DOC.20071009.0015

QA: QA

MDL-MGR-GS-000005 REV 02

September 2007

Dike/Drift Interactions

Prepared for:
U.S. Department of Energy
Office of Civilian Radioactive Waste Management
Office of Repository Development
1551 Hillshire Drive
Las Vegas, Nevada 89134-6321

Prepared by:
Sandia National Laboratories
OCRWM Lead Laboratory for Repository Systems
1180 Town Center Drive
Las Vegas, Nevada 89144

Under Contract Number
DE-AC04-94AL85000

DISCLAIMER

This report was prepared as an account of work sponsored by an agency of the United States Government. Neither the United States Government nor any agency thereof, nor any of their employees, nor any of their contractors, subcontractors or their employees, makes any warranty, express or implied, or assumes any legal liability or responsibility for the accuracy, completeness, or any third party's use or the results of such use of any information, apparatus, product, or process disclosed, or represents that its use would not infringe privately owned rights. Reference herein to any specific commercial product, process, or service by trade name, trademark, manufacturer, or otherwise, does not necessarily constitute or imply its endorsement, recommendation, or favoring by the United States Government or any agency thereof or its contractors or subcontractors. The views and opinions of authors expressed herein do not necessarily state or reflect those of the United States Government or any agency thereof.

QA: QA

Dike/Drift Interactions

MDL-MGR-GS-000005 REV 02

September 2007

ACKNOWLEDGMENTS

Supporting author was Branko Damjanac. Daniel Billaux, Douglas Alde, Stephen Nelson, and Patricia Bernot contributed to previous revisions.

INTENTIONALLY LEFT BLANK

Model Signature Page/Change History

Complete only applicable items.

1. Total Pages: 496

2. Type of Mathematical Model

☒ Process Model ☐ Abstraction Model ☐ System Model

Describe Intended Use of Model

3. Title

Dike/Drift Interactions

4. DI (including Revision No. and Addendum No.):

MDL-MGR-GS-000005 REV 02

	Printed Name	Signature	Date
5. Originator	Ed Gaffney		28Sep07
6. Independent Technical Reviewer for	Jean Younker		10/3/07
7. Checker	Dwayne Kicker		10/3/07
8. QCS/Lead Lab QA Reviewer	Sounia Kassabian-Darnell		10/03/07
9. Responsible Manager/Lead	Greg Valentine for		10/04/07
10. Responsible Manager	Tom Pfeifle for		10/4/07

11. Remarks

Change History

12. Revision No. and Addendum No.	13. Description of Change
00	Original issue
01	Documents new analyses for dike propagation and the "dog-leg" scenario, incorporates revised text for transparency and traceability, and incorporates relevant text (magma cooling, models) related to igneous activity postemplacement phenomena from *Igneous Intrusion Impacts to Waste Package and Waste Form*, REV 01 (MDL-EBS-GS-000002). This report is being archived and all relevant information will be contained in *Dike Drift Interactions* REV 01. This document is a complete revision and no change bars are provided.
02	Documents new analyses for dike propagation from depth including the effects of geologic structure and stratigraphy and the effects of topography, for the environment in the repository after intrusion including magmatic pressures after intrusion and magma chilling in backfilled drifts and for reaction between water and basalt; incorporates revised text for transparency and traceability; incorporates material originally presented in the *Magma Dynamics at Yucca Mountain, Nevada* analysis report (ANL-MGR-GS-000005 REV 00); eliminates discussion of gas flow between drifts and of chemical reaction between water and basalt that was included in *Dike*

	Drift Interactions REV 01; and provides additional validation for models. Condition Reports 5384, 5438, 5600, 6009, 6044, 6363, 8032, 8656 are addressed in this revision: CR-5384, -5438 and -6044 no longer apply to this document because it no longer models chemical reaction between basalt and seepage water; a simple literature review on natural analogue sites is provided instead in Section 6.6; CR-5600 by replacement and complete reconstruction of the DIRS report; CR-6009 by including discussion regarding the various values to approximate waste package diameter in different sections of the report; CR-6363 by discussion in Appendix A; CR-8032 deals with gas flow between drifts which is not included in Rev02; CR-8656 by revision of the output DTN listing in Table 8-1. This document is a complete revision and no change bars are provided.

CONTENTS

Page

CONTENTS (Continued)

Page

CONTENTS (Continued)

Page

CONTENTS (Continued)

Page

CONTENTS (Continued)

Page

CONTENTS (Continued)

Page

FIGURES

Page

FIGURES (Continued)

Page

FIGURES (Continued)

Page

FIGURES (Continued)

Page

FIGURES (Continued)

Page

FIGURES (Continued)

Page

FIGURES (Continued)

Page

FIGURES (Continued)

Page

FIGURES (Continued)

Page

INTENTIONALLY LEFT BLANK

TABLES

Page

TABLES (Continued)

Page

ACRONYMS AND ABBREVIATIONS

CWP	cold waste package
DIRS	Document Input Reference System
DTNs	data tracking numbers
EBS	Engineered Barrier System
EPRI	Electric Power Research Institute
ESF	Exploratory Study Facility
FEPs	features, events, and processes
GPa	gigapascal (10^9 pascals)
HWP	hot waste package
ICPRP	Igneous Consequences Peer Review Panel
IVRT	Independent Validation Review Team
J/(g·K)	joules divided by grams times Kelvin
kg	kilogram
kJ	kilojoule (10^3 joules)
kN	kiloNewtons (10^3 Newtons)
LEFM	linear-elastic fracture mechanics
m	meter
MPa	megapascal (10^6 pascals)
NRC	U.S. Nuclear Regulatory Commission
OCB	outer corrosion barrier
Pa·s	Pascal-second
PGV	peak ground velocity
ppmv	parts per million volume
RHH	repository host horizon
s	second
SSC	site-specific canister
THC	thermal-hydrological-chemical
Tptpln	Topopah Spring lower nonlithophysal unit
Tptpul	Topopah Spring upper lithophysal unit
TSPA	total system performance assessment
TSw1, TSw2	Topopah Spring thermo-mechanical units

ACRONYMS AND ABBREVIATIONS (Continued)

TWP	technical work plan
W/(m·K)	watts divided by the product of meters times Kelvin
wt %	weight percent (percent by weight)

1. PURPOSE

1.1 SCOPE OF WORK

This report presents and documents the model components and analyses that represent potential processes associated with propagation of a magma-filled crack (dike) migrating upward toward the surface, intersection of the dike with repository drifts, and the environment in the drifts after intrusion. The model components that describe upward migration of a dike and the intrusion of magma into the drifts are referred to as the dike intrusion submodel. The model components that deal with the environment in drifts after intrusion are referred to as the post-intrusion environment submodel. Collectively, these submodels comprise a conceptual model for dike/drift interaction. The model components and analyses of the dike/drift interaction conceptual model provide the technical basis for assessing the potential impacts of an igneous intrusion on repository performance, including those features, events, and processes (FEPs) related to dike/drift interaction (Section 6.1). Specifically, these processes are represented by the following model components and analyses:

- *Analysis of Natural and Induced Stresses* (Stress Analysis)—An evaluation of regional, local, and thermally induced stresses that may influence crack propagation (Section 6.2).

- *Dike Propagation Model*—A numerical model representing a dike tip propagating toward the surface and the properties of magma ascending within the crack, considering the influence of rock properties, natural and induced stresses, presence of a repository, and compressibility of magma (Section 6.3).

- *Post-Intrusion Environment Model*—A model of the conditions in the repository after drifts have been filled with magma. This includes a model of the thermal history as magma solidifies and cools to ambient temperature, as well as supplemental analyses of magma pressures after intrusion, magma interactions with waste packages and waste forms, and magma chilling in backfilled drifts (Section 6.4). It establishes the boundary conditions for assessing the potential for secondary dike propagation from within the repository and for the performance of the engineered barriers. It also provides limits on the transport of temperature effects from an intruded drift. The analysis of magma chilling in backfilled drifts (Section 6.4.8.4) supports the conclusion that backfill would be ineffective in stopping the flow of the low-viscosity magma from one drift to another.

- *Analysis of Secondary Dike Propagation* (secondary dike or dog-leg analysis)—An evaluation of the potential for a secondary dike (dog-leg) to propagate to the surface from within the repository after magma initially fills repository drifts (Section 6.5).

- *Analysis of Reaction Seepage Water with Basalt under Normal In-Drift Conditions*—This review of literature evaluates the chemical composition of waters in contact with basalt at natural analogue sites (Section 6.6).

The sequence and description of the processes listed above represent the general evolution of the processes that would occur if an igneous event were to occur at a repository at Yucca Mountain. Figure 1-1 is a schematic representation of the stages related to an igneous event. The first

two stages, "initial encounter" and "magma intrusion," are discussed in the dike propagation model and magma flow analysis, as is the potential for continued movement to the surface. The "eruption" stage addresses the movement to the surface and into the atmosphere. This movement to the surface is discussed in *Magma Dynamics at Yucca Mountain, Nevada* (BSC 2005 [DIRS 174070]), which also addresses multi-phase magma intrusion phenomena. The eruption into the atmosphere is addressed in *Atmospheric Dispersal and Deposition of Tephra from a Potential Volcanic Eruption at Yucca Mountain, Nevada* (SNL 2007 [DIRS 177431]). The environment after intrusion is captured in the discussions of the magma-cooling model. This last stage includes transport of volcanic heat through the rock separating individual drifts.

The overall concept represented in this report is that of a dike propagating toward the surface and intersecting the repository. If the rising magma encounters the repository drifts, it flows into and along the intersected repository drifts, filling them. This overall concept also takes into consideration the very unlikely scenario of pressurized magma filling the drift, then breaking out to the surface along a separate pathway. This scenario is referred to as a "dog-leg" event (magma rises along the dike, flows along the intersected drifts, and then rises to the surface forming a secondary dike).

The characteristics and properties of magma that are used as input to the analyses and models in this report are identified and described in *Characterize Eruptive Processes at Yucca Mountain, Nevada*, (SNL 2007 [DIRS 174260]). The consequences of the dike intersecting the repository drifts and magma flow into the drifts are addressed in *Number of Waste Packages Hit by Igneous Events* (SNL 2007 [DIRS 177432]).

The models and analyses presented in this report support the total system performance assessment (TSPA) igneous intrusion-groundwater transport model case, and the results presented in this report support FEP screening (DTN: MO0706SPAFEPLA.001 [DIRS 181613]) by providing a quantitative description of the FEPs that may result in dike/drift interactions. Elements of this report are also used as input to the update of the probabilistic volcanic hazard analysis of a future igneous event at Yucca Mountain. The relationship of the conclusions of this report to the acceptance criteria of the U.S. Nuclear Regulatory Commission (NRC) *Yucca Mountain Review Plan, Final Report* (NRC 2003 [DIRS 163274]) is discussed in Appendix A.

This report also provides a technical basis for addressing the NRC's related key technical issues and information needs, specifically IA [Igneous Activity] 2.18 (Kokajko 2005 [DIRS 174026]) and IA 2.20 (Kokajko 2005 [DIRS 182964]):

IA 2.18 *Development of secondary magma flow pathways for the duration of a potential igneous event.* The dike propagation model results in Section 6.3 indicate that pressures in a drift will rise over a period of several seconds to minutes after first intersection, preventing a strong shock from forming to propagate down the drift (Section 6.3.5). New material related to magmatic pressures following an intrusion, including a literature review, an analysis of potential magma pressure changing mechanisms, and a discussion of the likelihood that such late-time pressures might result in a secondary pathway, is provided in Section 6.4.8.1. A

thermal analysis of magma flow over backfill in Section 6.4.8.4 provides a basis for assessing how far magma would flow in backfilled main drifts.

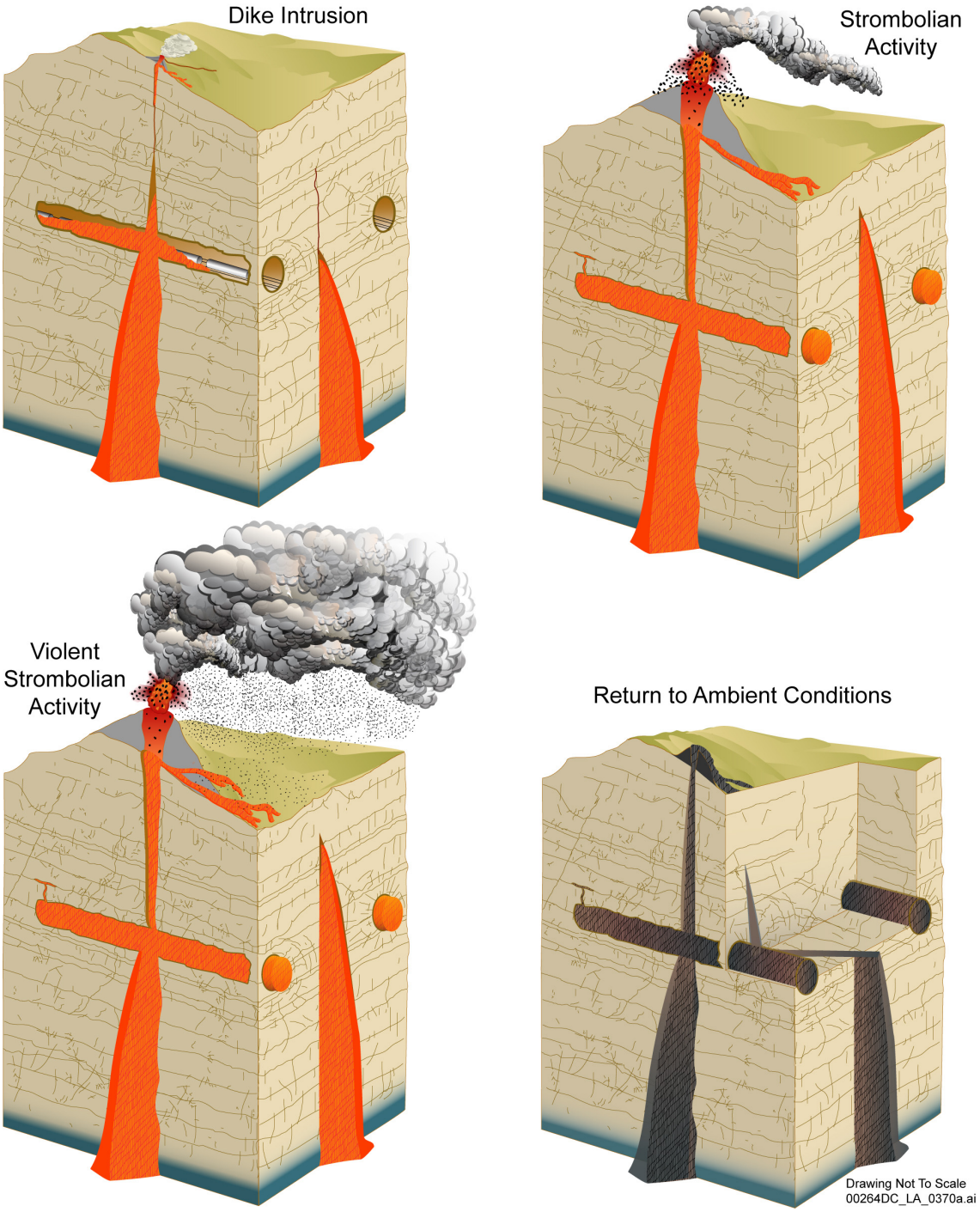

Source: For information purposes only.

Figure 1-1. Schematic Representation of the Stages of Interaction between a Volcanic Dike and Repository Drifts

IA 2.20 *Interaction between magma and waste forms.* New material from a literature search related to the reaction of corrosive volatile species with waste forms is provided in Section 6.4.8.3.3.

1.2 DIKE/DRIFT CONCEPTUAL MODEL

1.2.1 Dike Intrusion Submodel

The conceptual model of dike intrusion into the repository assumes that a dike originates at great depth (in the mantle or lower crust) and propagates upward due to the buoyancy of the magma relative to the rocks surrounding it. It is assumed that the composition of the magma in the dike is that of an alkali basalt with a few percent of water, which is dissolved in the silicate liquid at depth. As the dike approaches the surface, it encounters rocks less dense than basalt, but it retains buoyancy due to the exsolution of water vapor in the lower pressure environment of the upper several kilometers of the crust. This process is described in detail in *Characterize Eruptive Processes at Yucca Mountain, Nevada* (SNL 2007 [174260]).

The objective of the dike propagation modeling is to develop a representation of, and input conditions for, assessing the impacts of magma flow within a repository at Yucca Mountain, and to assess the interaction of the magma with the repository drifts, waste packages, and other engineered features. This objective is addressed with a deterministic approach that assumes an igneous event intersects the repository. Of particular importance are the:

- Phenomena that occur when the dike intersects the repository
- Pressure and temperature of the magma and characteristic behavior of the volatiles over time
- Width of the dike as a function of time, which relates to the rate of increase in the area of intersection and in the flow into a drift
- Effect of magma loss into the repository on the aforementioned items.

The dike-propagation model calculates the:

- Pressure conditions and dike parameters that would exist at the point of intersection with the repository, both at first encounter and over the duration of magma flow, which constrain an analysis of magma flow from the dike into a drift (Section 6.3.3)
- Effects of geologic structure and stratigraphy beneath the repository on dike propagation and the orientation of the dike trajectory (Section 6.3.4)
- Effects of topography and lateral variations of overburden stresses on dike intrusion into the repository (Section 6.3.5)

- Effects of compressibility of magma on dike propagation, which would alter the process of dike propagation (Section 6.3.6)

- Effects of in situ stress fields and thermally induced increased horizontal stresses at the repository level on development of the dike (Section 6.3.7).

The model provides support for determining boundary conditions related to dike propagation, including "leak-off" of magma into a drift. The model accommodates changing conditions to which the dike might react along a pathway, including the undisturbed area below the repository and the altered area around the repository, as well as conditions that would occur as the dike continues upward, after it has passed through the repository.

1.2.2 Post-Intrusion Submodel

The post-intrusion environment submodel addresses the environment that would result if magma were to fill an emplacement drift. The model describes the thermal conditions that would be expected for up to 100 years after magma entered an emplacement drift. Two-dimensional radial conductive cooling calculations at variable wall rock temperatures and aqueous wallrock saturations, as well as latent heat of crystallization effects, are considered. This thermal model component supports *Number of Waste Packages Hit by Igneous Events* (SNL 2007 [DIRS 177432]) by quantifying the thermal effect of a dike on nearby drifts. FEP 1.2.04.04.0A regarding this issue is listed in Table 6-1 and addressed in Section 6.4. It is supplemented by analyses that address:

- Pressures that could be generated if flow to the surface in the original dike were to be interrupted (Section 6.4.8.1)

- Interactions of magma with waste packages and waste forms (Section 6.4.8.3)

- Magma flow and cooling if drifts are backfilled (Section 6.4.8.4).

The secondary dike analyses address the phenomena that could result in a secondary dike originating from intruded emplacement drifts and propagating to the surface. The analyses address:

- The potential for the initiation of new fractures, or the dilation of existing joints around the drift, as a result of gradually pressurized magma within the drift (Section 6.5.1.2)

- Change in stresses adjacent to the repository due to the presence of the dike (Section 6.5.1.3)

- Effects of magma cooling on dike injection into cold rock (Section 6.5.1.4).

1.3 BACKGROUND

This version (Revision 02) of *Dike/Drift Interactions* enhances the technical basis for its technical outputs for use in other reports. It has been revised consistent with *Technical Work Plan for: Igneous Activity Analysis for Disruptive Events* (BSC 2006 [DIRS 178448]) for this activity.

1.3.1 Previous Reports

This report represents a major revision to information included in *Dike Propagation Near Drifts* (CRWMS M&O 2000 [DIRS 151552]). It significantly expands the numerical analytical support for the conceptual model of dike/drift interaction. Revision 01 of this report incorporated analyses and results from Revision 01 of *Igneous Intrusion Impacts on Waste Packages and Waste Forms* (BSC 2004 [DIRS 168960]). The magma-cooling model in Revision 01 of this report is incorporated into Revision 02 of this report. That model is augmented by new corroborative material to enhance confidence in the temperature results, which are unchanged. The model of basalt/seepage water chemical interaction that was included in Revision 01 is not contained in Revision 02; this effort is addressed in TSPA. Revision 02 of this report also incorporates material relating to development of and limitations to pressure in magma after intrusion that was originally presented in *Magma Dynamics at Yucca Mountain, Nevada* (BSC 2005 [DIRS 174070]). Revision 02 of this report does not include models of gas flow or of basalt/seepage water interaction that were included in Revision 01 (see Section 2).

Table 1-3 in Section 1.2.2.2 of the TWP (BSC 2006 [DIRS 178448]) lists activities that would lead to updating of this report. Those that are included in this report are:

- *Modify dike propagation model using FLAC3D to simulate effects of topography* (TWP, Section 2.2.2.2.2). This work is included in this report in Section 6.3.5.

- *Modify dike propagation model using UDEC code to simulate effects of preexisting faults, joints, and bedding structures on dike propagation* (TWP, Section 2.2.2.2.3). This work is included in this report in Section 6.3.4.

- *Revise magma cooling model to simulate magma cooling and drift conditions in the presence of the waste package and other EBS [Engineered Barrier System] components (e.g., backfill, invert), using FLAC3D* (TWP, Section 2.2.2.4.1). This work is included in this report in Section 6.4.7.2, but it is used to corroborate the previously provided output rather than to replace it.

- *Analyze interaction of magma with backfill in access drifts, using FLAC3D* (TWP, Section 2.2.2.4.2). This work is included in this report in Section 6.4.8.

- *Assess the effects of effusive magma flow on EBS, using FLAC or FLAC3D code* (TWP, Section 2.2.2.4.3). This work is included in this report in Section 6.4.8.3.3 and Appendix E.

1.3.2 Conceptual Model for Igneous Processes

Characterize Eruptive Processes at Yucca Mountain, Nevada (SNL 2007 [DIRS 174260]) provides a comprehensive discussion of the conceptual model for igneous activity at Yucca Mountain. The processes presented in this report are captured in the discussion of the igneous activity conceptual model.

An igneous event begins with ascent from a mantle source of magma as a dike (a magma-filled crack) that has a lower density than the surrounding rock. During magma ascent and decompression, which may be interrupted by temporary storage at intermediate levels, volatile gases such as H_2O and CO_2 exsolve and increase the volume of the magma. The resulting expansion drives the basaltic magma farther through the upper few kilometers of crust. Because volatiles may be concentrated near the crack tip of the ascending magma, the start of volcanism is frequently characterized by pyroclastic eruptions (volcanic explosions and aerial expulsion of clastic rock from a volcanic vent) of gas-rich magma. Based on analogue studies, the concentration of volatile species in basalts of the Yucca Mountain region is likely to range from 1 wt % to 4 wt %. This range is higher than in most alkali (sodium/potassium-rich) basalt magmas, possibly because the volatile species originated from smaller percentages of the partial melt of a hydrous lithospheric mantle source. The nature of these alkali basalts, which are enriched with incompatible elements (i.e., elements that more readily accumulate in mafic igneous melts), relative to other alkali basalts in the western United States is consistent with these values (SNL 2007 [DIRS 174260], pp. 6-11 to 6-12).

Basaltic magma is transported from a region of melting in the earth's mantle to the earth's surface through dikes. In the Yucca Mountain region, dikes are typically 1 m to 12 m wide (SNL 2007 [DIRS 174260], p. 6-19). The longest expected dike length in the Yucca Mountain region is less than 8 km and the recommended mean length is 2 km (SNL 2007 [DIRS 174260], p. 6-22). Based on the regional stress field of the upper crust and the effects of shallow crustal structures, dikes are expected to have orientations at the repository level that center on north, although other orientations, especially toward the northeast, are possible and are observed within the region (SNL 2007 [DIRS 174260], p. 6-22).

Although an ascending dike could be influenced by underlying geologic structure or by topographic and/or thermal-mechanical induced stress, the conceptual model described here indicates that the dike propagates through the repository; these conclusions are justified in Sections 6.3.4, 6.35, and 6.3.7, respectively. As the dike approaches the level of the drifts, the crack tip advances ahead of the magma front. When the magma within the dike reaches the level of the repository, magma will be available to flow into drifts. The flow regimes for basaltic magma can be homogeneous flow with small bubbles moving with the melt, bubbly flow with bubbles rising faster than the melt, or slug flow with bubble sizes approaching the width of the dike. Which flow regime is operative will be a function of many variables including but not limited to moisture content, other gases present, pressure, melt viscosity, and surface tension. For example, as the magma first encounters a drift, it may do so under slug flow; as time progresses and the magma front continues up the dike, flow entering the drift may become bubbly. For any of these flow regimes, the dike tip will precede the magma by several seconds to a few hours. Because the entry of magma from the dike into the drift is not necessarily instantaneous with intersection, it is unlikely that dike intersection will result in an abrupt

explosion into the drift. At the analogue Parícutin volcano, a new volcano in central Mexico, the initial crack broke the surface several hours before the first manifestation of weak pyroclastic eruptions began (Section 7.3.1.1.1).

The most likely scenario following dike intersection of repository drifts is that the dike continues to follow the path established by the dike tip and erupts to the surface without being deflected by the presence of the repository. An alternative, but unlikely, scenario is that the lateral diversion of magma into drifts results in sufficient pressurization of drifts to propagate a dike to the surface at a location some distance from the site of the initial dike intersection. This alternative scenario could potentially lead to more waste entrained during an eruption compared to the case of conduits developed only above the site of initial dike intersection. This is considered unlikely to occur because the model in Section 6.3 demonstrates that the cross-sectional area of contact between the dike and a drift will increase gradually over a period of several seconds or even minutes, precluding development of a strong shock propagating down the drift. The amount of waste potentially entrained in this scenario would depend on the length of drifts that transport magma to the site of the down-drift dike.

The rate and degree to which an intersected drift fills with magma depends on variables such as magma rise rate, magma viscosity, and the nature (effusive or pyroclastic) of the flow into the drifts. Magma rise rates between 1 m s^{-1} and 15 m s^{-1} are investigated, while viscosities range between 10 Pa·s and 40 Pa·s as presented in *Characterize Eruptive Processes at Yucca Mountain, Nevada* (SNL 2007 [DIRS 174260]).

1.4 LIMITATIONS OF MODELS AND ANALYSES

This section addresses the limitations of the model components and analyses that support the overall dike/drift interaction conceptual model.

1.4.1 Analysis of Natural and Thermal Stresses

The analysis of natural and thermal stresses in Section 6.2 considers that all material is linear elastic, except that two cohesionless Coulomb slip interfaces are used to represent the Ghost Dance and Solitario Canyon faults. Anelastic effects, which are likely to exist in the area, are not considered. The exclusion of anelastic effects has a very limited impact because the gravitational stresses are statically determined and, therefore, are correctly computed, and because the analyses of horizontal stresses are calibrated using field measurements.

1.4.2 Dike Propagation Model

The ultimate limit of the dike-propagation model is that dikes observed in the Yucca Mountain region were emplaced more than 100,000 years ago; therefore the process of emplacement was not observed. Dike propagation at other sites has been used to address the uncertainty of results in two ways. First, *Characterize Eruptive Processes at Yucca Mountain, Nevada* (SNL 2007 [DIRS 174260], Section 6.3.3, pp. 6-16 to 6-22) considered dike propagation as determined by field observation of Plio-Pleistocene volcanic centers in the Yucca Mountain region and in western North America. This analysis has been used to bound the inputs of the present dike propagation model. Second, field observations, laboratory studies, and analyses of rocks from

the 1943 eruption of Parícutin volcano (in west-central Mexico), which was observed from the first minutes of a crack opening at the surface in a plowed field, provide a unique insight into the processes that accompany dike intrusion and eruption at the surface. Taking into account the differences in geologic setting and magma characteristics between Parícutin and a hypothetical Yucca Mountain event, these insights have been applied to validate the results of the dike propagation model (Section 7.3.1.1.1).

A principal limitation of the dike propagation model is that it addresses the growth of a dike due to upward movement of an incompressible magma, whereas magma is expected to have varying degrees of compressibility (SNL 2007 [DIRS 174260], pp. 6-29 to 6-35). The effect of compressibility was addressed in *Final Report of the Igneous Consequences Peer Review Panel* (Detournay et al. 2003 [DIRS 169660], pp. 44 to 45), which concluded that the two significant differences resulting from compressibility are "…the substantial increase in the flow velocity at the magma front and the amount by which this exceeds the velocity of the magma front. Both effects increase the gas flux into the cavity relative to the flux out." They conclude that at "…cavity pressures below the dike normal stress (lower by an amount that exceeds the dike excess pressure, so perhaps a few MPa), the tip becomes unstable." Hence, the effect of compressibility would be to increase the tendency for the dike tip to accelerate as it approaches the ground surface. This will increase the likelihood that the crack tip will break through the surface before any magma reaches repository depth.

The uncertainty due to effects of magma compressibility is approximated in Section 6.3.6. That section applies an analysis using results for incompressible magmas of progressively lower densities at progressively decreasing depths to simulate some aspects of the behavior that would be expected for compressible magma that expanded and accelerated in a continuous manner as it approached the surface and the confining pressure dropped.

Another limitation of the dike propagation model is that viscous behavior of magma flowing in the dike is simplified. As noted in Section 1.3.2, any of three types of flow, homogenous, bubbly or slug, may occur in a dike when it approaches the surface. The approach taken in the dike propagation model is to use mathematical expressions that are based on Newtonian viscosity, with the value of the viscosity selected to be appropriate for the expected alkali basaltic magma flow regime. In some instances, results are presented for multiple viscosity values when it is desirable to highlight the effects of uncertainty in viscosity.

A number of other limitations are embedded in the model, including that the host rock behaves elastically and linearly and is a homogeneous, isotropic material and that the dike is a single fracture and the free surface is horizontal. The effect of these limitations is discussed in Section 6.3.2, where it is shown to be insignificant. For some of these limitations, further analysis is used to calculate the magnitude of the effect (e.g., topography for which the free surface is not horizontal is discussed in Section 6.3.5).

1.4.3 Analysis of Magma Flow

The limitations of the analysis of magma flow into drifts are, for the most part, the same as the ones for magma propagation from depth. An important analysis limitation is that the model treats the magma as a single incompressible phase (Section 1.4.2). The processes and effects

associated with expansion of bubbly or pyroclastic flow into a drift were not modeled. Therefore, the interaction between compressible-phase (pyroclastic) magma and the drifts, and between the pyroclastic-phase magma and repository components, has not been evaluated. Two-phase pyroclastic flow is addressed in *Magma Dynamics at Yucca Mountain, Nevada* (BSC 2005 [DIRS 174070]). However, the analysis of single-phase flow demonstrates that the drifts fill with magma within minutes and that all the waste packages contained in the intersected drifts will be engulfed in the magma (Sections 6.3.3.5.6 and 6.3.3.5.7). Therefore, the analysis of single-phase flow bounds the impacts to the waste package and waste form.

The analysis used to quantify the interaction of magma intrusion with waste packages in Section 6.4.8.3 is limited in its use of a constant viscosity, whereas the viscosity of silicate liquids increases rapidly with falling temperatures. This will result in overestimating the rate of magma intrusion into breached waste packages. An uncertainty exists with the alteration of waste forms, both glass and spent fuel, by interaction with magma. Little or no direct information on waste form–magma interactions is available. This uncertainty in possible phase changes results in a range of secondary oxide and silicate phases, as discussed in Section 6.4.8.3.3.

The analysis of the movement of waste packages by magma front pressure (Section 6.4.8.3.2) is limited by lack of a well-defined relationship between magma density and magma viscosity for highly vesiculated (50% to 75% vapor) and fragmented (more than 75% vapor by volume) pyroclastic-phase magma. This results in an increased level of uncertainty in the possible movement of waste packages.

1.4.4 Secondary Dike Analysis

A limitation of the secondary dike analyses is similar to those of the magma flow analyses. These analyses treat the magma flowing through a secondary crack as though it were a single incompressible phase, whereas sustained multiphase, pyroclastic-type flow may occur at some time during an igneous event. Pyroclastic flow is addressed in *Magma Dynamics at Yucca Mountain, Nevada* (BSC 2005 [DIRS 174070]). Nevertheless, the uncertainty in the consequences of a secondary dike propagating to the surface and distributing radioactive waste on the surface of the earth is captured within the distribution of the number of waste packages hit in a volcanic eruption through the repository (SNL 2007 [DIRS 177432], Section 8).

1.4.5 Basalt Cooling and Solidification Model

Cooling calculations are limited by parameter uncertainty representing the thermal diffusivity of basalt and host rock, as well as changes in this parameter as a function of temperature. Cooling calculations are also limited by the manner in which they represent and implement the latent heat of crystallization. However, validation studies documented in Section 7.3.2 indicate that these limitations are of little consequence to model predictions.

2. QUALITY ASSURANCE

Development of this report and supporting analyses are subject to *Quality Assurance Requirements Document* (QARD) (DOE 2007 [DIRS 182051]). This report was prepared under SCI-PRO-006, *Models*. The revision to this scientific model report is conducted in accordance with *Technical Work Plan: Igneous Activity Assessment for Disruptive Events* (BSC 2006 [DIRS 178448], Sections 1.2.2, 2.2.2, and 2.6). As review of this report was being completed, the technical work plan was revised (SNL 2007 [DIRS 182219]; the revision does not affect any of the discussion in this report. The following deviations have been made from the work scope as described in the technical work plan (TWP) (BSC 2006 [DIRS 178448]):

- *Qualify and implement EMSA code to dike propagation model to account for compressibility of magma and variations of stress with depth* (TWP, Section 2.2.2.2.1). This has not been accomplished, so no analyses using EMSA are contained in this report. There is no significant impact on model output or feeds to TSPA associated with not including these analyses because they were intended for corroboration only. Magma compressibility is addressed in Section 6.3.6 and variations of stress with depth in Section 6.3.7.

- *Address effects of repository thermal stresses on dike propagation* (TWP, Section 2.2.2.2.1). This work was to have used the EMSA code but has not done so, so it is not included in this report. There is no significant impact on model output or feeds to TSPA associated with not including these analyses because they were intended for corroboration only. The effects of repository thermal stresses on dike propagation are addressed in Section 6.3.7.

- *Analyze for potential development of secondary pathways (such as dog-leg dike); incorporate effects of wider range of pressure* (TWP, Section 2.2.2.2.3). This work was not completed before this report was finalized, so it is not included in this report. There is no significant impact on model output or feeds to TSPA based on the existing analyses to assess the possibility of a secondary dike propagation presented in Section 6.5.1.2.

- *Assess the effects of pyroclastic magma flow on EBS* (TWP, Section 2.2.2.4.3). This work was not undertaken before this report was finalized, so it is not included in this report. There is no significant impact on model output or feeds to TSPA because all waste packages are assumed to be compromised during an intrusive igneous event.

- *Assess the consequences of combined seismic and igneous events* (TWP, Section 2.2.2.4.4). This work was planned to assess the long-term function of bulkheads to block magma flow, but bulkheads were eliminated from the design, so the work was not done and is not reported in this report. Because bulkheads were eliminated from the design, there is no impact on the model or on feeds to TSPA.

- *Implement gas flow model to simulate migration of volatiles in gap between host rock and backfill, including migration into host rock and backfill* (TWP, Section 2.2.2.5). This work is not included in this revision because of the qualification status of the

TOUGHREACT code. Furthermore, all drifts are considered to be completely filled with magma if one drift is intersected, so there is no need to address migration of gases from intruded drifts to unintruded ones.

– *Review literature for basalt water chemistry and simulate the chemical effect of flow of water through cooled basalt using TOUGHREACT code* (TWP, (BSC 2006 [DIRS 178448]) Section 2.2.2.6). The literature review is included in this report in Section 6.7. The simulation is not included in this revision because of the qualification status of the TOUGHREACT and EQ3/6 codes. There is no significant impact on model output or feeds to TSPA because the chemical effect of water flowing through cooled basalt is addressed in *In-Package Chemistry Abstraction* (SNL 2007 [DIRS 180506]).

Table 2-3 in Section 2.6 of the TWP provides a listing of the models that will be documented in this report. The levels of confidence were assigned per the requirements of LP-2.29Q, *Planning for Science Activities,* which was in effect at the time that the TWP was approved. The levels of confidence for model validation activities performed under SCI-PRO-006, *Models*, are defined in SCI-PRO-002, *Planning for Science Activities*, and differ from those referenced in the TWP, (BSC 2006 [DIRS 178448]). The Level II confidence level in SCI-PRO-002 carries the equivalent requirements of the Level III confidence level described in LP-2.29Q. The Level I confidence level described in SCI-PRO-002 now incorporates both of the confidence levels (Levels I and II) found in LP-2.29Q.

An update to Table 2-3 of the TWP (BSC 2006 [DIRS 178448]) describing the model validation activities and related confidence levels that are documented in this report is provided in Table 2-1. Column 6 of Table 2-1 has been modified to reflect validation activities actually included in this report. Items that are not included in this report have been described in the bullets of the third paragraph of Section 2.

Table 2-1. Summary of Model Activities

Title	Model	Level of Confidence	Previously Validated?	Additional Validation Planned?	Additional Confidence Building Planned?
INTRUSIVE MODELING CASE					
Dike/Drift Interactions	Drift-Scale Gas Flow Model	II	Yes	No	Not included in this report.
	Dike Propagation from Depth Model	II	Yes	No	Base case for dike propagation from depth. Additional physical processes will be added to the current model as submodels.
	Submodel for Topography	I	No	Yes Section 2.6.4.2.1	The base case depicts a flat ground surface. The new submodel will add variable topography to represent the ground surface.

Table 2-1. Summary of Model Activities (Continued)

Title	Model	Level of Confidence	Previously Validated?	Additional Validation Planned?	Additional Confidence Building Planned?
INTRUSIVE MODELING CASE					
	Submodel for Structure Effects	I	No	Yes Section 2.6.4.2.1	New submodel to evaluate influence of geologic structure and stratigraphy on dike propagation from depth.
	Submodel for compressible magma	I	No	Yes Section 2.6.4.2.1	Not included in this report.
	Chemistry of Basalt/Water Seepage Model	II	No	Yes Section 2.6.4.2.2	Not included in this report.
	Basalt Cooling and Solidification Model	II	Yes	Yes Section 2.6.4.2.3	A new, higher-fidelity cooling analysis has been developed and used to validate the current models.

Source: *Technical Work Plan: Igneous Activity Assessment for Disruptive Events* (BSC 2006 [DIRS 178448], Table 2-3).

NOTE: Sections referred to in column 5 are sections in the TWP.
The last two rows in Table 2-1 are accurate transcriptions of the table in the TWP. However, the TWP table is erroneous in that the chemistry of basalt/water seepage model is Section 2.6.4.2.3 of the TWP, not Section 2.6.4.2.2 as listed in the table. The basalt cooling and solidification model is in Section 2.6.4.2.2 of the TWP instead of Section 2.6.4.2.3.

Table A-1 of the TWP lists *Yucca Mountain Review Plan, Final Report* (NRC 2003 [DIRS 163274]) acceptance criteria addressed in analysis reports or model reports. Item 4:(1)(c) states, "Where sufficient data do not exist, the definition of parameter values and conceptual models is based on appropriate use of other sources, such as expert elicitation conducted in accordance with appropriate guidance," but the box for this report is not checked. However, as stated in Section 7.2.1, parameter values developed by the Igneous Consequence Peer Review panel (a group of experts chosen for their expertise in fracture mechanics, dike propagation, magma properties, flow dynamics, and igneous processes) were used during model development of many of the models in this report to increase confidence.

In addition, the electronic management of data was accomplished in accordance with the controls specified in the TWP and IM-PRO-002, *Control of the Electronic Management of Information*. Unqualified inputs from external sources are justified for intended use in Appendix B per the requirements of SCI-PRO-006. The justification of external sources has been planned, using criteria that represent a subset of the methods and attributes required for qualification of data per SCI-PRO-001. These plans are included in Appendix B.

INTENTIONALLY LEFT BLANK

3. USE OF SOFTWARE

3.1 SOFTWARE TRACKED BY CONFIGURATION MANAGEMENT

The computer codes used directly in this modeling activity are summarized in Table 3-1. All software except exempt software (see Section 3.2) was fully qualified. All software was obtained from Configuration Management and is appropriate for the application. Qualified codes were used only within the range of validation, and have no limitations on their output within their intended use. All software except exempt software was fully qualified and was obtained from software Configuration Management per SCI-PRO-006.

FLAC3D V. 2.14 (STN: 10502-2.14-00 [DIRS 172323]) was used for the corroborative calculations reported in Appendix C. This software was obtained from Configuration Management and is appropriate for the application. This qualified code was used only within the range of validation and has no limitations on the output when used within its intended use.

FLAC V. 4.0 (STN: 10167-4.0-00 [DIRS 161953]) was used for the corroborative calculations reported in Appendix E. This software was obtained from Configuration Management and is appropriate for the application. This qualified code was used only within the range of validation and has no limitations on the output when used within its intended use.

Table 3-1. Computer Software

Software Title and Version (V)	Software Tracking Number	Code Usage	Computer Type Platform
NPHF2D V. 1.0 (DIRS 163665])	10904-1.0-00	Dike Propagation Model; performs numerical modeling supporting analysis of magmatic dike propagation and analysis of the dike/drift interaction where magma enters a drift, modified and requalified for this task. This code was developed specifically for fracture propagation to the surface; no other code can evaluate the number of physical phenomena required.	PC; Windows 2000/NT4.0
FLAC V. 4.0 [DIRS 161953]	10167-4.0-00	This is commercially available software that is used for a very broad range of geomechanical problems including hydraulic, mechanical, and thermal coupling.	PC; Windows 2000/NT 4.0
FLAC V. 4.04 [DIRS 172432]	10167-4.04-00	This is commercially available software that is used for a very broad range of geomechanical problems including hydraulic, mechanical, and thermal coupling. It is the same software as V. 4.0 but is also validated for fluid flow and coupled hydro-mechanical analyses.	PC; Windows 2000/NT 4.0
FLAC3D V. 2.1 (BSC 2002 [DIRS 161947])	10502-2.1-00	This is commercially available software that is used for a very broad range of geomechanical problems including hydraulic, mechanical, and thermal coupling. It is the preferred code for analyzing regional stresses, accounting for topography; and opening preexisting fractures by magma.	PC; Windows 2000/NT 4.0
FLAC3D V. 2.14 (BSC 2004 [DIRS 172323])	10502-2.14-00	This is commercially available software that is used for a very broad range of geomechanical problems including hydraulic, mechanical, and thermal coupling. It is the same software as V. 2.1 but is also validated for fluid flow and coupled hydro-mechanical analyses.	PC; Windows 2000

Table 3-1. Computer Software (Continued)

Software Title and Version (V)	Software Tracking Number	Code Usage	Computer Type Platform
UDEC V. 3.1 (BSC 2002 [DIRS 161949])	10173-3.1-00	Analyzes opening of preexisting fractures by magma. This was the only code available for hydromechanic behavior of fracture media.	PC; Windows 2000/NT 4.0
UDEC V. 3.14 (BSC 2004 [DIRS 172322])	10173-3.14-00	Analyzes opening of preexisting fractures by magma. Same software as V. 3.1, but also validated for fluid flow and coupled hydro-mechanical analyses .	PC; Windows 2000

3.2 EXEMPT SOFTWARE

Microsoft Excel, exempt as defined in IM-PRO-003, *Software Management*, was used in the cooling calculations described in Appendices C and D and in preparation of graphs and tables. The formulas used and their sources are described in those appendices, and the inputs and outputs are defined in the spreadsheets listed in Appendix G (for the calculations in Appendix C) or in the spreadsheet in output DTN: LA0307EG831811.001 (for Appendix D). No other software was used in the preparation of this document except for word-processing purposes.

Standard, built-in functions of Microsoft Excel 2000 for the Dell Inspiron 8000 and Dell Optiplex computers, Microsoft Excel for the Dell Inspiron 300m, or Microsoft Excel 97 for the Compaq V900 computer were used to calculate some parameters. Excel is used to support calculations in Sections 6.2, 6.3, 6.4, 6.5, 6.6, and 7.3. Some Microsoft Excel charts were converted to *.jpg* files using Microsoft PowerPoint 2003 on a Dell Inspiron 300m. Many "hand" calculations were confirmed using Microsoft Calculator V. 5.1 on a Dell Inspiron 300m. Also, Mathematica V. 4.2.0.0 is used for the three-dimensional magma flow calculation in Section 6.4. This software is exempt from the software validation requirements contained in IM-PRO-003. The formulas, inputs and outputs of those formulas, and additional information required for an independent technically qualified person to verify the results of analyses using exempt software are provided in Section 6 and in the data tracking numbers (DTNs) listed in Table 8-1.

3.3 USE OF UNQUALIFIED SOFTWARE

Two baselined software codes were used outside their validation range to develop preliminary output from this model report: FLAC3D V. 2.1 (STN: 10502-2.1-00 [DIRS 161947]) and UDEC V. 3.1 (STN: 10173-3.1-00 [DIRS 161949]). These software codes have subsequently been validated for the intended use and limitations as UDEC V. 3.14 (STN: 10173-3.14-00 [DIRS 172322]) and FLAC3D V. 2.14 (STN: 10502-2.14-00 [DIRS 172323]), as discussed in Table 3.1. All products from this report have been rerun, if originally unvalidated, after validation was complete.

All of the analyses that produced the preliminary output were rerun using the qualified software versions listed in Table 3.1. Comparisons of the output data were made, and the results were found to be nearly identical. The evaluation identified two files with minor differences (less than 1%) in the resulting output. The apparent reason for the differences was determined to be the result of interruptions during the running of the code in the preliminary runs. Per the requirements of SCI-PRO-006, the DTNs containing the preliminary output have been superseded with the output from the qualified software.

INTENTIONALLY LEFT BLANK

4. INPUTS

4.1 DATA, PARAMETERS, AND OTHER MODEL INPUTS

This subsection identifies all input parameters and other forms of model inputs that are used in the analyses detailed in this report.

Input information used in this report comes from several sources, which are summarized in Table 4-1. The data are fully appropriate for the discussion of dike/drift interactions in this report. The qualification status of the input sources is provided in the Document Input Reference System [DIRS] and documented in the Technical Data Management System for DTNs. The status of the input information quality may be confirmed by review of the DIRS database. The data from external sources have been qualified per the requirements of SCI-PRO-006 and are considered to be qualified for intended use. These qualifications are documented in Appendix B.

Data used to develop the model are not used to validate the model, per the requirements of SCI-PRO-006.

4.1.1 Data and Parameters

The input parameters for this report are listed in Table 4-1. Direct inputs from nonproject sources are qualified in Appendix B.

In many cases where a single value is given for a parameter, the value has been selected as a single value that is within the range of values in the cited document. Where the results of the input are not sensitive to the exact value of the input parameter, values may have been rounded while staying in the appropriate range. The parameters are discussed in Section 6 (as noted in Table 4-1, column 4).

The use of the values of density and specific heat of water are justified as established fact on the basis of the fact that their source is a standard textbook in thermodynamics. Other external sources are qualified for their use in this report in Appendix B. The other parameters are justified by having been generated under Yucca Mountain Project quality assurance standards. The values listed in Tables 4-1 and C-2 for rock-heat capacity are uniformly higher than the values in the listed source by 1 J kg^{-1} K^{-1}; the effect of this difference will be on the order of 0.1% in the temperatures listed in Table 4-1, or less than 1°C and within the expected precision of the table.

There are no direct inputs for the TSPA Igneous EBS Failure Fraction parameters because they are assumed to be 1. Inputs for corroboration in Appendices D and E are indirect input.

Table 4-1. Direct Input Parameters Used in Development of Models of Dike/Drift Interactions

Input Parameter	Value	Source	Where Discussed
Young's Modulus of Host Rock	15 GPa	Detournay et al. 2003 [DIRS 169660], Table 1-2	Sections 6.3.3, 6.3.4.4, and 6.3.7.3
Poisson's Ratio of Host Rock	0.21	Detournay et al. 2003 [DIRS 169660], Table 1-2	Sections 6.3.3 and 6.3.4.4

Table 4-1. Direct Input Parameters Used in Development of Models of Dike/Drift Interactions (Continued)

Input Parameter	Value	Source	Where Discussed
Toughness of Host Rock	0.3 MPa $m^{1/2}$	Detournay et al. 2003 [DIRS 169660], Table 1-2	Sections 6.3.3 and 6.3.4.4
Magma Density	751 kg m^{-3} to 2,282 kg m^{-3}	Detournay et al. 2003 [DIRS 169660], Table 1-2	Sections 6.3.3 and 6.3.7.3
Magma Viscosity	10 Pa·s to 40 Pa·s	Detournay et al. 2003 [DIRS 169660], Table 1-2	Sections 6.3.3 and 6.3.7.3
Density of Host Rock	2,400 kg m^{-3}	DTN: SNL02030193001.027 [DIRS 108410]	Section 6.3.3.3; Tables 6-2, 6-5, and 6-12
Magma Thermal Diffusivity	$0.1x10^{-6}$ m^2s^{-1} to 1×10^{-6} m^2s^{-1}	Detournay et al. 2003 [DIRS 169660], Table 1-2	Section 6.5.1.1.2; App. D Tables 6-33, D-1
Magma Rise Velocity	Various	Detournay et al. 2003 [DIRS 169660], p. 56	Section 6.3.3.5.6; Table 6-5
Input Parameters for Thermal Calculations	Various	DTN: LA0612DK831811.001 [DIRS 179987]	Table 6-34
Intrusion Temperature; Crystal-free Viscosity	Various	DTN: LA0612DK831811.001 [DIRS 179987]	Section 6.5.1.1.2, App. C, Section C1
Gravitational Constant	9.81 m s^{-2}	Incropera and De Witt 2002 [DIRS 163337]	Tables 6-2 and 6-5
Horizontal stresses in hole ESF-AOD-HFDR#1	2.9, 1.7, MPa	DTN: SNF37100195002.001 [DIRS 131356]	Sections 6.2.2, 6.3.3.3, and 6.3.3.4.1; Table 6-2
Density of rock units Tpcpv2, Tpcpv1, Tpbbt4, Tpy, Tpbt3, Tpp, Tpbt2, Tptrv3, Tptrv2, Tptrv1, Tptm, Tptrl, Tptpul, Tptpmn, Tptpll	1460, 1460, 1460, 1460, 1460, 1460, 1460, 1460, 1460, 2310, 2190, 2190, 1834, 2148, 1979, kg m^{-3}	DTN: MO0408MWDDDMIO.002 [DIRS 171483], file *Calculation Files\Material property\thermal properties TM units v2.xls,* tab "Conductivity and Density"	Section 6.3.3.3
Thickness of rock units Tpcpv2, Tpcpv1, Tpbbt4, Tpy, Tpbt3, Tpp, Tpbt2, Tptrv3, Tptrv2, Tptrv1, Tptm, Tptrl, Tptpul, Tptpmn, Tptpll	4.9, 4.2, 1.4, 10.4, 4.3, 20.8, 8.2, 2.8, 0.8, 1.0, 54.4, 9.1, 74.8, 36.8, 102.6, m	DTN: MO0408MWDDDMIO.002 [DIRS 171483], file *EarthVision Inputs & Outputs\Borehole_ESF -AOD-HFDR#1\results.xls*	Section 6.3.3.3
Elevation at surface	1285.1 m	DTN: MO0408MWDDDMIO.002 [DIRS 171483], file *EarthVision Inputs & Outputs\Borehole_ESF –AOD-HFDR#1\results.xls*	Section 6.3.3.3
Thermal Stresses Induced by Radioactive Decay of Waste	Various	DTN: MO0407SPAMTSHR.000 [DIRS 170679]	Figures 6-4, 6-5, and 6-6
Bulk Dry Rock Mass Thermal Conductivity	1.18 W m^{-1} K^{-1} to 1.49 W m^{-1} K^{-1}	DTN: SN0404T0503102.011 [DIRS 169129], file *ReadMe_Summery.doc*, Table 7-10	Table 6-28 and Appendix C, Table C-2

Table 4-1. Direct Input Parameters Used in Development of Models of Dike/Drift Interactions (Continued)

Input Parameter	Value	Source	Where Discussed
Bulk Wet Rock Mass Thermal Conductivity	1.77 W m^{-1} K^{-1} to 2.13 W m^{-1} K^{-1}	DTN: SN0404T0503102.011 [DIRS 169129], file *ReadMe_Summery.doc*, Table 7-10	Appendix C, Table C-2
Matrix Porosity	0.11 to 0.17	DTN: SN0404T0503102.011 [DIRS 169129], file *ReadMe_Summery.doc*, Table 7-10	Appendix C, Table C-2
Lithophysal Porosity	0.03 to 0.12	DTN: SN0404T0503102.011 [DIRS 169129], file *ReadMe_Summery.doc*, Table 7-10	Appendix C, Table C-2
Dry Bulk Density	1,830 kg m^{-3} to 2,210 kg m^{-3}	DTN: SN0404T0503102.011 [DIRS 169129], file *ReadMe_Summery.doc*, Table 7-10	Table 6-28 and Appendix C, Table C-2
Specific Heat Capacity of Solids	932 J kg^{-1} K^{-1} to 934 J kg^{-1} K^{-1}	DTN: SN0307T0510902.003 [DIRS 164196], file *rock_grain_heat_capacity (edited).xls*, tab: "Cp grain 25-325," cells X8:X11.	Appendix C, Table C-2
Heat Capacity of Rock	985 Jkg^{-1} K^{-1}	DTN: SN0402T0503102.010 [DIRS 170993], Section 6.8.4	Section 6.4.8.4.2; Table 6-28
Density of Water	982.3 kg m^{-3}	Incropera and DeWitt 2002 [DIRS 163337], Table A.6, p. 924	Appendix C, Section C1.3
Specific Heat of Water	4,186 J kg^{-1} K^{-1}	Incropera and DeWitt 2002 [DIRS 163337], Table A.6, p. 924	Appendix C, Section C1.3
Crystallization Sequence for Alkali Basalt	Nonnumeric	Detournay et al. 2003 [DIRS 169660], Appendix Table 2E	Section 6.4.8.1.3.1
Material Properties for Scoria	Various	Duncan et al. 1980 [DIRS 161776]	Table 6-26
Material Properties for Basalt	Various	Gupta & Seshagiri Rao 2000 [DIRS 174063], Tables 2 and 3	Section 6.4.8.1.3.3; Table 6-26
Friction Angle for Basalt	50°	Hoek and Brown 1997 [DIRS 170501], Fig. 8	Table 6-26
Magma Thermal Conductivity	0.6 W $m^{-1}K^{-1}$	Detournay et al. 2003, [DIRS 169660], Table 1-2	Section 6.4.8.4.2; Table 6-28
Coefficient of Thermal Expansion of TCw-PTn Unit in Regional Thermo-mechanical Analysis	4.46 × 10^{-6} K^{-1}	DTN: MO0408MWDDDMIO.002 [DIRS 171483], file *Calculation Files\Material property\thermal properties TM units v2.xls,* tab "Thermal Expansion"	Section 6.2.1

Table 4-1. Direct Input Parameters Used in Development of Models of Dike/Drift Interactions (Continued)

Input Parameter	Value	Source	Where Discussed
Thermal Conductivity of TSw1 Unit in Regional Thermo-mechanical Analysis	T <100°C, 1.77 W m^{-1} K^{-1} T ≥ 100°C, 1.22 W m^{-1} K^{-1}	DTN: MO0408MWDDDMIO.002 [DIRS 171483], file *Calculation Files\Material property\thermal properties TM units v2.xls,* tab "Conductivity and Density"	Section 6.2.1
Coefficient of Thermal Expansion of TSw1 Unit in Regional Thermo-mechanical Analysis	6.56×10^{-6} K^{-1}	DTN: MO0408MWDDDMIO.002 [DIRS 171483], file *Calculation Files\Material property\thermal properties TM units v2.xls,* tab "Thermal Expansion"	Section 6.2.1
Young's Modulus of TSw2-TSw3 Unit in Regional Thermo-mechanical Analysis	15.84 GPa	DTN: MO0408MWDDDMIO.002 [DIRS 171483] file *Calculation Files\Material property\rock mass strength v2.xls,* tab "Summary Data" Category 3	Section 6.2.1
Specific Heat of TSw2-TSw3 Unit in Regional Thermo-mechanical Analysis	T ≥ 114°C, 990 J kg^{-1} K^{-1}	DTN: MO0408MWDDDMIO.002 [DIRS 171483], file *Calculation Files\Material property\thermal properties TM units v2.xls,* tab "Specific Heat"	Section 6.2.1
Coefficient of Thermal Expansion of TSw2-TSw3 Unit in Regional Thermo-mechanical Analysis	T <50°C, 7.14×10^{-6} 50°C ≤ T < 75°C, 7.47×10^{-6} 75°C ≤ T < 100°C, 7.46×10^{-6} T ≥ 100°C, 9.07×10^{-6}	DTN: MO0408MWDDDMIO.002 [DIRS 171483], file *Calculation Files\Material property\thermal properties TM units v2.xls,* tab "Thermal Expansion"	Section 6.2.1
Poisson's ratio of TSw2-TSw3 Unit	0.2	DTN: MO0408MWDDDMIO.002 [DIRS 171483], file *Calculation Files\Material property\rock mass strength v2.xls,* tab "Intact Strength"	Section 6.2.1
Linear Heat –Source Power	1,450 W m^{-1}	SNL 2007 [DIRS 179354], Table 4-4, Parameter 05-03	Section 6.2.4
Preclosure Duration	50 years after final emplacement	SNL 2007 [DIRS 179466], Table 4-2, Parameter 06-01	Section 6.2.4
Repository Elevation	1,075 m	SNL 2007 [DIRS 179466], Table 4-1, Parameter 01-02	Section 6.2.4
Emplacement Drift Diameter	5.5 m	SNL 2007 [DIRS 179466], Table 4-1, Parameter 01-10	Table 6-5, Equation C-14
Emplacement Drift Spacing	81 m	SNL 2007 [DIRS 179466], Table 4-1, Parameter 01-13	Table 6-5, Equation C-15
Waste Package Thermal Conductivity	1.50 W m^{-1} K^{-1}	SNL 2007 [DIRS 179354], Table 4-4, Parameter 05-03	Table 6-14

NOTE: PTn, TCw, TSw1, TSw2, and TSw3 are thermo-mechanical tuff units in the Yucca Mountain region.

4.1.2 Use of Representative Assumed Values

The development of the in situ stress model of Section 6.2.2 and the thermal stress model of Section 6.2.4 were completed before the completion of *Drift Degradation Analysis* (BSC 2004 [DIRS 166107]) and used preliminary data that have since been modified and qualified in DTN: MO0408MWDDDMIO.002 [DIRS 171483]. As discussed in Section 5.1, these preliminary values for thermomechanical rock properties are treated as assumed values in this report and are documented in Appendix I, Table I-1; the values used for input (listed in Table I-1) are compared with the qualified values (column "Design Value" in Table I-1) as presented in DTN: MO0408MWDDDMIO.002 [DIRS 171483]. The sources for the qualified values presented in Table I-1 are provided in Appendix I, Table I-2.

The development of the numerical representation for the alternative thermal model in Section 6.3.7.2 was completed based on preliminary design concepts for the EBS components (See Assumption 5.4, Section 5). These values are compared to the design values in Appendix I, Table I-1. Impact assessments are also provided in Table I-1.

4.2 CRITERIA

The general requirements to be satisfied by the TSPA are stated in 10 CFR 63.114 (2007 [DIRS 180319]). The acceptance criteria that will be used by the NRC to determine whether the technical requirements of the license application associated with these integrated subissues, "Mechanical disruption of engineered barriers" (Section 2.2.1.3.2.3), "Volcanic disruption of waste packages" (Section 2.2.1.3.10.3), and "Airborne transport of radionuclides" (Section 2.2.1.3.11.3), have been met are identified in *Yucca Mountain Review Plan, Final Report* (NRC 2003 [DIRS 163274]).

Appendix A provides descriptions of how information in this report addresses the acceptance criteria of *Yucca Mountain Review Plan, Final Report* (NRC 2003 [DIRS 163274]).

4.3 CODES, STANDARDS, AND REGULATIONS

No standards, regulations, or code requirements other than those cited in Section 4.2 apply to this model.

INTENTIONALLY LEFT BLANK

5. ASSUMPTIONS

This section deals with conceptual assumptions used in the models covered by this report. Parameter assumptions, those dealing with the selection of a particular number or numbers as input values for the models, are described within the discussion of model inputs for each model component. Conceptual assumptions specific to each component of this report are also mentioned in the main text of Section 6, with references back to the discussion in this section; hence, only the subsection numbers for those discussions are identified here. Assumptions are grouped here according to the individual supporting models and analyses they affect.

5.1 IN SITU AND THERMALLY INDUCED STRESSES

Thermomechanical Properties of the Rock Mass

Assumption: The in situ stress and thermally-induced stress models make use of preliminary thermomechanical rock properties that were available before those submitted in qualified DTNs. It is assumed these preliminary values are representative of the qualified values both of which are documented in Appendix I, Table I-1.

Rationale: The calculations of in situ and thermally induced stresses at Yucca Mountain were completed using properties from Appendix C of *Drift Degradation Analysis* (BSC 2004 [DIRS 166107]) before final values for rock material properties reported in Appendix E of BSC (2004 [DIRS 166107]; DTN: MO0408MWDDDMIO.002 [DIRS 171483]) were developed. For most of the properties (Appendix I, Table I-1), the values used are within 20% of the qualified values, most of them within 10% or closer. Such variability is not unusual in the measurement and application of geologic properties as described in Appendix I, which also provides an impact assessment. For specific heats at temperatures between 95°C and 114°C, the variations can be up to 90%. In these cases, as stated in BSC (2004 [DIRS 166107], Appendix Q), the rock volume for temperatures over 95°C is localized adjacent to the drift wall and has a minimal effect on the mountain-scale stresses.

Confirmation Status: Confirmation is not required because the use of this assumption will not have a significant effect on model results.

Where Used: Sections 6.2.1, 6.2.2, and 6.2.4.

5.2 DIKE PROPAGATION FROM DEPTH

Pressure in Dike Tip Cavity

Assumption: The analysis of dike propagation from depth assumes that the pressure of the vapor in the cavity above the magma in the growing dike is negligible except as specifically noted to the contrary.

Rationale: The pressure will be substantially lower than either the horizontal far-field stress or the vapor pressure of the magma because the rock into which the dike is intruding has a very high gas permeability of 10^{-12} m^2/s (Detournay et al. 2003 [DIRS 169660]).

Confirmation status: Confirmation is not required because the extremely high permeability of the rocks surrounding the repository will prevent accumulation of high-pressure vapors. Gas pressures in the tip cavity that equal or approach the horizontal far-field stress will cause dike-tip instability. This means that the fracture that develops ahead of the ascending magma front will propagate rapidly to the surface, providing additional pressure release and establishing a pathway for magma to reach the surface.

Use in the Model: This assumption is used in Section 6.3.

Linear Elastic Fracture Mechanics

Assumption: The analysis of dike propagation from depth assumes that the approach of linear elastic fracture mechanics (LEFM) applies to the rock that the dike is penetrating.

Rationale: This assumption is required to make the problem mathematically tractable.

Confirmation status: Confirmation is not required because the effects of non-linearities are addressed in the model by varying the fracture toughness and in alternative models (Section 6.3.3.5.4). In both cases, the effects are found to be negligible.

Use in the Model: This assumption is used in Section 6.3.

Homogeneous, Isotropic Surrounding Rock

Assumption: The analysis of dike propagation from depth assumes that the rock into which the dike is intruding is homogeneous and isotropic.

Rationale: Realistic inhomogeneities cannot be efficiently modeled on the scale needed for the dike propagation model except for large-scale features such as faults and major lithologic boundaries. The variation of mechanical properties with direction in rocks is generally small, and disregarding them makes the mechanical deformation equations very much simpler, which allows the model to run more efficiently.

Confirmation status: Confirmation is not required because this is a standard assumption in geotechnical modeling. Furthermore, analyses in Section 6.3.4 relax this assumption by considering the effects of faults and other underlying geologic structures beneath the repository. Their effect is found to be minimal.

Use in the Model: This assumption is used in Section 6.3.

Magma is Newtonian Fluid

Assumption: The analysis of dike propagation from depth assumes that the deformation of magma is represented by Newtonian viscosity.

Rationale: Experimental data (Shaw 1972 [DIRS 126270], pp. 873 to 878) indicates that basaltic magmas near their liquidus are characterized by Newtonian rheology.

Confirmation status: Confirmation is provided by the experimental data of Shaw (1972 [DIRS 126270]).

Use in the Model: This assumption is used in Section 6.3.

Single Crack

Assumption: The analysis of dike propagation from depth assumes that the dike propagates as a single crack without any branching or reconnection.

Rationale: This assumption is required to make the model mathmatically tractable.

Confirmation status: Confirmation is not required because the field evidence (SNL 2007 [DIRS 174260], Appendix F) indicates that multiple fractures are likely to be most important at depths corresponding to horizons above the repository.

Use in the Model: This assumption is used in Section 6.3.

5.3 MAGMA FLOW INTO BACKFILLED DRIFTS FOR EFFUSIVE FLOW

Assumption: The analysis of magma flow over backfill in access drifts assumes that the gaps above the backfill are initially unobstructed by rubble or rockfall.

Rationale: Although near-field seismic events with annual frequencies one to two orders of magnitude greater than the igneous event may cause rockfall to partially or totally fill drifts for much of the postclosure period (SNL 2007 [DIRS 176828]), the extent and timing of such filling cannot be predicted precisely. Use of unobstructed dimensions will result in maximum exposure of waste packages and waste forms to magma. This assumption is further discussed in Section 6.4.8.4.2.

Confirmation status: The design configuration is the only configuration defined well enough to permit modeling. No confirmation is needed.

Use in the Model: This assumption is used in Section 6.4.8.4.

5.4 COOLING OF BASALT-FILLED DRIFTS

This section identifies relevant assumptions, along with their respective rationales, that are essential for process modeling and assessing the thermal impacts of igneous intrusion on drifts.

Identity of Thermal Properties of Magma and Tuff and Effects of Latent Heat

Assumption: It is assumed that thermal conductivity and thermal diffusivity of the magma are the same as the welded tuff, and that latent-heat effects related to magmatic crystallization have a minimal impact on the model.

Rationale: The properties of the magma that could intrude into the emplacement drift(s) are difficult to predict precisely. The assumption that the thermal properties (thermal conductivity and diffusivity) of the in-drift magma are the same as the drift wall rocks is reasonable.

Latent-heat effects are reasonably easy to simulate in cooling models; however the model is relatively insensitive to this as well. The sensitivity of these parameters to variation is examined in an alternative model in Section 6.4.7 and in the validation section (Section 7.3.2.1).

Confirmation Status: Sections 6.4.7 and 7.3.2.1 show that the results are not sensitive to these parameters. Therefore, no further confirmation is needed.

Use in the Model: This assumption is used in Section 6.4.

Heat Loss by Thermal Conduction

Assumption: It is assumed that heat loss from a magma-filled drift is accounted for by a thermal conduction model, with no contribution from radiation or fluid convection.

Rationale: Although the temperature of intruding magma is high enough for radiation to be an important heat transfer mechanism, the opacity of both the magma and the surrounding tuff to infrared radiation is so high that radiative heat transfer will not be effective in cooling magma in a drift. The heat capacity of air in voids in the tuff surrounding the drift is low enough that convective cooling is also not effective. The sensitivity of these parameters to variation is examined in an alternative model in Section 6.4.7.2 and in the validation section (Section 7.3.2.1).

Confirmation Status: Sections 6.4.7.2 and 7.3.2.1 show that the results are not sensitive to these parameters. Therefore, no further confirmation is needed.

Use in the Model: This assumption is used in Section 6.4.

Use of Representative Values for Design Input Parameters

Assumption: Based on preliminary concepts for the EBS components, representative values for the necessary design parameters were assumed to perform the simulations discussed in this report. These assumed values are provided in Appendix I, Table I-1.

Rationale: Many of the simulations were started before the direct confirming data were available in the design interface documents, so it was necessary to use preliminary values for the design of the EBS components. These values are compared to the direct confirming data values in Appendix I. Impact assessments are also provided in Appendix I, Table I-1. The assessments indicate that the use of the assumed representative values has a finite impact on the results presented in this report. However, as the alternative model does not provide any parameters to TSPA, there is no impact on the TSPA model.

Confirmation Status: Confirmation is not required because the use of this assumption was required to complete the analysis in a timely manner.

Where Used: Sections 6.4.7.2.

6. MODELS AND ANALYSES

The objective of the modeling discussed in this section is to provide a description of the mechanical, thermal, and chemical environment that waste packages and waste forms would experience should an igneous intrusive event intersect the repository and fill the drifts with magma. The consequences of an eruptive event, in which magma reached the surface after intersecting the repository, is addressed in *Atmospheric Dispersal and Deposition of Tephra from a Potential Volcanic Eruption at Yucca Mountain, Nevada* (SNL 2007 [DIRS 177431]). *Number of Waste Packages Hit by Igneous Events* (SNL 2007 [DIRS 177432]) presents an analysis of the quantity of waste packages impacted should an igneous event intersect the repository.

The dike/drift interaction conceptual model describes processes that would occur if an intrusion were to intercept the repository. The conceptual model consists of two submodels made up of several model components and analyses:

Dike-intrusion Submodel

- Natural and thermal stresses—analysis
- Dike propagation from depth—model
- Environment in repository up to solidification of magma—analysis
- Magma flow to the surface, either via a secondary dike or directly via the continuation of the dike to the surface—analysis.

Post-intrusion Submodel

- Transport to neighboring drifts of magmatic gases after magma emplacement—model
- Heating of neighboring drifts from the cooling of emplaced magma—model
- Seepage water alteration by reaction with intruded basalt in drifts—analysis.

This section of the report is organized as follows.

The features, events, and processes (FEPs) included in the model are described in Section 6.1.

The stresses active in the vicinity of the repository are an essential parameter of dike propagation. Therefore, Section 6.2 analyzes, for use in the later sections, the stresses in the region of the repository, both naturally occurring and those introduced from the engineered tunnels and subsequent heating from radioactive decay of waste.

To assess the interaction of the dike with an emplacement drift, one needs to define the physical conditions of its propagation until it effectively reaches the repository elevation. Section 6.3 discusses the propagation of the dike from depth and addresses propagation both with and without a thermal source in the repository, the effects of topography on dikes, the effects of underlying geology on propagation, and the effects of magma compressibility.

Section 6.4 models the environment following intrusion of magma into a drift and interactions with the waste packages and their contents. It is then possible to understand what happens after the drift has been filled. What temperatures are experienced by the Engineered Barrier System (EBS)? How much heat will flow between magma-filled drifts and adjacent drifts? What pressures can be expected in the magma and what gases will be present? What will be the impact of the magma on the waste packages and waste forms? Answers to these questions will support realistic scenarios for the transport of waste to the surface, and avoid unrealistic ones.

Section 6.5 analyzes the possibility that, after filling a drift, magma might open a secondary path to the surface at some distance from the original dike, with the magma flow being diverted through the drift and carrying the entire drift contents to the surface. This is commonly called the "dog-leg" scenario. Secondary dike propagation is analyzed for the case of effusive magma, with a brief consideration of the effect of magma compressibility.

Postemplacement effects are discussed in Sections 6.6, which presents a review of literature related to the composition of groundwater in contact with basalt.

This report considers a wide range of phenomena associated with dike propagation and magmatic interaction with drifts. Nevertheless, the range of possible interactions with waste packages, cladding, and drip shields encompasses an unusually broad range of uncertainty. As a result, it is not possible at this time to predict the precise behavior of the EBS components in the event of an igneous intrusion. However, the temperatures, pressures, corrosive vapors, and durations of exposure associated with an igneous intrusion into emplacement drifts support the assumption that waste canister/assembly, cladding, and drip shields contacted by magma will provide no added protection to waste forms against water.

6.1 FEATURES, EVENTS, AND PROCESSES ADDRESSED BY THE DIKE/DRIFT INTERACTION MODEL

Development of a comprehensive list of FEPs potentially relevant to postclosure performance of the Yucca Mountain repository is an ongoing, iterative process based on site-specific information, design, regulations, and better understanding of the characteristics and processes of an igneous event intersecting the repository. Table 6-1 provides a list of igneous-related FEPs (DTN: MO0706SPAFEPLA.001 [DIRS 181613]) that are included in the total system performance assessment (TSPA) through the use of the results of the calculations described in this document. The rationale for inclusion or exclusion of igneous-related disruptive-event FEPs is discussed in *Features, Events, and Processes: Disruptive Events*, which is included in DTN: MO0706SPAFEPLA.001 [DIRS 181613]. The analyses presented in the remaining parts of Section 6 support the technical bases for some of the exclusion arguments.

For the igneous intrusive scenario, the TSPA postulates that a hypothetical dike propagates upward during an unlikely intrusive event and intersects the repository, providing a source for magma to enter the repository drifts, subjecting waste packages and waste forms to very high temperatures, and exposing them to corrosive gases; it further postulates that, following intrusion, the chemistry of seepage waters may be altered by the presence of solidified basalt. For the igneous eruptive scenario, the TSPA postulates that, following or as an adjunct to an intrusive event, magma and ash, potentially with entrained waste, are released to the surface via

an eruptive conduit. The FEPs listed in Table 6-1 are part of the conceptual basis for such scenarios. This report provides supporting analyses to help constrain the potential consequences of the listed FEPs.

Table 6-1. Included Features, Events, and Processes for This Model Report

TSPA FEP Number, Name and Description	Section Where Disposition is Described
1.2.04.03.0A Igneous intrusion into repository - Magma from an igneous intrusion may flow into the drifts and extend over a large portion of the repository site, forming a sill, dike, or dike swarm, depending on the stress conditions. This intrusion could involve multiple drifts. The sill could be limited to the drifts or a continuous sill could form along the plane of the repository, bridging between adjacent drifts.	Section 6.3 contains the overall model description, assumptions and simplifications. Section 6.3.3 contains the mathematical description of the base-case model for dike propagation from depth, including potential effects of underlying faults, the potential for formation of sills, the effects of topography, the differences between dike propagation driven by an incompressible magma or by an expanding magma, and the effects of thermally induced stresses. Section 6.4 contains an analysis of the flow of magma into drifts and the temperature and pressure histories that would follow. Section 6.5 contains an analysis of secondary dike (or sill) propagation from magma-filled drifts.
1.2.04.04.0A Igneous intrusion interacts with EBS components - An igneous intrusion in the form of a dike may occur through the repository, intersecting the repository drifts, resulting in magma, pyroclastics, and volcanic gases entering the drift and interacting with the EBS components (drip shields, waste packages, pallet, and invert). This could lead to accelerated drip shield and waste package failure (e.g., attack by magmatic volatiles, damage by flowing or fragmented magma, thermal effects) and dissolution or volatilization of waste.	Section 6.4 contains an analysis of the flow of magma into drifts and its effects on waste packages and waste forms, and an analysis of the transport of heat through the host rock from an intruded drift to an adjacent drift. Section 6.6 contains a description of a model of postemplacement migration of volcanic gases out of a filled drift; the model can be used to determine effects on adjacent drifts. Section 6.6 contains a summary of analogue compositions of water in contact with basalt. Outputs related to igneous interaction with EBS components are found in Sections 8.2.2, 8.2.3, and 8.2.4.
1.2.04.04.0B Chemical effects of magma and magmatic volatiles - An igneous intrusion into the repository may be accompanied by the release of magmatic volatiles. The volatiles may affect in-drift chemistry (potentially leading to increased waste package corrosion), or may be absorbed by the host rock, where they could change the chemistry of the water seeping back into the drift following the intrusive event. Seepage water chemistry following magma cooling could also be affected by flowing through and interacting with the intruded basalt.	Section 6.4 contains an analysis of the flow of magma into drifts, of the temperatures and pressures that would result during cooling and solidification of the magma with enclosed waste packages, and of the interaction of magma with waste packages and waste forms. Section 6.6 contains a summary of analogue compositions of water in contact with basalt.
1.2.04.06.0A Eruptive conduit to surface intersects repository - As a result of an igneous intrusion, one or more volcanic vents may form at land surface. The conduit(s) supplying the vent(s) could pass through the repository, interacting with and entraining waste.	Section 6.3 contains an analysis of magma flow from a dike to a drift that is related to the potential location of eruptive conduits.

Source: DTN: MO0706SEPFEPLA.001 [DIRS 181613].

6.2 ANALYSIS OF NATURAL AND INDUCED STRESSES AT THE REPOSITORY

The stresses active in the vicinity of the repository are an essential parameter of dike propagation. The purpose of the simple analyses below is to assess the stress field that needs to be taken into account for the dike propagation computations. Vertical stresses are essentially governed by gravity and the topography in the neighborhood. Horizontal stresses in the absence of the repository have been measured. However, thermal loading due to the waste may have a profound effect on the horizontal stresses. Also, at a much smaller scale, the presence of a drift changes the stresses around the excavation.

This section is organized as follows:

- Section 6.2.1 discusses inputs used in the analysis
- Section 6.2.2 discusses the effect of topography
- Section 6.2.3 discusses the effect of excavation
- Section 6.2.4 assesses the effect of thermal loading.

The computations described below use FLAC3D V. 2.1 software (STN: 10502-2.1-00 [DIRS 161947]), which is qualified for this use.

6.2.1 Inputs for Topographic and Thermal Effects

A large-scale, three-dimensional analysis was used for calculation of in situ (topography-induced) and thermally induced stresses. Inputs for this model were:

- Regional topography
- Layout of the repository
- Ratios of horizontal principal stresses to the vertical stress
- Orientations of the horizontal principal stresses
- Stratigraphy in the vicinity of the repository
- Elastic properties (Young's modulus and Poisson's ratio) and density of each geological unit
- Thermal properties for each geological unit (conductivity, specific heat, and coefficient of thermal expansion)
- Position and mechanical properties (friction angle) of two faults in vicinity of the repository
- Heat released by the waste as a function of time and amount of heat removed by ventilation.

The calculations of in situ and thermally induced stresses at Yucca Mountain were completed using properties from Appendix C of *Drift Degradation Analysis* (BSC 2004 [DIRS 166107]) before final values for rock material properties reported in Appendix E of that report were developed. Therefore there is some discrepancy between the values used and properties in qualified DTNs so that some of the input values are assumptions as described in Section 5.1 and documented in Appendix I, Table I-1. However, the values used are qualified here for their intended use in Sections 6.2.2 and 6.2.4. When the source of the data is listed in Table 4-1 as DTN: MO0408MWDDDMIO.002 [DIRS 171483], the values are already qualified and any differences are due to rounding and will not be discussed.

For most of the other properties, the values used are within 20% of the qualified values, most of them within 10% or closer. Such variability is not unusual in the measurement and application of geologic properties. The result of these deviations are difficult to predict precisely, but because the resulting stresses are the result of cumulative calculations and variations do not appear to be coupled (i.e., not all the moduli are high or all the thermal conductivities low) the net result on the accuracy of the results in Sections 6.2.2 and 6.2.4 will be small. The values are therefore qualified for their use in Sections 6.2.2 and 6.2.4.

The specific heat valued used for temperatures between 95°C and 114°C for all units, as taken from Appendix C of *Drift Degradation Analysis* (BSC 2004 DIRS [166107]) are considerably higher than the qualified values from DTN: MO0408MWDDDMIO.002 ([DIRS 171483]). However, as stated in Appendix Q of *Drift Degradation Analysis* (BSC 2004 [DIRS 166107]), the rock volume for temperatures over 95°C is localized adjacent to the drift wall, and the time duration over 95°C is also limited to several hundred years, so the impact of this deviation is minimal and the data are qualified for their intended use.

For the deepest units, those underlying unit TSw3, the values for Young's modulus, Poisson's ratio and the coefficients of thermal expansion are assumed to be equal to those for units TSw2 and TSw3. For the other properties for the units beneath TSw3, the values used are within 10% of the qualified values from DTN: MO0408MWDDDMIO.002 ([DIRS 171483]). As no information is available for these units and the values have a minimal effect on the stress state at repository level, these data are qualified for their intended use.

The fault stiffness[1] was calculated after converting elastic properties (Young's modulus and Poisson's ratio of the TSw2 unit) from DTN: MO0408MWDDDMIO.002 [DIRS 171483] to bulk modulus and shear modulus using Equations 13 and 14 from Jaeger and Cook (1979 [DIRS 106219], p. 111). The resulting bulk and shear moduli were then used with the minimum cell dimension (64 m) as described in the FLAC3D users manual (Itasca 2002 [DIRS 160331], Equation 3.4).

6.2.2 Stress Due to Natural Topography

Large-scale, three-dimensional, thermo-mechanical analysis of regional stresses accounting for topography at the Yucca Mountain site was conducted using the FLAC3D V. 2.1 code. Detailed description of this analysis is found in *Drift Degradation Analysis* (BSC 2004 [DIRS 166107],

[1] The fault stiffness is a modeling parameter selected based on rule-of-thumb guidelines for efficient modeling.

Appendix C). The topography of the site and its representation in the model are shown in Figure 6-1. Contours of the vertical stress and orientations of the principal stresses are shown in Figure 6-2 (larger scale in the vertical plane at N232000).

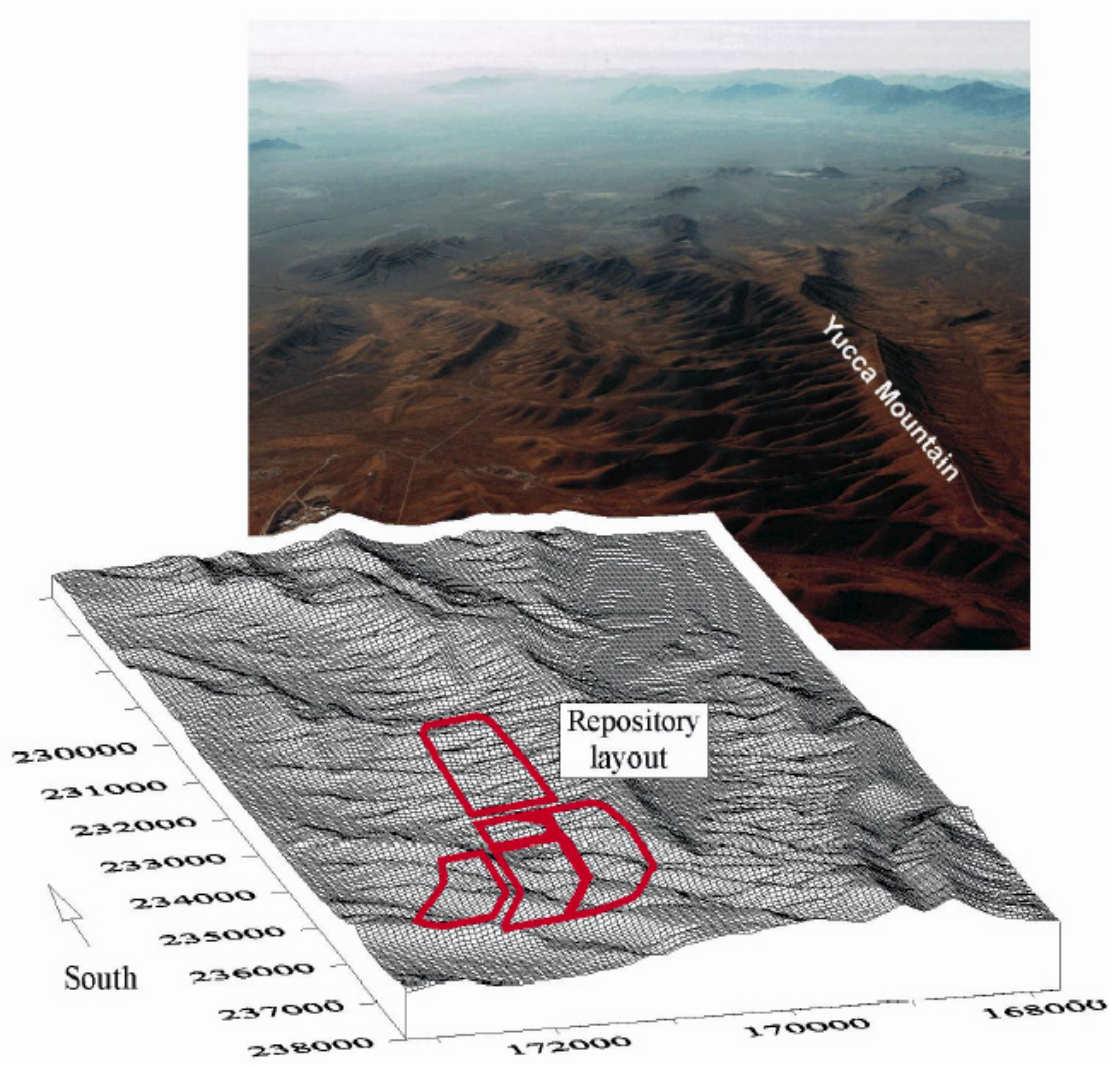

Source: BSC 2004 [DIRS 166107], Figure C-1a.

Figure 6-1. Topography at Yucca Mountain Nuclear Waste Repository Site

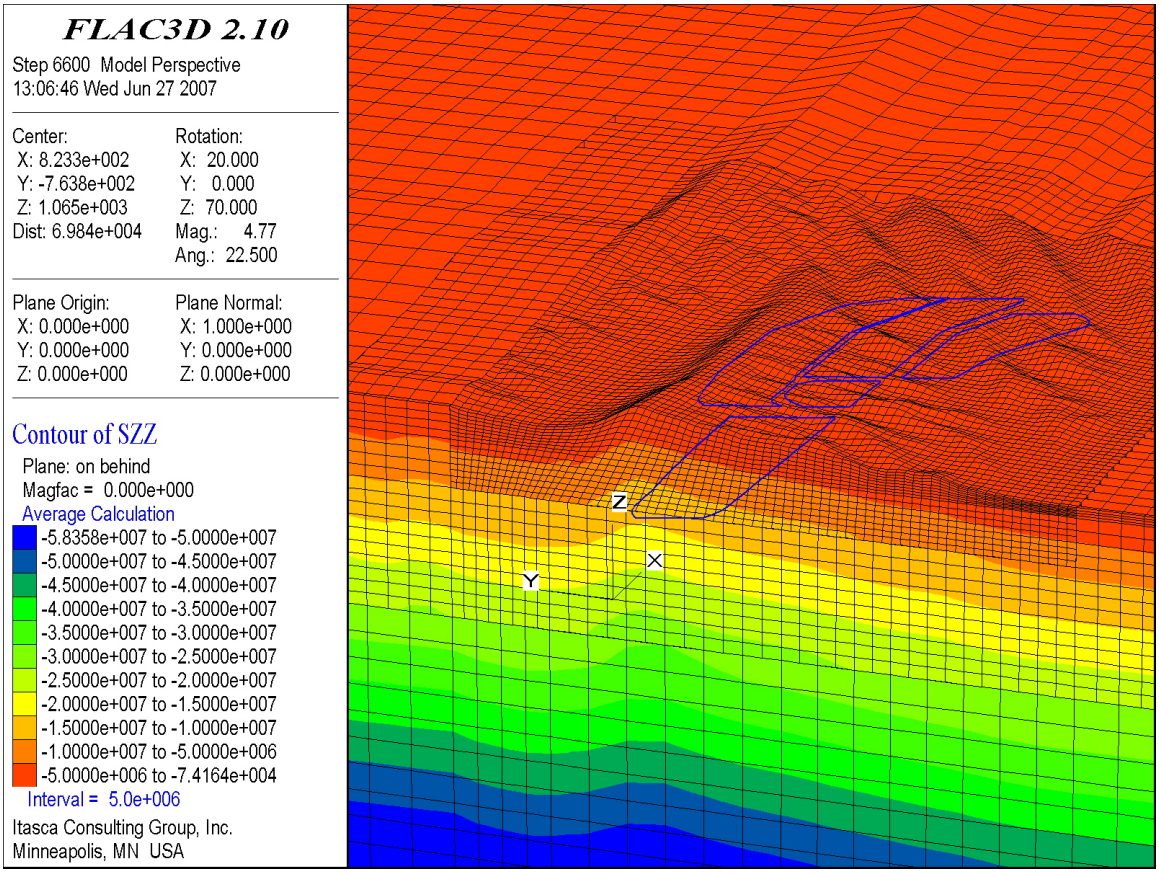

Output DTN: SN0707ISITUTIS.001, file *insitustresses.jpg*.

NOTES: Cross section through N232000 looking northwest.
Negative stresses are compressive. Stress scale in Pa.

Figure 6-2. Contours of Vertical Normal Stress Due to Topography at Yucca Mountain Nuclear Waste Repository Site

The in situ stress state at Yucca Mountain (before heating) is such that the vertical stress is the maximum principal compressive stress, whereas two other principal stresses of smaller magnitude are in the horizontal plane. The vertical in situ stress is gravitational (a function of topography and stratigraphy). The two orthogonal horizontal stresses are adjusted in the model (being statically undetermined) to match measurements of horizontal stresses (DTN: SNF37100195002.001 [DIRS 131356]); this provides the remaining constraint controlling how gravity, topography, stratigraphy, and two modeled faults interact to generate the horizontal stresses. The in situ stress profiles (normal stress components in the directions of the global coordinate axes) from the analysis, along the vertical scanline at (N171000, E235000), are shown in Figure 6-3. (The horizontal normal stresses in the directions of the global coordinate axes are almost coincident with the horizontal principal stresses.)

The repository is designed to be under the mountain—that is, the region of expected increased stresses. Heterogeneity of in situ stresses and rotation of the major principal stress from the vertical direction due to topography could affect the dike path and potentially divert it from the repository. It can be seen from the upward deflection of contours of vertical stress in Figure 6-2

that the topography above the repository will increase the vertical stress by less than 2 MPa, and that the vertical stress will remain the major principal stress. Note that the impact on horizontal stresses is significantly smaller. Since a dike tends to propagate towards the major principal stress, and since the vertical stress will remain major, based on current understanding of stress state, the topography at the Yucca Mountain will not cause deflection of the dike. Also, because horizontal stresses will be little affected, the impact on propagation will be minimal. A more detailed analysis of the effects of topography on dike propagation can be found in Section 6.3.5.

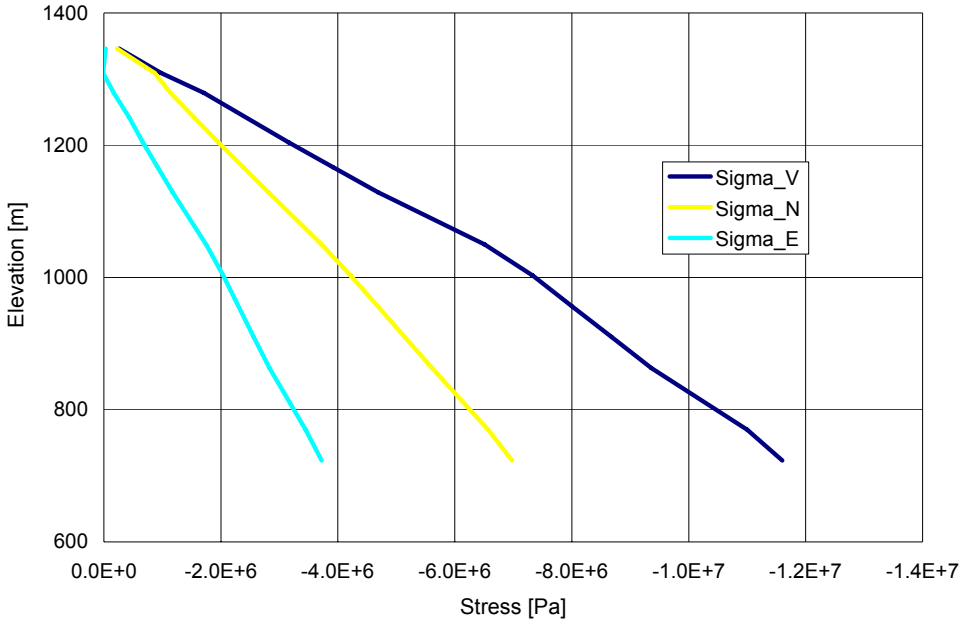

Output DTN: SN0707ISITUTIS.001, file *normal_stress_profiles.xls*, tab "ch initial."

NOTES: Sigma_V is the vertical stress; Sigma_N and Sigma_E are the two normal horizontal stresses in directions of the global coordinate axes. These normal stresses are almost coincident with principal stresses.
Repository elevation is approximately 1,070 m.

Figure 6-3. Variation of Initial in Situ Stresses with Depth at Yucca Mountain Nuclear Waste Repository along the Vertical Scanline at E171000, N235000

6.2.3 Stresses Due to Excavation of the Drift

The stress concentrations around a circular drift extending in the *z*-direction that are induced by the far-field stresses are well known and, at the tunnel wall, are given by Equations 6-1 to 6-4 (Jaeger and Cook 1979 [DIRS 106219], Section 10.4, pp. 249 to 254):

$$\sigma_\theta = (\sigma_x + \sigma_y) - 2(\sigma_x - \sigma_y)\cos(2\theta) - 4\tau_{xy}\sin(2\theta) \quad \text{(Eq. 6-1)}$$

$$\sigma_{zz} = \sigma_z - 2\nu(\sigma_x - \sigma_y)\cos(2\theta) - 4\nu\tau_{xy}\sin(2\theta) \quad \text{(Eq. 6-2)}$$

$$\tau_{\theta z} = 2(-\tau_{xz}\sin\theta + \tau_{yz}\cos\theta) \quad \text{(Eq. 6-3)}$$

$$\tau_{r\theta} = \tau_{rz} = 0 \quad \text{(Eq. 6-4)}$$

where:

θ = the angle about the drift axis as measured from the horizontal x-axis towards the vertical y-axis
σ_x, σ_y, σ_z = the far-field normal components of stress
τ_{xy} τ_{yz}, and τ_{zx} = the far-field shear stresses
σ_{zz} = the axial component of stress
σ_θ = the hoop stress
$\tau_{r\theta}$ and τ_{rz} = radial shear stress factors, which are zero at the tunnel wall (until pressurized by magma, which is considered in Section 6.5.1).

All of these stresses are at the drift wall, where the stress concentration is highest. Stress changes from the drift excavation are of limited spatial extent and decay quickly into the pillars separating drifts as a function of distance from the drift wall. The stress becomes almost equal to unperturbed, far-field stress state at a distance of three drift radii from the drift wall. Repository stresses will have an insignificant effect on dike propagation. The scale effect mentioned here is valid because the analyses consider a kilometer(s)-long dike propagating towards the surface. Later analyses addressing the secondary dike, or "dog leg," scenario in Section 6.5, consider propagation from the drift of a diverted dike with a length in the same range as the drift. In this case, excavation-induced stresses will need to be taken into account.

6.2.4 Thermal Stresses Induced by Radioactive Decay of Waste

On average, the vertical stresses (statically determined) would not change as a result of heating. If heating increases the magnitude of the horizontal principal stresses such that both become larger than the vertical principal stress, the repository could be shielded from potential volcanic intrusion for a period of time (while the conditions of such stress "inversion" exist).

The temperature and stress changes due to heat generated by the emplaced waste were simulated through the entire regulatory period of 10,000 years. Detailed description of this analysis is found in *Drift Degradation Analysis* (BSC 2004 [DIRS 166107]], Appendix C), which is based on a preclosure duration of 50 years (SNL 2007 [DIRS 179466], Parameter 06-01), and a linear heat load of 1,450 W/m (SNL 2007 [DIRS 179354], Table 4-4, Parameter 05-03). The maximum increase in horizontal stress due to heating occurs between 500 and 1,000 years after waste emplacement. Figures 6-4, 6-5, and 6-6 show the stress profiles after 500, 1,000, and 2,000 years, respectively, along the vertical scanline at N171000, E235000. The average elevation of the repository is approximately 1,075 m, as calculated from *Total System Performance Assessment Data Input Package for Requirements Analysis for Subsurface Facilities* (SNL 2007 [DIRS 179466]). Between 500 and 1,000 years of heating, the vertical stress becomes the least-compressive stress over a vertical range of approximately 200 m and, at most, 3 MPa smaller than the smaller horizontal principal stress (Figures 6-4 and 6-5). For times later than 1,000 years the stress difference and the spatial extent of the region with stress inversion decrease. After 2,000 years (Figure 6-6) of heating, normal stress in the east-west direction is only 1 MPa larger than the vertical stress.

Figures 6-4, 6-5, and 6-6 show that the stress change due to heating extends to a depth of about 200 m below the repository. Realistic potential for dike deflection may exist for a limited time during the regulatory period (between 500 and 2,000 years after waste emplacement). Also, because the change in horizontal stresses is sizeable, the propagation parameters (specifically, magma pressure) may be affected. Although the base case model does not address this, Section 6.3.7.3 evaluates the effect of these increased stresses on dike propagation.

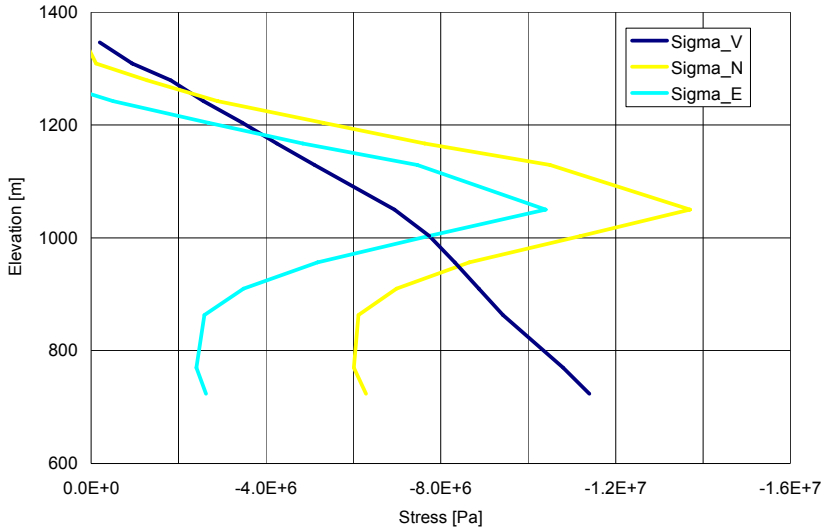

Output DTN: SN0707ISITUTIS.001, file *normal_stress_profiles.xls*, tab "ch 500."

NOTE: Sigma_V is the vertical stress; Sigma_N and Sigma_E are the two normal horizontal stresses in directions of the global coordinate axes. These normal stresses are almost coincident with principal stresses.

Figure 6-4. Predicted Variation of Stresses with Depth at Yucca Mountain Nuclear Waste Repository along the Vertical Scanline at E171000, N235000 after 500 Years of Heating

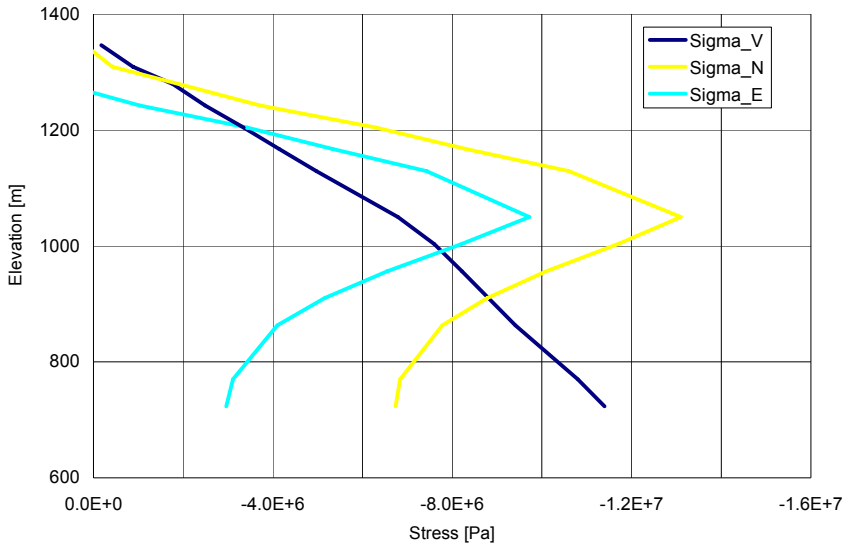

Output DTN: SN0707ISITUTIS.001, file *normal_stress_profiles.xls*, tab "ch 1000."

NOTE: Sigma_V is the vertical stress; Sigma_N and Sigma_E are the two normal horizontal stresses in directions of the global coordinate axes. These normal stresses are almost coincident with principal stresses.

Figure 6-5. Predicted Variation of Stresses with Depth at Yucca Mountain Nuclear Waste Repository along the Vertical Scanline at E171000, N235000 after 1,000 Years of Heating

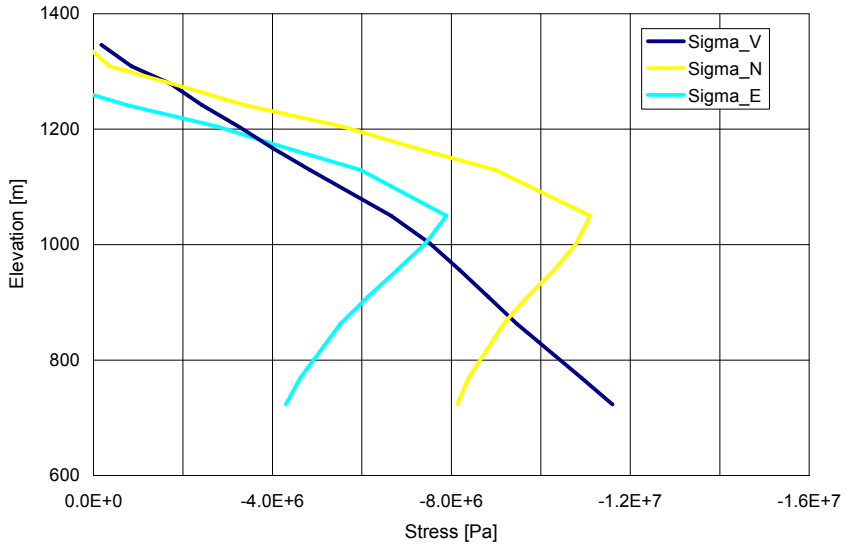

Output DTN: SN0707ISITUTIS.001, file *normal_stress_profiles.xls*, tab "ch 2000."

NOTE: Sigma_V is the vertical stress; Sigma_N and Sigma_E are the two normal horizontal stresses in directions of the global coordinate axes. These normal stresses are almost coincident with principal stresses.

Figure 6-6. Predicted Variation of Stresses with Depth at Yucca Mountain Nuclear Waste Repository along the Vertical Scanline at E171000, N235000 after 2,000 Years of Heating

6.2.5 Alternative Analysis of Stresses Due to Heating

A review of previous work and a new analysis of the effects of geologic features on thermally induced stress at Yucca Mountain was prepared by Smart (2004 [DIRS 178363]). After a summary of nine previous thermo-mechanical analyses, the review concentrated on the properties of fractures that had been mapped in the main drift of the Exploratory Studies Facility and the enhanced characterization of the repository block cross drift. This analysis used simple, first-order calculations "to demonstrate a large fraction of thermal-expansion strain from waste-generated heat can be accommodated through fracture closure. Thermally-induced [sic] stress, therefore, would be much smaller than suggested by the DOE [U.S. Department of Energy], reducing the likelihood for large-scale reorientation of the principal stresses" (Smart 2004 [DIRS 178363], p. ii).

6.2.6 Summary

Based on the results of the analyses presented above, the following results are carried forward to the dike propagation model presented in Section 6.3:

- Horizontal stresses at repository level are between 0.3 and 0.6 times the vertical stress
- Differential topography-induced stresses are considered negligible
- Excavation-induced stresses are considered negligible for the dike propagation from depth (although they may not be negligible for dike breakout at drift scale)
- Thermally induced stresses during the first two millennia may be significant, as addressed in Section 6.3.7.3.

6.3 DIKE PROPAGATION FROM DEPTH MODEL

In order to assess the interaction of the dike with a repository drift, the physical conditions of its propagation as the dike approaches and passes the repository elevation must be defined. Knowing these conditions (i.e., dike width, magma front velocity, magma pressure in the absence of a drift, and lag between crack tip and magma) will then enable analysis of the flow of the magma into the drift and its effect on further dike propagation (i.e., propagation from repository elevation to the surface). The purpose of this section is to obtain the range of physical conditions relevant for later analyses.

The model is described in Section 6.3.1, while the assumptions and simplifications involved are listed in Section 6.3.2. The base model described in Section 6.3 addresses dike propagation driven by incompressible magma in an isotropic, homogeneous, and two-dimensional half-space. The mathematical expression of the model, the uncertainties involved, and the relevant model inputs including the boundary and initial conditions are detailed in Sections 6.3.3.1, 6.3.3.2, and 6.3.3.3 respectively. The model results are detailed in Section 6.3.3.4. Alternative models are discussed in Section 6.3.3.5. This is followed by four analyses that relax the isotropic, homogeneous, two-dimensional assumptions of the base model. Section 6.3.4 looks at the effects of underlying structure and stratigraphy. The effects of thermally induced stresses are considered in Section 6.3.5, and effects of topography on dike propagation are addressed in

Section 6.3.6. A new dike propagation algorithm addressing compressible magma is analyzed in Section 6.3.7. Finally, a summary on dike propagation from depth (Section 6.3.8) spells out the inputs to be used in Section 6.4.

6.3.1 Model Description

6.3.1.1 Background

An igneous dike is magma that has propagated in a crack (usually nearly vertical) either upward from some deep source toward the surface or laterally from a source such as a volcanic conduit. This section addresses the former sort of dike. The high pressure of the magma in the dike pushes aside the surrounding rock, sometimes creating widths of several meters or more. Nevertheless, the restricted width of the dike induces frictional losses in the viscous magma that result in a pressure drop along the propagation direction of the dike. Thus, the overall dike propagation problem is an interaction that results in a balance between the high pressure that opens the dike and the appropriate width restriction that keeps the pressure at the required level through viscous losses.

This process is essentially a hydraulic fracturing problem (with some complications and some simplifications) and can only be modeled in any realistic sense by using a fully coupled hydro-mechanical-type model.

The basic components of a hydraulic fracture model include:

- The elastic deformation of the country rock due to the internal pressure of the fluid on the crack walls
- The viscous losses of the moving magma within the fracture
- Fluid losses into the surrounding medium
- A crack propagation criterion that accounts for the resistance of the rock to fracture.

The conceptual model for dike propagation is one that broadens a hydraulic fracture model for applications near a free surface. In general, hydraulic fracture models consider the propagation in an infinite medium, and effects near a free surface are not accounted for. Near-surface effects, like unstable growth and an altered width distribution, can be evaluated in the dike propagation model.

Inelastic processes associated with the crack tip are typically incorporated in hydraulic fracture models by way of fracture toughness, a measure of the energy required to open new crack surfaces. Although, large-scale geologic fractures, such as those produced by ascending magma, are not believed to have a strong dependence on fracture toughness, the model does address the effects of fracture toughness.

In general, a dike propagating from a source at depth would be expected to start out with a radial front that expands outward from the source. However, as the dike propagates, its height and length far exceed its width so that a two-dimensional approximation of dike propagation is a

reasonable approach for calculating dike parameters. As the dike approaches the repository level, horizontal confining stresses become very small and affect the propagation of the dike, but a two-dimensional model is still acceptable if it includes the effects of the free surface; this is addressed in the base model. As a dike rises into the upper crust beneath the repository, it will encounter different geologic layers (stratigraphy) and faults (structure) that have the potential to divert the dike from its original trajectory; this is addressed in the analysis of effects of structure and stratigraphy. If a dike approaches the repository during the first few thousand years while radioactive decay rates are still high enough to heat the surrounding rock by tens of degrees, the thermally induced stresses may become great enough to impede propagation; this is addressed in the analysis of thermally induced stresses. As the dike approaches the surface, the irregularity of the surface will affect dike propagation, both directly and by way of variation of stresses at a given horizon; this is addressed in the analysis of effects of topography. The above models and analyses assume the magma to be an incompressible fluid, but as the magma approaches the surface, dissolved gases (primarily water and CO_2) vaporize and the magma expands as a compressible fluid; this is addressed in the component for compressible magma.

6.3.1.2 Implementation

This section addresses the implementation of the base dike propagation model and four component analyses: structure and stratigraphy, thermally induced stresses, topography, and magma compressibility.

6.3.1.2.1 Base Model in a Homogeneous Half-Space

The elastic deformation associated with dike propagation, can be modeled using either analytic or numerical approaches. A numerical approach has much more flexibility and, therefore, is used in this application. In particular, the boundary element approach—specifically the displacement discontinuity method—is used here because of its simplicity and flexibility for crack problems (Crouch and Starfield 1983 [DIRS 139600]).

This method is based on the analytic solution to the problem of a finite line crack whose opposing sides have been displaced relative to one another in an infinite elastic solid. A crack is divided into N segments, each of which has a constant displacement over its segment, but every segment may have a different displacement from other segments. Because the analytic solution for a single element is known, the numerical solution is found by summing the effects of all N elements; however, in this application discontinuities in displacement between the elements are not known and must be calculated. If the pressure is known everywhere in the crack, then values of the elemental displacement discontinuities that are necessary to produce the pressure can be calculated by solving a system of equations. In this way, the general deformation of the crack can be determined as accurately as desired by increasing the number of elements.

The rock material that is deforming is considered to be a linear-elastic material characterized by Young's modulus, E, and Poisson's ratio, ν. This approach is clearly appropriate for small, fluid-filled fractures but may be questionable for large-scale dikes where many faults, joints, and bedding discontinuities may be intersected and respond anelastically. No methods are available for a nonlinear analysis.

The primary model approaches for magma flow are Newtonian viscosity and laminar flow in the lubrication approximation of the Navier-Stokes equation (Batchelor 1967 [DIRS 103289]). Many of the calculations used in this model are for magmas less dense than 1,300 kg m^3, which consist of more than 50% by volume gas. Such low densities are needed to maintain buoyancy at drift level, where the ratio (κ) of horizontal to vertical stress drops to approximately 0.5. The viscosity of such a mixture is uncertain, so a viscosity range of 10 Pa·s to 40 Pa·s, equivalent to the pure silicate liquid, is used.

The laminar approximation is valid for the flow rates, dike widths, and magma viscosities that are anticipated. The dimensionless parameter, Reynolds number, denoted $\mathrm{Re} = \rho_f v w/\mu$, signals a transition from laminar to turbulent flow of the fluid at $\mathrm{Re} \approx 2{,}200$ (Whan and Rothfus 1959 [DIRS 178373]). A typical set of magma/dike parameters are: a magma density (ρ_f) of 1,140 kg m^3, a dike width (w) of 1.5 m, a magma/dike velocity (v) of 10 m/sec, and a magma viscosity (μ) of 10 Pa·s; the Reynolds number is 1,710, implying laminar flow. The Reynolds number may exceed the threshold for the transition from laminar to turbulent flow in some cases, because of a wide dike fracture, high fluid density, or high velocity. No attempt is made to consider any transition effects because this would be largely speculative.

The viscous pressure drop along the propagation direction of the dike is calculated for laminar flow of a Newtonian fluid through parallel plates (Poiseuille flow) in the lubrication approximation. The Poiseuille flow approximation is valid because the dike width and magma velocity are very slowly varying functions of depth.

Standard hydraulic fracture models consider the leak-off of fracture-driving fluid into the surrounding rock formations. However, in the dike propagation case, the rock formations encountered by the dike will be impermeable to the viscous magma. Thus, no generalized leak-off is included in this model. However, leak-off of volatiles is still anticipated, which will reduce the pressure in the tip-cavity zone.

A crack propagation criterion is used in some hydraulic fracture models to include the effect of rock resistance to fracture, but it is also ignored in many models because the effects are negligible for large-scale fractures. In the dike propagation model, fracture toughness effects are included and can be evaluated. However, the scale of a dike is so large that it is not likely that the details of stress intensity calculations are strictly applicable. For example, the stresses are extremely large (on the order of several MPa) around the fracture tip and extend for many tens of meters. Damage, such as brittle fracture, likely occurs throughout this region, negating any rigorous use of linear-elastic fracture mechanics (LEFM). In this model, the fracture toughness can be used as a convenient parameter for assessing possible scale-dependent, anelastic behavior that may provide additional resistance to fracture growth.

As the propagating dike approaches the level of the drifts, the crack tip separates from the magma front because of the inability of the high-viscosity fluid to reach the very narrow tip. This separation results in a vapor-filled cavity above the magma, which is the first part of the propagating dike that encounters the drift. Cavity formation is followed some time later by magma. To evaluate tip-cavity effects, a range of values is used to assess reasonable values of a tip pressure that might develop. In conjunction with other aspects of the model, the tip pressure controls the length of the tip-cavity region.

Most hydrofractures produced for petroleum applications occur at depths where the effect of the free surface can be ignored. That is not the case at Yucca Mountain, where the repository would be a few hundred meters beneath the surface. The importance of the free surface should be evident from the relatively small ratio of the depth to the crack tip relative to the vertical extent of the dike.

Therefore, the dike propagation model in this report also includes the effect of a free surface in the deformation calculations. In this case, the solution for a displacement dislocation in a half space (Hills et al. 1996 [DIRS 163626]) is used. This formulation allows for the correct deformation in the proximity of a free surface.

The mathematical basis for this conceptual model of dike propagation is described in Section 6.3.3. The model, yielding the results presented in Sections 6.3.3.4.1 and 6.3.4.3.2, is implemented numerically with the Non-Planar Hydraulic Fracture 2D code, NPHF2D V. 1.0 (STN: 10904-1.0-00 [DIRS 163665]), described by Zhang et al. (2002 [DIRS 164368]).

The dike propagation model calculates the growth history of a dike propagating toward the surface in the vicinity of the repository. No attempt is made to model the topography of the site, as a complex surface topography formulation is beyond the capabilities of any current model. However, aspects of topographical features can be accounted for through the incorporation of a horizontal in situ stress distribution that reflects the stresses around the repository. Also, thermo-mechanical and fluid-mechanical simulations, using UDEC V. 3.14 (STN: 10173-3.14-00 [DIRS 172322]) and the same conceptual model for dike propagation, account for the horizontal stresses induced by thermal loading. UDEC V. 3.14 is qualified for this use.

As the magma rises in the dike, the flow is concentrated toward the center of the dike, with the magma at the very edge of the dike not moving upward at all. The shearing between the center of the dike and the walls will result in elongation of any vapor bubbles in that part of the magma, thus lowering the effective viscosity, so there may be a tendency for slug flow in the center of the dike.

There are two possibilities for the state of the magma in the center as it moves upward into the cavity. One possibility is that, as magma rises in the dike and approaches the cavity, it releases gas in a steady way. Stasiuk et al. (1996 [DIRS 164459]) describe a silicic volcanic conduit exposed in southwestern New Mexico that shows clear evidence of this process. The other possibility is that the liquid and vapor phases of the magma are so closely coupled that the release of gas is more catastrophic. The conceptual model adopted for the present report employs the former style because:

- The low viscosity of the basaltic melt will facilitate bubbles rising in the dike to release their gas at the fluid front
- Gas permeabilities of the repository host tuff are very high (on the order of 10^{-12} m^2/s, according to Detournay et al. 2003 [DIRS 169660]), which will permit much of the gas to leak out into the formation well ahead of the magma.

This is supported by findings of Detournay et al. (2003 [DIRS 169660], Section 3.3.3.3) and by processes described in *Characterize Eruptive Processes at Yucca Mountain, Nevada* (SNL 2007 [DIRS 174260], Section 6.3.2).

6.3.1.2.2 Component for Structural Effects

The base model introduced in Section 6.3.1.2.1 is based on a mathematical half-space occupied by a homogeneous, isotropic medium. In fact the geology in the Yucca Mountain region is complex with many different stratigraphic layers on all scales from centimeters to kilometers and is cut by faults of various angles and offsets. The underground interfaces represented by the structure and stratigraphy have some potential to divert magma rising from beneath the repository, either away from or toward the repository. The potential effects of structure and stratigraphy on dike propagation at Yucca Mountain are addressed in a structural-effects model component in Section 6.3.4. The results presented in Sections 6.3.4.5.1 and 6.3.4.5.2 are computed numerically with UDEC V. 3.14.

6.3.1.2.3 Component for Topography

The base model introduced in Section 6.3.1.2.1 is based on a mathematical half-space with gravity, which implies that the upper surface is flat and level. In fact the ground surface in the Yucca Mountain region is neither flat nor level but shows topographic variations of several hundred meters in the forms of ridges and valleys. This could affect both intrusive and extrusive magmatic activity due to both the pure geometric effect of some points being at lower elevations than others (if a dike intercepted the surface in the bottom of a valley, it might arrest further upward penetration of the magma under adjacent highlands) and the indirect effect of stresses in the ground being higher under hills than under valleys. A topographic-effects model component is presented in Section 6.3.5 to evaluate the magnitude of these effects and how they might modify dike propagation under Yucca Mountain. The results presented in Section 6.3.5.4 are obtained numerically with the FLAC3D code.

6.3.1.2.4 Component for Compressible Magma

The base model introduced in Section 6.3.1.2.1 is based on the magma being an incompressible fluid, whereas the magma is expected to have a component of volatile species, predominantly water, that will exsolve as it rises through the upper crust, thus generating bubbles and expanding the magma. The problem of dike propagation driven by an expanding magma, rather than an incompressible one, has no solution in the preexisting refereed literature. Section 6.3.6 presents an approximation developed by variation of the compressible model of Section 6.3.3.

6.3.1.2.5 Analysis of Thermally Induced Stresses

The base model introduced in Section 6.3.1.2.1 and the components described in Section 6.3.1.2.2 through 6.3.1.2.4 consider that the magnitude of the confining stresses in the ground beneath Yucca Mountain increase linearly with depth beneath the surface. During the first 2,000 years after emplacement, radioactive heat from the waste form will heat the surrounding rock causing it to expand. Reaction of the surrounding unheated rock mass will result in increased stress in the heated rock adjacent to the repository. An analysis of this effect

is included, implemented numerically with UDEC V. 3.14, with the results found in Section 6.3.7.4.

6.3.2 Assumptions and Simplifications

To make this a tractable problem, several simplifying assumptions have been incorporated in the model. These are summarized here:

1. Dike propagation can be treated in two dimensions: Although the problem of a dike propagating away from a deep magma source clearly is a three-dimensional problem, the behavior as the dike approaches the surface is considerably more constrained. Because the leading edge of the propagating crack is (ideally) an arc that is tangent to the surface when it erupts and its underground strike length may be much greater than its final surface expression, the flow of magma can safely be considered to be purely vertical. Also, the strike length of the dike is still large enough that out-of-plane effects do not impact the mechanical solution when the tip is nearing the surface (i.e., strike length is larger than the characteristic length of the problem, as mentioned later in Section 6.3.3.4). Thus, although the early-time modeling of the dike may not be accurate using a two-dimensional model, the late-time behavior (which is the behavior of interest) should be appropriately modeled using a two-dimensional approach that specifically takes account of the presence of the free surface.

2. Magma is incompressible: The analysis of dike propagation assumes that the magma is incompressible, whereas real magma is a mixture of liquid and gas (with or without solids) that can be highly compressible (SNL 2007 [DIRS 174260]). This is the standard assumption for hydrofracture analysis. The numerical model used is adapted from codes developed for oil field hydrofracture applications, which use water as the driving fluid. For these applications, incompressibility is a good assumption. Using the assumption of magma incompressibility in the magma flow model is not expected to have a major effect. Results from several incompressible magmas of successively lower densities are combined in Section 6.3.3.5 to approximate the effect of magma expansion on dike propagation. The assumption of incompressibility is relaxed in the analysis of dike propagation driven by compressible magma in Section 6.3.6.

3. Host rock behaves elastically: Elastic behavior is a reasonable assumption for small-scale pressurized fractures in the Earth but may be questionable for a dike-scale event. A dike would cross many joints, faults, bedding planes, and other discontinuities in the rock and would generate earthquakes as slippage occurs in response to the changes in stress generated by the inflated, propagating dike. However, such inelastic effects will generally serve to increase the width of the dike and decrease the pressure. These are competing effects at the repository level, with the pressure being the primary boundary condition for subsequent calculations of magma and gas flow, but the width of the dike provides a constraint on how much magma may be lost into the drift. As mentioned in assumption 10 below, “fracture toughness” is used to investigate the effect of any mechanism that resists fracture growth and thus increases the pressure.

4. Host rock behaves linearly: Most rocks have nonlinear behavior, with lower moduli (a) at low stress and (b) in the ground in the presence of joints and bedding planes. However, linear-elastic behavior would produce the greatest possible pressure.

5. Host rock is a homogeneous, isotropic material: Rocks are typically transversely isotropic due to bedding and are jointed and faulted. In addition, there are many stratigraphic units with different values of Young's modulus and Poisson's ratio. In general, the rock properties of the strata below the repository are not known, and characteristics of joints and faults deep in the Earth are not known. However, although it is true that the deformation at any one point is a cumulative effect of the deformation everywhere in the dike, the influence of any point on another point decreases with distance. Thus, in lieu of a capability to incorporate multiple layers (which the numerical model does not possess) and in the absence of detailed information on other rock properties, the dike behavior near the repository is best modeled by using the rock properties at the repository. This approach is the only assumption that can be made to obtain tractable models and sufficiently complete input parameters. The assumption of homogeneity is relaxed in the analysis of stratigraphy and structure in Section 6.3.4 and in the analysis of thermally induced stresses in Section 6.3.5.

6. Dike is a single fracture: Although many hydraulic fractures and dikes are known to exhibit multiple fracture strands and en echelon behavior, the overall dike behavior is still reasonably modeled with a single fracture. The more complex behavior observed in the field is due to complexities of the formation that are not known or otherwise available for modeling endeavors.

7. Magma is a Newtonian fluid: A Newtonian fluid is one that obeys Stokes' law of friction, for which the relationship between stress and rate of strain is linear. This formulation considerably simplifies calculations of fluid resistance and is known to apply to many common fluid systems. Although a more complex fluid rheology might be used (e.g., with yield stress and power-law behavior), it is more appropriate to remain within the analytically more tractable Newtonian framework and vary the viscosity to account for possible differences. The limitations associated with this assumption of Newtonian viscosity for modeling basaltic magma are discussed below in Section 6.3.4.

8. Magma flow is laminar: Laminar flow will occur for Reynolds numbers less than 2,200. However, Reynolds numbers do approach and even exceed 2,200 for some combinations of dike propagation calculated. These few cases are identified as the results are discussed.

9. Lubrication approximation is appropriate: The lubrication approximation is appropriate (and exact) for slow, steady motion of viscous fluids for which the viscous forces are considerably greater than the inertial forces, thus allowing the inertial forces to be neglected. These flows are also called *creeping motion*. Creeping motion can be considered as solutions of the full Navier-Stokes equations for cases with small Reynolds number (i.e., laminar flow). The lubrication approximation is appropriate

because flow in a long two-dimensional fracture is a "parallel flow," which is identical to the one-dimensional lubrication equation with the exception of an additional time derivative of the velocity and the dropping of one spatial derivative. Because hydraulic fractures—and deep dikes—are slowly varying with time and position, the time derivative is negligible, and the spatial derivative drops out as well. Consequently, the steady "parallel flow" approximation is the same as the one-dimensional lubrication equation:

$$q \equiv vw = -\frac{w^3}{\mu'}\left(\frac{\partial p_f}{\partial z}\right) \qquad \text{(Eq. 6-5)}$$

where q is the flux per unit length, v is the fluid velocity, w is the crack width, μ' is 12μ (μ is the dynamic viscosity), p_f is the fluid pressure, and z is the coordinate along the direction of crack propagation. In support of this reduction, the "lubrication approximation" has been used for 40 years in hydraulic fracturing (with even larger Reynolds numbers) with good success and no apparent discrepancies. Thus, this approximation is reasonable and appropriate for propagation from depth but may be less so very near the surface if magma begins accelerating.

10. Stress intensity factor governs tip behavior: LEFM is a discipline that has been well studied and is widely applicable to small-scale fractures in the laboratory, mines, concrete, and other typical engineering applications. In LEFM, the shape of the crack near its tip is governed by the relation in Equation 6-6:

$$w(z) = \frac{K'}{E'}(z-h)^{\frac{1}{2}}, \qquad \text{(Eq. 6-6)}$$

where $w(z)$ is here an explicit function of vertical position z, h is the vertical coordinate of the crack tip, and E' and K' are given by Equation 6-7:

$$K' = 4\left(\frac{2}{\pi}\right)^{1/2} K_{Ic} \quad \text{and} \quad E' = \frac{E}{1-\nu^2}, \qquad \text{(Eq. 6-7)}$$

with K_{Ic} being the host rock fracture toughness and E and v being Young's modulus and Poisson's ratio, respectively, also for the host rock.

However, in hydraulic fracturing, the fracture toughness of the rock is generally negligible, and the applicability of LEFM has been questioned for large-scale fractures propagating under internal pressure. The dike propagation problem is concerned with an even larger-scale feature and undoubtedly involves anelastic behavior in the surrounding rock. Thus, LEFM may not be strictly appropriate for this application. However, the LEFM formulation allows the fracture toughness to be used as a parameter that is indicative of the resistance of the rock to fracture, whatever the actual mechanism may be. Treated as a parameter, fracture toughness can be used to investigate the effect of any mechanism that resists fracture growth and thus increases the pressure.

11. Surface topography is a horizontal free surface: The surface topography at Yucca Mountain is relatively severe, but the dike propagation model treats it as a horizontal surface. Analysis of in situ stresses in Section 6.2.2 demonstrates that topography has negligible effect on the dike path and propagation parameters. The assumption of a flat surface is relaxed in the analysis of topography in Section 6.3.6.

6.3.3 Base Model: Dike Propagation from Depth in a Half-Space

6.3.3.1 Mathematical Description

Consider a liquid-filled vertical fracture propagating in a semi-infinite impermeable elastic medium that is impermeable to the liquid (Figure 6-7). The fracture is driven by the liquid (an incompressible Newtonian fluid), which is injected at the base of the fracture at a constant volumetric rate. The ascent of a two-dimensional dike in the Earth's crust can be represented by a vertical hydraulic fracture model if several simplifications are introduced to make the problem tractable:

- Plane strain conditions apply
- The magma is injected at infinity
- The dike propagates continuously in mobile equilibrium
- Lubrication theory and LEFM are applicable.

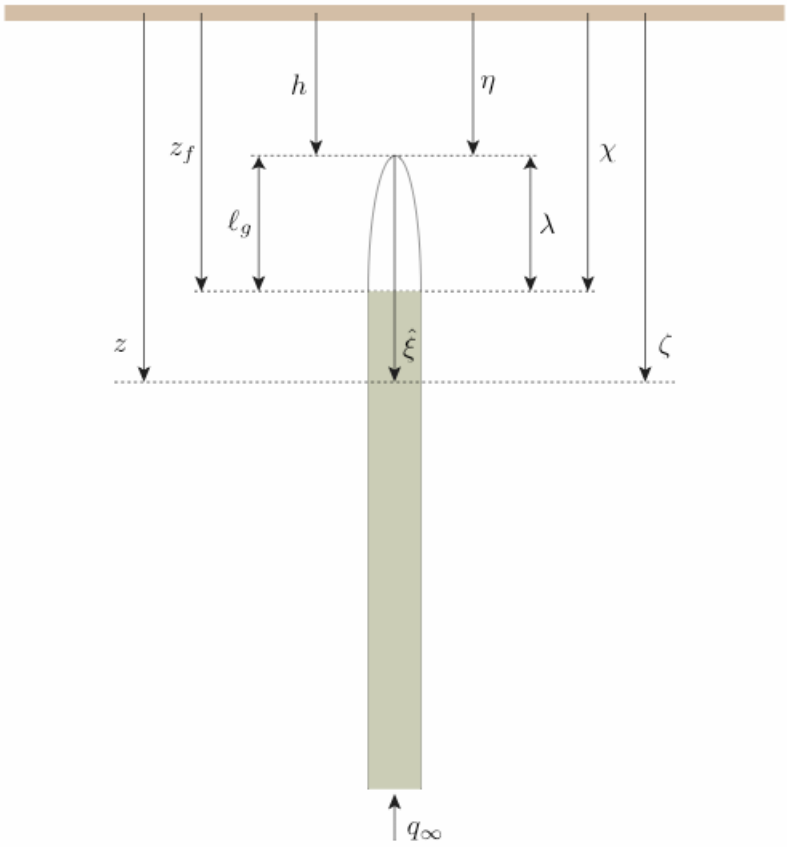

Source: For illustrative purposes only.

NOTES: The Roman symbols on the left side of the figure have dimensions of length.
The Greek symbols on the right are dimensionless scaled parameters as discussed in Section 6.4.3.2.

Figure 6-7. Plane-Strain, Fluid-Driven Vertical Fracture with a Lag Zone at the Tip

The material constants needed to represent deformation of the rock are Young's modulus, E, Poisson's ratio, ν, fracture toughness, K_{Ic}, and density, ρ_r, while the relevant constants for the fluid are the dynamic viscosity, μ, and the density, ρ_f.

The horizontal stress field, σ_o, is taken to vary with depth z according to $\sigma_0 = \sigma_c + \kappa\rho_r g z$, where σ_c is a constant stress, g is the acceleration of gravity, and κ is a number that is typically in the range $0.3 \leq \kappa \leq 1$. Finally, the boundary conditions at infinity correspond to a constant injection flow rate, q_∞.

The goal is to determine the fracture aperture, $w(z,t)$, the fluid pressure, $p_f(z,t)$ and the flow rate, $q(z,t)$, as functions of depth z and time t, as well as to determine the dependence of the solution on the problem parameters. Note that q is taken to be positive when directed upward, in the opposite direction to the z-axis.

Of particular interest is mapping the dependence of the solution on the injection rate, q_∞, and on the three material parameters, μ', E', K' defined previously. While E' is the plane strain modulus,

μ' and K' are introduced simply to keep equations uncluttered by numerical factors. For convenience, μ', E', and K' will be referred to as viscosity, elastic modulus, and toughness, respectively. The system of equations governing w, p_f, and q is summarized in Section 6.3.3.1.

6.3.3.1.1 Governing Equations

Elasticity Equation—The elastic relation between the fluid pressure, $p_f(z,t)$, and the fracture aperture, $w(z,t)$, is expressed by a singular integral equation (Hills et al.. 1996 [DIRS 163626]):

$$p_f(z,t) - \sigma_o(z) = E' \int_{h(t)}^{\infty} M(z,s) \frac{\partial w(s,t)}{\partial s} \mathrm{d}s \qquad \text{(Eq. 6-8)}$$

where $M(z, s)$ is an elastic kernel that accounts for the presence of a free surface:

$$M(z,s) = M_{\infty}(z,s) - \frac{1}{4\pi\,(z+s)} - \frac{2s}{4\pi\,(z+s)^2} + \frac{4s^2}{4\pi\,(z+s)^3} \qquad \text{(Eq. 6-9)}$$

with $M_{\infty}(z, s)$ denoting the Cauchy singular kernel for the infinite plane:

$$M_{\infty}(z,s) = \frac{1}{4\pi\,(z-s)} \qquad \text{(Eq. 6-10)}$$

Hereafter $p_f - \sigma_o$ is referred to as the net pressure p.

Lubrication—The equation governing the flow of viscous fluid in the fluid-filled zone is the non-linear Reynolds differential equation from the lubrication theory:

$$\frac{\partial w}{\partial t} = \frac{1}{\mu'} \frac{\partial}{\partial z} \left[w^3 \left(\frac{\partial p_f}{\partial z} - \rho_f g \right) \right] \qquad \text{(Eq. 6-11)}$$

This equation is obtained by combining Poiseuille's law (Equation 6-5) with the local continuity equation for an incompressible fluid:

$$\frac{\partial w}{\partial t} + \frac{\partial q}{\partial z} = 0 \qquad \text{(Eq. 6-12)}$$

For Poiseuille flow, $\partial w/\partial t$ is much less than the characteristic velocity of the problem, which is calculated below.

Boundary and Initial Conditions—The propagation criterion (Equation 6-6) imposes the asymptotic form of w at the tip, as given in Equation 6-13:

$$w \simeq \frac{K'}{E'} (z-h)^{1/2}, \quad z \to h \qquad \text{(Eq. 6-13)}$$

This criterion obviously implies that $w = 0$ at $z = h$.

At the fluid front, $z = z_f(t)$, the fluid pressure is the pressure p_{fo} in the lag zone and the velocity of the front corresponds to the average fluid velocity at the front. Hence, recalling that $q = vw$, Equation 6-14 gives:

$$p_f = p_{fo}, \quad \frac{\mathrm{d}z_f}{\mathrm{d}t} = \frac{w^2}{\mu'}\left(\frac{\partial p_f}{\partial z} - \rho_f g\right) \quad \text{at } z = z_f(t) \qquad \text{(Eq. 6-14)}$$

where the position of the fluid front, z_f, is given by:

$$z_f = h + \ell_g \qquad \text{(Eq. 6-15)}$$

with ℓ_g being the length of the tip cavity.

The condition at infinity corresponds to a constant injection rate, q_∞:

$$q = q_\infty \quad \text{at } z = \infty \qquad \text{(Eq. 6-16)}$$

It can actually be shown that this condition corresponds to a constant mean velocity, v_∞.

The set consisting of the elasticity equation (Equation 6-8), Poiseuille's law (Equation 6-5), fluid continuity (Equation 6-12), the propagation criterion (Equation 6-13), the conditions at the fluid front (Equation 6-14), and the flux at infinity (Equation 6-16) forms a complete system for determining $w(z,t)$, $p_f(z,t)$, $h(t)$ and $\ell_g(t)$, starting from known values of these quantities at an initial time, t_o. The issue of the initial conditions will be discussed below.

6.3.3.1.2 Scaling and Dimensionless Formulation

Scaling of this problem hinges on introducing the following characteristic quantities: length, ℓ_*; time, t_*; width, w_*; pressure, p_*; and flow rate, q_*. The values for these characteristic quantities will be determined in the following discussion. Using these quantities, the dimensionless depth, ζ, and time, τ, are defined as:

$$\zeta = z/\ell_* \quad \text{and} \quad \tau = t/t_* \qquad \text{(Eq. 6-17)}$$

the dimensionless fracture opening, $\Omega(\zeta, \tau)$, net pressure, $\Pi(\zeta, \tau)$, and flow rate, $\Psi(\zeta, \tau)$, as:

$$\Omega = w/w_*, \ \Pi = p/p_*, \ \Psi = q/q_* \qquad \text{(Eq. 6-18)}$$

and the depth of the fracture tip, $\eta(\tau)$, the length of the tip cavity, $\lambda(\tau)$, and the position of the fluid front, $\chi(\tau)$, as:

$$\eta = h/\ell_*, \ \lambda = \ell_g/\ell_*, \ \chi = z_f/\ell_* \qquad \text{(Eq. 6-19)}$$

From Figure 6-7, it can be seen that:

$$\chi = \eta + \lambda \qquad \text{(Eq. 6-20)}$$

Using Equations 6-17 through 6-19, the system of equations governing the variables $\Omega(\zeta, \tau)$, $\Pi(\zeta, \tau)$, $\Psi(\zeta, \tau)$, $\eta(\tau)$, and $\chi(\tau)$ becomes:

- Elasticity equation:

$$\Pi = \mathcal{G}_e \int_{\eta}^{\infty} M(\zeta, s) \frac{\partial \Omega}{\partial s} \mathrm{d}s \qquad \text{(Eq. 6-21)}$$

- Poiseuille's law:

$$\mathcal{G}_m \Psi = -\Omega^3 \left(\frac{\partial \Pi}{\partial \zeta} + \mathcal{G}_\gamma \right) \qquad \text{(Eq. 6-22)}$$

- Fluid continuity:

$$\mathcal{G}_w \frac{\partial \Omega}{\partial \tau} - \frac{\partial \Psi}{\partial \zeta} = 0 \qquad \text{(Eq. 6-23)}$$

- Fracture propagation criterion:

$$\Omega = \mathcal{G}_k \, (\zeta - \eta)^{1/2} \text{ as } \zeta \to \eta \qquad \text{(Eq. 6-24)}$$

- Boundary condition in the tip cavity:

$$\Pi = -\left(\mathcal{G}_s + \mathcal{G}_d \zeta \right), \ \eta < \zeta \leq \chi \qquad \text{(Eq. 6-25)}$$

- Boundary condition at the fluid front:

$$\mathcal{G}_m \mathcal{G}_w \dot{\chi} = \Omega^3 \left(\frac{\partial \Pi}{\partial \zeta} + \mathcal{G}_\gamma \right) \qquad \text{(Eq. 6-26)}$$

- Boundary condition at infinity:

$$\Psi = \mathcal{G}_q \text{ as } \zeta \to \infty \qquad \text{(Eq. 6-27)}$$

where the eight dimensionless groups $\mathcal{G}_e, \mathcal{G}_m, \mathcal{G}_\gamma, \mathcal{G}_w, \mathcal{G}_q, \mathcal{G}_k, \mathcal{G}_s, \mathcal{G}_d$ are defined as follows:

$$\mathcal{G}_e = \frac{E' w_*}{p_* l_*}, \ \mathcal{G}_m = \frac{\mu' q_* l_*}{w_*^3 p_*}, \ \mathcal{G}_\gamma = \frac{\delta' l_*}{p_*}, \ \mathcal{G}_w = \frac{w_* l_*}{t_* q_*}, \ \mathcal{G}_q = \frac{q_\infty}{q_*} \qquad \text{(Eq. 6-28)}$$

$$\mathcal{G}_k = \frac{K' \ell_*^{1/2}}{E' w_*}, \ \mathcal{G}_s = \frac{\sigma_c - p_{fo}}{p_*}, \ \mathcal{G}_d = \frac{\kappa \rho_r g \ell_*}{p_*} \qquad \text{(Eq. 6-29)}$$

The particular scaling used in this problem and, hence, the definitions of five characteristic quantities, ℓ_*, t_*, w_*, p_*, and q_*, are selected by setting the five dimensionless groups in Equation 6-28 all equal to one:

$$\mathcal{G}_e = \mathcal{G}_m = \mathcal{G}_\gamma = \mathcal{G}_w = \mathcal{G}_q = 1 \qquad \text{(Eq. 6-30)}$$

which sets the values of five characteristic quantities to:

$$\ell_* = \left(\frac{\mu' E'^3 q_\infty}{\delta'^4}\right)^{1/6},\ w_* = \left(\frac{\mu' q_\infty}{\delta'}\right)^{1/3},\ p_* = \left(\mu' E'^3 \delta'^2 q_\infty\right)^{1/6} \qquad \text{(Eq. 6-31)}$$

$$t_* = \left(\frac{\mu' E'}{\delta'^2 q_\infty}\right)^{1/2},\ q_* = q_\infty \qquad \text{(Eq. 6-32)}$$

with $\delta' = \left(\kappa\rho_r - \rho_f\right) g$. Finally, the three remaining dimensionless groups are renamed to:

$$\mathcal{G}_k \equiv \mathcal{K},\ \mathcal{G}_s \equiv \mathcal{S},\ \mathcal{G}_d \equiv \mathcal{D} \qquad \text{(Eq. 6-33)}$$

where $\mathcal{K}$ is a scaled toughness, $\mathcal{S}$ a scaled reference stress, and $\mathcal{D}$ a scaled relative host rock density:

$$\mathcal{K} = K'\left(\frac{1}{\mu' E'^3 q_\infty}\right)^{1/4},\ \mathcal{S} = \frac{\sigma_c - p_{fo}}{\left(\mu' E'^3 \delta'^2 q_\infty\right)^{1/6}},\ \mathcal{D} = \frac{\kappa\rho_r}{\kappa\rho_r - \rho_f} \qquad \text{(Eq. 6-34)}$$

This scaling is an extension of that used by Lister (1990 [DIRS 126877]) to solve the self-similar propagation of a dike, for the time-dependent case. This scaling collapses if $\delta' = 0$. In that case, an appropriate scaling would correspond to:

$$\mathcal{G}_e = \mathcal{G}_m = \mathcal{G}_d = \mathcal{G}_w = \mathcal{G}_q = 1,\ \text{when}\ \mathcal{G}_\gamma = 0 \qquad \text{(Eq. 6-35)}$$

from which new expressions for ℓ_*, t_*, w_*, p_*, and q_* can be derived:

$$l_* = \left(\frac{\mu'\, E'^3\, q_\infty}{g^4\, \kappa^4\, {\rho_r}^4}\right)^{\frac{1}{6}},\ w_* = \left(\frac{\mu'\, q_\infty}{g\, \kappa\, \rho_r}\right)^{\frac{1}{3}},\ p_* = \left(\mu'\, E'^3\, q_\infty\, g^2\, \kappa^2\, {\rho_r}^2\right)^{\frac{1}{6}} \qquad \text{(Eq. 6-36)}$$

$$t_* = \left(\frac{\mu'\, E'}{q_\infty\, g^2\, \kappa^2\, {\rho_r}^2}\right),\ q_* = q_\infty \qquad \text{(Eq. 6-37)}$$

In summary, the set of scaled governing equations can be written as:

$$\Pi(z,t) = \int_{\eta(t)}^{\infty} ds\ M(\zeta, s)\frac{\partial\Omega(s,t)}{\partial s},\ \Psi = -\Omega^3\left(\frac{\partial\Pi}{\partial\zeta} + 1\right),\ \frac{\partial\Omega}{\partial\tau} - \frac{\partial\Psi}{\partial\zeta} = 0 \qquad \text{(Eq. 6-38)}$$

with the propagation criterion and the conditions in the lag zone, at the fluid front, and at infinity given by Equations 6-39 to 6-42, respectively:

$$\Omega = \mathcal{K}\,(\zeta - \eta)^{1/2}\,,\ \zeta \to \eta \qquad \text{(Eq. 6-39)}$$

$$\Pi = -\,(\mathcal{S} + \mathcal{D}\zeta)\,,\ \eta < \zeta \le \chi \qquad \text{(Eq. 6-40)}$$

$$\dot{\chi} = \Omega^2 \left(\frac{\partial \Pi}{\partial \zeta} + 1\right),\ \zeta = \chi \qquad \text{(Eq. 6-41)}$$

$$\Psi = 1,\ \zeta \to \infty \qquad \text{(Eq. 6-42)}$$

The system of equations (Equations 6-38 to 6-42) is closed in the sense that it can be used to determine the solution $\mathcal{F}(\zeta, \tau; \mathcal{K}, \mathcal{S}, \mathcal{D})$ where $\mathcal{F} = \{\Omega, \Pi, \Psi, \eta, \chi\}$, given a suitable set of initial conditions.

The dependence of the solution on time arises through the boundary conditions in the tip cavity (which is changing with the depth η) and through the elastic kernel, which accounts for the distance to the free surface. The dependence on time, τ, can then be replaced by a dependence on the depth η, once the solution has been determined for $\eta = \eta(\tau)$. Thus, the solution can be expressed as $\bar{\mathcal{F}}(\zeta, \eta; \mathcal{K}, \mathcal{S}, \mathcal{D})$ with $\bar{\mathcal{F}} = \{\bar{\Omega}, \bar{\Pi}, \bar{\Psi}, \bar{\lambda}\}$. The overbar denotes that the field quantities depend on η instead of the time as the dependent variable.

6.3.3.1.3 Simplifications in the Case of the Dike Problem

It has been noted by various authors that rock toughness in the case of dike propagation through the Earth's crust often is not relevant, as $\mathcal{K} \ll 1$ (Spence and Turcotte 1985 [DIRS 127068]; Lister and Kerr 1991 [DIRS 126889]; Rubin 1995 [DIRS 164118]). Also, the case $\mathcal{S} = 0$ is an appropriate case. In other words, the particular solution $\mathcal{K} = \mathcal{S} = 0$ is very relevant. This solution is denoted by $\mathcal{F}_o(\zeta, \tau; \mathcal{D})$ or by $\bar{\mathcal{F}}_o(\hat{\xi}, \eta; \mathcal{D})$; it only depends on parameter $\mathcal{D}$. Because $\mathcal{K} = 0$, aperture Ω behaves at the dike tip according to Rice (1968 [DIRS 164405]):

$$\Omega \sim (\zeta - \eta)^{3/2}, \quad \zeta \to \eta \qquad \text{(Eq. 6-43)}$$

where the coefficient of proportionality is unknown *a priori*, as it is part of the solution. For this case, the condition of zero toughness is best imposed by:

$$\int_{\eta}^{\infty} \frac{\Pi(s)}{s^{1/2}}\,\mathrm{d}s = 0 \qquad \text{(Eq. 6-44)}$$

which uses the integral representation of the stress intensity factor. Note that the particular asymptotic behavior (Equation 6-43) is based on λ being not very small. (The term in $(\zeta - \eta)^{3/2}$ actually corresponds to the next term of the fracture opening expansion when $\mathcal{K} > 0$, according to LEFM.) When $\lambda \ll 1$, the behavior (Equation 6-43) takes place over a region so small that it is not visible in this scaling. Under these conditions, an intermediate asymptote develops:

$$\Omega \sim (\zeta - \eta)^{2/3}, \quad \zeta \to \eta \tag{Eq. 6-45}$$

(See Section 6.4.3.5 for a discussion of cases characterized by small tip cavities.)

It can be readily shown (as recognized by Lister 1990 [DIRS 126877] for the self-similar case) that the solution behaves at infinity as follows:

$$\Omega = 1, \ \Pi = \frac{1}{4\pi\zeta}, \ \zeta \to \infty \tag{Eq. 6-46}$$

The first of these equations implies that $w_\infty = w_*$.

The average scaled fluid velocity, Υ, is also found to be:

$$\Upsilon \equiv \Psi/\Omega = 1, \ \zeta \to \infty \tag{Eq. 6-47}$$

In dimensional terms, the average fluid velocity at infinity, v_∞, is given as:

$$v_\infty \equiv \frac{q_\infty}{w_\infty} = \frac{q_\infty}{w_*} = \left(\frac{\delta' q_\infty^2}{\mu'}\right)^{1/3} \tag{Eq. 6-48}$$

Actually, it is convenient to formulate the boundary conditions at infinity in terms of v_∞, rather than q_∞; hence, the characteristic quantities can be formulated as follows:

$$\ell_* = \left(\frac{\mu' E'^2 v_\infty}{\delta'^3}\right)^{1/4}, \ w_* = \left(\frac{\mu' v_\infty}{\delta'}\right)^{1/2}, \ p_* = \left(\mu' E'^2 \delta' v_\infty\right)^{1/4} \tag{Eq. 6-49}$$

$$t_* = \frac{\ell_*}{v_\infty}, \ q_* = v_\infty w_*$$

and the dimensionless groups become:

$$\mathcal{K} = K' \left(\frac{\delta'}{\mu'^3 E'^6 v_\infty^3}\right)^{1/8}, \ \mathcal{S} = \frac{\sigma_c - p_{f0}}{\left(\mu' E'^2 \delta' v_\infty\right)^{1/4}} \tag{Eq. 6-50}$$

with $\mathcal{D}$ remaining unchanged.

As is discussed in Section 6.3.6, boundary conditions for dike propagation are not given as a rate of magma influx at infinity, q_∞, but in terms of a dike opening at infinity, w_∞, and the dike velocity at infinity, v_∞. Therefore, it is more convenient to express scaling quantities and

dimensionless groups in terms of the dike opening and the dike velocity at infinity (i.e., at a large distance from the dike tip). Using Equation 6-48 and the second line of Equation 6-49 with $w_* = w_\infty$, the scaling quantities can be written as:

$$l_* = \left(\frac{E' w_\infty^3}{\mu' v_\infty}\right)^{1/2}, \; w_* = w_\infty, \; p_* = \left(\frac{\mu' E' v_\infty}{w_\infty}\right)^{1/2} \quad \text{(Eq. 6-51)}$$

$$t_* = \left(\frac{E'^2 w_\infty^3}{\mu'^2 v_\infty^3}\right), \quad q_* = w_\infty v_\infty \quad \text{(Eq. 6-52)}$$

and the dimensionless groups become:

$$\mathcal{K} = K' \left(\frac{1}{\mu' E'^3 v_\infty w_\infty}\right)^{1/4}, \; \mathcal{S} = \frac{\sigma_c - p_{f_0}}{\left(\mu' E' v_\infty / w_\infty\right)^{1/2}}, \; \mathcal{D} = \frac{\kappa \rho_r g {w_\infty}^2}{\mu' v_\infty} \quad \text{(Eq. 6-53)}$$

6.3.3.1.4 Self-Similar Problem of a Deep Dike

Formulation of the deep dike problem solved by Lister (1990 [DIRS 126877]) can be deduced from the more general equations derived in the previous subsections of this section. First, the equations are reformulated in terms of the moving coordinate $\hat{\xi} = \zeta - \eta$. The solution is now of the form $\hat{\mathcal{F}}(\hat{\xi}, \tau; \mathcal{K}, \mathcal{S}, \mathcal{D})$ where $\hat{\mathcal{F}} = \{\hat{\Omega}, \hat{\Pi}, \hat{\Psi}, \eta, \lambda\}$. The spatial and time derivative transform as:

$$\frac{\partial}{\partial \zeta} = \frac{\partial}{\partial \hat{\xi}}, \; \left.\frac{\partial}{\partial \tau}\right|_\zeta = \left.\frac{D}{D\tau}\right|_{\hat{\xi}} - \dot{\eta}\frac{\partial}{\partial \hat{\xi}} \quad \text{(Eq. 6-54)}$$

In summary, the set of governing equations can be written as:

$$\hat{\Pi} = \int_0^\infty \hat{M}(\hat{\xi}, \hat{s}; \eta) \frac{\partial \hat{\Omega}}{\partial \hat{s}} \mathrm{d}\hat{s}, \quad \hat{\Psi} = \hat{\Omega}^3 \left(\frac{\partial \hat{\Pi}}{\partial \hat{\xi}} + 1\right), \quad \frac{D\hat{\Omega}}{D\tau} - \dot{\eta}\frac{\partial \hat{\Omega}}{\partial \hat{\xi}} - \frac{\partial \hat{\Psi}}{\partial \hat{\xi}} = 0 \quad \text{(Eq. 6-55)}$$

where the elastic kernel $\hat{M}(\hat{\xi}, s; \eta)$ is now given by:

$$\hat{M}(\hat{\xi}, \hat{s}; \eta) = \hat{M}_\infty(\hat{\xi}, \hat{s}) - \frac{1}{4\pi\left(\hat{\xi} + \hat{s} + 2\eta\right)} - \frac{2(\hat{s} + \eta)}{4\pi\left(\hat{\xi} + \hat{s} + 2\eta\right)^2} + \frac{(4\hat{s} + \eta)^2}{4\pi\left(\hat{\xi} + \hat{s} + 2\eta\right)^3} \quad \text{(Eq. 6-56)}$$

with $M_\infty(z, s)$ denoting the Cauchy singular kernel for the infinite plane:

$$M_\infty(z, s) = \frac{1}{4\pi\left(\hat{\xi} - \hat{s}\right)} \quad \text{(Eq. 6-57)}$$

The propagation criterion and the conditions in the lag zone, at the fluid front and at infinity are given by Equations 6-58 to 6-61, respectively:

$$\hat{\Omega} = \mathcal{K}\hat{\xi}^{1/2},\ \hat{\xi} \to 0 \qquad \text{(Eq. 6-58)}$$

$$\hat{\Pi} = -\left[\mathcal{S} + \mathcal{D}\left(\hat{\xi} + \eta\right)\right],\ 0 < \hat{\xi} \leq \lambda \qquad \text{(Eq. 6-59)}$$

$$\dot{\eta} + \dot{\lambda} = -\Omega^2\left(\frac{\partial \Pi}{\partial \zeta} + 1\right),\ \zeta = \chi \qquad \text{(Eq. 6-60)}$$

$$\hat{\Psi} = 1,\ \zeta \to \infty \qquad \text{(Eq. 6-61)}$$

The equations of the problem solved by Lister (1990 [DIRS 126877]) can be deduced from the general system (Equations 6-55 through 6-61) if the dike is deep enough that the effect of the free surface is negligible and the solution is self-similar. It can be easily shown that self-similarity implies that the average magma velocity is constant along the dike and equal to the velocity of ascent of the dike. This approach implies, therefore, that:

$$\hat{M} = \hat{M}_\infty, \quad \frac{D\hat{\Omega}}{D\tau} = 0, \quad \dot{\lambda} = 0, \quad \dot{\eta} = -1 \qquad \text{(Eq. 6-62)}$$

The solution is now of the form $\hat{\mathcal{F}}_{ss}(\hat{\xi};\ \mathcal{K},\ \mathcal{S},\ \mathcal{D},\ \eta)$, where $\hat{\mathcal{F}}_{ss} = \{\hat{\Omega},\ \hat{\Pi},\ \hat{\Psi},\ \lambda\}$ and is governed by:

$$\hat{\Pi} = \int_0^\infty \hat{M}_\infty(\hat{\xi},\ \hat{s})\ \frac{\mathrm{d}\hat{\Omega}}{\mathrm{d}\hat{s}}\mathrm{d}\hat{s},\quad \hat{\Omega}^2\left(\frac{\mathrm{d}\hat{\Pi}}{\mathrm{d}\hat{\xi}} + 1\right) = 1 \qquad \text{(Eq. 6-63)}$$

and

$$\hat{\Omega} = \mathcal{K}\hat{\xi}^{1/2},\ \hat{\xi} \to 0;\ \hat{\Pi} = -\left[\mathcal{S} + \mathcal{D}\left(\hat{\xi} + \eta\right)\right],\ 0 < \hat{\xi} \leq \lambda;\ \hat{\Omega} = 1,\ \zeta \to \infty \qquad \text{(Eq. 6-64)}$$

Note, however, that a strictly self-similar solution does not exist, as depth η enters into the problem formulation via the boundary condition in the lag zone. Thus, within the approximation of self-similarity, the evolution problem is actually seen as a sequence of self-similar solutions.

Numerical solution of the system of equations (Equations 6-63 to 6-64) is given by Lister (1990 [DIRS 126877])[2]. This solution actually could be used as a suitable initial condition for the general problem—i.e.,

$$\mathcal{F}(\zeta - \eta_o, 0; \mathcal{K}, \mathcal{S}, \mathcal{D}, \eta) = \mathcal{F}_{ss}(\hat{\xi}; \mathcal{K}, \mathcal{S}, \mathcal{D}, \eta_o) \qquad \text{(Eq. 6-65)}$$

where $\eta_o \gg 1$. However, in practical terms, $\eta_o \simeq 2$, as the free-surface effect is negligible at those depths.

6.3.3.2 Uncertainties and Limitations

Uncertainties—Given that the dike propagation problem is relatively complex, any attempt at numerical modeling will have many embedded uncertainties. The approach taken in the base-case modeling is a two-dimensional model of a three-dimensional process. Because the large scale of a dike is very favorable for creating two-dimensional processes in the center of the dike, the effect of three-dimensional processes is not considered in this report.

Similar uncertainties exist with regard to fluid and rock properties. The modeling requires that the fluid be incompressible and the properties constant so that minimal differentiation (particularly vertically) within the magma is allowed except in the separate tip cavity. Clearly, there is also a large range of possible magma properties (viscosity and density) that could be employed, but evaluation of a range of conditions bounds the problem.

The boundary element approach also requires a constant material-property set for the host rock, so that no variation, either between layers or laterally, can be accommodated. Rather, a uniform, average condition is used in the calculation. This approach results in a model that does not account for stratigraphy. The effect of topography can be accounted for with respect to its effect on stress—which should be the dominating feature of topography—but other plausible effects (e.g., a modified free surface, rotation of the stress field) are so small that they need not be considered.

The dike propagation model is very flexible with respect to the far-field stress and either a density-defined stress field or an applied side load can be used. However, in the present model, the applied far-field stress affects only the condition of dike propagation. The stress gradient, which controls the magma pressure gradient, is defined by rock mass density and coefficient of lateral stress only. Consequently, magma buoyancy is independent of the applied far-field stress (e.g., repository-induced thermal stresses). Also, exact values for the stresses are based on only three stress measurements in the vicinity of Yucca Mountain (Stock et al. 1985 [DIRS 101027]) and on calculations of the stress field that might develop with heating of the repository (see Section 6.2.4).

For a large-scale dike, analysis of the important mechanisms suggests that the fracture criterion is immaterial for dike propagation. However, the application of LEFM principles to a problem of this scale has been questioned, and some other criterion could potentially be more appropriate.

[2] Lister uses $\hat{x}$, $\hat{h}$ and $\hat{p}$ to denote the characteristic quantities used to scale distance, dike width, and net pressure, respectively. These quantities are related to those defined here according to $\hat{x} = \ell_*/2$, $\hat{h} = w_*/2$, $\hat{p} = p_*/2$.

The LEFM approach was employed here, but elevated values of fracture toughness were considered to assess possible effects. Coupled with the fracture criterion is the pressure in the fluid-tip cavity. This pressure is controlled by the dike-fracture criterion, the permeability of the host rock, the pore pressure of the host rock, the exsolution of vapor from the magma, and the overall dike parameters. There is currently no method to calculate the tip-cavity pressure, so a range of values from atmospheric to considerably higher levels is employed.

Self-similar (far-field) conditions of dike ascent are defined by the dike aperture and magma velocity. The magma source is taken to be at a depth that is effectively equivalent to an infinite depth. The model allows only an injection-rate boundary condition at the source. It requires positive buoyancy of the magma to keep it moving vertically upward; otherwise, the magma will stagnate or form a sill. Ranges of magma density and the gradient of far-field stress were considered in the analysis.

Once the dike reaches the free surface, the calculations terminate. As a result, it is not possible to calculate any evolution of the conditions after intersection. Some speculations are offered about the continued development of the dike, but these are extrapolations of prior conditions.

Uncertainties in the future state, parameters, and processes are primarily those associated with the range of possible dike source conditions and magma properties. In situ stresses are not likely to change significantly except due to heating, which has already been accounted for using the thermo-mechanical response of the repository. Rock properties far from the repository drift will not change over this time frame, which is minute compared to usual geologic changes. The potential for changes in the rock properties adjacent to drifts has been addressed in *Drift Degradation Analysis* (BSC 2004 [DIRS 166107]). Thus, changes in magma outflow and viscosity are the most-likely variable properties. Because a range of these parameters is considered, it is expected that most future uncertainties have already been accounted for.

Limitations—The limitations of the dike propagation model are related to the simplifications discussed in Section 6.3.2. A limitation of the model is that the rock mass, which in reality is a heterogeneous, layered medium, is represented as homogeneous and isotropic. Another model limitation is that the actual ground surface topography cannot be represented. Instead, the ground surface is taken in the model to be planar. This is justified in Section 6.3.2.

A major limitation of the model is that it does not account for bulk density changes (compressibility) due to vesiculation of the magma, which is likely to occur as the magma rises above a depth of approximately 5 km (depending on the water content (SNL 2007 [DIRS 174260], Figure 6-4; Detournay et al. 2003 [DIRS 169660], Figure 2.1c) and could lead to density changes of a factor of two or more in the upper 2,000 m. To account for this, an approximation is developed in Section 6.3.8.2 to address the effect of magma compressibility.

An associated limitation of the model is that the rheology of the magma will be affected by the bubbles that form at less than 5 km depth (as described in the previous paragraph). At and below the magma front, the vapor fraction will be significant. The flow regimes for basaltic magma can be:

- Homogeneous with small, low Reynolds-number bubbles moving with the melt

- Bubbly flow with bubbles rising faster than the melt
- Slug flow with bubble sizes approaching the width of the dike (Vergniolle and Jaupart 1986 [DIRS 115585]).

Which flow regime is operative will be a function of many variables including, but not limited to, moisture content, other gases present, pressure, melt viscosity and surface tension. For example, as the magma first encounters a drift, it may do so under slug flow; as time progresses and the magma front continues up the dike, flow entering the drift may become bubbly. The viscosity of bubbly flow is very complicated and in certain cases will be non-Newtonian. This could include either shear thinning or shear thickening depending on the variables listed above (Detournay et al. 2003 [DIRS 169660], Appendix 2, p. 1, Figure 2B). Therefore, it is not possible to determine the effect of this uncertainty.

6.3.3.3 Model Inputs

The input data for the dike propagation model consist of formation (rock) properties, magma properties, boundary stresses, and dike parameters (Table 6-2). Those parameters derived from sources external to this document (direct input) are also listed in Table 4-1. Other values are included in Table 6-2 where data values have been selected from a range of data presented in the source cited, or are for illustrative purposes. The basis for selection of such values is discussed below. There are uncertainties in these parameters because of the scale of the calculations (several kilometers) and the possible changes in properties over such distances. Section 6.3.8.2 addresses the effects of expanding magma related to magma properties.

The ratio of horizontal stress to vertical stress (0.5) is calculated by dividing the horizontal stress by the vertical stress. The horizontal stress is taken as the average of two in situ stress measurements of the horizontal stress components at Borehole ESF-AOD-HFDR#1 (DTN: SNF37100195002.001 [DIRS 131356]). The vertical stress is calculated by summing the density of each overlying unit (DTN: MO0408MWDDDMIO.002 [DIRS 171483] multiplied by the thickness of that unit (DTN: MO0408MWDDDMIO.002 [DIRS 171483]) and multiplying the sum by the acceleration of gravity (Incropera and De Witt 2002 [DIRS 163337]). The thickness of the unit in which the measurements were made (17.8 m) is calculated by subtracting the elevation at which the measurement was made, which is assumed to be 1,033.3 m (SNL 1996 [DIRS 163645]), from the elevation of the top of unit Tptpll, which is 1,051.1 m according to DTN: MO0408MWDDDMIO.002[3] [DIRS 171483]. If the measurement location had been as high as the top of unit Tptpll, the vertical stress would be only 8% higher and the ratio would be 0.53 instead of 0.49. The larger number would round to the same input value of 0.5.

[3] The actual value is not in the source DTN (DTN: MO0408MWDDDMIO.002 [DIRS 171483]) but is calculated from the following values that are found there: 1,285.1 m (surface elevation) − 234.0 m (sum of all unit thicknesses above Tptpll) = 1,051.1 m.

Table 6-2. Inputs to Dike Propagation from Depth Model

Parameter	Value
Young's modulus of host rock (E) (Detournay et al. 2003 [DIRS 169660], Table 1-2)	15 GPa
Poisson's ratio of host rock (ν) (Detournay et al. 2003 [DIRS 169660], Table 1-2)	0.21
Density of host rock (ρ_r) (DTN: SNL02030193001.027 [DIRS 108410])	2,400 kg m^3
Toughness of host rock (K_{Ic}) (Detournay et al. 2003 [DIRS 169660], Table 1-2)	0.3 MPa-$m^{1/2}$
Magma density (ρ_f) (Detournay et al. 2003 [DIRS 169660], Figure 2-1e)	751 kg m^3 to 2,282 kg m^3
Magma viscosity (μ) (Detournay et al. 2003 [DIRS 169660], Figure 2-1e)	10 Pa·s to 40 Pa·s
Gravitational acceleration (g) (Incropera and DeWitt 2002 [DIRS 163337])	9.81 m/s^2
Horizontal stress components at Borehole ESF-AOD-HFDR#1 (DTN: SNF37100195002.001 [DIRS 131356])	2.9 MPa, 1.7 MPa
Density and thickness of each overlying unit (DTN: MO0408MWDDDMIO.002 [DIRS 171483])	Various
Elevation of the surface (DTN: MO0408MWDDDMIO.002 ([DIRS 171483])	1,285.1 m
Assumed Values	
Repository depth	300 m
Elevation at which the measurement was made	1,033.3 m
Ratio of minimum principal stress to vertical stress in host rock (κ) (coefficient of horizontal stress)	1.0
Pressure in dike tip (p_{f0})	0.0 MPa to 0.49 MPa
Far-field magma velocity (v_∞)	1 m/s to 15 m/s

The formation properties (those of the repository host rock) include Young's modulus, Poisson's ratio, and density, which have been measured and are available as qualified data. A fourth parameter, fracture toughness, has not been specifically measured for the repository. This lack is not a problem since fracture toughness is irrelevant at this scale because the rocks are already highly fractured prior to arrival of the crack tip and dike, and ascent of the dike is, therefore, accommodated by slip along these preexisting fracture surfaces (Rubin 1995 [DIRS 164118], p. 321; Rubin and Gillard 1998 [DIRS 169786], pp. 10,017 and 10,026; Rubin et al. 1998 [DIRS 169787], p. 10,011). In the analysis reported here, fracture toughness is treated as a parameter that is always small but may span a few orders of magnitude to account for non-ideal processes that may be associated with dike propagation.

Considering the scale (kilometers) of the analyzed problem and the fact that the main objective of the analysis is to describe phenomena associated with dike propagation in the vicinity of the repository, elastic properties (Young's modulus of 15 GPa and Poisson's ratio of 0.21) were selected to be representative of Topopah Spring thermo-mechanical units TSw1 and TSw2 (Detournay et al. 2003 [DIRS 169660], Table 1-2). The input value for density of rock mass (2400 kg m^3) was selected as representative of the saturated density of the Topopah Spring lower

nonlithophysal unit, Tptpln (DTN: SNL02030193001.027 [DIRS 108410]). Because the results can be rescaled for other formation property values, the exact values used in the inputs do not seriously constrain the applicability of the results.

The input magma properties are density and viscosity. Magma density varies depending on composition of magma but is also a function of depth (i.e., pressure). A range of magma densities between 751 kg m^3 and 2,282 kg m^3 was considered in the analysis. This range is derived from Detournay et al. (2003 [DIRS 169660], Figure 2-1e). Magma viscosity is a complicated function of composition (both silicate and volatile), temperature, and pressure. Many of the calculations used in this model are for magmas less dense than 1,300 kg m^3, which consist of more than 50% by volume gas. The viscosity of such a mixture is uncertain, so a viscosity range of 10 Pa·s to 40 Pa·s, equivalent to the pure silicate liquid, is used. The range of viscosities used in the analysis is derived from work by Detournay et al. (2003 [DIRS 169660], Figure 2-1e). Most of the results in this report are for a viscosity of 10 Pa·s, representing a fluid magma that would quickly fill the drifts. Some supplementary results for 40 Pa·s were also calculated.

The data range used for pressure in the dike tip is defined based on scaling calculations discussed further in Section 6.3.7.2. Results are derived from far-field magma velocity of 1, 5, 10, and 15 m/s to illustrate the effect of this variable.

Another input parameter is the far-field magma flux, q_∞. The far-field dike width is calculated from q_∞, the formation properties, and the magma properties.

The boundary stresses include the overburden stress, which is obtained by integrating the density of the overlying rock, and the distribution of the minimum principal horizontal in situ stress (against which the dike must open). The NPHF2D code uses the relation $\kappa = \nu/(1-\nu)$ from linear elastic theory. In order to obtain values of minimum principal horizontal stress consistent with stress measurements at Yucca Mountain for in situ conditions and consistent with the host rock density of 2,400 kg m^3 and Poisson's ratio of 0.21 in Table 6-2, the value of rock density input to the code was set artificially to the value of 9,022 kg m^3; the magnitude of this input number has no other effect on the calculation because inertial forces are neglected. The height of the overburden varies between 250 m and 400 m (BSC 2004 [DIRS 170029]). The depth to the repository horizon was assumed to be 300 m based on values from *Geologic Framework Model (GFM2000)* (BSC 2004 [DIRS 170029]).

In situ stress measurements (DTN: SNF37100195002.001 [DIRS 131356]) show that the ratio of the minor horizontal principal stress to the vertical stress is 0.361 and the ratio of the major horizontal principal stress to the vertical stress is 0.617. The ratio of the horizontal stress normal to the dike to the vertical stress (called the coefficient of horizontal stress) was set to 0.5 for the base model, approximating the average of those two values, with an assumed value of 1.0 being used to demonstrate the effect of this variable on the solution.

6.3.3.3.1 Boundary and Initial Conditions

The initial and boundary conditions required for analysis of fluid-driven fractures, in addition to the in situ stress state, are the initial depth of the fracture tip and the flow rate at the starting point of the fracture. The magma injection rate at the source depth may be cast in terms of the far-field magma velocity and the far-field dike width. However, on average, according to field observations (Rubin 1995 [DIRS 164118]), the dike openings are in a range between 0.1 m and 10 m. The range of far-field magma velocity for dike widths of 0.5 m, 1.5 m, and 4.5 m, calculated according to *Characterize Eruptive Processes at Yucca Mountain, Nevada* (SNL 2007 [DIRS 174260], Table 6-4), is 1, 5, and 12 m/s, respectively, if the buoyancy is 50 kg m^3.

It was shown in Section 6.3.3.3 and in Lister's study (1990 [DIRS 126865]) that, for the case of a semi-infinite dike, the dike opening and magma velocity at large distances from the dike tip are:

$$w_\infty = \left(\frac{\mu' q_\infty}{\delta'}\right)^{1/3} \quad \text{(Eq. 6-66)}$$

$$v_\infty = \left(\frac{\delta' q_\infty^2}{\mu'}\right)^{1/3} \quad \text{(Eq. 6-67)}$$

Combining relations from Equation 6-66 and Equation 6-67, the expression in Equation 6-68 is obtained:

$$v_\infty = \frac{\delta'}{\mu'} w_\infty^2 \quad \text{(Eq. 6-68)}$$

Equation 6-68 is plotted in Figure 6-8 for different values of the ratio $\delta'/\mu' \equiv (\kappa\rho_r - \rho_f)\, g/12\mu$. Using the plot in Figure 6-8, it is possible to select the far-field dike opening, w_∞, and far-field dike ascent velocity, v_∞, as function of controlling parameters, $\kappa\rho_r - \rho_f$ and μ. (At sufficient depth, the dike propagates as self-similar (Lister 1990 [DIRS 126877]). One of consequences of self-similarity is that the dike tip velocity, magma front velocity, and magma velocity are the same.) The range of velocities, v_∞, used in this simulation is taken to be from 1.0 to 15.0 m/s, covering the range calculated above. The range of values used for the far-field dike widths, w_∞, was from 0.12 m to 3.5 m. These parameters give a range of far-field injection rates, q_∞, from 0.12 m^2/s to 53 m^2/s.

The boundary conditions associated with the medium include the horizontal principal minimum in situ stress and overburden stress acting within the formation.

6.3.3.4 Model Results

In this model, the problem of dike propagation is calculated in dimensional form using the relations in Section 6.3.3.1; the results are then reformulated in dimensionless form, as is described in Section 6.3.3.2. The host rock density and magma density are combined into a dimensionless group called relative density, $\mathcal{D}$. Confining stress, pressure in the crack tip, magma viscosity, magma density, Young's modulus, Poisson's ratio, density of the host rock,

gravitational acceleration, and the magma supply rate are combined to form a dimensionless group called reference stress, $\mathcal{S}$. A third dimensionless group, called toughness, $\mathcal{K}$, is formed from the fracture toughness of the host rock, the elastic properties of the host rock, the magma viscosity, and the magma supply rate. Conditions of dike ascent are calculated from the values of these dimensionless groups, not directly from the dimensional parameters listed here as input. Complete results are found in output DTN: SN0304T0504203.001. These results are rescaled and plotted in output DTN: MO0408EG831811.004.

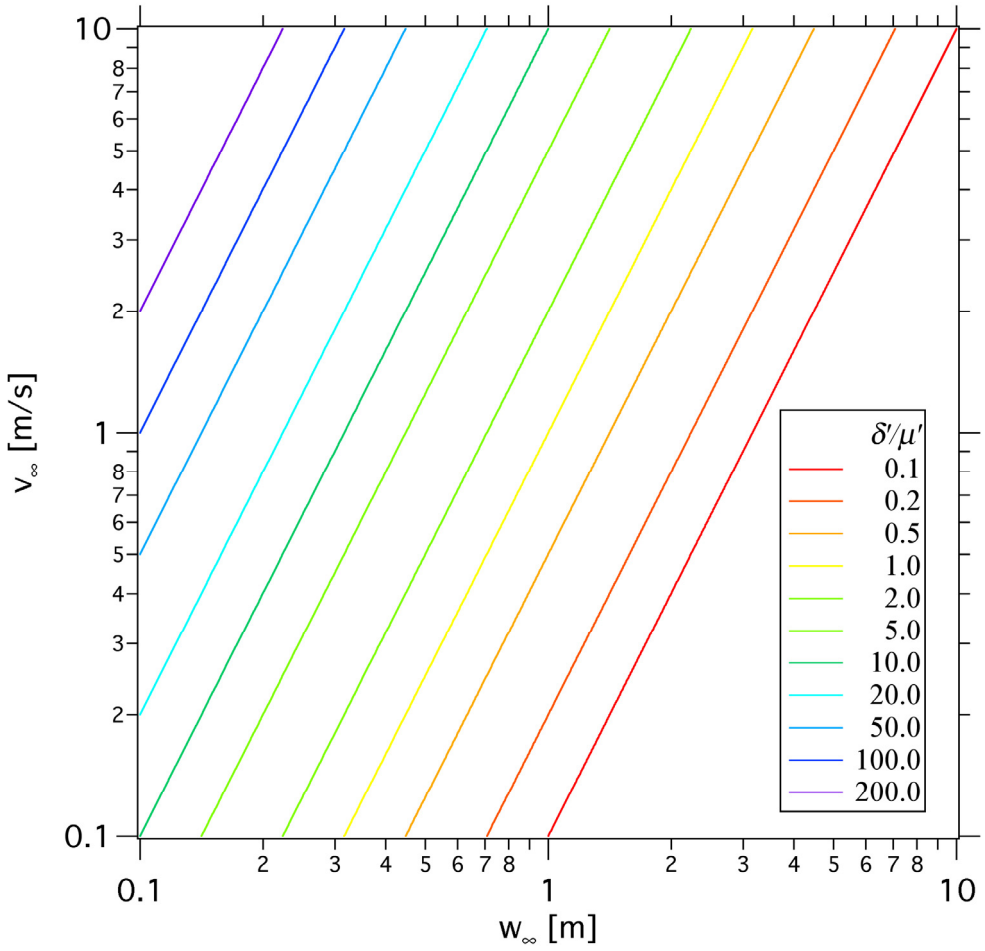

Source: For information only.

Figure 6-8. Relation between Far-Field Fluid Velocity and Far-Field Dike Opening from Equation 6-68

Results using a range of relative densities, $\mathcal{D}$, set to 2.67, 6.02, and 20.28 and reference stresses, $\mathcal{S}$, between –0.25 and 0.0 are given in this model report. A single value of toughness, $\mathcal{K}$, equal to 3.7×10^{-3} (corresponding to a host rock fracture toughness of 0.3 MPa·m$^{1/2}$) was used for all calculations that are discussed in detail, except that one calculation with a toughness of 0.37 was done, which demonstrated that the results are insensitive to values of this parameter.

The dimensionless fracture toughness for the range of mechanical parameters representative of the Yucca Mountain site has $\mathcal{K} \ll 1$. Consequently, if there is no leak-off into the repository, the problem solution is a function of two parameters only: $\mathcal{S}$ and $\mathcal{D}$.

The problem is solved first for the base case, in Section 6.3.4.4.1, with conditions of atmospheric pressure inside the tip cavity, $p_{fo} = 0$, and constant, far-field horizontal stress equal to zero, $\sigma_c = 0$. Under these conditions, $\mathcal{S} = 0$. The base case corresponds to the in situ conditions, unaffected by the repository (i.e., there is no increase in the horizontal stresses due to heating or leak-off into the repository drifts). Also, by considering the diffusivity of the gas in the rock formations (on the order of 10^{-12} m^2/s, according to Detournay et al. 2003 [DIRS 169660]), the assumption of atmospheric gas pressure inside the tip cavity, as in the base case described in Section 6.3.3.4.1, appears to be realistic. However, the problem was also analyzed for $\mathcal{S} < 0$, to investigate the effects of gas pressure inside the tip cavity in Section 6.3.4.4.2. Increased horizontal stresses due to repository heating, giving $\mathcal{S} > 0$, are addressed separately in Section 6.3.7 using a different numerical approach.

6.3.3.4.1 Base Case

Dimensionless results for $\mathcal{S} = 0$ and three values of $\mathcal{D}$ (2.67, 6.02 and 20.28) are shown in Figure 6-9. From these three dimensionless solutions, dimensional solutions are derived for various combinations of parameters: two effective rock mass densities $\kappa\rho_r$ (i.e., rock density multiplied by the horizontal stress coefficient), four magma velocities v_∞, and two magma viscosities μ. Derived parameters for each value of $\mathcal{D}$ and for a number of parameter combinations are shown in Table 6-3. The selected range of $\mathcal{D}$ covers the expected range of variation of $\kappa\rho_r - \rho_f$. The calculated value of Reynolds number is shown in the right-hand column; only three cases (shaded and in italics) fail to meet the criterion for laminar flow (Assumption 8, Section 6.3.2). Two others (shaded but not italicized) come within 10% of the turbulent limit. The curves shown in Figure 6-9 confirm that the solution is independent of $\mathcal{D}$ until the tip cavity develops (Zhang et al. 2002 [DIRS 164368]). As can be expected intuitively, the tip cavity forms earlier for smaller values of $\mathcal{D}$. For large values of $\mathcal{D}$, (i.e., $\mathcal{D} \sim O(10)$), the tip cavity forms "close" to the ground surface.

The dimensionless results from Figure 6-9 are rescaled using the relations from Section 6.3.3.2 to provide the results in dimensional form, assuming different values of v_∞. The positions of the dike tip and the fluid front as functions of time are shown in Figures 6-10 through 6-17.

For each value of $\mathcal{D}$, results are presented for two values for $\kappa\rho_r$: 2,400 and 1,200 kg m^3. The value of $\kappa\rho_r$ equal to 2,400 kg m^3 represents the case of a hydrostatic in situ stress state, in which the horizontal stress at the repository level (i.e., 300 m below the ground surface) would be 7.2 MPa. Measurements (DTN: SNF37100195002.001 [DIRS 131356]) at the site and knowledge of the regional stress state indicate that horizontal stress at the repository level is in the range of 3.5 MPa (i.e., κ is close to 0.5 for ρ_r = 2,400 g/m^3). Therefore, $\kappa\rho_r$ equal to 1,200 kg m^3 seems to be a better representation of the in situ stress state at Yucca Mountain.

The results are shown for four velocities, v_∞= 1, 5, 10 and 15 m/s. Corresponding dike openings, w_∞, were calculated from the condition that $\mathcal{D}$ remains invariant (Equation 6-53).

Most of the results were generated for magma viscosity equal to 10 Pa·s, with some results for a viscosity of 40 Pa·s, (Figures 6-16 and 6-17) resulting in wider dike apertures.

Table 6-3. Independent and Derived Parameters for Base-Case Simulations

Independent Parameters					Derived Parameters				
$\mathcal{D}$	v_∞ (m/s)	μ (Pa·s)	κ	$\kappa\rho_r$ (kg m^3)	ρ_f (kg m^3)	$\kappa\rho_r - \rho_f$ (kg m^3)	w_∞ (m)	q_∞ (m^2/s)	Reynolds number
2.67	15	10	1.0	2,400	1,501	899	0.452	6.78	1,018
2.67	10	10	1.0	2,400	1,501	899	0.369	3.69	554
2.67	5	10	1.0	2,400	1,501	899	0.261	1.30	196
2.67	1	10	1.0	2,400	1,501	899	0.117	0.12	18
6.02	15	10	1.0	2,400	2,001	399	0.678	10.18	2,035
6.02	10	10	1.0	2,400	2,001	399	0.554	5.54	1,109
6.02	5	10	1.0	2,400	2,001	399	0.392	1.96	392
6.02	1	10	1.0	2,400	2,001	399	0.175	0.18	35
20.28	15	10	1.0	2,400	2,282	118	1.245	18.68	4,262
20.28	10	10	1.0	2,400	2,282	118	1.017	10.17	2,321
20.28	5	10	1.0	2,400	2,282	118	0.719	3.59	820
20.28	1	10	1.0	2,400	2,282	118	0.322	0.32	73
20.28	15	40	1.0	2,400	2,282	118	2.490	37.35	2,131
20.28	10	40	1.0	2,400	2,282	118	2.033	20.33	1,160
20.28	5	40	1.0	2,400	2,282	118	1.438	7.19	410
20.28	1	40	1.0	2,400	2,282	118	0.643	0.64	37
2.67	15	10	0.5	1,200	751	449	0.639	9.58	720
2.67	10	10	0.5	1,200	751	449	0.522	5.22	392
2.67	5	10	0.5	1,200	751	449	0.369	1.84	139
2.67	1	10	0.5	1,200	751	449	0.165	0.16	12
6.02	15	10	0.5	1,200	1,001	199	0.959	14.39	1,440
6.02	10	10	0.5	1,200	1,001	199	0.783	7.83	784
6.02	5	10	0.5	1,200	1,001	199	0.554	2.77	277
6.02	1	10	0.5	1,200	1,001	199	0.248	0.25	25
20.28	15	10	0.5	1,200	1,141	59	1.761	26.41	3,014
20.28	10	10	0.5	1,200	1,141	59	1.438	14.38	1,641
20.28	5	10	0.5	1,200	1,141	59	1.017	5.08	580
20.28	1	10	0.5	1,200	1,141	59	0.455	0.45	52
20.28	15	40	0.5	1,200	1,141	59	3.522	52.83	1,507
20.28	10	40	0.5	1,200	1,141	59	2.876	28.76	820
20.28	5	40	0.5	1,200	1,141	59	2.033	10.17	290
20.28	1	40	0.5	1,200	1,141	59	0.909	0.91	26

Source: For illustrative purposes only.

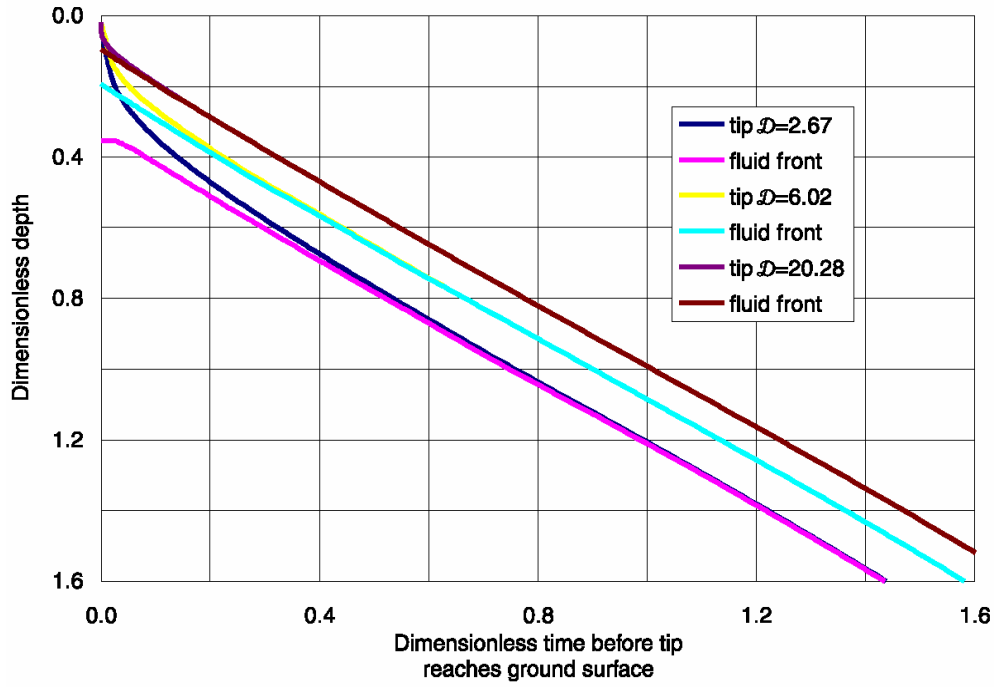

Output DTN: MO0408EG831811.004; file *Fig. 6-10 & 6-11.xls*, tab "c nondim positions summary."

Source: Output data calculation plots.

Figure 6-9. Dimensionless Solution for Dike Tip and Fluid Front as Functions of Time

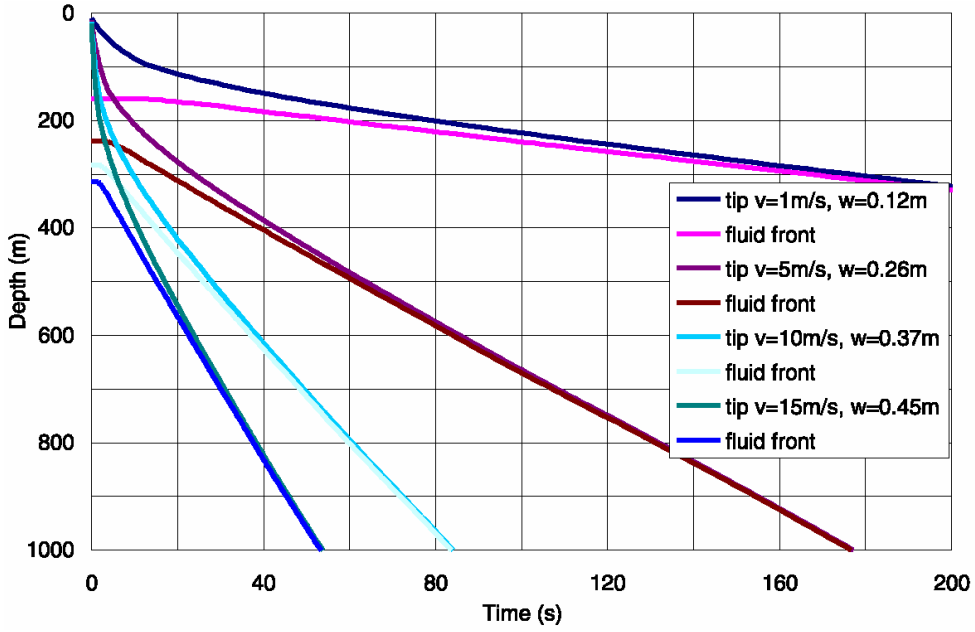

Output DTN: MO0408EG831811.004; file *Fig. 6-10 & 6-11.xls*, tab "c dim positions."

Source: Output data calculation plots.

NOTE: $\mathcal{D}$ = 2.67, $\kappa\rho_r$ = 2,400 kg m^3, μ = 10 Pa·s.

Figure 6-10. Dike Tip and Fluid Front as Functions of Time

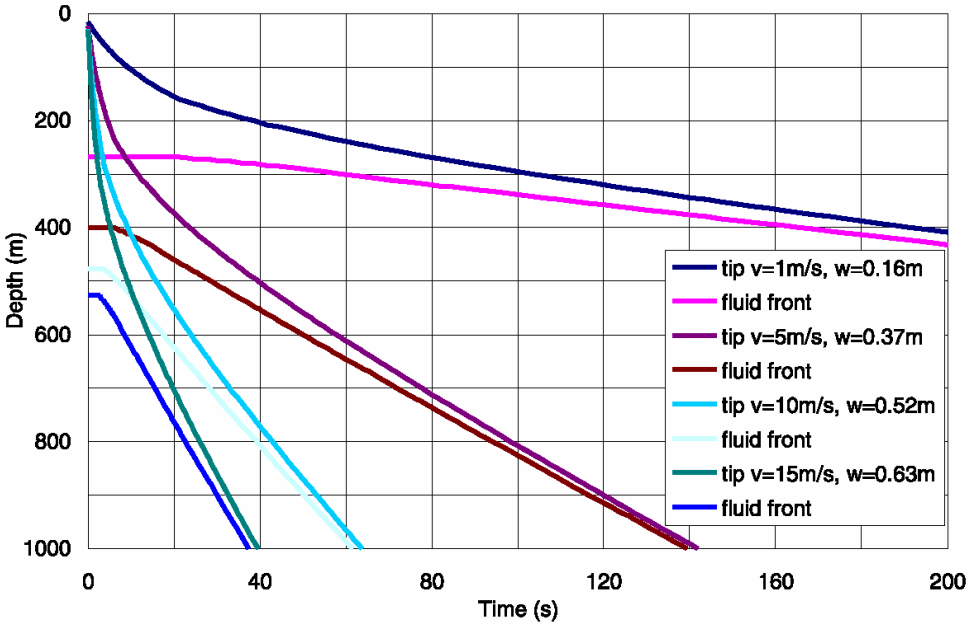

Output DTN: MO0408EG831811.004; file *Fig. 6-10 & 6-12.xls*, tab "c dim positions."

Source: Output data calculation plots.

NOTE: $\mathcal{D}$ = 2.67, $\kappa\rho_r$ = 1,200 kg m^3, μ = 10 Pa·s.

Figure 6-11. Dike Tip and Fluid Front as Functions of Time

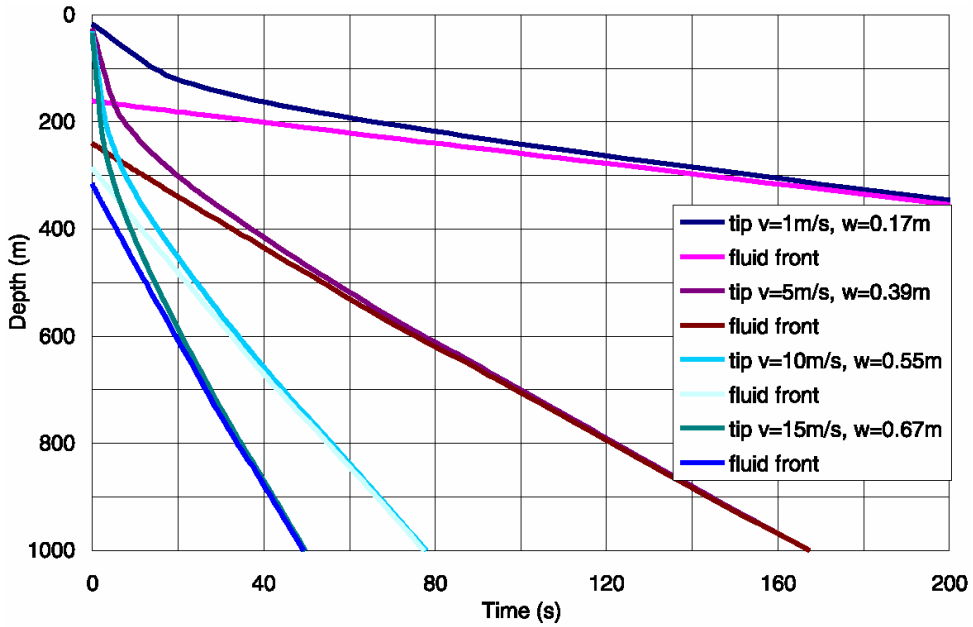

Output DTN: MO0408EG831811.004; file: *Fig. 6-13.xls*, tab: "c dim positions."

Source: Output data calculation plots.

NOTE: $\mathcal{D}$ = 6.02, $\kappa\rho_r$ = 2,400 kg m^3, μ = 10 Pa·s.

Figure 6-12. Dike Tip and Fluid Front as Functions of Time

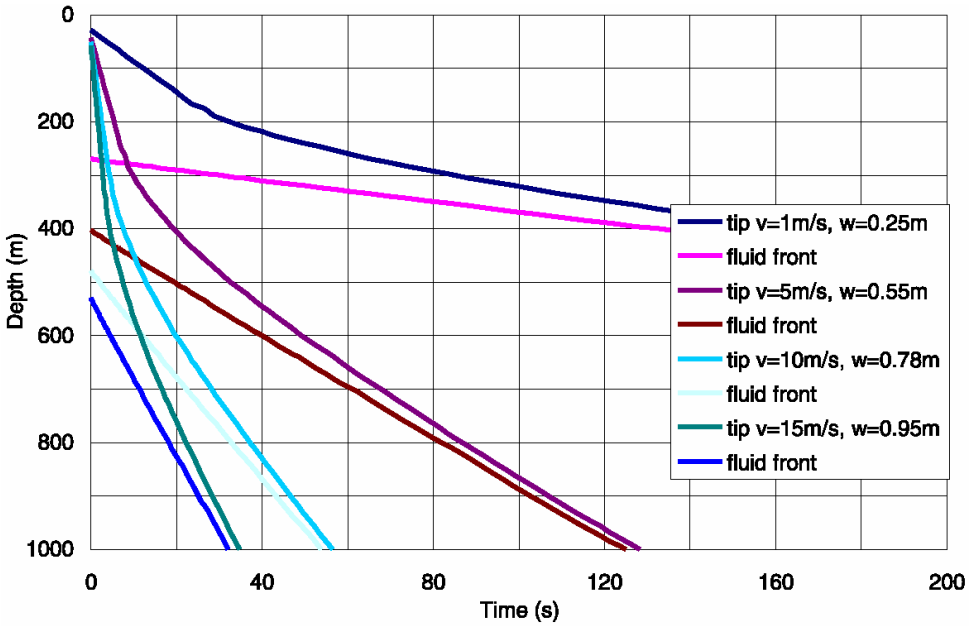

Output DTN: MO0408EG831811.004; file *Fig. 6-14.xls*, tab "c dim positions."

Source: Output data calculation plots.

NOTE: $\mathcal{D}$ = 6.02, $\kappa\rho_r$ = 1,200 kg m^3, μ = 10 Pa·s.

Figure 6-13. Dike Tip and Fluid Front as Functions of Time

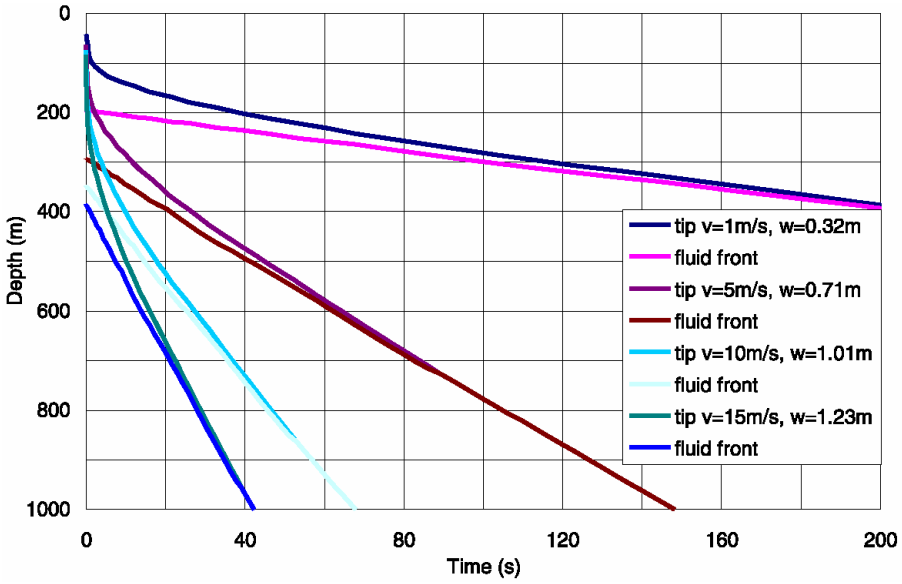

Output DTN: MO0408EG831811.004; file *Fig. 6-15.xls*, tab "c dim positions."

Source: Output data calculation plots.

NOTES: Flow parameters for v=10 m/s, 15 m/s indicate nonlaminar flow.
$\mathcal{D}$ = 20.28, $\kappa\rho_r$ = 2,400 kg m^3, μ = 10 Pa·s.

Figure 6-14. Dike Tip and Fluid Front as Functions of Time

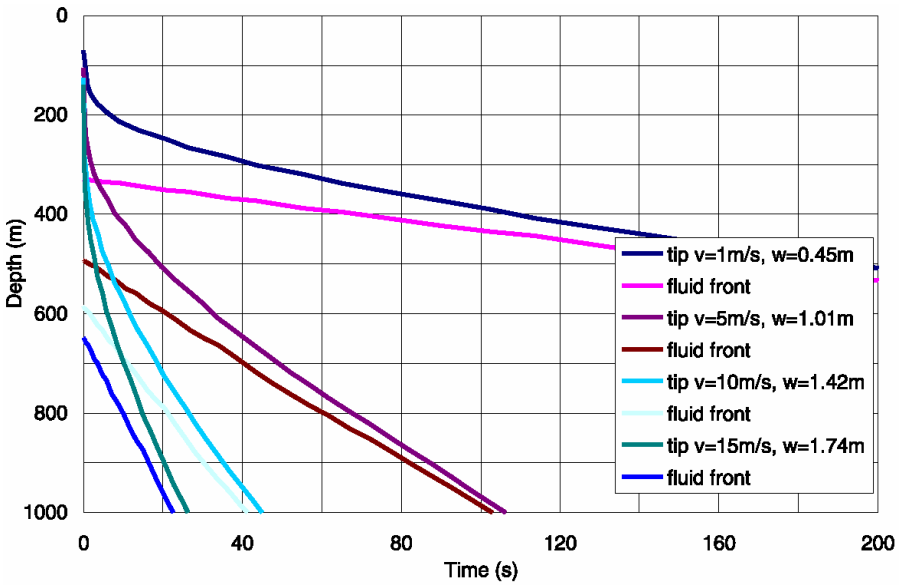

Output DTN: MO0408EG831811.004; file: *Fig. 6-16.xls*, tab: "c dim positions."

Source: Output data calculation plots.

NOTES: Flow parameters for v=15 m/s indicate nonlaminar flow.
$\mathcal{D}$= 20.28, $\kappa\rho_r$= 1,200 kg m^3, μ = 10 Pa·s.

Figure 6-15. Dike Tip and Fluid Front as Functions of Time

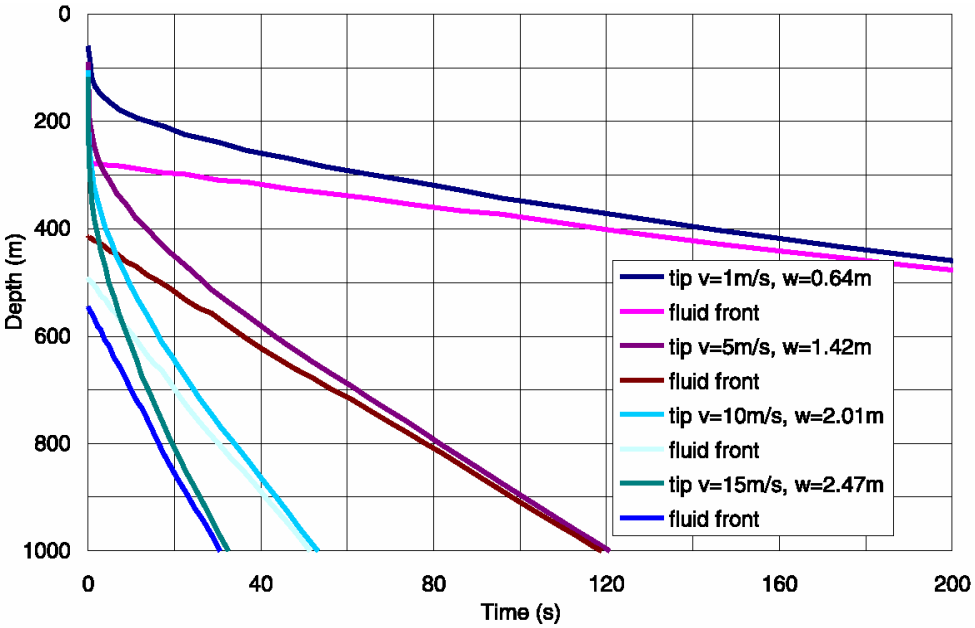

Output DTN: MO0408EG831811.004; file: *Fig. 6-17.xls*, tab: "c dim positions."

Source: Output data calculation plots.

NOTES: Flow parameters for v=15 m/s indicate nonlaminar flow.
$\mathcal{D}$= 20.28, $\kappa\rho_r$= 2,400 kg m^3, μ = 40 Pa·s.

Figure 6-16. Dike Tip and Fluid Front as Functions of Time

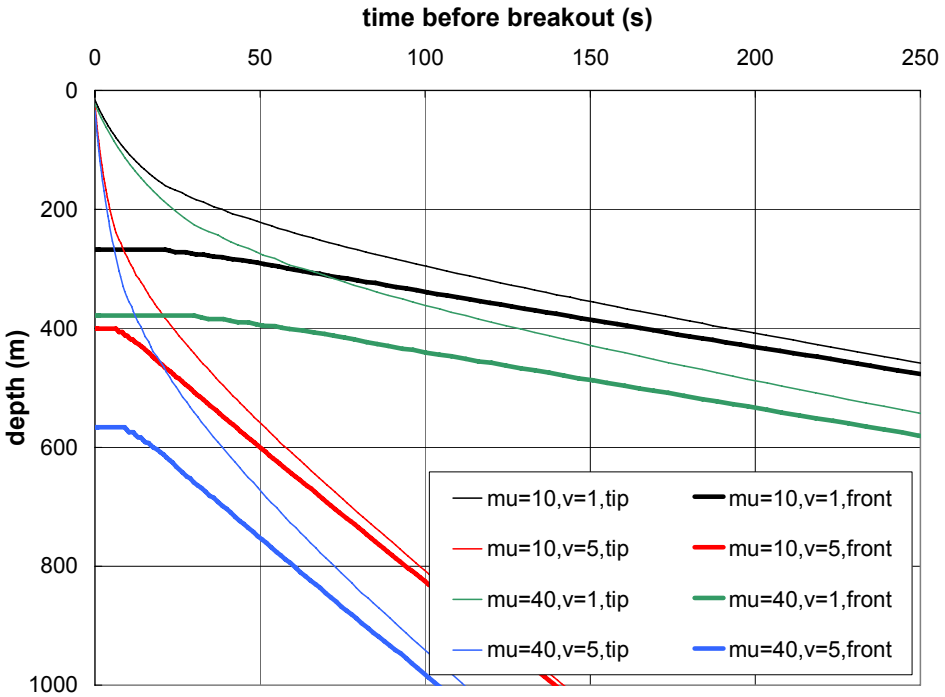

Output DTN: MO0408EG831811.003; file: *Fig. 6-18.xls*, tab: "varyMu,RhoRk1200."

Source: Output data calculation plots.

NOTE: $\mathcal{D}$ = 20.28, $\kappa\rho_r$ = 1,200 kg m^3, μ = 10 Pa·s or μ = 40 Pa·s.

Figure 6-17. Dike Tip and Fluid Front as Functions of Time

In all cases considered, the tip cavity forms before the dike tip reaches the repository level (nominally 300 m). The cavity size at the repository level varies from case to case. Because the length scale decreases as δ' increases (Equation 6-49), the solutions for $\kappa = 1.0$ (i.e., $\kappa\rho_r = 2{,}400$ kg m^3) yield shorter cavity lengths than solutions for the more relevant, $\kappa = 0.5$ (i.e., $\kappa\rho_r = 1{,}200$ kg m^3). Similarly, the dike opening, w_∞, for a given velocity, v_∞, is smaller for $\kappa = 1.0$ than $\kappa = 0.5$. Note that some of the widths obtained are small (lower than 0.2m) and could result in freezing of the magma. However, these values are retained to show the relative effect of the parameters. Results for $\kappa = 0.5$ indicate (see Figures 6-11, 6-13, and 6-15) that the magma does not reach the repository level (i.e., a 300-m depth) before the dike tip reaches the ground surface, except for the lowest velocity cases considered (i.e., $v_\infty = 1$ m/s with $\mathcal{D} = 2.67$ where $w_\infty = 0.16$ m (Figure 6-11), and $\mathcal{D} = 6.02$ where $w_\infty = 0.25$ m (Figure 6-13); these two cases are at the lower end of realistic dike widths). In these two cases, the length of the tip cavity is between 100 m and 200 m when the magma is at the repository horizon. In the case of $\mathcal{D} = 20.28$, illustrated in Figure 6-15, the tip cavity is longer than 300 m when the dike tip reaches the ground surface. As expected from Equation 6-49, an increase in magma viscosity, μ results in an increase in the tip cavity length, as illustrated in Figures 6-16 and 6-17 (for $\mu = 40$ Pa·s), compared to results in Figures 6-14 and 6-15 (for $\mu = 10$ Pa·s).

As expected from Equation 6-51, an increase in magma viscosity, μ, results in an increase in the tip cavity length. This is evident from Figure 6-17 where results for different viscosities are plotted for $\mathcal{D}$ = 20.3. Increasing the viscosity from 10 Pa·s to 40 Pa·s for a fixed far-field velocity of 1 m/s doubles the cavity length at depth. As the crack tip approaches the surface, the effect is not quite so large, but the cavity length at breakout is still approximately 40% greater for the higher viscosity. For the lower velocity, this increase is enough that the magma does not reach the nominal 300-m repository level before breakout.

One objective of the dike propagation analysis is to estimate the magma pressure history at the repository level as the dike passes through the repository. However, the NPHF2D simulation stops when the dike tip reaches the ground surface. Consequently, the model does not provide the pressure history at repository depth in those cases where the magma does not reach the repository level by the time the tip reaches the ground surface. In other cases, when the magma is at the repository level before the dike ruptures the ground surface, the history is usually provided for only a short period.

To account for the strike dimension of the dike, the proper solution requires a three-dimensional model of fluid flow in the preexisting fracture (there being then no need for simulation of fracture propagation). For present purposes, a pragmatic approach was adopted. The pressure profile in the magma behind the front remains invariant until magma is close to the ground surface. The only change in the net pressure profile is a variation of the minimum, which is controlled by the net pressure inside the cavity and is equal to the horizontal far-field stress.

The net pressure profiles and pressure histories for two values of $\mathcal{D}$ are shown in Figures 6-18 to 6-21. The net pressure profiles for $\mathcal{D}$ equal to 2.67 and 20.28 at different times (the earliest being when the magma reaches a repository depth of 300 m) are shown in Figures 6-18 and 6-20, respectively. Clearly, in the case of $\mathcal{D}$ = 20.28 (Figure 6-20), all four pressure profiles (at four different times) have the same shape. All curves could have been obtained by horizontally translating the curve for t = 4,086 s and truncating those portions below the line corresponding to the horizontal far-field stress. This argument can be applied to pressure profiles at t = 1,339 s and t = 1,367 s for $\mathcal{D}$ = 2.67 shown in Figure 6-18. However, the pressure profile at t = 1,392 s does not follow the same trend. The reason is that, in the case of $\mathcal{D}$ = 2.67, there is an effect on the magma front velocity when the dike tip approaches the ground surface (see Figure 6-9): the magma front stalls. The low lateral confinement and a large decrease in elastic stiffness as the dike tip approaches the ground surface accommodate the influx of additional magma without forward movement of the magma front.

The pressure and time histories at the repository level can be approximated by advecting the pressure profile at the repository horizon using the known fluid front velocity. Pressure histories constructed using such an approach for $\mathcal{D}$ equal to 2.67 and 20.28 for different velocities (1 m/s, 5, 10, and 15 m/s) are shown as curves in Figures 6-19 and 6-21. (Only the curve for 1 m/s velocity is a pressure history at the depth of 300 m. Other curves are at different depths, which correspond to the same dimensionless depth as a 300-m depth for a 1 m/s curve). The calculated pressure histories (labeled "sink data") at the repository depth for the case in which v_∞ = 1 m/s are shown as discrete points in Figures 6-19 and 6-21. The agreement between pressure histories

derived from pressure profiles and fluid velocities, and the actual pressure-time history at the sink is very good.

It appears from the pressure history plots in Figures 6-19 and 6-21 that the two major factors controlling the evolution of magma pressure at a given depth are the far-field horizontal stress and magma front velocity. From these computations, the maximum magma pressure is at most 1 MPa larger than the horizontal far-field stress at the given depth[4]. Therefore, the maximum magma pressure at a 300-m depth is approximately:

- 4.6 MPa in the case of $\kappa\rho_r$ = 1,200 kg m^3 (horizontal far-field stress 3.6 MPa)
- 8.0 MPa in the case of $\kappa\rho_r$ = 2,400 kg m^3 (horizontal far-field stress is 7.6 MPa).

Clearly, a larger magma front velocity results in a larger rate of pressure change at a given depth. The length of the tip cavity provides a measure of the distance over which the magma pressure behind the front changes from zero to the maximum value. Consequently, as the tip cavity becomes shorter, the pressure gradient becomes larger, and the rate of pressure change at a given depth increases.

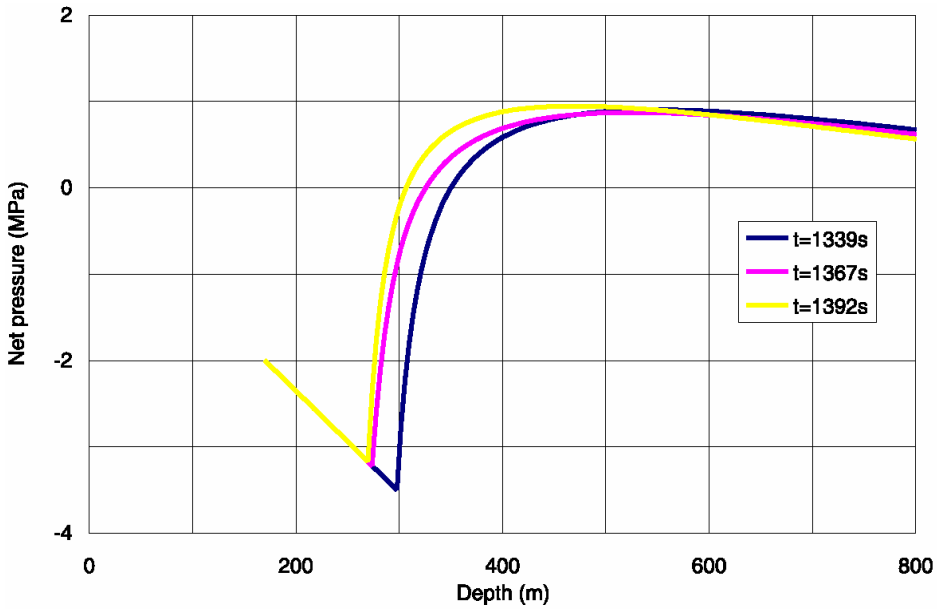

Output DTN: MO0408EG831811.004; file: *Fig. 6-19 & 6-20.xls*, tab: "c v=1."

Source: Output data calculation plots.

NOTE: $\mathcal{D}$ = 2.67, $\kappa\rho_r$ = 1,200 kg m^3, μ = 10 Pa·s, v_∞ = 1 m/s, w_∞ = 0.16.

Figure 6-18. Net Pressure Profile as a Function of Depth

[4] This is lower than the "few MPa" suggested by Dr. Rubin in his independent technical review of an early version of this report (Section 7.3.1.1.2 and Appendix F). This is a result of the specific magma and far-field dike properties and the elastic properties used in this analysis.

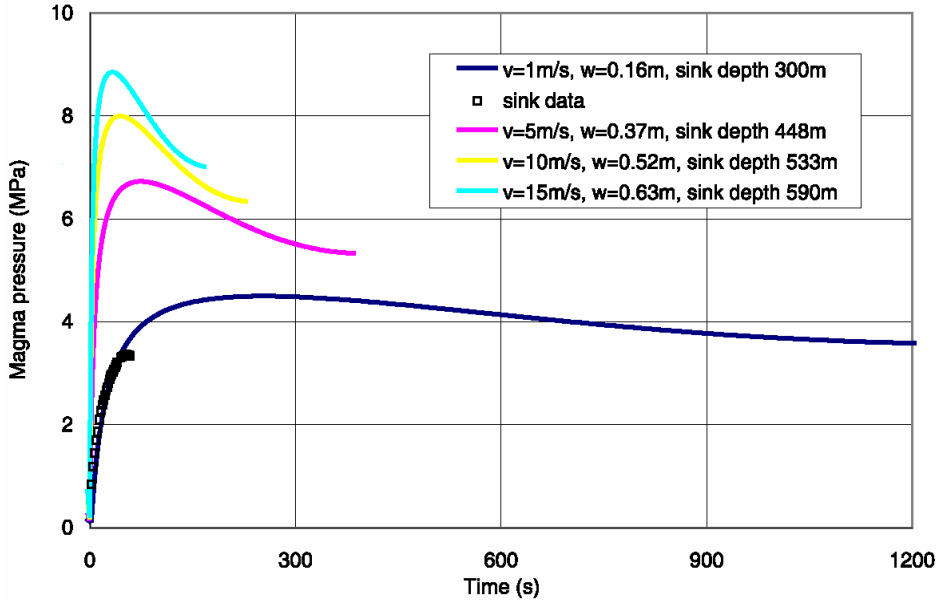

Output DTN: MO0408EG831811.004; file: *Fig. 6-19 & 6-20.xls*, tab: "c pressure histories."

Source: Output data calculation plots.

NOTE: $\mathcal{D}$ = 2.67, $\kappa\rho_r$ = 1,200 kg m^3, μ = 10 Pa·s.

Figure 6-19. Pressure History at Points Similar to Repository Depth

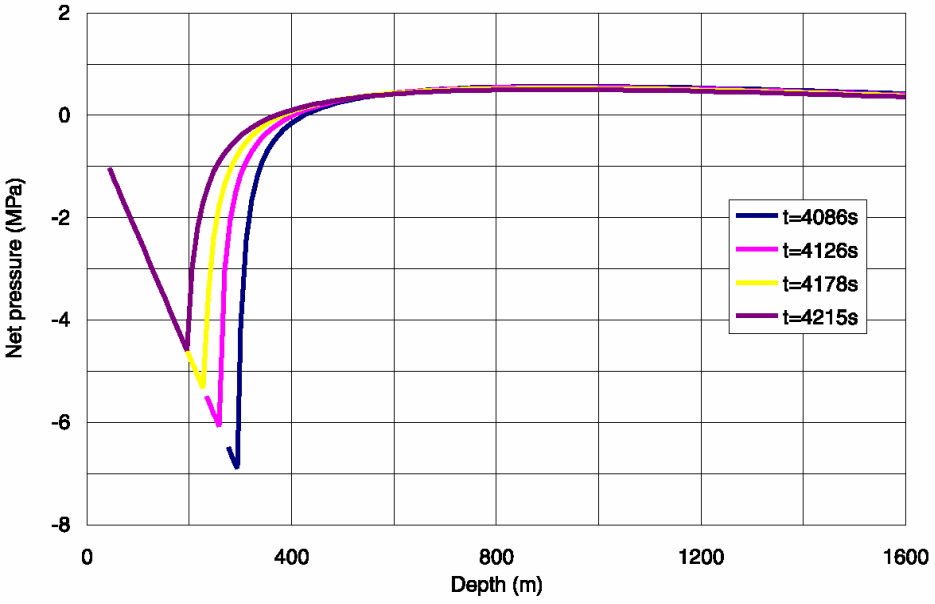

Output DTN: MO0408EG831811.004; file: *Fig. 6-21 & 6-22.xls*, tab: "c v=1."

Source: Output data calculation plots.

NOTE: $\mathcal{D}$ = 20.28, $\kappa\rho_r$ = 2,400 kg m^3, μ = 10 Pa·s, v_∞ = 1 m/s, w_∞ = 0.32 m.

Figure 6-20. Net Pressure Profile as a Function of Depth

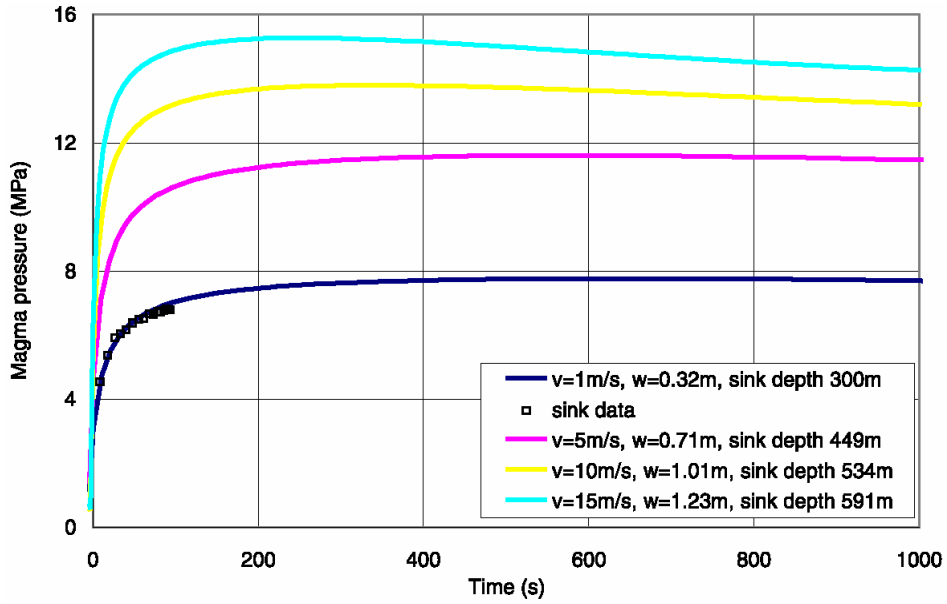

Output DTN: MO0408EG831811.004; file: *Fig. 6-21 & 6-22.xls*, tab: "c pressure histories."

Source: Output data calculation plots.

NOTES: Flow parameters for v=10 m/s, 15 m/s indicate non-laminar flow.
$\mathcal{D}$ = 20.28, $\kappa\rho_r$ = 2,400 kg m^3, μ = 10 Pa·s.

Figure 6-21. Pressure History at Points Similar to Repository Depth

6.3.3.4.2 Effect of Pressure inside the Tip Cavity

Magmas contain volatile components, mainly H_2O and CO_2. At high pressures, the gases are completely dissolved in the magma. The magma pressure falls as the magma approaches the ground surface, exsolution takes place, and gases form bubbles inside the melt. The volumetric percentage of the bubbles increases as the magma pressure decreases. Near the tip cavity, the gases in the magma can move (due to the pressure gradient) and be released into the cavity. As pressure builds inside the cavity, the gases leak off into the surrounding rock formations. The model discussed in this report does not simulate any of these processes. However, a simplified analysis (Detournay et al. 2003 [DIRS 169660]), based on consideration of the gas diffusivity in tuff at Yucca Mountain, shows that the cavity gas pressure will be insignificantly larger than the gas pressure in the surrounding formation (i.e., atmospheric pressure). Because this is a simplified analysis, the effect of gas pressure inside the tip cavity on the conditions of dike propagation was investigated. Table 6-4 shows the independent and derived parameters developed as inputs to evaluate the effect of gas pressure inside the tip cavity, using the same conventions that were used in Table 6-3.

The results of the numerical model are illustrated in Figures 6-22 through 6-27. The dimensionless results are in Figures 6-22 and 6-25; the dimensional results are shown in Figures 6-23, 6-24, 6-26, and 6-27. Two cases were considered: $\mathcal{D} = 2.67$, $\mathcal{S} = -0.25$ and $\mathcal{D} = 20.28$, $\mathcal{S} = -0.20$. The former corresponds to 1.00 MPa, and the latter to 0.48 MPa cavity gas pressure in the case of $\kappa\rho_r$ = 2,400 kg m^3, μ = 10 Pa·s and v_∞= 1 m/s. The most realistic values are obtained with $\kappa\rho_r$ = 1,200 kg m^3 and yield pressures of 0.49 MPa to 0.20 MPa.

Table 6-4. Independent and Derived Parameters for Non-Zero Cavity Tip Pressure Simulations

Independent Parameters					Derived Parameters					
$\mathcal{D}$	$\mathcal{S}$	v_∞ (m/s)	κ	$\kappa\rho_r$ (kg m^3)	ρ_f (kg m^3)	$\kappa\rho_r - \rho_f$ (kg m^3)	w_∞ (m)	q_∞ (m^2/s)	$\sigma_c - p_{f0}$ (MPa)	Reynolds Number
2.67	−0.25	15	1.0	2,400	1,501	899	0.452	6.78	-1.98	1018
2.67	−0.25	10	1.0	2,400	1,501	899	0.369	3.69	-1.79	554
2.67	−0.25	5	1.0	2,400	1,501	899	0.261	1.30	-1.50	196
2.67	−0.25	1	1.0	2,400	1,501	899	0.117	0.12	-1.00	18
20.28	−0.20	15	1.0	2,400	2,282	118	1.245	18.68	-0.95	4,262
20.28	−0.20	10	1.0	2,400	2,282	118	1.017	10.17	-0.86	2,321
20.28	−0.20	5	1.0	2,400	2,282	118	0.719	3.59	-0.72	820
20.28	−0.20	1	1.0	2,400	2,282	118	0.322	0.32	-0.48	73
2.67	−0.25	15	0.5	1,200	751	449	0.639	9.58	-1.66	720
2.67	−0.25	10	0.5	1,200	751	449	0.522	5.22	-1.50	392
2.67	−0.25	5	0.5	1,200	751	449	0.369	1.84	-1.26	139
2.67	−0.25	1	0.5	1,200	751	449	0.165	0.16	-0.84	12
20.28	−0.20	15	0.5	1,200	1,141	59	1.761	26.41	-0.80	3,014
20.28	−0.20	10	0.5	1,200	1,141	59	1.438	14.38	-0.72	1,641
20.28	−0.20	5	0.5	1,200	1,141	59	1.017	5.08	-0.61	580
20.28	−0.20	1	0.5	1,200	1,141	59	0.455	0.45	-0.41	52

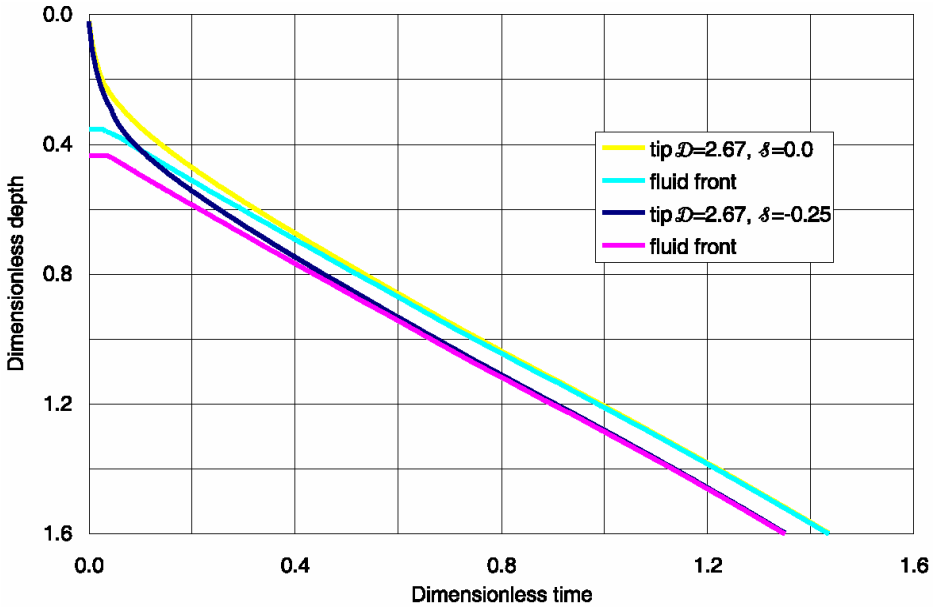

Output DTN: MO0408EG831811.004; file: *Fig. 6-23 & 6-24.xls*, tab: "c nondim positions."

Source: Output data calculation plots.

NOTE: Graphic shows the effect of $\mathcal{S}$ for $\mathcal{D}$ = 2.67.

Figure 6-22. Dimensionless Solution for Dike Tip and Fluid Front as Functions of Time

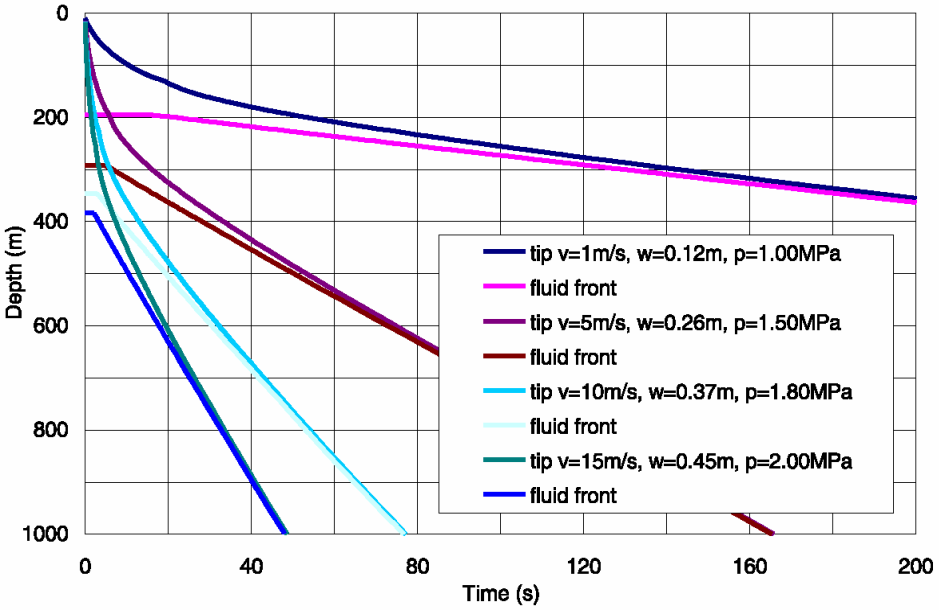

Output DTN: MO0408EG831811.004; file: *Fig. 6-23 & 6-24.xls*, tab: "c dim positions."

Source: Output data calculation plots.

NOTE: $\mathcal{D}$ = 2.67, $\mathcal{S}$ = -0.25, $\kappa\rho_r$ = 2,400 kg m^3, μ = 10 Pa·s.

Figure 6-23. Dike Tip and Fluid Front as Functions of Time

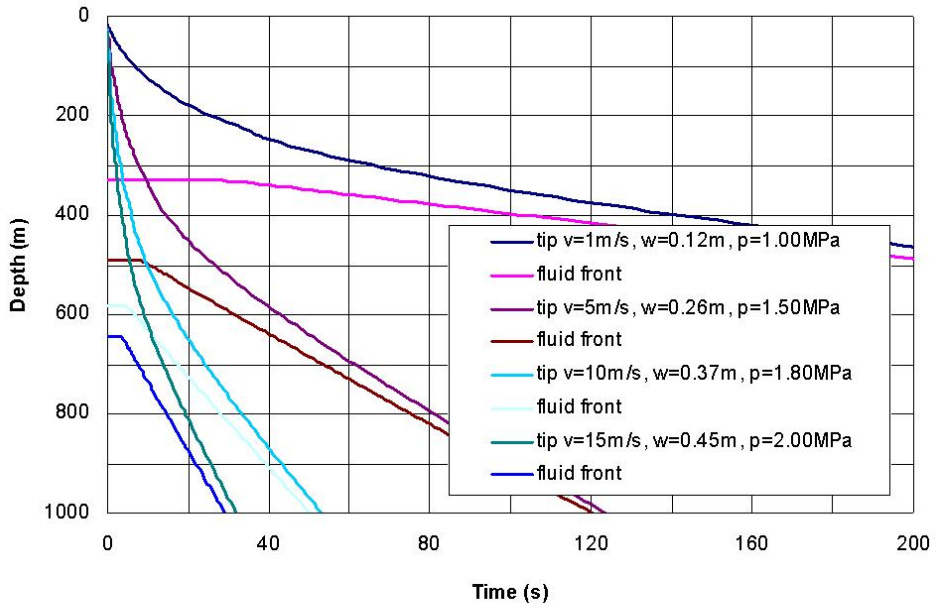

Output DTN: MO0408EG831811.004; file: *case28-1200Fig6-25.xls*, tab: "c dim positions."

Source: Output data calculation plots.

NOTE: $\mathcal{D}$ = 2.67, $\mathcal{S}$ = -0.25, $\kappa\rho_r$ = 1,200 kg m^3, μ = 10 Pa·s.

Figure 6-24. Dike Tip and Fluid Front as Functions of Time

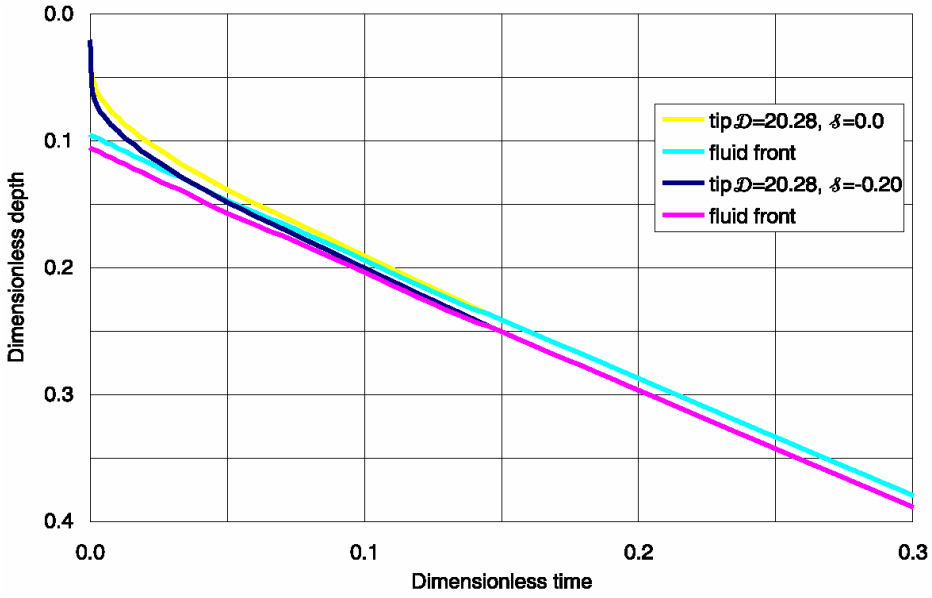

Output DTN: MO0408EG831811.004; file: *Figs. 6-26 & 6-27.xls*, tab: "c nondim positions."

Source: Output data calculation plots.

NOTE: Graphic shows the effect of $\mathcal{S}$ for $\mathcal{D}$ = 20.28.

Figure 6-25. Dimensionless Solution for Dike Tip and Fluid Front as Functions of Time

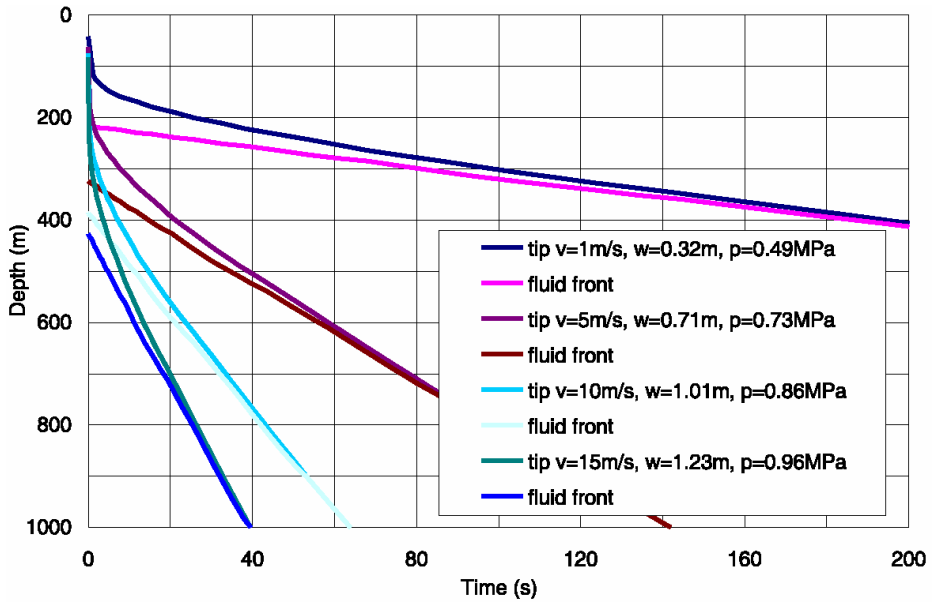

Output DTN: MO0408EG831811.004; file: *Figs. 6-26 & 6-27.xls*, tab: "c dim positions."

Source: Output data calculation plots.

NOTES: Flow parameters for v=10 m/s, 15 m/s indicate nonlaminar flow.
$\mathcal{D}$ = 20.28, $\mathcal{S}$ = -0.2, $\kappa\rho_r$ = 2,400 kg m^3, μ = 10 Pa·s.

Figure 6-26. Dike Tip and Fluid Front as Functions of Time

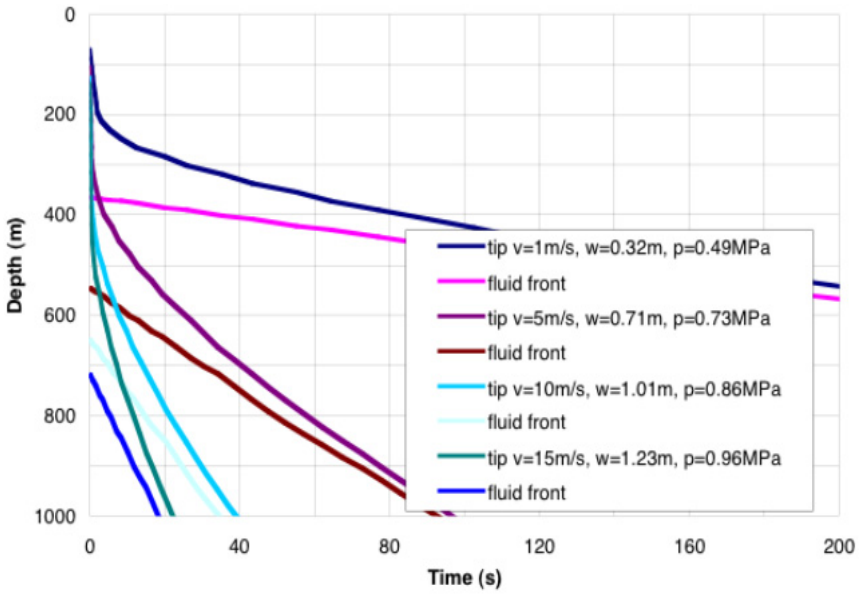

Output DTN: MO0408EG831811.004; file: *case14-1200Fig6-28.xls*, tab: "c dim positions."

Source: Output data calculation plots.

NOTES: Flow parameters for v=15 m/s indicate nonlaminar flow.
$\mathcal{D}$ = 20.28, $\mathcal{S}$ = -0.2, $\kappa\rho_r$ = 1,200 kg m^3, μ = 10 Pa·s.

Figure 6-27. Dike Tip and Fluid Front as Functions of Time

The cavity gas pressure does not significantly affect the velocity of the magma front. The velocity of the dike tip is affected, particularly when the tip gets close to the ground surface (i.e., when the cavity pressure becomes a significant proportion of the horizontal far-field stress). Thus, the cavity pressure increases the cavity length. Because the cavity is longer, the magma will be deeper when the crack tip reaches the surface. For example, comparing Figure 6-24 with Figure 6-11, it is seen that even the small added pressure in the cavity causes the crack tip to reach the surface before the magma reaches the repository.

Neglecting the cavity gas pressure would overpredict the rate of magma pressure change in repository drifts.

6.3.3.5 Alternative Models for Dike Propagation

There are a number of analytic and commercial oil and gas hydraulic-fracture models available (including those used in geothermal hot-dry-rock and waste-injection applications), and there are hydraulic-fracture models adapted to the igneous dike problem. Each of these applications is discussed and considered.

6.3.3.5.1 Analytic Solutions of the Hydraulic-Fracture Problem

Although analytic solutions may not be sufficiently versatile to solve complex problems with free surfaces and loss into repositories, they are quite adequate for solving fracture propagation problems in general homogeneous media and are thus useful for comparisons and parameter estimation. The first hydraulic-fracture models were developed using a combination of two

landmark papers on the topic. These included a paper by Perkins and Kern (1961 [DIRS 163644]) and another by Howard and Fast (1958 [DIRS 163628]) with an appendix by Carter that was the basis for constructing a joint model.

Perkins and Kern (1961 [DIRS 163644]) considered two-dimensional fractures in Cartesian and radial geometries with laminar and turbulent flow for Newtonian and pseudoplastic rheologies. In the Cartesian geometry, the dimensions of the dike are a width (w) in the direction of crack opening, a length (L) in the direction of crack propagation, and a height (H) orthogonal to the other two. This situation can be analyzed as a two-dimensional problem as long as L is very large compared to w. Perkins and Kern (1961 [DIRS 163644]) took the two previously developed width equations for fractures inflated by constant pressure (Sneddon 1946 [DIRS 163648]):

$$w = \frac{2(1-\nu^2)(p-\sigma)L}{E}, \text{ for Cartesian geometry} \quad \text{(Eq. 6-69)}$$

and

$$w = \frac{8(1-\nu^2)(p-\sigma)R}{\pi E}, \text{ for radial geometry} \quad \text{(Eq. 6-70)}$$

where:

p = pressure of fluid in dike
σ = stress component normal to the dike
R = radius of the dike
E = Young's modulus of the confining rock
ν = Poisson's ratio of the confining rock.

To this, they added two pressure-drop equations. The first, for linear flow through an elliptic cross section, was of the form:

$$\frac{dp}{dx} = \frac{32Q\mu}{\pi Hw^3} \quad \text{(Eq. 6-71)}$$

where:

x = the spatial coordinate in the L-direction
Q = the volume flux of the driving fluid
μ = the dynamic viscosity of the driving fluid.

The second, for radial flow through a constant-aperture fracture, was as follows:

$$p = p_w - \frac{6Q\mu \ln[r/r_w]}{2\pi w^3} \quad \text{(Eq. 6-72)}$$

where:

p = the pressure at radius r
p_w = the driving pressure
r_w = the radius of the source flux, Q, where the dike width is w.

In addition, Perkins and Kern (1961 [DIRS 163644]) added a mass-conservation formulation and solved for widths and pressures, obtaining equations of the form:

$$w_{\max} = 3\left[\frac{2\left(1-\nu^2\right)Q\mu L}{E}\right]^{\frac{1}{4}} \text{ for the Cartesian case} \qquad \text{(Eq. 6-73)}$$

and:

$$w_{\max} = 3\left[\frac{\left(1-\nu^2\right)Q\mu R}{\pi^2 E}\right]^{\frac{1}{4}} \text{ for radial conditions} \qquad \text{(Eq. 6-74)}$$

where $w_{\max}$ is the maximum fracture width.

Using volumetric considerations (e.g., volume = flow rate × time), the length of the fracture could be found as:

$$L = 0.6\left[\frac{EQ^3}{2\left(1-\nu^2\right)\mu H^4}\right]^{\frac{1}{5}} t^{\frac{4}{5}} \text{ for the Cartesian case} \qquad \text{(Eq. 6-75)}$$

and

$$R = \left[\frac{EQ^3}{16\pi^2\left(1-\nu^2\right)\mu}\right]^{\frac{1}{9}} t^{\frac{4}{9}} \text{ for radial conditions.} \qquad \text{(Eq. 6-76)}$$

where t is time.

The contribution by Howard and Fast (1958 [DIRS 163628]) to the hydraulic-fracturing problem was the incorporation of leak off into the reservoir in the form of a square-root-of-time approximation. Although leak off into the surrounding rocks is not necessary for dike propagation, an appendix in their paper written by R.D. Carter (Howard and Fast 1958 [DIRS 163628], Appendix) provided a more accurate coupling of width, pressure, and leak-off equations. Carter's equation, as it is known, expresses the area (height × length) of a fracture as a function of the width, leak-off, flow rate, and time. Coupled with equations from Perkins and Kern's report (1961 [DIRS 163644]), and Equations 6-75 and 6-76, this solution allowed for analytic calculations of fracture growth in a much more exact form than the Perkins and Kern solution (1961 [DIRS 163644]). Nevertheless, the Perkins and Kern solution (1961 [DIRS 163644]) is very useful in estimating fracture parameters for most situations and can be

used as a check on any model that predicts the length, width, and pressure of a fracture that has a constrained height. In this case, height is the major dimension not aligned with fluid flow; length is the major dimension aligned with fluid flow. This type of fracture has an elliptic crack profile (e.g., in the minor dimension).

Nordgren (1972 [DIRS 163641]) applied the Carter-type (1961 [DIRS 163644], Appendix) solution for fractures in the Cartesian case and obtained:

$$w_{\max} \approx 2.5\left[\frac{2\left(1-\nu^2\right)Q^2\mu}{EH}\right]^{\frac{1}{5}} t^{\frac{1}{5}} \quad \text{(Eq. 6-77)}$$

and

$$L = 0.68\left[\frac{EQ^3}{2\left(1-\nu^2\right)\mu H^4}\right]^{\frac{1}{5}} t^{\frac{4}{5}} \quad \text{(Eq. 6-78)}$$

which is a relatively small change over the Perkins and Kern (1961 [DIRS 163644]) solution.

Geertsma and de Klerk (1969 [DIRS 163624]) provided analytic solutions for two-dimensional fractures that had a constant-width profile (e.g., the fracture extends to infinity or exhibits full slip at some boundary). For such a case, the width is given by:

$$w_{\max} \approx 2.27\left[\frac{2\left(1-\nu^2\right)Q\mu L^2}{E}\right]^{\frac{1}{4}} \text{ for the Cartesian case} \quad \text{(Eq. 6-79)}$$

and

$$w_{\max} \approx 2\left[\frac{2\left(1-\nu^2\right)Q\mu R}{E}\right]^{\frac{1}{4}} \text{ for radial conditions.} \quad \text{(Eq. 6-80)}$$

Because the dike propagation modeling being performed here is applying the two-dimensional approximation used by Geertsma and de Klerk (1969 [DIRS 163624]), these equations are most appropriate for direct comparison with the model results.

Although such analytic conceptual models are useful for parameter estimation, they are not appropriate for the dike propagation problem near the free surface and with a sink point at some single location. Thus, these models cannot be used to provide the detail needed for understanding magma flow into a shallow repository due to an intersecting dike.

6.3.3.5.2 Industrial Hydraulic-Fracture Models (Oil and Gas Applications)

Industrial hydraulic-fracture models are based on the same concepts as the analytic solutions given above, but numerical solutions allow considerable flexibility, particularly with respect to

height evolution and length factors. Some of the major available industrial packages are FracPro, Stimtech, MFrac, and TerraFrac, each available from a software provider.

Because these are proprietary industrial models, no exact accounting for their equations, algorithms, and applications can be made, but general principles associated with these models are documented in the literature and elsewhere. The most significant differences between the analytic solutions and the industrial models are the ability to handle variable height growth (into other layers having different stresses and other properties), compressible fluids (e.g., for foam-fracturing fluids), and proppant transport (e.g., for carrying sand to keep the fracture open after the treatment ends and the pressure drops). Many other factors can also be accounted for, such as different types of leak-off behavior, different fracture-tip propagation conditions, three-dimensional coupling effects, and others.

An overview of these types of models, a comparison of their results, and references for the equations/algorithms can be found in reporting Warpinski et al. (1993 [DIRS 163649]; 1994 [DIRS 163657]). In general, the review papers show that these models can result in widely different fracture geometries (and pressures) for the same input parameters, largely because of many unknown factors in the algorithms. In addition, these models are primarily appropriate for fracturing far away from the free surface in layered media (where fractures are relatively confined between horizontal strata). These limitations clearly make the industrial models unsuitable for the present application, and no further use is made of these models.

6.3.3.5.3 Hydraulic-Fracture Dike-Propagation Models

There are a number of models of dike propagation using hydraulic-fracture models but with the addition of the effects of buoyancy (buoyancy is normally ignored in most hydraulic-fracture models). Buoyancy has been found to be important for its effect on upward growth of the dike and for the effect of magma density on the width profile of the dike. Examples of these models are those of Spence and Turcotte (1985 [DIRS 127068]; 1990 [DIRS 127086]), Lister (1990 [DIRS 126865]; 1995 [DIRS 163635]), Lister and Kerr (1991 [DIRS 126889]), and Turcotte et al. (1987 [DIRS 134364]), among others. These models have quite adequately shown how the buoyancy effects are a critical element of dike propagation.

However, none of these models has a free surface that can model the changing behavior of the dike as the surface is approached. No other use is made of these models except as validation comparisons.

6.3.3.5.4 Damage-controlled Dike Propagation Model

Meriaux et al. (1999 [DIRS 178355]) have proposed an alternative to models of the type based on linear-elastic fracture mechanics that form the basis of the base model and of the models discussed in Section 6.3.8.1.2. The LEFM approach results in a stress singularity at the crack tip and requires a value for the fracture toughness, K. The damage model rather assumes that the crack process produces a damage zone surrounding the crack tip with reduced elastic stiffness, thereby eliminating the need for a value of K. In principal, this could have significant effect on the crack-propagation velocity. But Meriaux et al. (1999 [DIRS 178355]) conclude that "v [crack tip velocity] and the large-scale behaviour are given by the $K = 0$ solution of LEFM,"

and that a rough order of magnitude of the length scale l_d of the damage zone is "of the order of a metre." They conclude "that dyke propagation is governed by the fluid timescale rather than the damage timescale," which is in agreement with the base conceptual model described above.

6.3.3.5.5 Electric Power Research Institute Analysis of Dike Propagation

The Electric Power Research Institute (EPRI) published an analysis of potential igneous processes at Yucca Mountain (EPRI 2004 [DIRS 171915]). The institute's analysis of dike propagation from depth coincides closely with the analysis in this section, with one major exception. The least compressive stress during the first 2,000 years after closure will reach 10 MPa, with the horizontal components exceeding vertical. EPRI concluded, "the potential for an extrusive release in the first 2,000 years is zero" (EPRI 2004 [DIRS 171915], Section 3.3). Regarding intrusion of the repository, EPRI states:

> Radiogenic heating, and associated modifications of the stress field, are at a maximum soon after repository closure. It is reasonable to assume that, under these conditions, in which the vertical principal stress is double the horizontal, that the probability of a dike intrusion into the repository is zero. At 2,000 years after closure and thereafter, the probability of dike intrusion through the repository is set at the PVHA [probabilistic volcanic hazard analysis] value of 1.6×10^{-8}/yr. It is assumed that the modification of the stress field is related to the heat generation of the repository, which gradually decreases over this 2000-year period.
>
> From the "reasonable expectation" case, therefore, the probability of dike intrusion into the repository for the expected case is considered to increase linearly between 0 at time zero (i.e., time of repository closure) and 1.6×10^{-8}/yr at 2,000 years. This approach is considered to be a reasonable intermediate approach between the bounding approach used in past analyses (i.e., in which the deflection effect is ignored), and assuming a zero probability for the first 2,000 years.

Section 6.3.7.3 shows that, because of the finite extent of the increased confining stresses during the first 2,000 years after repository closure, dike propagation will not be stopped by the thermal stress field; it will merely be slowed down until the dike at depth widens enough to push the crack tip through the repository.

6.3.3.5.6 Magma Flow into Drift

The purpose of this section is to analyze the flow of the magma into the drifts and its effect on further dike propagation (i.e., propagation from repository elevation to the surface), using the conditions in the dike as computed in Section 6.3. This will lend insight into the process of magma filling the drifts, considering such questions as:

- Does the magma front continue up the original dike at the same speed?
- Does magma stall while the drift is filling?

- What pressures can be expected in the magma while the drift is filling, and after the drift has filled?

- What are the effects of magmatic temperatures on waste packages and waste forms?

Answers to these questions allow the development of realistic scenarios for assessing the impacts to waste packages and the elimination of unrealistic scenarios.

The analyses described in this section are executed using FLAC3D V. 2.14 (BSC 2004 [DIRS 172323]). This code is qualified and is used here within its range of intended use.

Approximations and Simplifications – Several approximations that were already detailed and justified in Section 6.3.2 are also used in this analysis:

- The host rock behaves elastically

- The elastic response of the host rock is linear

- The host rock is a homogeneous and isotropic material

- The dike is a single fracture

- The free surface is horizontal

- The lubrication approximation is valid (i.e., that the flow is laminar, the viscosity is Newtonian, and that inertial forces are not important).

In addition to the ones mentioned above, a few simplifications are different from the ones in Section 6.3.

The fracture toughness is taken to be negligible (i.e., the propagation of the dike is not affected by the energy needed to break the rock at the crack tip). Therefore, the dike propagation can be simulated using a preexisting crack along the vertical path of the dike. Section 6.3.2 discusses the supposition that fracture toughness is negligible for dike propagation.

The magma entering the drift from the dike is considered to be partially degassed so that it does not explosively decompress. This approximation is used in the analysis of flow within the dike as described in this section. It is consistent with observations (in Hawaii and at Parícutin in Mexico) of magma behavior prior to magma reaching the surface.

The analysis treats the pressure as atmospheric at the intersection between the dike and the drift; therefore, the flow in the drift is not explicitly represented. In reality, some pressure buildup will take place. In this regard, the analysis presented in this section effectively provides an upper bound for the amount of magma flowing into the drift, which overestimated the magma inflow rate into the drift and underestimated the time required for magma to fill the drifts. A complementary analysis using a fully coupled dike flow/drift flow formulation is also presented in this section (Results: Backpressure Effects on Dike-Drift Interaction).

The analysis treats the magma entering the drift as free of obstructions, such as waste packages, backfill, or rubble. These features, if considered, may impact the thermal and mechanical characteristics of the magma as it flows into the drift.

Magma Flow within the Dike – FLAC3D V. 2.14 (BSC 2004 [DIRS 172323]) is fully capable of simulating coupled fluid-mechanical problems. For the specific analysis of dike propagation, magma flow is confined to one vertical layer of zones only; there is no flow in the rest of the model. The fluid-flow model implemented in the numerical code uses Darcy's law as a transport law:

$$Q_i = \sum_{j=1}^{3} k_{ij} \frac{\partial (p - \rho_f z g)}{\partial x_j} \qquad \text{(Eq. 6-81)}$$

where Q_i is the specific discharge or volumetric flow rate per unit area, k_{ij} is the permeability tensor, p is magma pressure, ρ_f is magma density, z is elevation relative to a reference plane, g is the gravitational constant, and the summation convention is applied to repeated indices. However, the magma flow rate per dike width is considered to follow the cubic law, which is a special form of the Poiseuille law (Bird et al. 1960 [DIRS 103524]) for the case of flow between parallel plates:

$$Q_i = -\frac{a^3}{12\mu} (p - \rho_f z g)_i \qquad \text{(Eq. 6-82)}$$

where a is the dike aperture and μ is magma viscosity. To correctly simulate magma flow inside the dike, the permeability tensor of the zones that represent the dike is calculated during the simulation according to the following relation:

$$k_{ij} = \delta_{ij} \frac{a^3}{12\mu d} \qquad \text{(Eq. 6-83)}$$

where d is the thickness of the layer of zones that represent the dike and δ_{ij} is the Kronecker symbol.

The dike thickness is not explicitly represented in the model because it is zero initially, and even later, when the dike opens due to magma injection, it is much smaller than any characteristic length of the model. Instead, an arbitrary small value, d, is selected to be the thickness of zones that represent the dike. With the correction of permeability shown in Equation 6-83, the arbitrary number has no effect on the model solution. The dike aperture, a, is calculated during the simulation as a function of model deformation.

Description of Input—Inputs used in the analysis are shown in Table 6-5. Those parameters derived from sources external to this document (direct input) are also listed in Table 4-1. Magma density for this analysis uses a restricted subset of the values used previously in Table 6-2. A restricted subset was selected to minimize computation time while still providing a demonstration of the effect of key variables where the effect may not be readily discernible from the underlying equations. For example, fluxes in the dike vary as the third power of the dike width; therefore, two values were selected to show a typical range. A single value for magma

viscosity was selected from the viscosities in Table 4-1 because the linear dependence of flow rate on viscosity can be extended readily to other viscosities. The bulk density of the host rock is the same as that used in Section 6.3.5. The value of magma compressibility is set to 50 MPa as a number required by the code but chosen such that it does not affect the results. Acceleration of gravity has been rounded up to 10 m/s^2 from the value of 9.8 m/s^2 given by Incropera and DeWitt (2002 [DIRS 163337]). Calculational products developed in previous sections are used here.

Table 6-5. Inputs to Dike-Drift Interaction Analysis

Parameter	Value
Drift Diameter (SNL 2007 [DIRS 179466])	5.5 m
Half of Drift Spacing (SNL 2007 [DIRS 179466])	40.5 m
Young's Modulus of Host Rock (Detournay et al. 2003 [DIRS 169660], Table 1-2)	15 GPa
Bulk Density of Host Rock (DTN: SNL02030193001.027 [DIRS 108410])	2,400 kg m^3
Bulk Viscosity of Magma (μ) (Detournay et al. 2003 [DIRS 169660], Figure 2-1e)	10 Pa·s
Magma Buk Modulus	50 MPa
Magma Rise Velocity (Detournay et al. 2003 [DIRS 169660], p. 56)	1 m/s
Gravitational Acceleration (g) (Incropera and DeWitt 2002 [DIRS 163337])	10 m/s^2

Two combinations of model parameters with different magma densities and, therefore, two different dike widths were simulated. These two cases correspond to two of the dike-propagation cases studied in Section 6.3 (Table 6.3). Both cases correspond to a magma-front velocity far from the ground surface of 1 m/s. The dike width far from the ground surface can be calculated from the input values (Section 6.3.3.3). Consequently, the first case, or "wide-aperture case," corresponds to a dike aperture (far from the ground surface) of 0.45 m; Case 2, or "narrow aperture case," corresponds to a dike aperture (far from the ground surface) of 0.25 m. Note that far-field velocity and the far-field dike width are used as approximations for the velocity of magma and the width of the dike when magma reaches the drift elevation, as discussed in Section 6.3.7. Besides the inputs from Section 6.3 already associated with these two cases, this analysis requires the drift diameter, drift spacing, and magma compressibility.

Initial and Boundary Conditions—The geometry used for the numerical simulations of dike propagation is shown in Figure 6-28. The model represents the portion of the dike between the vertical plane along the drift and the vertical symmetry plane halfway between the drifts. Symmetry conditions are used on those two planes in the mechanical and the flow simulations.

The model extends 900 m below the repository level and 600 m on each side perpendicular to the dike. A stress-boundary condition is applied on the model vertical boundaries parallel with the dike. The bottom model boundary is restrained in the vertical direction. The top model boundary corresponding to the ground surface is free.

The magma is injected into the dike at the bottom of the model. The vertical in situ stress in the rock mass is gravitational. In the same manner as in Section 6.3, the stress state in the horizontal plane is taken to be isotropic, with magnitude of the horizontal principal stress equal to half of the vertical stress magnitude.

One vertical layer of zones represents the dike, with magma flow into this layer simulated as explained in Section 6.4.2.

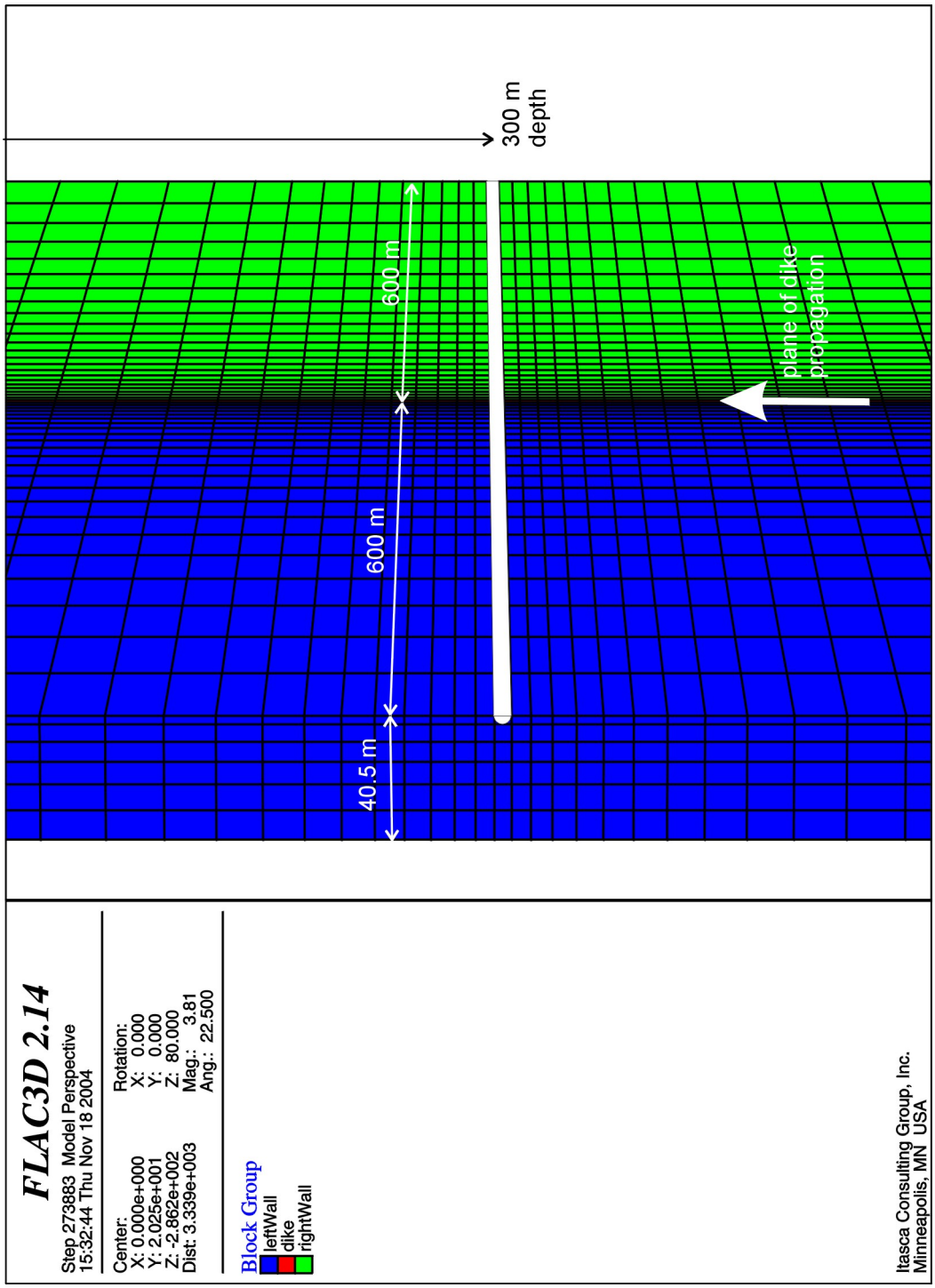

Output DTN: MO0411EG831811.001; file: *MO0411EG831811.001_Disk1/figures/fig6-37.jpg*.

Source: Output calculation data plot.

Figure 6-28. Geometry of the Dike Model

Results: Wide-Aperture Case

The results for the wide-aperture case are illustrated in Figures 6-29 through 6-34.

Figure 6-29 shows the contours of the horizontal stress perpendicular to the dike and the displacement vectors at the end of the simulation, at which time the crack tip is between 125 m and 100 m deep. The plot illustrates that, far from the dike tip and the magma front (i.e., at the bottom of the model), the magma pressure and pressure gradient are determined by the in situ conditions in the rock mass. The maximum displacement results in the dike aperture of 0.47 m, which is close to the far field dike aperture of 0.45 m. This result indicates that the artificial bottom boundary is sufficiently far from the repository level.

The magma flow rate out of the dike as a function of time (Figure 6-30) shows a progressive increase of magma loss after the magma has reached the level of the drift at time 540 s after the start of simulation. The initial acceleration of the flow into the drift is approximately 0.1 m^3/s^2. After another 1,100 s, the flow rate out of the model is 18.1 m^3/s. This is already very close to steady state in which the complete magma flow rate inside the dike ($Q = 1.0$ m/s $\times$ 0.45 m $\times$ 40.5 m = 18.23 m^3/s) would be diverted into the drift. Integration of the flux out of the dike shows that a 500-m-long drift is filled 15 minutes (900 s) after the magma has reached the repository level.

Positions of the magma front at three different states during the simulation (all states are after the magma front has reached the repository level) can be determined from contour plots of saturation shown in Figures 6-31 through 6-33 (the magma front coincides with the contour line of 50% saturation). Figure 6-33 corresponds to the end of the simulation, at a time slightly larger than the time needed to fill the drift. Therefore, Figure 6-33 shows a slight overestimation of the level reached by the magma when the drift is full. It seems that, in this case, the magma front moves to a maximum of approximately 80 m above the repository level before the drift is filled with magma.

Contours of the magma pressure and the flow vectors for the same point in time are shown in Figure 6-34. Although the flow vectors are obviously diverted toward the drift, it is clear that the entire flow is not diverted into the drift, in agreement with Figures 6-31 through 6-33.

Because the magma rises higher in the dike between the drifts than it does directly above a drift (Figures 6-31 and 6-32) and the magma pressure is higher between drifts than at the intersection (Figure 6-34), an argument can be made that the presence of drifts could result in conduit formation along a dike being concentrated between drifts rather than at the dike/drift intersection. However, the mechanics that lead to the localization of conduits along a dike is not well enough known for such an argument to be considered a strong one.

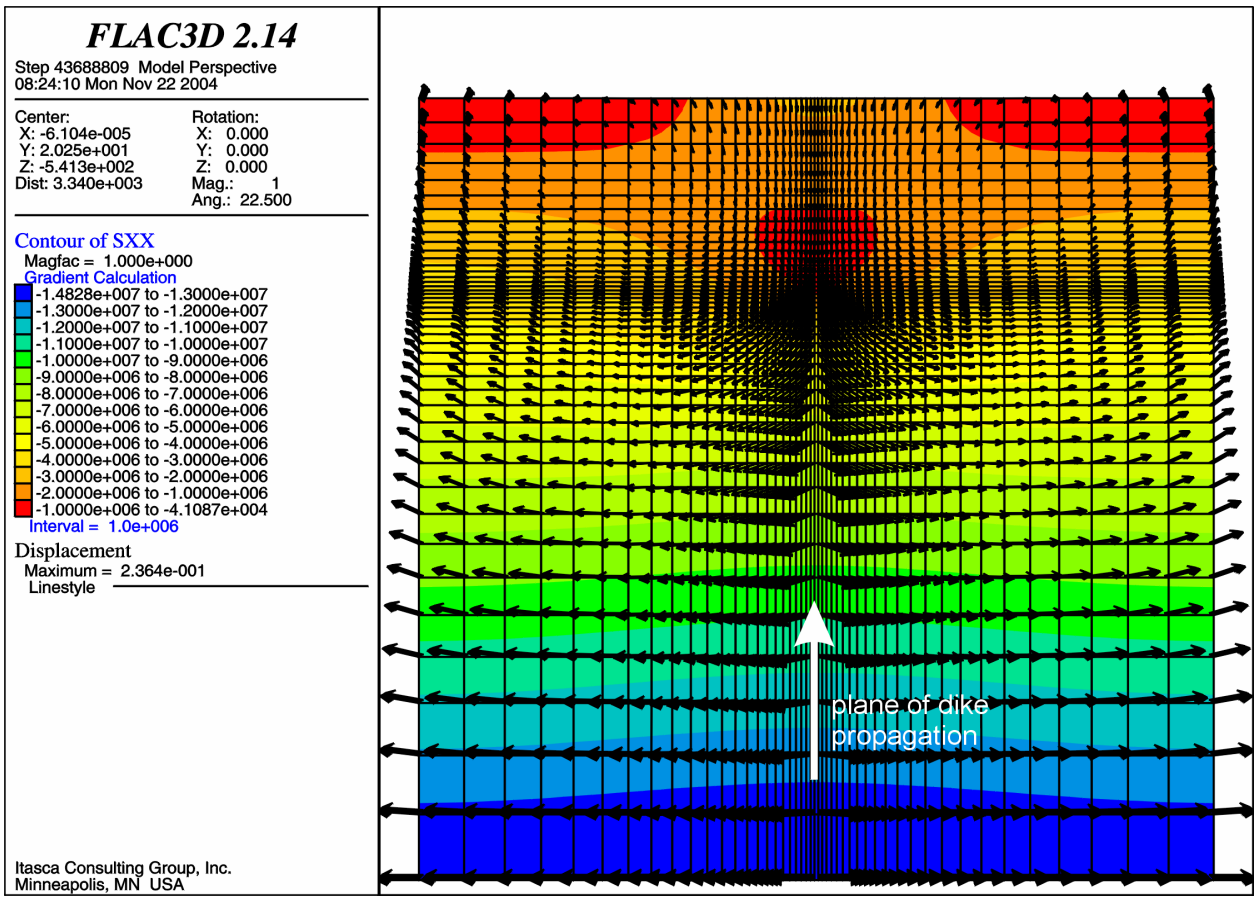

Output DTN: MO0411EG831811.001; file: *MO0411EG831811.001_Disk1/figures/fig6-38.pcx*.

Source: Output calculation data plots.

Figure 6-29. Contours of Horizontal Stress (Pa) Perpendicular to the Drift and Displacement Vectors (m) After 1,642 Seconds of Simulation: Wide-Aperture Case

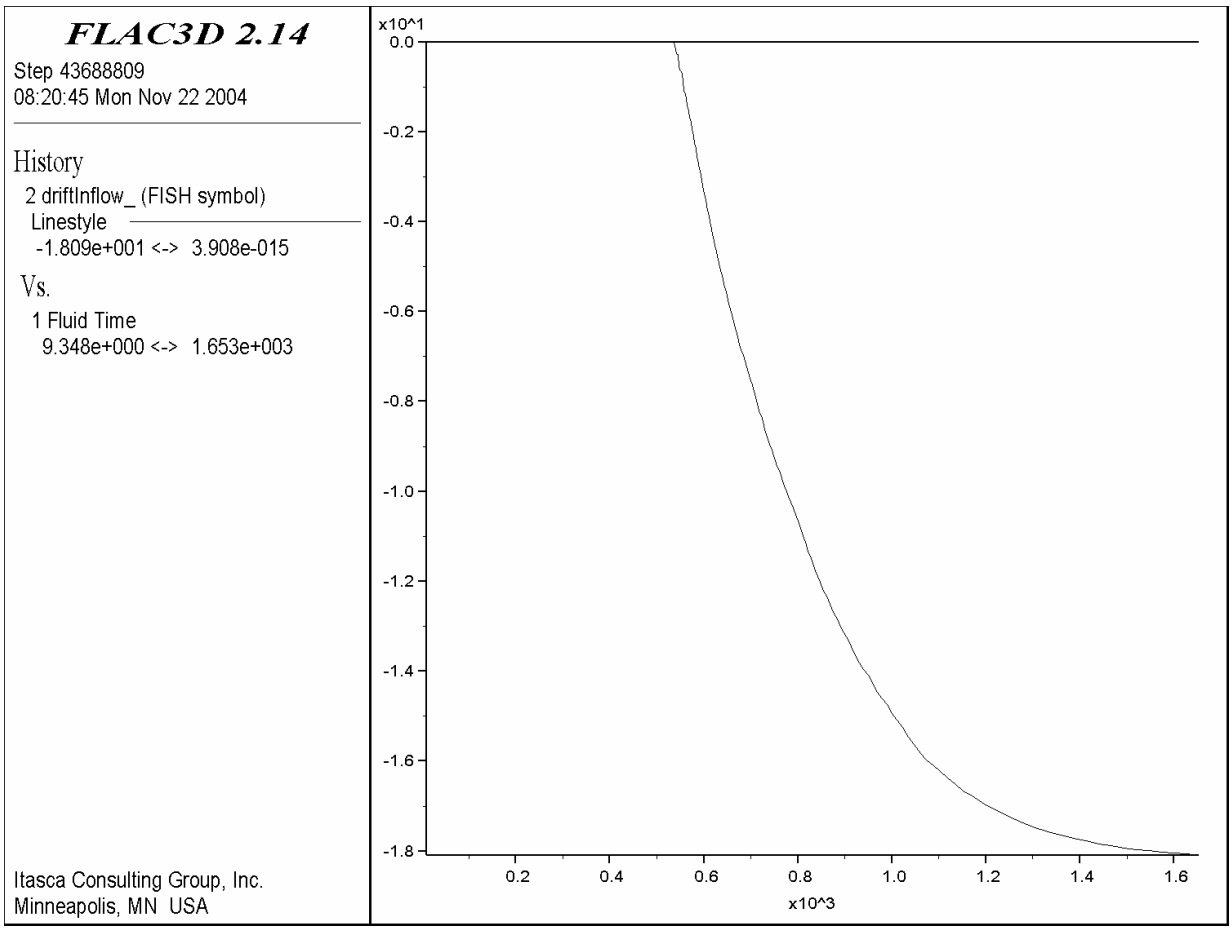

Output DTN: MO0411EG831811.001; file: *MO0411EG831811.001_Disk1/figures/fig6-39.pcx*.

Source: Output calculation data plot.

NOTES: Negative flow rates indicate flow from dike into drift.
Vertical axis is magma flow rate (×10); horizontal axis is time ($\times 10^3$).

Figure 6-30. Rate of Magma Flow (m^3/s) From the Dike into the Drift as a Function of Time (s): Wide-Aperture Case

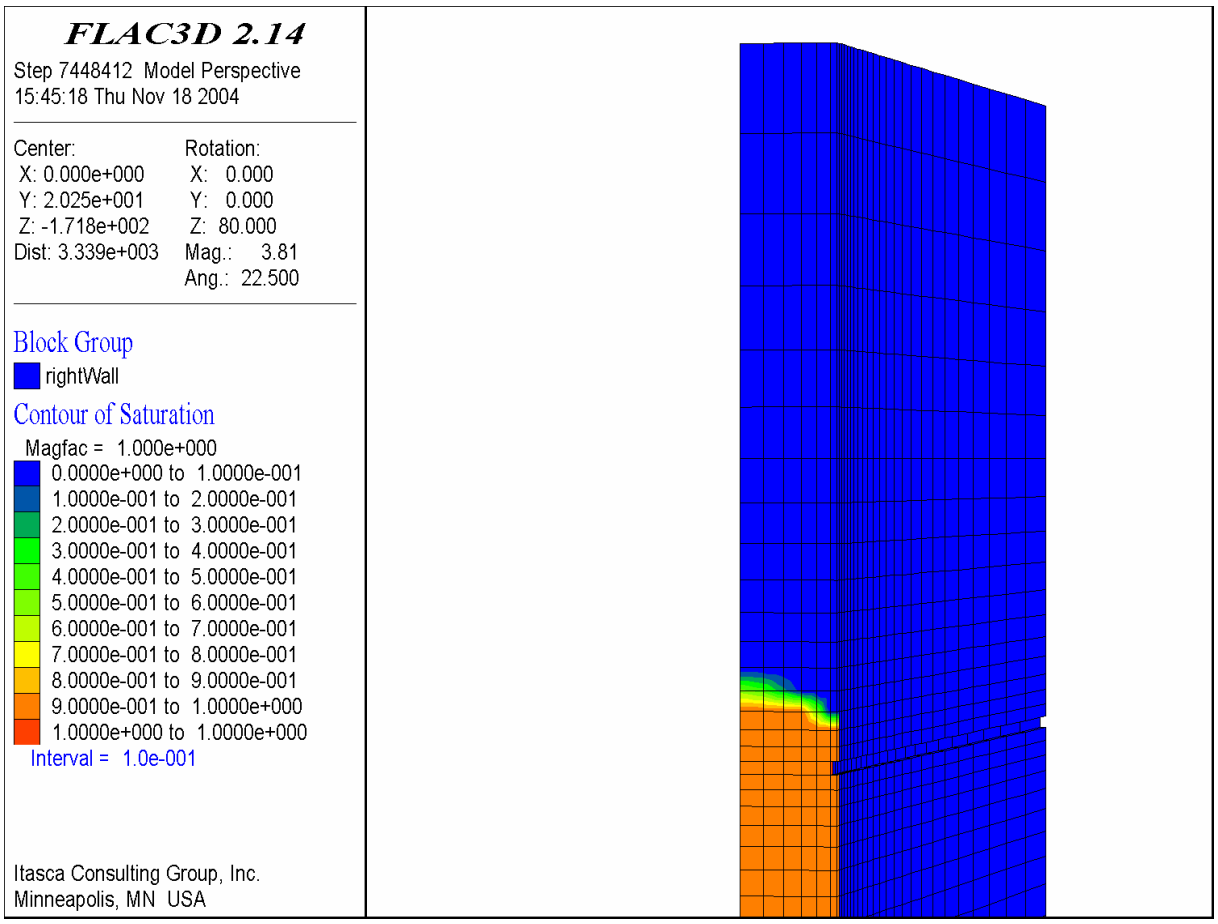

Output DTN: MO0411EG831811.001; file: *MO0411EG831811.001_Disk1/figures/fig6-40.pcx*.

Source: Calculation data plots.

NOTES: The left wall of the dike is hidden.
Drift shown by notch along the right edge and indentation in the blue zone.
The scale is given by the drift depth (300 m).
Position of the magma front corresponds to saturation 0.5.

Figure 6-31. Contours of Saturation of Dike with Magma 602 Seconds after Start of Simulation: Wide-Aperture Case.

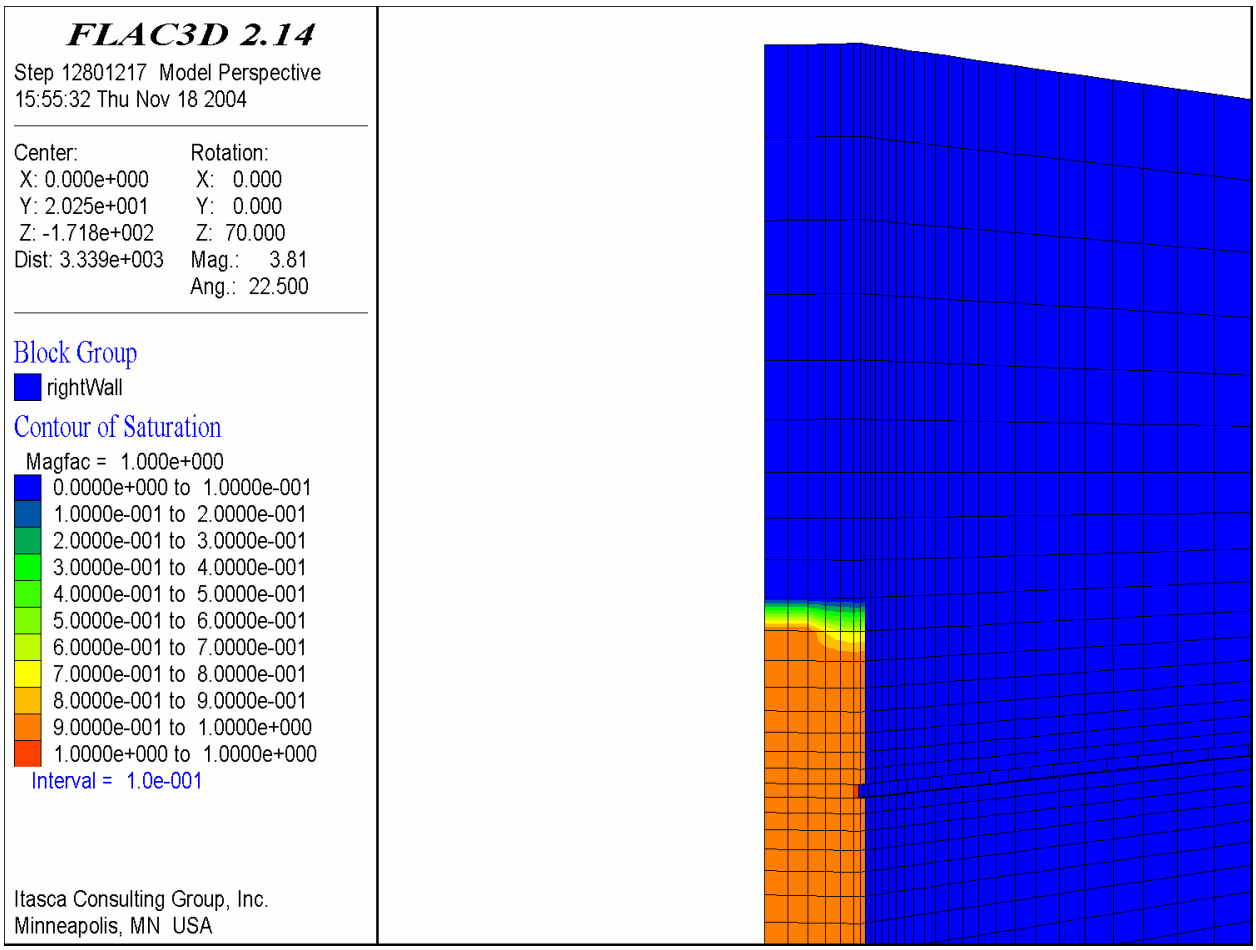

Output DTN: MO0411EG831811.001; file: *MO0411EG831811.001_Disk1/figures/fig6-41.pcx*.

Source: Calculation data plots.

NOTES: The left wall of the dike is hidden.
The scale is given by the drift depth (300 m).
Drift shown by notch along the right edge and indentation in the blue zone.
The position of the magma front corresponds to saturation 0.5.

Figure 6-32. Contours of Saturation of Dike with Magma 798 Seconds after Start of Simulation: Wide-Aperture Case

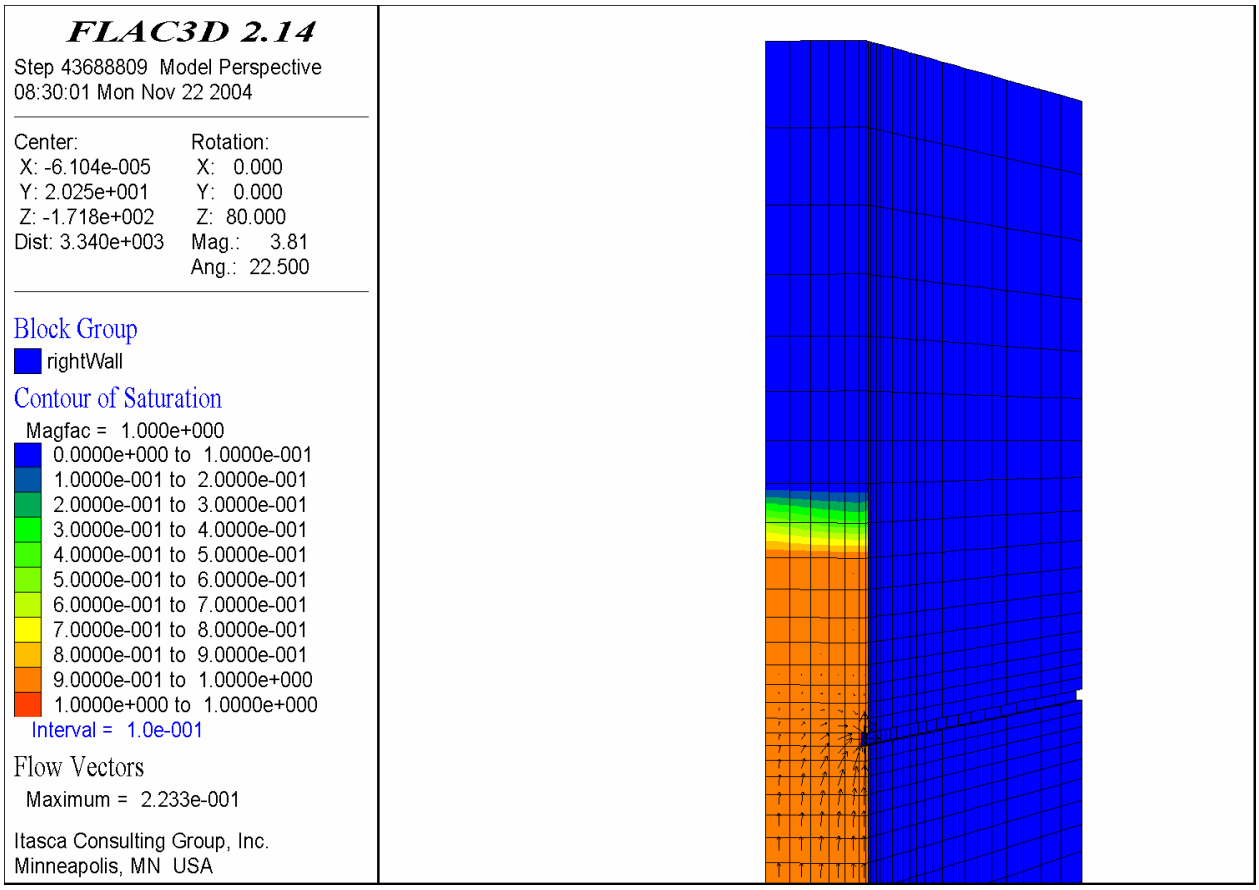

Output DTN: MO0411EG831811.001; file: *MO0411EG831811.001_Disk1/figures/fig6-42.pcx*.

Source: Calculation data plots.

NOTES: The left wall of the dike is hidden.
Drift shown by notch along the right edge and indentation in the blue zone.
The scale is given by the drift depth (300 m).
The position of the magma front corresponds to saturation 0.5.

Figure 6-33. Contours of Saturation of Dike with Magma 1,642 Seconds after Start of Simulation: Wide-aperture Case

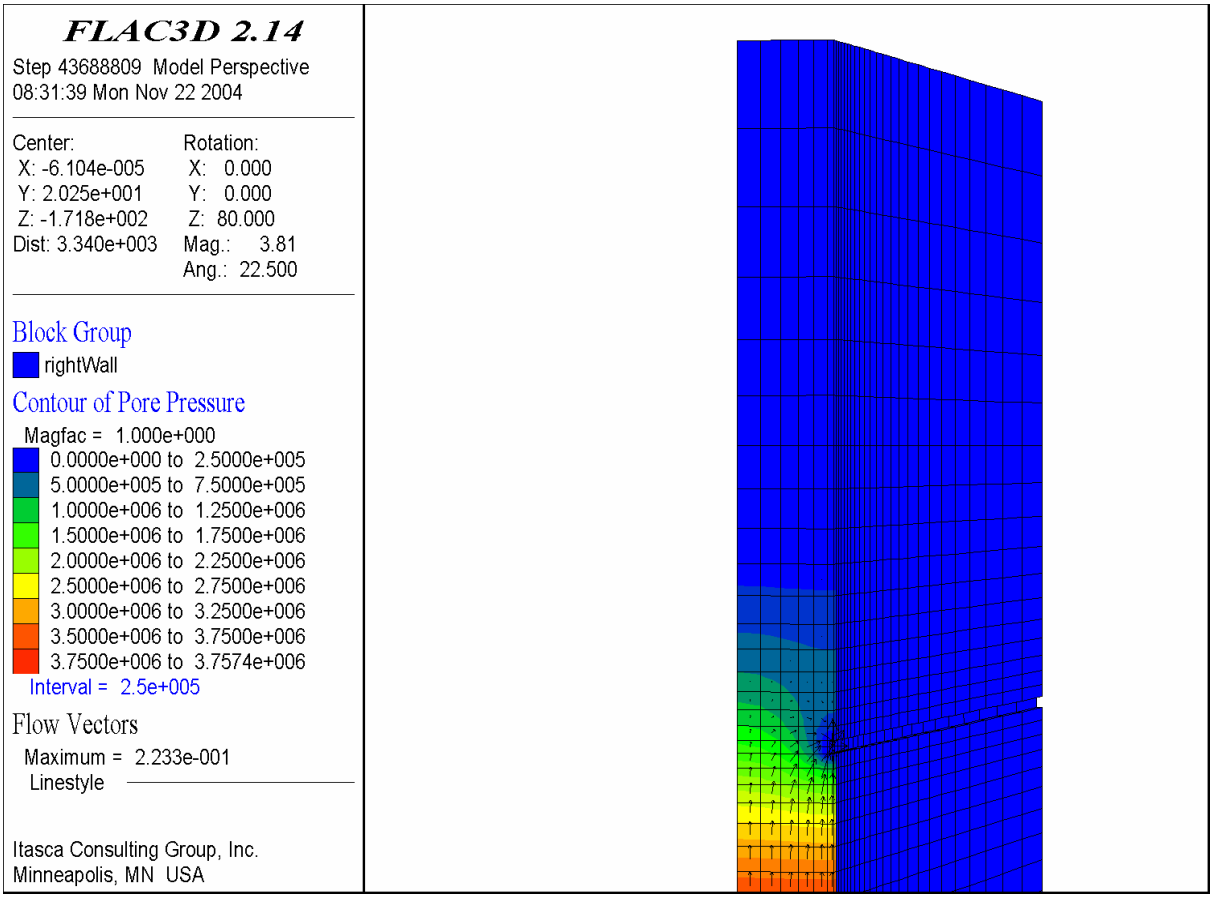

Output DTN: MO0411EG831811.001; file: *MO0411EG831811.001_Disk1/figures/fig6-43.pcx*.

Source: Calculation data plots.

NOTES: The left wall of the dike is hidden.
The scale is given by the drift depth (300 m).
Drift shown by notch along the right edge and indentation in the blue zone.

Figure 6-34. Contours of Magma Pressure (Pa) Inside the Dike 1,642 Seconds after Start of Simulation: Wide-Aperture Case

Results: Narrow-Aperture Case

Figures 6-35 to 6-37 illustrate the results of the narrow-aperture case. From Figure 6-35, it appears that the magma reaches the drift 740 s after the start of the simulation. The initial rate of increase of flow into the drift is 0.05 m^3/s. It then takes another 1,200 s after magma starts to flow into the drifts for the narrow aperture case to approach steady state (at the end of the simulation, the flow rate is 9.9 m^3/s compared to a full diversion steady state rate of Q = 1.0 m/s × 0.25 m × 40.5 m = 10.13 m^3/s). Integration of the flux out of the dike shows that a 500-m-long drift is filled 25 minutes (1,500 s) after the magma has reached the repository level, and 2,240 s after the start of the simulation. Therefore, in this case, steady state is achieved and the magma front stalls before the drift is completely filled. The maximum elevation the magma front can reach is approximately 120 m above the repository level (saturation contours shown in Figure 6-36), which is more than in the wide-aperture case. Contours of the magma pressure and the flow vectors for the narrow-aperture case are shown in Figure 6-37.

In both cases analyzed, the magma does not reach the ground surface before the drifts are filled with the magma. Therefore, it is necessary to investigate conditions of magma injection into preexisting joints inside the drifts to assess potential for a secondary dike or "dog leg" scenario (Section 6.5).

Results: Back-Pressure Effects on Dike-Drift Interaction

The numerical analysis in this section differs from the previous analyses by explicitly accounting for the coupling between flow in the dike and flow in the drift. This analysis is used simply to ensure that the condition of atmospheric pressure in the drift mentioned in Section 6.4.1 is appropriately justified.

The same two cases (wide- and narrow-aperture) are used to investigate the effect of coupling. These simulations are identical to the previous ones, except the magma pressure at the intersection between the dike and the drift, instead of being fixed at atmospheric, is calculated using the solution for fluid flow in a circular pipe.

Detournay et al. (2003 [DIRS 169660], Appendix 3.5, p. 62) give the equation for the volume flow rate through a circular pipe, Q_{pipe}, as:

$$Q_{pipe} = \frac{\pi a^4}{8 \mu L} P \qquad \text{(Eq. 6-84)}$$

P = pressure drop along the filled section of pipe
Q_{pipe} = inflow rate into the drift
L = drift length filled with magma
μ = magma viscosity
a = drift radius.

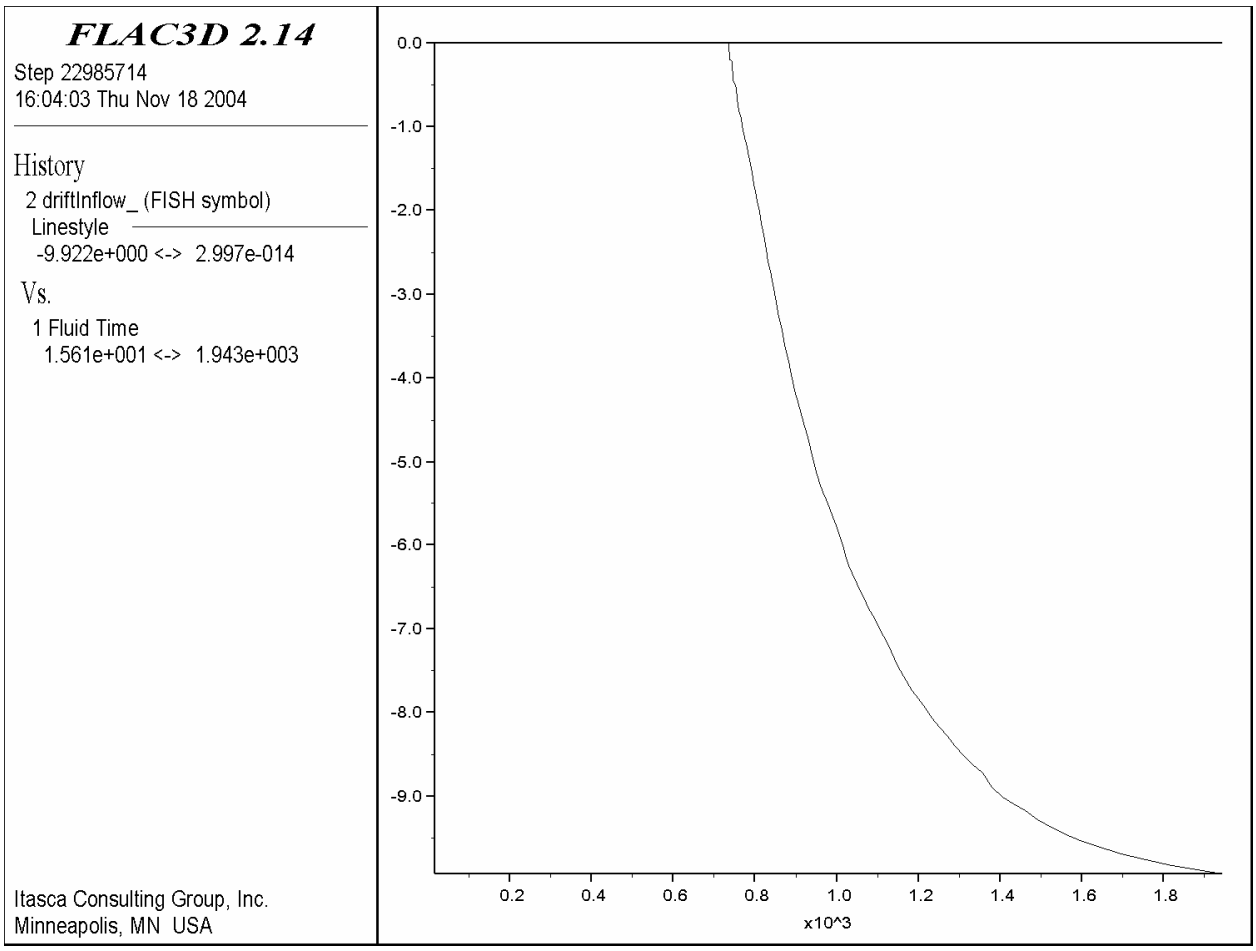

Output DTN: MO0411EG831811.001; file: *MO0411EG831811.001_Disk1/figures/fig6-44.pcx*.

Source: Output calculation data plot.

NOTES: Negative flow rates indicate flow from dike into drift.
Vertical axis is magma flow rate (×10); horizontal axis is time ($\times 10^3$).

Figure 6-35. Rate of Magma Flow (m^3/s) from the Dike as a Function of Time (s): Narrow-Aperture Case

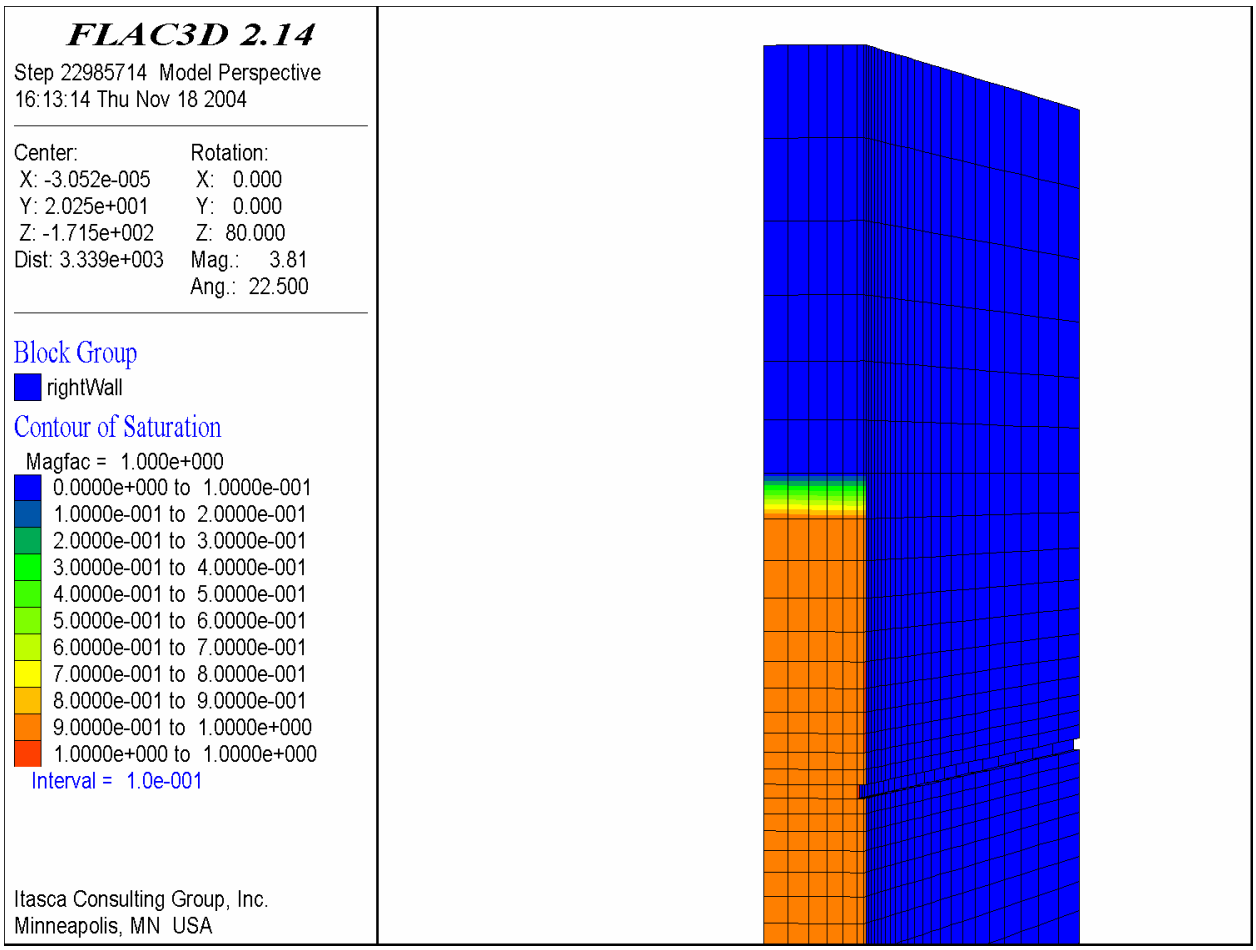

Output DTN: MO0411EG831811.001; file: *MO0411EG831811.001_Disk1/figures/fig6-45.pcx*.

Source: Output calculation data plots.

NOTES: The left wall of the dike is hidden.
The scale is given by the drift depth (300 m).
The position of the magma front corresponds to saturation 0.5.

Figure 6-36. Contours of Saturation of Dike with Magma 1,943 Seconds after Start of Simulation: Narrow-Aperture Case

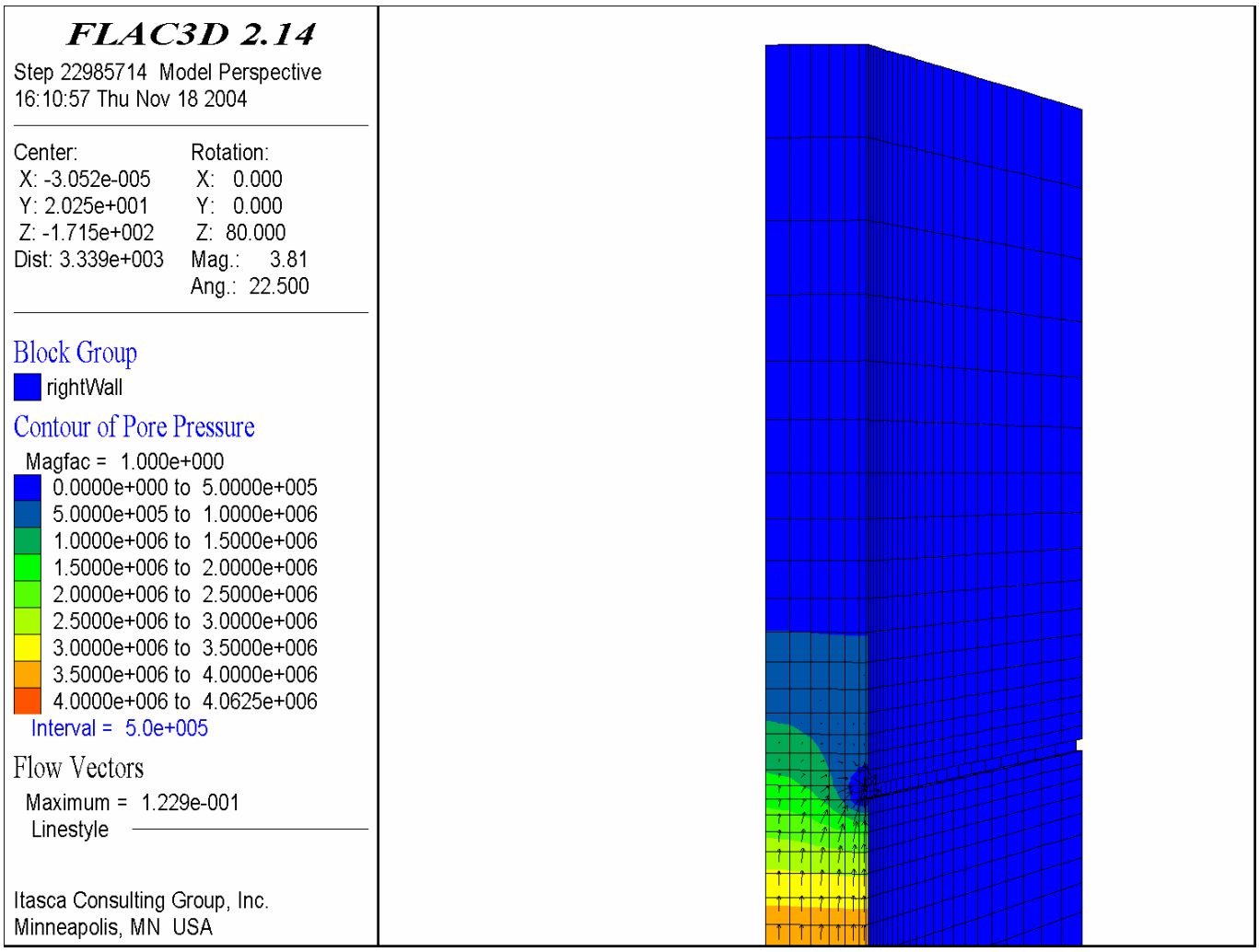

Output DTN: MO0411EG831811.001; file: *MO0411EG831811.001_Disk1/figures/fig6-46.pcx*.

Source: Output calculation data plots.

NOTES: The left wall of the dike is hidden.
The scale is given by the drift depth (300 m).

Figure 6-37. Contours of Magma Pressure (Pa) Inside the Dike 1,943 Seconds after Start of Simulation: Narrow-Aperture Case

Rearranging the expression for the inflow rate and including the time dependence yields the desired expression for the pressure history at the intersection:

$$P(t) = \frac{8\mu L(t)}{\pi a^4} q(t) \qquad \text{(Eq. 6-85)}$$

where:

q is the new notation for the inflow rate into the drift.

The drift length filled with magma at any time can be calculated by integrating the inflow rate:

$$L(t) = \frac{\int_0^t q(\tau) d\tau}{\pi a^2} \qquad \text{(Eq. 6-86)}$$

The order of magnitude of magma pressure was estimated at the intersection by applying the above formulae for the following case:

- 300 m of the drifts are filled with magma
- The entire magma flow from the dike is diverted into the drift ($Q = 1.0$ m/s × 0.45 m × 40.5 m = 18.23 m^3/s)
- There are no obstacles to flow inside the drifts (i.e., $a = 2.75$ m).

The resulting pressure drop in the drift is 2.4 kPa. From the perspective of magma pressures inside the dike (which are on the order of MPa), the calculated pressure at the intersection is practically zero. Therefore, the original approximation seems to be appropriate.

To investigate the extreme case of pressure increase caused by such obstacles to flow as waste packages, drip shields, and eventual rockfall from partial drift degradation, the numerical simulation of the dike/drift interaction was conducted with the drift diameter ($2a$) of only 1.5 m in the calculation of pressure. Simulations were carried out for both wide- and narrow-aperture dike cases.

Figures 6-38 and 6-39 show the inflow rates into the drift as calculated in the original models (zero pressure at intersection) and in the coupled models with a restricted diameter, for the wide and narrow aperture case respectively. The effect of coupling is very small, particularly at early times when the pressure at the intersection is small. Later, the effect increases but remains insignificant. The effect is slightly greater for the wide-aperture case.

For the parameters considered, the above analysis demonstrates that coupling between the magma flow in the dike and the drift is one way only. Even for an extreme case of resistance to flow inside the drifts, the pressure at the intersection between the dike and the drift does not increase sufficiently to affect the flow inside the dike. In other words, the analyses are equivalent for all practical purposes.

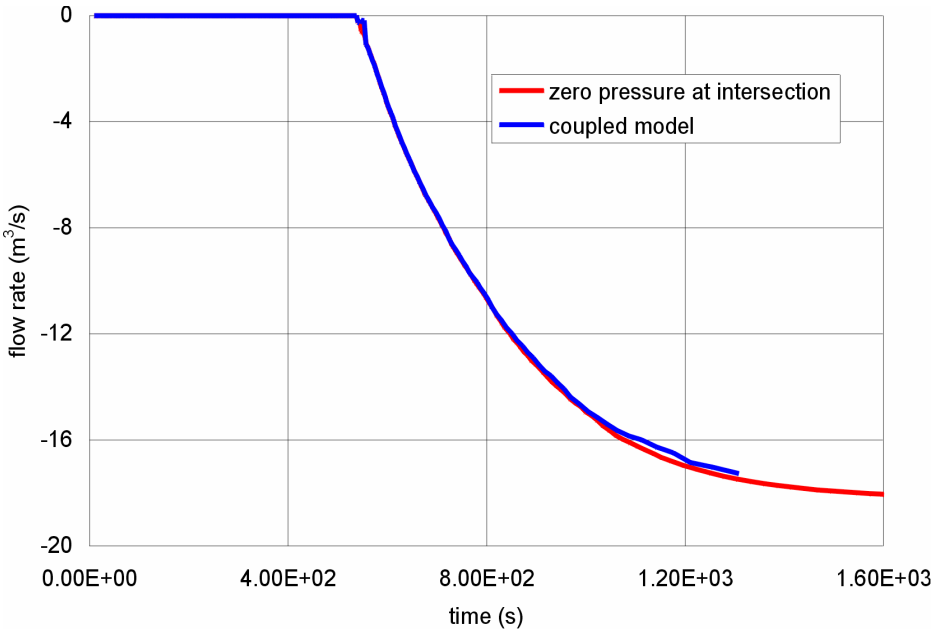

Output DTN: MO0411EG831811.001; file: *MO0411EG831811.001_Disk1/figures/fig6-47.pcx*.

NOTE: Flow rates are positive when entering the model.

Figure 6-38. History of the Rate of Magma Inflow from the Dike as a Function of Time: Wide-Aperture Case

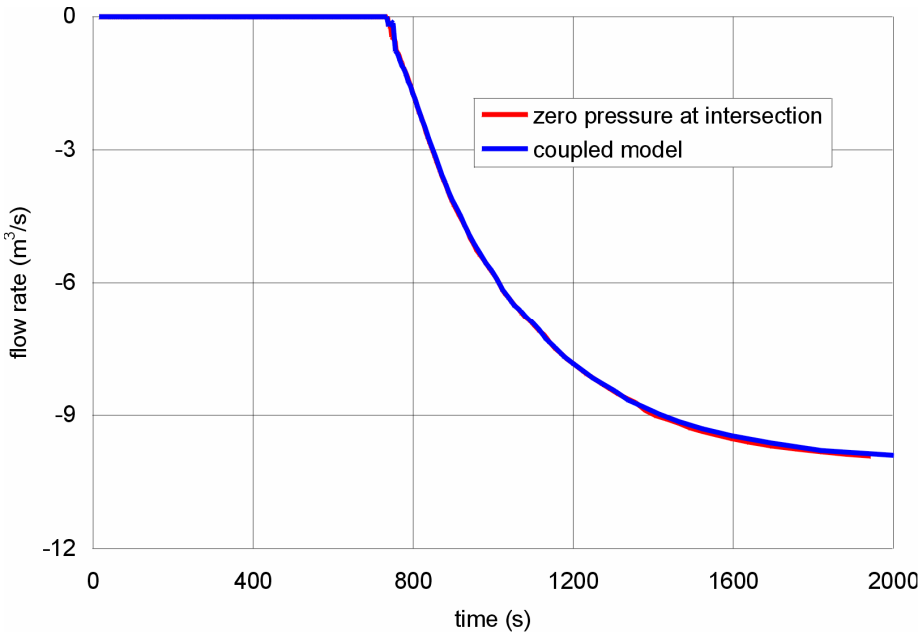

Output DTN: MO0411EG831811.001; file: *MO0411EG831811.001_Disk1/figures/fig6-48.pcx*.

NOTE: Flow rates are positive when entering the model.

Figure 6-39. History of the Rate of Magma Inflow from the Dike as a Function of Time: Narrow-Aperture Case

6.3.3.5.7 Analytic Solution for Effusive Flow into Drift

In this analysis, magma rises in the dike (starting at the level of the bottom of the drifts at $t=0$) driven by a velocity as deduced in Section 6.3. At any time, the volume of magma rising above the base of the drifts can either flow into the drift or continue up the dike. The amount going into the drift is taken to be the minimum of that calculated by the three equations described in Section 6.4.7.2.

Initially, the magma flows into the drift (radius a) as it would flow through a weir of circular cross section until the height of the magma reaches the top of the drift. After the magma height (H) exceeds that of the drift, the problem is analogous to a fluid draining out of a tank through an orifice. Because the dike is fairly thin (on the order of 1 m with about 80 m between drifts) and the magma has a viscosity substantially larger than water (on the order of 10 Pa·s to 40 Pa·s), for $H >> 2a$, the orifice equation is modified to include the effect of viscous drag in the dike following the method outlined by Detournay et al. (2003 [DIRS 169660], Appendix 3.5).

When the drift becomes sufficiently filled that viscous drag in the drift may control loss from the dike, the magma flow into the drift is calculated from the pipe-flow equation balanced by viscous drag in the dike.

Idealizations and Simplifications—The weir equation will give an overestimate of the flow into the drift because it considers that material flowing into the drift does not build up just inside the drift to decrease the head driving flow over the weir. Any frictional losses at the weir interface are also ignored. Similar comments apply to the orifice equation. Further, these equations ignore the effect of viscosity in the dike itself. As shown in the analysis of Section 6.3.3.5.6, the magma surface in the dike is not at a uniform height, as is the case in this analysis.

The definition chosen for L (the length of the drift filled with magma) leads to inaccuracy in the discharge Q that is difficult to predict simply. This approximation is equivalent to taking the magma front in the drift to be vertical, which it certainly will not be. Early in the flow history, the fact that viscous drag on the walls only occurs along the bottom of the flow will probably result in greater discharge. Later, as the length, L, becomes long compared to the slope times the drift diameter, this approximation will become closer to reality.

The idealization of the drift cross section as being perfectly circular ignores the drift invert, which is on the order of 4% of the cross-sectional area of the entire drift. The result will be a slight decrease in the hydraulic radius of the drift and in the volume of the drift and a change of the real weir cross section that will be considerable at the earliest times of the flow. The decrease in the hydraulic radius will result in slightly lower discharge rate from the dike into the drift. The decrease in the volume of the drift will lead to a shorter time to fill the drift at a fixed discharge rate. These two effects have an opposite sign but do not exactly cancel each other.

The analysis idealizes the blockage of the drift to be only obstruction by waste packages, packed end to end. This approach ignores the effects of rails, pallets, and drip shields, and the effects of gaps between waste packages on the flow. The presence of rails, pallets, and drip shields will reduce the total volume to be filled by the magma and will increase the viscous drag forces. The gaps between waste packages will result in a larger volume to be filled and a longer time to fill

the drift with magma. The effects of drag are expected to dominate resulting in a larger time required for magma to fill the drift.

Drift Degradation Analysis (BSC 2004 [DIRS 166107], Sections 6.3 and 6.4) indicates that rock degradation and seismic activity during the first 10,000 years after emplacement is likely to cause considerable rockfall. The analysis presented in this section does not take such potential drift blockage into account.

Mathematical Formulation—The governing equations are those for flow of a liquid over a weir (weir equation, $H << 2a$), out of a tank through a circular orifice well below the top of the liquid in the tank (orifice equation, $2a << H$), radially toward a point of discharge between two parallel plates (plate-drain equation), and through a pipe (pipe equation). The first two equations (Henderson 1966 [DIRS 164124]) are used separately. A simultaneous solution to the pipe equation and the plate-drain equations is used for $H << 2a$. Geometric configuration and nomenclature are illustrated in Figure 6-40.

The weir equation for a weir of arbitrary shape is:

$$Q(H) = \sqrt{2g} \int_0^H dh \sqrt{h}\, w(h) \qquad \text{(Eq. 6-87)}$$

where $Q(H)$ is the discharge rate through the weir of the fluid at height, H, above the bottom of the weir, $w(h)$ is the width of the weir at depth (h) below the magma height, and g is the gravitational acceleration.

For a weir or orifice of circular cross section with radius a and $0 \le H \le 2a$, $w(h)$, the equation for flow of liquid out of a tank through a circular orifice is given by

$$\begin{aligned} w(h) &= 2\sqrt{a^2 - (a - H + h)^2} \\ &= 2\sqrt{(H - h)(2a - H + h)} \end{aligned} \qquad \text{(Eq. 6-88)}$$

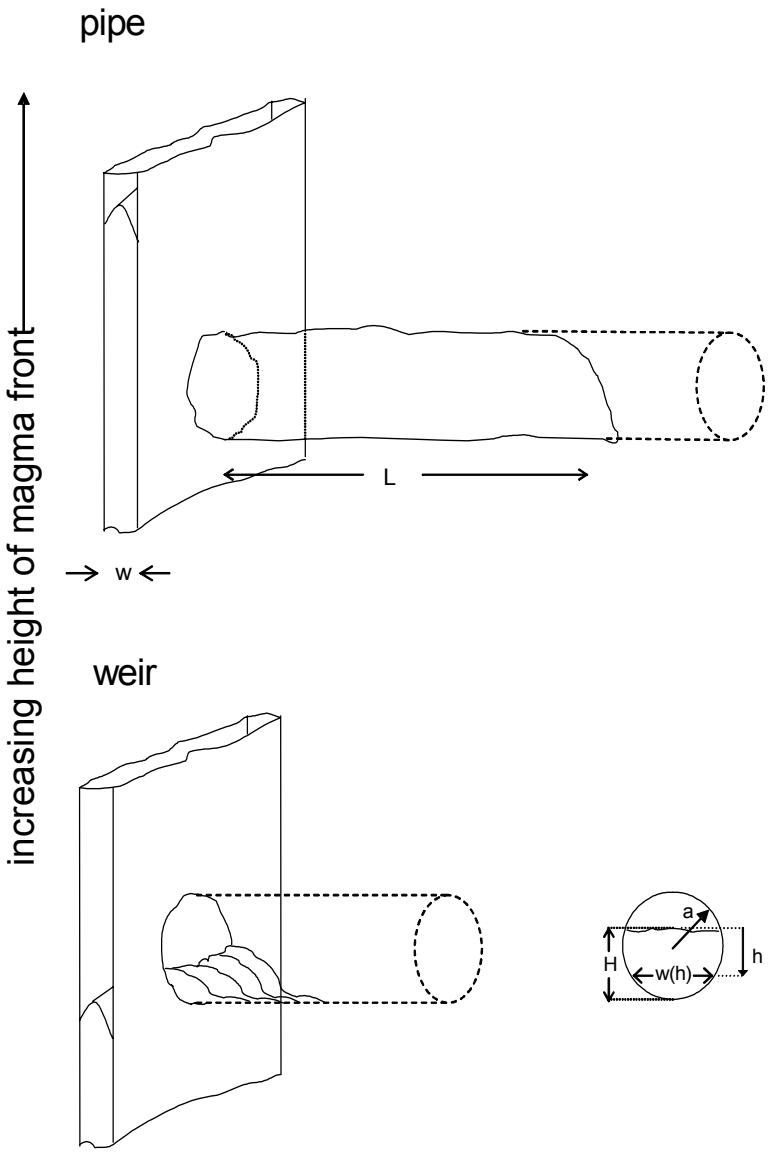

Source: For information purposes only.

NOTE The figure represents flow of magma for two distinct situations. In the lower drawing, the magma has not risen to the top of the drift, and a weir equation (Equation 6-89) is used. In the upper drawing, viscous drag in either the dike or the drift limits flow and Equation 6-92 or 6-98 is appropriate.

Figure 6-40. Schematic Representing Flow of Magma from Dike into Drift

The flow rate equation becomes:

$$\begin{aligned} Q(H) &= \sqrt{2g}\int_0^H dh\, 2\sqrt{h}\sqrt{(H-h)(2a-H+h)} \\ &= 2\sqrt{2gH^5}\int_0^1 dx\,\sqrt{x\left((2a/H)-x\right)(1-x)} \\ &= 4H^2\sqrt{ga}\int_0^1 dx\,\sqrt{x\left(1-(H/2a)x\right)(1-x)} \\ &= \frac{\pi}{2}H^2\sqrt{ag}\;{}_2F_1\left(-\frac{1}{2},\frac{3}{2};3;\frac{H}{2a}\right) \end{aligned} \qquad \text{(Eq. 6-89)}$$

$$= \frac{\pi}{2}H^2\sqrt{ag}\left(1+\frac{(-1/2)(3/2)}{1!3}\frac{H}{2a}+\frac{(-1/2)(-1/2+1)(3/2)(3/2+1)}{2!(3)(3+1)}\left(\frac{H}{2a}\right)^2+\cdots\right)$$

where the symbolic substitution has been made in the integral, $x = (H- h)/H$, and ${}_2F_1(a,b;c;z)$ is the hypergeometric function (Abramowitz and Stegun 1972 [DIRS 156927], Section 15.3). For $H = 2a$, the flow rate reduces to:

$$Q(H) = (64/15)a^2\sqrt{ag} \qquad \text{(Eq. 6-90)}$$

For $H > 2a$, the flow rate is given by:

$$Q(H) = \sqrt{2g}\int_{H-2a}^{H} dh\sqrt{h}w(h) \qquad \text{(Eq. 6-91)}$$

where $w(h)$ is given by Equation 6-88. This yields a result similar to Equation 6-89:

$$\begin{aligned} Q(H) &= \sqrt{2g}\int_{H-2a}^{H} dh\; 2\sqrt{h}\sqrt{(H-h)(2a-(H-h))} \\ &= 2\sqrt{2g}(2a)^{5/2}\int_0^1 dx\,\sqrt{x\left((H/2a)-x\right)(1-x)} \\ &= 8a^2\sqrt{2gH}\int_0^1 dx\,\sqrt{x\left(1-(2a/H)x\right)(1-x)} \\ &= \pi a^2\sqrt{2gH}\;{}_2F_1\left(-\frac{1}{2},\frac{3}{2};3;\frac{2a}{H}\right) \end{aligned} \qquad \text{(Eq. 6-92)}$$

The symbolic substitution, $x = (H-h)/2a$, has been made in the integral. This reduces to the orifice equation for flow from a half-space through a circular hole of radius a for $H>>2a$, as expected:

$$Q = \pi a^2\sqrt{2gH} \qquad \text{(Eq. 6-93)}$$

The equation for flow out of a dike into a pipe is derived following the method of Detournay et al. (2003 [DIRS 169660], Appendix 3.5, p. 62), which gives the volume flow rate from a dike through a circular hole q_{out} as:

$$q_{out} = \frac{2\pi a w^3}{12\mu} \frac{d/2a}{\log(d/2a)} \frac{\rho g H - P}{d/2} \quad \text{(Eq. 6-94)}$$

and the flow rate down the drift, q_{pipe}, as:

$$q_{pipe} = \frac{\pi a^4}{8\mu L} P \quad \text{(Eq. 6-95)}$$

where w is the width of the dike, μ is the magma viscosity, d is the spacing between drifts, ρ is the magma density, H is the height of magma above the drift, P is the pressure at the dike/drift interface, and L is the length of drift that is filled with magma.

Several things should be noted regarding differences between Equations 6-94 and 6-95, above, and Equations (3) and (4) of Detournay et al. (2003 [DIRS 169660]). First, the variable, w, in Detournay et al. (2003 [DIRS 169660]), represents the half-width of the dike, whereas the w in this document represents the full width of the dike. Thus, when comparing the above equations with those of Detournay et al. (2003 [DIRS 169660]), each occurrence of w in the equations in that study must be changed to $w/2$. Further, equations (2) and (3) of Detournay et al. (2003 [DIRS 169660]) are both too small by a factor of 2. Finally, the factor of 5.3 used by Detournay et al. (2003 [DIRS 169660], Equation (3)), is the factor of $(d/2a)/\log(d/2a)$ in Equation 6-94. The expression in Equation 6-94 is explicitly used because the variable, a, is corrected as by Detournay et al. (2003 [DIRS 169660], Equation (4)) for the presence of waste packages in the drift.

Equating q_{out} and q_{pipe} and solving for P yields the flow rate under the dual constraint of flow in the dike and flow in the drift (pipe-flow equation). After rearranging, placing this result in Equation 6-95 yields the equation for flow from the dike to the drift:

$$q_{pipe} = \frac{\pi a w^3}{3\mu d} \frac{d/2a}{\log(d/2a)} \rho g H \left[1 + \frac{8}{3} \frac{d/2a}{\log(d/2a)} \frac{a w^3 L}{d a^4} \right]^{-1} \quad \text{(Eq. 6-96)}$$

Defining a "scaling volume," V^*, as:

$$V^* = \frac{a w^3}{3d} \frac{d/2a}{\log(d/2a)} \quad \text{(Eq. 6-97)}$$

simplifies Equation 6-96 to:

$$q_{pipe} = V^* \frac{\pi \rho g H}{\mu} \left(1 + 8 \frac{V^* L}{a^4} \right)^{-1} \quad \text{(Eq. 6-98)}$$

The time development of flow into the drift is a solution to one of two differential equations described in the *Mathematica* notebook contained in output DTN: LA0602DA831811.001, where the flow into the drift is taken to be Equation 6-89 for $H \leq 2a$ and the minimum of Equations 6-92 and 6-98 for $H > 2a$.

Description of Input—The variables in Equations 6-89, 6-92, and 6-98 are the acceleration of gravity g, drift radius a (half the drift diameter), the filled drift length L, the distance between drifts d, the magma density ρ, and the magma viscosity μ. Most of the inputs are equivalent to the inputs described in Section 6.4.3 and are found in Table 4-1 and shown in Table 6-5. The calculations were done for a dike width calculated internally from the magma viscosity, the magma supply rate and the scaled relative density (which was taken from Table 6-3 to be $\mathcal{D} = 20.28$ with $\kappa\rho_r = 1{,}200$ kg m^3). The parameters are equivalent to those used in Section 6.4.5.1 (wide-aperture case). The height of magma over the weir, H, in Equations 6-89 and 6-92 is internally generated in the analysis. For Equation 6-98, the filled drift length, L, is calculated internally as the cumulative discharge from prior flow divided by the cross-sectional area of the drift. In order to demonstrate the effects of deviations of magma viscosity and magma supply rate, calculations of magma flow have been done with two values of viscosity and two magma rise velocities, using values from Table 6-3 in Section 6.3.7.1. Sources for these parameters are found in Table 4-1. The 1-m value assumed for the radius of a waste package (Table 6.6) is within the range of dimensions for waste packages planned for the repository.

Initial and Boundary Conditions—The initial condition consists of magma beneath the end of the drift at the height of the invert. The magma is moving upward at the chosen magma far-field velocity. The drift is a horizontal tube, the diameter of which is four times the hydraulic radius; the drift is initially empty (except for the decreased hydraulic radius in obstructed cases).

All surfaces except the magma-free surface, if any, are rigid, and the equations are based on a no-slip boundary.

Results—Eight cases have been evaluated for effusive flow of magma into drifts. The eight cases cover variations in magma far-field velocity and in magma bulk viscosity, as well as whether the drifts are empty or filled with waste packages. These cases are listed in Table 6-6. Note that the second case in this table corresponds to the wide-aperture case in Section 6.4.5.

Table 6-6. Cases Evaluated for Effusive Magma Flow into Drift

Magma Viscosity (Pa·s)	Waste Package Radius (m)	Magma Rise Velocity (m/s)
40	0	1
10	0	1
40	1	1
10	1	1
40	0	10
10	0	10
40	1	10
10	1	10

The results are presented in Figures 6-41 through 6-43, showing, respectively, the discharge rate out of the dike as a function of time, the length of drift filled as a function of time, and the height that magma rises above the drift invert.

Figure 6-41 shows this analysis predicts steady state is reached in about 8 s for the case ($v = 1$ m/s, $\mu = 10$ Pa·s, empty drift), which corresponds to the wide-aperture case in Section 6.4.5. Figure 6-43 shows that the magma will not rise more than 3 m above the drift. This is compared with the results from the previous analysis: steady state not achieved before the drift is filled, 900 s after magma reaches the drift, and a magma rise of about 80 m. The alternative analytical analysis is biased toward large flows because it only considers viscous drag in the dike after the pipe-flow condition occurs. It is presumed that better agreement between the models would be obtained if viscous forces in the dike were coupled to the weir equations (Equations 6-89 and 6-92).

This analysis does not address the phenomena associated with multiphase flow of magma into a drift. This subject is addressed in *Magma Dynamics at Yucca Mountain, Nevada* (BSC 2005 [DIRS 174070]).

6.3.3.5.8 EPRI Analysis of Magma-Drift Interactions

The EPRI published an analysis of potential igneous processes at Yucca Mountain (EPRI 2004 [DIRS 171915]). That analysis of magma-drift interaction provides a description of thermal effects in magma flowing in the drift. The study notes that surface temperatures of lava flows in Hawaii are as low as 450°C because "radiative cooling allows the surface temperature to drop several hundred degrees within minutes" (EPRI 2004 [DIRS 171915], Section 4.1.2, p. 4-4). The EPRI analysis concludes, "These observations and analyses, predominantly reflecting conditions on the surface, are expected to be conservative compared to conditions in a drift. Flow into a drift is characterized by a higher surface area to volume ratio of the surroundings, which allows higher rates of heat loss than would be experienced at the ground surface. Consequently, in-drift heat losses from magma into waste packages and the surrounding rock would be higher than heat losses into the ground at the surface. Therefore, the same mass of magma would cool more quickly in a drift than on the surface" (EPRI 2004 [DIRS 171915], Section 4.1.2, p. 4-5). As the report notes, radiative cooling is a major contributor to the rapid cooling of lava surfaces. However, radiative cooling will be inhibited in an underground environment where the surrounding solid surface (the back of the drift) will heat up quickly. In addition, convective cooling due to movement of air will be less efficient in a 5.5-m-diameter drift than in the open atmosphere. Therefore, the model in this report is preferred over the EPRI analysis.

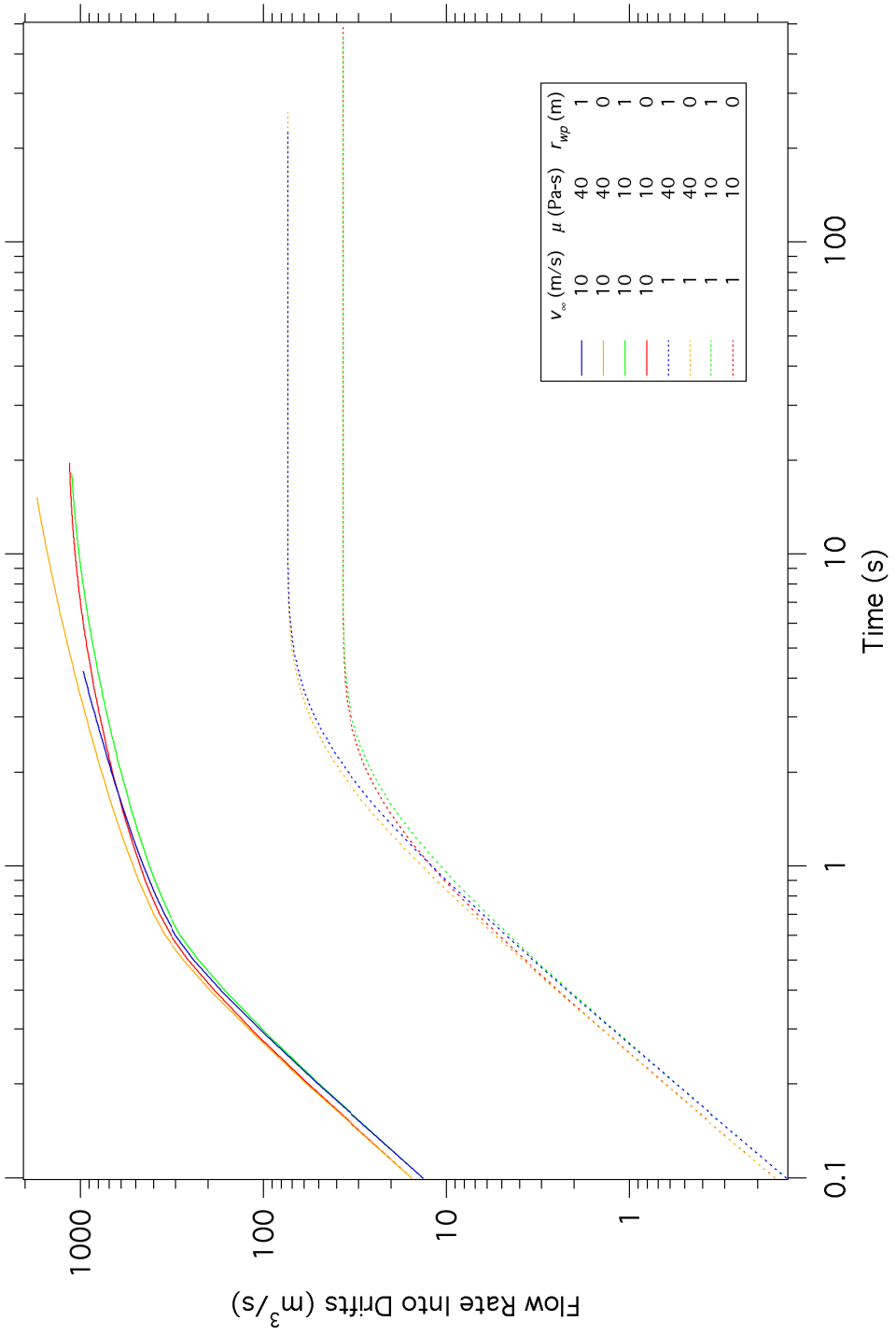

Output DTN: LA0602DA831811.001; file: *Igor Data\Graph1.png.*

Source: Output data plots.

Figure 6-41. Discharge Rate for Effusive Magma Flowing into Drifts as a Function of Time

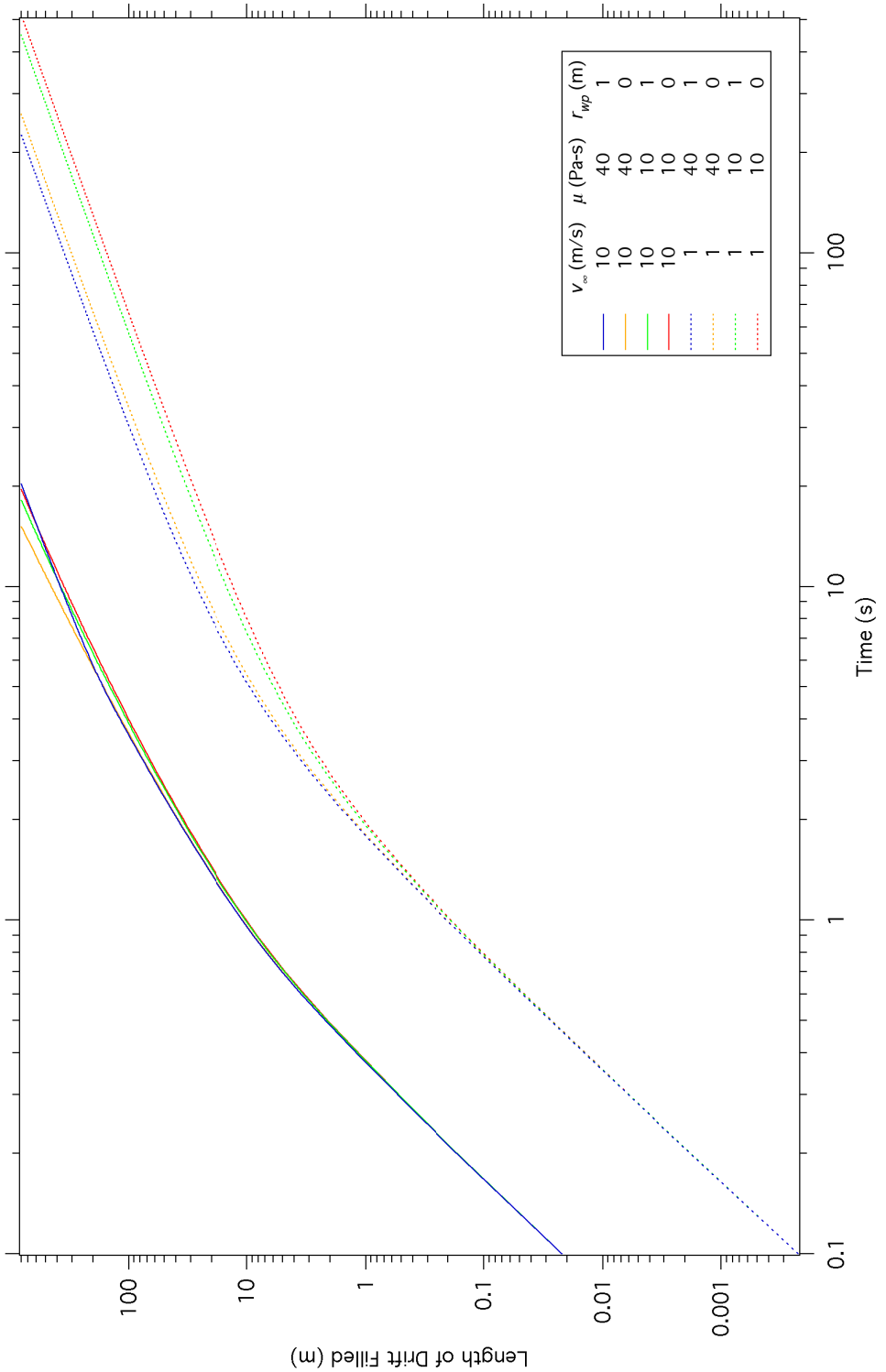

Output DTN: LA0602DA831811.001; file: *Igor Data\Graph2.png*.

Source: Output sata plots.

Figure 6-42. Length of Drift Filled by Effusive Magma Flowing into Drifts as a Function of Time

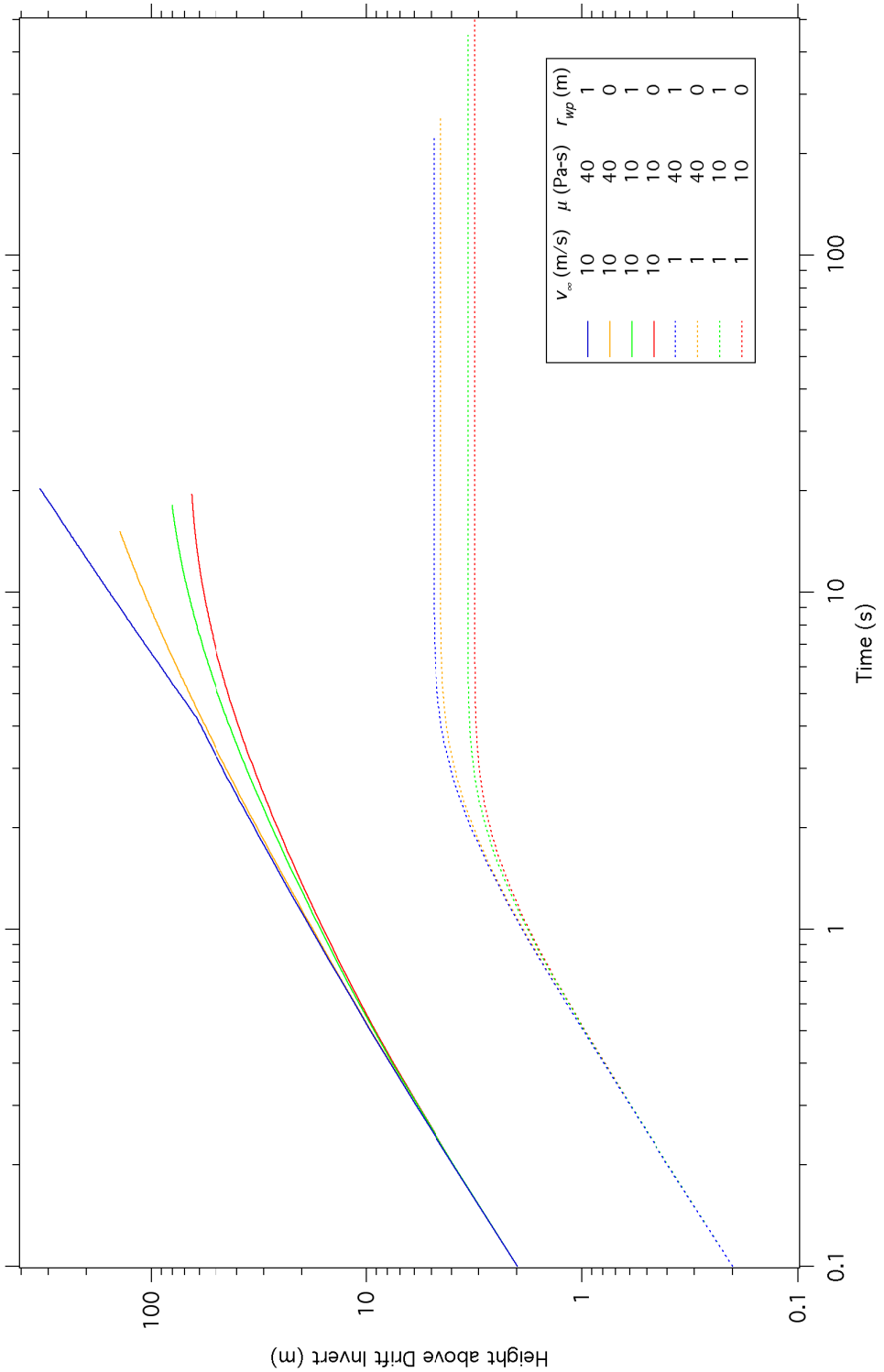

Output DTN: LA0602DA831811.001; file: *Igor Data\Graph0.png*.

Source: Output data plots.

Figure 6-43. Height of Magma in Dike above Invert for Effusive Magma Flowing into Drifts as a Function of Time

6.3.4 Component for Effect of Structure and Stratigraphy

A large number of faults characterize the structural geology of the Yucca Mountain area (Day et al. 1998 [DIRS 100027]). Because faults are discontinuities in the rock mass, they could have an effect on potential dikes in the vicinity of Yucca Mountain (Connor et al. 2000 [DIRS 149935]). When a fracture tip intersects a discontinuity in any medium (including a rock mass), the singularity in the vertical plane will disappear, which could effectively result in fracture arrest or diversion into the plane of discontinuity. In addition, faults, as discontinuities or regions filled with broken, rubblized rock mass, can be regions of increased permeability, providing preferential paths for magma flow.

It has been observed in the Paiute Ridge area of southern Nevada (Carter, Krogh, and Valentine 1996 [DIRS 160928]) that most dikes occupy preexisting normal faults. The effect of faults on dike propagation in the vicinity of Yucca Mountain and the possibility of diversion of potential dikes propagating under Yucca Mountain are investigated here. In this section, the results of an approximate analytical method are corroborated with the results of numerical simulations.

Figure 6-44 shows an east-west geologic cross section near Yucca Mountain (at coordinate 760,000N based on Nevada coordinate system central zone), as developed by Day et al. (1998 [DIRS 100027]). The location of the Exploratory Study Facility (ESF) is indicated in the figure. The repository will be located at the same elevation as the ESF, extending to the west relative to the ESF. The entire repository will be located within the Topopah Spring Tuff.

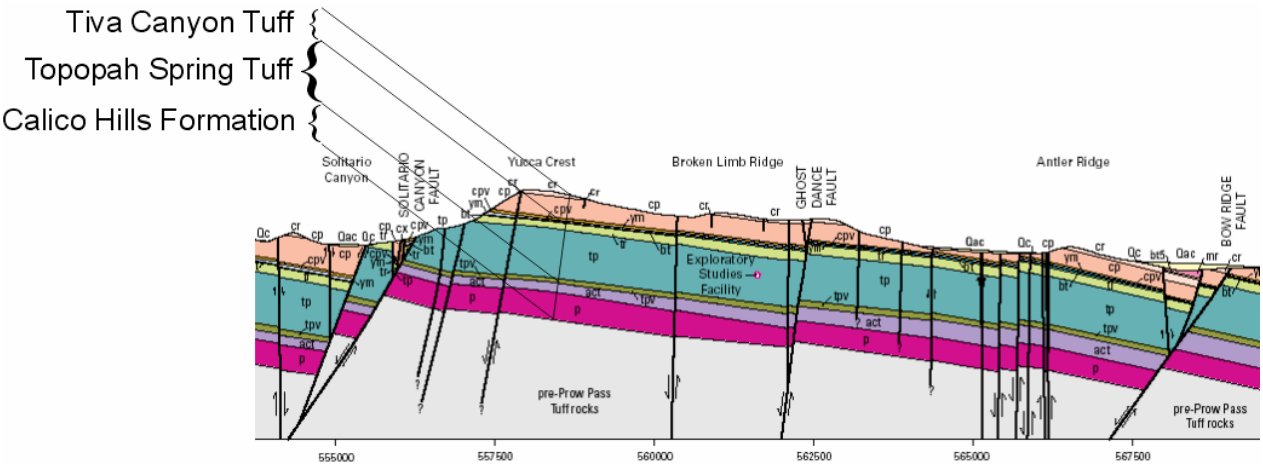

Source: Day et al. 1998 [DIRS 100027].

NOTE: Graphic shows a roughly vertical east-west cross section.

Figure 6-44. Geological Cross Section of the Yucca Mountain Area

Faults near Yucca Mountain generally strike north with variable dips ranging from relatively shallow (45°–50°) to steep (75°–85°) (Day et al. 1998 [DIRS 100027]). Two block-bounding faults surrounding Yucca Mountain are the Solitario Canyon Fault (on the west side of Yucca Mountain) and the Bow Ridge Fault (on the east side of Yucca Mountain), both dipping at roughly 55°–60°. Intrablock structures (Day et al. 1998 [DIRS 100027]) are relatively minor

faults that lie entirely within the structural blocks defined by block-bounding faults. The Ghost Dance Fault is the main intrablock fault within the central part of the potential repository area. It is entirely an intrablock fault with no surface connection to any known block-bounding fault (Day et al. 1998 [DIRS 100027]). Any connection at depth of the Ghost Dance Fault with block-bounding faults is inferential.

6.3.4.1 Model Description

Dikes are magma-driven hydraulic fractures, usually propagating vertically upward through the rock mass. The magma front lags behind the fracture tip at a distance determined by the magnitude of stresses normal to the dike plane (Section 6.3.3.4.2). The lag is small, or disappears completely, when the stresses are large (e.g., at great depth), but can be very large (200 m - 300 m) as confinement decreases at shallow depths, near the ground surface.

This analysis considers a fault in brittle material, so it is applicable only in the upper crust, where the rocks fail in a brittle manner. Faults are discontinuities in the rock mass that have undergone some relative shear displacement. Consequently, cohesion and toughness (resistance to fracture) in the fault plane itself could be low. In this analysis, the low cohesion of the fault is taken to vanish altogether, making diversion into a fault more likely than it might be in nature. The compressive normal stresses keep the fault closed; the build-up of finite shear stresses in the fault plane before the fault slips is defined by the friction angle.

Fracture toughness of many different rocks on the scale of intact samples usually tested in laboratory is of the order of 1 MPa $m^{1/2}$ (values for many different rock types are given in Section 6.3.4.6.3). The effective fracture toughness of rock mass on a large scale (the scale relevant for dike propagation) is probably less, because of the effect of preexisting fractures within the rock mass. As the dike tip propagates through the rock mass, a portion of its path is through the intact rock (which has a finite toughness of the order of 1 MPa $m^{1/2}$), while some portion is along preexisting fractures. The dimensionless dike-propagation analysis (Section 6.3.3.1.2) shows that even a fracture toughness of 1 MPa $m^{1/2}$ is relatively small, having a second-order effect on dike propagation (e.g., magma pressures, magma front velocity, dike opening), and can be neglected in an analysis. However, small but finite toughness of the rock mass becomes important when considering interaction between the dike and a preexisting fault, which has no toughness.

As a dike approaches a fault, it can either turn into the fault (Figure 6-45) or continue propagating along the original path, vertically upward. The dike tip gets "arrested" when it intersects the fault in a situation in which the cohesive strength (or toughness) in the fault plane is very low and the hanging wall is intact and has finite toughness—that is, the stress singularity, which is ahead of the dike tip when the dike is away from interfaces (such as faults), cannot penetrate into the hanging wall of the fault even though the tip has reached the fault. Fracture initialization and propagation in the hanging wall of an intact fault can occur only if the magma pressure in the portion of the dike below the fault can cause tensile stresses in the hanging wall of the fault that exceed the tensile strength of the rock mass. Such an effect is possible if tensile and shear strengths of the fault are sufficiently large. For faults with no cohesion, the dike can cause sufficient tension in the hanging wall of shallow dipping faults only (e.g., a dip angle of 40° or less). However, there is a mechanism, discussed in the following paragraph, which can

cause continuation of dike propagation in the vertical direction even when the rock (total) horizontal stress in the hanging wall is compressive.

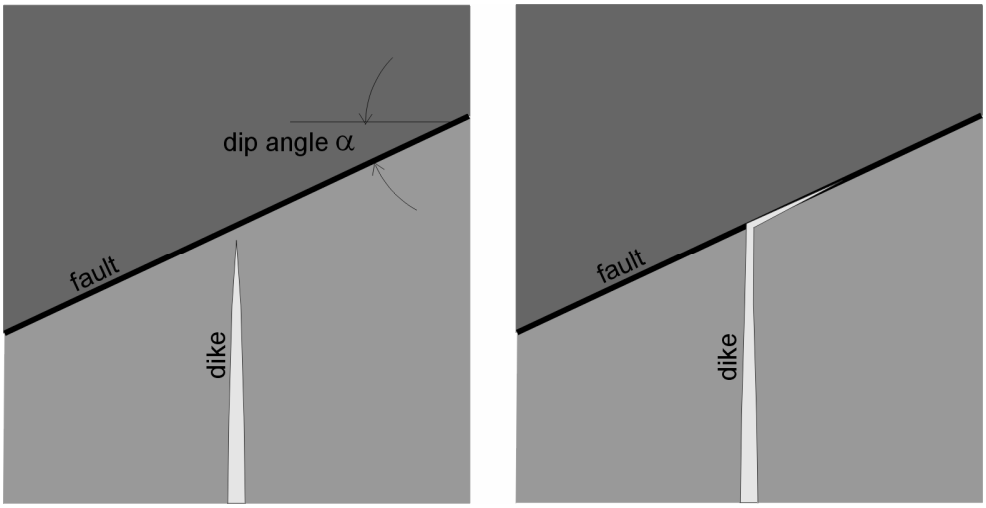

Source: For illustrative purposes only.

Figure 6-45. Diversion of the Dike into the Fault Dipping at Angle α

Rock masses in the upper crust are rarely completely intact. Fractures exist on different scales, from grain-size to the kilometer scales (e.g., faults). Most likely, the hanging wall will contain fractures of a varying length, α, between a tenth of a meter to few meters. Figure 6-46 illustrates this situation with subvertical fractures. The spacing of fractures of different sizes will also vary from one location to another, depending on a number of factors, including rock type, stress state, and tectonic history. After magma reaches the intersection and magma pressure increases to eventually open and start flowing into the fault, it will also fill and pressurize the joints in the hanging wall (Figure 6-46). As the fault length filled with magma increases, a greater number and more representative sample of hanging wall fractures will be exposed to magma pressure. If the pressure (relative to the rock stress acting on the fracture plane) required to propagate any of the hanging wall fractures is less than the pressure required to open and flow along the fault, the dike will resume propagation in the vertical direction. A simple analysis of dike/fault interaction for subvertical hanging wall fractures is presented in the next section.

When the stress state is such that the vertical stress is greater than the stress normal to the dike plane, as at Yucca Mountain, dike propagation will be slowed for some time after the tip reaches the fault.[5] After the magma pressure at the dike/fault intersection builds up sufficiently to open the fault (i.e., becomes equal to or greater than the stress normal to the fault plane) or initialize the fracture in the hanging wall, the magma will start flowing into the fault (Figure 6-45) or continue along the original path. The excess pressure required to open the fault or fracture the hanging wall, compared to the original pressure required to propagate the dike in the vertical direction, will cause an additional opening of the portion of the dike below the intersection with the fault.

[5] A dike is usually oriented perpendicular to the least compressive normal stress. If the rock mass strength is isotropic, a stress state with the greatest principal stress directed vertically will favor vertical dike propagation.

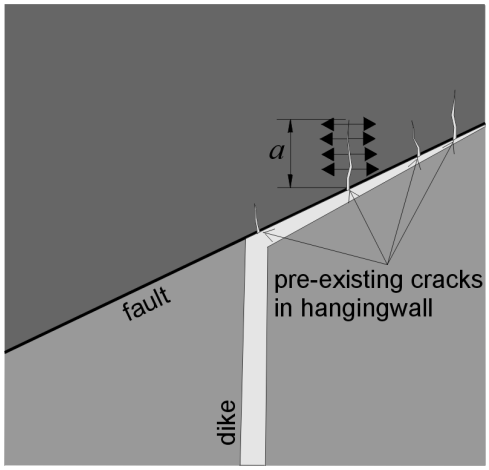

Source: For illustrative purposes only.

Figure 6-46. Mechanism for Propagation of a Dike in the Fault Hanging Wall

6.3.4.2 Mathematical Description

Interaction between the dike and faults was numerically investigated using UDEC V. 3.14. Calculations were carried out in two stages. In the first, purely mechanical stage, the initial equilibrium stresses in the analyzed domain were determined. "Roller" boundary conditions were applied at the base. The top surface was stress-free. Stress boundary conditions were applied on the far-field vertical boundaries. These stresses were in equilibrium with the in situ horizontal stress, which is 50% of the vertical gravitational stress.

In the UDEC calculations, the dike propagation and magma flow can only occur along preexisting discontinuities. There are two different ways to simulate hydro-mechanical joint behavior in UDEC calculations. If the joint represents a preexisting fracture in a rock mass, which is permeable even when it is completely closed because of residual permeability due to joint surface roughness, the fluid can flow along the joint even if it is closed (i.e., there is a normal stress on the joint). This approximation is used for a joint that represents a fault and for a joint that represents the dike when the rock has no fracture toughness (e.g., it is heavily jointed). In the second approximation, a joint represents a potential fracture path that initially is unfractured, so that flow along the joint cannot take place until the joint is fractured (either as a result of opening or shearing) as dictated by the stresses acting in the joint plane. The second approach is more appropriate for dike representation in the case of finite toughness of the rock mass.

6.3.4.3 Uncertainties and Limitations

The fluid flow inside the joints in UDEC was approximated by laminar flow between the parallel plates. This approximation certainly is not appropriate for flow along the faults while they are closed under in situ normal stress. However, if magma is injected into a fault and it opens, the parallel plate flow approximation will become adequate. The initial fault aperture in the flow calculation approximated by the flow between parallel plates was assumed to be 1 cm, uniformly throughout the analyzed domain, irrespective of fault depth. Due to an increase in confinement

(stress acting normal to the fault plane), the effective permeability of the faults probably decreases with depth. However, the variability of fault permeability as a function of depth is inconsequential in these calculations because the initial fault permeability is negligible compared to the permeability of the dike propped open by magma pressure (aperture on the order of 1 m).

6.3.4.4 Input Parameters

In the initial state of dike propagation analysis, the joint that represents the potential dike path is prefractured along a relatively short segment (200 m) at the base of the calculation domain. As magma is injected at the base, at the rate of 0.45 $m^2 s^{-1}$ (cf., case $\mathcal{D}$ = 20.28, v_∞ = 1 m s^{-1}, μ = 10 Pa·s, and κ = 0.5 in Table 6-3), the magma pressure in the dike builds up, fracturing the rock ahead of the dike tip and pushing the magma upward. Magma is represented as a slightly compressible fluid with a bulk modulus of 50 MPa, a density of 1,000 kg m^3 (within 12% of the 1,141 kg m^3 for the case cited), and a viscosity of 10 Pa·s. Gravitational acceleration is approximated as 10 m/s^2.

The situation illustrated in Figure 6-45, a dike intersecting a fault, is analyzed. Fault angles ranged from 10° to 80°, in increments of 10°. The dike intersects the fault at a 2-km depth in all cases. Rock mass properties, given in Table 6-7 are consistent with those of Table 6-2 for dike propagation.

Table 6-7. Mechanical Properties of the Rock Mass for Simulation of Analytic Approximation

Property	Value
Density (kg m3)	2,400
Young's Modulus (GPa)	15
Poisson's ratio	0.21

Source: Table 6-2 in this document.

The pressure required to pry open the fault at the intersection between the dike and the fault was investigated numerically. The numerical results are compared with the simple predictions based on the analytic approximation of Section 6.3.4.6.3 (which does not account for the stress changes caused by the dike). The geometry of the numerical representation and magma pressure distribution along the dike (and fault) during simulation of the fault dipping at 80° are shown in Figure 6-47.

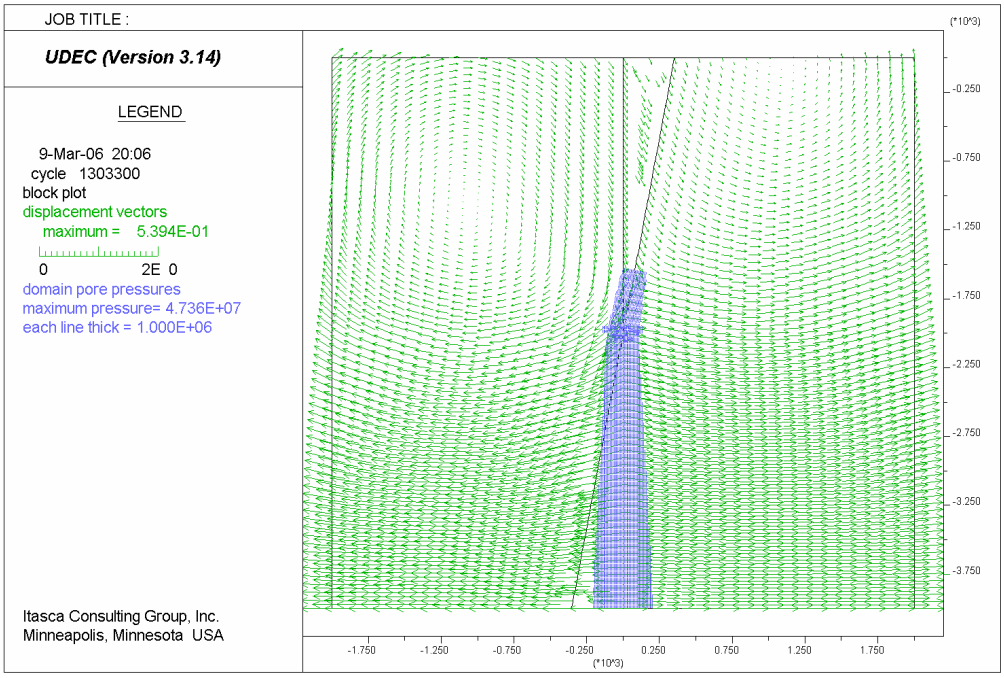

Source: Output DTN: MO0610SPADIKEP.000, file *pressures.xls*.

Figure 6-47. Displacements (m) and Magma Pressures (Pa) after Dike Diversion into the Fault Dipping at 80°

6.3.4.5 Model Results

The evolutions of magma pressures at the dike/fault intersection in the numerical simulations are shown in Figure 6-48. The pressure estimates based on the analytic approximation (Section 6.3.4.6.2) are included in the plot as dashed lines. The maximum magma pressures calculated using two methods are also listed in Table 6-8. The results indicate that the initial stress transformation provides a good estimate (error within 15%) for fault dip angle greater than 60°. The difference between the two predictions increases for the range of dip angle between 30° and 60°. For the angles investigated, the greatest difference is for a dip angle of 40°. In that case, the maximum numerically calculated magma pressure is 28.8 MPa, while the initial stress transformation yields the normal stress on the fault plane (i.e., the pressure required to open the fault) of 38 MPa. (The difference is approximately 24%.) It appears, based on the results presented in Figure 6-48 that the initial stress transformation provides an even worse estimate for a fault dip angle equal to or smaller than 30°. However, the numerical results in Figure 6-48 (for the total simulated time up to 1.6×10^4 s or approximately 4.5 h) do not provide the maximum pressure for dip angles between 10° and 30°. The magma pressure at the intersection is still increasing at the end of the simulation.

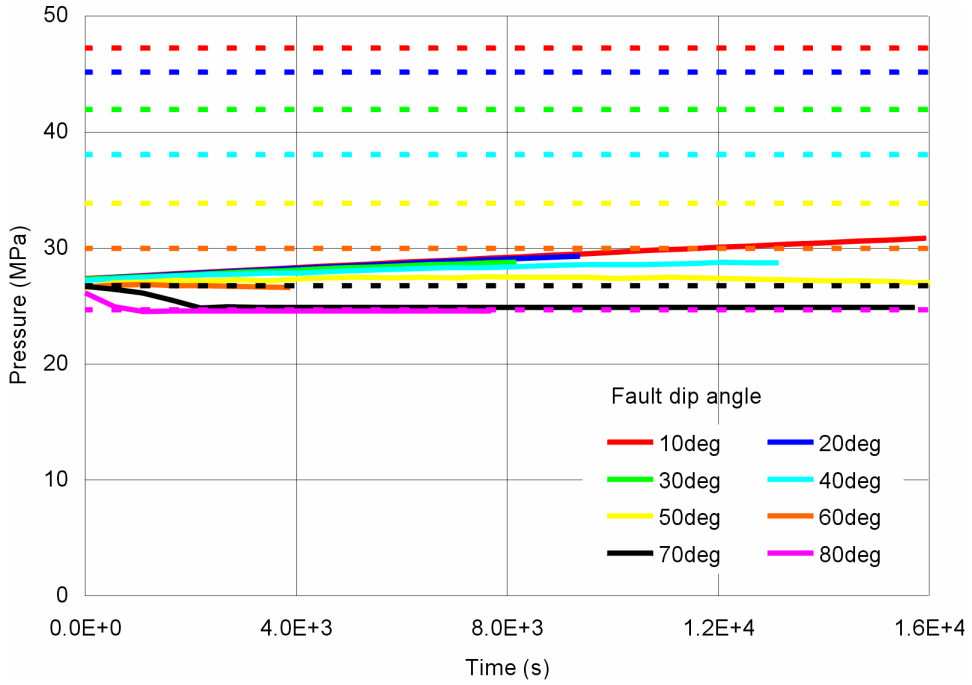

Source: Output DTN: MO0610SPADIKEP.000, file *pressures.xls*.

NOTE: The pressures required to open the fault estimated based on the analytic approximation of Section 6.3.4.6.2 are shown as dashed lines.

Figure 6-48. Evolution of Pressures at Dike/Fault Intersection Calculated Numerically Compared to the Estimates Based on the Initial Stress Transformation

Table 6-8. Results of Numerical Study of an Analytic Solution

Fault dip angle, α (°)	Numerical prediction		Pressure based on analytic solution (MPa)	Fault open?
	Max. pressure (MPa)	Final pressure (MPa)		
10		30.9[a]	47.2	no
20		29.4[a]	45.2	no
30		28.8[a]	42.0	no
40	28.8	28.8	38.1	yes
50	27.6	27.1	33.9	yes
60	26.9	26.6	30.0	yes
70	26.8	24.9	26.8	yes
80	26.2	24.6	24.7	yes

[a] The pressure when the simulation was terminated.

Source: Output DTN: MO0610SPADIKEP.000, file *pressures.xls*.

The contours of the vertical stress, as well as the dike and fault normal deformation at the point 4.4 hr after magma has reached the dike/fault intersection (approximately the final state from Figure 6-48) for the case of a 10° fault dip angle are shown in Figure 6-49. Clearly the fault has not even started to open yet. The contours of the vertical normal stress indicate that the vertical normal stresses along the fault are well in excess of 40 MPa. In fact, the maximum normal stresses on the fault, along the segment of the fault above the intersection, at the stage when the magma reaches the intersection (as extracted from the numerical calculations), are 45.95 MPa,

42.44 MPa, and 38.00 MPa for fault dip angles of 10°, 20° and 30°, respectively. These stresses, which represent the asymptotes of magma pressures required to open the fault, are in good agreement with the magma pressures calculated by the initial stress transformation (Table 6-8 and dashed lines in Figure 6-48). Furthermore, in the limit when the fault dip angle is 0°, the magma pressure prediction required to open the fault must be correct because the intrusion of the dike causes only the horizontal stress to change.

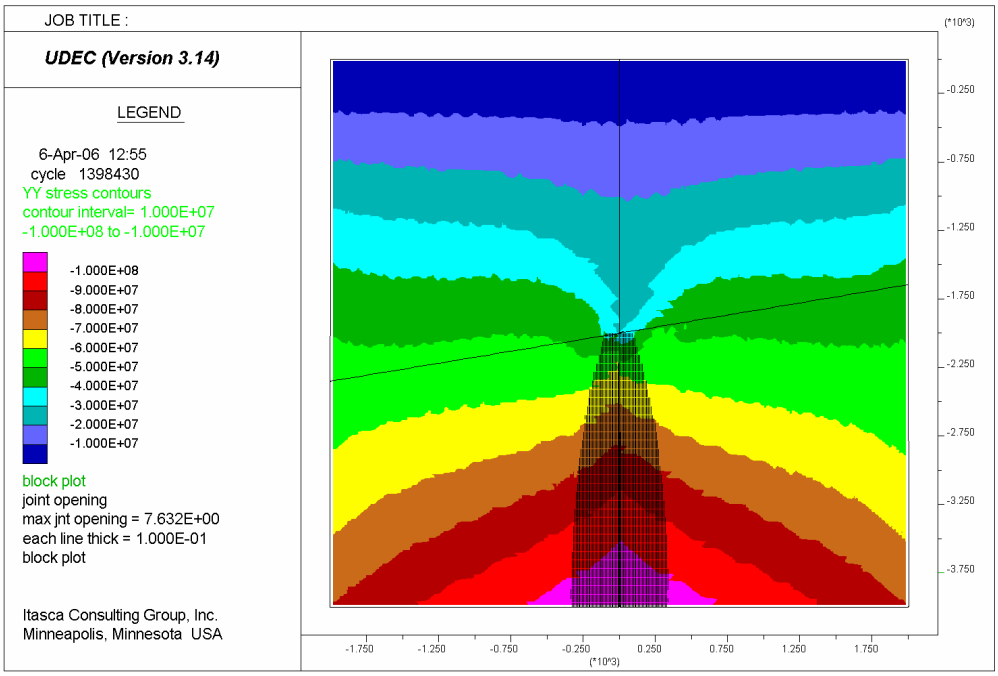

Source: Output DTN: MO0610SPADIKEP.000, file *pressures.xls*.

Figure 6-49. Contours of Vertical Normal Stress (Pa) and Dike Deformation (m) 4.4 Hours After Magma has Reached the Intersection with a 10° Dipping Fault

6.3.4.5.1 Simulation of Dike Propagation below Yucca Mountain

The geometry used for the numerical analysis of dike/fault interaction below Yucca Mountain is shown in Figure 6-50. A possible dike path, unaffected by faults, is predefined by the vertical fracture below Yucca Mountain (indicated by the dashed line in Figure 6-50). The calculation domain is approximately 15 km wide; the bottom of the domain is 7 km below the ground surface. The calculation is two-dimensional and is intended to approximate the cross section shown in Figure 6-44. The topography and lithology in the vicinity of Yucca Mountain and the repository (but not over the entire width of the calculation domain) are included in a simplified way.

Although three different layers can be distinguished from the bottom of the Calico Hills Formation to the ground surface, they were assumed to have the same mechanical properties in all simulations. The details of geology near the ground surface do not have significant (if any) effect on dike/fault interaction, which occurs approximately 3.5 km below the ground surface. At depths greater than 1 km, there is significant uncertainty regarding lithology and no data on the mechanical properties of the different units. Therefore, the rock mass below the Calico Hills Formation was represented as a homogeneous material.

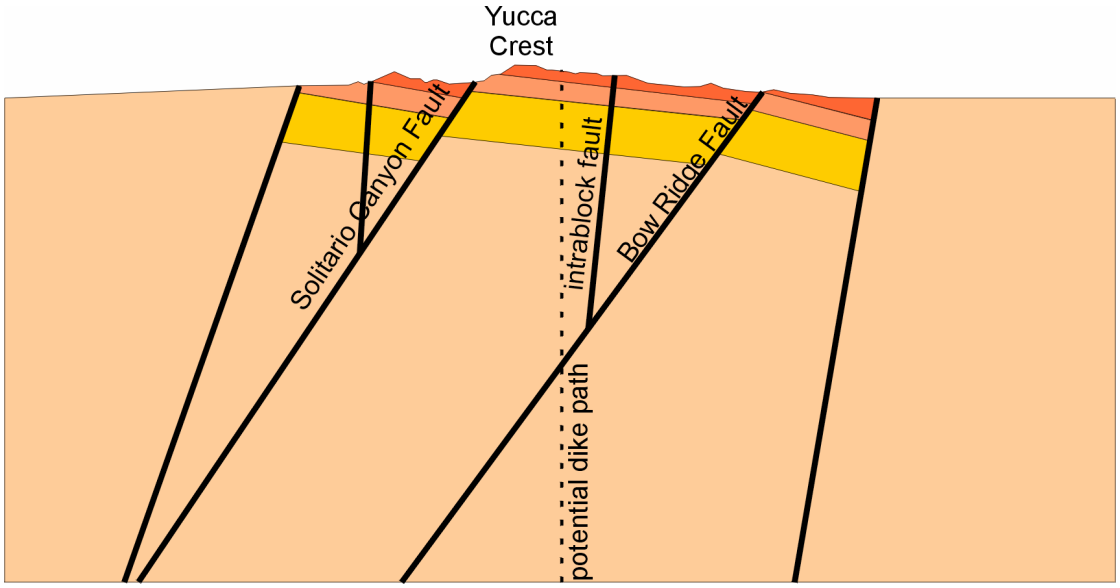

Source: For illustrative purposes only.

Figure 6-50. Geometrical Representation used in the Numerical Simulation of Dike Propagation below Yucca Mountain

In all calculations, the rock mass was considered to be linearly elastic. The rock mass mechanical properties used in the calculations are listed in Table 6-9. Two cases were addressed:

- Case 1: All rock properties were Type 1
- Case 2: The rock properties of Calico Hills and higher rocks were Type 1; lower rocks were Type 2.

Table 6-9. Mechanical Properties of the Rock Masses

Property	Type 1	Type 2
Density (kg m3)	2,400	2,400
Young's Modulus (GPa)	15	25[a]
Poisson's ratio	0.21	0.21

[a] value is assumed to simulate stiffer rock.

Source: see Table 6-2.

Two block-bounding faults (the Solitario Canyon Fault and the Bow Ridge Fault), which are the main structures that can affect dike propagation below Yucca Mountain, are extended to the base of the calculation domain (Figure 6-50) based on dip angles inferred from Figure 6-44. It was assumed that the intrablock fault within the block formed by the Solitario Canyon Fault and the Ghost Dance Fault does not extend below its intersection with the Bow Ridge Fault. In all calculations, the faults (subvertical structures in Figure 6-50) and the interfaces between different geological units (subhorizontal structures in Figure 6-50) are represented as cohesionless contacts, which slip as governed by the Coulomb law. The effect of different friction angles in the faults and interfaces on the results of calculations is investigated by using values of 30°, 45°,

and 55°. Considering that the faults and the interfaces between the different units are represented in the calculations as planar, while, in reality, there is a considerable amount of roughness, the friction angle of 30° is a lower bound of the fault friction angle on the scale of this calculation. If the faults are continuous, as they are represented in the calculations, their effective friction angle probably does not exceed 55°. A fault is represented in the calculation as a discontinuity of no physical thickness. In reality, faults are usually zones of rubble and clay a few meters thick. The joint stiffness in the numerical calculation, which represents the deformability of the fault zone, is a function of different factors, including fault zone thickness and the type of material filling the fault zone. The calculations were carried out for joint stiffnesses of 5 GPa, 10 GPa, and 20 GPa/m (BSC 2004 [DIRS 166107], Table E-5).

6.3.4.5.2 Results

The depth at which a dike can intersect the Bow Ridge Fault below Yucca Mountain (assuming extrapolation of the fault shown in Figure 6-50) is in the range between 5,250 m and 3,300 m. The dip angle of the Bow Ridge Fault is approximately 55°. The conditions of interaction between the potential dike and the Bow Ridge Fault are indicated as green squares (for depths of 3,300 and 5,250 m) in Figure 6-51. The plot indicates that the dike will most likely propagate vertically upward unless there are no preexisting fractures of length equal to or greater than 0.1 m, or the rock toughness exceeds 10 MPa $m^{1/2}$, which is unlikely.

For this situation to be analyzed numerically, magma flow is allowed in the joint that represents the dike even when the joint is still unfractured. This condition corresponds to the bounding scenario in which the rock mass has no toughness or has very long preexisting cracks in the fault hanging wall. The stress state only controls the potential for dike diversion into the intersected fault. Because the vertical stress is two times greater than the horizontal stress, the dike continues along the vertical path (Figure 6-52).

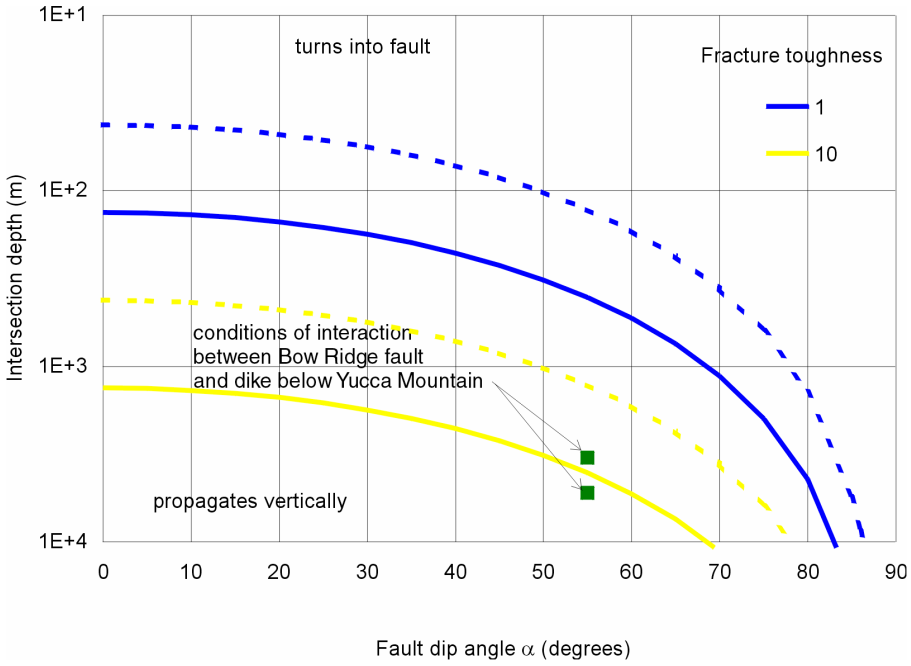

Source: Output DTN: MO0610SPADIKEP.000, file *depth dev.xls*.

NOTE: The solid lines are for 0.1-m-long preexisting hanging wall fractures; the dashed lines are for 1.0-m-long preexisting hanging wall fractures.

Figure 6-51. Evaluation of Potential for Dike Diversion into the Bow Ridge Fault below Yucca Mountain

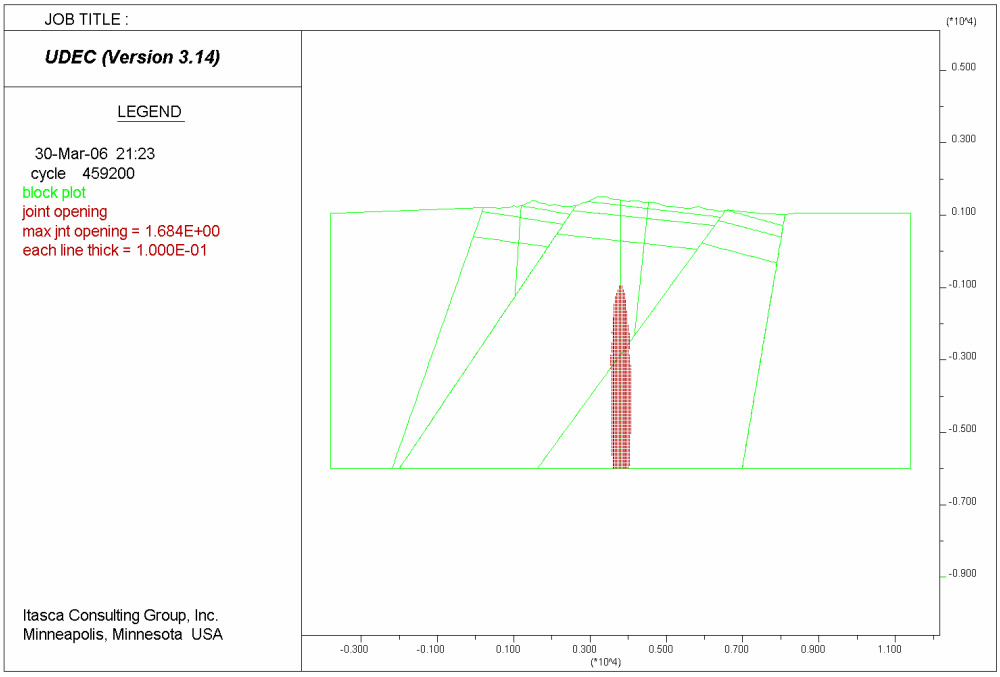

Source: Created for illustrative purposes only.

Figure 6-52. Opening (m) of the Dike at the Stage When the Dike Tip is above the Dike/Fault Intersection if the Dike Propagates through the Fault

The other, unlikely, situation that the potential dike would turn into the Bow Ridge Fault is simulated by assuming that magma cannot flow along the joint that represents the dike path, unless the joint is fractured (either opened or slipped). As mentioned previously, when the dike intersects the fault, it is unable to continue propagation along the original path, because magma pressure inside the dike and fault does not create a stress concentration in the hanging wall sufficient for fracture propagation. Consequently, magma turns into the Bow Ridge Fault. Dike apertures at four different stages during simulation of the dike/fault interaction are shown in Figures 6-53 through 6-56. Before reaching the intersection with the Bow Ridge Fault, the dike opening is of the order of 1 m. After the intersection, the dike is unable to continue along the original path. Because the normal stress on the fault plane is greater than the normal stress on the dike plane, an increase in magma pressure is required before the magma can open the fault and start flowing along the fault. Propagation is stalled until sufficient pressure builds up. A consequence of this magma pressure increase is the additional opening of the section of the dike below the intersection. However, after magma starts flowing along the Bow Ridge Fault, and reaches the intersection between the Bow Ridge Fault and the steeply dipping intrablock fault, it will turn into the steeply dipping fault, along the path with smaller normal stress.

As magma is injected into faults, the effective normal stress in the fault plane drops to zero, causing the faults to slip and the relaxation to zero of any shear stress that could have existed in the fault planes. An interesting effect of slip on the intrablock fault is the opening on the hanging wall side of the subhorizontal structures (which represent interfaces between different geological units) as magma approaches the ground surface. This response is consistent with observations by Valentine and Krogh (2006 [DIRS 177282]) in the Paiute Ridge area of sills forming at shallow depths in the hanging wall of normal faults that have been intruded by dikes.

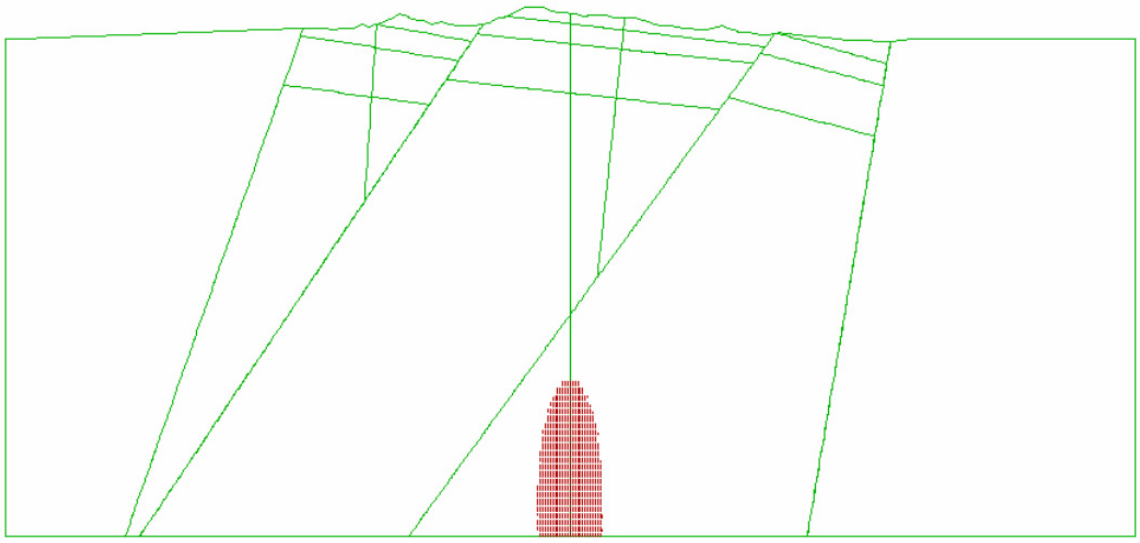

Source: Output DTN MO0610SPADIKEP.000, file *\dike_fault\step1.sav*.

Figure 6-53. Evolution of Dike and Fault Opening in UDEC Simulations before Magma has Reached Fault

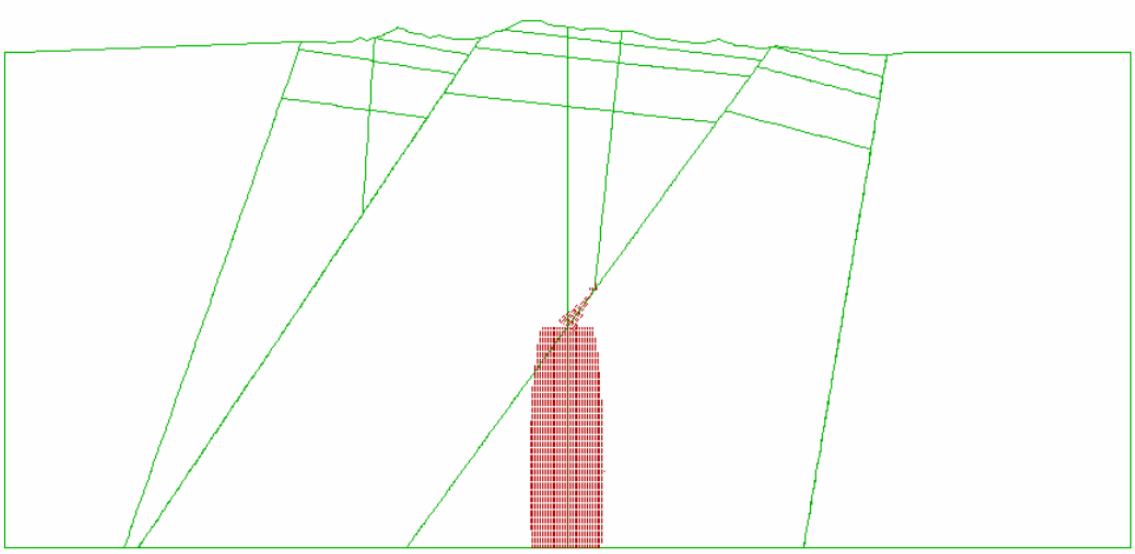

Source: Output DTN MO0610SPADIKEP.000, file *dike_fault**step2.sav*.

Figure 6-54. Evolution of Dike and Fault Opening in UDEC Simulations after Magma has Penetrated Shallower Dipping Fault

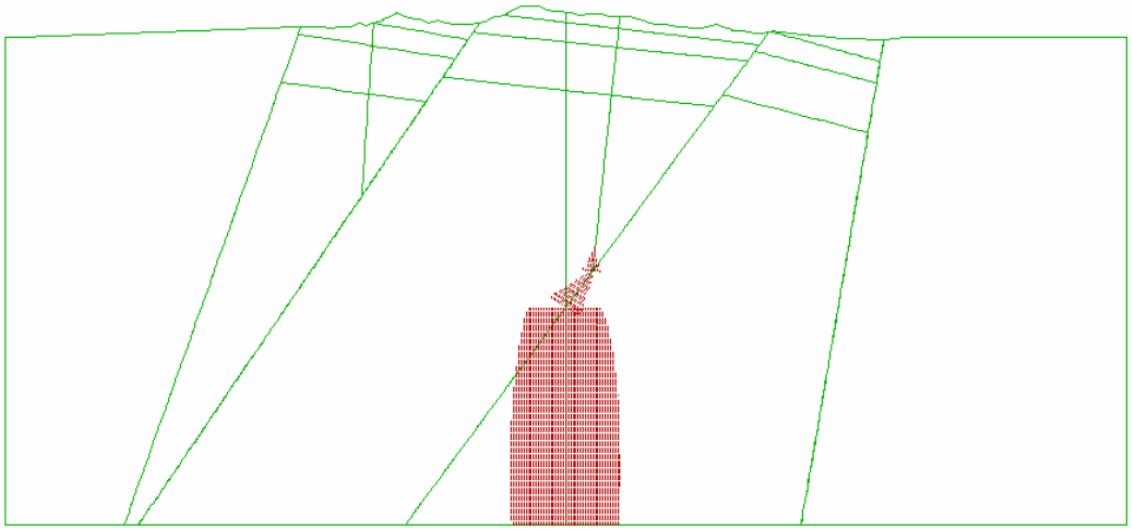

Source: Output DTN MO0610SPADIKEP.000, file *dike_fault**step3.sav*.

Figure 6-55. Evolution of Dike and Fault Opening in UDEC Simulations after Magma Enters Steeper Fault

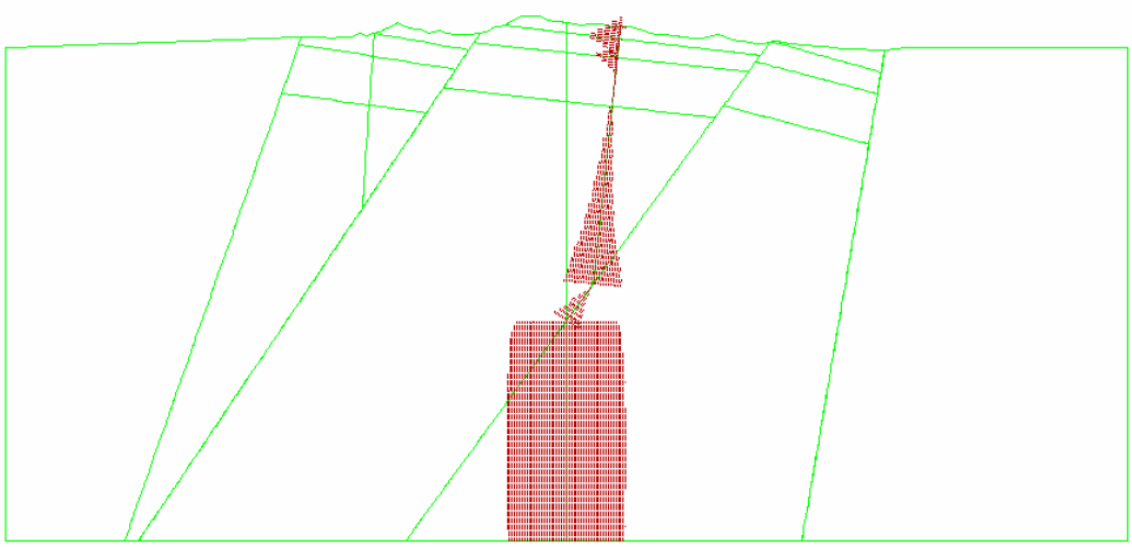

Source: Output DTN MO0610SPADIKEP.000, file *\dike_fault\step4.sav*.

Figure 6-56. Evolution of Dike and Fault Opening at End of Simulation

A detail of deformation of the fault and subhorizontal interfaces, caused by magma intrusion into preexisting faults, is shown in Figure 6-57. The interfaces open near the ground surface. The deep interface does not open at all; the greatest opening of 1.9 m is on the shallowest interface. Opening of the subhorizontal interfaces is a consequence of the slip on the steeply dipping fault. The magnitude of the slip on the fault is of the order of 4 m, which is consistent with the contour plots of vertical displacements shown in Figure 6-58 for two values (45° and 55°) of friction angle on the fault. The results, shown in Figures 6-54 through 6-58, are obtained for a 45° friction angle in the fault plane, a 20-GPa fault stiffness, and Case 2 set of mechanical properties below the bottom of the Calico Hills Formation from Table 6-9. Other analyzed sets of input properties yield different magnitudes but qualitatively the same mechanism of deformation.

The interaction between dikes and faults is analyzed here. Of particular interest is the potential dike/fault interaction below Yucca Mountain, the effect of such interaction on the probability of the dike diversion below Yucca Mountain away from the repository, and the reduction of volcanic hazard for the repository.

Although the rock mass fracture toughness is not an important factor in the analysis of dike propagation, it becomes important when the potential for dike diversion into intersected faults is assessed. If the hanging wall were unfractured, the continuation of dike propagation along the original vertical path would be possible only in cases of shallow dipping faults intersected by a dike. Otherwise, magma and the dike would always turn into the fault. Real rocks are almost always fractured and have finite toughness. The injection of magma into rock mass fractures and their pressurization can cause the hanging wall of the fault to fracture.

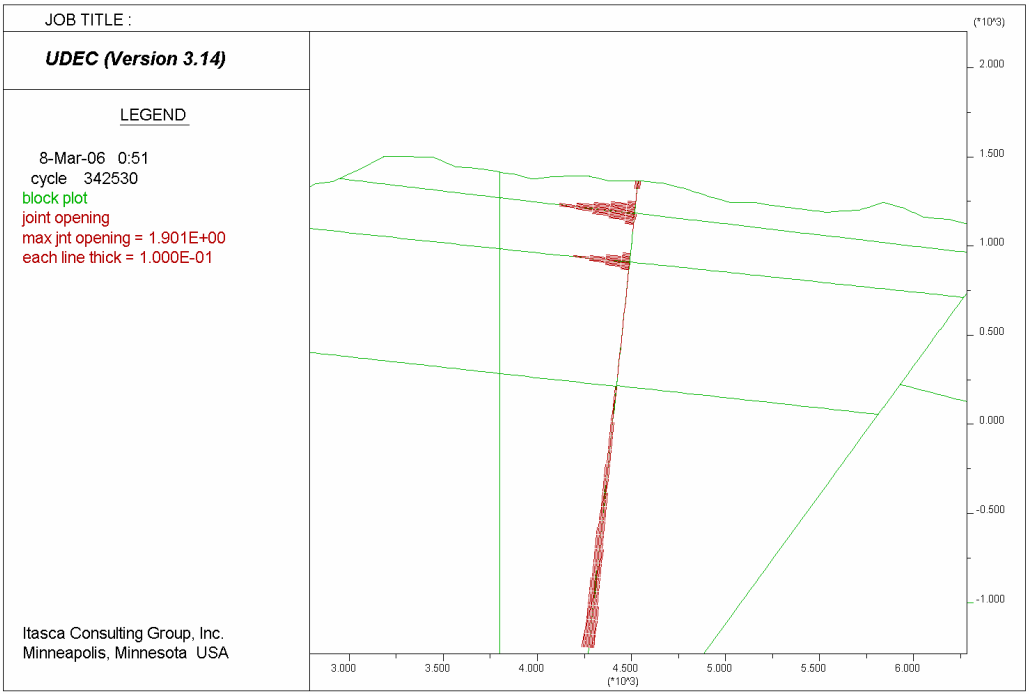

Source: Output DTN MO0610SPADIKEP.000, file *\dike_fault\step4.sav*.

Figure 6-57. Detail of Fault and Interface Deformation (m) at the End of Simulation

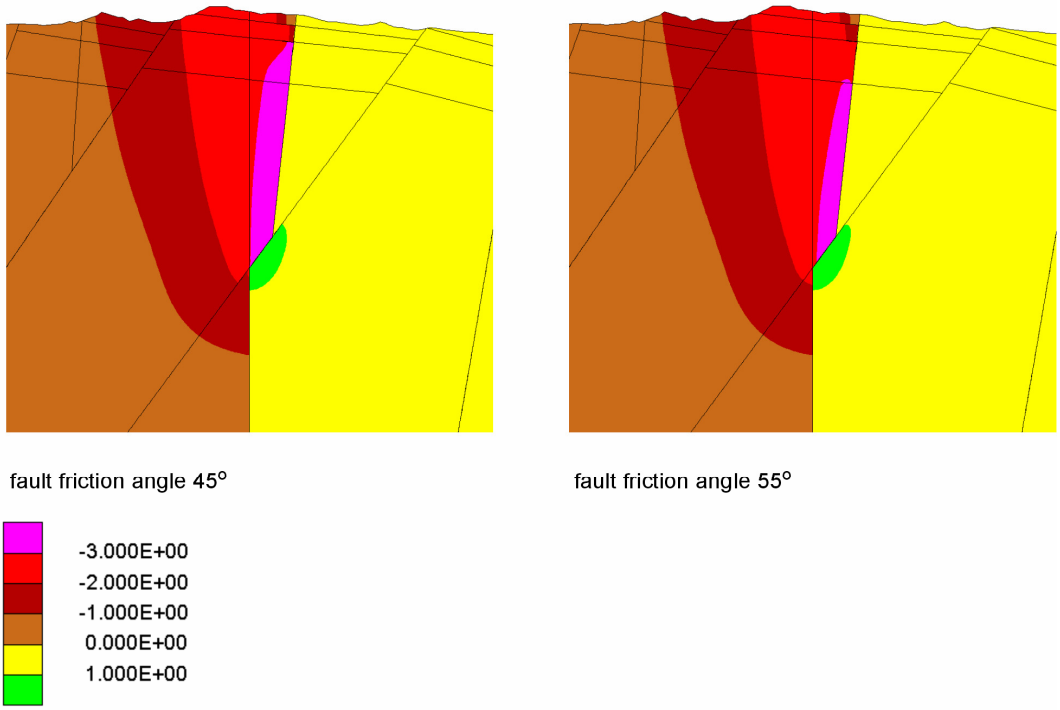

Source: Created for illustrative purposes only.

NOTE: Displacement magnitudes are shown in meters.

Figure 6-58. Contours of Vertical Displacement as Functions of Friction Angle of the Faults

It is very difficult (if it is even possible) to analyze numerically the conditions for fracturing a hanging wall at the intersection. This problem involves the consideration of very different length scales. The stresses and pressures are defined on the kilometer scale, while conditions for propagation of preexisting fractures must be analyzed on the centimeter scale. Therefore, the potential for dike diversion into a fault was analyzed using a simple analytical approach, which yields a criterion for dike diversion as a function of the fault dip angle, depth of intersection, preexisting fracture length, and rock toughness.

For the conditions below Yucca Mountain, where the Bow Ridge Fault is the block-bounding fault extending below the repository, a simple analysis indicates that the dike will most likely continue propagating vertically upward after it intersects the Bow Ridge Fault. Even if magma would be diverted into the Bow Ridge Fault (e.g., in the unlikely event that the fault hanging wall has only fractures much shorter than 0.1 m or the fracture toughness exceeds 10 MPa $m^{1/2}$), it would flow along the Bow Ridge Fault until it reaches another steeply dipping structure, at which point magma would turn again along the steeply dipping structure.

6.3.4.5.3 Discussion of Results

The potential for dike diversion into a fault after it intersects the fault cannot be completely assessed in UDEC calculations. If the dike path is represented as a joint that does not allow flow until it is fractured, the dike will propagate along that path until it intersects the first fault. At that stage, when the dike tip reaches the fault, the dike tip will be "arrested." The only mechanism for continuation of fracturing in the intact (unfractured) fault hanging wall is if the magma pressure in the section of the dike below the fault causes sufficient tension in the hanging wall before shearing or opening of the fault. In case of relatively weak (i.e., no cohesion), steeply dipping (e.g., greater than 50°) faults, that is the unlikely outcome. In reality, the preexisting fractures in the hanging wall could provide a mechanism for vertical dike propagation. The representation of 1-m or shorter fractures sufficiently discretized to investigate the potential for their propagation in the calculation domain (15 km in size) is not practical. Instead, the potential for dike diversion into a fault is estimated based on the alternative model described in Section 6.3.4.5 (Table 6-8).

6.3.4.6 Alternative Models

Three alternative models are discussed: the model of Young et al. (1994 [DIRS 178376]), an analysis by Gudmundsson and Philipp (2006), and an analytical solution coupled with an alternative numerical method.

6.3.4.6.1 Model of Young, McKague, and Terhune

Young et al. (1994 [DIRS 178376]) used two-dimensional numerical models to investigate the diversion of magma from a vertical dike into a fault. They considered three situations: a 60°fault at 1,000 meters depth, an 80° fault at 1,000 meters, and an 80° fault at 300 meters. They did not model the entire block from below the intersection of the dike with the fault to the surface; instead they considered a block of a few hundred meters around the intersection. Their input parameters are similar to those used in Section 6.3.4.4, except that the tensile strength of the rock in the hanging wall was 20 MPa. Such a value for tensile strength would correspond to a

maximum crack length in the hanging wall of less that 1 millimeter if the fracture toughness were on the order of the 0.4 $MPa \cdot m^{1/2}$ used in the analysis of Section 6.3.6.

They found that both 80° faults captured the magma flow but that the outcome was uncertain for the 60° fault. The model results in Section 6.3.4.5 suggest that, had their computational grid been large enough to extend the calculations to greater time, the 60° fault at 1,000 meter depth would also have captured the flow from the vertical dike.

6.3.4.6.2 Model of Gudmundsson and Philipp

Gudmundson and Philipp (2006 [DIRS 181324]) analyzed the distribution of stresses in layered rock between the surface and a buried magma chamber. Their two-dimensional models considered two types of configurations: (1) a circular magma chamber beneath three relatively thick, flat-lying layers, and (2) a circular magma chamber in the lower levels of a thick section of relatively thin, sloping layers. For both configurations, the layers alternated between high stiffness and low stiffness. For configuration (1) they considered both high stiffness between low and low stiffness between high. The pressure field developed in response to pressurization of the magma chamber was calculated and the orientations of the principal stresses were determined.

Their analysis of configuration: found that the maximum principal stress direction tended to be vertical at the low-stiffness-over-high-stiffness interface, but tended to be horizontal at the high-stiffness-over-low-stiffness interface. Because a vertical orientation of maximum principal stress is favorable for dike formation, they concluded that alternating layers would discourage upward dike migration. The same effect resulted in a down dip migration of the center of maximum principal stress concentration above the magma chamber in the stack of tilted layers. They also reported field observations that supported their analysis.

The analysis of Gudmundsson and Philipp (2006 [DIRS 181324]) can be applied to the situation at Yucca Mountain on two scales. On the basin scale, the rocks beneath Yucca Mountain consist of layers dipping to the east. Beneath approximately 2 km of Tertiary tuffs is a sequence of over 5 km of Paleozoic carbonates, shales, and sandstones, which overlay Precambrian rocks (Potter et al. 2002 [DIRS 160060], cross sections A-A′ and D-D′). The tuffs have lower stiffness than the Paleozoic rocks, in general, so the analysis of Gudmundsson and Philipp (2006 [DIRS 181324]) would not indicate an environment hostile to dike propagation into the tuffs. If layers of lower stiffness shale in the Paleozoic section were thick enough, they could hinder upward progress of a dike.

6.3.4.6.3 Analytic Solution

This section presents an analytical solution for the injection of a viscous fluid from a vertical crack (i.e., a dike) into a preexisting crack inclined at some angle to the dike (i.e., a fault). McDuffie et al. (1994 [DIRS 178354]) presented a brief description of an analysis similar to the simple stress analysis presented here.

The condition for a fracture of length a (illustrated in Figure 6-45) in the hanging wall of a fault with dip α to propagate can be written as:

$$K_I \geq K_{IC} \quad \text{(Eq. 6-99)}$$

where K_I is the stress intensity factor at the fracture tip due to magma pressure inside the fracture, and K_{IC} is the fracture toughness (with respect to mode I fracture propagation) or resistance of the rock to fracture propagation. Table 6-10 provides a summary of laboratory investigations of fracture toughness of a wide range of rock types. The stress intensity factor for a fracture inside an infinite or semi-infinite domain can be written in the following form:

$$K_I = \beta p_{\text{eff}} \sqrt{\pi a} \quad \text{(Eq. 6-100)}$$

where p_{eff} is the effective magma pressure inside the fracture, equal to the difference between the magma pressure, p, and stress normal to the fracture plane, σ:

$$p_{eff} = p - \sigma. \quad \text{(Eq. 6-101)}$$

In these calculations the normal stress on the fracture plane is approximated by the far-field rock mass stress $\sigma = \sigma_x$. This approximation is reasonable for relatively steeply dipping and weak faults for which the dike cannot cause significant stress changes in the hanging wall. The coefficient β accounts for different geometries or boundary conditions of the fracture propagation problem. For example, in the case of a uniformly pressurized fracture in the edge of a semi-infinite domain, under plane strain conditions, β is 1.12 (Rice 1968 [DIRS 164405). (This case also represents the fracture that has the length in the out-of-plane direction much greater than the fracture dimension perpendicular to the surface. In the case of a semi-circular, penny-shaped fracture in the surface of a semi-infinite domain, the coefficient β for the maximum stress intensity factor is 0.72 (Barsom and Rolfe 1987 [DIRS 178342]).

The magma pressure required to divert a dike into a fault must be equal to or greater than the stress normal to the fault plane (i.e., sufficient to open the fault). In the stress state in which the principal stresses are vertical (σ_y) and horizontal (σ_x), the stress normal to a fault dipping at an angle α, can be approximated as:

$$\sigma_n = \sigma_x \sin^2 \alpha + \sigma_y \cos^2 \alpha. \quad \text{(Eq. 6-102)}$$

Equation 6-102 is only an approximation of the normal stress on the fault because it does not account for the effect of the dike itself on the stress state in the vicinity of the dike/fault intersection. This effect is investigated numerically, and it is demonstrated (Section 6.3.4.5) that, for a wide range of angles α, Equation 6-102 provides a good approximation, with an error less than 25%.

Table 6-10. Typical Values for Fracture Toughness

Source	Rock Type	Value (MPa $m^{1/2}$)
Balme et al. 2004 [DIRS 182314]	Iceland basalt	2.17 – 3.78
	Aetna basalt	1.5 – 2.06
	Vesuvius basalt	2.18 – 2.24
Basham et al. 1993 [DIRS 182275]	An eastern basalt	3.46
	Berea sandstone	1.26
Funatsu et al. 2004 [DIRS 178348]	Kimachi sandstone	0.47 – 0.6
	Tage tuff (zeolitized)	0.43 – 0.63
Matsuki et al. 1991 [DIRS 182276]	Ogino tuff	1.0 – 1.1
Momber 2004 [DIRS 182315]	Granite	0.80
	Rhyolite porphyry	1.17
	Limestone	1.21
	Schist	2.70
Donovan and Karfakis 2004 [DIRS 182316]	Fine-grained granite	0.88 – 0.91
	Coarse-grained granite	0.62
	Dolomitic limestone	1.33 – 1.40
	Sioux quartzite	1.24

By combining Equations 6-101 and 6-102, the effective stress inside the fracture in the fault hanging wall can be approximated as:

$$p_{\text{eff}} = \sigma_x(\sin^2\alpha - 1) + \sigma_y \cos^2\alpha \qquad \text{(Eq. 6-103)}$$

By combining Equations 6-99, 6-100, and 6-103, the critical fracture length, a_{cr}, for which a dike will continue propagating vertically upward instead of turning into the fault can be written as:

$$a_{\text{cr}} \geq \frac{1}{\pi}\left\{\frac{K_{IC}}{\beta\left[\sigma_x(\sin^2\alpha - 1) + \sigma_y \cos^2\alpha\right]}\right\}^2 . \qquad \text{(Eq. 6-104)}$$

If the vertical stress is assumed to be gravitational, $\sigma_y = \gamma d$ (where γ is the unit weight of the rock mass and d is the depth), and the horizontal stress is proportional to the vertical stress, $\sigma_x = \kappa\sigma_y$, the critical fracture length required for a dike to propagate vertically upward into the hanging wall can be expressed as:

$$a_{\text{cr}} \geq \frac{K_{IC}^2}{\pi(\beta\gamma d)^2\left[\kappa(\sin^2\alpha - 1) + \cos^2\alpha\right]^2} \qquad \text{(Eq. 6-105)}$$

Similarly, the critical depth, d_{cr}, for a given fracture length, a, for which the dike will continue to propagate vertically can be written as:

$$d_{cr} \geq \frac{K_{IC}}{\beta\gamma\sqrt{\pi a}\left[\kappa\left(\sin^2\alpha - 1\right) + \cos^2\alpha\right]} \qquad \text{(Eq. 6-106)}$$

Using $\beta = 1.12$ (i.e., the coefficient for an edge fracture in an infinite half-plane), the unit weight of the rock mass, $\gamma = 0.024$ MN/m^3, and coefficient of horizontal stress, $\kappa = 0.5$, the condition for dike diversion or propagation vertically through the fault plane is derived as a function of depth and the fault dip angle for different preexisting fault hanging wall fracture lengths and fracture toughness. The results are shown in Figure 6-59. Each line divides the plane into two domains. The domain above a line corresponds to a combination of parameters for which this simple analysis predicts diversion of the magma into the faults; the domain below a line corresponds to a combination of parameters for which the dike is predicted to propagate through the fault vertically upward.

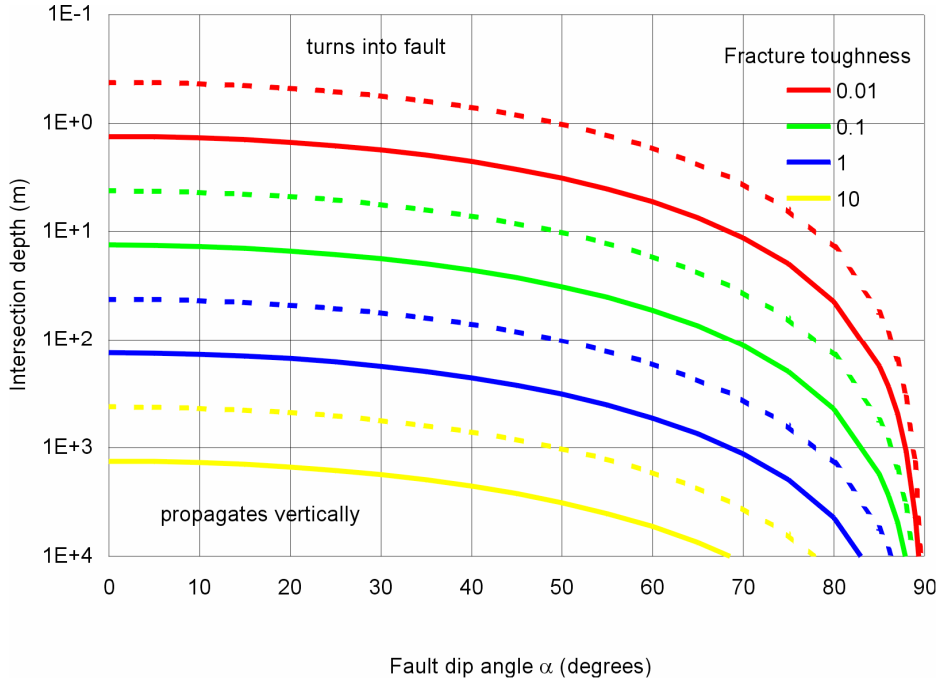

Source: Output DTN: MO0610SPADIKEP.000, file *depth.xls.*

NOTE: The solid lines are for 0.1-m long preexisting hanging wall fractures; the dashed lines are for 1.0-m long preexisting hanging wall fractures.

Figure 6-59. Critical Depth at which the Dike Propagates Vertically through the Fault as a Function of Fault Angle, Fracture Toughness, and Hanging Wall Fracture Length

The results of the simple analysis of the dike/fault interaction and conditions for dike diversion into the preexisting fault, summarized in Figure 6-51, indicate some plausible trends. It is more likely that a dike will turn into a fault at shallower depths. At greater depths the tendency of a dike is to propagate vertically upward because the pressure required to open the fault increases

relative to the magma pressure required for vertical dike propagation, making dike diversion less likely. It is also more probable that the dike will turn into a steeply dipping fault than into a shallow fault. Again, the explanation for this trend is that the pressure required to open the fault in excess of the pressure required to propagate the dike vertically increases with a decrease in the dip angle (as long as the coefficient of the horizontal stress, κ, is less than 1.0).

As expected, it is more likely that the dike will propagate vertically upward for a small fracture toughness and if the fault hanging wall is fractured with relatively long, closely-spaced vertical fractures. Fracture spacing does not directly enter the analysis but is important in the selection of the fracture length used to assess dike diversion potential. The characteristic fracture length, *a*, used in the calculations should be the average fracture length with a typical spacing of the order of meters, making such fractures ubiquitous. In the case of longer but more widely spaced fractures, magma will flow along the fault until it reaches that long vertical fracture, when it will turn again into the vertical fracture.

6.3.5 Component for the Effect of Topography on Dike Propagation

The effect of topography on a dike path and potential for dike deflection due to topography-induced stresses underneath Yucca Mountain were analyzed in Section 6.2.2. Based on stress trajectories determined from the mountain-scale thermo-mechanical model, it was concluded that variation of the stress state (both the magnitude and orientation of the principal stresses) due to the topography is insufficient to cause deflection of the dike propagating under the mountain at a greater depth, directing it to rupture the ground surface and erupt in the valley. This analysis did not address the effect of topography on the magma flow field inside the dike plane, potentially redirecting magma flow inside the dike plane from the region under the mountain into the region under the valley. Nonuniform magma flow field inside a dike plane is a consequence of variable dike aperture. Two reasons for variable dike aperture are finite strike length of the dike and non-uniform topography-induced stress field. For isotropic, homogeneous conditions, the largest dike aperture will be the in the middle of the dike in the horizontal cross section. The aperture reduces to zero at both ends of the dike. The flow rate will be the largest in the middle and smallest at both ends, resulting in a curved magma front with the magma front in the middle of the dike leading ahead (above) the magma front at the edges. Similarly, topography-induced nonuniform in situ stresses will cause greater flow rates in the region of smaller stresses than in the region of larger stresses.

The topography also has a geometrical effect on the spatial distribution of the probability of a dike rupturing the ground surface. It is more probable that the magma front will reach the ground surface in a valley. (Because of lower elevations, the valleys will be reached first by the upwardly propagating magma front.) Once the ground surface is ruptured in the valley, the dike aperture will be larger under the valley, and there will be larger probability for eruption localization in the valley. Assuming that there are no other factors affecting dike path (e.g., structures), all these considerations lead to the expectation that it is more likely that a dike will rupture the ground surface and erupt in a valley than somewhere on a mountain range. These hypotheses were investigated numerically. The calculations were carried out with the finite difference code, FLAC3D V. 2.14 (BSC 2004 [DIRS 172323].

6.3.5.1 Mathematical Description

The dike location, path, and strike length are inputs to the calculation, not parts of the solution. The dike length in the plan view is assumed to be 4 km. The analyzed position and orientation of the dike relative to the topography are indicated in Figure 6-60. The dike is striking at 30° NE. Simple two-dimensional calculations were conducted in the process of selecting optimum model and zone sizes. These preliminary analyses have demonstrated that the square-shaped model with the edge length of 24 km in the plan view is sufficiently large to reduce an error due to model finite size to only a few percent in displacement. The model height averages 7.5 km. The element size is variable. The largest zones have 400-m edge length; the smallest zones have 100-m edge length. The geometry of the numerical representation showing the topography and dike projection on the ground surface is presented in Figure 6-61. Magma flow is confined to a single layer of zones indicated in Figure 6-61 as block group "dike." The thickness of that layer of zones in the numerical representation is 50 m. The actual dike aperture used in the calculation of magma flow is unrelated to the zone size but is a function of dike-wall deformation. The hydraulic conductivities of the zones representing the dike are calculated in the same way as explained in detail in Section 6.3.3.5.6.

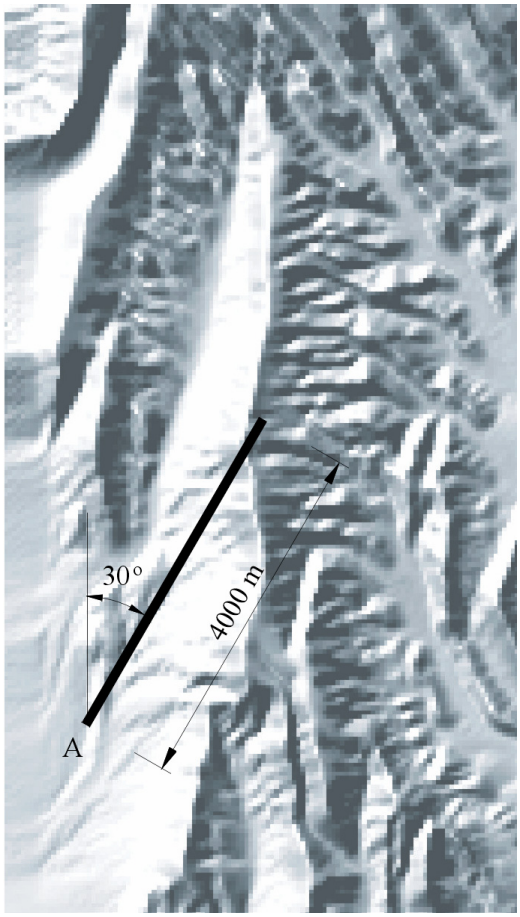

Source: For illustrative purposes only.

NOTE: Geographical coordinates of "tip" A are 168250, 228136.

Figure 6-60. Position of the Dike Relative to the Topography of Yucca Mountain

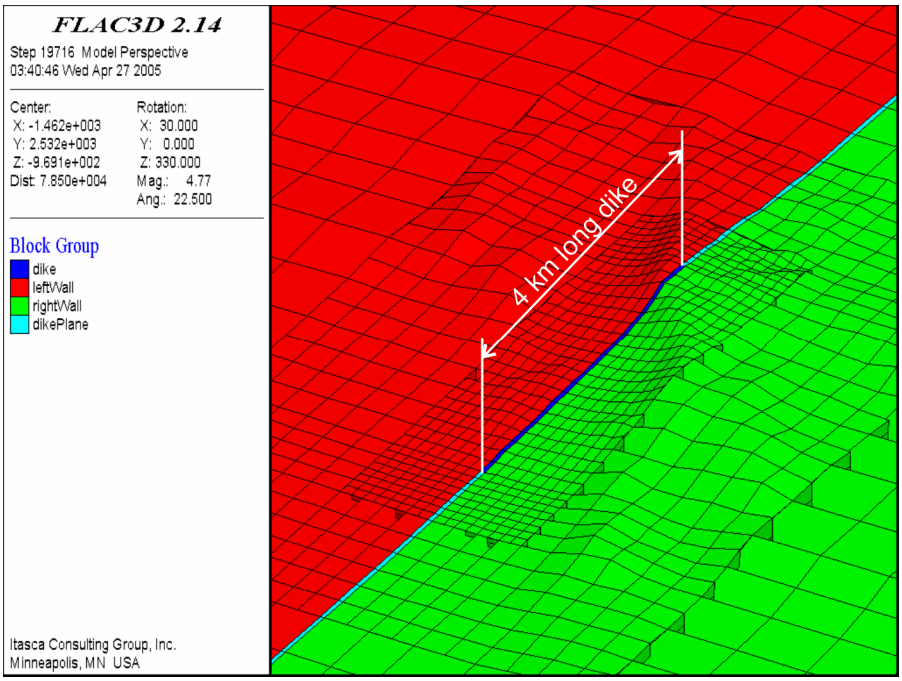

Source: For illustrative purposes only.

Figure 6-61. Representation of the Dike in the Numerical Calculation

6.3.5.2 Uncertainties and Limitations

This calculation represents the interaction of a single dike of fixed orientation with a ridge shaped like Yucca Mountain. However, there is uncertainty regarding the orientation of any dike that might intrude into the region as described in *Plan for the Expert Elicitation to Update the Probabilistic Volcanic Hazard Analysis (PVHA) for Yucca Mountain, Nevada* (SNL 2007 [DIRS 181325]). The uncertainty associated with the properties of the host rock and the magma has been discussed above in Section 6.3.3.

Limitations of the calculation are that it does not simulate the process of crack propagation and that the path of the dike is predetermined by the computational mesh. These limitations do not affect the conclusions regarding the effect of surrounding topography on the likelihood of an eruption along the strike of a dike.

6.3.5.3 Inputs

The same input parameters as those assumed in the wide-aperture case discussed in Section 6.3.3.5.6 are used in this calculation. The input parameters, which are consistent with case $\mathcal{D} = 20.28$, $v_\infty = 1$ m s^{-1}, $\mu = 10$ Pa·s, and $\kappa = 0.5$ in Table 6-3, are listed in Table 6-5. The magma is injected into the dike at the bottom of the model at the constant, uniform rate (along the crack) of 0.45 m^2/s. The boundary condition on the surface (where the dike intersects the topography) is zero pressure. Magma viscosity is 10 Pa·s and the density is 1,141 kg m^3. In situ vertical stress is gravitational, corresponding to the average rock-mass density of 2,400 kg m^3. The horizontal in situ stresses are isotropic, with a magnitude of the principal stresses equal to

50% of the vertical stress. There is a "roller" boundary condition on the model bottom boundary in the entire simulation. The top of the model is a stress-free surface. The stress boundary condition in equilibrium with the in situ stress state is applied on the vertical model boundaries. The initial dike opening is 5 cm. The simulation was carried out until the steady state was reached. The repository and interaction between the dike and the repository were not represented in the calculation.

In order to separate the geometrical and stress effects of the topography on magma flow and localization of eruption, two additional calculations were conducted.

The first calculation was aimed at investigating the effects of topography-induced stresses, and the initial calculation of the in situ stresses was done using the geometrical representation that included the actual topography. In the subsequent step, during the simulation of dike propagation, the portion of the grid above the horizontal level 200 m below the repository level (and below the relief base) was deleted and replaced with a non-uniform vertical load, equal to the varying weight of the removed grid. Consequently, the topography-induced stresses were represented in the calculation, but the geometrical effect of the topography was neglected.

In the second calculation, aimed at investigating the geometrical effects of the topography, it was assumed that the portion of the grid above the horizontal level 200 m below the repository level (and below the relief base) had negligibly small density of 24 kg m^3 compared to assumed average density of the tuff of 2,400 kg m^3. (The numerical code FLAC3D requires finite density for each zone in the model.) Consequently, the geometrical effect of the topography is represented in the calculation, but the topography-induced stresses are neglected.

6.3.5.4 Model Results

The results of the simulations indicate that the magma front is practically horizontal while the magma front is relatively far from the ground surface (i.e., outside the range of topography influence), although the magma discharge vectors (i.e., magma volumetric flow rate per unit dike width) vary along the length of the dike. The contours of saturation (between 0 and 1) and discharge vectors (averaged over the dike zone thickness of 50 m) are shown in Figure 6-62. The region of large saturation gradient roughly corresponds to the location of the magma front. When the magma front gets within the range of the influence of topography (as shown Figure 6-63), it becomes curved, with the front in the middle (which also happens to be underneath the valley) leading above the front at the dike edges. In the steady state (Figure 6-64), the magma front rises to the level of the repository even at the dike edge under the mountain, but the ground surface is ruptured in the valley and the entire magma flow is directed toward the region of eruption. A mode of deformation induced in the surrounding rock by the dike is illustrated in Figures 6-65 and 6-66. As the dike approaches the ground surface, the deformation and flow localize in the valley.

The effect of magma near the edges of the dike reaching the repository level will be relatively small, from the perspective of containment of the nuclear waste. Figures 6-67 and 6-68 show, at two different scales, the contours of average magma velocity magnitude and discharge vector field (averaged over the dike zone thickness of 50 m) inside the dike. Large velocities are localized in the middle of the dike and particularly at the location of the rupture of the ground

surface in the valley (Figure 6-67). The magma average velocity magnitudes close to the dike edge at the repository level are relatively small. Figure 6-68 indicates velocities (near the repository level) ranging between 0 and 0.05 m/s (compared to more than 3.1 m/s at the location of ground surface rupture shown in Figure 6-67). It is very likely, considering relatively small velocities and dike apertures (less than 0.1 m according to Figures 6-69 and 6-70), that magma, which could potentially reach the repository, will solidify before reaching the ground surface.

The results of two additional calculations are shown in Figures 6-71 and 6-72. Contours of vertical stress shown in Figure 6-71 illustrate that, although the topography is not explicitly represented in this calculation, the effect of topography on vertical stresses is accounted for. Magma discharge vectors (averaged over the dike zone thickness of 50 m) in the steady state (also shown in Figure 6-71) indicate that stresses do affect the magma flow but to a lesser extent than when both stress and geometrical effects are included (e.g., Figure 6-64). In this case, the magma discharge vectors are oriented slightly away from the region of the increased stresses under the mountain. The results of the calculation in which the topography effects on the stress field are not accounted for (Figure 6-72) indicate that geometry alone also affects the magma flow and localization of the eruption.

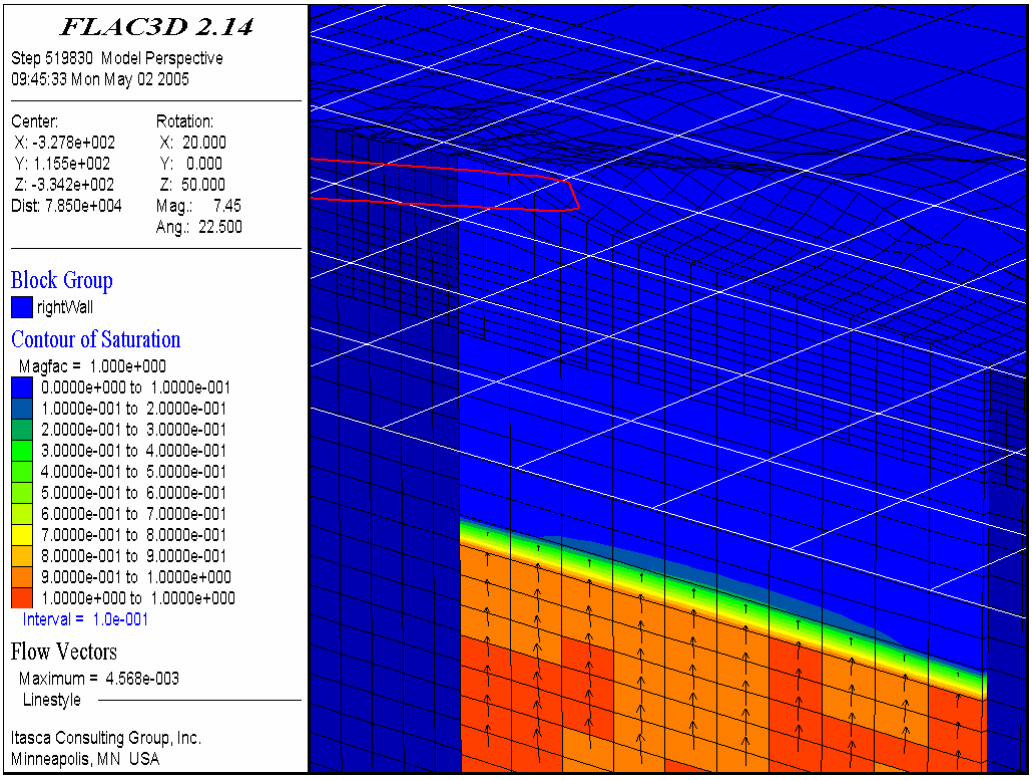

Output DTN: MO0705TOPODIKE.000; file: *nominal\step17.sav*.

NOTE: Outline of the repository is shown in red. The rectangular grid shown in white is in the horizontal plane of the repository. The middle horizontal line is in the dike plane.

Figure 6-62. Saturation Contours and Magma Discharge Vectors Averaged over the Dike Zone Thickness (50 m) at State when the Magma Front is Below the Range of Topographical Influence

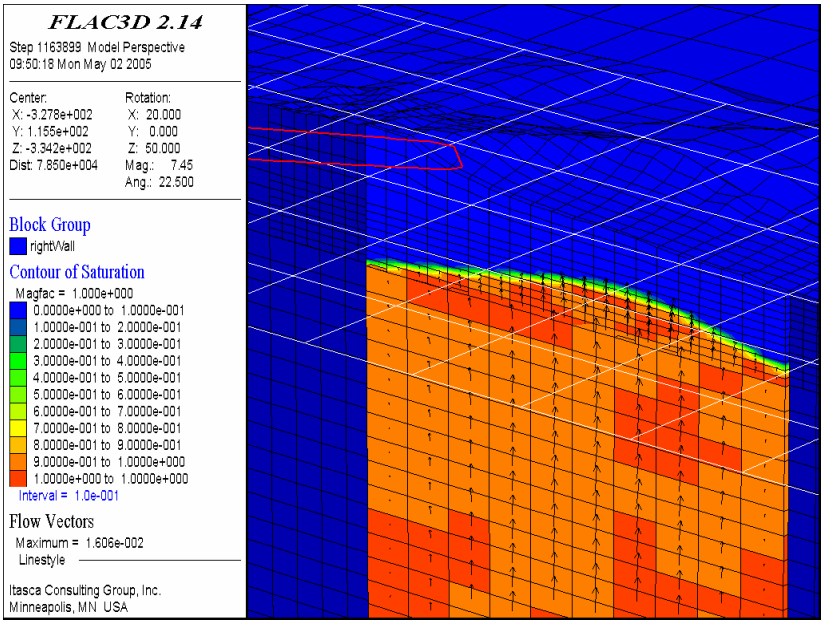

Output DTN: MO0705TOPODIKE.000; file: *nominal\step22.sav*.

NOTE: Outline of the repository is shown in red. The rectangular grid shown in white is in the horizontal plane of the repository. The middle horizontal line is in the dike plane.

Figure 6-63. Saturation Contours and Magma Discharge Vectors Averaged over the Dike Zone Thickness (50 m) at a State when the Magma Front Approaches the Ground Surface

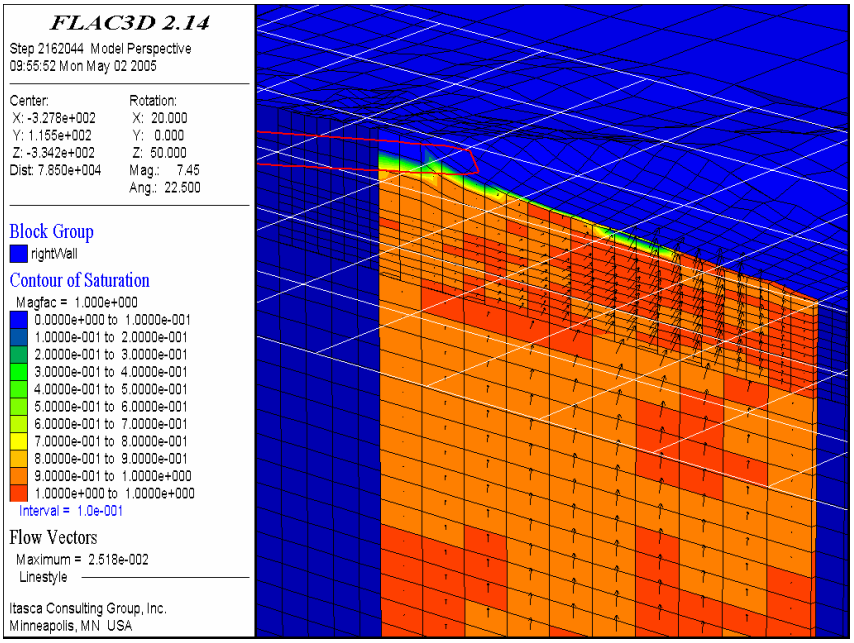

Output DTN: MO0705TOPODIKE.000; file: *nominal\step26.sav.*

NOTE: Outline of the repository is shown in red. The rectangular grid shown in white is in the horizontal plane of the repository. The middle horizontal line is in the dike plane.

Figure 6-64. Saturation Contours and Magma Discharge Vectors Averaged over the Dike Zone Thickness (50 m) at the Steady State

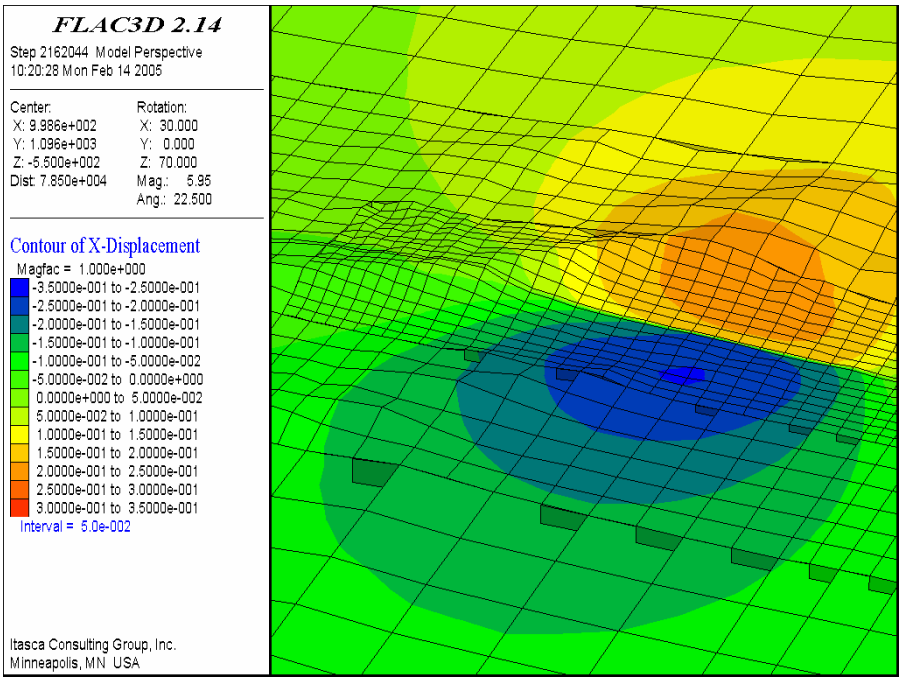

Output DTN: MO0705TOPODIKE.000; file: *nominal\step26.sav*.

Figure 6-65. Contours of Dike-induced Horizontal Displacements (m) Normal to the Dike Shown on the Ground Surface at the Steady State

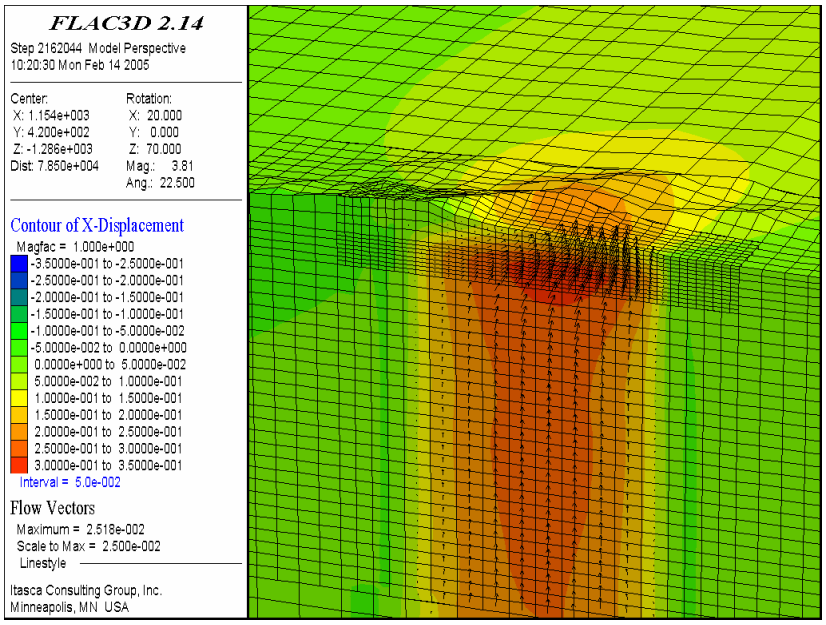

Output DTN: MO0705TOPODIKE.000; file: *nominal\step26.sav*.

NOTE: Dike is shown on the ground surface and in cross section in the dike plane.

Figure 6-66. Contours of Dike-induced Horizontal Displacements (m) Normal to the Dike and Magma Discharge Vectors Averaged over the Dike Zone Thickness (50 m) at the Steady State

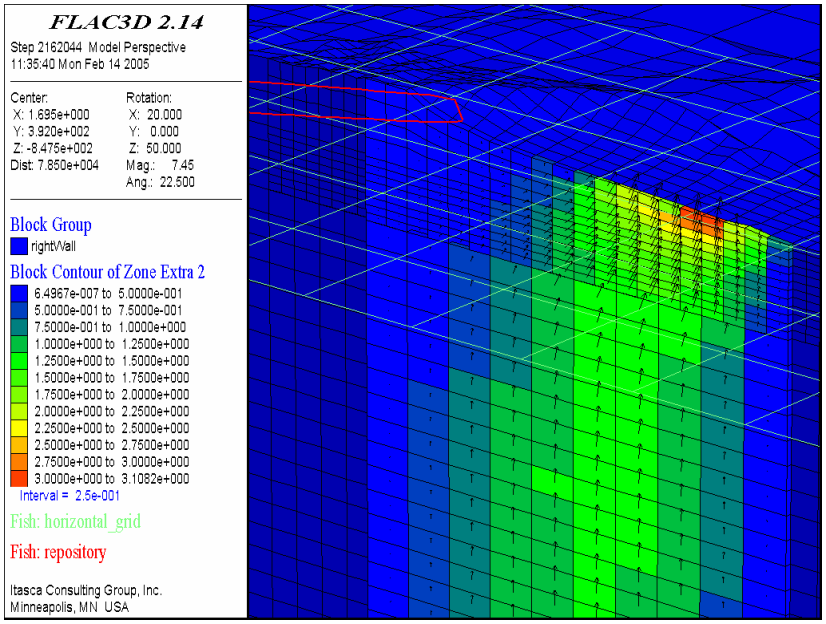

Output DTN: MO0705TOPODIKE.000; file: *nominal\step26.sav*.

NOTE: Outline of the repository is shown in red. The rectangular grid shown in white is in the horizontal plane of the repository. The middle horizontal line is in the dike plane.

Figure 6-67. Block Contours of Average Magma Velocity Magnitude (m/s) and Magma Discharge Vectors Averaged over the Dike Zone Thickness (50 m) at the Steady State

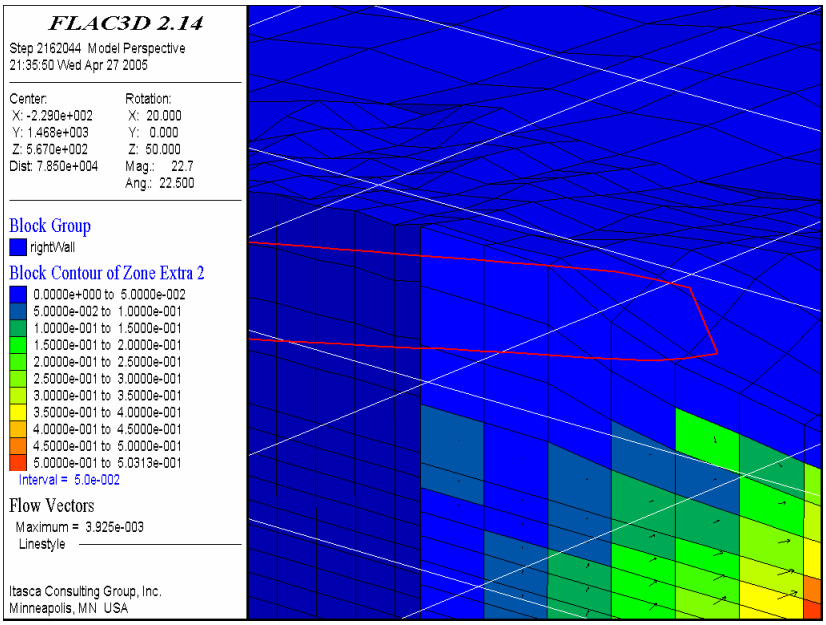

Output DTN: MO0705TOPODIKE.000; file: *nominal\step26.sav*.

NOTE: Outline of the repository is shown in red. The rectangular grid shown in white is in the horizontal plane of the repository. The second horizontal line from the bottom of the figure is in the dike plane.

Figure 6-68. Detail near the Repository of Block Contours of Average Magma Velocity Magnitude (m/s) and Magma Discharge Vectors Averaged over the Dike Zone Thickness (50 m) at the Steady State

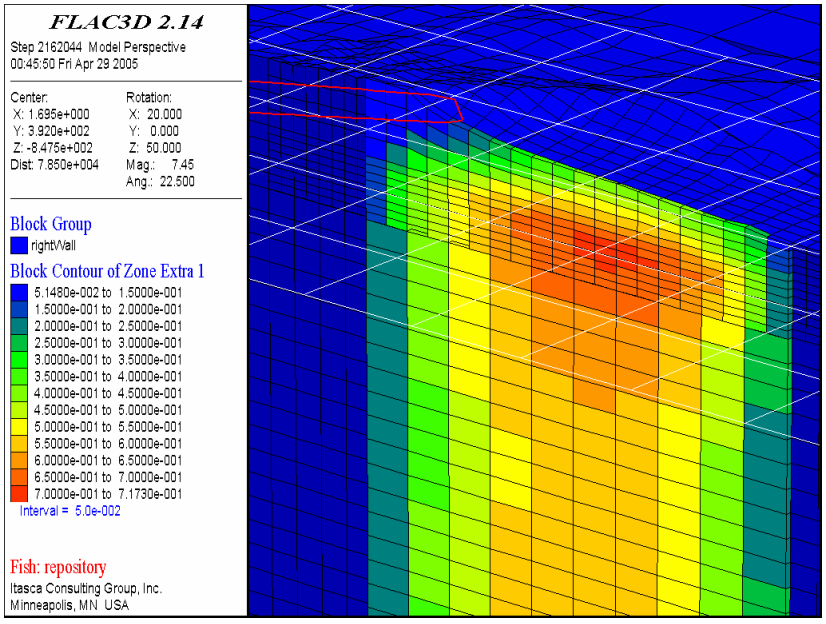

Output DTN: MO0705TOPODIKE.000; file: *nominal\step26.sav*.

NOTE: Outline of the repository is shown in red. The rectangular grid shown in white is in the horizontal plane of the repository. The middle horizontal line is in the dike plane.

Figure 6-69. Block Contours of Dike Aperture (m) at the Steady State

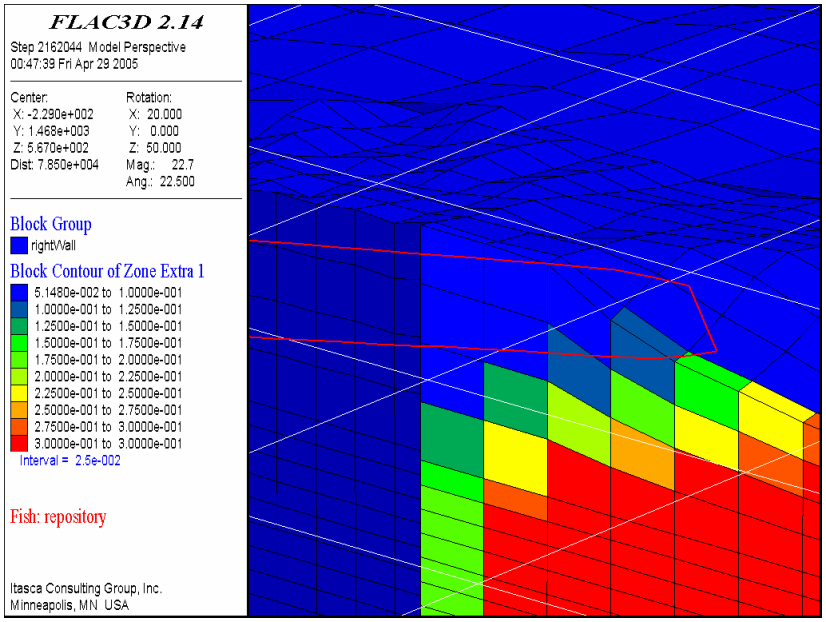

Output DTN: MO0705TOPODIKE.000; file: *nominal\step26.sav*.

NOTE: Outline of the repository is shown in red. The rectangular grid shown in white is in the horizontal plane of the repository. The second horizontal line from the bottom of the figure is in the dike plane.

Figure 6-70. Detail near the Repository of Block Contours of Dike Aperture (m) at the Steady State

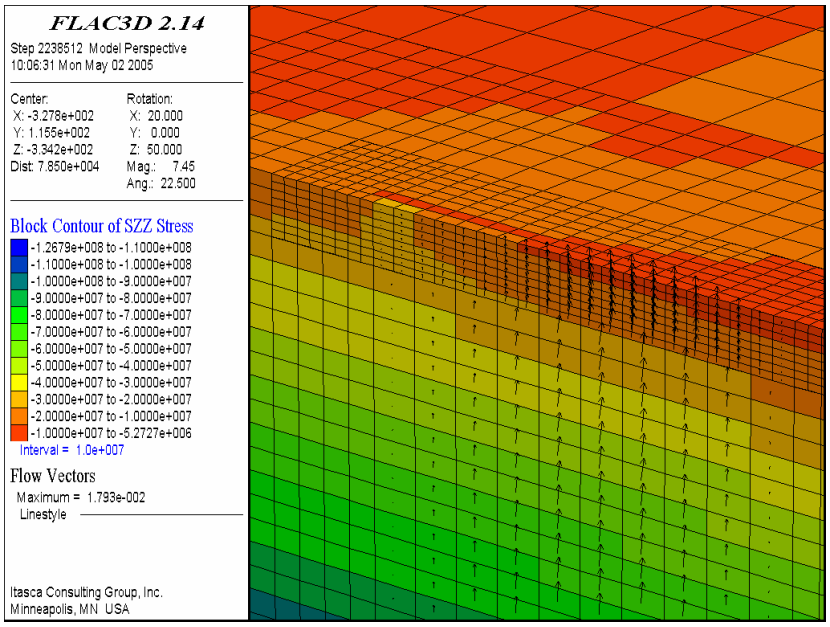

Output DTN: MO0705TOPODIKE.000; file: *flat\step30.sav*.

NOTE: Dike is shown on the ground surface and cross section in the plane of the dike.

Figure 6-71. Calculation for Flat Upper Boundary: Contours of Dike-induced Horizontal Displacements (m) Normal to the Dike and Magma Discharge Vectors Averaged over the Dike Zone Thickness (50 m) at the Steady State

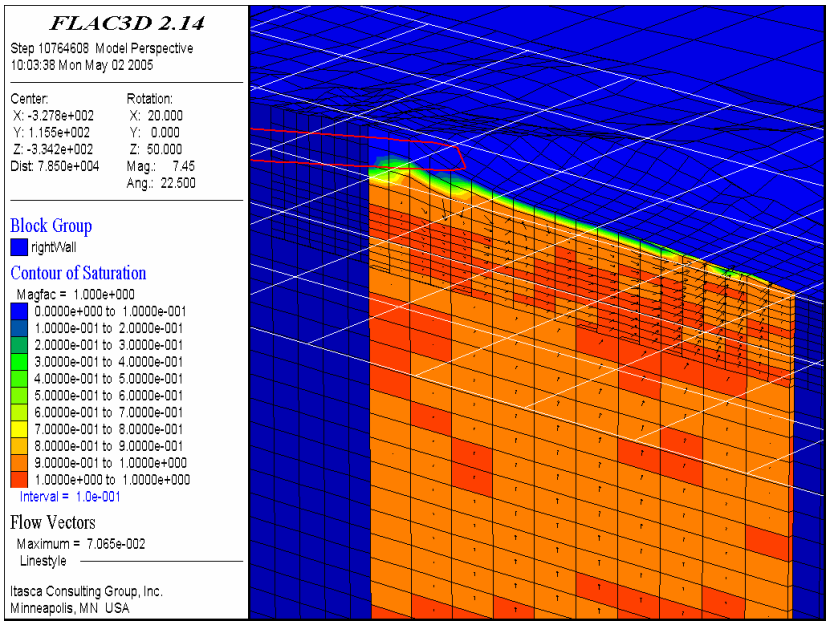

Output DTN: MO0705TOPODIKE.000; file: *density\step33.sav*.

NOTE: Outline of the repository is shown in red. The rectangular grid shown in white is in the horizontal plane of the repository. The middle horizontal line is in the dike plane.

Figure 6-72. Calculation for In-situ Stress Field Unaffected by Topography: Saturation Contours, and Magma Discharge Vectors Averaged over the Dike Zone Thickness (50 m) at the Steady State

The effect of topography on magma flow inside the dike plane and on localization of the eruption was investigated numerically for the particular location of a dike relative to Yucca Mountain. The calculation was carried out assuming the rock mass to be homogeneous and isotropic. No other geological features that could affect the dike path or magma flow inside the dike were considered in the calculation. For such conditions and analyzed geometry (i.e., topography and dike location), the calculations indicate that a dike will first rupture the ground surface in the valley. Subsequently, based on purely mechanical effects on variable dike aperture (i.e., not considering the effect of magma solidification on the change in dike aperture), the magma flow will localize in the region of initial surface rupture. The calculation indicates that magma will eventually reach the repository level in the portion of the dike which intersects the repository. However, the magma velocities and the dike aperture in that region are predicted to be relatively small. The additional calculations indicate that the observed effects of topography are due to both topography-induced stress changes and geometrical effects of the topography.

6.3.5.5 Alternative Models

In a pair of papers, Pinel and Jaupart (2004 [DIRS 178358], 2004 [DIRS 176896]) presented analytic models of the interaction between magma and an overlying edifice. Although their models represent new eruption from a previously active center, either a shield volcano or a steeper-sided stratovolcano, the principles of their analyses must also apply to topographic effects related to mountainous topography of primarily erosional origin.

In the first of these studies (2004 [DIRS 178358]), the authors note that the excess mass of the edifice causes confining stresses beneath it to rise above those at the same horizon beneath the adjacent plains. The edifice in their model was idealized as a right cylinder and the magma was taken to be in a symmetrical body on the axis through the cone. They identify three possible regimes for magma disposition beneath the edifice: (1) the magma may simply be stored in place, (2) it may erupt through the summit, or (3) it may propagate horizontally out from under the edifice. They state that "with no edifice, a horizontal dike is always tallest at the injection point, implying that, if it is able to breach the surface, it does so in the focal area." But with the increased stresses under an edifice, the top of the magma in a horizontally propagating dike rises as it moves out from the axis. This may result in eruptions several edifice radii out from under the edifice, especially for large edifices (>~3 km radius) and low density magmas such as would be likely for high water-content alkali basalts found at Lathrop Wells (SNL 2007 [DIRS 174260]).

In the second study (Pinel and Jaupart 2004 [DIRS 176896]), Pinel and Jaupart consider the effect of volatiles on the penetration of an edifice by rising magma. In this analysis, they address both conical and linear edifices. For the linear edifice, they conclude that a basaltic magma with 1% dissolved water could rise through the axis of a linear ridge with a 0.5-km-high peak; for a magma with 3% dissolved volatiles, the magma could rise through a linear ridge well over a kilometer high.

Neither of these models is directly relevant to the problem of dike propagation at Yucca Mountain. But they do provide important insights into the applicability of the results of the model presented in Section 6.3.5.4. The first analysis (Pinel and Jaupart 2004 [DIRS 178358]) provides another example of how topography can cause the diversion of a dike from its original upward path. In this case, only the effect of topography-induced stresses acts, not the geometry of the topography itself. The second analysis (Pinel and Jaupart 2004 [DIRS 176896]) suggests that some caution is required in applying the conclusion of Section 6.3.5.4 that magma will be diverted away from its original trajectory when the effect of volatiles dissolved in the magma is taken into account.

6.3.6 Approximation for Compressible Magma

It is important to understand what occurs between the time the magma reaches the drifts and the time the fracture reaches the surface; once the fracture reaches the surface, it will be very unlikely that the magma in the drift can be pressurized sufficiently to open a new path to the surface. An approximation was developed to describe the effect of expanding magma as it moves upward by combining results for different magma densities from the calculations of Section 6.3.3.4. The specific numerical inputs are given in Table 6-11. The magma density below 750 m is 1,140 kg m^{-3} with a far-field velocity of 1 m s^{-1}; the magma expands to 1,000 kg m^{-3} at 750 m and to 750 kg m^{-3} above 500 m, with the far-field velocity increasing so that the product of density times velocity times dike width is constant (conserving mass flux). This analysis illustrates the type of changes that could be expected for an expanding magma. It does not take into account any interaction with a drift.

Table 6-11. Inputs for Approximation for Expanding Magma

Depth, z (m)	Magma Density (kg m^{-3})	v_∞ (m s^{-1})	w (m)	$\mathcal{D}$ (cf. Sec. 6.3.3.4)
< 500	750	2.6	0.26	2.67
500 < z < 750	1,000	1.6	0.31	6.02
> 750	1,140	1.0	0.45	20.28

Figure 6-73 shows the result. Expansion of rising magma will be accompanied by acceleration of the magma, which, in turn, will augment the acceleration of the crack tip as the tip approaches the surface. In the approximation illustrated, the magma-front velocity is approximately 2.3 m/s between 400 and 340 m in depth. The crack tip arrives at the surface three minutes earlier than it would have had no expansion of the magma occurred as it rose toward the surface. Selection of the depths (750 and 500 m) for expansion in this approximation is arbitrary. Clearly, if magma began expanding at a deeper horizon, the surface arrival would be even earlier than the three minutes seen in Figure 6-73.

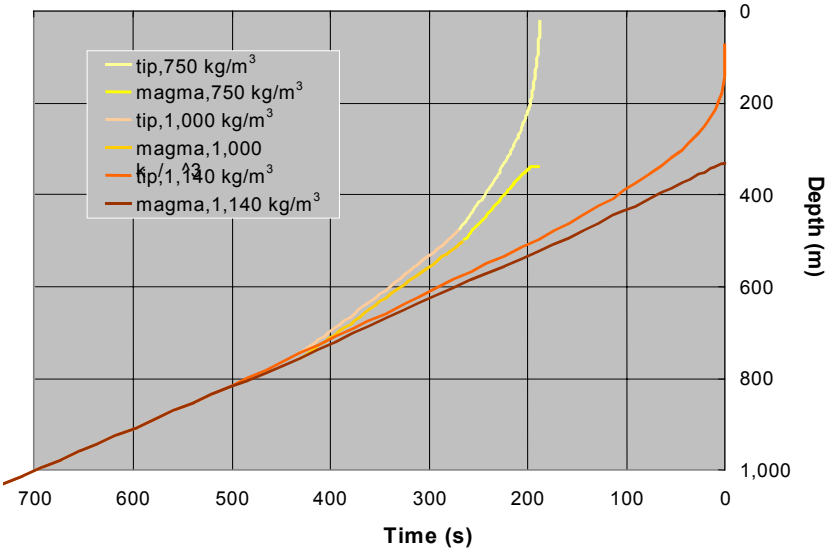

Output DTN: MO0408EG831811.002; file: *Sl2YccaMtn.xls*, tab: "depth(t)750."

NOTE: The brown and orange (for tip) curves show the dike propagation for a dike ($\mathcal{D}$ = 20.3) with a magma density 1,140 kg m^3, a far-field velocity 1.00 m/s, and a far-field dike width of 0.45 m. The light orange and tan (for tip) lines between 750 m and 500 m are results for a dike ($\mathcal{D}$ = 6.02) with magma density 1,000 kg m^3, a far-field velocity of 1.64 m/s, and a far-field dike width of 0.31 m; these lines shifted earlier by 142 s to align with the results for $\mathcal{D}$ = 20.3 at 750 m. The yellow and light yellow (for tip) lines above 500 m are results for a dike ($\mathcal{D}$ = 2.67) with magma density 750 kg m^3, a far-field velocity 2.60 m/s, and a far-field dike width of 0.26 m shifted by 260 s.

Figure 6-73. Approximate Magma and Crack Propagation for an Expanding, but Still Effusive, Magma

6.3.7 Analysis of Effect of Thermally Induced Stress Increases

The analysis of thermally induced stresses in a large-scale model (Section 6.2.4) shows that the least compressive horizontal stress increases to a maximum of approximately 10 MPa at the repository level. This maximum stress occurs in a limited volume of the rock mass and over a limited time span. On the one hand, this thermally induced increase in horizontal stress could "pinch" the dike tip and force it to turn in the direction of the maximum compressive principal stress (between 500 and 2,000 years after waste emplacement, this direction is horizontal approximately 80 m below and above the repository), thus forming a sill. On the other hand, if the dike proceeds vertically through the highly stressed repository, the magma pressure in the dike may be much larger than the pressure computed for nonthermally increased stresses.

6.3.7.1 Mathematical Description

In this section these effects are investigated numerically, using the distinct element code UDEC V. 3.14. This code solves the same equations for fluid flow as NPHF2D (Equation 6-15), except for the fracture criterion (Equation 6-13). In these simulations, the magma intrudes into preexisting cracks, the locations of which are determined by the geometric mesh used.

6.3.7.2 Uncertainties and Limitations

One of the greatest uncertainties in dike propagation is the path the dike will take. This is due to inherent uncertainty in the location, length, and orientation of fractures in the rock through which the crack is propagating. This uncertainty is addressed in the present analysis by using a collection of randomly oriented intersecting fractures (see Section 6.3.7.3) to simulate weak rock.

6.3.7.3 Inputs

A set of properties representative of the conditions studied in the previous sections was used; these are presented in Table 6-12.

Table 6-12. Model Parameters

Rock Young's Modulus[a] (GPa)	Rock Density[b] (kg m^3)	Horizontal Stress Ratio, κ[c]	Magma Density[a] (kg m^3)	Magma Viscosity[a] (Pa·s)	Magma Bulk Modulus* (MPa)	Magma Injection Rate* (m^2/s)
15	2,400	0.5	1,000	10	50	0.45

* Specified value.

Sources: [a] Detournay et al. 2003 [DIRS 169660], Table 1-2, Figure 2-1e.
[b] DTN: SNL02030193001.027 [DIRS 108410].
[c] Calculated in Section 6.3.3.3.

These parameters correspond to a value of the dimensionless parameter $\mathcal{D} = 6$, a width at infinity $w_\infty = 0.30$ m, and a fluid velocity at infinity $v_\infty = 1.5$ m/s. The velocity used is, therefore, in the lower end of the range used for the base case (Table 6-3). The magma density used is a rounded value (Section 6.3.3.4.1); density is not a controlling factor in secondary dike propagation, hence a single value is used to demonstrate the effects of other variables on the process. A value for

bulk modulus of the magma, which is required by the code employed, is specified but has no effect on the results as long as it is much greater than any pressure in the magma.

The analyses were carried out in two sets. Although the external sizes of both types of simulations are the same (4,000-m wide and 2,000-m high), the objective of the large-scale ones is dike propagation over the entire height of the model, while the small-scale simulations deal with dike propagation from a depth of 500 m. The geometry of the large-scale simulations is shown in Figure 6-74. There is only one joint (i.e., the dike path is predetermined but not the solution of the problem). The geometry of the small-scale simulations is shown in Figures 6-75 and 6-76. It includes a rectangular box (1,000-m wide and 500-m high) cut into a large number of polygonal blocks, which are discretized internally to become fully deformable. These "Voronoi polygons" (Itasca 2002 [DIRS 160331]) have an average size of 30 m. The polygonal block boundaries define the crack or joint locations.

Voronoi polygons do not create any preferential orientation; the behavior of an assemblage of such polygons is isotropic by construction. The joints between blocks form a network with no preferential direction that can accommodate a number of possible dike paths. If the block size is sufficiently small, the dike path on the scale of the model is therefore defined by the conditions that control the direction of dike propagation (e.g., stress state ahead of the dike tip). To demonstrate that the results are not dependent on any particular model geometry, each small-scale simulation was solved for two different statistical realizations of the Voronoi block geometry. Also, the validity of the computation was checked by comparing the width of the dike computed in the simulation and the analytical value of w_∞ as given above, before applying the thermal load.

Both large-scale and small-scale simulations were applied to an in situ initial stress state and a stress state 1,000 years after waste emplacement (the maximum temperature of the rock mass, on the scale of the repository, will be reached approximately 1,000 years after waste emplacement). The in situ stress state is characterized by the gravitational vertical normal stress and the horizontal normal stress, which is taken as half of the vertical stress. The "1,000-years" stress state is computed by performing a coupled thermo-mechanical simulation, using the temperature field in the east-west vertical cross section through the middle of the repository, as calculated in the mountain-scale thermo-mechanical model (BSC 2004 [DIRS 166107], Appendix C). This field is imported in UDEC V. 3.14 (BSC 2004 [DIRS 172322]). The contours of increase in temperature, as imported, are shown in Figure 6-77. The contours of the corresponding horizontal stress increase, calculated for a coefficient of linear thermal expansion of 10^{-5} K^{-1}, are shown in Figure 6-78. (The largest stress increase is expected in the horizontal direction.) The vertical profile of the horizontal stress along the joint (shown in Figure 6-79) shows a higher effect than the average of the horizontal stress profiles in Section 6.2.4. This is expected because of the two-dimensional nature of these new simulations. Still, the model size and the boundary conditions used in the thermo-mechanical calculation in UDEC are satisfactory.

In all mechanical simulations, the lower horizontal boundary of the simulation has "rollers" (i.e., it is free to move laterally and restrained in the normal direction); the top horizontal boundary represents the ground surface and is stress free (the ground surface is flat in these analyses). The vertical boundaries have "rollers" during the thermo-mechanical calculation.

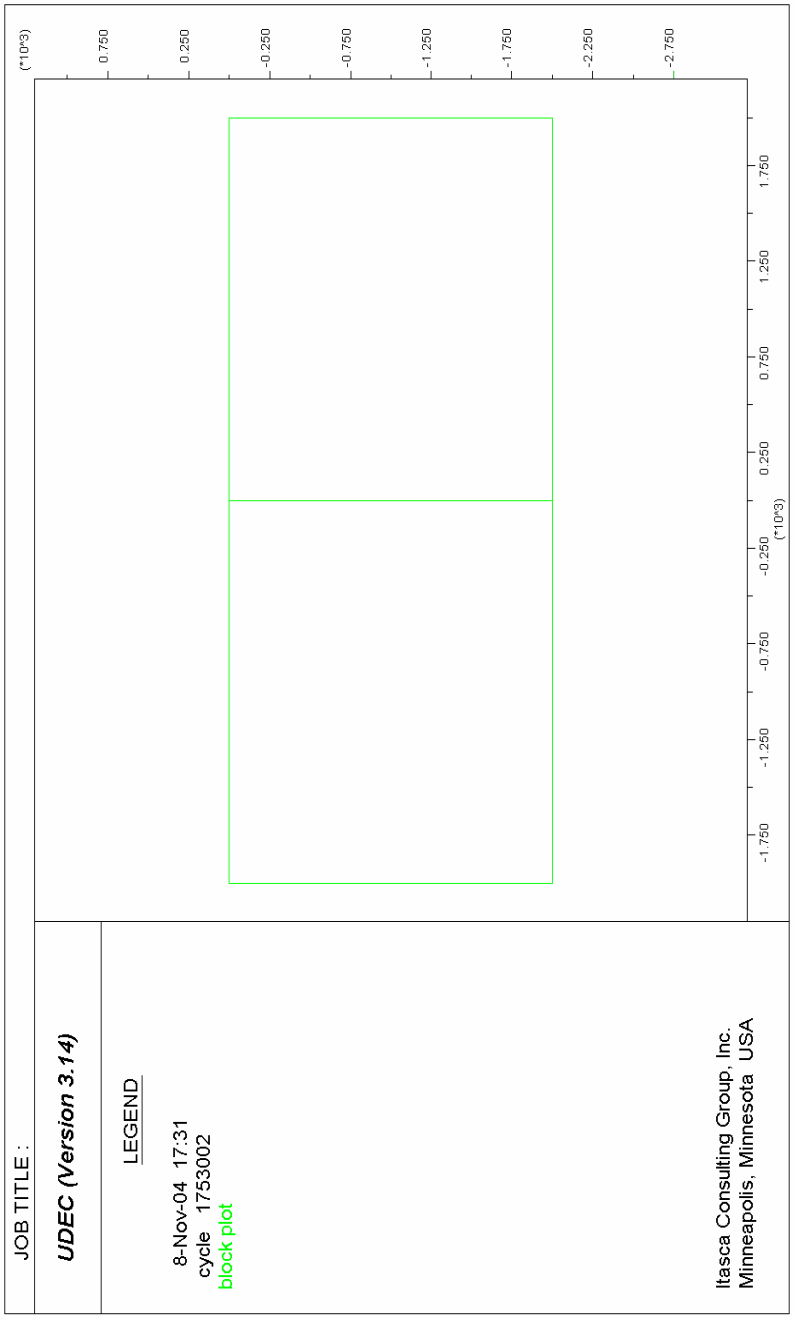

Output DTN: MO0411EG831811.000; file: *MO0411EG831811.000_Disk 1.zipVFigure 6-29.*

Figure 6-74. Large-Scale UDEC Model 2,000-m Deep by 4,000-m Wide, in Two Blocks

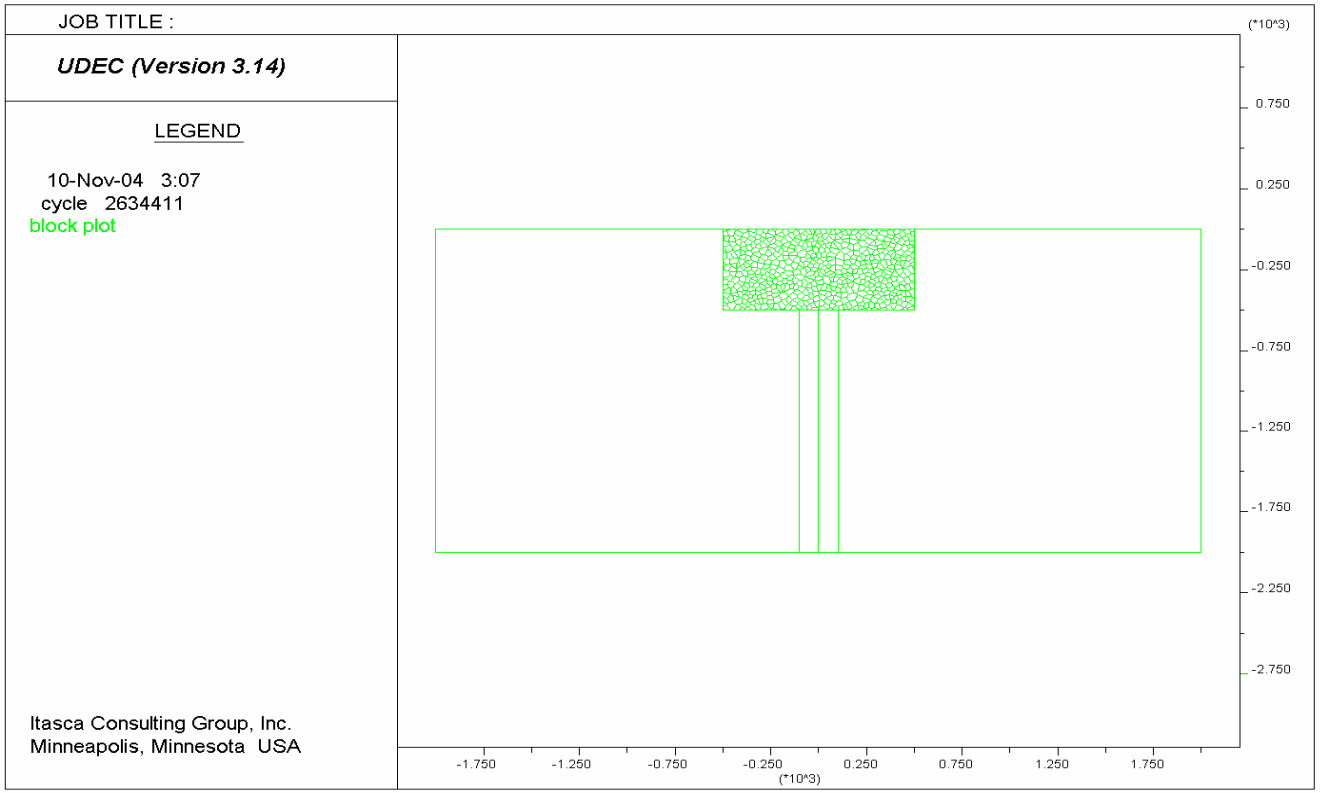

Output DTN: MO0411EG831811.000; file: *MO0411EG831811.000_Disk 1.zip\Figure 6-30*.

Figure 6-75. UDEC Model 2,000-m Deep by 4,000-m Wide, in Two Blocks With Voronoi Polygons in the 500-m-Deep by 1,000-m-Wide Rectangle Near the Surface

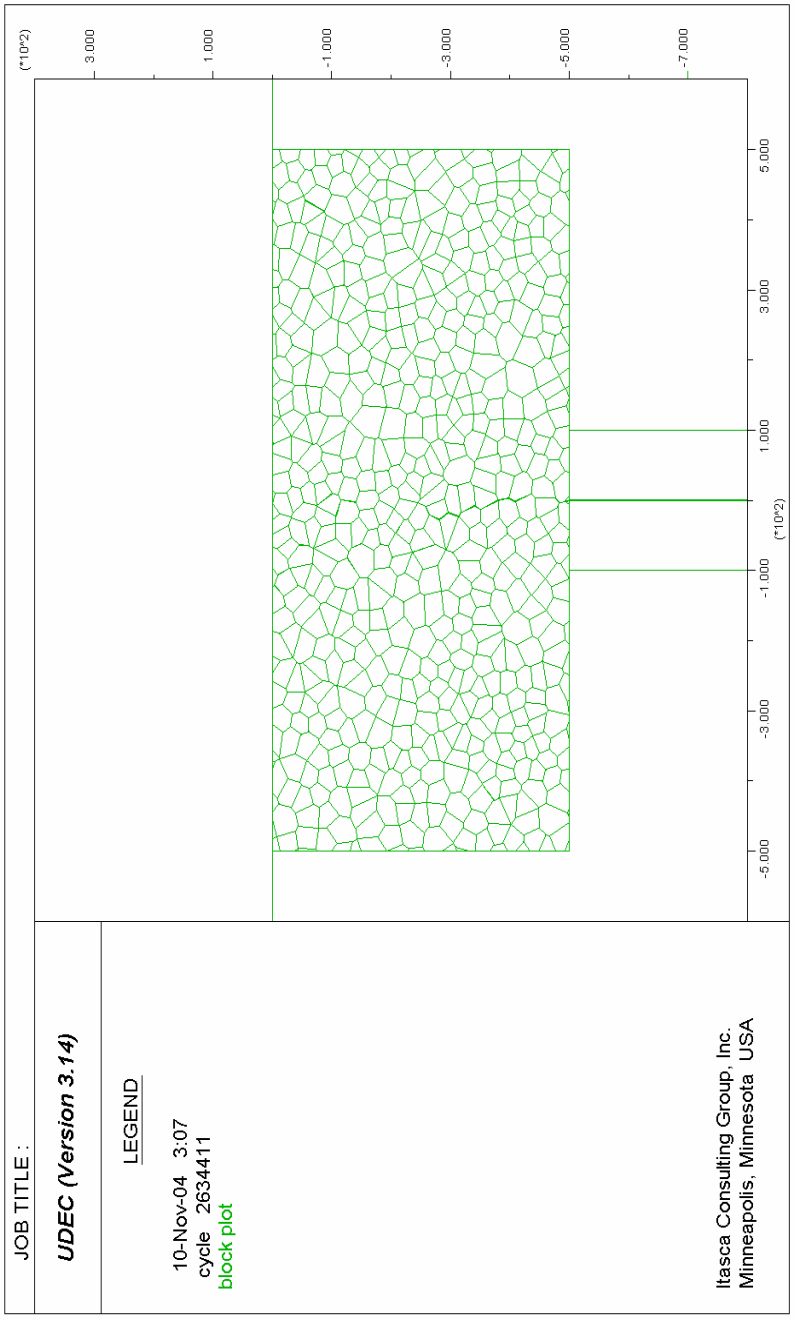

Output DTN: MO0411EG831811.000; file: *MO0411EG831811.000_Disk 1.zip\Figure 6-31.*

NOTE: Graphic shows a detail near the ground surface; the block of polygons is 500-m deep by 1,000-m wide.

Figure 6-76. UDEC Model with Voronoi Polygons near The Surface

The magma ascent simulations are fully coupled fluid-mechanical computations, starting either from the in situ stress state (initial case), or from the stress state computed as described for the 1,000-year case. In these computations, constant stress vertical boundaries replace the previous "rollers" with corresponding reactions (in equilibrium with the stress state inside the model).

For magma ascent computations, the boundary conditions involve a specified magma injection rate at the bottom and a constant zero pressure at the top. In the large-scale simulations, the volumetric fraction of magma in the joint is initially zero. Consequently, the initial magma pressure is also zero. The magma pressure and volumetric fraction of magma in the dike in the large-scale simulations, at the time when the magma front reaches the depth of 500 m below the ground surface, are used as the initial state in the small-scale flow simulations. A small-scale simulation is first equilibrated for the initial magma pressure distribution imported from the large-scale simulation.

The mesh size (discretization of Voronoi polygons) is on the order of 10 m.

6.3.7.4 Results

The objective of the large-scale simulations is not only to provide the initial conditions for the small-scale model but also to investigate the effect of the stress field on the velocity of dike propagation. A summary of the stress field effect obtained is shown in Figure 6-80 as a plot of the position of the magma front as a function of time. In addition to the aforementioned cases (in situ stress state and the nominal case for the repository state 1,000 years after waste emplacement), two additional cases are included:

- Thermally induced stresses 1,000 years after waste emplacement, for a dike propagating 500 m to one side of the center of the repository. This was done to illustrate the variability in dike propagation that might result from varying dike trajectories.

- Much higher confining stresses similar to thermally induced stresses 1,000 years after waste emplacement but with a coefficient of linear thermal expansion five times greater than the coefficient of TSw2 geological units at Yucca Mountain in which the repository will be located. This was done to demonstrate that the model will result in sill formation, as would be expected in the presence of extremely high confining stresses.

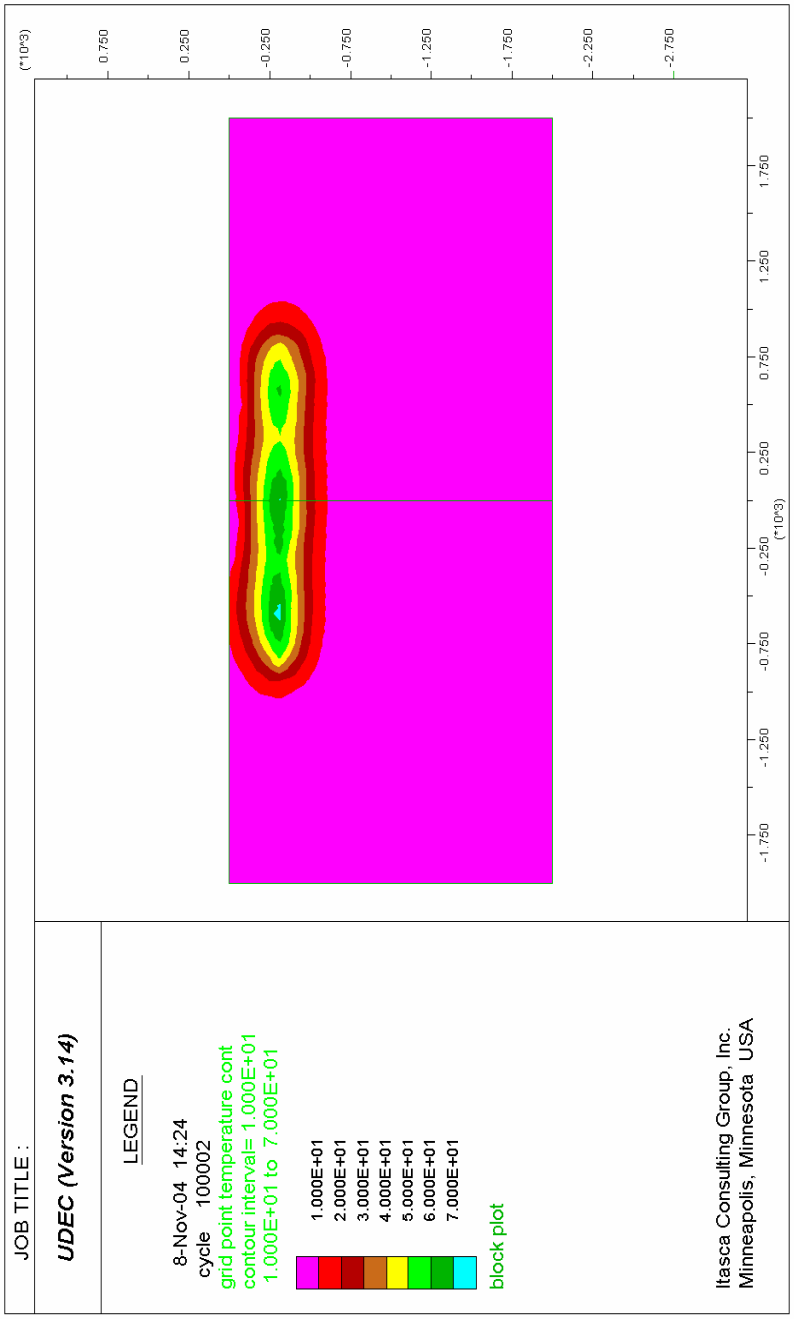

Output DTN: MO0411EG831811.000; file: *MO0411EG831811.000_Disk 1.zipVFigure 6-32.*

Figure 6-77. Contours of Temperature Increase (°C) 1,000 Years after Waste Emplacement

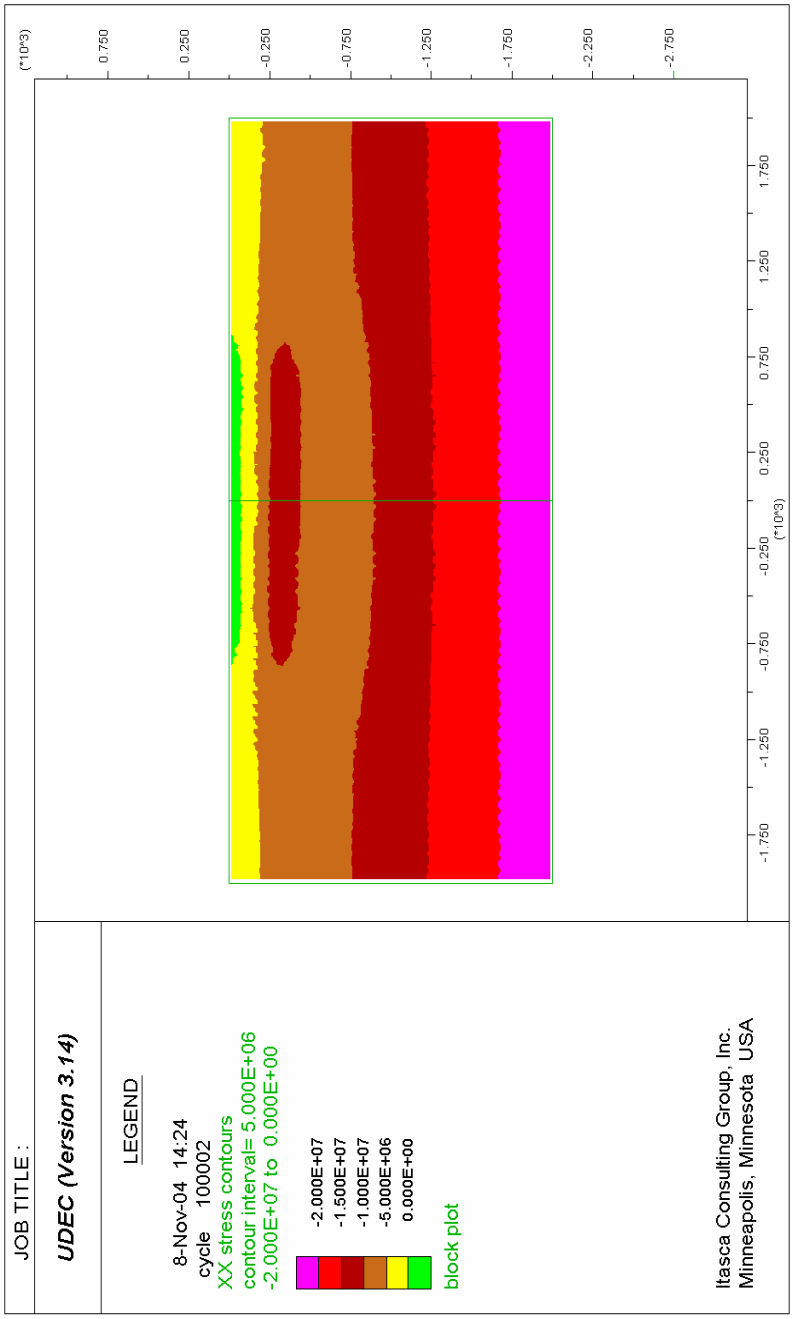

Output DTN: MO0411EG831811.000; file: *MO0411EG831811.000_Disk 1.zip\Figure 6-33.*

Figure 6-78. Contours of Horizontal Stress (Pa) 1,000 Years after Waste Emplacement

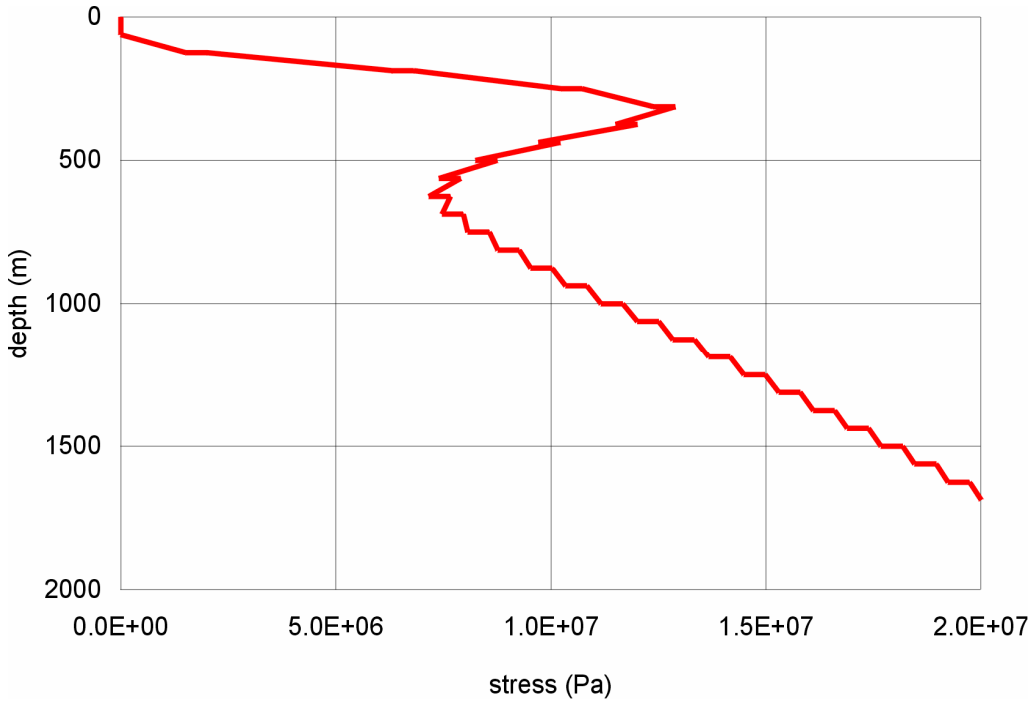

Output DTN: MO0411EG831811.000; file: *MO0411EG831811.000_Disk 1.zip\Figure 6-34*.

NOTE: Horizontal "steps" are a result of projection of two values from three-dimensional model onto a single line; stresses used as input to the two-dimensional calculation were averaged, so no steps occurred.

Figure 6-79. Vertical Profile of Horizontal Stress 1,000 Years after Waste Emplacement

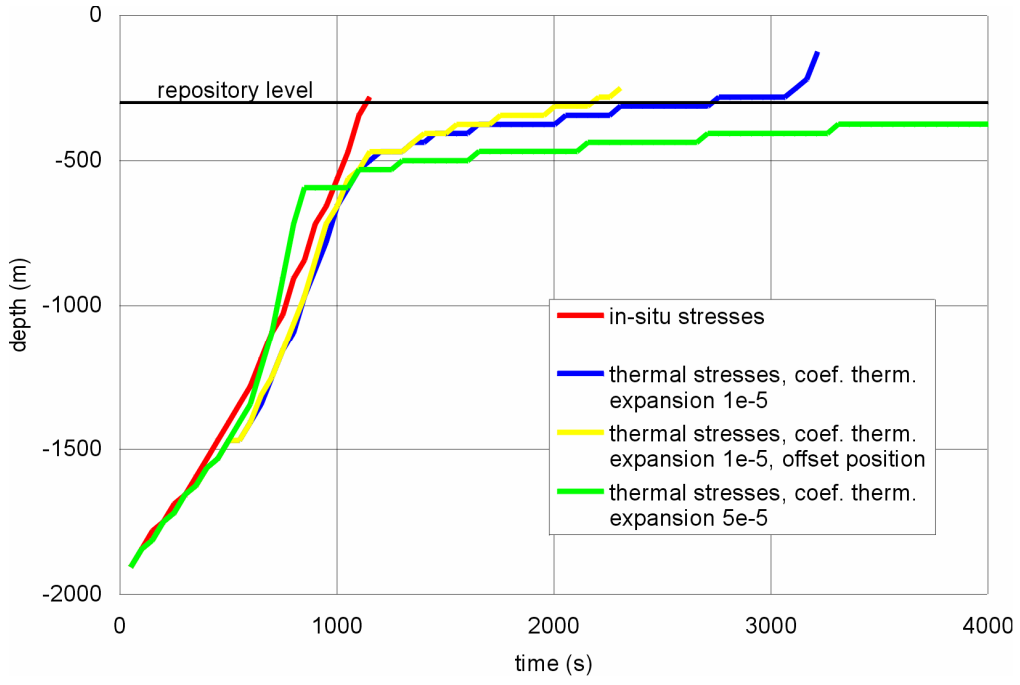

Output DTN: MO0411EG831811.000; file: *MO0411EG831811.000_Disk 1.zip\Figure 6-35*.

Figure 6-80. Position of Magma Front as a Function of Time – Large-Scale Model

The results indicate that thermally induced stresses 1,000 years after waste emplacement significantly affect dike propagation. When the dike approaches the region of increased horizontal stresses approximately 200 m below the repository, the dike tip and the magma front slow down. In the nominal case, the magma front velocity, after increasing from 0.7 m/s to more than 1 m/s when reaching a depth of 800 m, slows to approximately 0.1 m/s upon reaching the repository level. The magma front advances from 500 m depth to 300 m depth (the repository horizon) in approximately 2,000 s. The slow-down is less pronounced if the dike is propagating closer to the edges of the repository, because the thermally induced horizontal stresses are smaller at the edges than in the middle of the repository. An increased coefficient of thermal expansion logically results in even more slowdown. Once the dike passes through the region of increased horizontal stresses, the tip and magma front suddenly accelerate due to the very large horizontal stress gradient (Figure 6-79) above the repository.

Two states of the flow model for the single-joint case 1,000 years after waste emplacement are shown in Figures 6-81 and 6- 82 (any asymmetry in these figures is an artifact from the plotting). The result shown in Figure 6-81 is at an early time and is not yet affected by either the thermal stresses or the free surface. The cavity between the dike tip (the location can be determined from the profile of dike opening) and the magma front (the location can be determined from the profile of magma pressure) is between 50 m and 100 m in length. That cavity almost completely disappears in the later result when the dike propagation has stalled (shown in Figure 6-82). The magma pressure increases at relatively short distances from the tip, but remains unchanged elsewhere as it is controlled by far-field horizontal stress boundary conditions. However, the dike opening significantly increases and the dike propagation is retarded by the large confining stress.

Thermally induced stresses 1,000 years after waste emplacement (Figure 6-5) create a stress field a few hundred meters below and above the repository in which the horizontal principal stress is the most compressive (more compressive than the vertical principal stress). The crack tip extends in the direction of the most compressive principal stress in the region ahead of the crack tip.

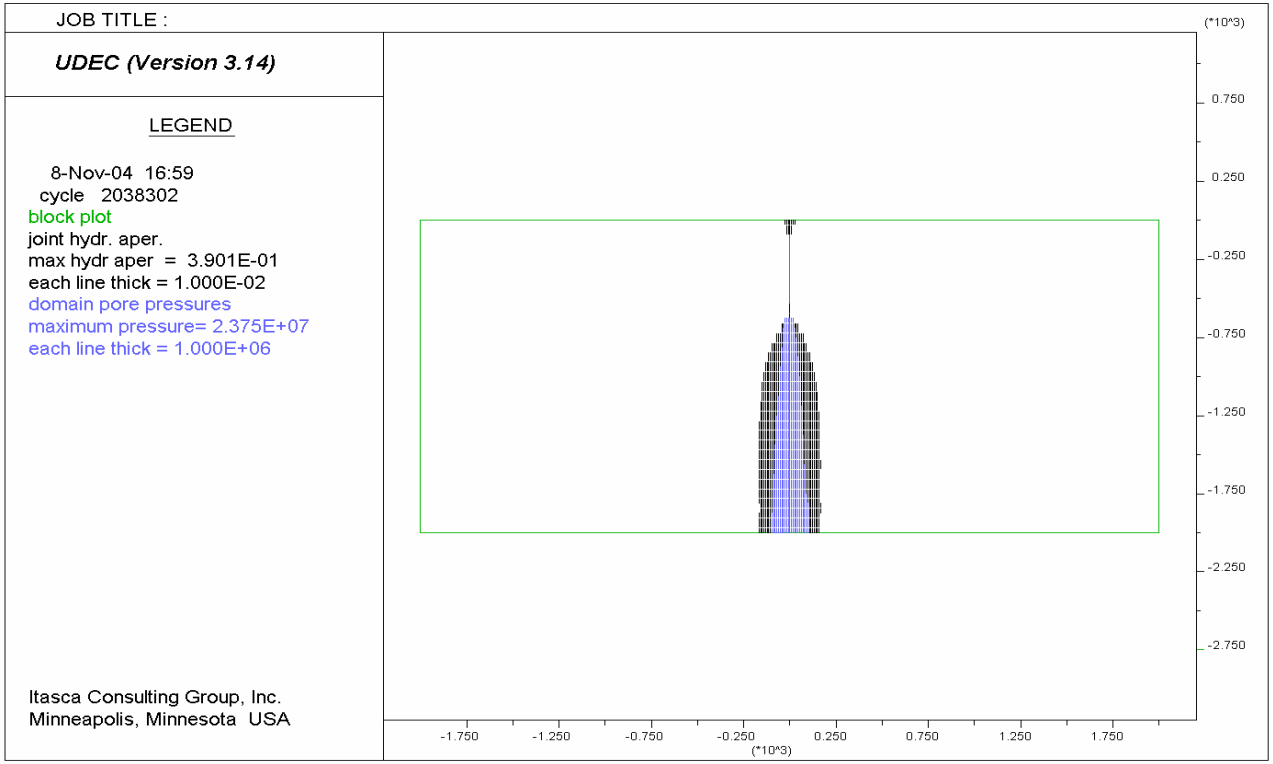

Output DTN: MO0411EG831811.000; file: *MO0411EG831811.000_Disk 1.zip\Figure 6-36*.

NOTE: Green outline is 2,000 m deep by 4,000 m wide; maximum aperture is 0.39 m, maximum pressure is 23.7 MPa. Pressure (Pa) is shown in blue; aperture (m) is shown in black.

Figure 6-81. Pressure and Aperture along the Dike Propagating in the Middle of the Repository 1,000 Years After Waste Emplacement – 1,000 Seconds after Start of Simulation

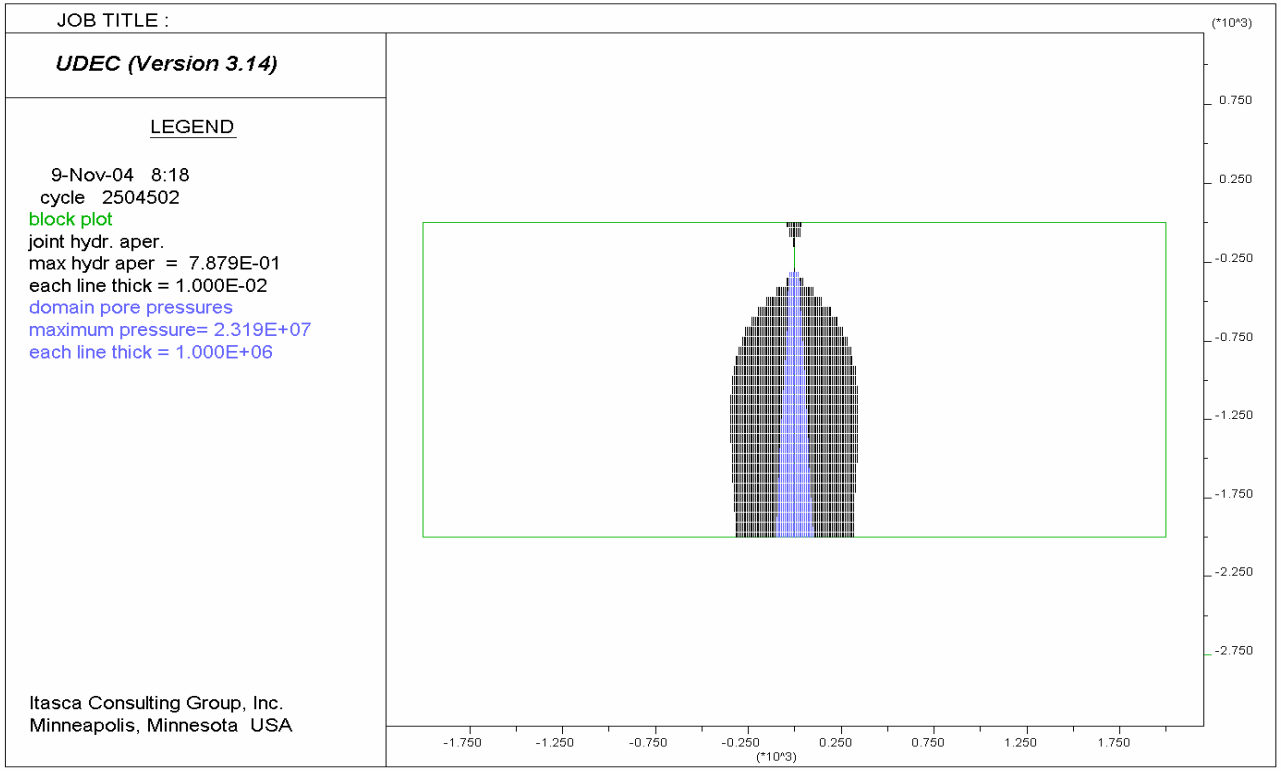

Output DTN: MO0411EG831811.000; file: *MO0411EG831811.000_Disk 1.zip\Figure 6-36a*.

NOTE: Green outline is 2,000 m deep by 4,000-m wide; maximum aperture is 0.79-m, maximum pressure is 23.2 MPa.

Figure 6-82. Pressure (Pa) and Aperture (m) Along the Dike Propagating in the Middle of the Repository 1,000 Years After Waste Emplacement–2,500 Seconds after Start of Simulation

In the large-scale simulations, the dike is constrained by the computational model to propagate along the predefined joint vertically upward. The possibility of sill formation is investigated with the small-scale simulations. The stress field ahead of the tip is a combination of the preexisting state and the effect of the crack and the pressure inside the crack on that stress field. Therefore, the crack path does not always coincide with the trajectories of the most compressive principal stress existing before the crack propagates: because of the change of stress due to the presence of the dike itself, the tip will deviate more gradually than the in situ principal stresses. The sharpness of the deviation will depend on the magnitude of the stress difference. Also, in the simulations, the sharpness of the deviation obviously depends on the size of the Voronoi polygons. Initially, all joints have the same properties. In the nominal case, as well as in the case with a dike position offset 500 m to the left and right of the center of the repository toward the edges, the dike propagation is essentially vertical (shown in Figures 6-83 and 6-84). This is an indication that the thermal stresses are not expected to cause dike deflection and sill formation under conditions likely to occur at Yucca Mountain. However, dike deflection cannot be ruled out entirely, because the size of the Voronoi polygons may prevent the simulation from producing a sharp enough deflection. The analysis did not consider the effect of a horizontal discontinuity that could arrest vertical dike propagation and provide a preferred horizontal path for magma flow, resulting in more-favorable conditions for sill formation.

If the model fails to produce a sill under such conditions, the conclusion that sill formation will not occur under expected thermal stress conditions would not be credible. Therefore, a final simulation was performed to demonstrate that the model correctly simulates formation of a sill under the repository if confining stresses are extremely high. To obtain such a case, the coefficient of linear thermal expansion was increased to 5×10^{-5} K^{-1} (this coefficient is on the order of 10^{-5} for all geological units at Yucca Mountain (BSC 2004 [DIRS 166107])). This analysis is not intended to approximate any condition that is expected to occur at Yucca Mountain; it is included only to show that the model is capable of yielding a sill under some (unrealistically extreme) conditions. The results for this extreme case are shown in Figure 6-85. The calculated maximum horizontal stresses are approximately 50 MPa. Propagation of the dike in the original vertical direction is slowed down, as indicated in Figure 6-80. However, because the dike is free to "choose" the path in the model, the state after approximately 5,000 s (shown in Figure 6-85) shows a sill beginning to form at the boundary of the box discretized into Voronoi blocks as indicated by the horizontal extension of the high-pressure region (black). Because sill formation in this case starts exactly at the lower edge of the box with Voronoi blocks, the position where dike deflection begins is a model artifact and is an upper limit to the location where sill formation would be expected if the box extended farther down. If the model was continued to a longer time under the same driving condition, it is expected that the sill would propagate horizontally until reaching the edge of the repository, where it would revert to a vertical dike form of intrusion.

The positions of the magma front as functions of time (Figure 6-86) extracted from the small-scale simulations, show the same trend as observed from the large-scale model. The zero time in Figure 6-86 is offset from that in Figure 6-80 by about 1,000 s. The dike propagating in the middle of the repository will be pinched by the thermal stresses 1,000 years after waste emplacement, and the magma front will slow down to approximately 0.1 m/s. The effect closer to the edges of the repository will be less.

The pressure histories extracted from the simulations at the repository level (i.e., approximately 300 m below the ground surface) are shown in Figure 6-87. The pressure history for the in situ stress state follows the trend observed in the simulations from Section 6.3.7.1. The difference between the maximum magma pressure and the horizontal far-field stress is close to 1 MPa. With thermally induced stresses, the maximum magma pressure is 6 MPa, much less than the peak horizontal stress of approximately 13 MPa.

The analysis of the effect of thermally induced stress increases on dike propagation has shown the following:

- The magma velocity decreases for the stress state expected 1,000 years after waste emplacement, at approximately 200 m below the repository level, from more than 1 m/s (for the analyzed case) to approximately 0.1 m/s
- After passing the repository level, the dike tip and magma front accelerate again
- Slow-down is slightly greater if the dike propagates in the middle of the repository rather than at the edge of the repository.
- For the expected maximum stress increase 1,000 years after waste emplacement, and for a homogeneous and isotropic rock mass (as represented by the isotropic Voronoi polygons), no dike deflection was produced in the model. However, the possibility of a deflection cannot be ruled out entirely because of possible effects of details of Voronoi block orientations and size.

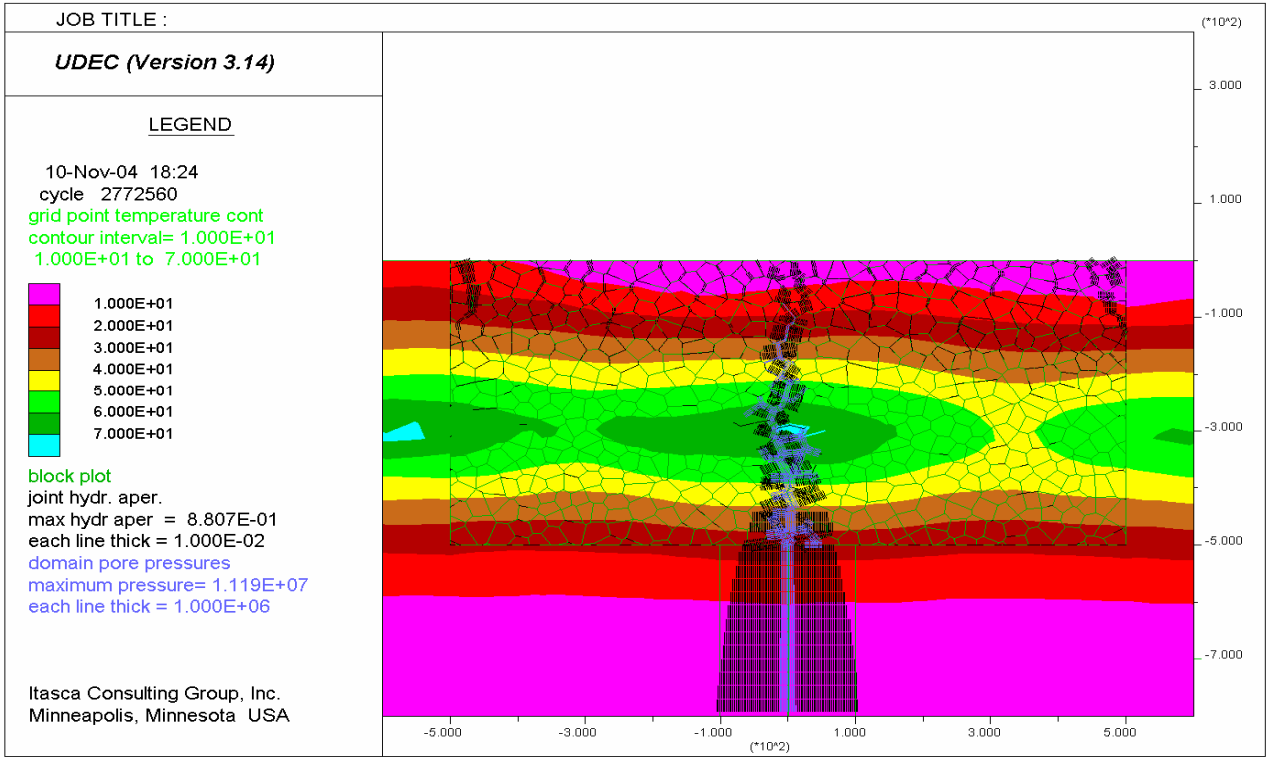

Output DTN: MO0411EG831811.000; file: *MO0411EG831811.000_Disk 1.zip\Figure 6-36b*.

NOTES: Thickness of the black line proportional to dike opening, maximum aperture, is 0.75-m; thickness of the blue line proportional to magma pressure, maximum pressure, is 10.7 MPa. Region filled with green polygons is 500 m deep by 1,000-m wide.
Graphic illustrates temperature increase contours (°C), dike opening (m), and magma pressure (Pa).

Figure 6-83. Dike Path Propagating in the Middle of the Repository 1,000 Years after Waste Emplacement

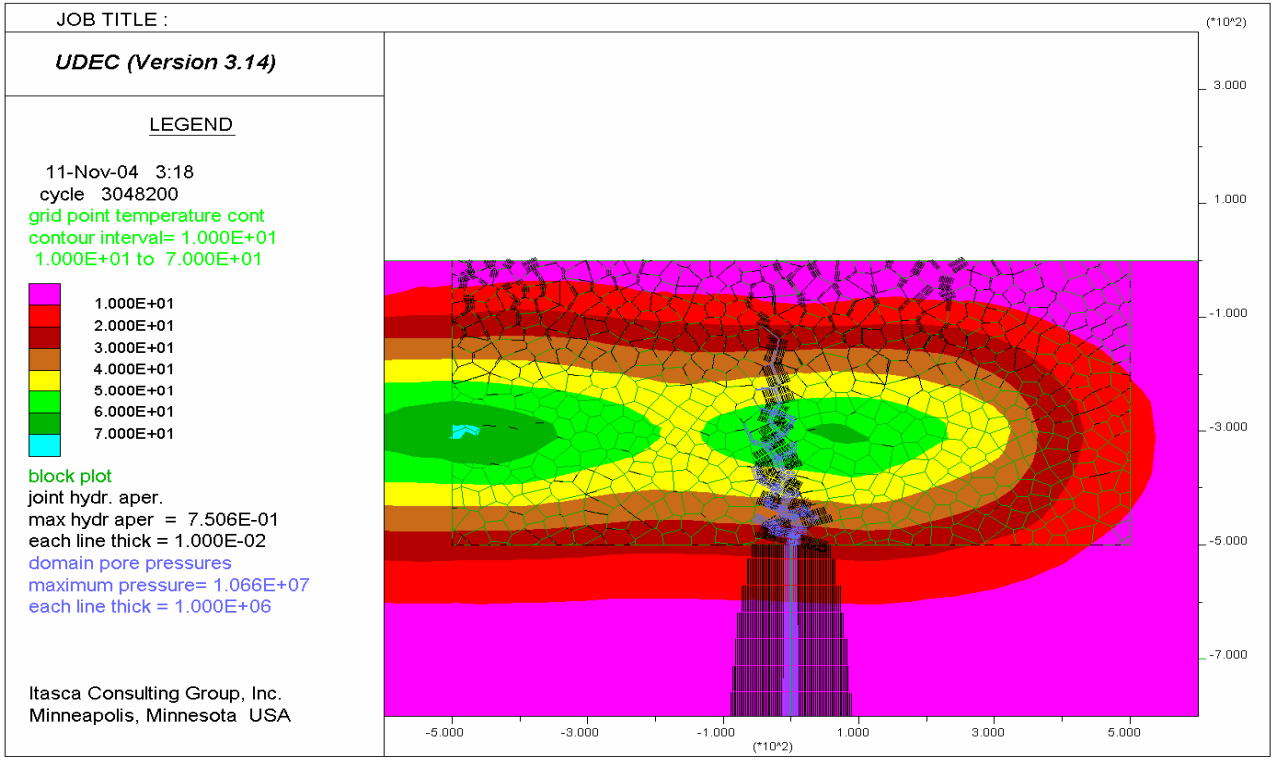

Output DTN: MO0411EG831811.000; file: *MO0411EG831811.000_Disk 1.zip\Figure 6-36c*.

NOTES: Thickness of the black line proportional to dike opening; thickness of the blue line proportional to magma pressure.
Graphic shows temperature increase contours (°C), dike opening (m), and magma pressure (Pa).

Figure 6-84. Dike Path Propagating 500 m Offset from the Middle of the Repository 1,000 Years After Waste Emplacement

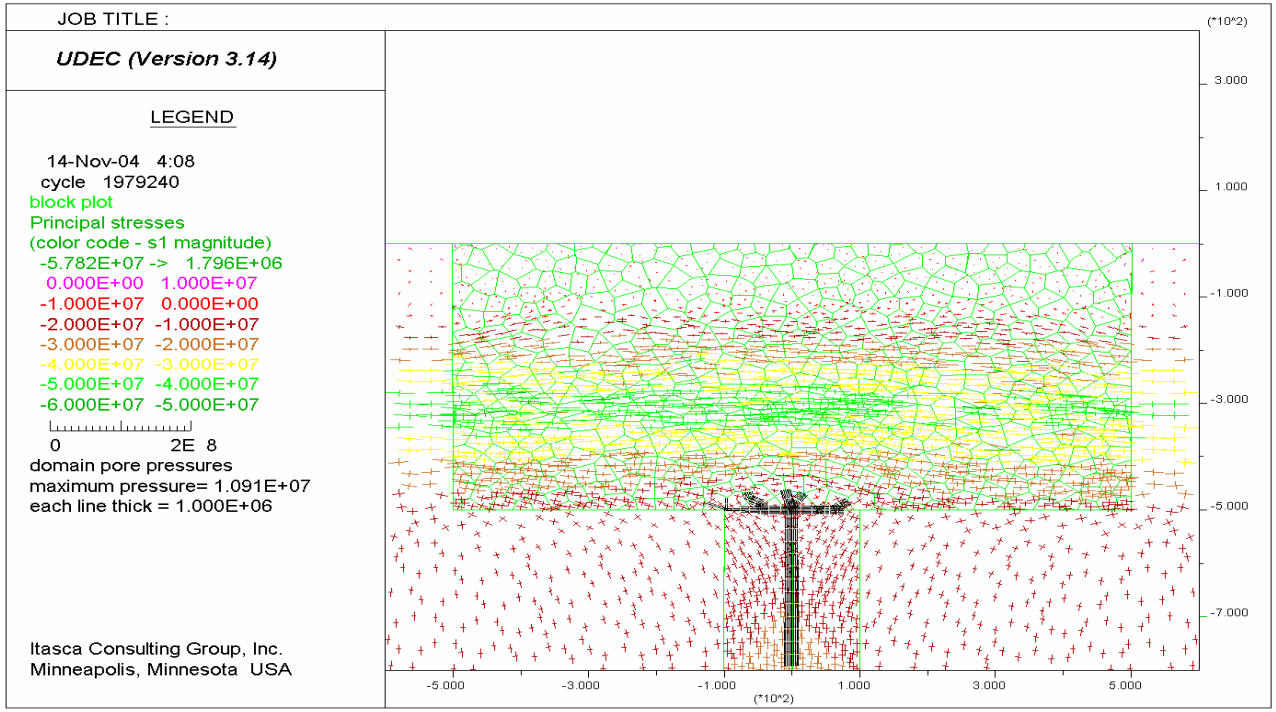

Output DTN: MO0411EG831811.000; file: *MO0411EG831811.000_Disk 1.zip\Figure 6-36d*.

NOTE: Thickness of the black line proportional to magma pressure.
Graphic assumes a coefficient of thermal expansion of 5×10^{-5}.

Figure 6-85. Pressure (Pa) and Stress Tensors Colored By Magnitude Of Major Principal Stress (Pa) Along The Dike Propagating In The Middle of The Repository 1,000 Years after Waste Emplacement

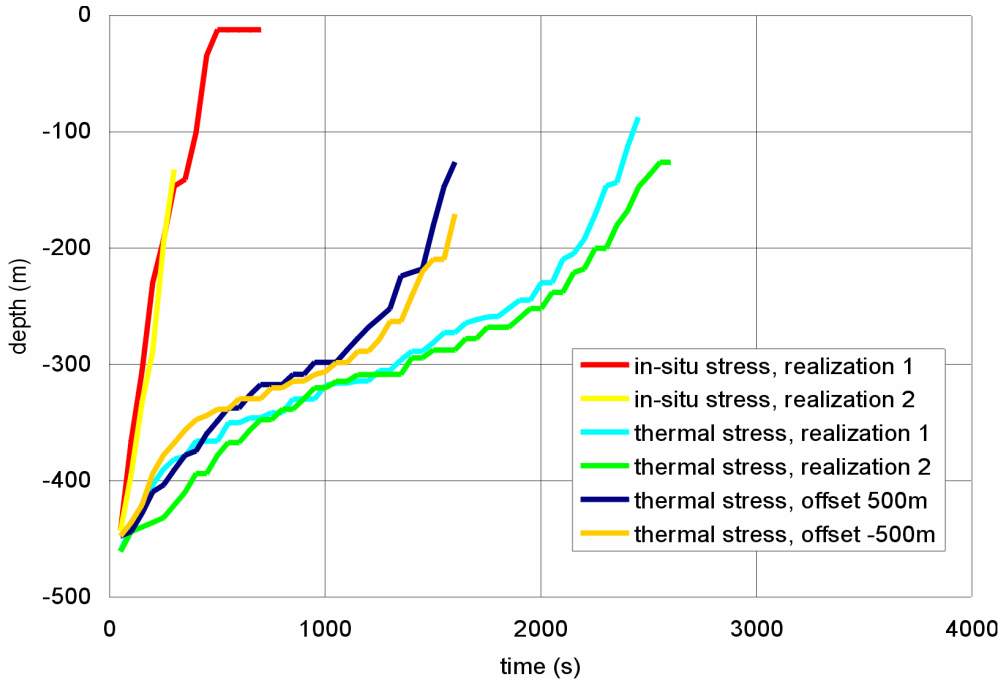

Output DTN: MO0411EG831811.000; file: *MO0411EG831811.000_Disk 1.zip\Figure 6-36e*.

Figure 6-86. Position of the Magma Front as a Function of Time – Small-Scale Model

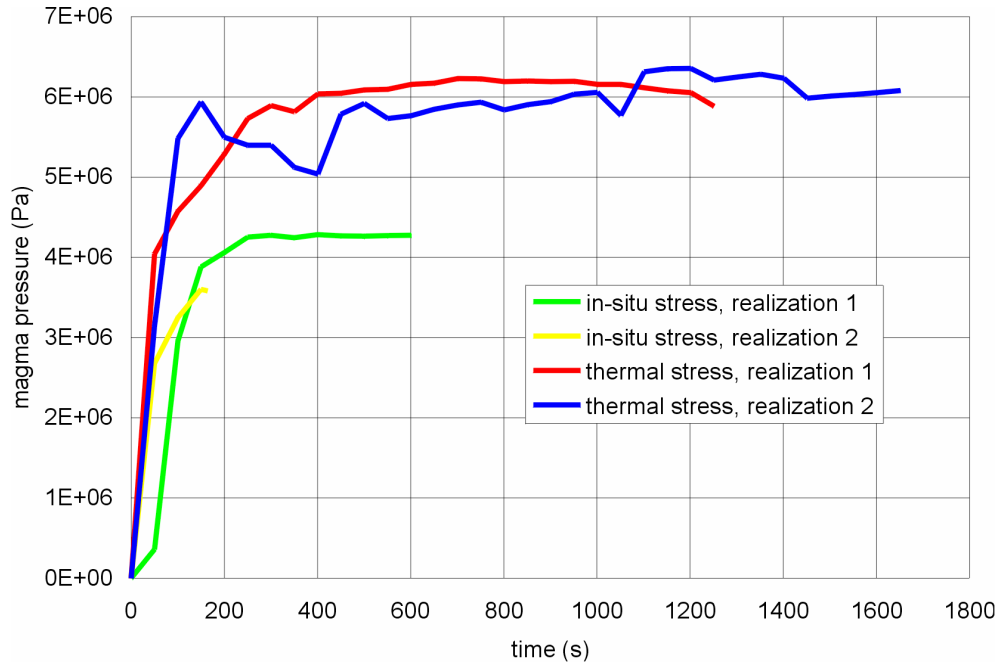

Output DTN: MO0411EG831811.000; file: *MO0411EG831811.000_Disk 1.zip\Figure 6-36f*.

Figure 6-87. Pressure Histories in Magma as a Function of Time at the Repository Horizon – Small-Scale Model

The magma pressure at the repository level for the stress state 1,000 years after waste emplacement and after the dike breaks through the region of increased horizontal stresses, is expected to be in the range of 6 MPa, which is much less than the maximum thermally induced stress increase. This maximum magma pressure limitation agrees well with the calculations showing the difficulty of sill formation.

6.3.8 Summary

6.3.8.1 Base Model for Incompressible Magma

Dike ascent driven by incompressible magma was analyzed for a variety of conditions. The effects of vertical gradients of horizontal stress, far-field dike velocity and opening, pressure inside the tip cavity, and additional horizontal confinement were considered. Although the dimensional results were provided for different values of v_∞ (up to 15 m/s) and $\kappa \rho_r$ (up to 2,400 kg m^3), the primary focus was on v_∞ = 1 m/s and 10 m/s, and on $\kappa\rho_r$ = 1,200 kg m^3.

The maximum magma pressure in the dike, in the absence of a drift, at the repository elevation, was computed to be about 1 MPa above in situ stress conditions (i.e., 4.5 MPa for a horizontal far-field stress of 3.5 MPa). Thermally induced horizontal stresses only increase the magma pressure by a fraction of the increase of horizontal stresses: while horizontal stresses reach 13 MPa (i.e., an increase close to 10 MPa), the magma pressure reaches only 6 MPa, a 1.5-MPa increase over magma pressures computed using nonthermal horizontal stresses. When uncertainty in the far-field width of the dike is taken into account, it is concluded that maximum magma pressures at the repository during dike emplacement will be at most a few MPa greater than the in situ confining stress (Section 7.3.1.1.2 and Appendix F). With this reservation, both the thermal and non-thermal periods are covered.

The tip of the crack speeds up when approaching the surface, therefore lengthening the cavity behind the dike tip, which is free of magma. In all cases, the cavity has grown to a significant length when the magma reaches the repository elevation. In fact, for the most realistic cases mentioned above, the dike tip has reached or is about to reach the surface when the magma reaches the repository.

The velocity of the ascending incompressible magma stays constant when approaching the repository level, except in the lower buoyancy cases (Figure 6-9) for which the magma slows down. The width of the dike at the repository level is essentially the same as w_∞, since the magma flow rate is constant and the magma velocity does not vary much. An increase of up to 20% in width was calculated, but that increase is not significant compared to the range of parameters analyzed. The magma front velocity and dike width are not considered to be significantly different from the values at infinity.

6.3.8.2 Variations from Base Model

The effects of structure and stratigraphy on dike propagation were investigated. It was found that deep range-bounding faults are not likely to divert magma. Diversion of magma into a fault is more likely for faults with steep dips (> 60° to 70°) and only at shallow depths (less than a few hundred meters). If magma is captured by such a fault and the fault slips, conditions may

become favorable for the intrusion of sills at shallow depths along bedding planes in the hanging wall.

An analysis of a dike approaching an irregular surface composed of ridges and valleys found that magma flow in a dike whose strike cuts across the ridges will be diverted away from the highlands because of the higher overburden stress beneath. Such dikes will have a tendency to erupt in lowlands rather than on ridges.

Propagation of dikes driven by compressible magma is not expected to be radically different from that driven by incompressible magma. However, it was found that dikes with compressible magma will accelerate as they approach the surface more than those with incompressible magma.

Analysis shows that thermally induced stresses will slow the penetration of a dike into the repository but will not result in formation of a sill beneath it. Thermal stresses will result in higher magma pressures at the repository horizon.

6.4 ENVIRONMENT IN REPOSITORY AFTER INTRUSION

The style of magma flow into emplacement drifts would depend on details of the distribution of volatiles within the rising magma in a dike. At one extreme, if less than approximately 0.5 wt % of volatiles remained in the magma that first encountered an emplacement drift, the flow of magma into the drifts would be dominated by the viscosity of the liquid portion of the magma; such flow is called effusive and is described in Sections 6.3.3.5.6 through 6.3.3.5.8. At the other extreme, if the magma had a volatile content of 3 wt % or more that was well-mixed with the liquid phase when a drift were encountered, the magma would expand rapidly into the drift as the volatiles exsolved from the magma. This would result in a turbulent two-phase flow of the type called pyroclastic; such flow in drifts is described in *Magma Dynamics at Yucca Mountain, Nevada* (BSC 2005 [DIRS 174070]).

6.4.1 Model Description

The complete model of the environment in the repository following an intrusion calculates temperatures in and surrounding a drift after it has been filled with magma as described in Sections 6.4.2 through 6.4.6. Alternative models are addressed in Section 6.4.7. Several supplemental analyses that further define the post-intrusion environment, including effects on waste packages and waste forms, are discussed in Section 6.4.8. The environment in the repository after intrusion is summarized in Section 6.4.9.

6.4.1.1 Magma Cooling and Solidification Model

This model addresses the evolution of the temperature of the waste package, invert, surrounding rock mass, and magma after magma intrusion into the emplacement drift. Magma intrusion is considered for the upper bounding case of a completely molten magma at 1,150°C (referred to as the effusive case). Five initial temperature states of the surrounding rock mass were considered: 25°C, 50°C, 100°C, 150°C, and 200°C. The model is a one-dimensional analytic solution based on heat transfer by conduction after the magma fills the drift and latent heat is neglected. Effects of latent heat and two-dimensionality are addressed in alternative models.

Section 6.4.2 presents the assumptions and simplifications of the model, while the mathematical description is found in Section 6.4.3. Uncertainties and limitations are discussed in Section 6.4.4. The inputs for the simulations are listed in Section 6.4.5. The results of the analyses for both hot and cold waste packages are included in Section 6.4.6. Finally, as noted above, alternative models are discussed in Section 6.4.7.

6.4.1.2 Supplemental Analyses

Further details of the environment in the repository following intrusion are developed in three supplemental analyses in Section 6.4.8. An analysis of magmatic pressures after intrusion is presented in Section 6.4.8.1, followed by consideration of magma interactions with waste packages and waste forms in Section 6.4.8.2, and a treatment of magma chilling in backfilled access drifts in Section 6.4.8.3.

6.4.2 Assumptions and Simplifications

The model of magma cooling simplifies the actual conditions in the following ways:

- The geometry is simplified to a one-dimensional cylindrical configuration so that heat flow along the length of the drift is not addressed. This is justified because the length of a drift is two orders of magnitude larger than its radius. A further justification is that the separation between waste packages is almost two orders of magnitude smaller than the length of an individual drift.

- All media in the calculation are treated as isotropic and homogeneous.

- The waste packages themselves are not included explicitly in the calculations. This simplification is justified in that it makes the problem analytically tractable. The extent of error introduced into the solutions is evaluated in an alternative model in Section 6.4.7.2.

6.4.3 Mathematical Description

Consider a drift 5.5 m in diameter and 637-m long created in tuff at a depth of 300-m below the surface and where the ambient tuff temperature is approximately 30°C. The ratio of the length to the diameter of the excavation is >100. Thus, for the vast majority of the volume of the drifts, heating can be treated as a cylindrical one-dimensional heat-flow problem. If a drift were to be instantaneously and entirely filled with basaltic magma at a temperature of approximately 1,150°C (SNL 2007 [DIRS 174260], Table 6-5, 0.5 wt % water), the tuff surrounding the drift would begin to heat up as the magma cooled, and the temperature profile through the drift and surrounding rock would evolve with time.

The temperature distribution for magma filling an emplacement drift can be estimated using an idealized model of one-dimensional unsteady heat conduction in a cylinder (i.e., drift) subject to constant heat content. This simplified model may be used to estimate the length of time it takes for the repository to cool back to any temperature of interest. The contribution of latent heat and heat transfer due to convection is neglected in the base case, although the effects of latent heat are considered in Appendix C, Section C3.1. Any advection of gases in the surrounding host

rock, as well as the release of volatiles from the cooling magma will enhance the cooling rate; thus, these purely convective calculations will tend to underestimate magmatic and host-rock cooling rates with respect to the mass flow of hot gases.

In this model, the temperature of the repository host rock is considered to be between 25°C and 200°C at the time of the intrusion. The thermal properties of the magma are considered the same as those for the densely welded tuff for a first-order analysis. Details for the heat conduction model are presented, along with pertinent equations, in Appendix C, Section C1.

6.4.4 Uncertainties and Limitations

Uncertainties arising from the lack of certainty of the properties of tuff are addressed in Section 6.4.6, where properties of both wet and dry tuff are used to develop separate solutions, and in Appendix C, Section C4, which presents results for temperature history at a radius of 10 m from the centerline of the drift for eight variations of conductivity representing high and low values of input parameters. For all cases, the peak temperature at that range is between 75°C and 81°C and occurs just later than one year after intrusion.

6.4.5 Inputs

The inputs to the magma cooling model are found in Appendix C, Tables C-2 and C-3. The input parameters in these tables were all developed under Yucca Mountain quality assurance standards and meet the requirements of SCI-PRO-006 for direct input. In addition, properties of water, which are established fact, are cited in Appendix C, Section C1.3.

6.4.6 Model Results

The results of the magma cooling model are presented in Table C-4 in Appendix C, Section C2. Sensitivity to country rock consisting of either wet or dry tuff is found in Appendix C, Section C2. Analyses of the sensitivity of the results to latent heat of crystallizing magma and to saturation of the tuff are found in Appendix C, Section C3. The results are contained in output DTN: LA0702PADE01EG.001. The values are summarized in Table 6-13.

6.4.7 Alternative Models

Two alternative models have been considered. The first, in Section 6.4.7.1, is an approximate analytic solution that includes the effects of latent heat, which were not included in the base model. The second alternative model consists of numerical solutions in two dimensions that also include the effects of latent heat and of radioactive heat from hot waste packages. This is described in Section 6.4.7.2.

6.4.7.1 Analytic Solution

An alternative model for heat flow from a magma filled drift is considered. This model is similar to the first but includes the effects of latent heat. This analysis is presented in full detail in Appendix D.

6.4.7.2 Two-Dimensional Numerical Solutions

Two-dimensional numerical analyses were conducted to investigate the effects of off-axis position of waste packages in a drift and of variations in magmatic temperature. These analyses also included the effects of magmatic latent heat of crystallization and of radiogenic heat on waste packages. Two radiogenic heat states were considered: a "cold waste package" (CWP) case, with no heat source in the waste package, and a "hot waste package" (HWP) case, with an internal heat source in the waste package and with preheated surrounding rock.

Table 6-13. Lookup Tables for Temperature (°C) of Intruded Drifts

Time after Intrusion	Pre-intrusion Temperature									
	25°C		50°C		100°C		150°C		200°C	
Years	$T_{r=0m}$	$T_{r=3m}$	$T_{r=0m}$	$T_{r=3m}$	$T_{r=0m}$	$T_{r=3m}$	$T_{r=0m}$	$T_{r=3m}$	$T_{r=0m}$	$T_{r=3m}$
0	1,150	1,150	1,150	1,150	1,150	1,150	1,150	1,150	1,150	1,150
0.1	1,003	608	1,006	620	1,012	644	1,019	668	1,026	692
0.2	740	479	749	494	768	524	786	553	804	583
0.3	564	399	577	416	603	449	629	483	655	516
0.4	452	342	467	360	498	396	529	432	560	468
0.5	377	299	394	318	428	356	462	394	497	431
0.6	323	266	341	286	378	325	415	364	452	403
0.7	283	240	303	260	341	300	380	341	418	381
0.8	253	218	273	239	313	281	353	322	392	363
0.9	229	201	249	222	290	264	331	306	372	349
1	209	186	230	208	272	251	314	293	356	336
2	119	112	142	136	187	182	233	228	279	274
3	87.7	84.9	111	109	158	156	206	203	253	251
4	72.1	70.5	96.0	94.5	144	142	192	190	240	238
5	62.7	61.7	86.8	85.8	135	134	183	183	232	231
6	56.4	55.7	80.7	80.0	129	129	178	177	227	226
7	51.9	51.4	76.3	75.8	125	125	174	173	223	222
8	48.6	48.2	73.0	72.6	122	122	171	171	220	220
9	45.9	45.6	70.5	70.2	120	119	169	168	218	217
10	43.9	43.6	68.4	68.2	118	117	167	167	216	216
20	34.4	34.4	59.2	59.2	109	109	158	158	208	208
30	31.3	31.3	56.1	56.1	106	106	156	156	205	205
40	29.7	29.7	54.6	54.6	104	104	154	154	204	204
50	28.8	28.8	53.7	53.7	104	104	153	153	203	203
60	28.1	28.1	53.1	53.1	103	103	153	153	203	203
70	27.7	27.7	52.6	52.6	103	103	152	152	202	202
80	27.4	27.4	52.3	52.3	102	102	152	152	202	202
90	27.1	27.1	52.0	52.0	102	102	152	152	202	202
100	26.9	26.9	51.8	51.8	102	102	152	152	202	202
Source file name	*Heat Conduction - Dry TPTPLL*		*Heat Conduction - Dry TPTPLL 50C*		*Heat Conduction - Dry TPTPLL 100C*		*Heat Conduction - Dry TPTPLL 150C*		*Heat Conduction - Dry TPTPLL 200C*	

Source: Located in tab: "Lookup Tables" in named spreadsheets in Appendix G.

Output DTN: LA0702PADE01EG.001.

NOTE: $T_{r=0}$ is the centerline temperature and $T_{r=3}$ is the temperature at the edge of the drift.

6.4.7.2.1 Assumptions and Simplifications

It is assumed that the 950°C magma has 30% of voids. Consequently, in the 1,223 K (950°C) case, magma density was reduced by 30% compared to the effusive magma properties because a basaltic magma at such temperature would most likely have been emplaced in a pyroclastic fashion that would result in a large void fraction. The thermal conductivity is reduced by the same proportion.

It is assumed that there are no heat sinks or sources other than the latent heat of magma crystallization and heat generated by radioactive decay in the waste packages.

Although the waste package has a relatively complex structure, including the outer barrier (Alloy 22), inner vessel (stainless steel) and the internals, it is represented in the calculations as a homogeneous medium with thermal properties equal to those of the waste package internal cylinder.

The diameter of the waste package used in this analysis is 1.72 m (see Assumption 5.4, Section 5); the exact value used has a minor effect on the result, with a smaller diameter leading to higher peak temperatures and a larger diameter leading to lower peak temperatures. The bottom of waste package is located approximately 0.19 m above the invert, which has a maximum depth of 0.84 m. The emplacement pallet and the drip shield, which have relatively small mass, are not included in the calculations. (Per unit length of the emplacement drift, the total mass of the pallet and the drip shield is approximately 15% of the waste package mass.) The entire space inside the drift not occupied by the waste package and the invert is filled with magma. Because of two-dimensional approximation, the gap of 0.1 m between the ends of the waste packages is not accounted for in the calculations. This approximation has insignificant effect on the results of the calculation, because the gap length of 0.1 m is small compared to the 5.0-m length of the waste package.

6.4.7.2.2 Mathematical Description

If the magma is emplaced in the drift instantaneously and it experiences no further loss or gain of mass, the cooling and heat transfer is governed by the conservation of energy:

$$\frac{\partial T}{\partial t} = \nabla \cdot (\kappa \nabla T) - \mathbf{u} \cdot \nabla T + q \qquad \text{(Eq. 6-107)}$$

where:

- T = temperature
- t = time
- κ = thermal diffusivity
- $\mathbf{u}$ = the magma convective velocity vector
- q = represents heat sources and sinks.

This equation describes the change of temperature with time (left-hand side), with the right-hand side summing the effects of thermal conductivity (first term) and thermal convection (second term) with heat sources and sinks (third term).

Numerical solutions to Equation 6-107 were obtained with FLAC3D on a computational grid representing an emplacement drift filled with magma and with a waste package below the drift axis. Details of the grid and other inputs are in Section 6.4.5.

6.4.7.2.3 Uncertainties and Limitations

When magma temperature drops below the solidification temperature, the specific heat should be reduced to its original (unmodified) value. This was done for the hotter intrusion temperatures analyzed but not for the cooler ones. The effect of using increased specific heat independently of the temperature is not significant but does result in increased temperatures, particularly in the CWP scenario.

6.4.7.2.4 Inputs

The emplacement drift has a 5.5-m-diameter circular cross section. The analyzed geometry of the problem is illustrated in Figure 6-88.

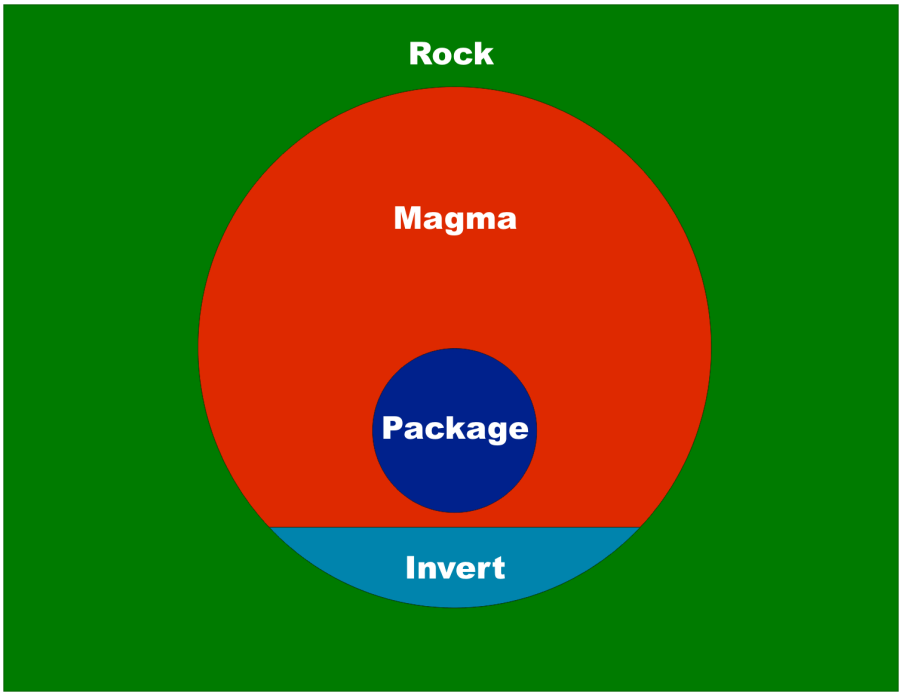

Source: For Illustrative purposes only

Figure 6-88. Geometry of the Problem Around the Drift

Two initial temperatures are considered for the magma: 1,423 K (1,150ºC) is approximately the upper limit for liquidus temperatures tabulated in SNL (2007 [DIRS 174260], Table 6-5), and 1,223 K (950ºC) is approximately the effective solidification temperature from Detournay et al. (2003 [DIRS 169660]). The thermal properties used in the analysis are listed in Table 6-14. (Thermal diffusivity is defined as conductivity divided by the product of heat capacity and density.) The specific heat of magma listed in the table and used in the calculations is increased from a value of 1,100 (Detournay et al 2003 [DIRS 169660]) to account for the latent heat of

solidification (2,635 J $kg^{-1}K^{-1}$ for higher-temperature magma, 1,945 J $kg^{-1}K^{-1}$ for the lower). When magma temperature drops below the solidification temperature (1,229 K for the higher-temperature magma, 1,174 K for the lower-temperature magma (DTN: MO0411EG831811.002)), the specific heat should be reduced to its original (unmodified) value. This was done for the higher temperature magma analyses but not for the lower temperature ones (see Section 6.4.7.2.3).

Table 6-14. Thermal Properties of Rock Mass, Invert, Waste Package, and Magma

Property	Value	Comments
Country Rock		
Conductivity [W m^{-1} K^{-1}]	1.18	Value for Topopah Spring upper lithophysal (Tptpul) strata, lowest among four repository host horizon (RHH) units
Heat capacity [J kg^{-1} K^{-1}]	985	The same value listed for four RHH units
Density [kg m^{-3}]	2,043	Average density for four RHH units.
Diffusivity[1] [m^2 s^{-1}]	5.86×10^{-7}	
Fill		
Conductivity [W m^{-1} K^{-1}]	0.16	Average of three measurements
Heat capacity [J kg^{-1} K^{-1}]	760	
Density [kg m^{-3}]	1,225	
Diffusivity[a] [m^2 s^{-1}]	1.72×10^{-7}	
Magma, Effusive[b]		
Conductivity [W m^{-1} K^{-1}]	0.60	Mid-point of range
Heat capacity [J kg^{-1} K^{-1}]	1,100, 1,945, or 2,635	Assumption (see text)
Density [kg m^{-3}]	2,556	Values for 2 wt % water content, no porosity
Diffusivity[1] [m^2 s^{-1}]	1.21×10^{-7}	
Waste Package		
Conductivity [W m^{-1} K^{-1}]	1.50	Thermal conductivity at 400 K. Because of representation of the waste package as a homogeneous medium temperature dependence was not considered. Source: SNL 2007 [DIRS 179354], Table 4-4, Parameter 05-03.
Heat capacity [J kg^{-1} K^{-1}]	432	Assumed value based on diffusivity and conductivity. See Assumption 5.4, Section 5, and Appendix I.
Density [kg m^{-3}]	3,470	Calculated from information for the 21-PWR waste package: mass (m=41,700 kg), length (L=5.024 m), diameter (D=1.756 m), and gap between waste packages (d=0.1 m). See Assumption 5.4, Section 5, and Appendix I. $\rho = \frac{4m}{\pi D^2 (L+d)}$
Diffusivity[a] [m^2 s^{-1}]	1.00×10^{-6}	Thermal diffusivity at 400 K

[a] Diffusivity is calculated by dividing conductivity with heat capacity and density.

[b] Thermal conductivity and density of 950°C magma are 70% of those for 1,150°C magma. The diffusivity is same for both.

Source: Sources for data not explicitly given in Table 6-14 are provided in Table 6-28.

For the HWP scenario, the initial rock-mass temperature is determined using the information presented in Figure 6-3 of *Repository Twelve Waste Package Segment Thermal Calculation* (BSC 2003 [DIRS 164726]), which is included here as Figure 6-89. Magma intrusion is assumed to occur when the peak temperature of the waste package is reached (i.e., 485.5 K approximately 30 years after waste emplacement, as indicated in Figure 6-89). The corresponding temperatures at the drift wall and at three points inside the rock mass (i.e., at 1, 5, and 20.25 m from the drift center (this latter value is considered to be "between drifts")) also are obtained from the curves in Figure 6-3 of *Repository Twelve Waste Package Segment Thermal Calculation* (BSC 2003 [DIRS 164726]). The values are listed in Table 6-15.

The temperature in the rock mass is initialized axisymmetrically using linear interpolation (radially with reference to the center of the drift) between those values. The initial temperatures in the waste package and invert are assumed to be uniform and equal to 485.5 K and 473 K (drift wall), respectively. The waste package acts as a heat source in the calculations for the HWP scenario. The analysis assumed the average linear heat load of the waste packages without correction for ventilation effect is plotted versus time in Figure 6-90. The initial power output of the waste packages in the simulations is equal to the heat load (approximately 800 W/m from Figure 6-90) at the time when the temperature of the waste package reaches the maximum. Subsequently, the linear power output decays as indicated in Figure 6-90. The linear heat load is divided by the area of the waste package in cross section to provide a volumetric heat load for input in the FLAC3D simulations.

For the CWP scenario, the initial temperature in the waste package, rock mass and invert is 293 K; the waste package is not a heat source.

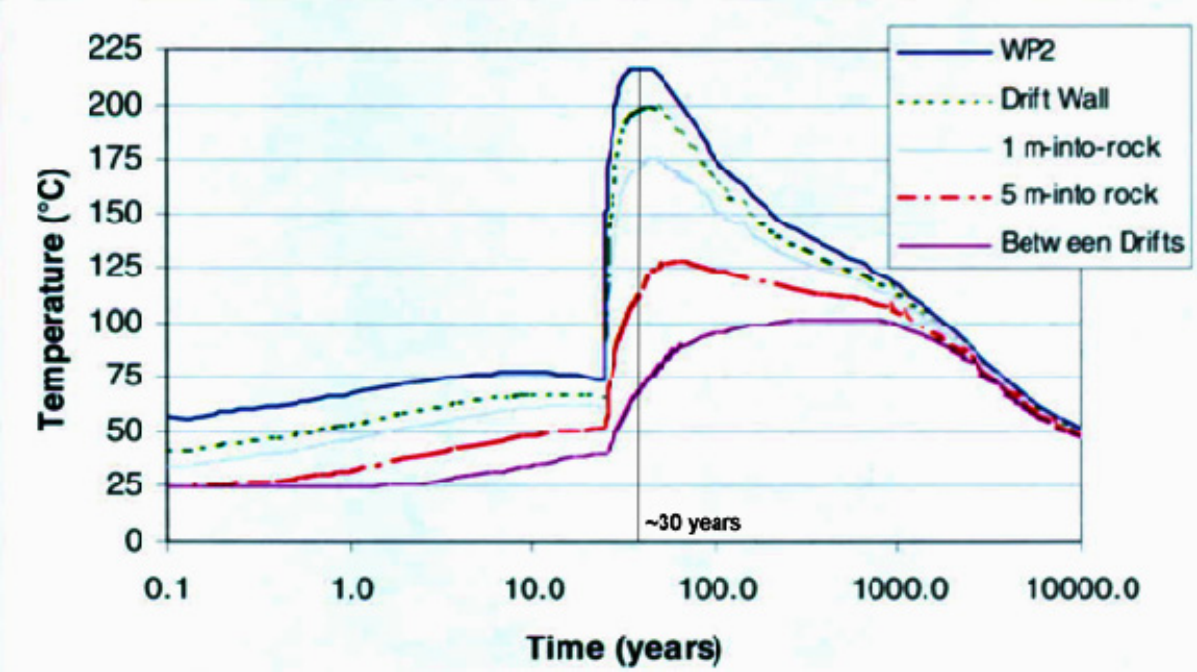

Source: For illustrative purposes only; see Assumption 5.4, Section 5.

NOTE: To convert to temperature in kelvins (K), add 273.

Figure 6-89. Temperature Histories in Repository and Surrounding Rock Including 25 Years of Ventilation Time

Table 6-15. Initial Temperature Data — HWP Scenario

	Radial Distance from Drift Center (m)	Temperature (K)
Waste package		485.5
Drift wall	2.75	473
1 m into rock	3.75	448
5 m into rock	7.75	385.5
Quarter Pillar Distance	20.25	335.5

Source: Output DTN: MO0705FREEZING.000.

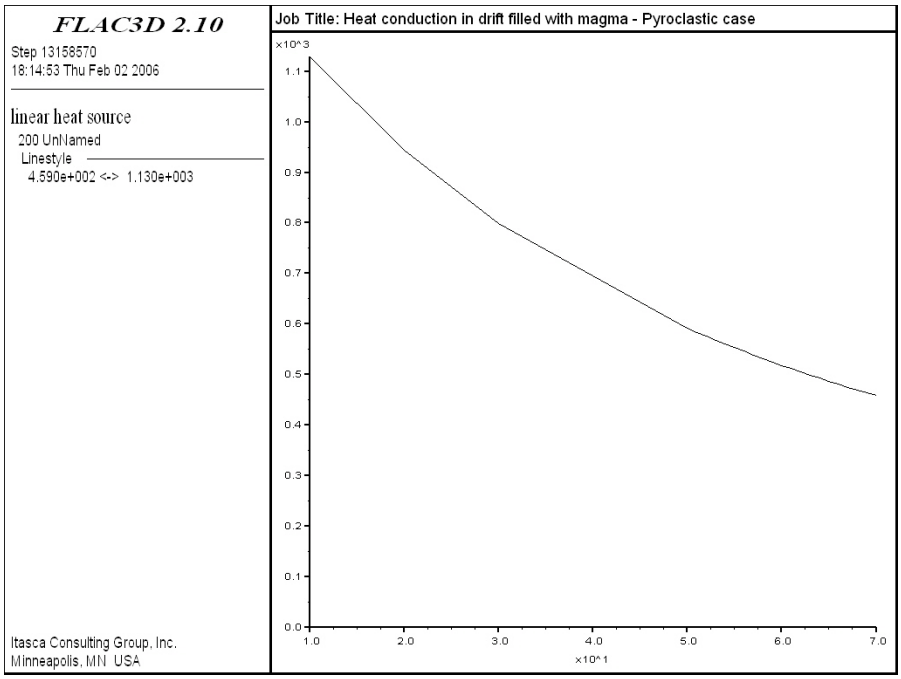

Source: Source: For illustrative purposes only; see Assumption 5.4, Section 5.

Figure 6-90. Linear Heat Load (W/m) versus Time (year)

The FLAC3D grid used for the simulations includes an outer block of zones that represents the rock mass around the drift. For cases with magma temperatures of 1,423 K (1,150°C), the outer block extended to a 150-m radius. For 1,223 K (950°C) magma, the outer block extended to a 100-m radius for the HWP case and to 70 m for the CWP case. A close-up view of the grid around the drift is shown in Figure 6-91. The system of reference axes, also shown in the figure, has the z-axis pointing up along the plane of symmetry, the x-axis pointing to the right, and the origin located at the top of the waste package. The locations of history points within the drift are shown in Figure 6-92; locations of history points within the rock mass are shown in Figure 6-93. History points are tabulated in Tables 6-16 and 6-17 for the drift and the rock mass, respectively.

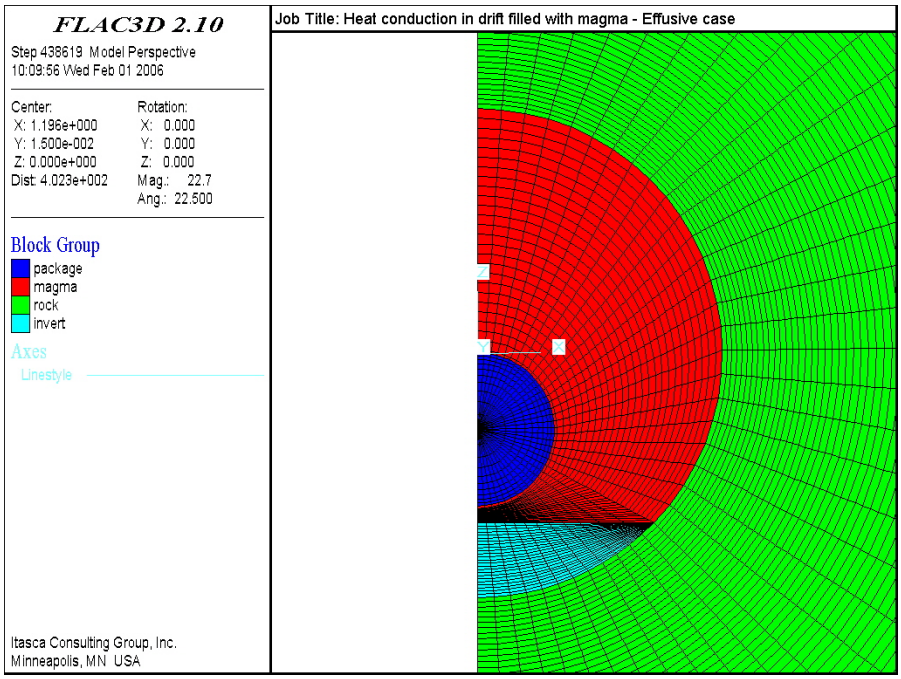

Source: For Illustrative purposes only.

Figure 6-91. FLAC3D Grid — Close-up View around the Drift

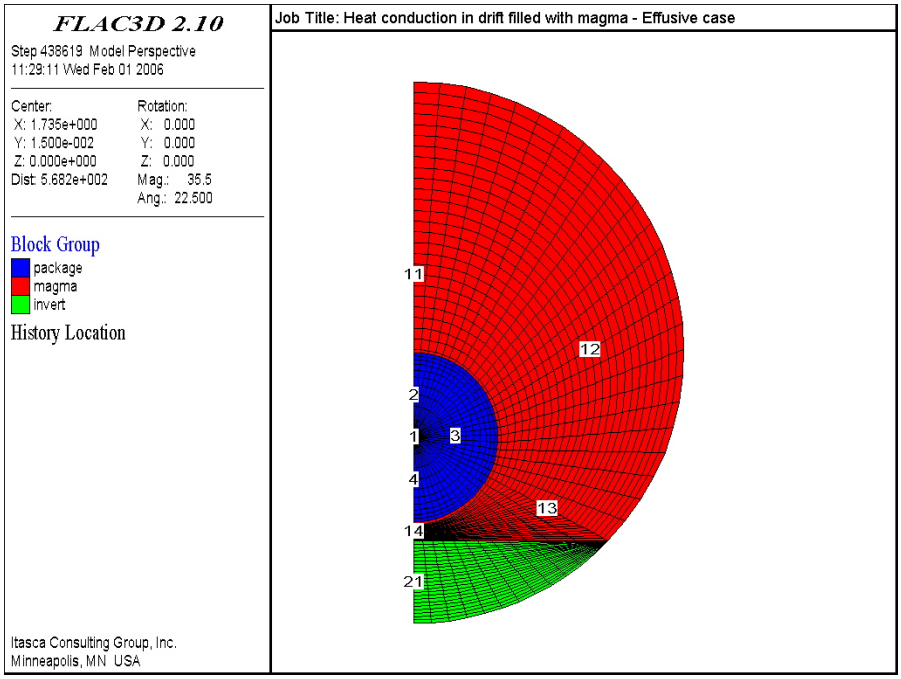

Source: For Illustrative purposes only.

Figure 6-92. FLAC3D Grid and Location of History Points within the Drift

Table 6-16. Location of History Points within the Drift

History Label	x (m)	z (m)
1	0	−0.86
2	0	−0.43
3	0.43	−0.85
4	0	−1.29
11	0	0.79
12	1.80	0.04
13	1.36	−1.58
14	0	−1.81
21	0	−2.33

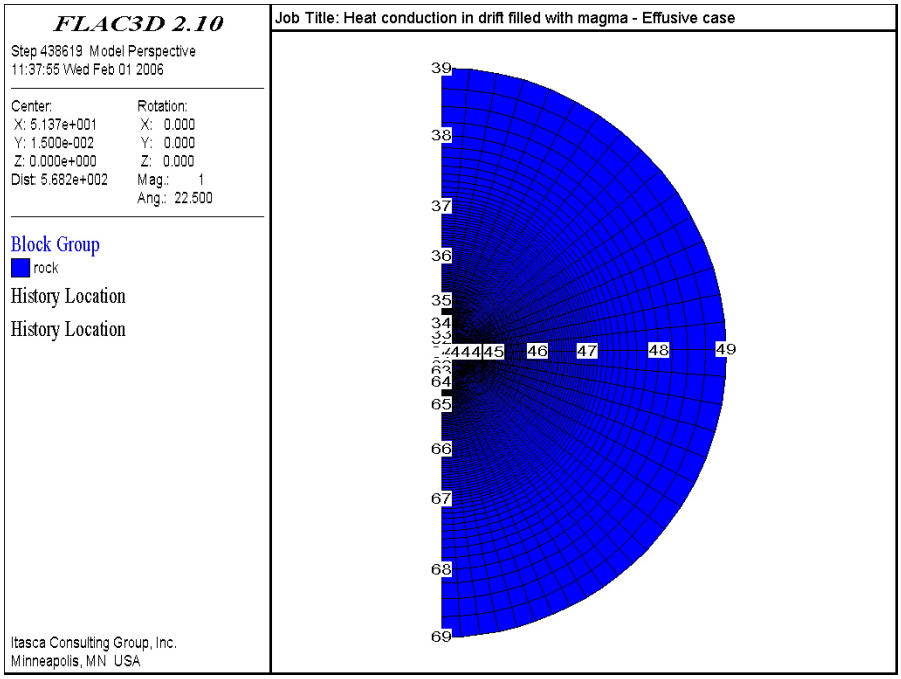

Source: For Illustrative purposes only.

Figure 6-93. FLAC3D Grid and Location of History Points within the Rock Mass

Table 6-17. Location of History Points within the Rock Mass

History Label	x (m)	z (m)
31	0	3.76
32	0	4.75
33	0	6.77
34	0	10.65
35	0	18.87
36	0	34.82
37	0	52.75
38[a]	0	78.34
39[a]	0	102.75
41	3.76	0.04
42	4.75	0.06
43	6.77	0.08
44	10.64	0.13
45	18.87	0.22
46	34.82	0.41
47	53.75	0.62
48[a]	78.33	0.92
49[a]	102.74	1.21
61	0	−3.76
62	0	−4.75
63	0	−6.77
64	0	−10.65
65	0	−18.87
66	0	−34.82
67	0	−52.75
68[a]	0	−78.34
69[a]	0	−102.75

[a] These history points apply only to the HWP scenario.

The FLAC3D grid used for the CWP scenario simulations is similar to the one used in the 1,150°C HWP scenario except that the radius of the outer block used to model the rock mass around the drift is smaller. The number, label, and location of most history points (see Figures 6-94 and 6-95 and Tables 6-15 and 6-16) are the same as those used in the HWP scenario analyses. The only exceptions are history points 38, 39, 48, 49, 68, 69, whose locations are updated as tabulated in Table 6-18.

Table 6-18. Location of History Points — CWP Scenario

History Label	x (m)	z (m)
38	0	62.68
39	0	72.75
48	62.67	0.74
49	72.75	0.85
68	0	−62.68
69	0	−72.75

6.4.7.2.5 Model Results

The results of two-dimensional heat conduction analyses are presented in the following sections. The results for an initial magma temperature at 1,423 K (1,150°C), are reported in Section 6.4.7.2.5.1; the results for an initial magma temperature at 1,223 K (950°C) are reported in Section 6.4.7.2.5.2. Symmetry across the vertical plane through the axis of the drift is used in the simulations to reduce the problem size. The heat conduction analysis is carried out to a time of 100 years after magma intrusion for cases with magma initially at 1,423 K (1,150°C) and to 30 years for the cooler magma.

6.4.7.2.5.1 Results for 1,423 K (1,150°C) Magma Case

HWP Scenario—The analyses provide an estimate for the magma, package, and rock mass cooling time for the effusive magma case (i.e., magma intrusion at the time when the waste package reaches the peak temperature and acts as a heat source). The rock mass temperature is initialized at the values estimated to exist 30 years after emplacement of the waste, according to the description in Section 6.4.7.2.4. Temperature is initialized at 485.5 K (212.2°C) in the waste package and at the intrusion value in the magma. Also, a time-dependent heat source is applied in the waste package as discussed in Section 6.4.7.2.4. Results for the HWP scenario are presented first, followed by results for the CWP.

The evolution of temperature versus time at monitoring points located within the waste package, magma, and invert is shown for the first year (365 days) in Figures 6-94, 6-95, and 6-96, respectively (see Figure 6-92 and Table 6-15 for locations). The maximum waste-package temperature in Figure 6-94, recorded at monitoring point 2 (the upper part of the waste package, Figure 6-92), is about 1,417 K (1,144°C) for this case. In Figure 6-94, it can be observed that the magma temperature at monitoring point 14, located between the waste package and the invert, is seen first to decrease, dropping below the effective solidification temperature, $T_s = 1174$ K (901°C), in less than 3.5 days. It then increases above T_s before decreasing again, falling below T_s about half a year after intrusion. (At that stage, this point has the slowest cooling rate compared to other temperature histories in the magma.) This non-monotonic effect occurs because the point, being very close to the relatively cool waste package and invert, first cools down, transferring heat to the waste package and the invert; subsequently, the point receives heat from the rest of the magma and from the waste package, which heats up under the influence of the larger body of magma. The maximum invert temperature, recorded at monitoring point 21 (center of invert in Figure 6-92), is about 918 K (645°C) for this case.

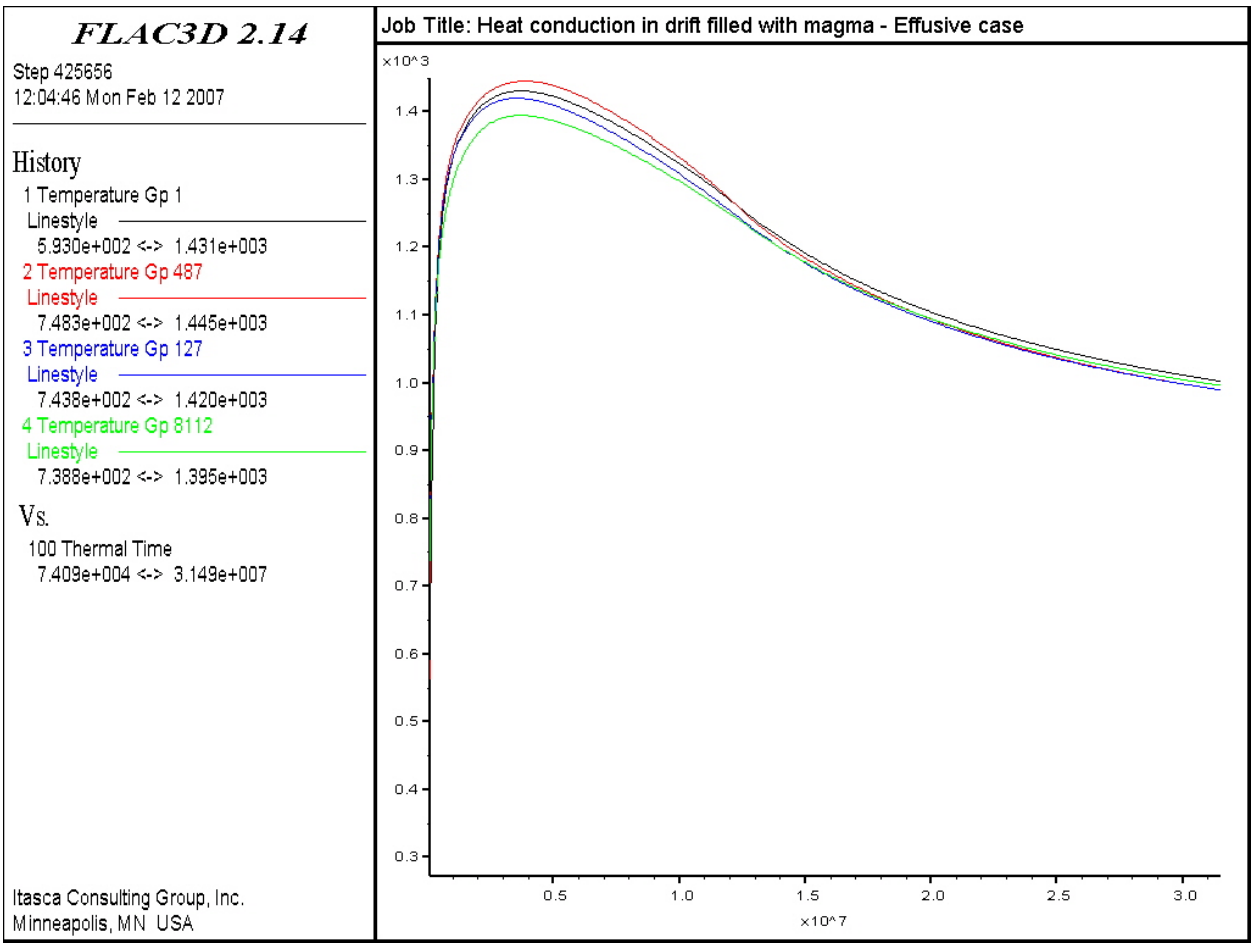

Source: Output DTN: MO0705FREEZING.000, file *\effusive\maximum temperature\figure7.jpg.*

Figure 6-94. Temperature Histories (temperature in K, time in s) in the Waste Package during the First Year: 1,423 K (1,150°C) Case—HWP Scenario

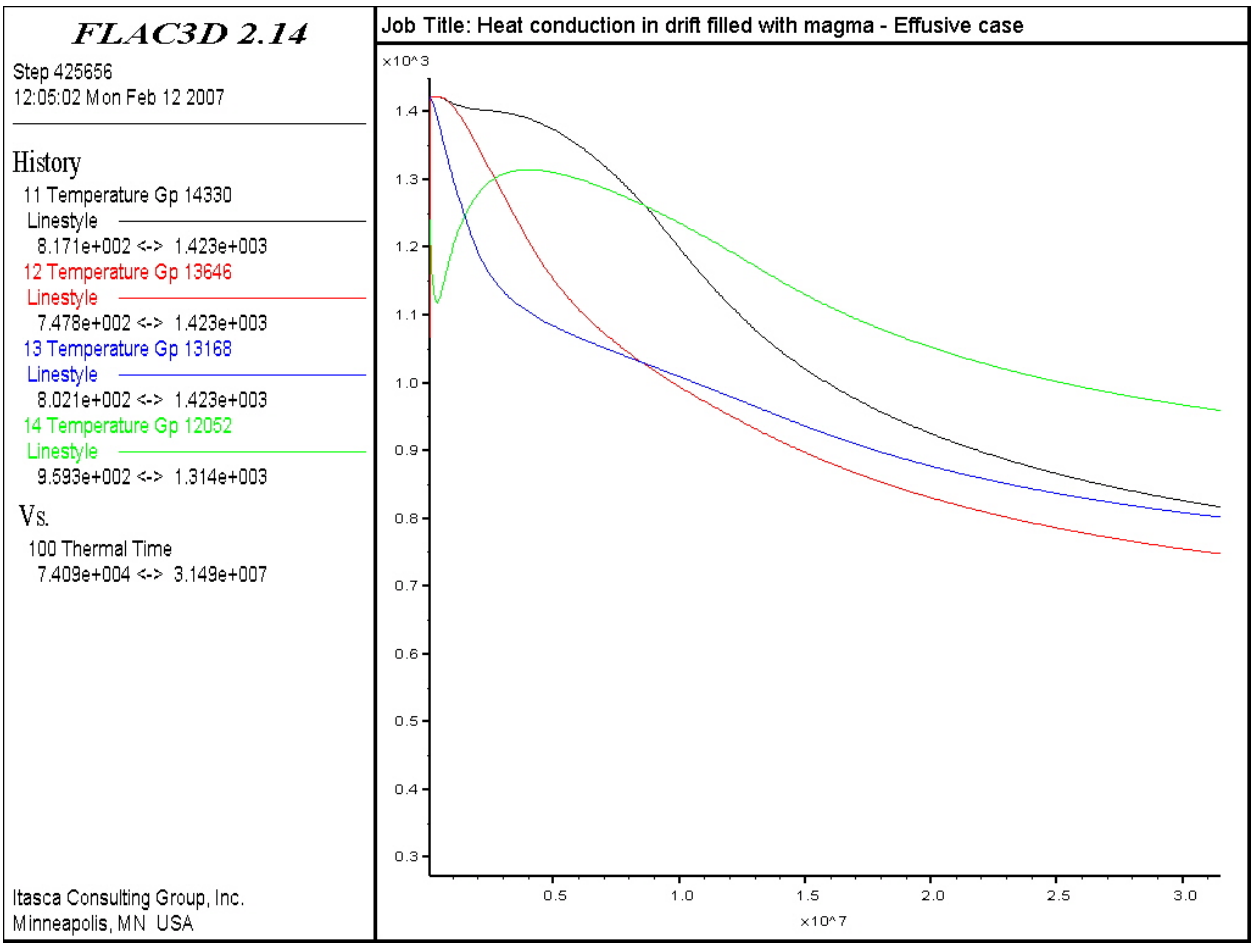

Source: Output DTN: MO0705FREEZING.000, file *\effusive\maximum temperature\figure8.jpg*.

Figure 6-95. Temperature Histories (temperature in K, time in s) in the Magma during the First Year: 1,423 K (1,150°C) Case—HWP Scenario

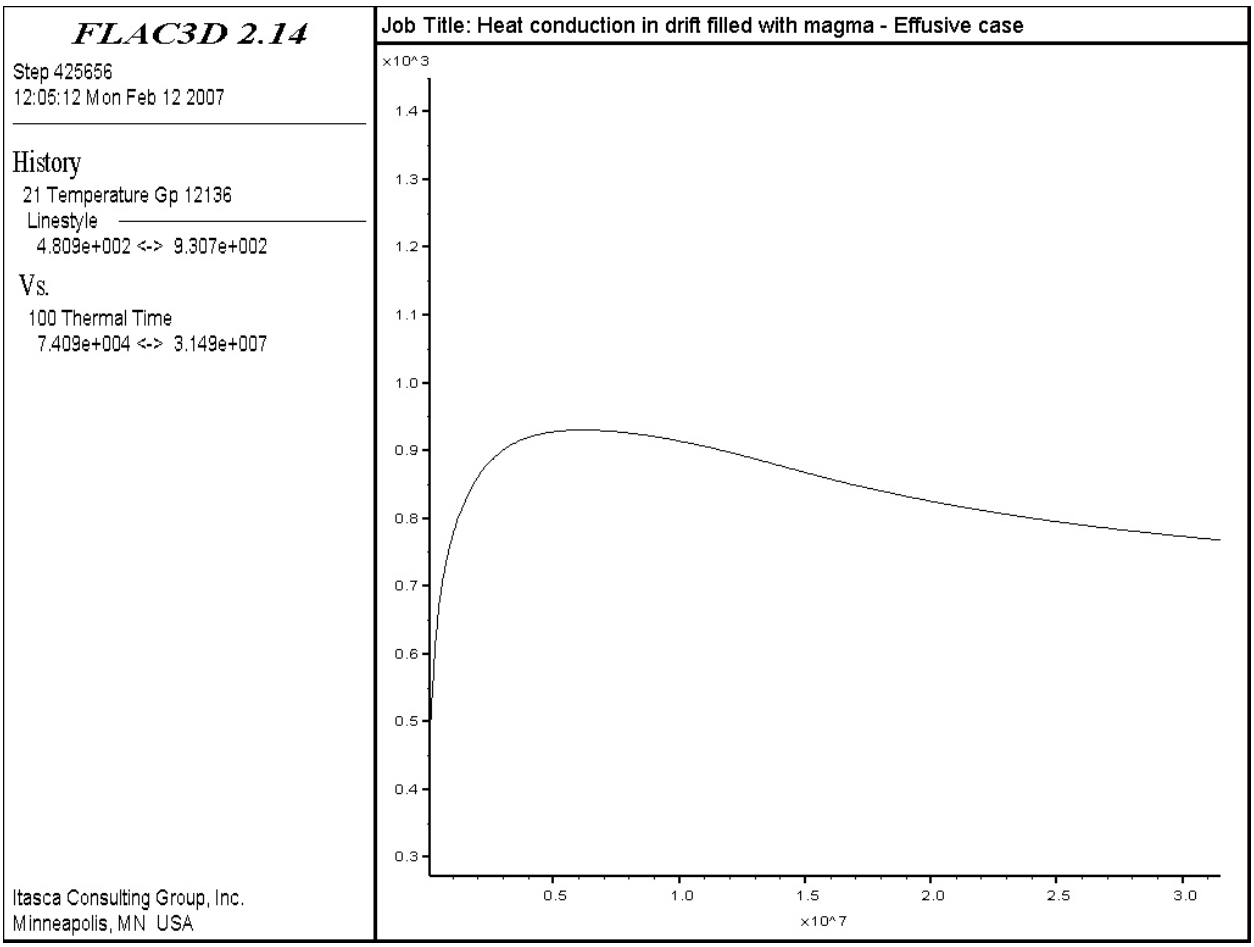

Source: Output DTN: MO0705FREEZING.000, file \effusive\maximum temperature*figure9.jpg*.

Figure 6-96. Temperature Histories (temperature in K, time in s) in the Invert during the First Year: 1,423 K (1,150°C) Case—HWP Scenario

The evolution of temperature at the monitoring points for 100 years after intrusion is shown in Figures 6-97, 6-98, and 6-99 for the waste package, for the magma, and for the invert, respectively. These figures show a sharp temperature decrease during the first three years after intrusion (by which time, the temperature reaches about 900 K (627°C) in the waste package), followed by a more gentle decrease. The temperatures at points 1, 11, and 12, recorded 1, 5, 10, 50, and 100 years after intrusion, are listed in Table 6-19. The rate of temperature decrease derived from the 10- and 50-data is about 4.5 K yr^{-1} in the waste package (point 1) and about 3 K yr^{-1} in both the magma (point 11) and invert (point 21). One hundred years after intrusion, the temperatures at monitoring points 1 (waste package), 11 (magma) and 21 (invert) are about 555 K (282°C), 488 K (215°C), and 486 K (213°C), respectively.

Table 6-19. Temperature (K) Within the Drift: Effusive Case—HWP Scenario

	Temperature				
History Label	**1 year (K)**	**5 years (K)**	**10 years (K)**	**50 years (K)**	**100 years (K)**
1 = waste package	1,003	874	843	660	555
11 = magma	817	691	673	559	488
21 = invert	768	684	667	556	486

Source: Output DTN: MO0705FREEZING.000, file *\effusive\maximum temperature\effus.sav.*

NOTE: To convert to °C, subtract 273.

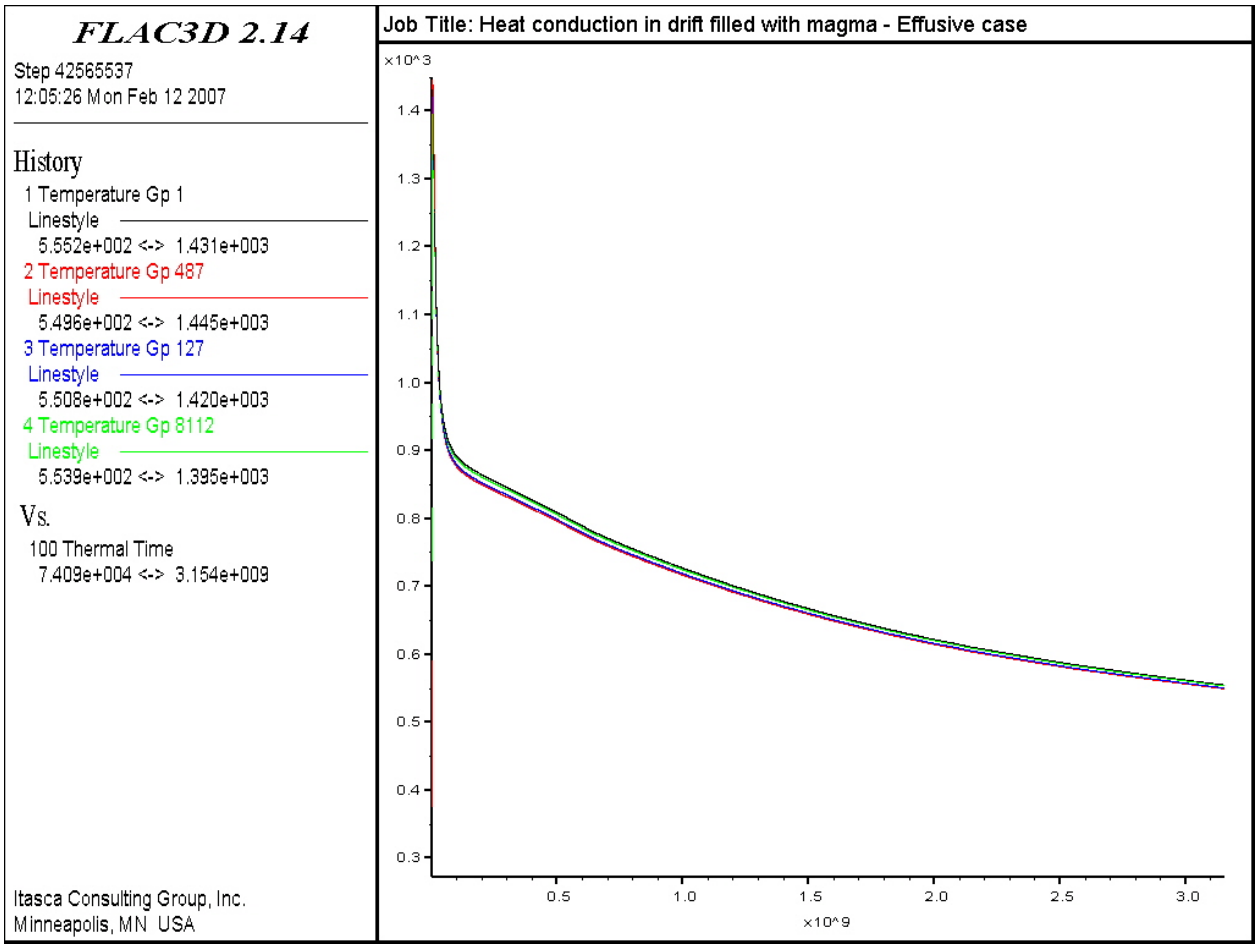

Source: Output DTN: MO0705FREEZING.000, file *\effusive\maximum temperature\figure10.jpg.*

Figure 6-97. Temperature Histories (temperature in K, time in s) in the Waste Package over 100 Years: 1,423 K (1,150°C) Case—HWP Scenario

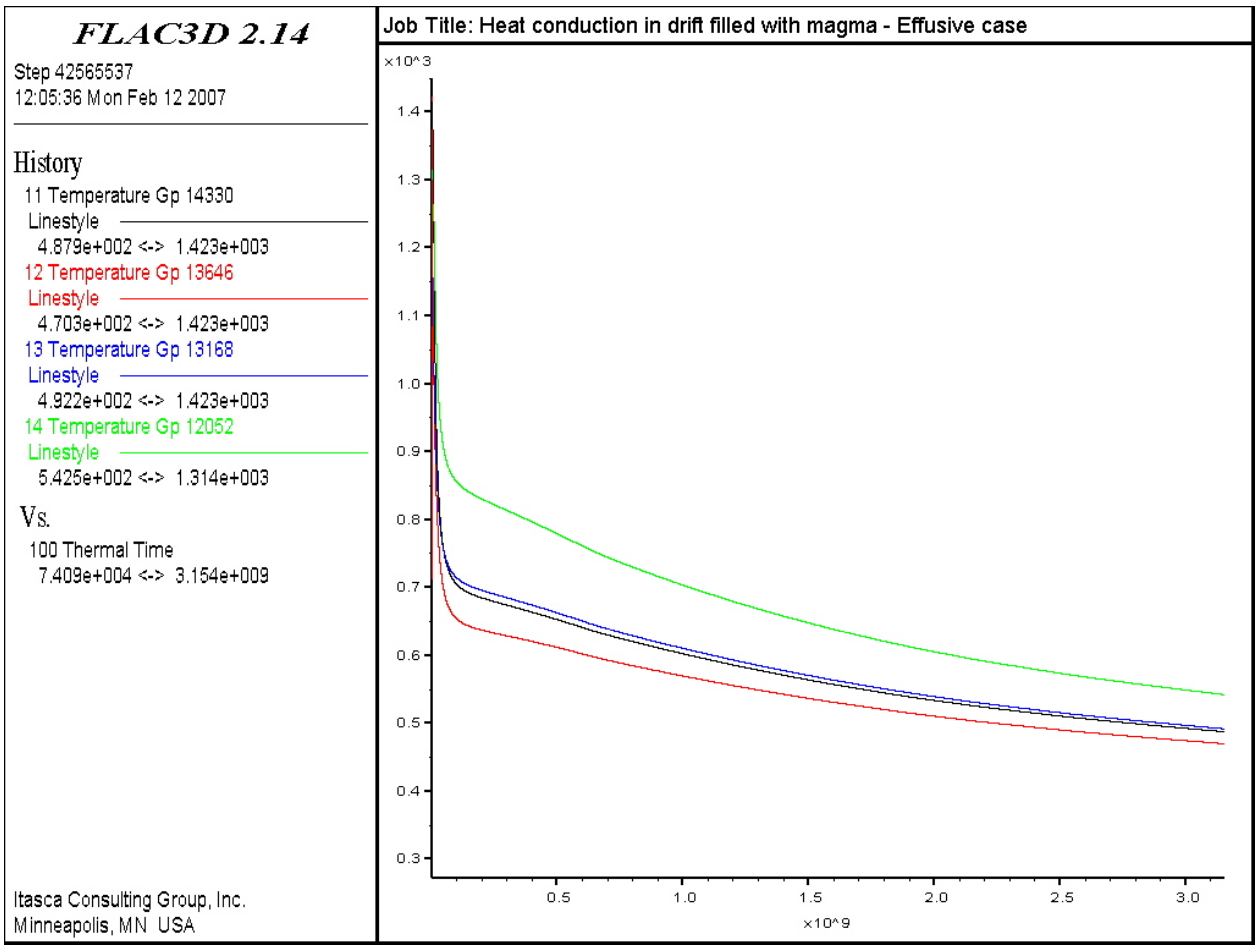

Source: Output DTN: MO0705FREEZING.000, file *\effusive\maximum temperature\figure11.jpg*.

Figure 6-98. Temperature Histories (temperature in K, time in s) in the Magma over 100 Years: 1,423 K (1,150°C) Case—HWP Scenario

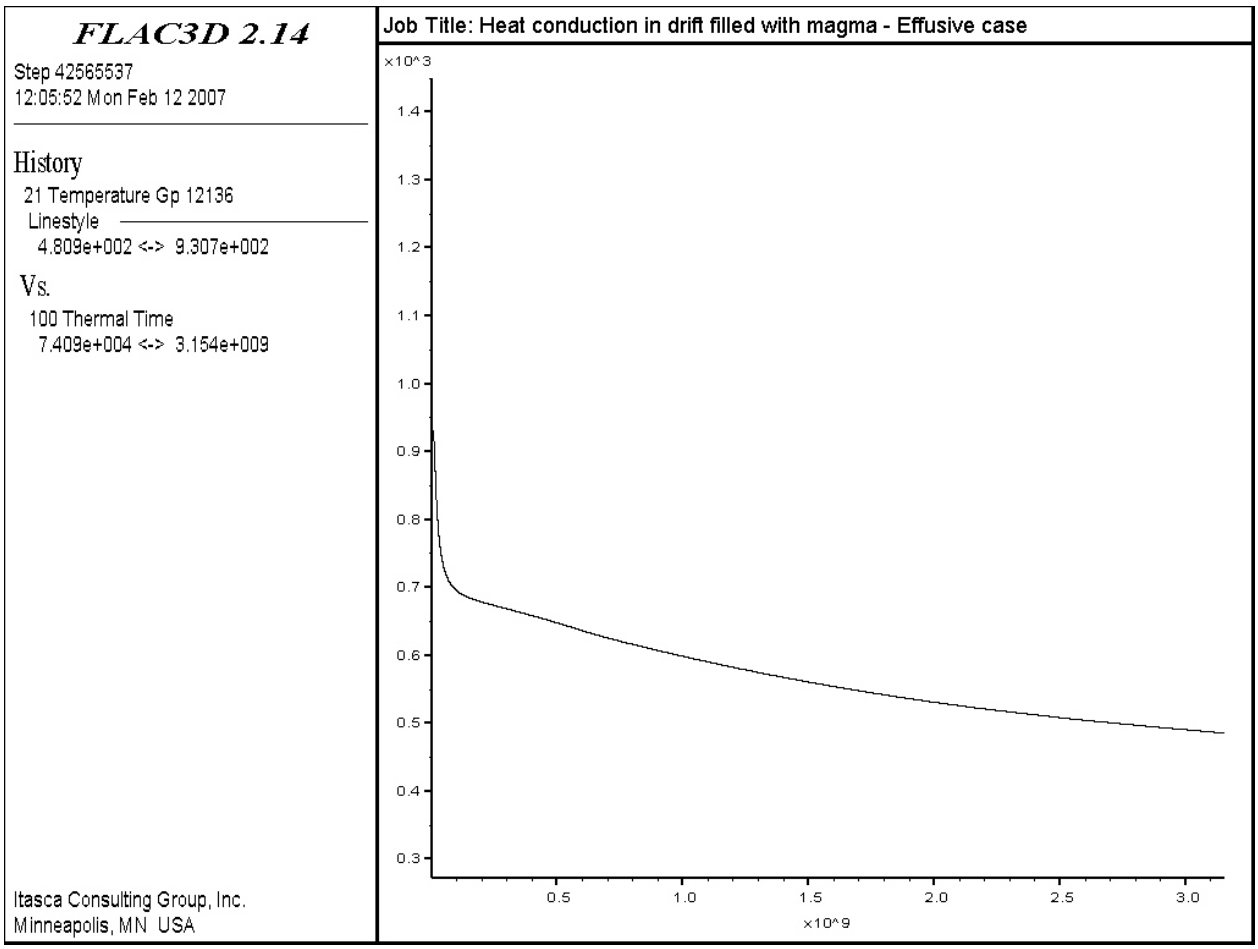

Source: Output DTN: MO0705FREEZING.000, file *\effusive\maximum temperature\figure12.jpg*.

Figure 6-99. Temperature Histories (temperature in K, time in s) in the Invert over 100 Years: 1,423 K (1,150°C) Case—HWP Scenario

The evolution of temperatures at the monitoring points in the rock mass above, sideways to, and below the drift (see Figure 6-93 and Table 6-16 for locations) is shown for the first 100 years after intrusion in Figures 6-100, 6-101, and 6-102, respectively. Table 6-20 provides the calculated rock-mass temperatures 1, 5, 10, 50, and 100 years after intrusion at selected monitoring points located at a distances of about 3.8, 11, and 35 m from the center of the drift (see Table 6-16 for locations of history points). One year after intrusion, temperatures decrease within a radius of about 10.5 m from the center of the drift (i.e., approximately history point 34) and increase at a slow rate beyond that. Contours of temperature at the end of the 100 simulation are shown in Figures 6-103 (within the drift) and 6-104 (within the rock mass).

Table 6-20. Rock Mass Temperature (K) for Selected Monitoring Points: 1,423 K (1,150°C) Case — HWP Scenario

	Temperature				
History Label	**1 year [K]**	**5 years [K]**	**10 years [K]**	**50 years [K]**	**100 years [K]**
31 = 3.8 m above	579	508	503	458	421
34 = 11 m above	407	414	416	406	386
36 = 35 m above	312	314	319	338	340
41 = 3.8 m to side	589	528	522	470	428
44 = 11 m to side	406	418	421	410	388
46 = 35 m to side	312	314	319	339	341
61 = 3.8 m below	573	533	528	474	431
64 = 11 m below	399	420	424	412	390
66 = 35 m below	312	314	319	340	341

Source: Output DTN: MO0705FREEZING.000, file *\effusive\maximum temperature\effus.sav*.

NOTE: To convert to °C, subtract 273.

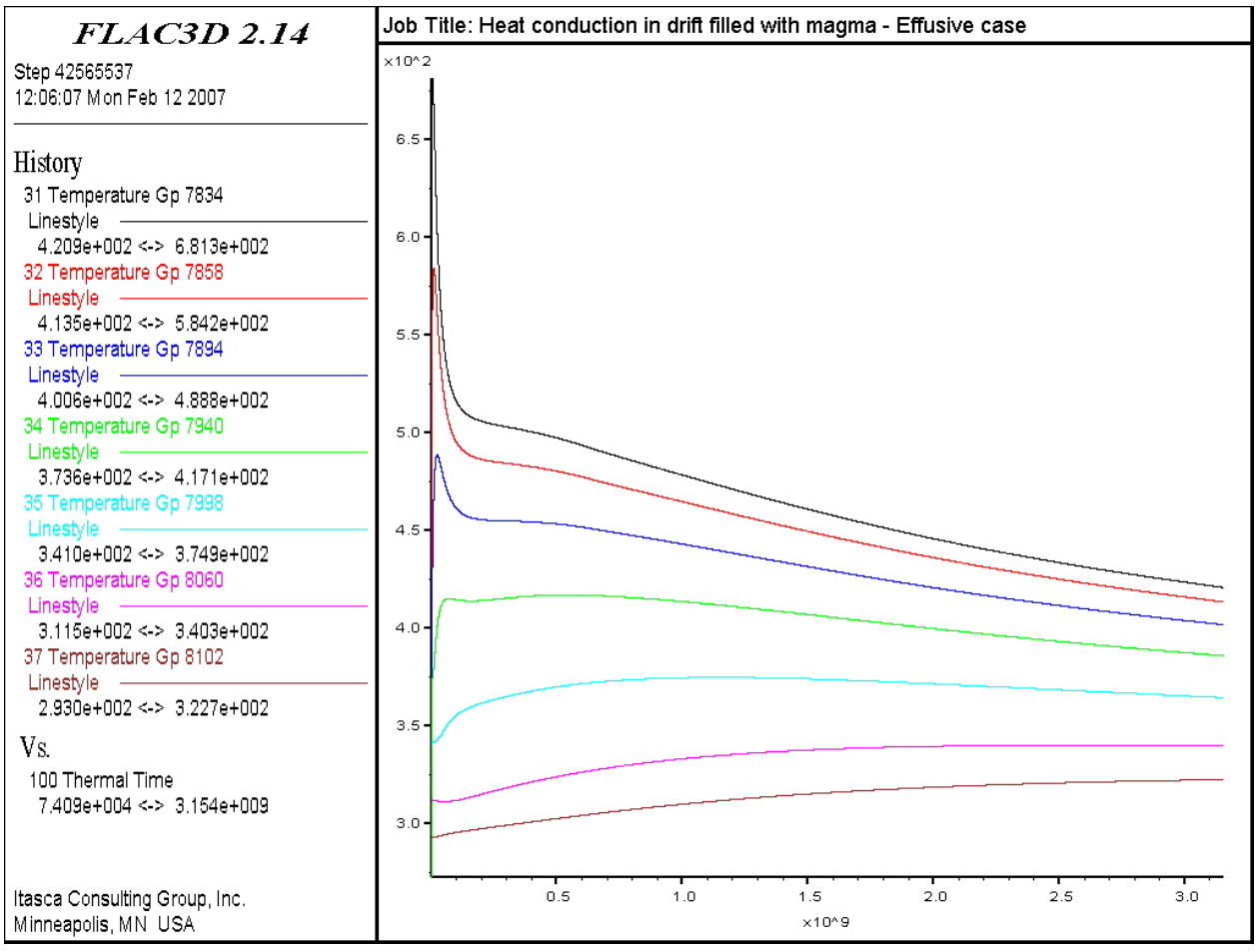

Source: Output DTN: MO0705FREEZING.000, file *\effusive\maximum temperature\figure13.jpg*.

Figure 6-100. Temperature Histories (temperature in K, time in s) in the Rock Mass above the Drift over 100 Years: 1,423 K (1,150°C) Case—HWP Scenario

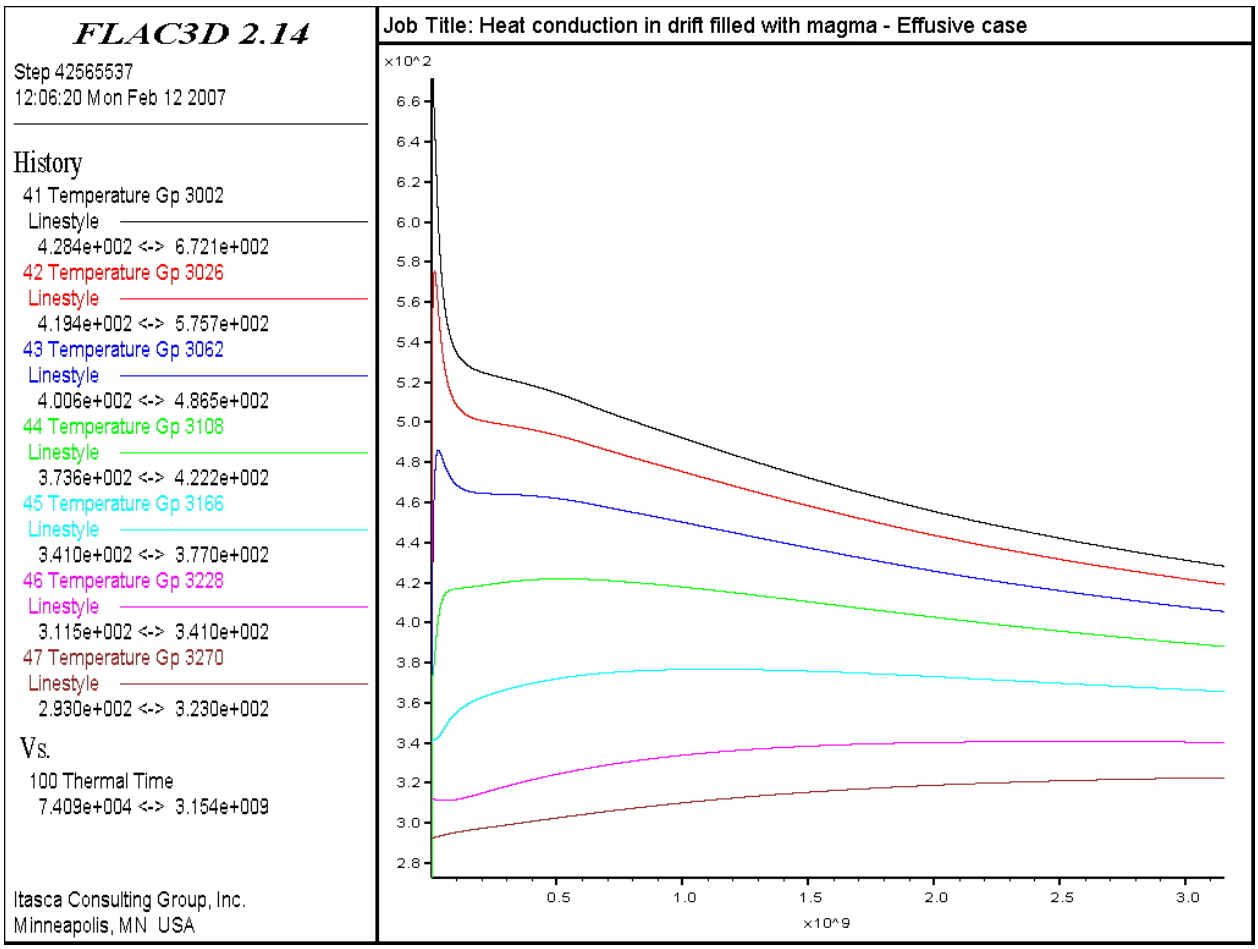

Source: Output DTN: MO0705FREEZING.000, file *\effusive\maximum temperature\figure14.jpg*.

Figure 6-101. Temperature Histories (temperature in K, time in s) Sideways in the Rock Mass over 100 Years: 1,423 K (1,150°C) Case—HWP Scenario

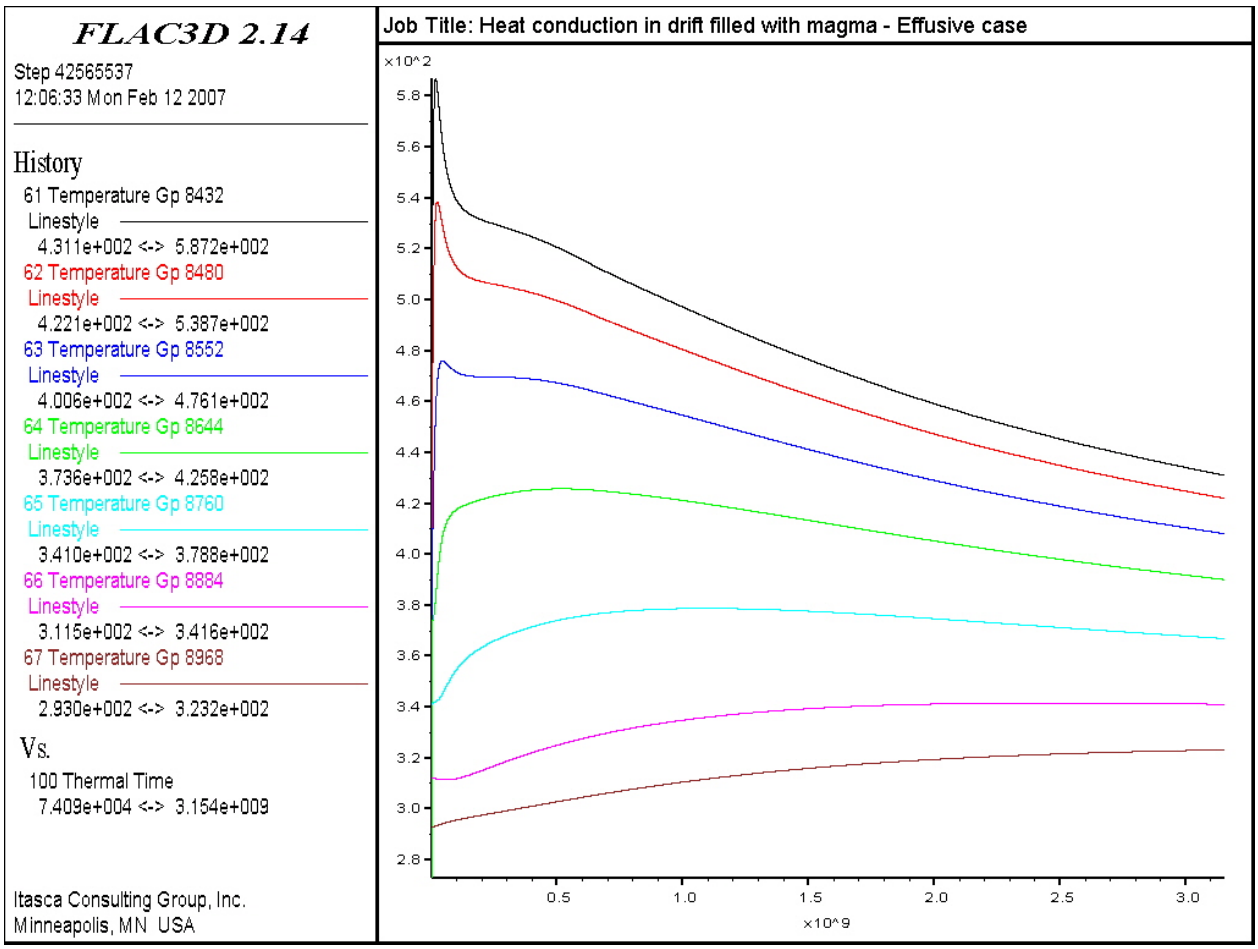

Source: Output DTN: MO0705FREEZING.000, file *\effusive\maximum temperature\figure15.jpg.*

Figure 6-102. Temperature Histories (temperature in K, time in s) in the Rock Mass below the Drift over 100 Years: 1,423 K (1,150°C) Case—HWP Scenario

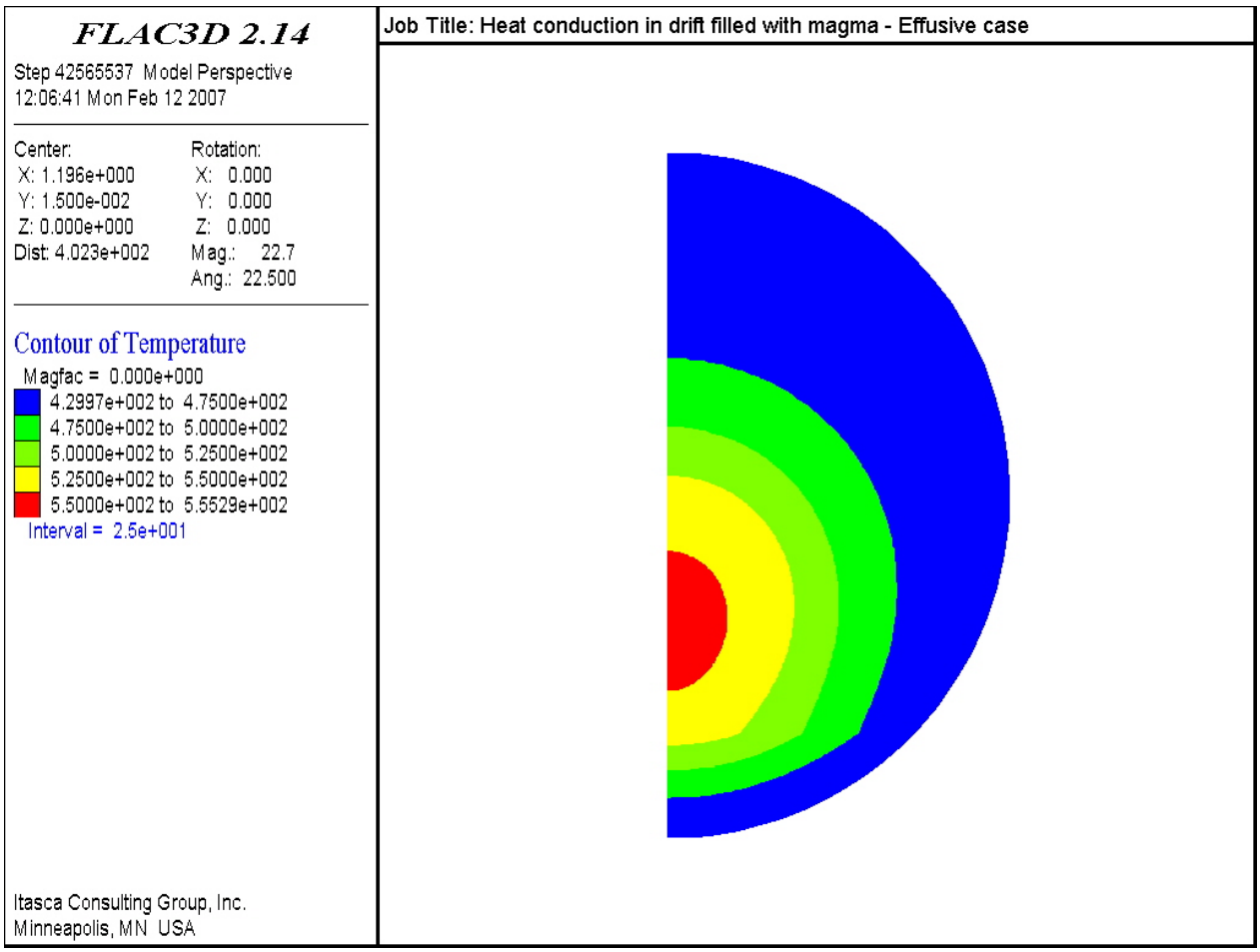

Source: Output DTN: MO0705FREEZING.000, file *effusive\maximum temperature\figure16.jpg*.

NOTE: To obtain temperature values in °C, subtract 273.

Figure 6-103. Temperature Contours (K) within the Drift after 100 Years: 1,423 K (1,150°C) Case—HWP Scenario

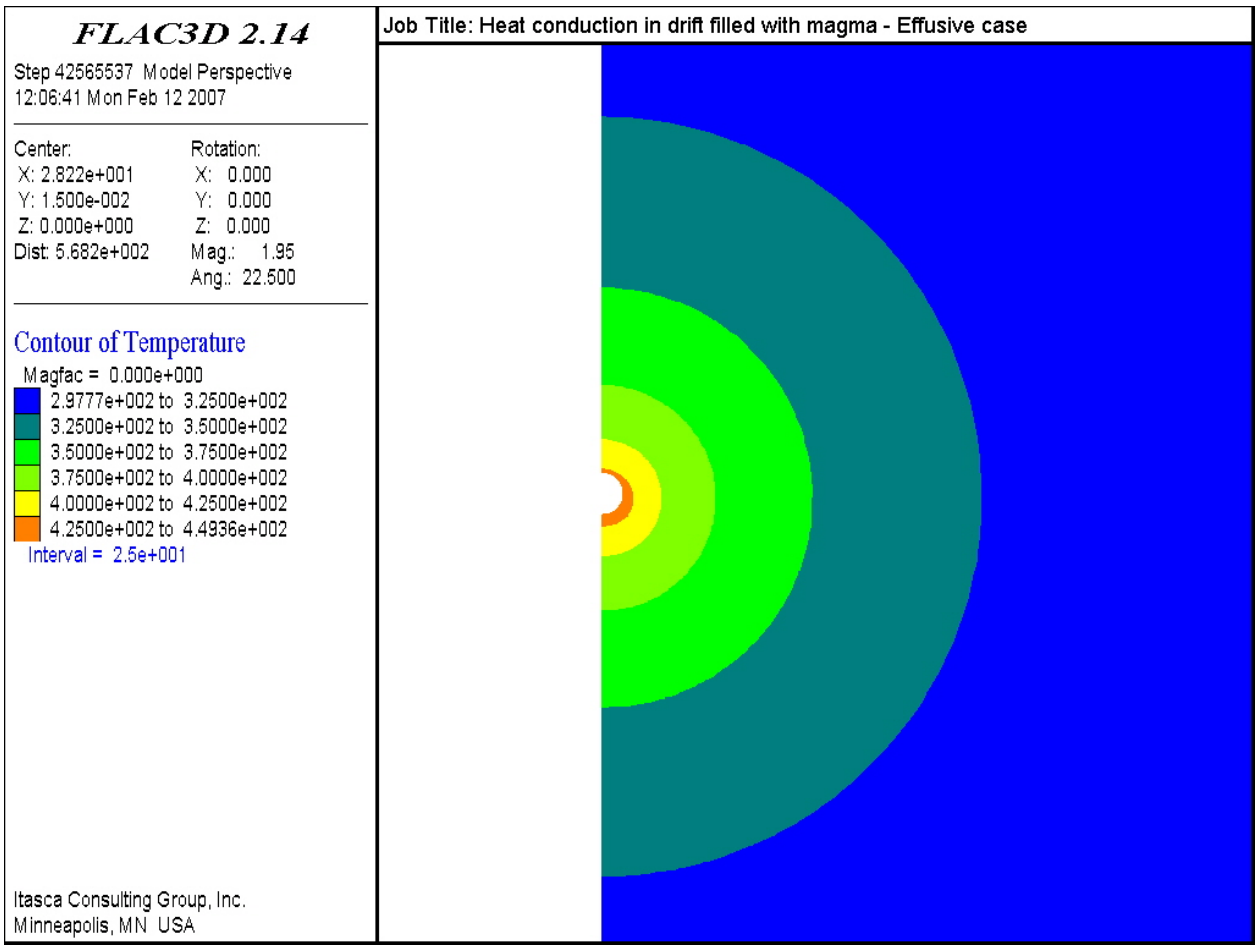

Source: Output DTN: MO0705FREEZING.000, file *\effusive\maximum temperature\figure17.jpg*.

NOTES: The white region in the center is the drift.
To obtain temperature values in °C, subtract 273.

Figure 6-104. Temperature Contours (K) within the Rock Mass after 100 Years: 1,423 K (1,150°C) Case—HWP Scenario

CWP Scenario—The results of two-dimensional heat conduction analyses, providing temperature estimates for the magma, package and rock mass cooling time for the CWP scenario (with magma intrusion at a time when the waste package temperature is approximately the same as the ambient temperature and the radiogenic heat source in the waste package is negligible) are presented in this section. The initial rock-mass and waste-package temperature is 293 K (20°C). Magma temperature in the calculations is initialized at the magma intrusion temperature of 1,423 K (1,150°C). The heat conduction analysis is carried out to a time of 100 years after magma intrusion.

The evolution of temperature versus time at monitoring points located within the waste package, magma, and invert are shown for the first year (365 days) in Figures 6-105, 6-106, and 6-107, respectively. The maximum waste-package temperature in Figure 6-107, recorded at monitoring point 2 (the upper part of the waste package in Figure 6-92), is about 1,280 K (1,007°C) for this

case. The maximum invert temperature, recorded at monitoring point 21 (center of invert in Figure 6-92), is about 764 K (491°C) for this case.

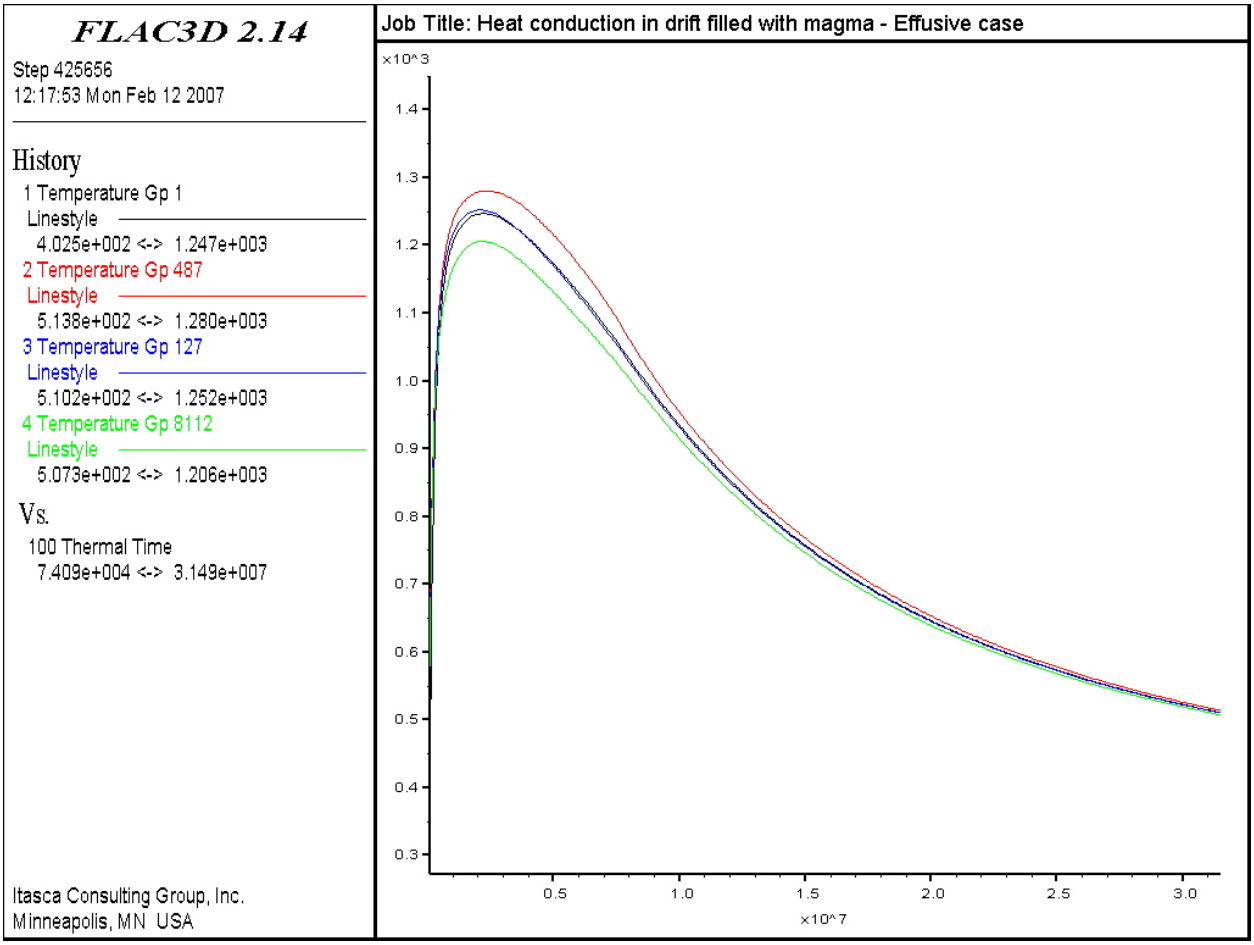

Source: Output DTN: MO0705FREEZING.000, file *\effusive\20deg\figure18.jpg*.

Figure 6-105. Temperature Histories (temperature in K, time in s) in the Waste Package During the First Year: 1,423 K (1,150°C) Case—CWP Scenario

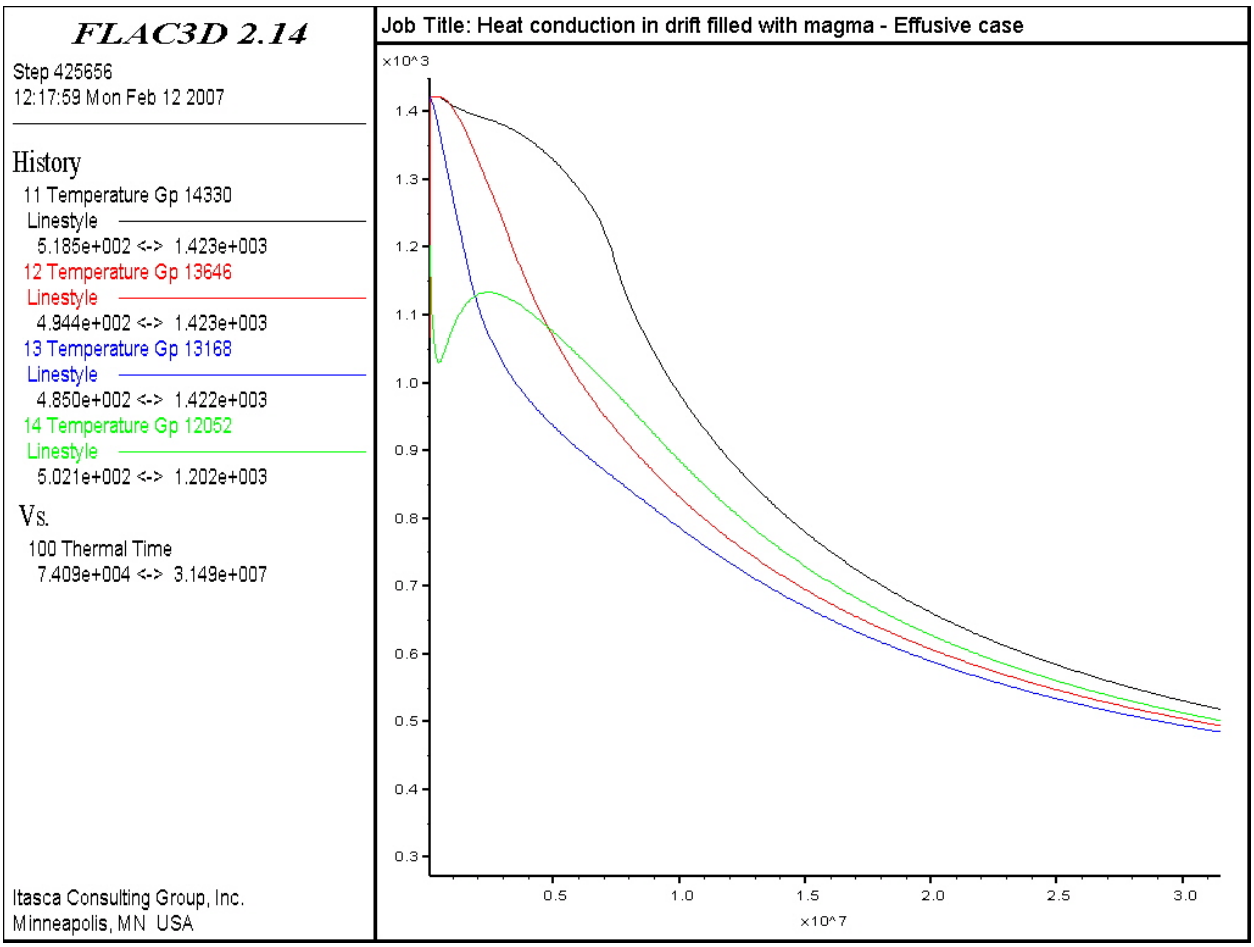

Source: Output DTN: MO0705FREEZING.000, file *\effusive\20deg\figure19.jpg*.

Figure 6-106. Temperature Histories (temperature in K, time in s) in the Magma during the First Year: 1,423 K (1,150°C) Case—CWP Scenario

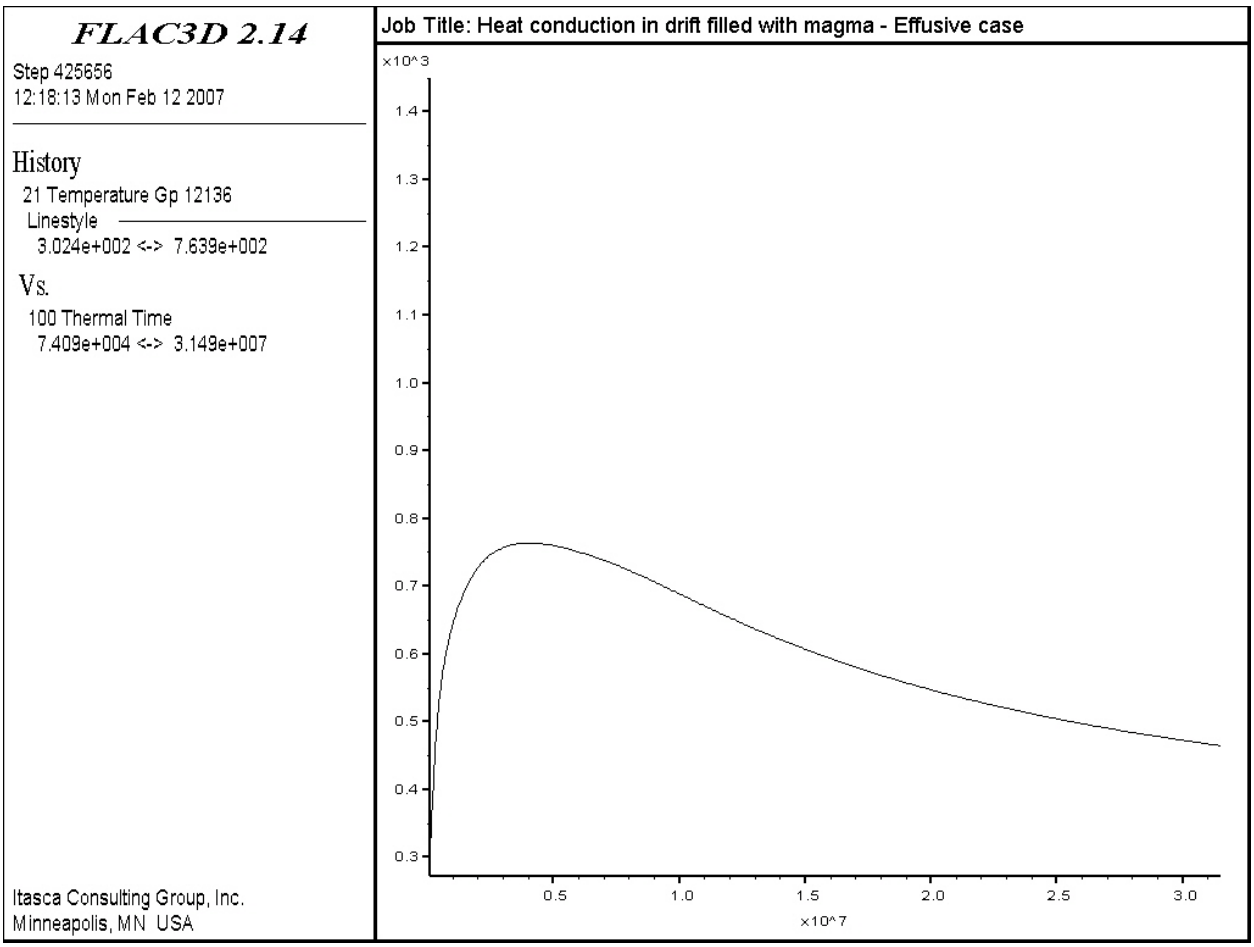

Source: Output DTN: MO0705FREEZING.000, file \effusive\20deg*figure20.jpg*.

Figure 6-107. Temperature Histories (temperature in K, time in s) in the Invert During the First Year: 1,423 K (1,150°C) Case—CWP Scenario

The evolution of temperature at the monitoring points for 100 years after intrusion is shown in Figures 6-108, 6-109, and 6-110 for the waste package, the magma, and the invert, respectively. These figures show that at least 90% of the temperature drop at the monitoring points occurs during the first five years after intrusion, by which time all the temperatures are below the boiling temperature of water. After one year, the temperatures at monitoring points 1 (waste package), 11 (magma), and 21 (invert) are about 510 K (237°C), 518 K (245°C), and 465 K (192°C), respectively. After five years, the same three temperatures are about 329 K (56°C), 330 K (57°C), and 328 K (55°C). After 10 years, the same three temperatures are about 311 K (38°C), 311 K (38°C), and 310 K (37°C). After 50 years, the same three temperatures are all about 296 K, (23°C). After 100 years, the temperatures at all monitoring points 1 (waste package), 11 (magma), and 21 (invert) have equilibrated down to a value of about 295 K (22°C).

The evolution of temperatures at the monitoring points in the rock mass above, sideways to, and below the drift (see Figure 6-93 and Table 6-16 for locations) are shown for 100 years after intrusion in Figures 6-111, 6-112, and 6-113, respectively. Contours of temperatures at the end

of the 100-year simulation are shown in Figure 6-114 (within the drift) and Figure 6-115 (within the rock mass).

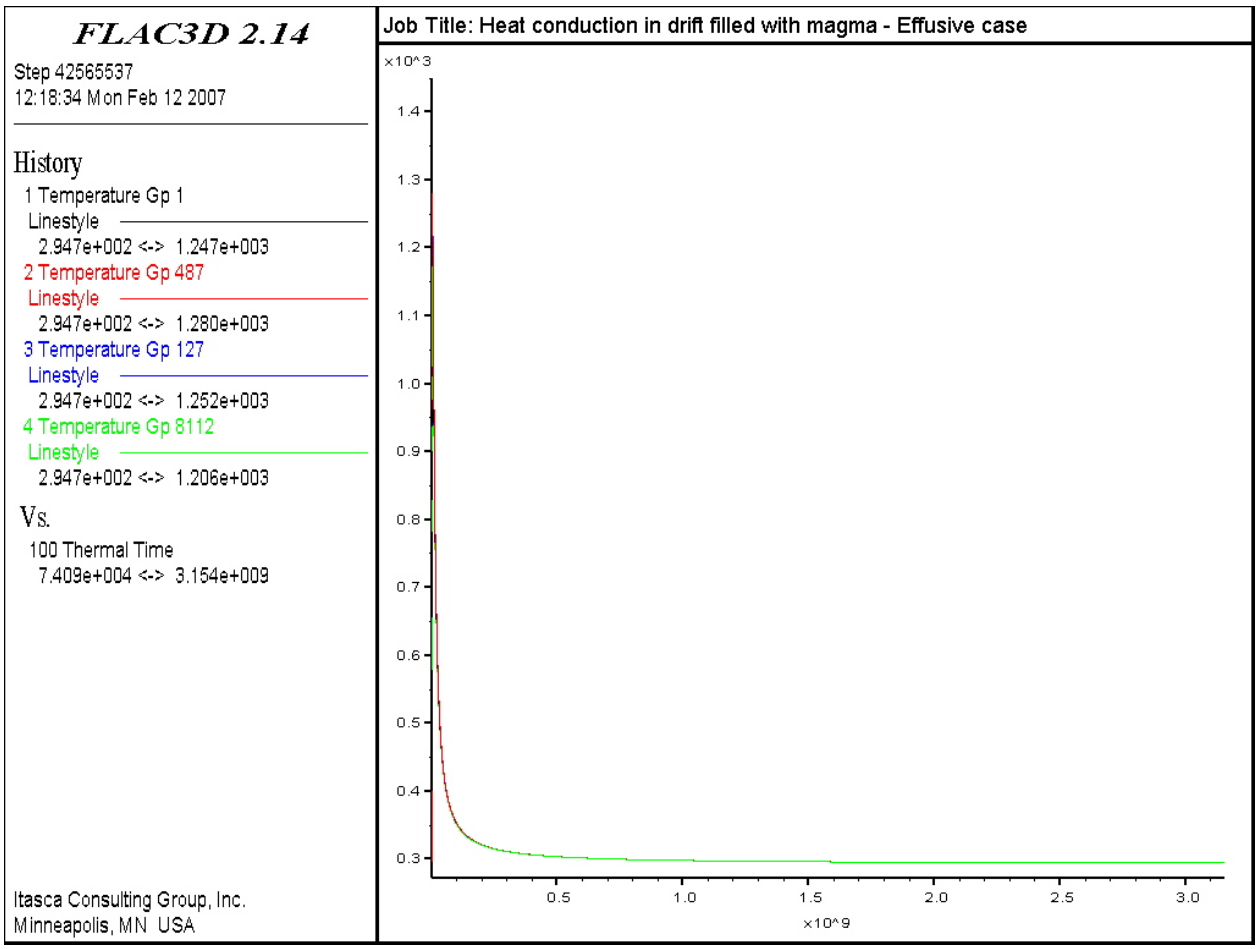

Source: Output DTN: MO0705FREEZING.000, file *\effusive\20deg\figure21.jpg*.

Figure 6-108. Temperature Histories (temperature in K, time in s) in the Waste Package over 100 Years: 1,423 K (1,150°C) Case—CWP Scenario

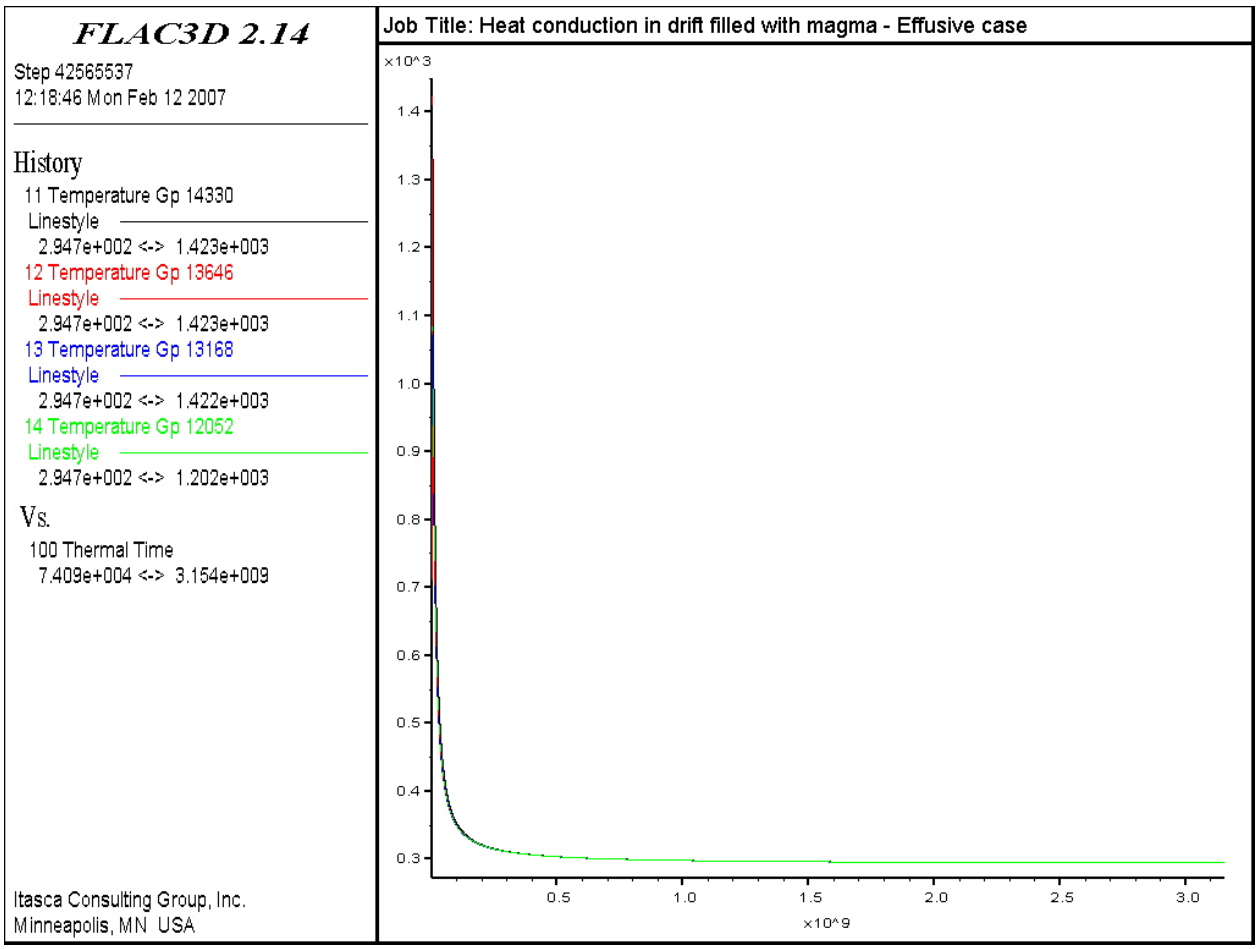

Source: Output DTN: MO0705FREEZING.000, file \effusive\20deg*figure22.jpg*.

Figure 6-109. Temperature Histories (temperature in K, time in s) in the Magma over 100 Years: 1423 K (1150°C) Case — CWP Scenario

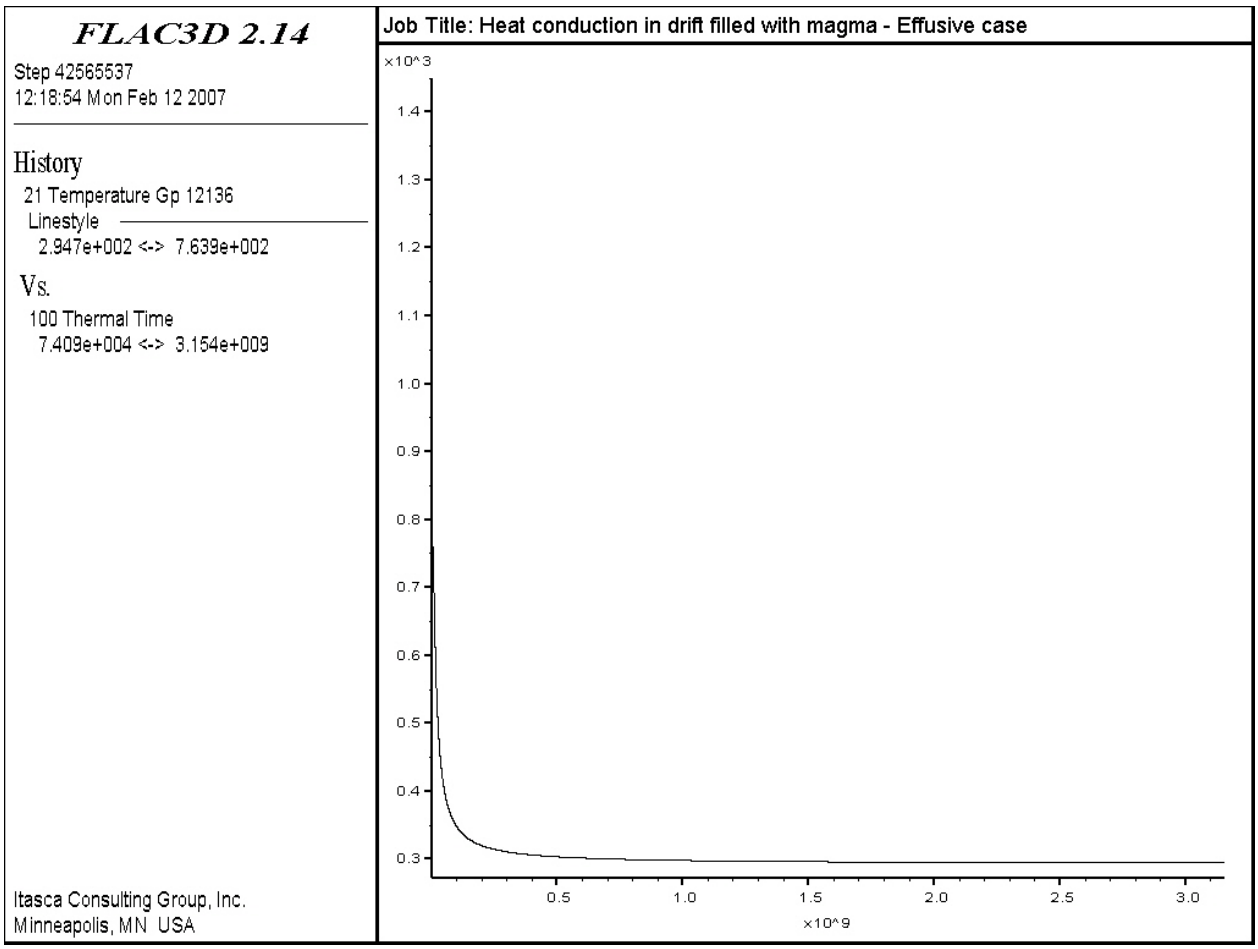

Source: Output DTN: MO0705FREEZING.000, file *\effusive\20deg\figure23.jpg.*

Figure 6-110. Temperature Histories (temperature in K, time in s) in the Invert over 100 Years: 1,423 K (1,150°C) Case—CWP Scenario

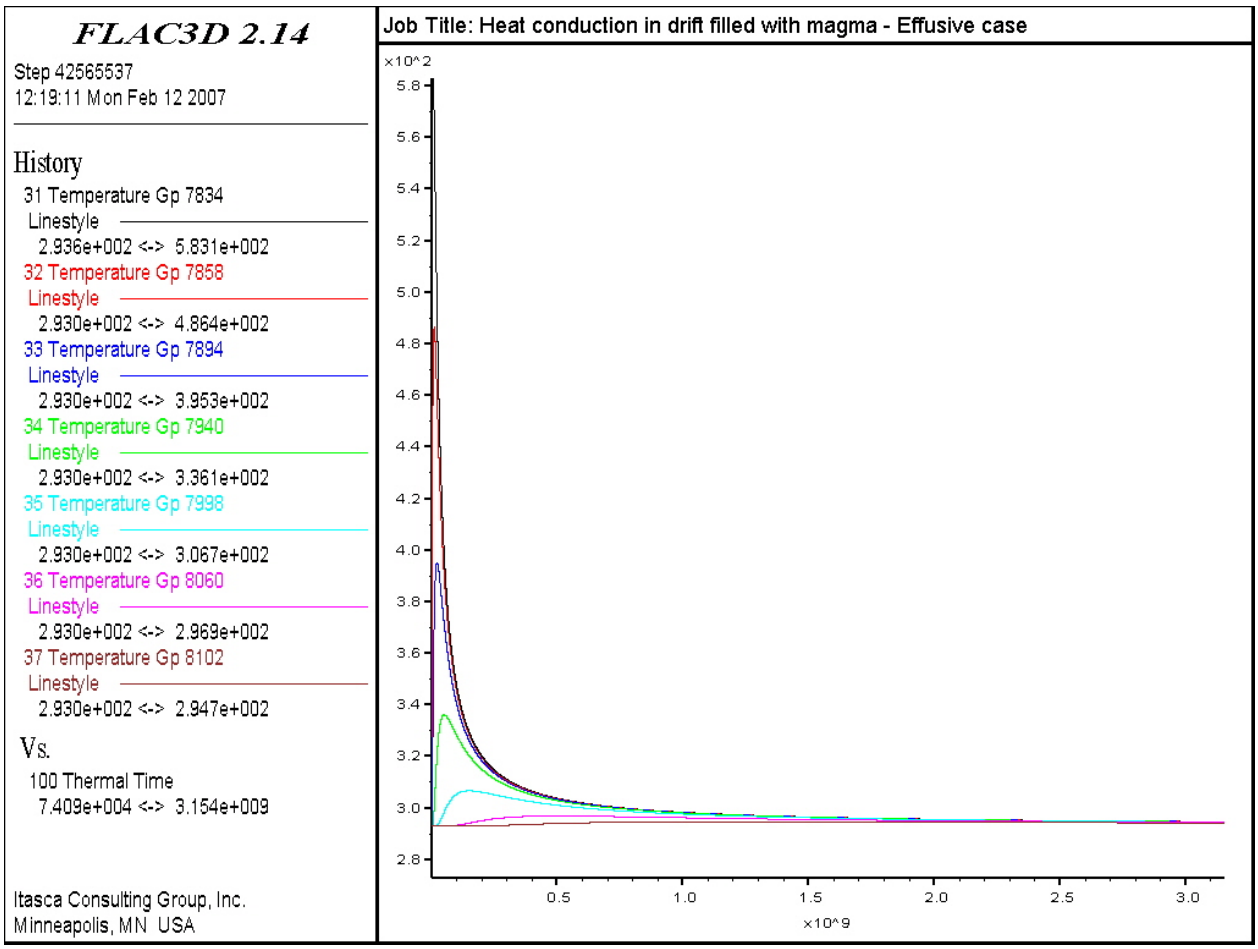

Source: Output DTN: MO0705FREEZING.000, file *\effusive\20deg\figure24.jpg.*

Figure 6-111. Temperature Histories (temperature in K, time in s) in the Rock Mass above the Drift over 100 Years: 1,423 K (1,150°C) Case—CWP Scenario

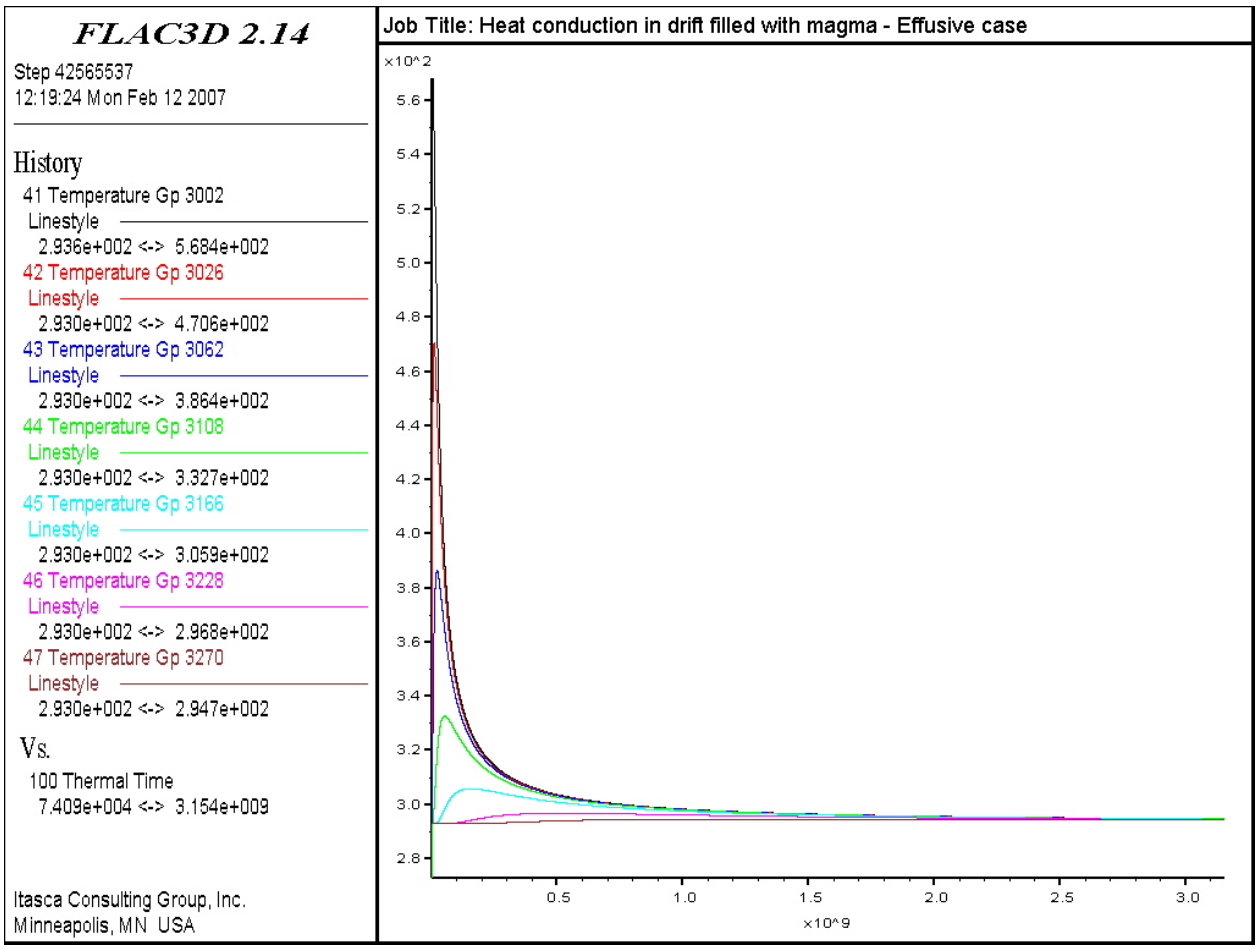

Source: Output DTN: MO0705FREEZING.000, file *\effusive\20deg\figure25.jpg*.

Figure 6-112. Temperature Histories (temperature in K, time in s) Sideways in the Rock Mass over 100 Years: 1,423 K (1,150°C) Case—CWP Scenario

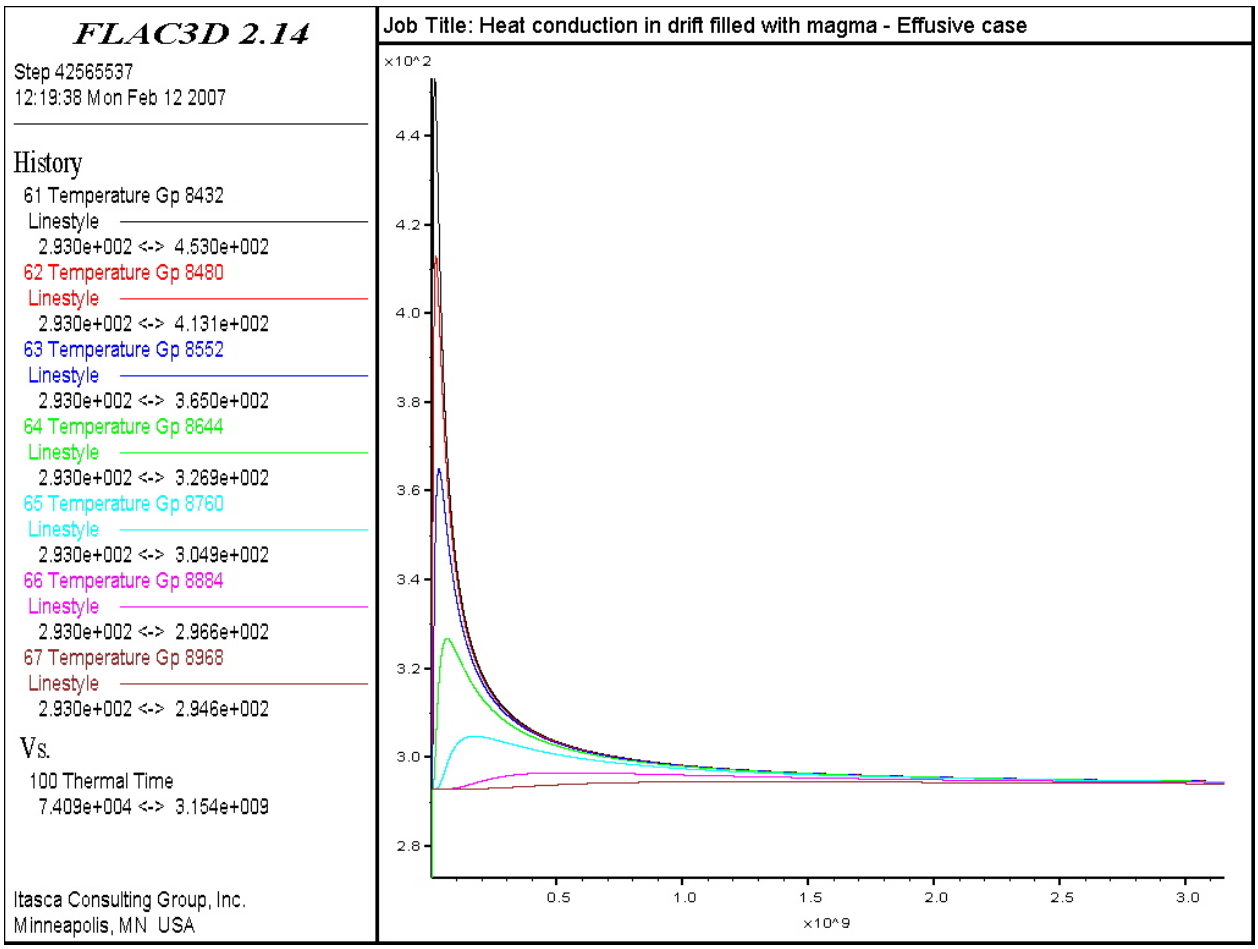

Source: Output DTN: MO0705FREEZING.000, file *\effusive\20deg\figure26.jpg*.

Figure 6-113. Temperature Histories (temperature in K, time in s) in the Rock Mass below the Drift Over 100 Years: 1,423 K (1,150°C) Case—CWP Scenario

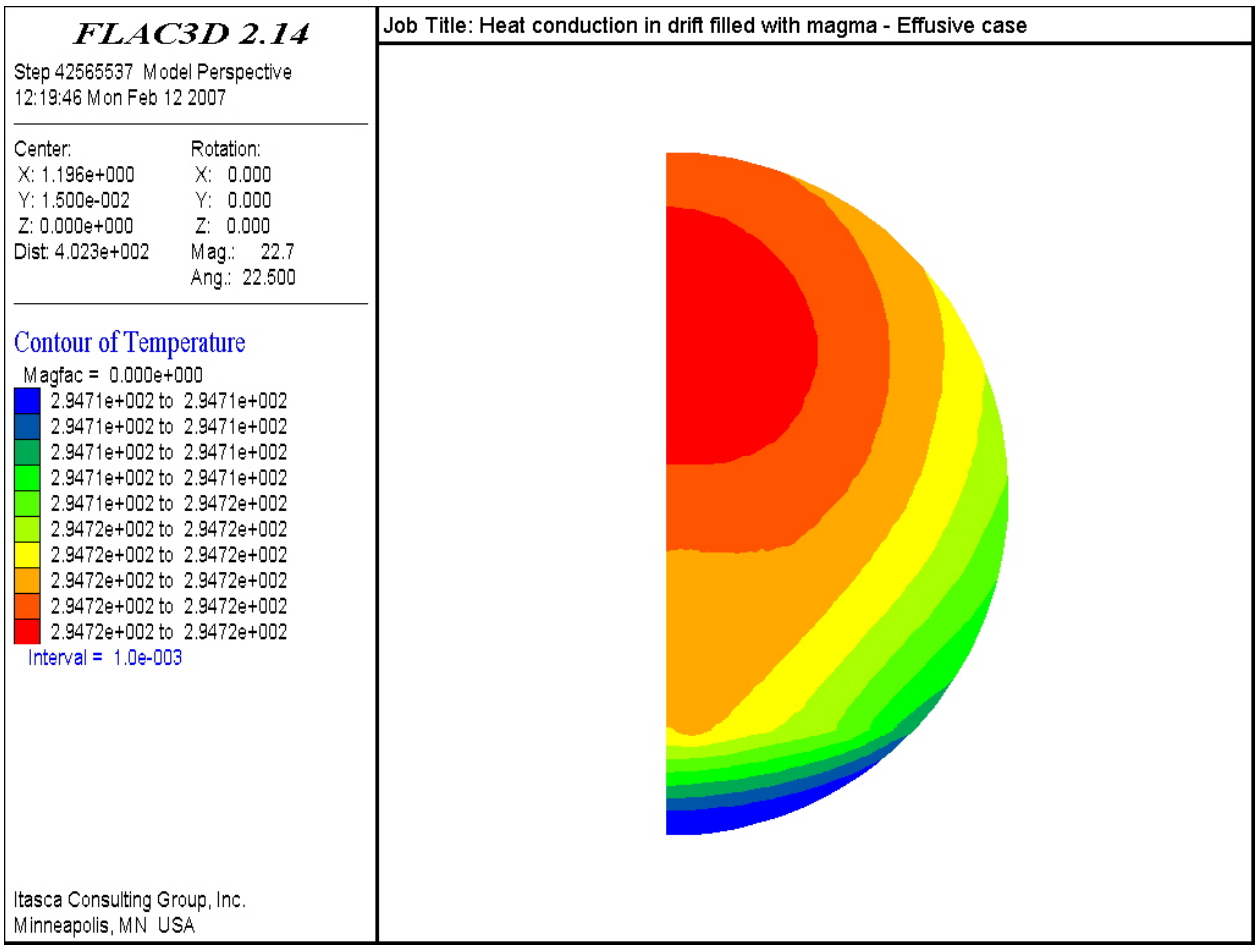

Source: Output DTN: MO0705FREEZING.000, file *\effusive\20deg\figure27.jpg*.

NOTE: To obtain temperature values in °C, subtract 273.

Figure 6-114. Temperature Contours (K) within the Drift after 100 Years: 1,423 K (1,150°C) Case—CWP Scenario

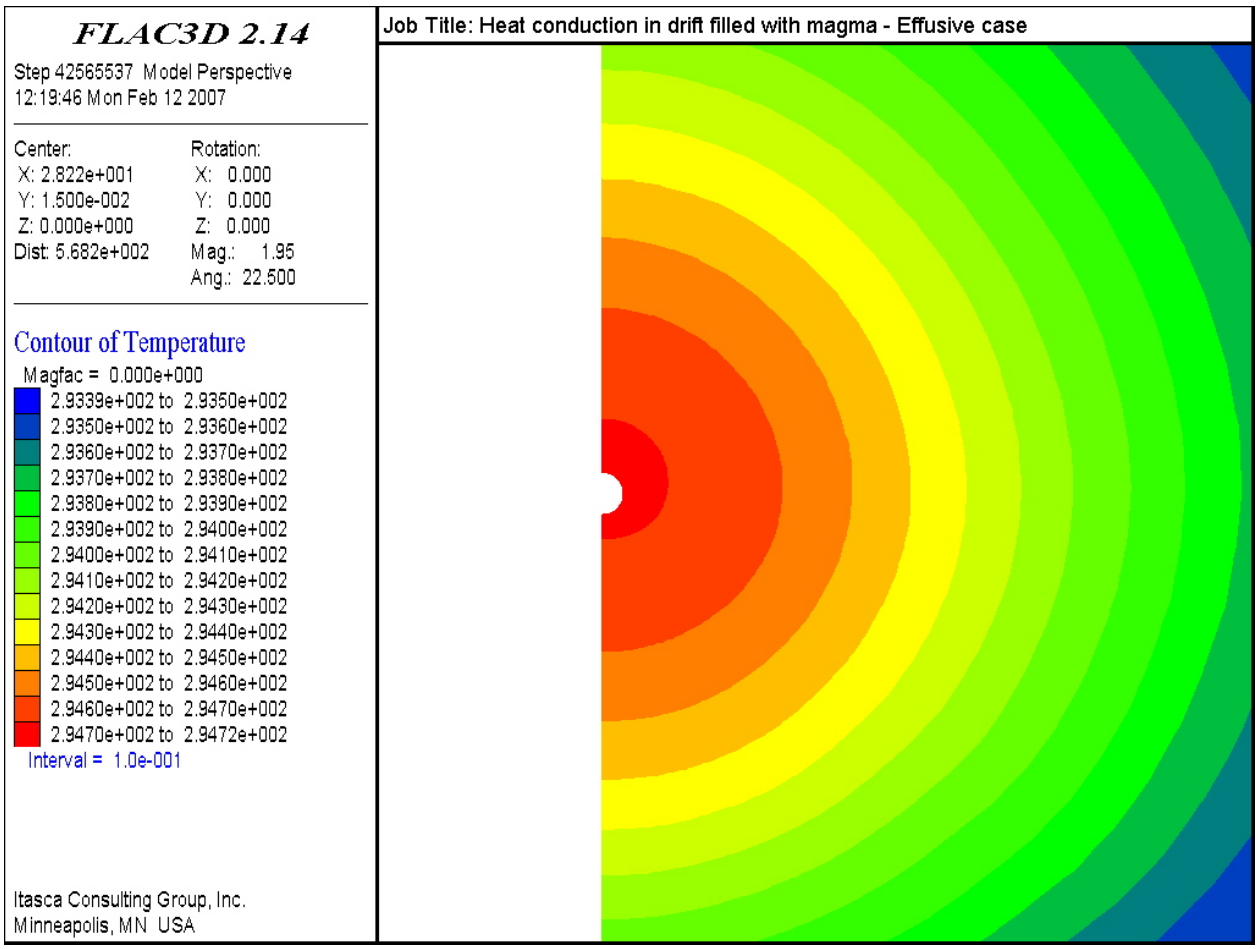

Source: Output DTN: MO0705FREEZING.000, file *\effusive\20deg\figure28.jpg*.

NOTE: To obtain temperature values in °C, subtract 273.

Figure 6-115. Temperature Contours (K) within the Rock Mass after 100 Years: Effusive Case—CWP Scenario

6.4.7.2.5.2 Results for the 1,223 K (950°C) Intrusion Case

HWP Scenario - The analyses provide an estimate for the magma, waste package, and rock mass cooling time for the HWP scenario (i.e., magma intrusion at the time when the waste package reaches the peak temperature and acts as a heat source).

The evolution of temperature versus time at monitoring points located in the waste package, magma and invert for the 1,223 K (950°C) case (T_0 = 1,223 K) is shown for the first year in Figures 6-116, 6-117, and 6-118, respectively. The maximum waste-package temperature, recorded at monitoring point 2 (the upper part of the waste package in Figure 6-92), is about 1,261 K (988°C) (compared to 1,417 K (1,144°C) for the effusive case). As with the effusive case, the non-monotonic behavior of magma temperature at the point between the waste package and the invert (point 14, see Figure 6-92 and Table 6-16) is observed. The temperature at point 14 drops to a local minimum of 887 K, which is below the solidification temperature, T_0 = 1,174 K (901°C), compared to 1,067 K (794°C) for the effusive case. Because of the lower

intrusion temperature, the temperature at that location never rises above the solidification temperature, T_s, again. The maximum invert temperature in Figure 6-118, recorded at monitoring point 21 (center of invert), is about 630 K (357°C) for this case (compared to 918 K (645°C) for the effusive case).

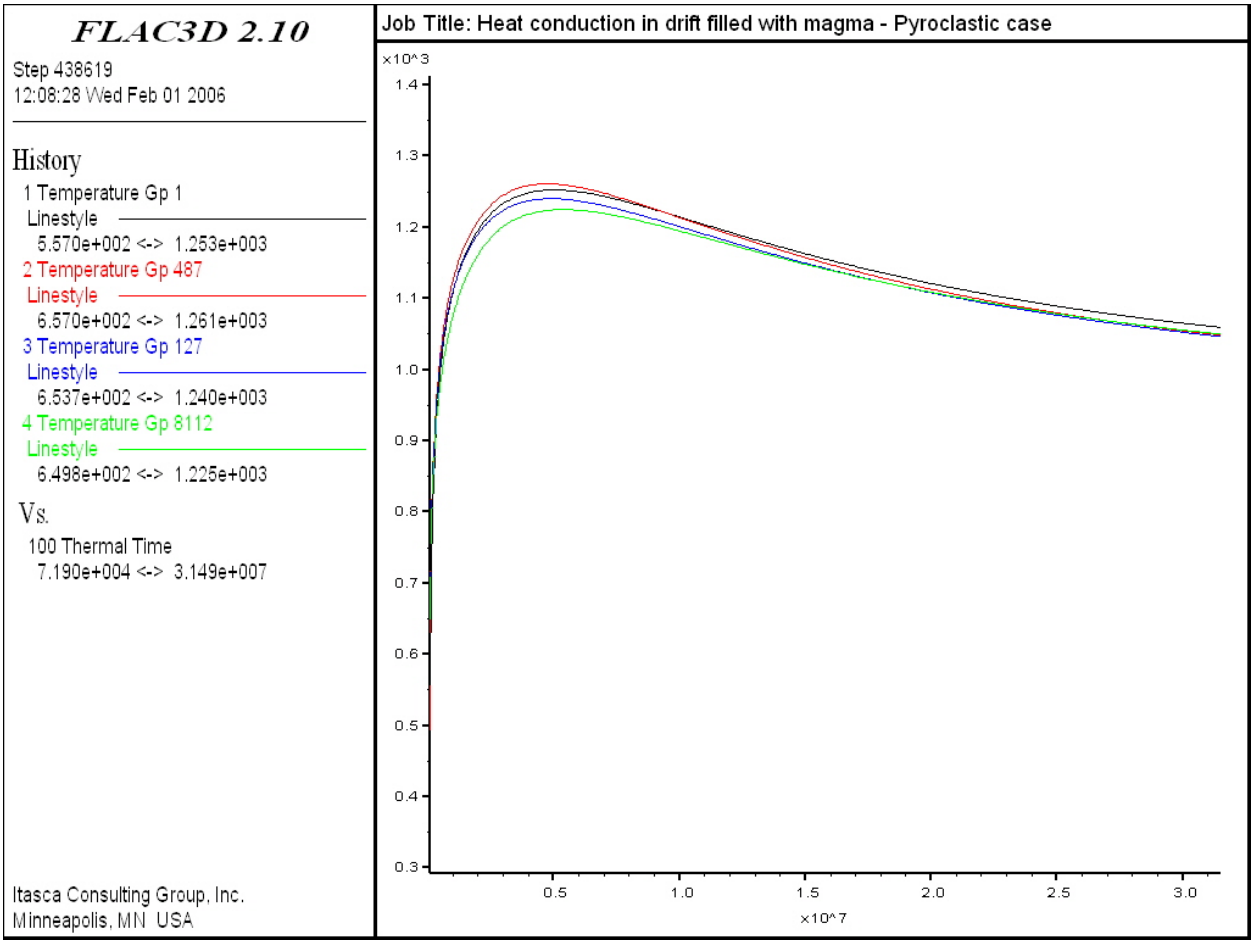

Source: Output DTN: MO0705FREEZING.000, file *\pyroclastic\maximum temperature\package-1.jpg*.

Figure 6-116. Temperature Histories (temperature in K, time in s) in the Waste Package during the First Year: 1,223 K (950°C) Case—HWP Scenario

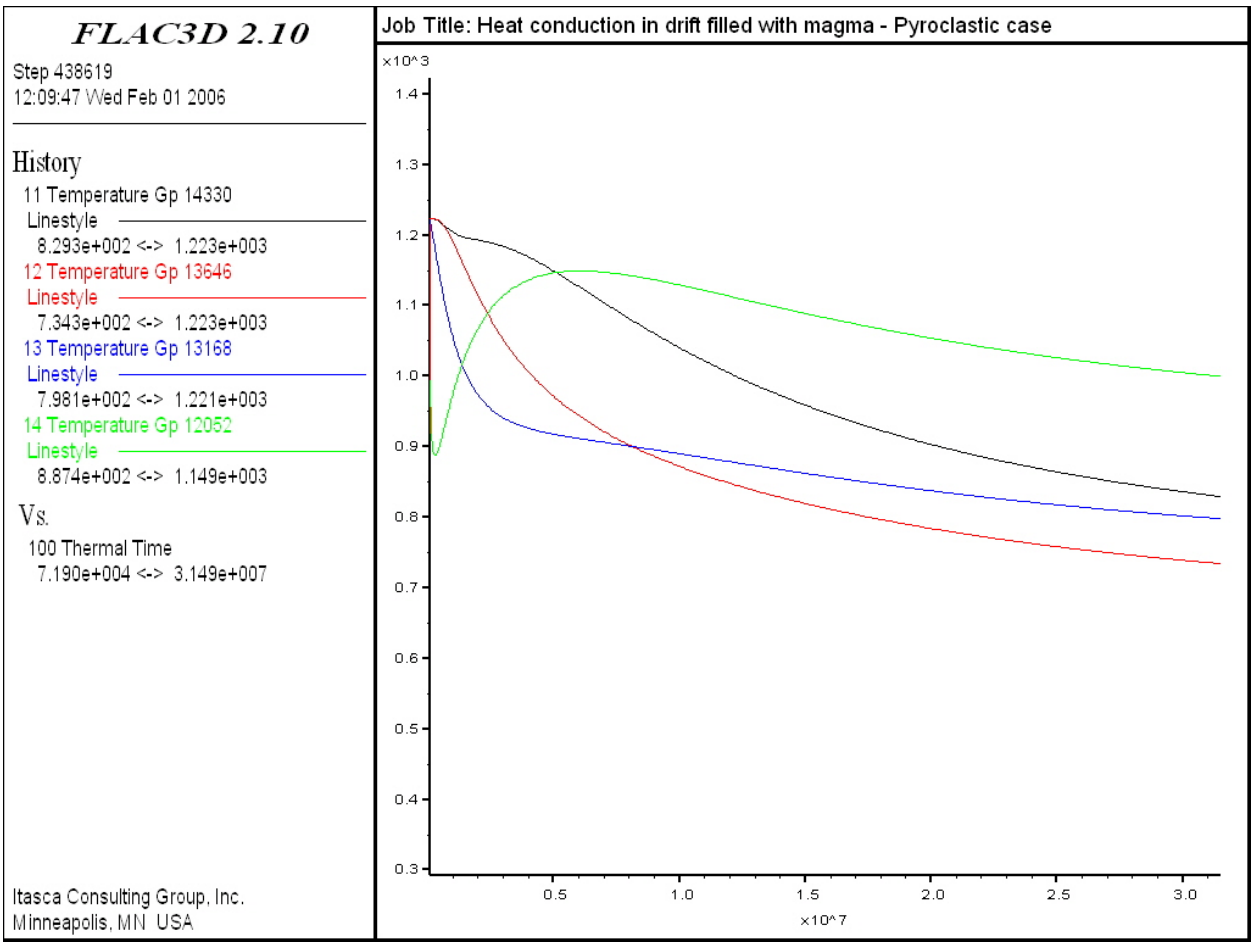

Source: Output DTN: MO0705FREEZING.000, file *\pyroclastic\maximum temperature\magma-1.jpg*.

Figure 6-117. Temperature Histories (temperature in K, time in s) in the Magma during the First Year: 1,223 K (950°C) Case—HWP Scenario

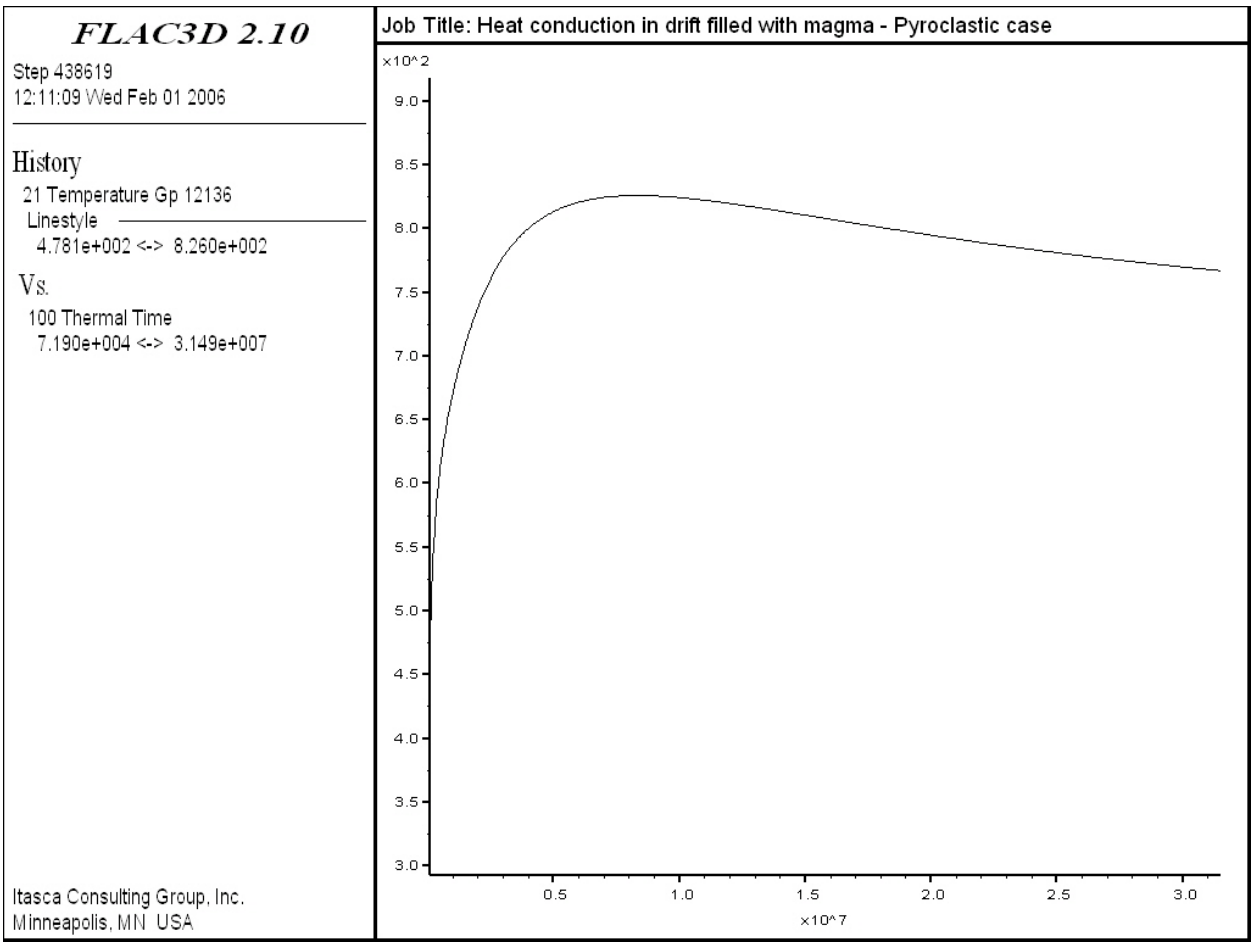

Source: Output DTN: MO0705FREEZING.000, file *\pyroclastic\maximum temperature\invert-1.jpg*.

Figure 6-118. Temperature Histories (temperature in K, time in s) in the Invert during the First Year: 1,223 K (950°C) Case—HWP Scenario

The evolution of temperature at the monitoring points for 30 years after intrusion is shown in Figures 6-119, 6-120, and 6-121 for the waste package, the magma, and the invert, respectively. The plots again show a sharp temperature drop during the first three years of the simulation, followed by a steady decrease of temperature at the lower rate of about 6.4 K for the waste package (point 1), 3.7 K for the magma (point 11), and 3.5 K for the invert (point 21). The temperature data from which the rates are derived are shown in Table 6-21. The rates (derived from the 10- and 30-year data) are slightly higher than those observed for the effusive case. Comparing data in Tables 6-19 and 6-21 for times longer than five years, it is interesting to note that, for a given time, higher temperatures are reached in the 1,223 K (950°C) case than in the effusive case. This is due to the lower conductivity of the cooler magma. Thirty years after intrusion, the temperatures at monitoring points 1 (waste package), 11 (magma), and 21 (invert) reach the values of 800 K (527°C), 641 K (368°C) and 631 K (358°C), respectively (compared to 738 K (465°C), 611 K (338°C), and 606 K (333°C), respectively, in the effusive case).

Table 6-21. Temperature Data within the Drift: 1,223 K (950°C) Case—HWP Scenario

History Label	1 year (K)	5 years (K)	10 years (K)	30 years (K)
1	1,059	959	928	800
11	829	731	714	641
21	767	714	700	631

Source: Output DTN: MO0705FREEZING.000.
To convert to °C, subtract 273.

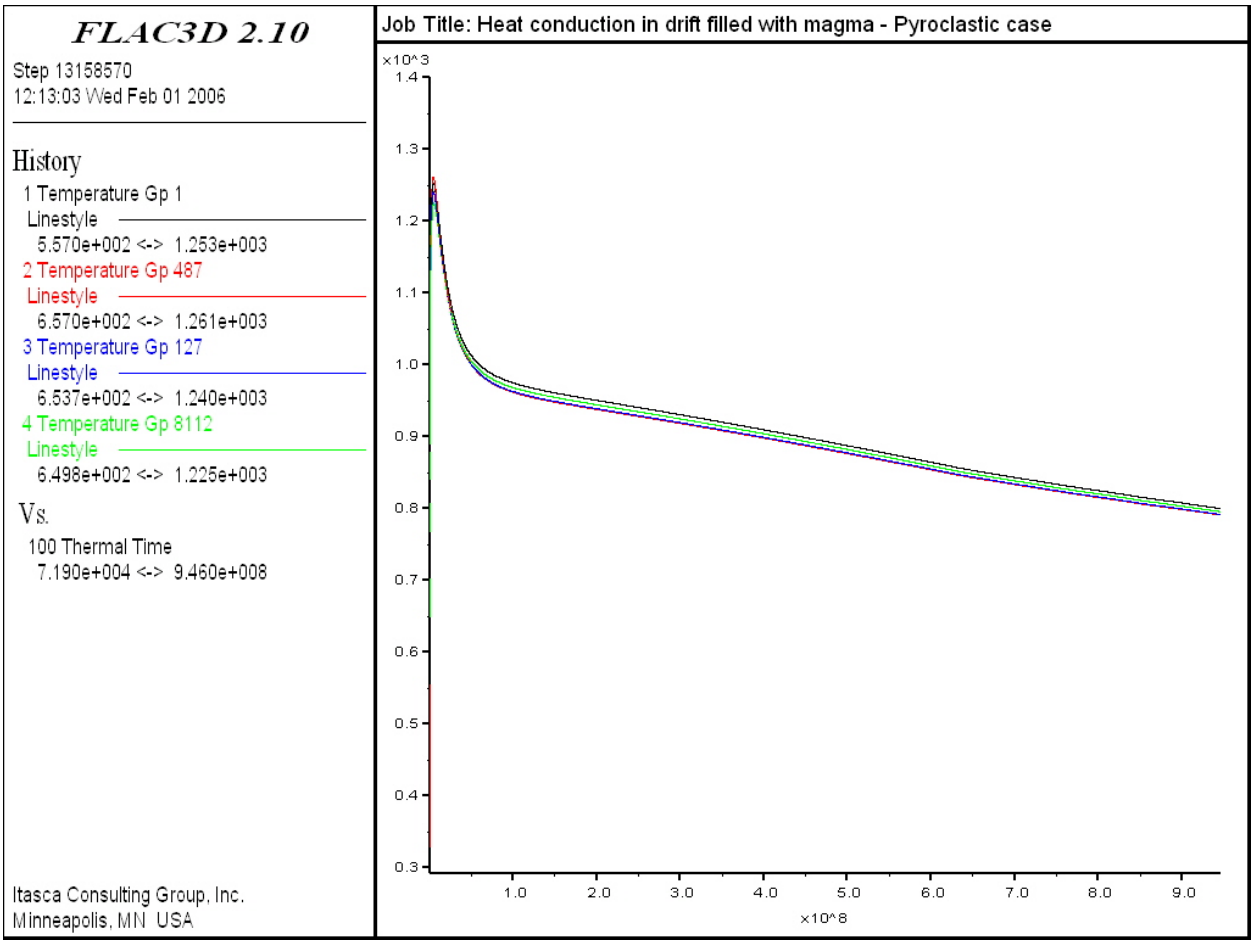

Source: Output DTN: MO0705FREEZING.000, file *\pyroclastic\maximum temperature\package-30.jpg*.

Figure 6-119. Temperature Histories (temperature in K, time in s) in the Waste Package over 30 Years: 1,223 K (950°C) Case—HWP Scenario

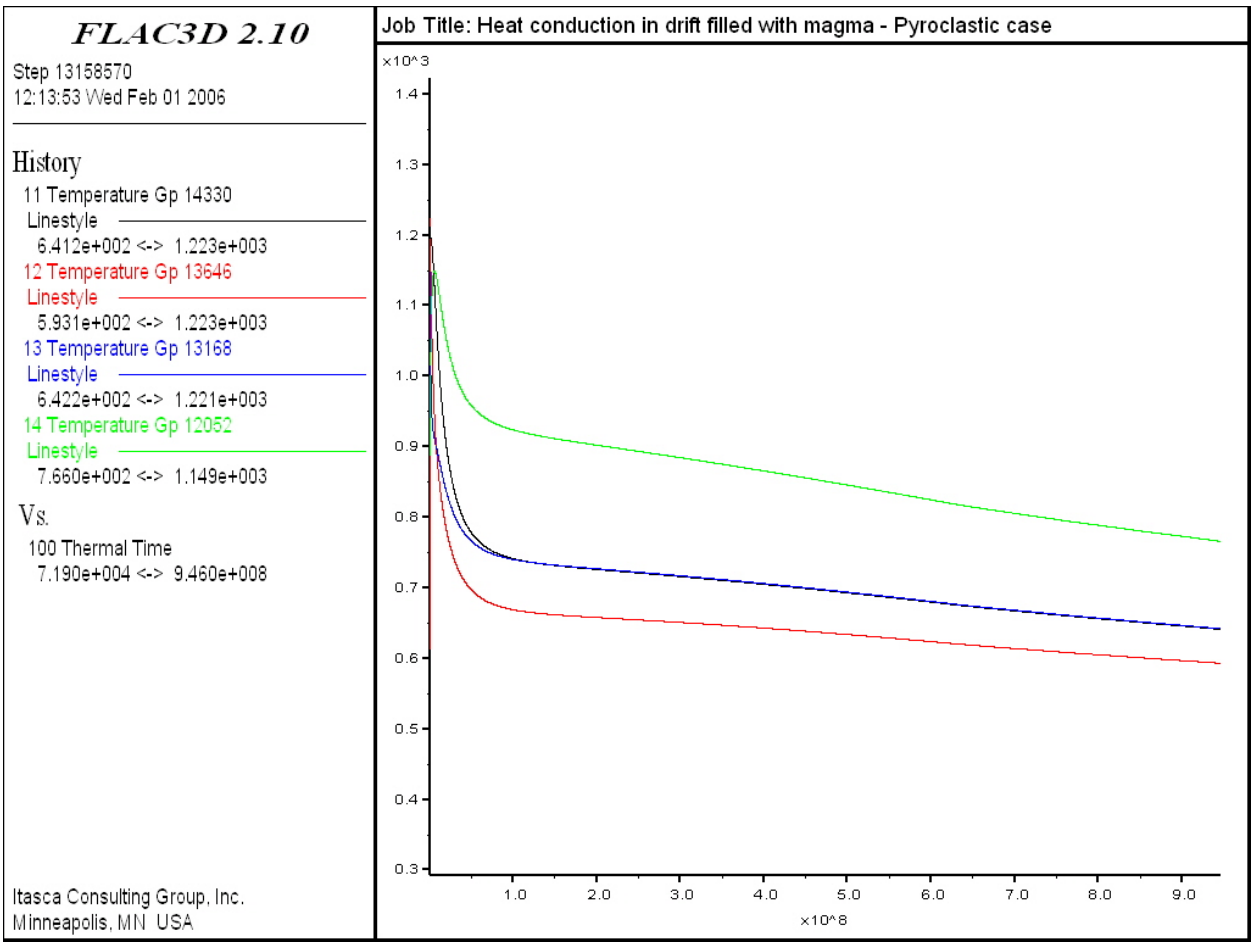

Source: Output DTN: MO0705FREEZING.000, file *\pyroclastic\maximum temperature\magma-30.jpg.*

Figure 6-120. Temperature Histories (temperature in K, time in s) in the Magma over 30 Years: 1,223 K (950°C) Case—HWP Scenario

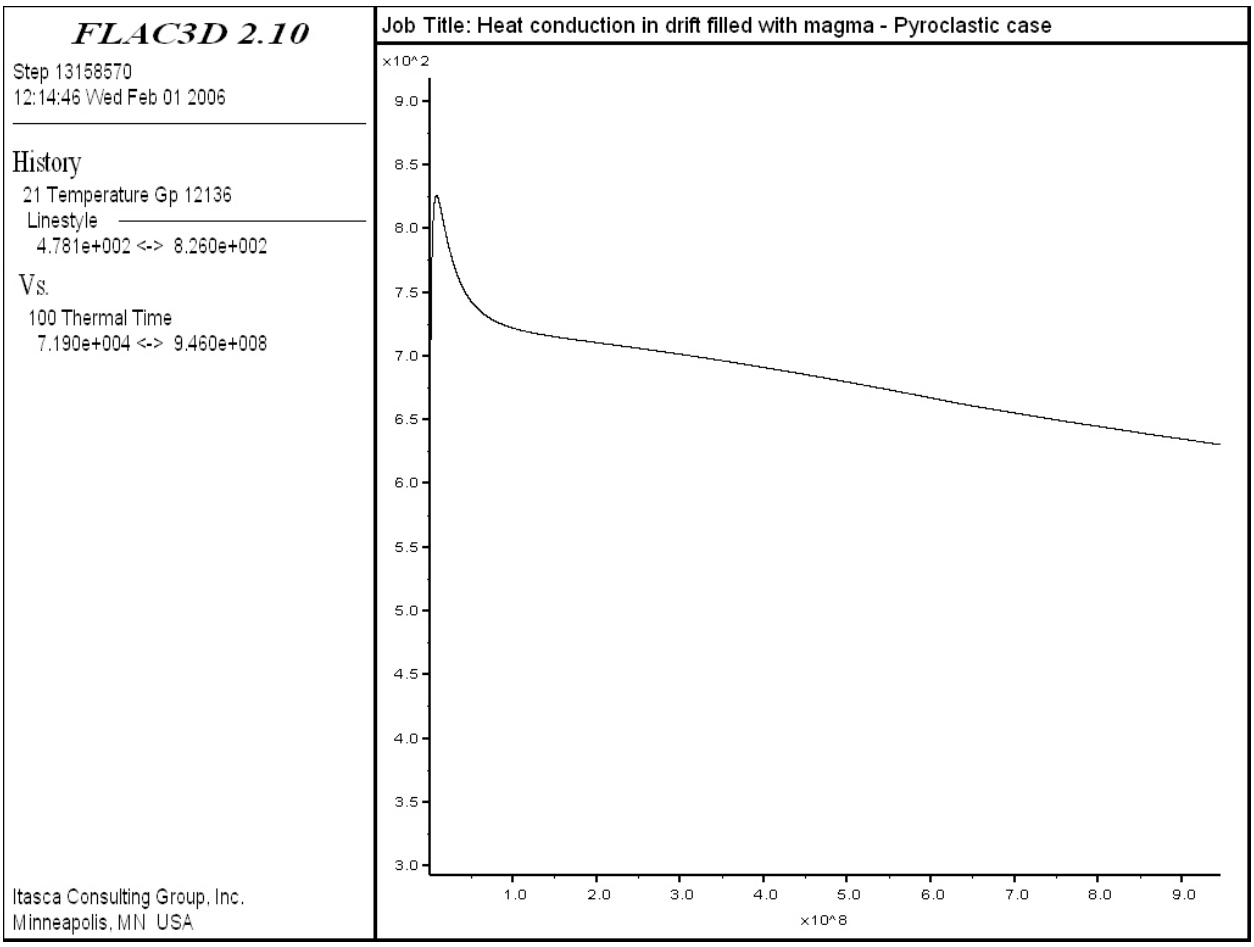

Source: Output DTN: MO0705FREEZING.000, file *\pyroclastic\maximum temperature\invert-30.jpg*.

Figure 6-121. Temperature Histories (temperature in K, time in s) in the Invert over 30 Years: 1,223 K (950°C) Case—HWP Scenario

The evolution of temperature at the monitoring points in the rock mass above, sideways to, and below the drift (see the locations of the history points in Figure 6-93 and Table 6-17) is shown in Figures 6-122, 6-123, and 6-124, respectively. Table 6-22 provides the calculated rock-mass temperature 1, 5, 10, and 30 years after intrusion, for selected monitoring points located at distances of about 3.75 m, 10.65 m, and 34.82 m from the center of the drift. One year after intrusion, temperatures are predicted to decrease within a radius of about 10.5 m from the center of the drift and to increase at a slower rate beyond that radius. Contours of temperature at the end of the 30-year simulation are shown in Figure 6-125 (within the drift) and Figure 6-126 (within the rock mass).

Table 6-22. Rock Mass Temperature for Selected Monitoring Points: 1,223 K (950°C) Case—HWP Scenario

History Label	1 year [K]	5 years [K]	10 years [K]	30 years [K]
31	533	495	494	477
34	396	406	410	413
36	312	313	318	332
41	545	517	516	493
44	395	411	417	418
46	312	313	318	333
61	546	534	532	505
64	392	416	423	423
66	312	313	319	334

Source: Output DTN: MO0705FREEZING.000.

NOTE: To convert to °C, subtract 273.

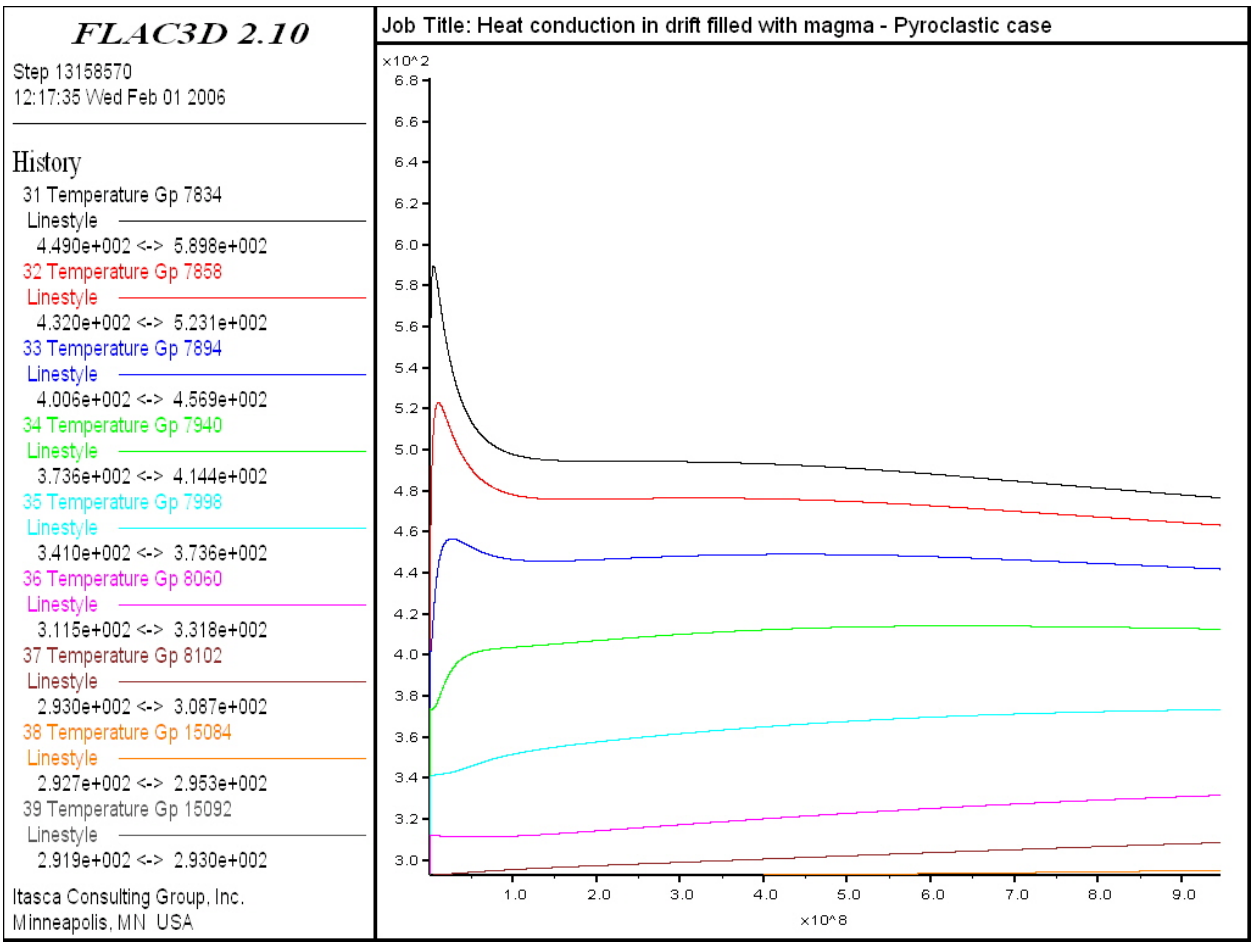

Source: Output DTN: MO0705FREEZING.000, file *\pyroclastic\maximum temperature\rockup.jpg*.

Figure 6-122. Temperature Histories (temperature in K, time in s) in the Rock Mass above the Waste Package over 30 Years: 1,223 K (950°C) Case—HWP Scenario

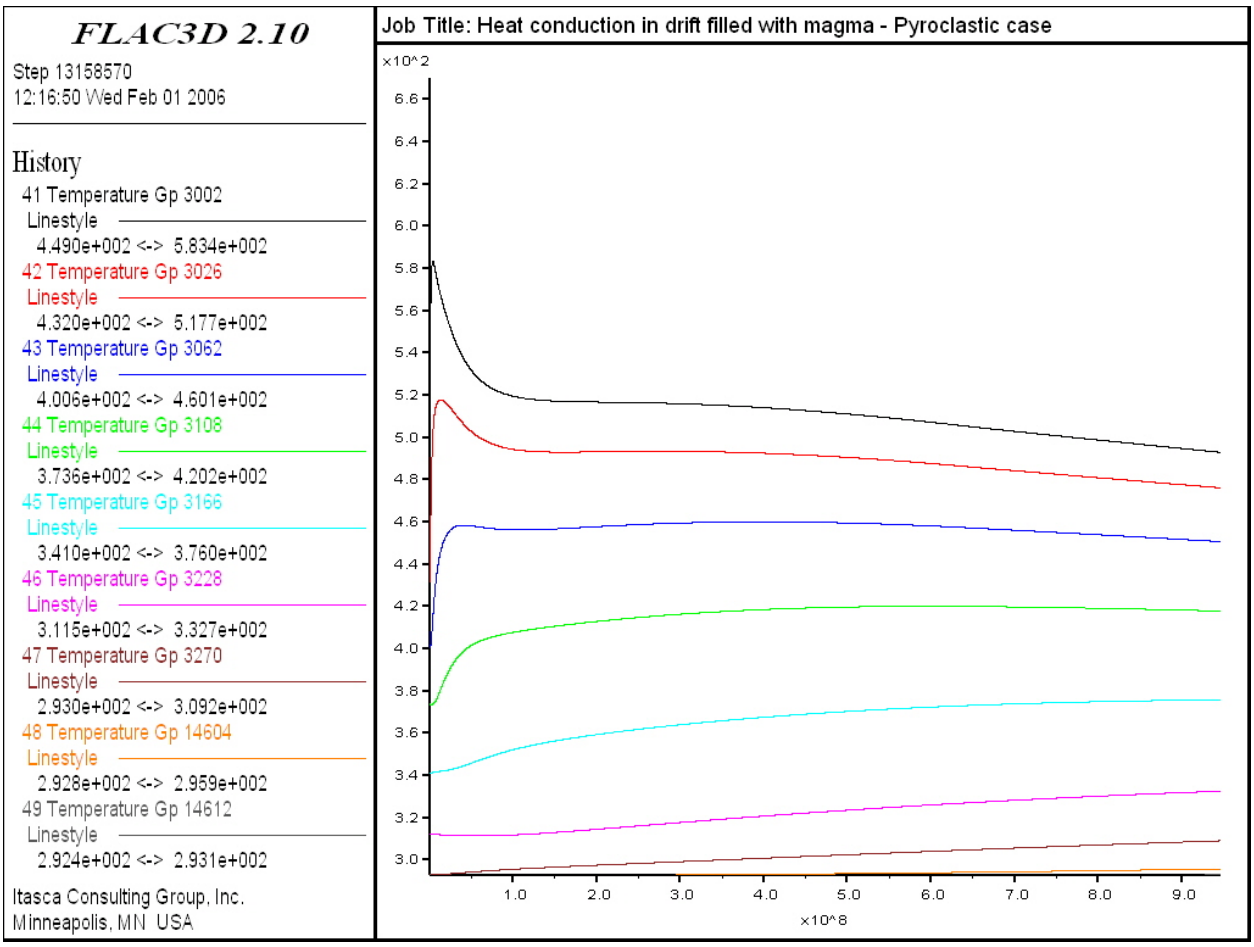

Source: Output DTN: MO0705FREEZING.000, file *\pyroclastic\maximum temperature\rockright.jpg*.

Figure 6-123. Temperature Histories (temperature in K, time in s) in the Rock Mass beside the Waste Package over 30 Years: 1,223 K (950°C) Case—HWP Scenario

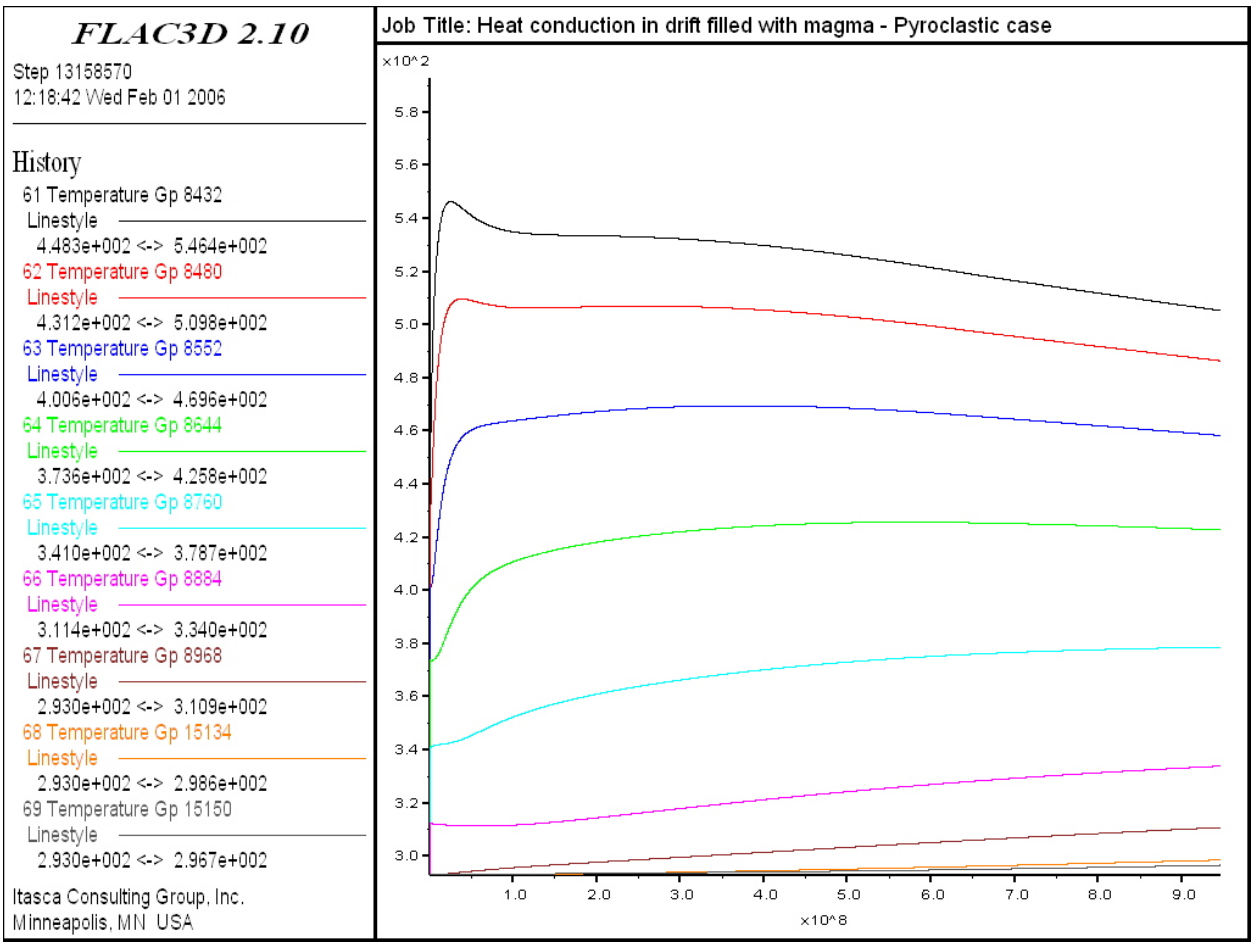

Source: Output DTN: MO0705FREEZING.000, file *\pyroclastic\maximum temperature\rockdown.jpg.*

Figure 6-124. Temperature Histories (temperature in K, time in s) in the Rock Mass below the Waste Package over 30 Years: 1,223 K (950°C) Case—HWP Scenario

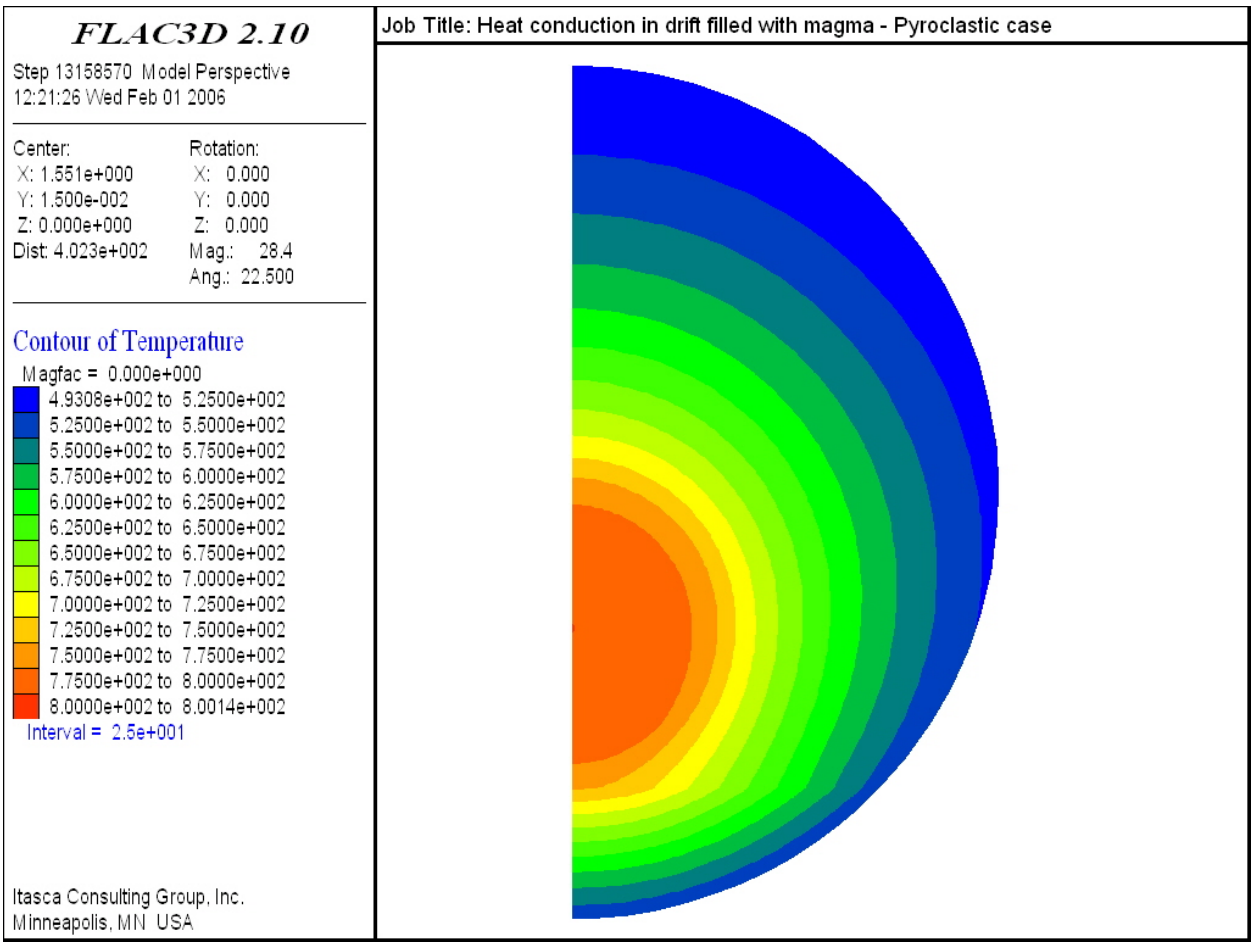

Source: Output DTN: MO0705FREEZING.000, file *\pyroclastic\maximum temperature\mpi-30.jpg*.

Figure 6-125. Temperature Contours (K) within the Drift after 30 Years: 1,223 K (950°C) Case—HWP Scenario

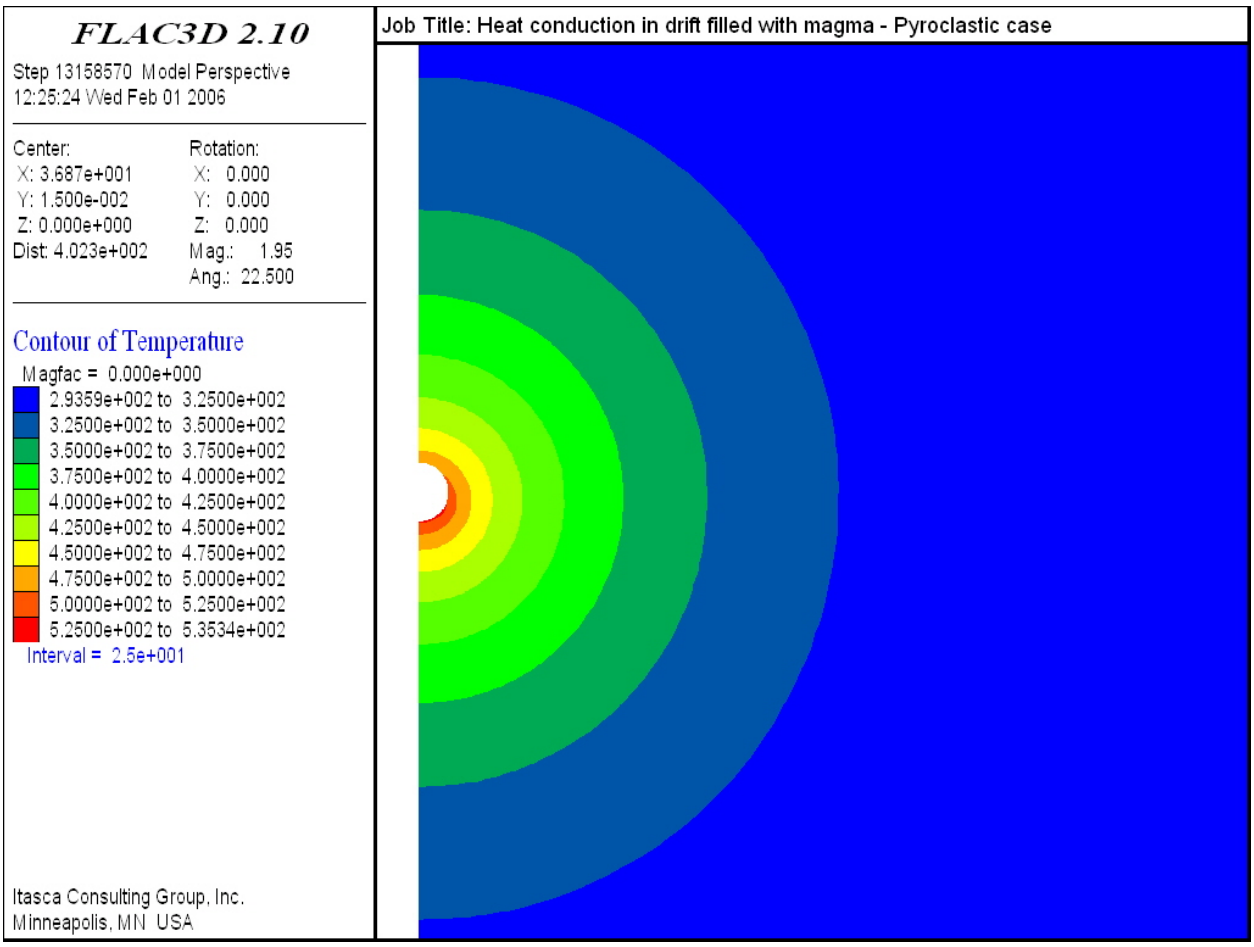

Source: Output DTN: MO0705FREEZING.000, file *\pyroclastic\maximum temperature\temp-30.jpg*.

Figure 6-126. Temperature Contours (K) within the Rock Mass after 30 Years: 950°C Case—HWP Scenario

CWP Scenario—The evolution of temperature versus time at monitoring points located inside the waste package, magma, and the invert for the 1,223 K (950°C) intrusion case is shown for the first year in Figures 6-127, 6-128, and 6-129, respectively. The maximum waste-package temperature, recorded at monitoring point 2 (the upper part of the waste package in Figure 6-92), is about 1,023 K (750°C) compared to 1,243 K (970°C) for the 1,423 K (1,150°C) case. The maximum invert temperature, recorded at monitoring point 21 (center of invert) in Figure 6-129, is about 630 K (357°C) for this case compared to 753 K (480°C) for the 1,423 K (1,150°C) case.

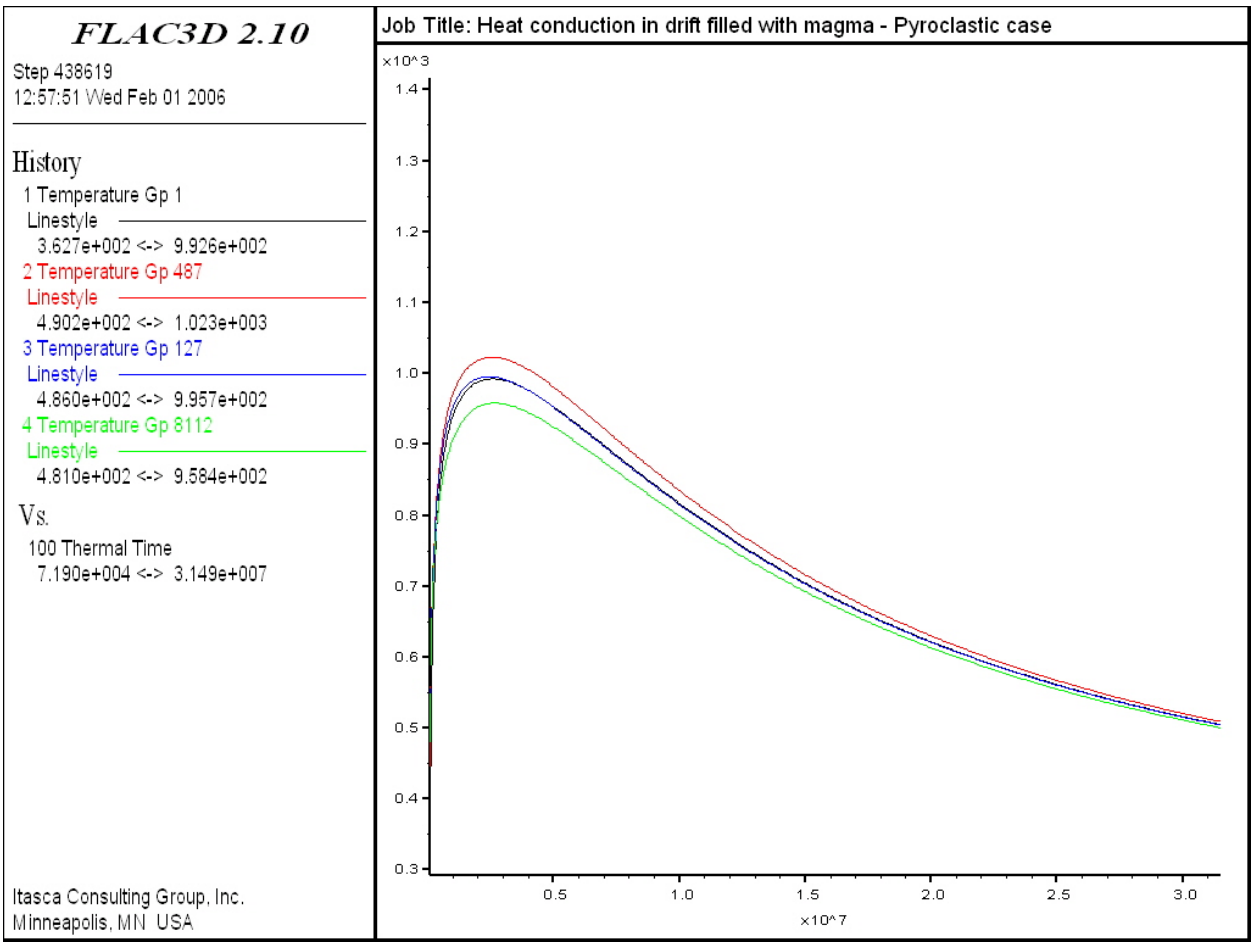

Source: Output DTN: MO0705FREEZING.000, file *\pyroclastic\20deg\package20-1.jpg*.

Figure 6-127. Temperature Histories (temperature in K, time in s) in the Waste Package During the First Year: 1,223 K (950°C) Case—CWP Scenario

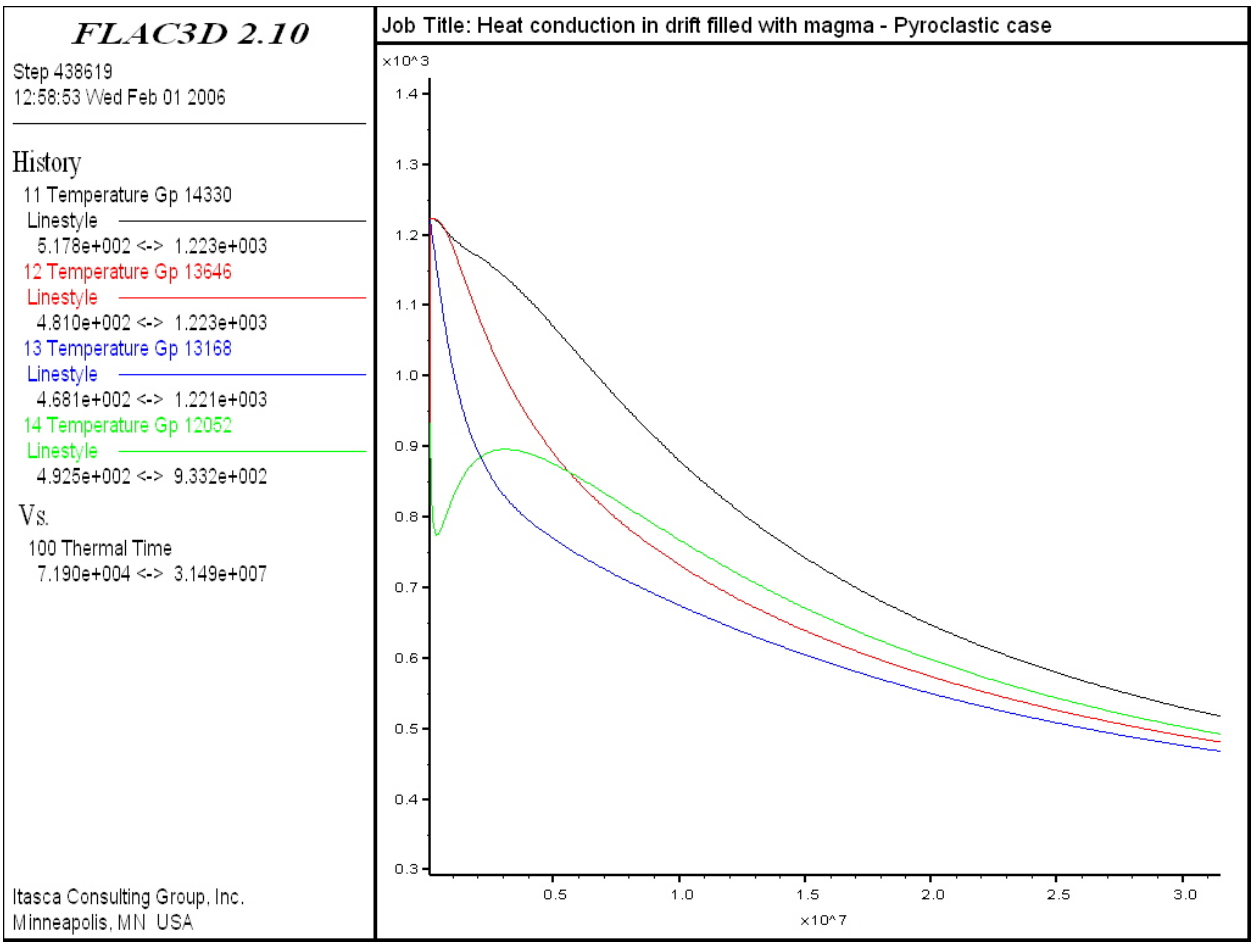

Source: Output DTN: MO0705FREEZING.000, file *\pyroclastic\20deg\magma20-1.jpg*.

Figure 6-128. Temperature Histories (temperature in K, time in s) in the Magma During the First Year: 1,223 K (950°C) Case—CWP Scenario

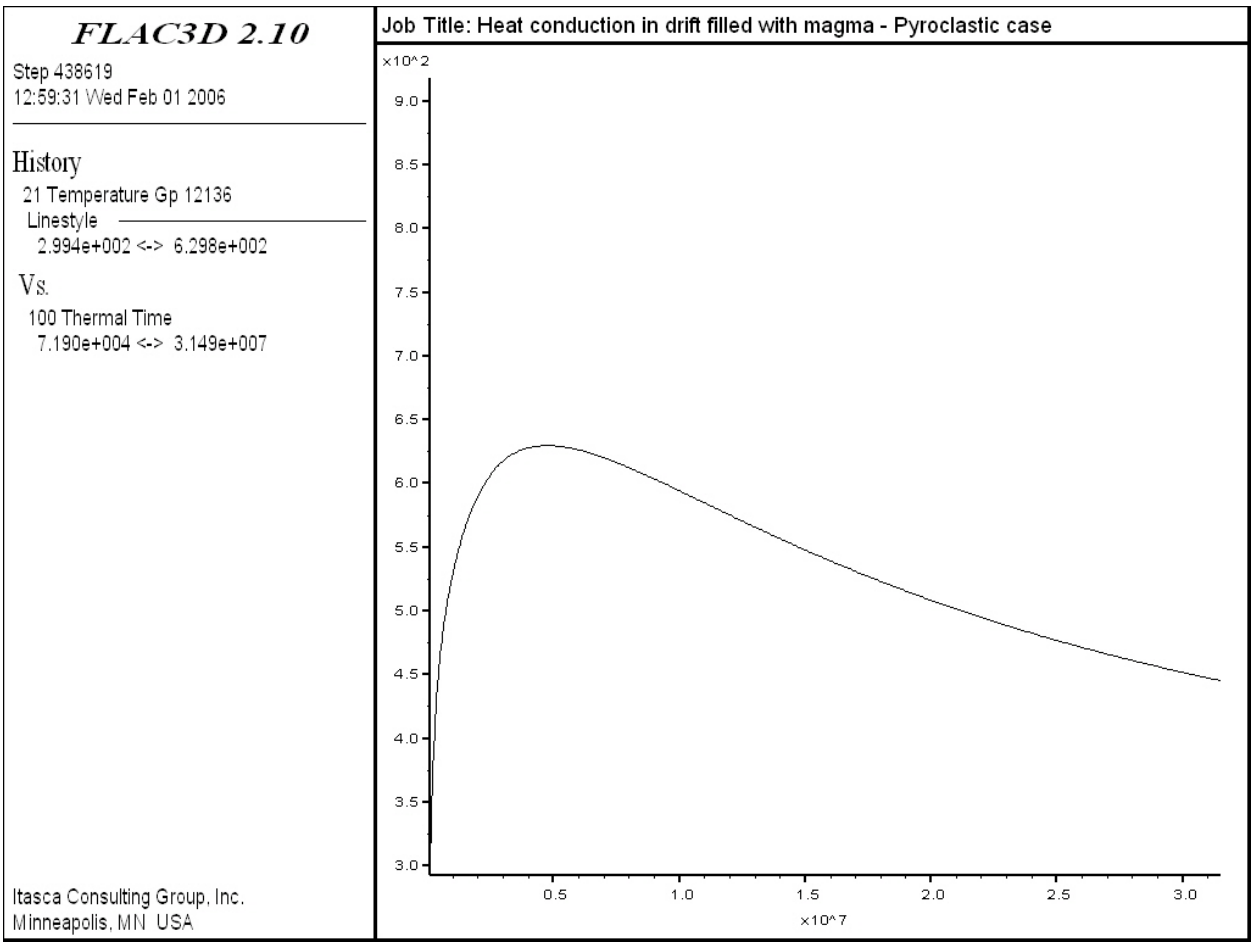

Source: Output DTN: MO0705FREEZING.000, file *\pyroclastic\20deg\invert20-1.jpg*.

Figure 6-129. Temperature Histories (temperature in K, time in s) in the Invert during the First Year: 1,223 K (950°C) Case—CWP Scenario

The evolution of temperature at the monitoring points over 30 years after intrusion is shown in Figures 6-130, 6-131, and 6-132 for the waste package, the magma, and the invert, respectively. After 30 years, the temperatures at monitoring points 1 (waste package), 11 (magma), and 21 (invert) have equilibrated down to a value of about 298 K. The plots in Figures 6-130 through 6-132 again show that at least 90% of the temperature drop at the monitoring points occurs during the first six years of the simulation.

The evolution of temperature at the monitoring points in the rock mass above, sideways to, and below the drift (see Figure 6-93 and Table 6-16 for locations) is shown in Figures 6-133, 6-134, and 6-135, respectively. Contours of temperature at the end of the 30-year simulation are shown in Figure 6-136 (within the drift) and Figure 6-137 (within the rock mass).

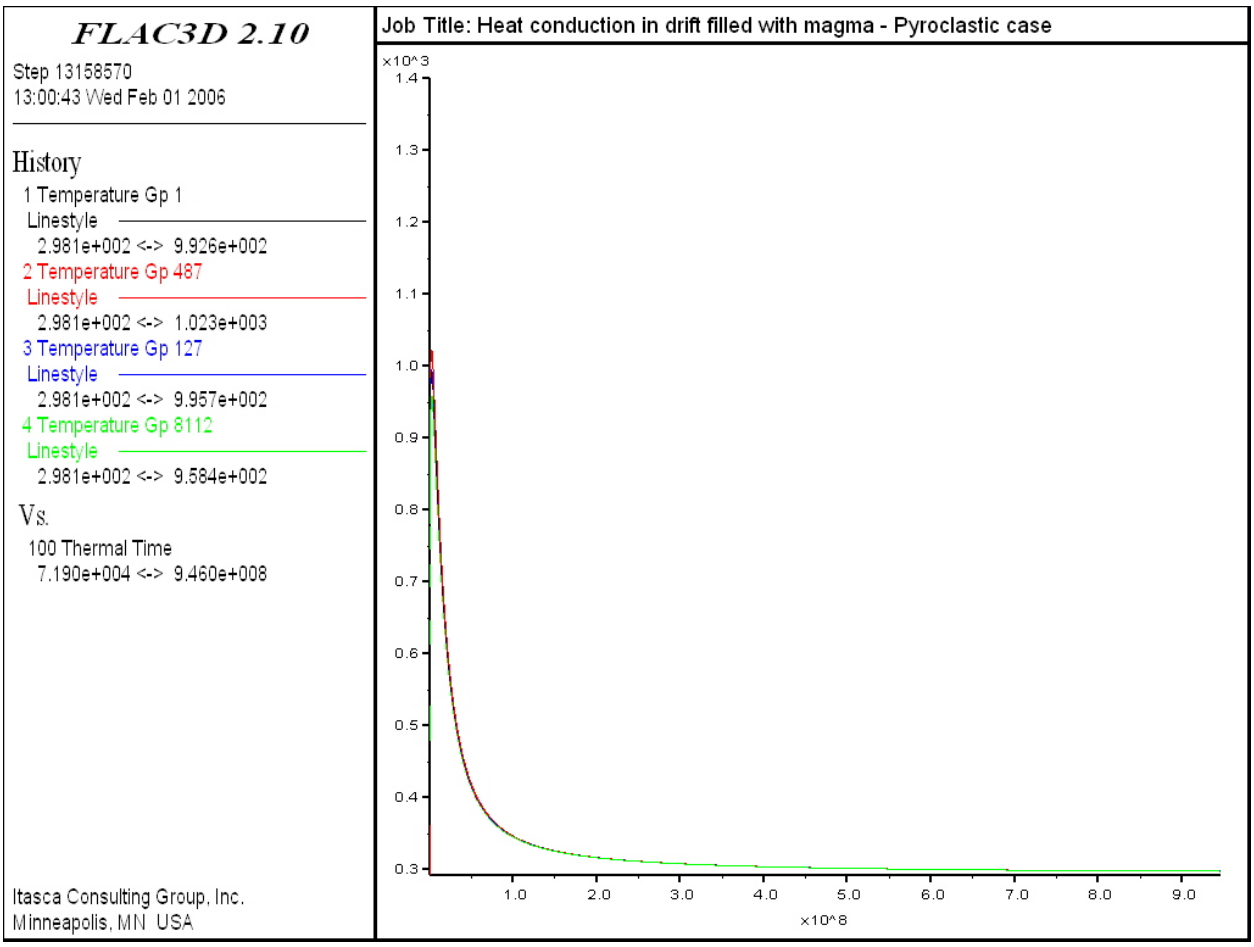

Source: Output DTN: MO0705FREEZING.000, file *\pyroclastic\20deg\package20-30.jpg*.

Figure 6-130. Temperature Histories (temperature in K, time in s) in the Waste Package over 30 Years: 1,223 K (950°C) Case—CWP Scenario

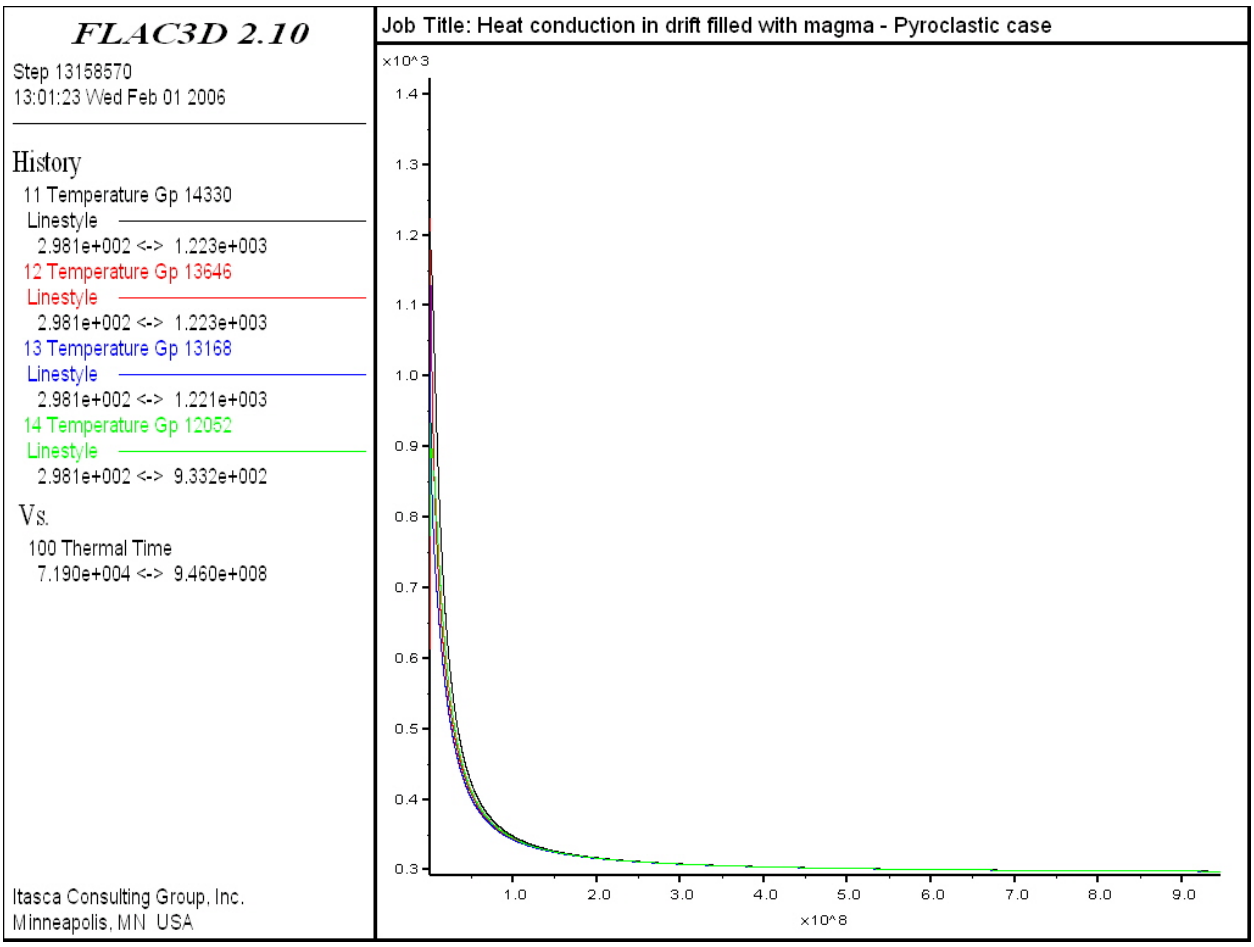

Source: Output DTN: MO0705FREEZING.000, file \pyroclastic\20deg*magma20-30.jpg*.

Figure 6-131. Temperature Histories (temperature in K, time in s) in the Magma over 30 Years: 1,223 K (950°C) Case—CWP Scenario.

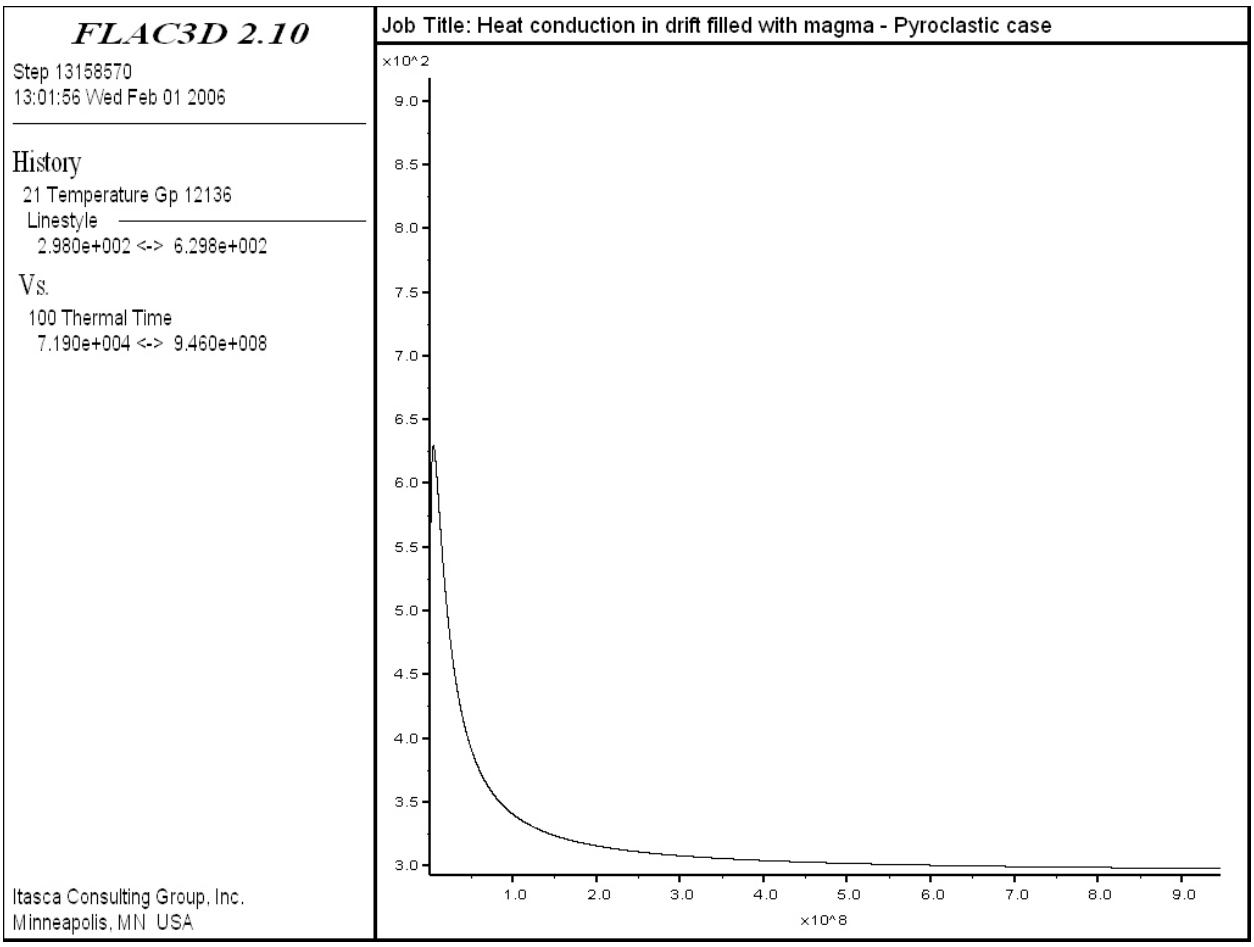

Source: Output DTN: MO0705FREEZING.000, file *\pyroclastic\20deg\invert20-30.jpg*.

Figure 6-132. Temperature Histories (temperature in K, time in s) in the Invert over 30 Years: 1,223 K (950°C) Case—CWP Scenario

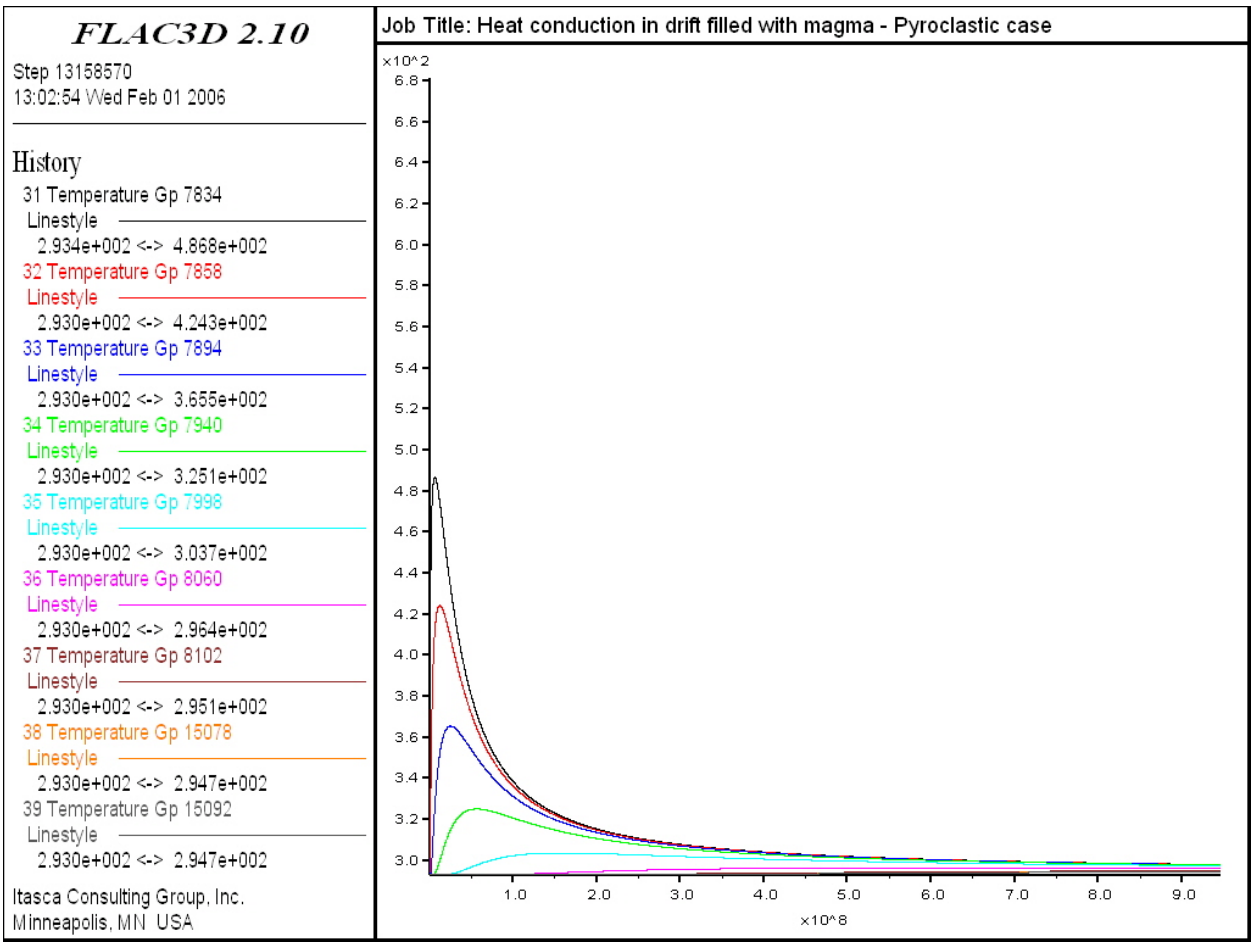

Source: Output DTN: MO0705FREEZING.000, file *\pyroclastic\20deg\rockup20-30.jpg*.

Figure 6-133. Temperature Histories (temperature in K, time in s) in the Rock Mass above the Waste Package over 30 Years: 1,223 K (950°C) Case—CWP Scenario

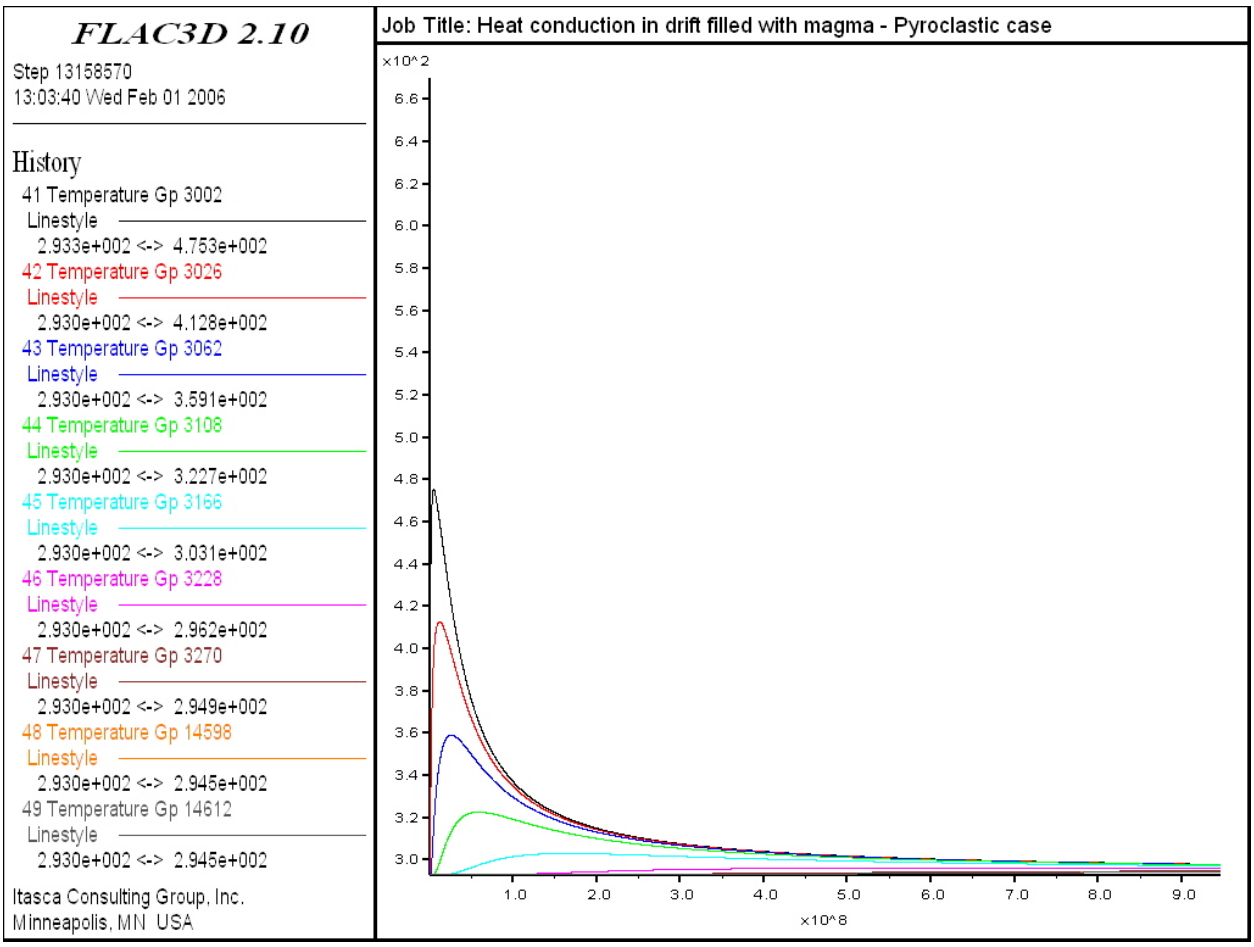

Source: Output DTN: MO0705FREEZING.000, file *\pyroclastic\20deg\rockright20-30.jpg*.

Figure 6-134. Temperature Histories (temperature in K, time in s) in the Rock Mass beside the Waste Package over 30 Years: 1,223 K (950°C) Case—CWP Scenario

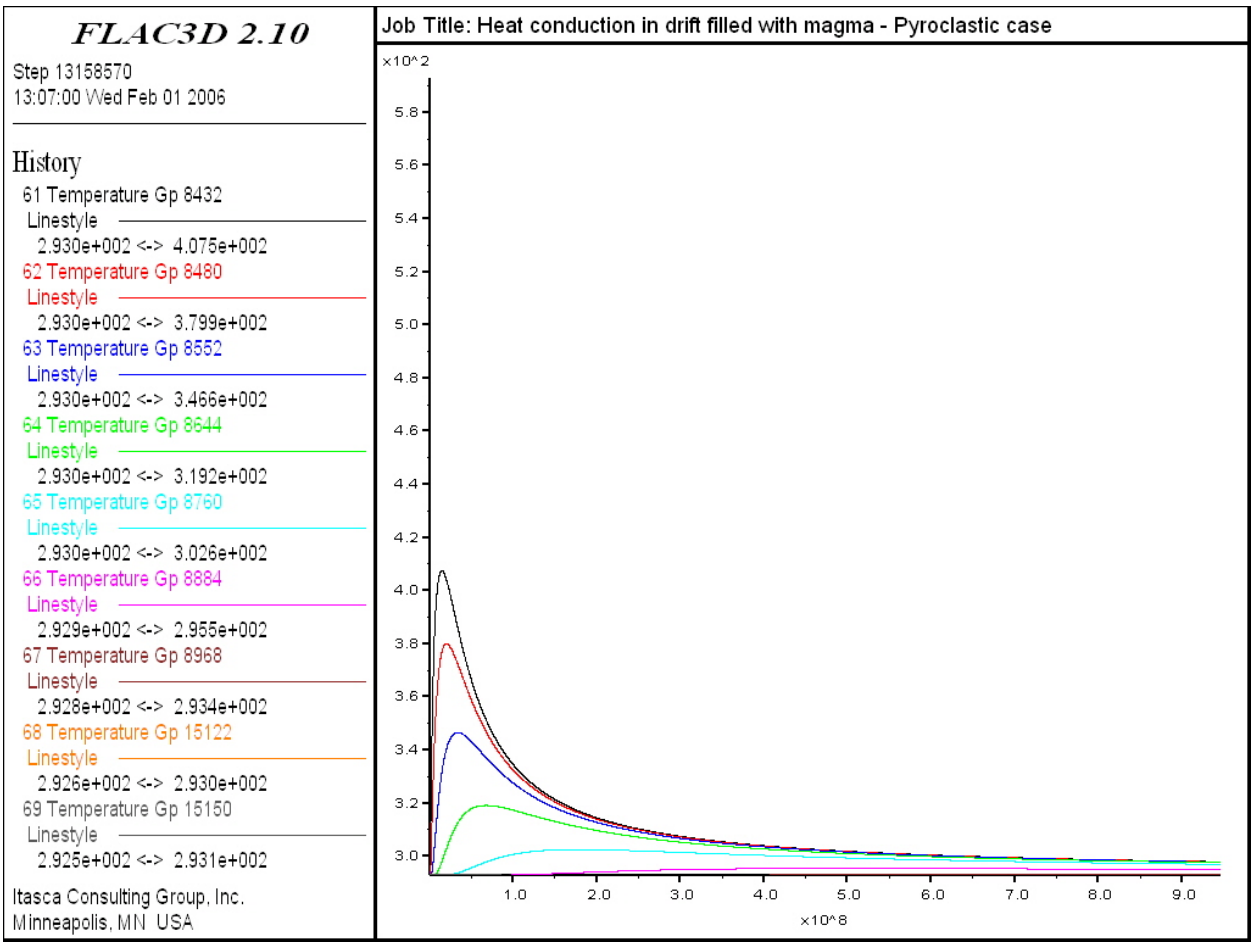

Source: Output DTN: MO0705FREEZING.000, file *\pyroclastic\20deg\rockdown20-30.jpg*.

Figure 6-135. Temperature Histories (temperature in K, time in s) in the Rock Mass below the Waste Package over 30 Years: 1,223 K (950°C) Case—CWP Scenario

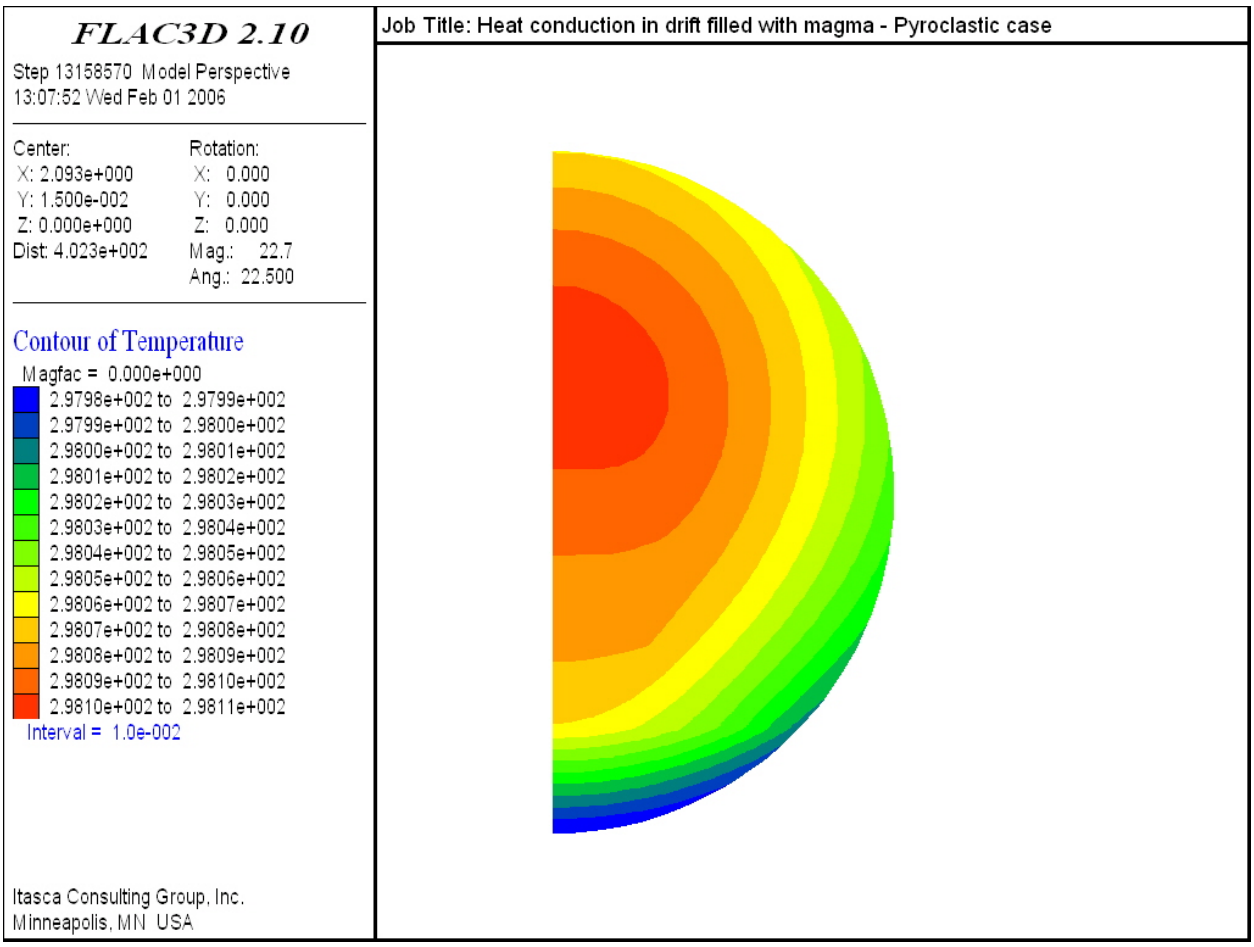

Source: Output DTN: MO0705FREEZING.000, file *\pyroclastic\20deg\mpi20-30.jpg*.

Figure 6-136. Temperature Contours (K) Within the Drift after 30 Years: 1,223 K (950°C)—CWP Scenario

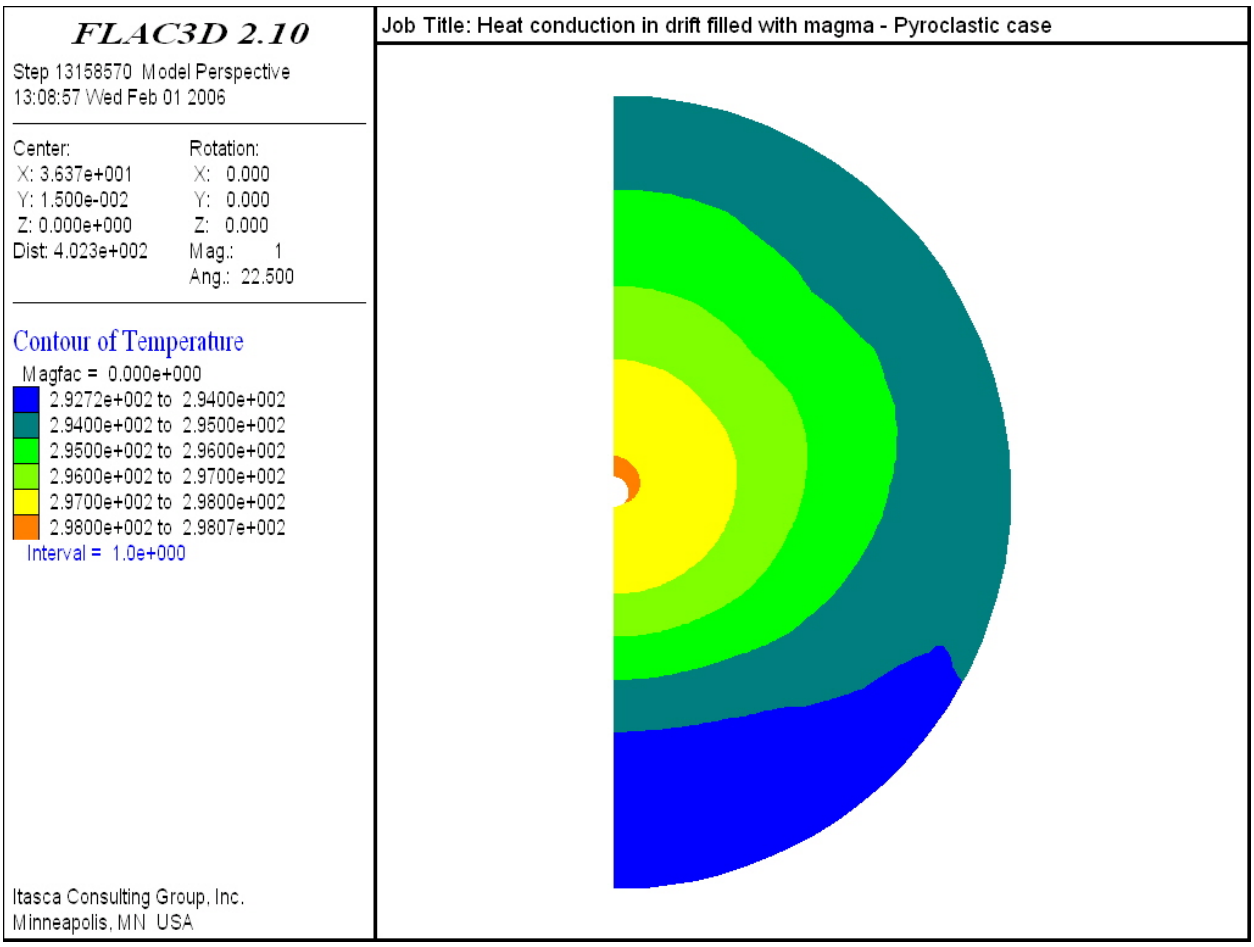

Source: Output DTN: MO0705FREEZING.000, file *\pyroclastic\20deg\temp20-30.jpg*.

Figure 6-137. Temperature Contours (K) Within the Rock Mass after 30 Years: 1,223 K (950°C) Case—CWP Scenario

6.4.7.2.6 Discussion of Alternative Numerical Model

Two sets of numerical simulations were carried out for the HWP and CWP scenarios to study the evolution of temperature in the waste package, invert, and surrounding rock mass after magma intrusion into the emplacement drift. In the HWP scenario, magma intrusion occurs when the peak temperature is reached in the waste package. In the CWP scenario, the intrusion takes place when, in the long term, temperatures in the waste package and the rock mass have returned to ambient temperature. The analyses are two-dimensional and are based on heat transfer by conduction after the magma fills the drift. Peak temperatures in the waste package and the invert fill, as well as durations above several temperatures, are summarized in Table 6-23.

Table 6-23. Peak Temperatures and Durations for Waste Packages, Invert Fill, and Crown

Scenario	Waste Package					Invert			Crown
	T_{max} (°C)	$t_{>T=250°C}$	$t_{>T=350°C}$	$t_{>T=800°C}$	$t_{>T=940°C}$	T_{max} (°C)	$t_{>T=550°C}$	$t_{>T=650°C}$	$t_{>T=100°C}$
CWP, 1150°C	974	351 d	248 d	93 d	45 d	490	0	0	2.3 y
HWP, 1150°C	1,158	>100 y	63 y	259 d	165 d	658	39 d	0	>100 y
CWP, 950°C	748	350.3 d	242.1 d	0	0	356	0	0	1.93 y
HWP, 950°C	988	>30 y	>30 y	308.7 d	99.9 d	553	34 d	0	>30 y

Source: Output DTN: MO0705FREEZING.000, files *\effusive\20deg\effus.sav, \effusive\maximum temperature\effus.sav*, *\pyroclastic\20deg\pyroc.sav* and *\pyroclastic\maximum temperature\pyroc.sav.*

NOTE: To convert to K, add 273.

The results of the simulations for the HWP scenario show that the temperature in the waste package (monitoring point 1) is about 734 K (461°C) 30 years after intrusion, falling to about 555 K (282°C) after 100 years, for the 1,423 K (1,150°C) case. The temperature in the magma (point 11) is 611 K (338°C) for the 1,423 K (1,150°C) case. For times longer than one year after intrusion, the recorded temperatures at monitoring points within the drift are higher for the 1,223 K (950°C) case than for the 1,423 K (1,150°C) case, while temperatures at monitoring points within the rock mass are lower for the 1,223 K (950°C) case than the 1,423 K (1,150°C) case. This effect is attributed to the lower conductivity of the magma in the 1,223 K (950°C) case. One year after intrusion, temperatures in the rock mass are seen to decrease within a radius of about 10.5 m from the center of the drift, and to increase at a slow rate beyond that.

The simulations for the CWP scenario show that at least 90% of the temperature drop at the monitoring points occurs during the first six years after intrusion, by which time all the temperatures are below the boiling point of water. The maximum recorded waste-package temperature (monitoring point 2) is about 1,243 K (970°C) for the 1,423 K (1,150°C) case and 1,023 K (750°C) for the 1,223 K (950°C) case. Also, 30 years after intrusion, the temperatures at monitoring points in the waste package (point 1), magma (point 11), and invert (point 21) have equilibrated down to a value of about 302 K (29°C) for the 1,423 K (1,150°C) case and 298 K (25°C) for the 1,223 K (950°C) case.

The analyses provide estimates of the temperature excursion of the invert fill following an intrusion. This is important because the invert fill will consist of crushed tuff that will become plastic at temperatures above its glass transition temperature. Values for glass transition temperature of acidic rocks average about 873 K (600°C) (Grunder et al. 2005 [DIRS 178351]), with Giordano et al. (2005 [DIRS 178350]) reporting a fairly low value of 821 K (548°C) for dacite and Russell and Quane (2005 [DIRS 176667]) reporting a high of 923 K (650°C) for a dry rhyolite. Invert fill subjected to temperatures above the glass transition would not provide firm support to the pallets or waste packages. Only for the HWP scenario with a hot magma (1,423 K or 1,150°C) does the temperature in the center of the invert fill (point 21) rise above 773 K (500°C), and it barely exceeds 923 K (650°C). In that case temperatures above 823 K (550°C) are expected to last for about eight months. However, the upper surface of the invert fill will be closer to the temperatures experienced by the thin layer of magma between the bottom of the waste package and the invert fill (point 14). Here temperatures will reach or exceed 898 K (625°C) for a period lasting from days (in the 1,223 K (950°C) CWP scenario) to about three years (in the 1,423 K (1,150°C) HWP scenario).

The results of this section are provided only for initial rock temperatures of 293 K (20°C) and 473 K (200°C). To estimate the temperature for times when the wall rock is at an intermediate temperature, it is recommended that one of two approaches be used. For temperatures within approximately 50 K of either end temperature, the temperature may be estimated by adding (or subtracting) the difference of the model initial temperature and the initial temperature for which the result is desired to (or from) the model result. For temperatures that are more intermediate, an average of the two initial temperature results, weighted by the initial temperature for which the result is desired, may be used.

A comparison of the results of this alternative model with those of the base model is presented in Section 7.3.2.1.

6.4.8 Supplemental Analyses

The models and alternative models for thermal evolution of the repository resulting from magmatic intrusion presented in Sections 6.4.1 through 6.4.7 are supplemented by analyses of magmatic pressures (Section 6.4.8.1), magma interactions with waste packages and waste forms (Section 6.4.8.2), and magma chilling in backfilled drifts (Section 6.4.8.3).

6.4.8.1 Magmatic Pressures after Intrusion

The magnitude of pressures that may occur in a magma-filled drift is important in assessing the fate of waste packages engulfed by an intrusion and in assessing the potential for later eruption, which might carry waste form to the surface. This section provides a review of relevant literature, analysis of potential magma pressurization and depressurization mechanisms, and synthesis of "typical" pressure histories.

6.4.8.1.1 Literature Review

Vergniolle and Jaupart (1986 [DIRS 115585]) find that some features of basaltic eruptions suggest that they occur in a separated flow regime (that is, with the gas flow largely being separated from the movement of magma), as opposed to more viscous magmas such as dacite, where the flow is homogeneous.

Bardintzeff and Bonin (1987 [DIRS 178341]) provide an excellent discourse on the mechanism of magma pressurization due to crystallization. Basically, for a basaltic magma with any finite water content, crystallization first removes anhydrous crystals such as olivine or pyroxene from the magma, forcing all of the water into the remaining silicate liquid. The higher water fraction results in a higher pressure.

Tait et al. (1989 [DIRS 178364]) discuss the appropriate value to use for the tensile strength of a volcanic edifice:

> "The overpressure at which fracture occurs is determined by the tensile strength of the surrounding rocks. For pristine basalt and granite Touloukian et al. (1981 [DIRS 178366]) give 8.6 ± 1.4 and 13.8 ± 2.1 MPa respectively. Values for sedimentary rocks are generally a factor of 2 or 3 less than those of basalt. However, the rocks of a volcanic structure are likely to be penetratively fractured

> as a result of eruptive and tectonic events, so values determined in the laboratory on small, homogeneous samples must be treated as upper limits. For example, Einarsson and Brandsdottir [1980 [DIRS 178346]] studied the lateral propagation of a dyke in the Krafla rift zone [in northern Iceland] away from the magma chamber. The tip (traced by seismic events) followed a $t \propto 1/2$ law in accordance with a simple model of magma flow, and they deduced overpressures in the chamber of 1-4 MPa. Rubin and Pollard [1987 [DIRS 178361]] obtained estimates of 3-11 MPa from an analysis of bladelike dikes. The overpressure is equal to twice the tensile stresses at the chamber margin (Appendix A), suggesting tensile strengths of 0.5-5 MPa, much less than quoted above for pristine basalt. In the following, we assume maximum tensile strengths of 8 MPa, though it is likely that values less than this may be appropriate in natural situations." [Appendix A refers to the paper of Tait et al. (1989 [DIRS 178364]), not to this report.]

They note that less than 3% crystallization is required to produce the 4 MPa overpressures at Krafla found by Einarsson and Brandsdottir (1980 [DIRS 178346]). They use the approximation that the magma pressure at failure of the reservoir is $P = P_i + 2\sigma$, where P_i is the initial reservoir pressure, and σ is the tensile strength. In their applications to Krafla and Kilauea (Hawaii), Tait et al. (1989 [DIRS 178364]) use $\sigma = 5$ MPa.

Fagents and Wilson (1993 [DIRS 178347]) modify the earlier model of Wilson (1972 [DIRS 178374]) to estimate the distances to which blocks may be accelerated by a volcanic explosion. They analyzed data from three sites to develop a range of possible driving pressures, launch velocities and driving gas fractions. At Arenal, in Costa Rica, they conclude that a block travelling 5 km had launch conditions in the range of 5 to 30 MPa, 300 to 400 m s^{-1}, and 4% to 10% gas. At Ngauruhoe, in New Zealand, they state, "pressures of 1 to 10 MPa, gas mass fractions of 0.02 to 0.06 and velocities of 220 to 250 m s^{-1} would have sent a 0.8 m projectile to a distance of 2.5 km." For an Alaskan maar, they find source values of 0.1 to 5 MPa, 82 to 85 m s^{-1}, and 5% to 10% gas.

Fagents and Wilson (1993 [DIRS 178347]) also discuss the strength of material constraining gas expansion prior to an eruption, which, for the cases they considered, ranges from unconsolidated glacial till at the Ukinrek maar in Alaska to dense, coherent rock at Arenal. They state:

> However, even massive rocks have joints which limit their strength. In volcanic areas, the scenario which represents the greatest strength is where the caprock is a layer of recently emplaced lava or magma intruded at shallow depth. The melt may have invaded cracks in the pre-existing country rocks and will have chilled against them and at any exposed margins, and the uncooled parts of the magma will be weak because they are largely fluid. However, the zones intermediate between these regions will be solid and uncracked, thus having their maximal strength. A tensile strength of $\sigma = 20$ MPa is probably an upper limit for such a material (Roberts 1969 [DIRS 178359]; Murrell 1969 [DIRS 178356]; Tait et al. 1989 [DIRS 178364]). The pressure acting inside a spherical cavity in this material required to cause failure in tension is then $2\sigma = 40$ MPa (Tait et al. 1989

[DIRS 178364]). The values we have found it necessary to infer above are all significantly smaller than this upper limit.

Woods (1995 [DIRS 178375]) describes a model of ballistic ejection that has been used to estimate magma pressures. He cites previous works by Self et al. (1979 [DIRS 178362]), Kieffer (1981 [DIRS 178353]) and Turcotte et al. (1990 [DIRS 178367]). According to Woods (1995 [DIRS 178375]), Self et al. (1979 [DIRS 178362]) used a model of an explosion where motion of a cap on a reservoir is produced by expansion of the trapped gas. However, Woods (1995 [DIRS 178375]) calls the resulting pressures "rather large" (an expression that is not quantified), and no account is made of the history of decompression during the acceleration. Woods further notes that the model employed by Turcotte et al. (1990 [DIRS 178367]) follows the approach used by Kieffer (1981 [DIRS 178353]) on the Mount St. Helens blast (in Oregon in the U.S.) and is more complete than Self's, with the reservoir being volatile saturated liquid (not gas) and the volatiles instantaneously exsolving as a rarefaction wave propagates into the reservoir. This mixed-phase assemblage then expands isothermally, yielding ejecta velocities up to 400 m/s.

Woods (1995 [DIRS 178375]) then modifies the Turcotte model by considering adiabatic expansion. He cites Tait et al. (1989 [DIRS 178364]) to the effect that driving pressures "typically" will be below 10 MPa ("100 bars"). Woods (1995 [DIRS 178375]) also considers the effects of gravity and wall friction in the eruptive conduit. He uses shock tube theory to calculate a simple upper bound on the velocity of material exiting the conduit. He finds that the velocity generated by magma of a given pressure varies little if only half of the ejecta mass is in thermal equilibrium with the vapor, but if only 5% of the ejecta heat reaches the gas, the ultimate velocity will be about 25% less and about 63% less at 1% equilibration. Woods (1995 [DIRS 178375]) draws no conclusions as to the likely range of pressures in reality.

Nakada et al. (1999 [DIRS 178357]) report 5-cm-diameter breadcrust bombs from the June 8, 1991, eruption of the Unzen (Japan) volcano thrown as far as 5 km from the source, with vertical velocities measured at about 100 m/s. From this, they infer a driving pressure of about 10 MPa for a bulk density for the projectiles of about 2,000 kg m^3.

Boorman et al. (2003 [DIRS 178343]) describe the generation of a high-pressure vapor-dominated phase in the Bushveld-layered intrusive complex in the Republic of South Africa. To support their contention that crystallization leads to such phases, they present analyses using PELE, a Windows-based extraction (Boudreaux 1999 [DIRS 178344]) of the more complete MELTS code (Ghiorso and Sack 1995 [DIRS 178349]), to follow chemical and mineralogical changes in a cooling mafic magma. For a confining pressure of about 200 MPa (equivalent to depths of 7 or 8 km), they found pressure increases of about 20 MPa during cooling of 20 K to 150 K.

Vergniolle and Caplan-Auerbach (2004 [DIRS 178372]) cite estimates by Morrissey and Chouet (1997 [DIRS 181320]) of vent pressures of 0.2 to 5 MPa during the eruption of the Sakurajima (Japan) volcano, the same range for Mount Ruapehu (New Zealand), 1.4 MPa at Shishaldin (in Alaska's Aleutian Islands chain), between 5 MPa and 6 MPa at Ngauruhoe, and ≥5 MPa at Mount Pinatubo (on the island of Luzon in the Philippines), and by Kieffer (1981 [DIRS 178353]), 7.5 MPa for Mount St. Helens**.**

Vergniolle et al. (2004 [DIRS 181321]) report that Hagerty et al. (2000 [DIRS 178352]) found that observed atmospheric-pressure sensor records from Arenal were well reproduced by a 3.4 MPa overpressure source buried 12 m below the surface. They also note that "At Stromboli [one of the Aeolian Islands off the north coast of Sicily in Italy], the initial overpressure at the approximate depth of 300 m is of the order of 11 MPa [Vergniolle 1998 [DIRS 178371]], in agreement with seismic studies (Chouet et al., 2003 [DIRS 178345])."

6.4.8.1.2 Relevance to Yucca Mountain

The literature cited above concerns magma pressures in a wide variety of environments ranging from ultramafic to rhyolitic compositions and including depths ranging from only a few meters to as deep as 7 km. Many of them deal with explosive eruptions, which are not the subject of this report. Consequently, discussion is provided below to address the relevance of these results to the alkali basaltic igneous activity at Yucca Mountain.

The discussion of Bardintzeff and Bonin (1987 [DIRS 178341]) demonstrates the validity of the thesis that crystallization of a relatively dry magma will increase the water content. Tait et al. (1989 [DIRS 178364]) found that less than 3% crystallization is required to produce the 4 MPa overpressures at Krafla. Rubin and Pollard (1987 [DIRS 178361]) indicate that only a small percentage of crystallization can cause overpressures equal to the in situ horizontal stress (as illustrated in Figure 6-3 and as reported by Stock et al. 1985 [DIRS 101027]) at Yucca Mountain. The analyses of Boorman et al. (2003 [DIRS 178343]) provides a numerical implementation of the water concentration mechanism of Bardintzeff and Bonin (1987 [DIRS 178341]). As such it provides a quantitative illustration of the magnitude pressures generated during crystallization for three different mafic magma compositions, although at much higher ambient pressure than would be appropriate to the proposed repository. Together, these four papers leave no doubt that partial crystallization of a magma will generate overpressures in the remaining liquid of a few MPa to 10 MPa or more. An illustration specific to Yucca Mountain is presented below (Section 6.4.8.1.3.1).

A second issue related to the relevance of the cited pressure estimates is that of magma composition. Vergniolle (1998 [DIRS 178371]) finds an 11 MPa overpressure at a basalt site, compatible with the value in Section 6.4.8.1.3. This is "in agreement" with seismic work by Chouet et al. (2003 [DIRS 178345]). Tait et al. (1989 [DIRS 178364]) use a model with overpressure of ~10 MPa, required for failure to apply to Kilauea and Krafla, both basalt sites. However, Einarsson and Brandsdottir (1980 [DIRS 178346]) found that the lower overpressures of 1 to 4 MPa in their model were consistent with observed dike injection rates at Krafla. In an analysis of blade-like dikes, Rubin and Pollard (1987 [DIRS 178361]) estimated overpressures of 3 to 11 MPa. Other estimates, below 7.5 MPa, are for rhyotile to andesite compositions. Thus, it is concluded that the pressure increases in a cooling magma are relevant to the crystallization of an alkali basalt magma such as that at the Lathrop Wells volcano, a natural analogue for a potential igneous event at Yucca Mountain.

That such pressures could build up inside an emplacement drift without the volatile components escaping through fissures is supported by the formation of a ductile zone between the high pressure core of solidifying basalt and the surrounding brittle rock. A semi-quantitative discussion of the formation of this ductile zone, which would act as a seal, preventing high gas

pressures from venting into the tuff, is included at the end of Section 6.4.8.1.3.1. The upper end of this range of pressures may be outside the range of conditions associated with basaltic volcanism of the type found in the Yucca Mountain region; however, they are included in this analysis for completeness.

6.4.8.1.3 Potential Magma Pressure Changing Mechanisms

Section 6.4.8.1.3.1 presents an analysis of the magma pressurization mechanism described by Bardintzeff and Bonin (1987 [DIRS 178341]), using an approach similar to that of Boorman et al. (2003 [DIRS 178343]). A discussion of mechanisms that might limit pressures in a crystallizing magma is provided in Section 6.4.8.1.3.2, and analyses of several potential scenarios in which magma breaks out at the surface, thereby reducing pressures at repository level, are found in Section 6.4.8.1.3.3.

6.4.8.1.3.1 Magma Pressurization Analysis

The pressurization mechanism of Bardintzeff and Bonin (1987 [DIRS 178341]) can be illustrated for an alkali basalt magma such as the Lathrop Wells basalt using data from *Final Report of the Igneous Consequences Peer Review Panel* (Detournay et al. 2002 [DIRS 169660]), the thermal analysis in Appendix D, and *Characterize Eruptive Processes at Yucca Mountain* (SNL 2007 [DIRS 174260]). Results of these reports can be reworked to estimate the increase in water content that would occur when a magma with only a small fraction of water crystallizes, after which the pressure generated can be estimated analytically. In this analysis, the volatiles are considered to be trapped in the interior of the drift, being prevented from venting into the porous country rock by a layer of plastically deformable hot—perhaps even partially molten—rock surrounding the core that contains the waste packages. Thus, as the volume of silicate liquid dissolving a fixed mass of volatiles decreases, the pressure generated by those volatiles in solution increases.

Inputs and Assumptions—The Igneous Consequences Peer Review Panel (ICPRP) provided plots of weight percent of solids in alkali basalt magmas with various water contents and at various pressures (Detournay et al. 2002 [DIRS 169660], Appendix Table 2E), showing that the sequence of crystallization of alkali basalt magma at decreasing temperatures below the liquidus depends on the initial pressure and on the bulk water content. Results for two cases are summarized in Table 6-24, which presents the weight fraction of various solid phases as a function of temperature for magma initially at 100 MPa with 2 wt % of water and for dry magma initially at 10 MPa. Both the temperatures and the percentages were read off the ICPRP plots cited; accuracy of tabulated temperature differences (ΔT) are on the order of 2 K (for dry) to 5 K (for wet); accuracies of percentages are on the order of 1%.

Table 6-24. Crystallization Sequences for Alkali Basalt.

T (K)	T (°C)	ΔT (°C)=(K)	Wt % Solid					
			Total	ol	sp	plag	cpx	ap
2% water, 100 MPa								
1,430	1,157	0	0	0.0	0.0	0.0	0.0	0.0
1,373	1,100	57	5	2.5	2.5	0.0	0.0	0.0
1,323	1,050	107	23	3.5	7.0	3.0	9.0	0.5
1,273	1,000	157	40	4.5	9.5	12.0	13.0	1.0
1,223	950	207	50	5.0	12.0	19.0	13.0	1.0
Dry, 10 MPa								
1,457	1,184	0	0	0.0	0.0	0.0	0.0	0.0
1,438	1,165	19	3	0.0	0.0	3.0	0.0	0.0
1,418	1,145	39	16	5.5	0.0	11.5	0.0	0.0
1,398	1,125	59	32	9.0	0.0	23.0	0.0	0.0
1,378	1,105	79	53	9.0	5.0	32.0	7.0	0.0

Source: Output DTN: SN0705MAGPRESS.001 file *Meltfraction.pdf*.

NOTE: ol = olivine, sp = spinel, plag = plagioclase, cpx = clinopyroxene, ap = apatite.

The relation between water content and magma pressure is taken from Equation 6-1 of *Characterize Eruptive Processes at Yucca Mountain,* Nevada (SNL 2007 [DIRS 174260]), which is inverted to:

$$P = \left(\frac{n}{6.8 \times 10^{-8}} \right)^{10/7} \qquad \text{(Eq. 6-108)}$$

If the assumption is made that the volume of the combined mass of magma and crystals does not change during crystallization and that no gas escapes that volume, the mass fraction of water in the magma after X wt % has crystallized will be related to the original mass fraction of water, n_o, by:

$$n = \frac{n_0}{1 - X/100} \qquad \text{(Eq. 6-109)}$$

Because all of the minerals in Table 6-24 are denser than the original magma (2,663 kg m^3 for dry magma to 2,474 kg m^3 for magma with 4 wt % water (SNL 2007 [DIRS 174260], Table 6-5)), this assumption is suspect. However, the density of the residual liquid will be less than that of the original uncrystallized magma, which will compensate, to some extent, for the higher densities of the crystals.

Results—Equations 6-108 and 6-109 can be combined to yield a relation between wt % crystallization and magma pressure. This relation is illustrated in Figure 6-138.

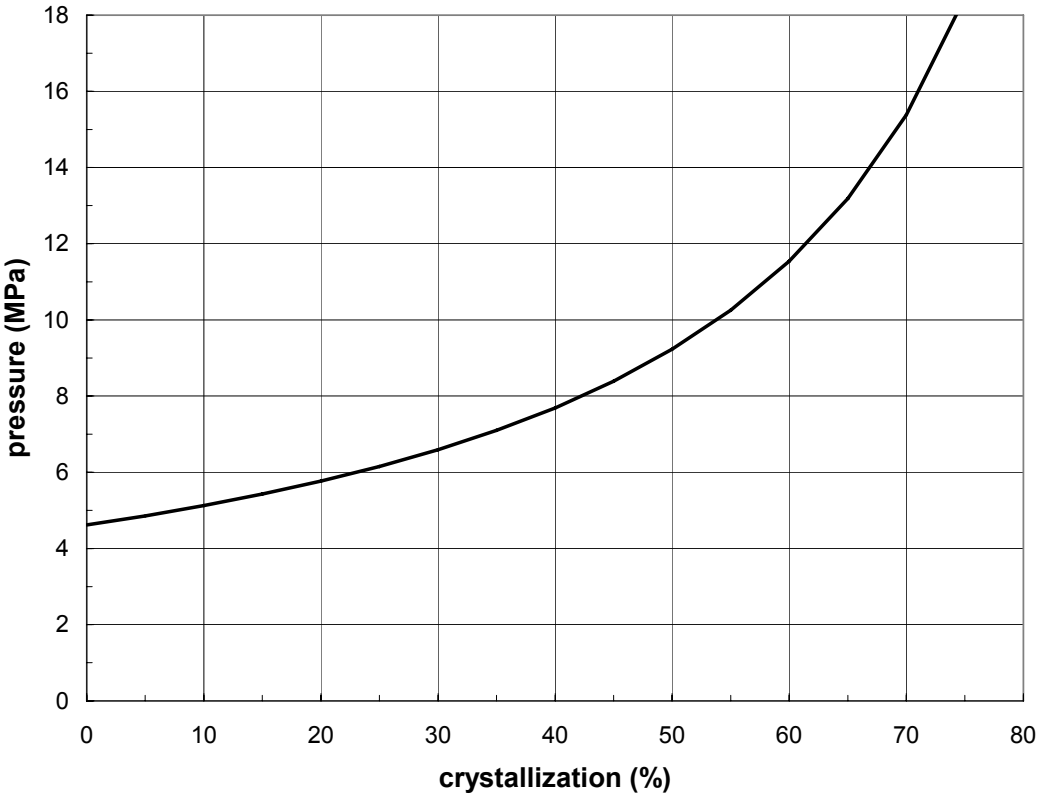

Output DTN: SN0705MAGPRESS.001, file: *CrystallizationPressure.xls*; tab: "P(%) (3)."

Figure 6-138. Relation of Magma Pressure to Degree of Crystallization for Alkali Basalt

When this relation is combined with the sub-liquidus temperatures needed to generate degrees of crystallization, the relation between temperature drop and magma pressure shown in Figure 6-139 results. This is plotted in terms of sub-liquidus temperature, because the actual liquidus temperature depends critically on both the concentration of water present and the pressure, as does the rate of crystallization (c.f., Table 6-24).

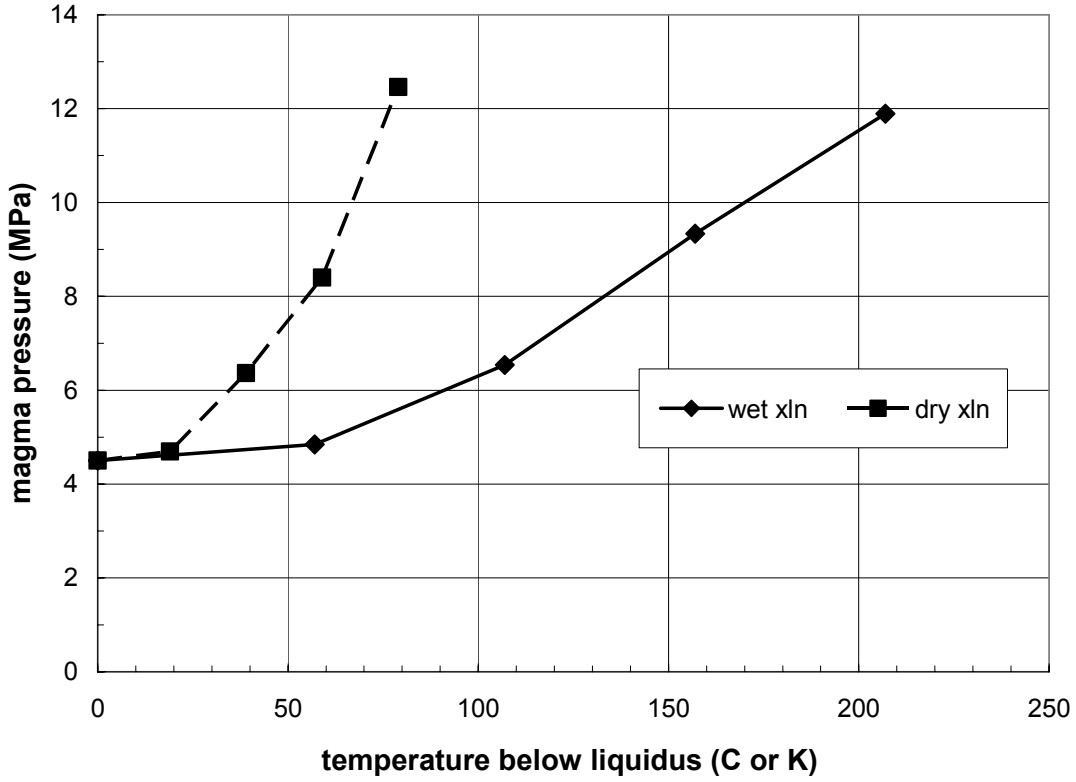

Output DTN: SN0705MAGPRESS.001, file: *CrystallizationPressure.xls*; tab: "P(dT)."

Figure 6-139. Relation of Magma Pressure to Degree of Sub-liquidus Cooling for Two Different Crystallization Histories for Alkali Basalt Magma

Discussion—The alternative thermal model in Section 6.4.7.2 presents two-dimensional calculations of the cooling of an emplacement drift, including both waste packages and invert fill, inundated with 1,423 K (1,150°C) magma. These calculations considered both "cool" waste packages with no internal heat sources and "hot" waste packages with a decaying internal heat source initially just above 1,100 W/m. From Figure 6-139, it is seen that isochoric pressures would increase by approximately 8 MPa when temperatures in the magma drop more than about 70 K to 200 K below the liquidus. Based on the cooling histories in Figures 6-108 and 6-97, pressures would increase by by approximately 8 MPa after one to two months for crystallization following the dry or wet paths, respectively, in a drift with "cool" waste packages or after 1.5 to 3 months in a drift with "hot" waste packages.

This estimate of pressurization rate can be used to infer the strain rates that would be associated with crystallization-induced pressures. To an order of magnitude, the elastic strain rate, $\dot{\varepsilon}$, produced by inflating a void in an elastic body will be:

$$\dot{\varepsilon}_{el} = \left(\frac{dP}{dt}\right) \Big/ E \,, \qquad \text{(Eq. 6-110)}$$

where dP/dt is the rate of pressurization, and E is Young's modulus of the surrounding rock (typically about 15 GPa for tuff at Yucca Mountain). If pressures build to 8 MPa over two months, dP/dt is 1.5 $Pa \cdot s^{-1}$. The elastic strain rate then would be on the order of 10^{-10} s^{-1}. Although plastic (or creep) strain rates may exceed the elastic strain rate by a few orders of magnitude, an overall deformation rate of $<10^{-6}$ should be an upper limit for defining the brittle-ductile transition for such loading. The synthesis by Rocchi et al. (2002 [DIRS 178360], especially Figures 6 through 8, pp. 34-35 and 38) of basalt deformation data over a wide range of temperatures and stresses indicates that, at such low strain rates, even at the modest confining stresses appropriate for repository depth, hot sub-solidus basalt will deform in a ductile fashion. The data in the low-stress region of interest are sparse, at best, but existing data indicate that hot basalt will be ductile under these conditions. A ductile zone between the high-pressure core of solidifying basalt and the surrounding brittle rock could act as a seal, preventing high gas pressures from venting into the tuff. Although this conclusion will apply to cylindrical shapes such as conduits and drifts, it is less clear how a pressurized dike will respond. It is possible that pressurization of a dike may not be relevant, as a dike only 1 m thick would be expected to solidify completely within only two days after magma flow has stopped, and it would cool enough in less than a week to permit brittle fracture (as estimated by rescaling the results in the upper part of Figure D-1 in Appendix D) by the square of the dike width. (This calculation is located in output DTN: SN0705MAGPRESS.001, file *DikeCoolingTimes.xls*).

The results of this section provide an illustration of the extent to which crystallization of magma can generate high pressures. However, because of the limiting approximations and assumptions, it is just an illustration. The estimates must be considered as approximate upper limits because of the assumptions that the volumes of the solid and liquid phases do not decrease during crystallization. An accurate calculation of the pressures generated in a fixed volume can be done with the same MELTS program (Ghiorso and Sack 1995 [DIRS 178349]) used by the ICPRP to calculate the crystallization sequences in Appendix Table 3E of Detournay et al. (2002 [DIRS 169660]), but that code is not qualified for Yucca Mountain applications. It is also an upper limit, because the assumption is made that no gas escapes. Extrapolation to complete crystallization using Equation 6-109 indicates an infinite pressure, which clearly is not possible. At some pressure, the surrounding solidified magma must fracture and allow some of the gas to escape. Nevertheless, a cylindrical pressure vessel surrounded by a ductile layer, with both of them enclosed in a massive elastic material, is a standard recipe for strong confinement of high-pressure gases.

6.4.8.1.3.2 Pressure Limiting Mechanisms

According to two-dimensional analyses such as those in Section 6.3.3.4 for incompressible fluids, the pressure in a dike at some distance below the magma front is practically equal to the component of the in-situ stress normal to the plane of the dike. At repository depth beneath Yucca Mountain, minimum in situ stress is about 3.6 MPa (Stock et al. 1985 [DIRS 101027]). A short distance below the magma front, the pressure could exceed in situ stress by approximately 1 MPa. While the dike is propagating, the maximum magma pressure at repository depth can reach 4.6 MPa, based on computations found in Section 6.3.3.4.1. Thus, it would seem that pressures as high as 11 MPa (Vergniolle 1998 DIRS 178371]) or 10 MPa (Tait et al. 1989 [DIRS 178364]) will not arise at Yucca Mountain because they would drive the dike horizontally.

However, greater magma pressures than those inside the dike could be generated in an isolated drift or in a conduit because they are cylinders, not sheets. For a cylinder, the limiting pressure that will cause hydrofracture of the surrounding rock is given by the following formula (Goodman 1980 [DIRS 101966], Equation 4.8, page 114):

$$P = 3\sigma_n - \sigma_N + T \qquad \text{(Eq. 6-111)}$$

where σ_n is the least confining stress normal to the axis of the cylinder, σ_N is the greatest confining stress normal to the axis of the cylinder, and T is the tensile strength of the country rock. (The convention used in this equation is that the compressive stresses are positive.) Assuming that the horizontal principal stresses are equal and using values consistent with the discussion of the previous paragraph, this would limit pressures in an isolated vertical cylinder, such as a conduit at a depth of 300 m at Yucca Mountain, to 7.2 MPa, assuming the horizontal confining stress is isotropic and equal to half the vertical overburden stress (i.e., $\sigma_n = \sigma_N = 3.6$ MPa plus the tensile strength of the rock). Similarly, the maximum magma pressure inside an isolated horizontal cylinder, such as a drift, would be limited to 3.6 MPa ($\sigma_n = 3.6$ MPa, $\sigma_N = 7.2$ MPa, with the greatest stress being vertical) plus the tensile strength of the rock. If the fracture toughness, K_{Ic}, of the country rock at repository confining stresses is about 1 MPa·m^{½} (Funatsu et al. 2004 [DIRS 178348]) and the length, a, of the longest pre-existing crack intersecting the cylinder is 1 m, the tensile strength of the surrounding tuff is $T = K_{Ic}\cdot(\pi\cdot a)^{-½} = 0.56$ MPa. Taken together, the limit rises to about 4.2 MPa, or as much as 5.4 MPa if cracks are only 0.1 m long.

However, even that may not constitute a true upper limit, as the outer portions of either type of cylinder would include a zone of solidified but plastically deformable hot basalt that would retard fracture propagation. Such a material with relatively small shear stiffness (and strength) when pressurized by magma against relatively stiff country rock would develop an almost isotropic compressive stress state, never going into tension. Before it ruptures by exceeding rupture strain, this material will provide an excellent seal to magma inside the cylinder. This effect would also limit formation of a "dog-leg" secondary hydrofracture to provide an alternative path for waste form to reach the surface. It might be possible to estimate a more realistic upper limit using a full visco-elasto-plastic analysis, but that would require verifiable values for constitutive properties for hot basalt at temperatures just below and just above the solidus, which are not available.

Even though pressure in a cylinder can exceed the horizontal confining stress, at some point the conduit or drift may intersect a planar dike that is still fluid, so the limit set out in the first paragraph of this section needs to be addressed. That limit is based on a two-dimensional analysis with an infinite strike length. For finite strike length L, the aspect ratio, w/L, of a crack is related to the excess pressure ($P_d = P - \sigma_h$) and the elasticity of the host rock (G = shear modulus, ν = Poisson's ratio) by Equation 6-112 (Valentine and Krogh (2006 [DIRS 177282]):

$$\frac{w}{L} = \frac{P_d}{G(1-\nu)}. \qquad \text{(Eq. 6-112)}$$

Excess pressures calculated with this formula (Table 6-25) indicate that a dike with L = 1 km would inflate from a = 0.45 m to a = 1.0 m as the total pressure rose from 7 MPa to just over 11 MPa. The relation is linear, so a vertical blade-like dike with L = 500 m would inflate to only 0.5 m; one with L = 1,500 m would inflate to 1.5 m.

Table 6-25. Magma Pressures in Equilibrium with Three-Dimensional Dikes at Yucca Mountain.

P_{total} (MPa)					
w(m)↓ \ l(m)→	**500**	**1,000**	**1,500**	**2,000**	**4,000**
0.3	8.2	5.9	5.1	4.7	4.1
0.45	10.6	7.1	5.9	5.3	4.4
0.5	11.4	7.5	6.1	5.5	4.5
0.75	15.3	9.4	7.5	6.5	5.0
1	19.2	11.4	8.8	7.5	5.5
1.5	27	15.3	11.4	9.4	6.5
3	51	27	19.2	15.3	9.4
7	113	58	40	31	17.3

Source: Output DTN: SN0705MAGPRESS.001, tab "[Calc]" of file *dikeWidthPressure.xls*.

Pressures up to 20 MPa or 30 MPa would result in inflations up to 1.5 m to 3 m, which are at the low end of dike apertures found at Paiute Ridge by Valentine and Krogh (2006 [DIRS 177282]). On the other hand, this formula is valid for an elastic crack, which cannot propagate laterally. In a typical rock mass, overpressures of less than 0.1 MPa are needed to cause a 1-km-long crack to propagate in the strike direction. Furthermore, Valentine and Krogh (2006 [DIRS 177282]) propose that the crust was in a tensile or near-tensile state during dike intrusion at Paiute Ridge, so that wider dikes were accompanied by reactivation of the faults and extension of the country rock. Thus, it is concluded that pressures of that order are unlikely to be sustained in a dike, as magma crystallizes after intrusion at Yucca Mountain.

6.4.8.1.3.3 Depressurization Scenarios

This section presents analyses addressing various aspects of the movement or blockage of magma during a potential intrusion into drifts at Yucca Mountain. These situations are representative of some geometries that potentially could develop at some time during the course of an igneous event, but they should be considered as upper-limiting cases. Three cases in which the primary path for magma to reach the surface is blocked are analyzed, addressing blockage by slumping of scoria, solidification during a pause in eruption, or blockage by faulting. The potential for magma breakout is evaluated in these cases. These analyses apply numerical codes to simulate the specific conditions. Direct input parameters, simplifications, and idealizations are discussed in each subsection.

Three different scenarios or configurations for blockage of magma in a conduit or dike were considered as shown in Figures 6-140 through 6-142. Figure 6-140 considers magma flow through a conduit feeding a scoria cone and involves the blockage of magma by loose scoria slumping inward, blocking the vent with solidification of underlying magma, resulting in a solid plug at the top of the conduit. Whether the slumping prevents magma flow long enough to

permit the solidification, or a temporary halt in magma flow allows the scoria to slump inward, this scenario is intended to examine the phenomena that would be expected following a pause in building of a scoria cone such as the one at Lathrop Wells volcano. The second configuration (Figure 6-141) arises from a temporary interruption of magma supply to a lava flow leading to formation of a plug of solidified magma blocking a conduit. This scenario investigates the effect of intermittency of magma supply to an effusive eruption that has produced a lava flow. A third scenario (Figure 6-142) may arise if a syn-eruptive displacement on a fault cuts a feeder dike at depth. This case addresses one effect of earthquakes that frequently accompany volcanic activity including dike injection. All three analyses provide information on the limits of pressure that might build up in a dike if flow were halted; this can be related to estimates of how closely a dike can approach a drift before it will break through the intervening rock (SNL 2007 [DIRS 177432], Appendix G). The third scenario also provides insight into the potential for magma to be diverted from its original path to a different path along a newly formed fault.

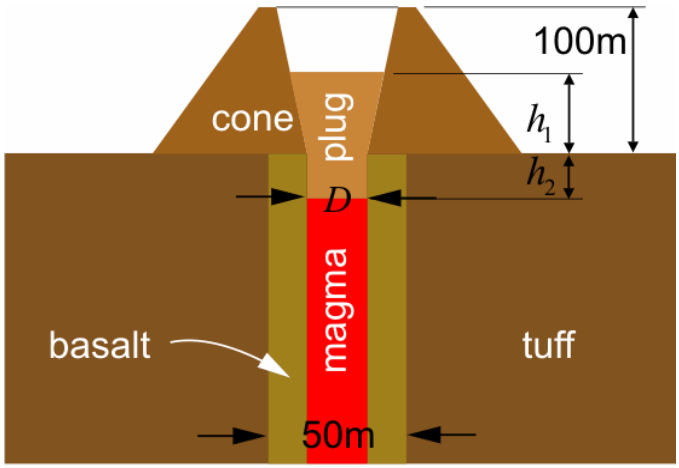

Source: For illustration purposes only.

NOTE: Axially symmetrical about the center of the conduit.

Figure 6-140. Configuration for Analysis of Pressure Build-Up by Slumping in a Scoria Cone

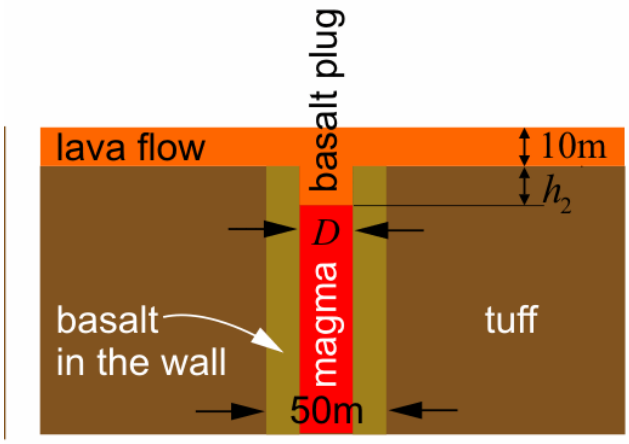

Source: For illustration purposes only.

NOTE: Axially symmetrical about the center of the conduit.

Figure 6-141. Configuration for Analysis of Pressure Build-Up under a Lava Flow

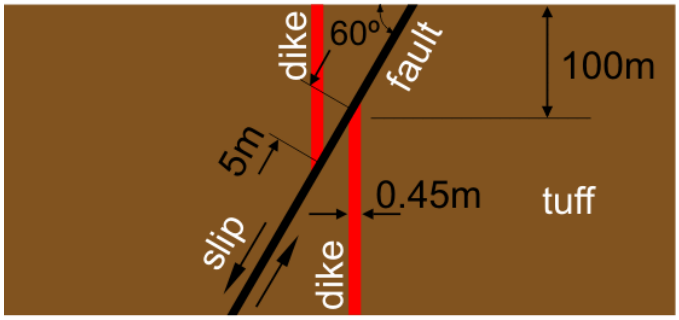

Source: For illustration purposes only.

Figure 6-142. Configuration for Analysis of Pressure Build-Up for Dike Cut by Fault

Slumping: *Inputs*—Roller boundary conditions (fixed displacement normal to the boundary, free in the tangential direction) were applied at the bottom of the calculation (150 m below the original ground surface for the conduits, 500 m for the dike) and the vertical far-field boundaries (240 m from the axis of the conduit or 500 m on either side of the dike). Gravitational acceleration of 9.81 m/s^2 (rounded from Incropera and DeWitt 2002 [DIRS 163337], Table A-6) acted vertically downward throughout. All materials were represented as elastic, perfectly plastic, Mohr- Coulomb materials having the properties listed in Table 6-26.

Table 6-26. Material Properties

Material	Density (kg m^3)	Bulk Modulus (MPa)	Shear Modulus (MPa)	Cohesion (MPa)	Friction Angle (°)	Tensile Strength (MPa)	Source
Loose scoria	1,300	16.7	10	0	40	0	Assumed equivalent to generic gravel-like material, and estimated based on Duncan et al. 1980 [DIRS 161776], Table 5 and Equation 3. Cohesion of 0.1 MPa is for undisturbed scoria. Stiffness (shear modulus) of loose scoria is assumed to be 50% of stiffness of undisturbed scoria.
Undisturbed scoria	1,500	33.3	20	0.1	40	0	
Basalt	2,960	25,000	19,500	32.7	50	27	Gupta and Seshagiri Rao 2000 [DIRS 174063], Tables 2 and 3, except friction angle from Hoek and Brown 1997 [DIRS 170501], Figure 8, with geologic strength index (GSI) ~90 and m_i = 25. GSI is index for rock mass characterization. m_i is parameter in failure criteria listed by Hoek and Brown 1997 [DIRS 170501].
Tuff	2,310	16,800	12,100	3.9	57	2.35	Assumed based on data presented in Appendix I, Tables I-1 and I-2. Bulk modulus and shear modulus are calculated from modulus of elasticity and Poisson's ratio (E = 29.36 GPa, *v = 0.21)* of TCw unit.

Values for bulk and shear moduli in this table, if not directly presented in the cited source documents, were developed from the inputs cited using the relations $K = E/3(1-2v)$, and $G=E/2(1+v)$, where K = bulk modulus (or modulus of elasticity), G = shear modulus, E = Young's modulus, and v = Poisson's ratio (Timoshenko and Goodier 1970 [DIRS 121096], pp. 10 and 11). The values used for rock mass properties of tuff are assumed based on a design document (BSC 2003 [DIRS 163439], Table 5-9) and justified in Appendix I (Table I-1 and I-2). The elastic properties are within 6%. Strength values (including cohesion and friction angle) have larger deviations (see Table I-1), but all of these values are very small compared to the solidified basalt that separates the magma from the tuff, and so will have a minor effect on the results of the analysis. The zone of solid basalt surrounding the conduit is assumed to be 50 m in diameter, the mode of the distribution presented in DTN: LA0612DK831811.001 [DIRS 179987]. The cross-sectional area of the conduit actively transporting magma is assumed to be either 5 m or 15 m in diameter. These values include the recommended mean conduit diameter (15 m) given in DTN: LA0612DK831811.001 [DIRS 179987] and a value between the minimum (1 m) and the mean (8 m) of the dike width from the same source. This range of input values is intended to illustrate the nature of variations that could arise from natural variability. The higher value is consistent with the statement in *Characterize Eruptive Processes at Yucca Mountain, Nevada* (SNL 2007 [DIRS 174260], Section 6.3.3.3) that the whole cross-sectional area of a conduit may not be active at the same time. A low value will result in large values for magma pressure required to break through a blockage. The larger value is expected to be

representative of conduits which are likely to form in a potential Yucca Mountain eruptive volcanic event.

The scoria cone is assumed to have a height of 100 m, an outer slope of 50°, and a summit crater diameter twice the diameter of the conduit at the base of the cone (i.e., 30 m for a 15-m conduit diameter, and 10 m for 5-m conduit diameter). The height is on the order of the Lathrop Wells volcano (~140 m) (SNL 2007 [DIRS 174260], Appendix C, Section C4). The angle of the outer slope of the cone has a negligible effect on the results of the calculations in that the effect of the angle on the stresses beneath the cone and breakout pressure is secondary. The summit crater diameter was selected to result in a relatively steep slope inside the crater. A steeper slope of the crater wall will result in a larger breakout pressure. The assumed geometry of the crater inside the cone is possible, because the calculations showed that the wall of the crater inside the cone was stable under static conditions for the selected properties of the undisturbed scoria. Because it is expected that an average slope of the crater wall will be smaller than the assumed slope, the selected geometry yields an overestimate of the breakout pressure. Higher breakout pressures will increase the potential for formation of a secondary dike out of a drift.

Computational Approach—This analysis of blockage by scoria slumping into an eruptive cone used the FLAC code, V. 4.04 (STN 10167-4.04-00 [DIRS 172432]) with an axisymmetric mesh (Figure 6-8a). Undisturbed scoria properties (Table 6-26) were used to represent the volcanic cone; the plug was treated as loose scoria (Table 6-26). The interface between the loose and undisturbed scoria was assumed to have a friction angle of 30°, except for three calculations where the interface friction angle was 40°. The mechanical properties of solidified basalt used in this analysis, as listed in Table 6-26, were for room temperature. Rocchi et al. (2004 [DIRS 173995]) found that the mechanical properties of basalt are not affected by temperatures below 600°C, so the effect of temperature on mechanical properties was not included in the calculations. Calculations considered various heights of the scoria plug, both above and below ground, two different conduit diameters, and two different values for the friction angle between the plug and the conduit wall.

The calculation proceeded in three steps. First, stresses due to cone construction and convergence around the conduit after the magma overpressure in the conduit dropped to zero were calculated. Then, the plug was generated inside the conduit and the calculation was run to equilibrium, generating horizontal stresses at the contact between the plug and the conduit wall due to lateral deformation of the plug under gravity. Finally, uniform magma overpressure was applied on the conduit walls and the bottom of the plug. Magma overpressures were increased in increments of 0.25 MPa and stresses were allowed to equilibrate before the next pressure increment. Breakout was manifested by the inability of the simulation to achieve equilibrium.

Results—A summary of the breakout pressures calculated assuming different dimensions of the scoria plug is listed in Table 6-27. Two breakout mechanisms (hydrofracture and shear failure) were considered.

Sensitivity of breakout pressure prediction to the diameter of the conduit and the friction angle was investigated in the calculations by varying those two parameters. Increase in friction angle resulted in increase of the breakout pressure (cases 10 and 12 relative to cases 4 and 6, respectively) as did a smaller conduit diameter (cases 13 and 15 relative to cases 1 and 3,

respectively). When the breakout was the result of a shearing mechanism (highlighted rows in Table 6-27), upper-bound plug accelerations were calculated and are listed in the last column of Table 6-27. These accelerations are based on the entire resistance (i.e., friction, tensile, and shear strength of scoria) to plug movement vanishing at the onset of breakout; the only forces acting are gravity, inertia, and magma pressure. Accelerations are tabulated only for cases where the pressure required to push the entire scoria plug upward is less than the hydrofracture pressure.

There are two possible mechanisms for magma breakout from the plugged conduit. A first mechanism is that the entire scoria plug may move upward; in most cases this would include portions of the undisturbed volcanic cone. The second involves development of hydrofractures in the conduit wall. When the hydrofracture mechanism is expected to result from magma pressures lower than would be needed to move the scoria plug, the breakout pressure is indicated in Table 6-27 in parentheses along with the pressure needed to move the plug.

Based on the stress field around the pressurized conduit, such hydrofractures would initially be vertical; however, upon propagating into the rock mass, they may intersect fractures of other orientations before reaching the surface. Propagation of hydrofractures was not analyzed directly, only the conditions (pressure) required for fracture initiation. The pressures listed in Table 6-27 are calculated using the tensile strength of basalt measured by Gupta and Seshagiri Rao (2000 [DIRS 174063], Table 3), which was determined on intact samples of relatively small size, for which preexisting fractures and defects in the tested specimens were small compared to the size of the tested sample.

Actual in situ tensile strengths may be either higher or lower. On the one hand, thermal cycles may cause fracturing of the basalt in the conduit, resulting in significant reduction of the tensile strength compared to values determined on the intact samples. Rocchi et al. (2004 [DIRS 173995], Table 3) measured the tensile strength of small basalt samples and reported a value of 6.4 MPa. Pressures needed to initiate hydrofractures listed in Table 6-27 are based on this value. If the tensile strength of the basalt rock (in the immediate wall of the conduit) is 6.4 MPa and if the scoria plug fills a portion of the conduit below the ground surface (h_2>0), then hydrofracture of the conduit wall is expected at magma pressures near 10 MPa (cases 6, 8, 9, 11, and 12).

On the other hand, if a layer of basalt, plastically deformable due to near-solidus temperatures but contained by surrounding elastic basalt and tuff, could block hydrofractures, much higher magma pressures could build up. So the high tensile strength of Gupta and Seshagiri Rao (2000 [DIRS 174063], Table 3) was used in order to reach high enough magma pressures to investigate the second mechanism (i.e., to determine deformations of the plug and cone). Figure 6-143 shows the deformation of the scoria plug (arrows or “vectors”) and plasticity conditions in the cone for (a) case 3 and (b) case 1, illustrating the failure mechanism when the critical pressure is achieved. In both cases, deformation shortens the scoria plug and moves it upward.

Table 6-27. Magma Breakout Pressures

Case No.	h_1 (m)	h_2 (m)	D (m)	Friction Angle (°)	Breakout Pressure[a] (MPa)	Acceleration (m/s^2)
1	20	0	15	30	0.5	16
2	60	0	15	30	2.7	19
3	100	0	15	30	7.0 (5.8)	
4	20	25	15	30	1.8	28
5	60	25	15	30	8.8	51
6	100	25	15	30	19.6 (9.6)	
7	20	50	15	30	6.9*	71
8	60	50	15	30	21.0 (10.1)	
9	100	50	15	30	32.7 (10.2)	
10	20	25	15	40	5.6*	87
11	60	25	15	40	24.3 (9.7)	
12	100	25	15	40	27.8 (9.7)	
13	20	0	5	30	0.8*	25
14	60	0	5	30	9.5 (7.5)	
15	100	0	5	30	10.0 (7.5)	

[a] Critical breakout pressure required to move the entire scoria plug. The value in parentheses is the pressure that causes hydrofracture of the conduit wall. The expected breakout pressure is the smaller of the two.

Source: Output DTN: MO0705BREAKOUT.000, case 1 from FLAC save files in folder \scoria plug\conduit_00mPlug_20mConePlug\; case 2 from FLAC save files in folder \scoria plug\conduit_00mPlug_60mConePlug\; case 3 from FLAC save files in folder \scoria plug\conduit_00mPlug_100mConePlug\; case 4 from FLAC save files in folder \scoria plug\conduit_25mPlug_20mConePlug\; case 5 from FLAC save files in folder \scoria plug\conduit_25mPlug_60mConePlug\; case 6 from FLAC save files in folder \scoria plug\conduit_25mPlug_100mConePlug\; case 7 from FLAC save files in folder \scoria plug\conduit_50mPlug_20mConePlug\; case 8 from FLAC save files in folder \scoria plug\conduit_50mPlug_60mConePlug\; case 9 from FLAC save files in folder \scoria plug\conduit_50mPlug_100mConePlug\; case 10 from FLAC save files in folder \scoria plug\conduit_25mPlug_20mConePlug_fric40\; case 11 from FLAC save files in folder \scoria plug\conduit_25mPlug_60mConePlug_fric40\; case 12 from FLAC save files in folder \scoria plug\conduit_25mPlug_100mConePlug_fric40\; case 13 from FLAC save files in folder\scoria plug\conduit_00mPlug_20mConePlug_5mRadius\; case 14 from FLAC save files in folder \scoria plug\conduit_00mPlug_60mConePlug_5mRadius\; case 15 from FLAC save files in folder \scoria plug\conduit_00mPlug_100mConePlug_5mRadius\.

NOTE: Highlighted rows indicate breakout resulting from a shearing mechanism.

Figure 6-144 illustrates tangential stress profiles in the solidified basalt immediately adjacent to the conduit wall (i.e., 1.25 m from the wall) for several magma pressures for a scoria plug filling the entire 100-m depth of the scoria cone and extending 25 m beneath the original ground surface (case 6, Figure 6-144(a)) or 50 m (case 9, Figure 6-144(b)). Depths in Figure 6-144 are relative to the original (pre-cone) ground surface. The hydrofracture pressure is the smallest magma pressure that generates the tensile stress in the wall equal to the tensile strength of the basalt. The tensile strength measured by Rocchi et al. (2004 [DIRS 173995], Table 3) is indicated by the dashed vertical line. For case 3 where $h_2 = 0$ (Table 6-27), the hydrofracture pressure is only 6.5 MPa, almost equal to the 7 MPa required to displace the entire scoria plug.

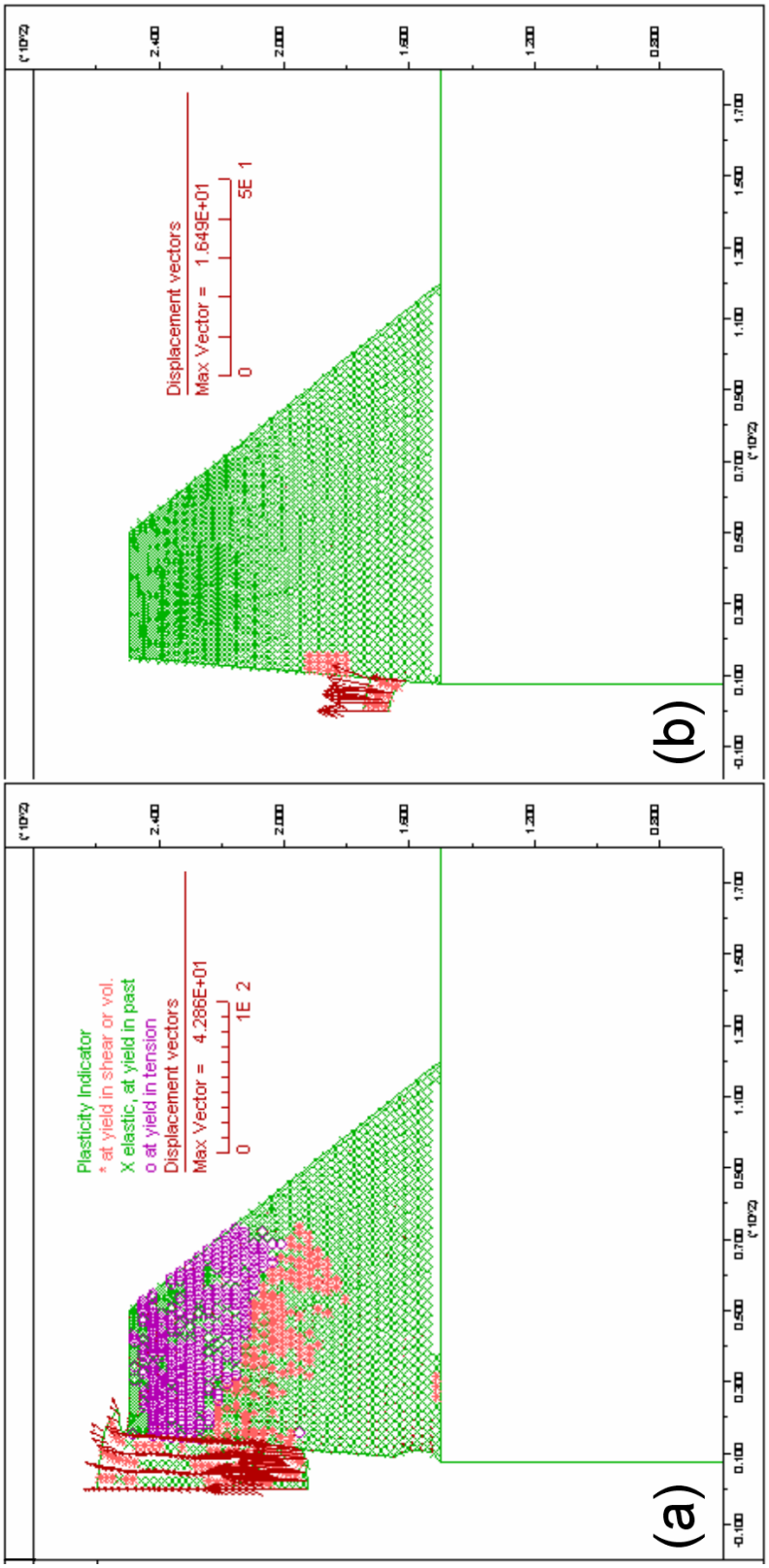

Source: Output DTN: MO0705BREAKOUT.000, files *\scoria plug\conduit_00mPlug_100mconeplug\temp_bad_geometry.sav* and *\scoria plug\conduit_00mPlug_100mconeplug\temp_bad_geometry.sav*.

NOTE: All dimensions and vector lengths are in meters.

Figure 6-143. Yielding and Deformation of Scoria Cones Fully Blocked to Various Depths

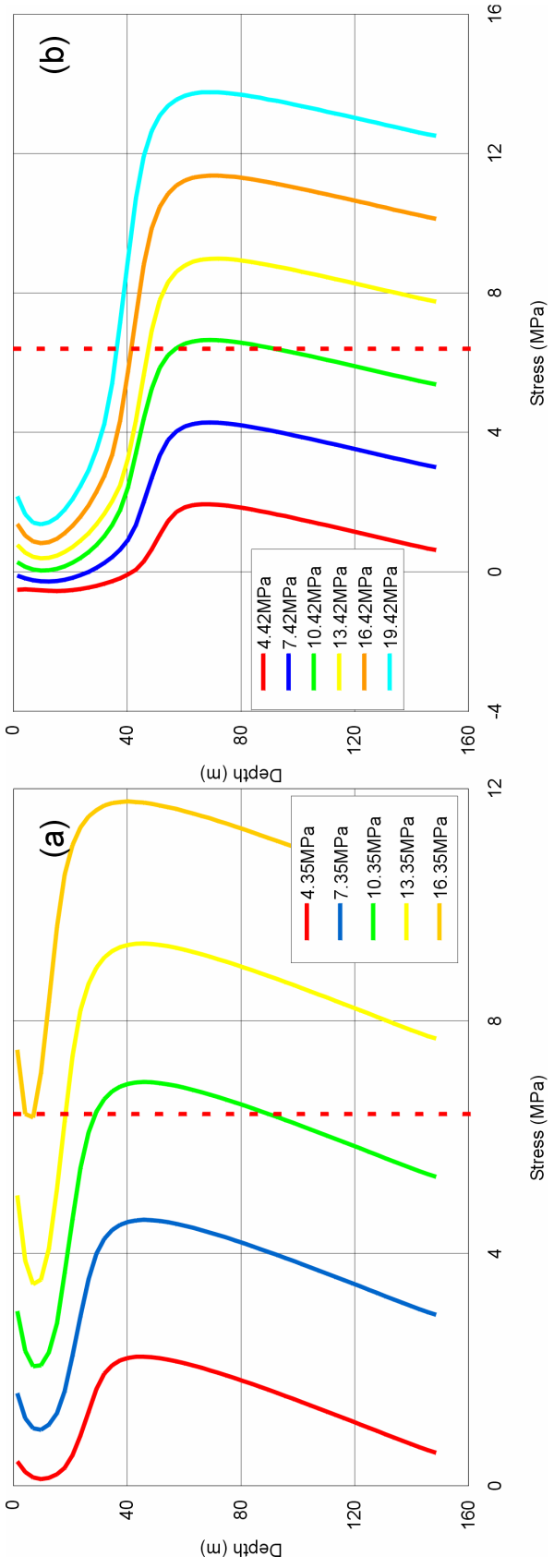

Source: Output DTN: MO0705BREAKOUT.000, FLAC save files in folders (a) \scoria plug\conduit_25mPlug_100mConePlug and (b) \scoria plug\conduit_50mPlug_100mConePlug.

NOTE: The vertical dashed line is tensile strength measured by Rocchi et al. (2004 [DIRS 173995], Table 3) and is used for interpretation.

Figure 6-144. Tangential Stresses around a Conduit Blocked by Slumping into a Scoria Cone for Different Magma Pressures

Interpretation—In the case of hydrofracture, it is expected that the magma pressure will decay relatively gradually after the breakout at the conduit boundary wall. Such cases are indicated in Table 6-27 as unshaded. The hydrofracture pressure is virtually independent of plug height (h_1) as can be seen by comparing case 8 with case 9 or case 11 with case 12. On the other hand, comparison of case 6 with case 9 indicates that h_2 does affect the pressure needed for breakout by hydrofracture; this is because the breakout will occur at greater depth (as is indicated by the depths of the maxima in Figure 6-144). A simple extrapolation of hydrofracture pressure based on a linearly elastic stress analysis can be made to estimate behavior of deeper plugs if it is assumed that the rock mass is homogeneous and isotropic. With this approach, the hydrofracture pressure for blockage by slumping or lava solidification will increase by about 0.23 MPa for every 10-m increase in the depth, h_2. This may be compared with the 0.6-MPa difference between breakout magma pressures with $h_2 = 25$ m (case 6) and $h_2 = 50$ m (case 9). Hydrofracture pressures calculated in this analysis are similar to those used in analysis of secondary breakout pressures in Section 6.5.1, so no deviations from the response predicted there is to be expected.

When the breakout is a result of a shearing mechanism, which involves deformation of the entire scoria plug, the breakout can occur as a rapid, perhaps explosive, event resulting in acceleration of material to several times normal gravitational accelerations. The main reason for rapid breakout is a sudden decrease in shear resistance (strain softening and/or reduction of friction as a function of relative velocity) between the disturbed and undisturbed scoria and within the undisturbed scoria as a result of plug movement and deformation. This analysis does not allow proper estimates of velocities of ejecta that could result but indicates the potential for the violent ejection of projectiles from a collapsing cone. Furthermore, magma pressures calculated to break through blockages by shearing failure of a scoria cone may be over three times those used in analysis of secondary breakout pressures in Section 6.5.1. If such shear failure is realistic, the higher pressures used in the analysis of secondary breakout Section 6.5.1.2 may be slightly low with respect to secondary dike formation.

Solidification: *Inputs*—The solidified lava flow is selected to be 10 m thick, and the solidification extends 30 m below the base of the flow into the conduit. The thickness is in accord with the finding presented in *Characterize Eruptive Processes at Yucca Mountain, Nevada* (SNL 2007 [DIRS 174260], Section C4). Rescaling the magma cooling results of Appendix D (Figure D-1 (lower plot)) to the diameter of the dike (15 m) indicates that complete solidification would be expected to have encompassed approximately the outer 80% of the radius of the conduit after about three months. This was simplified to a single depth for computational efficiency.

Computational Approach—This analysis considered a case where magma supply pauses so that the surface basalt flow stops, with the solidification extending 30-m deep into the underlying conduit (Figure 6-142b). The solidified lava flow on the top of the conduit was taken to be 10 m thick. The sequence used for analysis of breakout of the solidified basalt plug was the same as for the scoria plug. These calculations were done with FLAC V. 4.04 with an axisymmetric mesh using the input parameters listed in Table 6-26.

Results—Results for breakout after blockage by solidification (Figure 6-142b) are illustrated in Figure 6-145, which shows tangential stresses adjacent to the conduit for a magma pressure of 10.26 MPa. Stresses at the wall would be sufficient to generate radial hydrofractures in basalt with a tensile strength of 6.4 MPa as determined by Rocchi et al. (2004 [DIRS 173995], Table 3). Such hydrofractures would result in radially propagating dikes that might look similar to the dikes around the central conduit at Paiute Ridge (Valentine and Krogh 2006 [DIRS 177282]) if exposed by later erosion.

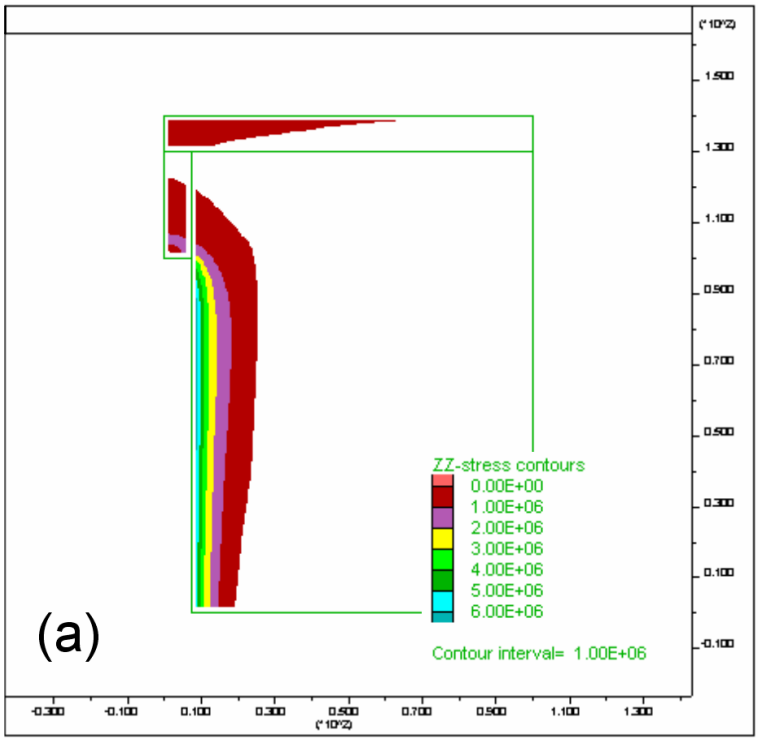

Source: Output DTN: MO0705BREAKOUT.000, file *\solidified magma plug\temp38.sav*.

NOTE: Dimensions are in meters (m). Stresses are in pascals (Pa).

Figure 6-145. Tensile Stresses Surrounding Conduit Blocked by Freezing

Faulting: *Inputs*—For problem formulation, the analyzed fault is selected to be a normal (dip-slip) fault with a dip of 60°, with a strike parallel to the dike, and a throw of 5 m. The fault intersects the dike at a depth of 100 m. This fault geometry is typical of observed faults in the Yucca Mountain region, as described in *Yucca Mountain Site Description* (BSC 2004 [DIRS 169734], Section 4.3.2.2, Table 4-9). The parallel strike is selected so as to make the problem two-dimensional. The fault throw is very large for a volcanic-related earthquake but is only a factor of about two larger than the maximum measured per-event slippage in the Yucca Mountain region (BSC 2004 [DIRS 169734], Table 4-9).

The in situ horizontal stresses for the analyses in this section are selected to be one-half of the overburden stress. This is consistent with field measurements of in situ stresses at Yucca Mountain (see Section 6.3.3.3). The fault and the original dike above the fault are assumed to have initial hydraulic apertures of 5 mm. Calculation of dike propagation after displacement by

a normal fault requires an initial fracture of some width (aperture) for any potential magma flow path (dike). A 5-mm value was selected as the initial aperture of the fault and of the potential vertical continuation to represent slightly open pathways but to minimize any bias as to which pathway the magma will follow in the calculations.

Computational Approach—This analysis addressed cutting of a dike by a fault as shown in Figure 6-142c. A vertically propagating dike, with a 0.45-m aperture, was offset by a 60°-dipping normal fault 100 m below the ground surface. The fault slip was 5 m. A plane-strain, two-dimensional, coupled hydro-mechanical problem was analyzed using the numerical code UDEC V. 3.14. The input parameters for the calculations were the same as those used in the wide-aperture case discussed in Section 6.3.3.5.6. The initial hydraulic aperture of the dike below the intersection was assumed to be 0.45 m. Both the fault and the original crack above the dike were assumed to have an initial hydraulic aperture of 5 mm. The initial magma pressure in the segment of the dike below the intersection was in equilibrium with the horizontal stresses. Magma was injected at the bottom of the analysis at the rate of 0.45 m^2/s per unit strike length, and the calculation was run until it reached steady state.

Results—Figure 6-146 shows the dike aperture distribution at the end of the faulted simulation (i.e., at steady state). The fault offset has forced the magma to turn and continue along the fault toward the surface, albeit with a reduced aperture of only ~0.15 m. The pressure increased from its pre-faulting equilibrium pressure of 1.2 MPa to a maximum of 1.42 MPa, before decaying over the next 200 s to a new equilibrium value near 1.3 MPa. All of these pressures are less than the 1.5-MPa component of confining stress normal to the fault at this depth. The difference, which is not large, results from a moment (force times distance), or leverage effect, such that the higher pressure in the source dike, acting at the dike-fault intersection, causes the upper fault block to incrementally rotate clockwise, thus opening the fault aperture.

Interpretation—This analysis demonstrates that magma may follow an active fault to the surface if it cuts an active dike, but it does not require such behavior. The results indicate that a magma pressure of about 1.4 MPa would be needed to open a fault cutting a dike 100 m below the surface. The pressure required to inject magma into a fault that has just cut a dike should vary with depth in a manner similar to hydrofracture pressure, as described in the first paragraph of this section. If a fault were to block a dike just above the repository (at a nominal 300-m depth) the expected magma pressure might rise as high as 6 MPa before magma moved to follow the new fault. This pressure is similar to those used in analysis of secondary breakout pressures in Section 6.5.1.2, so no deviations from the response predicted in that report are found.

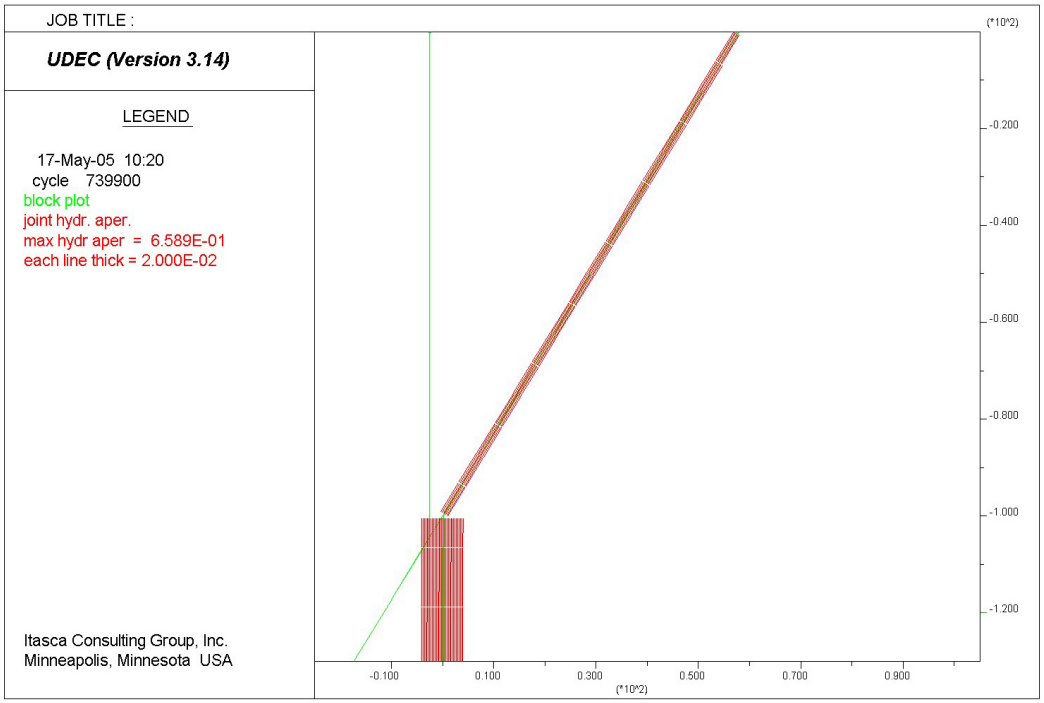

Source: Output DTN: MO0705BREAKOUT.000, file *\dike slip\step9.sav*.

NOTE: Dimensions are in meters (m). The width of the red line is proportional to dike aperture (m).

Figure 6-146. Magma Diversion by a Fault Cutting a Dike

Summary: For a conduit blocked by a lava flow, it was determined that the solidified basalt surrounding the magma would fail in tension when magma pressures exceeded about 9 MPa to 10 MPa, resulting in radial hydrofractures and releasing the magma pressures.

For a conduit blocked by slumped scoria, pressures needed to blow out the scoria were generally less than about 5 MPa, except for cases where the scoria blockage was extensive. For more extensive blockages, pressures as high as 20 to 30 MPa would be needed to blow out the scoria, but radial hydrofracture at about 10 MPa would relieve pressures before the lava blockage failed.

The pressures calculated for these two scenarios are pressures at the bottom of the blockage, which ranged from 10 m for the lava flow to as much as 100 m for the deeper scoria blockages. Pressures at repository depth would be higher by the hydrostatic head of the magma column between the blockage depth and the repository. For a magma density of 2,400 kg m^3, that head would be in the range of 3 MPa to 7 MPa, varying with both blockage depth and repository depth.

For a dike cut by a syn-volcanic fault, it was found that the magma could follow the fault to the surface with a pressure increase of less than 1.5 MPa. The analysis of the effect of preexisting faults on dike propagation in Section 6.3.4 found that diversion of a dike into a fault was more likely for high-angle faults and for intersections nearer the surface. Thus, faulting is not expected to be a factor in generation of high magmatic pressures at Yucca Mountain.

6.4.8.1.4 Summary and Conclusions

The substantial literature on the pressures experienced by magmatic systems during eruption and during crystallization was reviewed. Estimates of magmatic pressures near the surface for a wide range of cases reported range up to about 10 MPa. The fundamental process by which magmatic pressures increase during an igneous episode is the early crystallization of anhydrous minerals, which leaves the residual magma with higher water content. This process has been calculated to generate pressure increases in deep magmas on the order of 20 MPa. These results were found to be relevant to Yucca Mountain in terms of the composition of the magmatic systems evaluated and the magmatic chemical processes considered in the analyses.

The bulk of this section has addressed potential magma-pressure changing mechanisms. An approximation to magma pressurization during crystallization was developed using crystallization sequences developed by Detournay et al. (2002 [DIRS 169660]) for either dry magma at 10 MPa or magma with 2 wt % water at 100 MPa, following each case from the liquidus to about 50% crystallization. The dry magma achieved 53% crystallization at only 79 K below the liquidus, whereas 50% of the wet magma crystallized after a drop in temperature of 207 K. In this analysis, the volatiles are considered to be trapped in the interior of the drift, being prevented from venting into the porous country rock by a layer of plastically deformable hot, perhaps even partially molten, rock surrounding the core that contains the waste packages. The calculated magma pressures were between 10 MPa and 13 MPa under those conditions, respectively.

Mechanisms that would limit pressure in a dike or conduit were also investigated. The primary mechanism is the development of hydrofractures driven into the surrounding country rock by the pressurized magma, although the possibility of explosive eruption was considered and found to be unlikely. For pressures within cylindrical bodies in tuff, pressure limits were estimated to be about 8 MPa for vertical cylinders (conduits). However, plastic deformation of a layer of ductile basalt near its solidus that would surround the cylinders likely will permit higher pressures to be reached. This effect may preclude secondary breakout after a drift has filled with magma from being a viable threat to repository function.

When the analyses of this section are taken as a whole, it is concluded that pressures above 10 MPa are likely to develop in magma crystallizing in a repository. The upper limit is difficult to predict, but in view of the literature on pressures in actual volcanic events it seems unlikely to be much above 15 MPa.

6.4.8.2 Magma Cooling Rates

This section presents an analysis of how fast such an opening dike would be chilled by the surrounding cold rock to the extent that magma could no longer feed the crack-tip region and force the crack to continue growing. The analysis follows that of *Final Report of the Igneous Consequences Peer Review Panel* (Detournay et al. [DIRS 169660], Appendix 3.4, p. 53). From *Conduction of Heat in Solids* (Carslaw and Jaeger 1959 [DIRS 100968], Chapter 11, Section 11.2), the thickness of the chilled margin, δ, of a sheet of magma in cold rock with no advection is:

$$\delta = 2\lambda_d \sqrt{\kappa t} \qquad \text{(Eq. 6-113)}$$

where:

t = time
κ = thermal diffusivity

and where:

parameter λ_d is the solution to:

$$\frac{\sqrt{\pi}\Lambda}{k(T_m - T_r)} = \frac{e^{-\lambda_d^2}}{\lambda_d}\left[\frac{1}{1+erf(\lambda_d)} - \frac{T_m - T_s}{(T_m - T_r)erfc(\lambda_d)}\right] \qquad \text{(Eq. 6-114)}$$

where:

Λ = latent heat of fusion for the magma
k = thermal conductivity
T_m = initial magma temperature
T_s = temperature at which the magma viscosity becomes high enough to stop dike growth
T_r = temperature of the surrounding rock
erf and *erfc* = error function and the complementary error function, respectively.

The simplifying approximation is made that all properties of the magma and the host rock are identical. The parameter λ_d is solved for by trial and error given values of the other parameters in the equations.

6.4.8.2.1 "Solidification" Temperatures

The determination of "solidification" temperatures, T_s, is described next. To stop a newly forming dike by "thermal death," it is not necessary that the magma freeze completely. As the fraction of crystals increases in the magma, the apparent viscosity of the mixture increases dramatically. A complete treatment of this phenomenon is beyond the scope of this report, but an approximate analysis is presented to describe the major effects of partial crystallization. The apparent viscosity, $\mu_A(T)$, of a partially crystallized magma at temperature T below its liquidus temperature T_L is given by:

$$\mu_A(T) = \mu_o(T)\left(1 - \frac{(T_L - T)}{(T_L - T_{\phi_{mx}})}\right)^{-2.5} e^{(T_L - T)0.04k^{-1}} \qquad \text{(Eq. 6-115)}$$

where:

$\mu_0(T)$ = the viscosity of the pure liquid at T

ϕ_{mx} = the maximum crystal volume fraction that will allow flow

$T_{\phi_{mx}}$ = the temperature at which the volume fraction of solids is ϕ_{mx}.

This equation is derived from Griffiths (2000 [DIRS 163625], Equation 2 by way of Equation 3) with the following postulates:

(1) The initial temperature is the liquidus temperature, so the initial volume fraction of solids is 0

(2) The volume fraction of crystals varies linearly with temperature

(3) ϕ_f is equal to ϕ_{mx} with $T_f = T_{\phi_{mx}}$.

Estimates of ϕ_{mx} in the literature, summarized by Griffiths (2000 [DIRS 163625]), range from 0.4 to 0.6; the central value, 0.5, has been used in this analysis. Temperatures at which the magma is 50% solidified are derived from figures for the appropriate water content in Detournay et al. (2003 [DIRS 169660], Appendix, Table 2E). Temperatures from the figures were adjusted downward by the difference in liquidus temperature between that source and *Characterize Eruptive Processes* (SNL 2007 [DIRS 174260], Table 6-5, p. 6-14) in order to obtain consistent values for the analysis. For water contents not calculated by Detournay et al. (2003 [DIRS 169660]), temperatures were interpolated or extrapolated from values at other water contents. Viscosities of the pure liquid were calculated at the liquidus with the method of Shaw used in *Characterize Eruptive Processes at Yucca Mountain, Nevada* (SNL 2007 [DIRS 174260]). This will underestimate the effective viscosity because it:

- Does not take into account the increase in viscosity of the pure liquid as it cools
- Does not consider any increase in viscosity due to increasing silica content of the remaining liquid when crystals begin to form
- Does not consider the existence of a glass transition temperature, which will cause very large increases in the viscosity of the remaining liquid.

Using this relation, the apparent viscosity of partially crystallized alkali basalt magmas of several water contents as functions of temperature both above and below their liquidus temperatures is shown in Figure 6-147. The effect of only 10% to 20% crystals on the rheology of the partially crystallized magma is dramatic. This increase in percent crystals results in an increase in viscosity of 1.5 to 2 orders of magnitude, as roughly indicated by the highlighted region (labeled *15%.xls*) in Figure 6-147.

In light of the very rapid increase of apparent viscosity as temperatures drop, the temperature at which the apparent viscosity reaches 1,000 Pa·s has been chosen as T_s in Table 6-33 (Section 6.5.1.1.2).

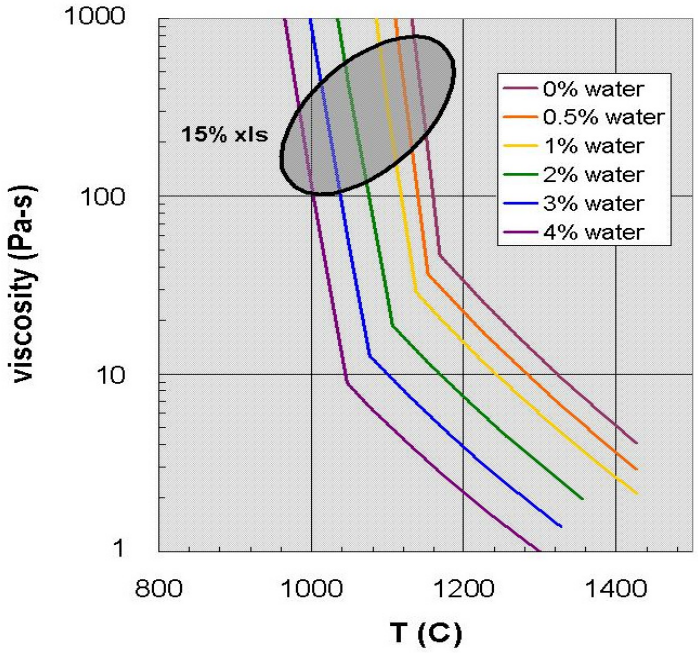

Output DTN: MO0411EG831811.002; file: *MO0411EG831811.002_Disk8.zip\Figures 6-75 & 6-76.zip\Shaw viscosity.xls*.

NOTES: Liquidus is indicated by the break in slope of each plotted curve; xls = crystals.

Figure 6-147. Apparent Viscosity of Alkali Basalt Magmas during Crystallization

6.4.8.3 Magma Interactions with Waste Packages and Waste Forms

This analysis addresses potential interactions of alkali basalt magma with a generic waste package. This waste package has outer 70-mm-thick shells (20-mm Alloy 22 and 50-mm Stainless Steel Type 316NG) with similar end closures. Internal components consist of a tubular lattice combining sheets of stainless steel for structural support, borated stainless steel to absorb neutrons, and aluminum as thermal shunts. These components contain the waste form in rods made up of cylindrical pellets of oxide fuel clad with zirconium metal.

Basaltic magma that may come in contact with waste package materials undoubtedly has the ability to modify their physical and chemical properties, but it is very difficult to predict, with confidence, the resulting effects. However, all such effects are expected to be deleterious to the integrity of waste packages and waste forms.

The physical and chemical environment of waste package and waste form materials in contact with active magma will include temperatures in the range of 825°C to 1,100°C cooling to below 700°C over about one to nineteen months (Figures 6-94, 6-105, 6-116, and 6-127), abundant steam and other potentially corrosive or reactive volatiles including SO_2, HCl, and, possibly, HF (SNL 2007 [DIRS 174260], Table 6-4). In addition, the magma will be flowing at least during the initial emplacement phase of the magmatic activity.

Section 6.4.8.3.1 analyzes the degradation of waste packages in the igneous environment. This includes material in response to Independent Validation Review Team (IVRT) concerns IGI-5, IGI-WP/WF-4, and IGI-WP/WF-7 on the igneous vapor environment and, in an appendix, a failure analysis of the elasto-plastic deformation of a composite waste package due to external magma pressures. Drip shields are expected to provide no more protection from seepage water after an intrusion than do waste packages. Section 6.4.8.3.2 presents an analysis of the potential for magma to move waste packages. The effect of the magmatic environment on waste forms is addressed in Section 6.4.8.3.3, which discusses the IVRT concern IGI-WP/WF-4. An alternative analysis by EPRI is summarized in Section 6.4.8.3.4. Conclusions are found in Section 6.4.8.3.5.

6.4.8.3.1 Degradation of Waste Packages

Analyses presented in Appendix E support the premise that an igneous intrusion would render ineffective the drip shields, waste packages, and cladding in the dike-intersected emplacement drifts (i.e., the waste package and associated components would no longer provide protection from seepage water). The temperature of the intruding magma may approach 1,200°C (BSC 2004 [DIRS 174260], Table 6-5). Although the melting temperatures of Alloy C-22 (1,357°C) and Stainless Steel Type 316NG (1,375°C) (BSC 2005, Section 5.1 [DIRS 173492]]) are above the magma temperature, the metals would likely lose their tensile strength and deform plastically at magmatic temperatures.

Chemical Considerations: Corrosion would also be enhanced. Analyses in Section 6.4.8.1 indicate that, after magma has filled the drifts, pressures could rise to near 8 MPa as magma rises to the surface. Furthermore, if a blockage occurs, preventing further extrusion onto the surface or during partial solidifications after magma flow has ceased, pressures could reach 15 MPa as the volatiles are excluded from the solid phases and confined to a progressively smaller volume of silicate liquid. (The discussion following Equation 6-110 in Section 6.4.8.1.3.1 indicates that hydrofracture breakout from a contained cylinder that is pressurized by partial crystallization is not likely to occur at pressures of this magnitude.) Combining a nominal 10 MPa pressure, which would be expected one or two months (i.e., 700 to 1,500 hours) after flow ceased (Section 6.4.8.1.3.1), at a nominal 1,100°C with the composition of magmatic volatiles from *Characterize Eruptive Processes at Yucca Mountain, Nevada* (SNL 2007 [DIRS 174260], Table 6-4), it is concluded that waste packages can be subjected to a highly corrosive vapor consisting of partial pressures of 7.3 MPa steam, 1.4 MPa CO_2, 945 kPa $S0_2$, 120 kPa H_2, 87 kPa HCl, 74 kPa H_2S, 57 kPa CO, 41 kPa S_2, and 17 kPa HF. These high partial pressures of corrosive gases must be addressed in an analysis of the corrosion of waste packages and waste forms. If the standard deviations from *Characterize Eruptive Processes at Yucca Mountain, Nevada* (SNL 2007 [DIRS 174260], Table 6-4) are subtracted from the mean in the analysis, the partial pressures of many of the gases are still considerable: 5.3 MPa steam, no CO_2, 50 kPa $S0_2$, 50 kPa H_2, no HCl, 5 kPa H_2S, no CO, 1 kPa S_2, and 9 kPa HF.

Once a drift is filled with magma, the magma will begin to cool. In the course of this cooling, minerals will crystallize over a range from 1,100°C to 800-900°C. All of these crystals are essentially volatile-free so that the proportion of volatiles left in the liquid fraction will increase as the volume in which they are contained decreases and the liquid becomes more and more viscous. It is expected that it will take approximately two months for magma to chill to the solidus temperature. This is the cause of high pressures that can lead to late-time explosive

eruptions such as those modeled in Section 6.4.3.1.3. At some point, the pressure and concentration gradients will be high enough that the volatiles will find their way into bubbles and/or cracks that will provide a long-term supply of high-pressure corrosive gas to interact with waste packages. For a waste package that is contained in the interior of the cooling magma, it is reasonable to expect that the pressures at and in the waste package will be gas pressures due to these volatile constituents. The pressures would eventually be relieved by cooling cracks forming first at the outer edge of the drift and moving inward. Although such cracks might begin at the outer edge of the drift at between one and two months, they would not be expected to reach the waste package until temperatures in the interior of the drift had fallen to about 750°C or below. Thus, it is expected that gas pressures at the waste package could be considerably higher than 8 MPa for at least a couple of months.

Findings of a literature review on the performance of materials similar to Alloy 22 waste packages and titanium drip shield materials in magmatic environments (Gordon 2003 [DIRS 163357], Section 5), suggest that the structural integrity of these materials would be compromised. For example, Stainless Steel Types 310 and 446, exposed to Hawaiian basaltic lava at 1,300°C and 2 psi (15 kPa) gauge pressure for 100 hours, underwent extensive reaction, while Alloy 718 suffered a loss of structural integrity. During the course of magma cooling, waste packages and canisters or assemblies will be subject to corrosion, the degree of which may vary depending on their composition, magma contact temperature, and in situ geochemical environment. Magma temperatures, pressures, and geochemical environment in the drift, influenced by the magma composition and volume of exsolving volatile gases, such as H_2O, H_2, CO_2, CO, SO_2, S_2, HCl, HF, and H_2S may have a significant impact on corrosion rates. Literature review findings related to oxidation, sulfidation, and corrosion behavior and rates of Alloy 22 waste package materials, drip shield titanium alloy, and similar alloys in magmatic environments shed light on the potential degree of corrosion (Gordon 2003 [DIRS 163357], Section 2).

One study of binary and ternary alloys containing various amounts of molybdenum and chromium and exposed to basaltic magma at 1,150°C for periods of 24 hours and 96 hours shows that the formation of secondary phases and oxidation or sulfidation of metals is extremely dependent on metal composition (Douglass 1983 [DIRS 166999]). For a nickel alloy with 20% chromium and 10% molybdenum, a maximum corrosion (oxidation) rate of about 7 mm/yr was obtained as estimated from metallography reported by Ehrlich and Douglass (1982 [DIRS 101097]). Another finding, from a qualitative study of various alloys in contact with Hawaiian basalt lava, indicates that Stainless Steel Types 310 and 446 reacted extensively with the degassed lava while Udimet 700 and Alloy 718 suffered a loss of structural integrity (Gordon 2003 [DIRS 163357], Section 5). Findings from another study, conducted at 727°C for 96 hours, indicate that, under a reducing atmosphere of 1.5% H_2S and 98.5% H_2, the corrosion is significantly higher than in an oxidizing-sulfidizing environment with 59% argon, 3% O_2, 36.5% H_2, and 1.5% H_2S (Gordon 2003 [DIRS 163357], Section 2). All of these corroborative findings suggest that metals embedded in the cooling basalt magma would be subjected to various degrees of corrosion. Drip shields are expected to provide no more protection from seepage water after an intrusion than do waste packages.

Mechanical Considerations: Mechanical properties of the alloy comprising the main waste package external components, developed in BSC 2005 [DIRS 173802]), indicate 1,000 creep strengths of only 2 MPa (for Stainless Steel Type 316) to 3 MPa (for Alloy 22) at 1,100°C and that these strengths increase to only about 15 MPa to 33 MPa, respectively, at 900°C.

Analyses of pressure that would develop within waste packages as the result of gas equilibration at high temperatures have been conducted (BSC 2005 [DIRS 173492]). The results indicate that, as the internal temperatures near the magmatic temperature, the resulting stresses on the packages would exceed the tensile strength of the package materials and that package would fail. Furthermore, if a package were corroded or otherwise weakened, it would have a lower tensile strength that could be exceeded by even lower internal pressure. Although these calculations were done for a very low value of external magmatic confining pressure, this would provide a possible mechanism for package breaching even in the event of a very low-volume intrusion that did not completely fill an emplacement drift.

Based on the information provided on the performance of waste package materials under high temperatures and high internal pressures, the following interpretations are made regarding the expected performance of waste packages engulfed in magma at initial temperatures approaching 1,100°C. At this temperature, the waste packages and their internals will quickly heat to near-magma temperatures; depending on whether the waste package is initially hot or cold and whether the magma is at near-liquidus temperature or considerably cooler, the analyses in Section 6.4.7 indicate waste package temperatures ranging from over 1,100°C (Figure 6-94) to 825°C (Figure 6-127). This will produce high pressures within the waste packages. The non-corroded waste packages will not rupture from the internal pressures; however, the heat and external load of the magma will cause the waste packages to lose strength and deform plastically, collapsing onto their internal components. Some form of breaching may occur, and the cladding is likely to fail at such temperatures.

A more likely condition that the waste packages could encounter would be the pressures generated in the magma as it begins to crystallize (Section 6.4.8.1.3.1). An analysis detailed in Appendix E indicates that, in response to external pressures of 4 MPa, 8 MPa, and 12 MPa at temperatures of 1,100°C, waste packages would fail as creep strains exceeded the strain limits of the end-cap materials. Such conditions are expected to be seen by all waste packages in flooded emplacement drifts because the source of pressure is inherent in the magma itself. As a result, magma could enter the waste packages. As the magma cools further within the waste package, more gas will be released and vesicles will form. The end result would be a waste package containing vesicular basalt (i.e., containing isolated millimeter-to-centimeter size spheroidal voids) with few large internal voids.

Even though magma may penetrate a waste package, the magma outside of the waste package is expected to stagnate once the drift has filled (on the order of 1,000 s) so that there are not likely to be driving forces that would result in flow through a waste package. In view of these results, it is safe to conclude that significant amounts of magma will not flow through waste packages, and that the waste forms will remain inside the waste packages.

6.4.8.3.2 Movement of Waste Packages by Magma

The possibility that magma movement can carry waste packages to the surface, either through drifts or along a drift into an erupting conduit, has been analyzed.

The velocity of magma required to move a waste package can be estimated from the density and dimensions of the waste packages and the density of the magma. The range of waste package density is from 2,940 kg m^3 to 4,280 kg m^3 (BSC 2004 [DIRS 177432]). If the magma is completely degassed, its density (ρ_m) will be 2,663 kg m^3 (SNL 2007 [DIRS 174260], Table 6-5). Although the dimensions of the waste packages vary, an approximate calculation of buoyant, viscous, and dynamic forces indicates that movement of waste packages in magma will not be facilitated. A 5-m-long waste package with a diameter of 1.5 m (volume = V_{WP} = 8.9 m^3) with a bulk density, ρ_{WP}, of 2,940 kg m^3 will be subject to a net downward buoyant force of 24 kN (($\rho_{WP} - \rho_m$) * g * V_{WP}); for a density of 4,280 kg m^3, the force will be 140 kN (kilonewtons). For lower magma densities, these forces will be correspondingly larger. Viscous forces on the waste package can be estimated from the magma viscosity (μ), the area of the package (A_{WP}) subject to drag, and the distance normal to that surface (dr) across which the velocity decreases (dv_m) to the free-field velocity ($F_{visc} = A_{WP}\,\mu(\mathrm{d}v_m/\mathrm{d}r)$). A waste package 5-m-long and 1.5 m in diameter has a cylindrical surface of 24 m^2; if the velocity increases to a free-field value of 1 m/s over 1 m radially from the package, the viscous drag will amount to only 2.4 kN for a magma viscosity of 100 Pa·s. The load due to dynamic pressure ($P_{dyn} = \rho_m v_m^2$) of moving magma with density ρ_m impacting on the end of a waste package at 1 m/s would be similar to that from viscous drag on the cylindrical surface. Even the combined force almost certainly would be too small to mobilize a package subject to a downward load of 24 kN to 140 kN.

The viscous forces and the dynamic pressure increase with magma velocity, and a magma velocity of 1 m/s is considered to be the speed of rising magma below the exsolution depth, which is on the order of a kilometer (SNL 2007 [DIRS 174260]). Any increase in magma velocity will be accompanied by expansion of the magma. In the simplest model of magma expansion in a dike or conduit of fixed area, mass flux is conserved so that an increase in velocity from 1 m/s to 5 m/s, for example, would coincide with a drop in density by the same factor. Thus, a velocity of 5 m/s would be associated with a magma density of only about 500 kg m^3. Such a medium moving at 5 m/s would exert a dynamic force on the end of a waste package of 22 kN; but it is difficult to envision a scenario in which the end of a package could be impacted by magma to move the package toward a dike or conduit. Viscous drag also depends on the velocity of the magma, but it is not possible to predict accurately what the viscosity of magma with a density of 500 kg m^3 would be. Such a magma would be fragmented (SNL 2007 [DIRS 174260]), meaning that the continuous phase would be vapor rather than silicate liquid. The viscosity of the fragmented magma would probably be very low relative to the pure liquid. Counteracting the effect of increased velocity will be an increase in downward gravitational force due to lower buoyancy in the less-dense magma. Unsupported gravitational forces on packages in magma of 500 kg m^3 will be between 211 kN and 330 kN. Hence, it can be concluded that viscous drag will not be able to move intact waste packages in drifts as the magma expands. Magma of density 500 kg m^3 would have to move faster than 15 m/s to 20 m/s in order to lift waste packages in a conduit.

Even if the waste packages do not move in response to magma motion, some settling is likely due to softening of the crushed rhyolite tuff that comprises the invert fill material (Section 6.4.7.2). For waste packages that are hot at the time of intrusion, much of the invert fill will experience temperatures above its glass transition temperature for five months to three years. This is ample time for the pallets to sink into the softened invert fill. There is no reason to expect that rotation of the waste packages would not accompany such settlement. For cold waste packages, less heating of the invert fill would occur, but the upper tenth of a meter or more of the fill would still reach glass transition, so that rotations cannot be ruled out in that condition as well.

6.4.8.3.3 Effect on Waste Forms

Very little work has been done relevant to the ability of direct contact with magma to modify the physical and chemical properties of waste forms, making it impossible to predict precisely their behavior in the event of the entry of basaltic magma into repository drifts. As a result, a limited discussion regarding the kinds of expected behaviors is presented below.

The spent commercial fuel rods are composed of UO_2, a ceramic with a high melting temperature, ranging from approximately 2,600°C (Todreas and Kazimi 1990 [DIRS 107735], p. 307 for light-water reactor fuels) to 2,800°C (Lide 2002 [DIRS 160832], p. 4-92 for UO_2). Therefore, commercial spent nuclear fuel exposed to magma will not melt directly at magmatic temperatures (up to approximately 1,169°C) (SNL 2007 [DIRS 174260], Table 6-5).

However, when waste canisters/assemblies and fuel claddings are damaged, the fuel pellets/rods may be assimilated into cooling basalt magma. Under this scenario, three types of processes may alter spent fuel rods: chemical interaction between the waste forms and the metal of waste canisters/assemblies and cladding, chemical interaction between waste forms and the magma, and physical changes to the waste form.

Chemical interactions may occur between cladding and spent fuel. Hofmann and Kerwin-Peck (1984 [DIRS 164038]) conducted experiments between UO_2 and Zircaloy-4 under isothermal and transient temperatures of 1,000°C to 1,700°C and at 0.1 MPa to 8 MPa for a duration of 1 to 150 minutes. These experiments showed that, under reducing conditions, oxygen from UO_2 is transported to the Zircaloy via the gas phase, and, as a result, uranium metal is formed. Uranium then diffuses to react with zirconium to form a layer of U-Zr alloy at about 800°C to 1,150°C. Subsequently, several other solid solution layers of interactive U-Zr and Zr-oxides are formed at lower temperatures. However, there is considerable uncertainty relative to the work of Hofmann and Kerwin-Peck (1984 [DIRS 164038]) as to the range of oxygen fugacities that will be obtained during an intrusive scenario.

The presence of magmatic gases can also affect Zircaloy cladding in a relatively short time after the gases contact the cladding at temperatures near 1,100°C. Kinetic corrosion-rate calculations suggest that Zircaloy cladding can be significantly damaged by corrosion in a matter of days in the presence of water vapor at temperatures between 250°C to 360°C (Hillner et al. 1998 [DIRS 100455]). Also, Fe-Zr and Ni-Zr liquid eutectics begin to form at about 940°C and would likely lead to failure of the fuel cladding if the temperature were to increase above about 940°C (Haskin et al. 2002 [DIRS 171570], Figure 3.1-4).

In addition, radionuclides in the waste could be incorporated into crystallizing silicate mineral phases, or form higher oxide phases. Westrich (1982 [DIRS 100492]) found that up to 20% by weight of UO_2 was soluble in molten basalt. Reactions with volcanic gases are also likely. Tananaev et al. (1961 [DIRS 181322]) report that "a number of papers describe the fluorination of uranium dioxide with gaseous hydrogen fluoride at high temperature. At the Second International Conference on the Peaceful Uses of Atomic Energy, brief details were given of methods which can be used under industrial or laboratory conditions for the preparation of UF_4 by the action of gaseous hydrogen fluoride on uranium dioxide at 600°- 700°."

The thermodynamic stability of secondary phases likely to form in cooling basalt is poorly known, and it is difficult to predict which phases, if any, might form. Fission products (e.g., cesium and technetium) may also be incorporated into new mineral phases, with the size and charge of fission-product ions exerting primary control as to the resulting minerals that might contain them. Some fission products (e.g., cesium and strontium) may also be volatilized by the high temperatures. Thus, there is great uncertainty as to which phases and minerals are likely to accommodate the suite of radionuclides in spent-fuel and glass waste forms.

As temperatures decrease after initial emplacement and under oxidizing conditions, uranium oxide is expected to fragment, which increases the surface area of the waste (BSC 2004 [DIRS 169987], Section 6.2.2). This fragmentation and subsequent increase in surface area would make it more susceptible to transport under nominal conditions. Oxidation of UO_2 fuel in the presence of water-rich volatiles exsolving from cooling basalt magma may also occur (Einziger et al. 1991 [DIRS 126446]). UO_2 dissolution at room temperature is reported to be enhanced by additional iron and SO_4 (Bhatti et al. 1998, [DIRS 181323] p. 263) and to be substantial (Bhatti et al. 1998, [DIRS 181323] p. 260).

A fraction of waste packages within the repository will contain radionuclides in a glass matrix. If glass waste is contained within waste packages, glass would be expected to re-melt and resolidify as the drift cooled. The slow cooling would be expected to result in a smaller amount of cracking relative to cooling at higher rates and, therefore, a lower release rate (although no credit is taken for this phenomenon). The extent of devitrification will depend on the composition of the glass, temperature, and cooling rate. Borosilicate high-level radioactive waste glasses are currently formulated to avoid formation of phases, such as nepheline ($NaAlSiO_4$), because they lead to a composition change in the glass. Likewise, glass additives are controlled to avoid both the formation of soluble inclusion phases, such as lithium metasilicate (Li_2SiO_3), and glass/glass-phase separation.

Less certain, however, are possible chemical interactions between exposed and partially degraded glass waste and basalt magma. Given the low melting temperature of glass waste and the large difference in composition between glass waste and basalt magma, some reaction between them is inevitable. One possibility is that the interaction might result in the rimming of olivine crystals with pyroxene or in the crystallization of pyroxene rather than olivine in regions of the cooling drift that are rich in glass. Much as with spent fuel, however, there remains considerable uncertainty as to the exact nature of materials that may be formed by reactions between glass and magma. Menard et al. (1996 [DIRS 171053]) report that, when R7T7 borosilicate glass is corroded by sulfate solutions, "uranium was found essentially in aqueous

form" with "the presence of carbonate ions increasing its solubility by creating stable complexes."

In summary, although the range of possible secondary mineral phases that may form cannot presently be constrained, it is nonetheless expected to comprise silicate and oxide minerals, although salts can not be ruled out. As oxide and silicate minerals tend to have slow dissolution rates compared to salts, significantly enhanced dissolution rates of minerals due to reaction of waste with basalt magma within drifts are not anticipated.

6.4.8.3.4 EPRI Analysis of Magma-Waste Interaction

The Electric Power Research Institute recently published an analysis of potential igneous processes at Yucca Mountain (EPRI 2004 [DIRS 171915]). This analysis is extensive and includes the interaction between magma and waste packages (EPRI 2004 [DIRS 171915], Section 5) and waste forms (EPRI (2004 [DIRS 171915], Section 6). The following paragraphs summarize these findings and provide commentary on their relation to this report.

A most dramatic analysis is presented wherein a 4-m-diameter by 5-m-long cylinder of magma moving vertically parallel to its axis at 100 m/s impacts a horizontal 21-PWR waste package at midlength (EPRI 2004 [DIRS 171915], Section 5.2). The waste package is modeled in considerable three-dimensional detail including:

- Outer and inner shells
- Outer, middle, and inner top lids
- Spreader and spacer rings
- Top and bottom trunion rings
- Inner and outer bottom lids
- Inner vessel structural guides
- Fuel basket assembly
- Fuel tubes and fuel assemblies (EPRI 2004 [DIRS 171915], Section 5.2.2.1) with elastic-plastic models for four different materials (EPRI 2004 [DIRS 171915], Section 5.2.2.2).

The magma has a density of 2,600 kg m^3 with very low tensile and shear strength (EPRI 2004 [DIRS 171915], Section 5.2.2.3). The initial condition has an internal gas pressure of 150 kPa. After an initial transient lasting approximately 10 ms, the waste package moves upward at 35 m/s to 40 m/s, with its lower side dented inward by a third to a half of a meter, the dent encompassing the entire length and the lower half of the circumference. This deformation is sufficient to cause very great damage to the structural guides, the fuel basket assembly, and the fuel assemblies (EPRI 2004 [DIRS 171915], Section 5.2.3). However, there was no tearing of the inner structural shell, and the integrity of both end closures and of the package as a whole

was maintained during the 30 ms of the simulation. They also note that, "Under the extreme magma conditions assumed for the analysis, the waste package will likely sustain a secondary impact with the roof of the chamber at an impact velocity of about 120 fps (36.6 m/s). This is equivalent to a drop from 224 ft (68 m), which is seen as extremely conservative compared to conditions in the drift." The EPRI report (EPRI 2004 [DIRS 171915], Section 5.2.4) concludes by noting:

> The force applied to the waste package in this analysis was far in excess of the expected range of force that might be experienced by an actual waste package inside the repository drift. Despite the large conservatism of the analysis, the waste package survived without loss of containment capability.… EPRI's position is that the analyses reported in this section eliminate mechanical impact of magma on a waste package within the repository drift during a volcanic event as a credible failure mechanism for waste packages at Yucca Mountain.

This analysis applies a large load to the waste package. As argued in Section 6.4.8.2, if the magma velocity were as high as 100 m/s, it would be unlikely that the density of magma averaged over the dike cross section would attain even half the value used in the EPRI analysis (EPRI 2004 [DIRS 171915]).

The EPRI analysis also considered erosive effects of flowing magma: "Mechanical erosion of the waste package could occur if the hardness of the solid material entrained in the flowing magma exceeds that of Alloy 22. No suitable data were found to judge the possibility of waste package erosion by flowing magma," (EPRI 2004 [DIRS 171915], Section 5.3). Regarding erosion-corrosion, the analysis (EPRI 2004 [DIRS 171915], Section 5.3) concludes:

> At elevated temperatures, Alloy 22 is protected from corrosion by an oxide (or sulfide) scale. An estimate of the maximum rate of erosion-corrosion can be obtained by assuming that erosion of the surface prevents the formation of a stable scale. Short-term corrosion rates of Ni-based alloys in molten magma and glasses are of the order of 10's of μm/day over the temperature range 1000-1200°C. The extent of erosion-corrosion of the waste package during the eruption would amount to a maximum of 0.4-2.0 mm. Therefore, waste package failure due to erosion-corrosion by flowing magma is highly unlikely.

The EPRI report analyzes the effects of internal pressurization during the thermal transient due to intrusion (EPRI 2004 [DIRS 171915], Section 5.4). Addressing "pinhole" rupture due to overpressurization, the report calculates that internal pressures after magma has engulfed a waste package will be compressive until the magma has solidified, thereafter increasing to approximately 0.45 MPa and then slowly declining to just over 0.3 MPa in 200 days. As a result, the maximum hoop stresses will be 19 MPa, whereas the 0.2% offset strength of Alloy 22 under those conditions will be at least 50 MPa. The EPRI study concludes, "It is unlikely that the waste package shell will plastically deform, let alone undergo ductile failure, during the thermal transient. This conclusion applies equally to the weld material as to the outer shell of the waste package" (EPRI 2004 [DIRS 171915], Section 5.4.1). Creep rupture of the shell is considered "unlikely because geometrical constraints [from the solidified magma surrounding the waste package] limit the amount of strain" (EPRI 2004 [DIRS 171915], Section 5.4.2). The differences

between these findings and those of Section 6.4.8.1 occur because the EPRI analysts employed different inputs than are used in this report.

The EPRI report also addresses corrosion of waste packages by magma (EPRI 2004 [DIRS 171915], Section 5.5). It presents results of new experiments with remelted Hawaiian basalt and Alloy 22 (EPRI 2004 [DIRS 171915], Section 5.5.1). The results were similar to those applied in Section 6.4.8.1 of this report. The EPRI analysis (EPRI 2004 [DIRS 171915]) used a magma composition without corrosive gases such as H_2S, SO_2, or HCl to attack Alloy 22. It also included a probabilistic calculation of waste-package corrosion with a range of activation energies (0, 40, 100 kJ/mole) and a range of temperature ranges over which corrosion occurred. The study found that the maximum corrosion depth was 5.26 mm and occurred when corrosion continued down to temperatures as low as 800°C (EPRI 2004 [DIRS 171915], Section 5.5.2). The differences between the EPRI results and those of Section 6.4.8.3.1 can likely be attributed to the absence of reactive gases, sulfur species, and halides.

6.4.8.3.5 Conclusion

When considering the results of these studies, it is important to remember that limited time will be available for interaction between magma, waste forms, and waste package materials. As demonstrated in Sections 6.4.6 and 6.4.7 and in Appendix D, temperatures at the centerline of the drift will have relaxed to below solidus temperatures in approximately 60 days, and reaction rates typically decline in an exponential fashion with decreasing temperature.

The heat and pressures associated with magmatic intrusion and crystallization in drifts that have been intruded are expected to render waste packages ineffective in isolating waste from seepage water when it returns after drifts have cooled. In addition, magma could enter most waste packages.

The heat and oxidizing environment of the intrusion will cause extensive fragmentation of oxide wastes. Glassy wastes are not expected to be substantially changed by an intrusion. Little is known about chemical reactions that might occur between basalt and waste forms. They are nonetheless expected to comprise silicate and oxide minerals, although salts cannot be ruled out.

The outputs from this section are found in EBS Failure Fractions (output DTN: LA0702PADE01EG.002). They include three parameters used in the TSPA GoldSim model. Fraction_DS_Failed_Ign_Input represents total damage of the drip shield and has a value of 1. Fraction_WP_Failed_Ign_Input represents total damage of the waste package and has a value of 1. Clad_Failure_Frac_Ign_Input represents total failure of the commercial spent nuclear fuel cladding and has a value of 1.

6.4.8.4 Magma Chilling in Backfilled Drifts

Tight backfilling of the access drifts, particularly under conditions of remote emplacement, would be extremely difficult and costly to accomplish. Therefore, it is expected that there will be a gap between the top of backfill and the crown of the drift. The size of the gap may increase subsequent to emplacement of the backfill, as a result of backfill settlement induced by relatively low intensity of ground shaking, or it can decrease or close completely, as a result of crown collapse induced by stronger ground motions. Although the amount of settlement is uncertain

(depending on the initial relative density of the backfill and the number and intensity of seismic events), some settlement of backfill will certainly occur.

This section reports on the results of numerical simulations to estimate the time required by the tip of a magma intrusion, flowing atop a partially backfilled emplacement drift, to cool below the effective solidification temperature, using a three-dimensional simulation accounting for transport of heat by advection as well as loss by conduction. The parameters for the simulation are listed in Section 6.4.8.4.2. The results of the analyses are included in Section 6.4.8.4.3. The analyses are based on heat transfer only; they do not address temperature-dependent viscosity of magma or any effects of mixing of backfill into magma. Section 6.4.8.4.4 discusses the results and presents conclusions regarding the movement of magma into unintruded emplacement drifts.

6.4.8.4.1 Analytical Method

The analysis assumes magma entering the backfilled drift is degassed, resulting in effusive flow. This is justified by the long flow path (hundreds of meters) needed to fill the unintruded emplacement drift, which would allow time for much of the volatile content to escape into the porous tuff. The velocity of effusive flow, calculated with Equation 6-95, will be between a centimeter and a meter per second. The tip of the magma flowing down the drift into the gap will continuously encounter cold rock and backfill. Because of heat loss into these media, it will gradually cool down. As a result, its viscosity will increase and its velocity will decrease. When temperature at the magma front drops below the effective solidification temperature (1,174 K as derived in Section 6.4.8.2.1), magma will stop flowing. The process of magma flow in the gap on the top of backfill was analyzed numerically with FLAC3D. Heat conduction was analyzed around the magma tip moving at the steady velocity past the media (rock and backfill) at ambient temperature (293 K). The magma intrusion temperature was 1,379 K. The simulation was carried out for different gap dimensions.

6.4.8.4.2 Assumptions, Uncertainties and Key Parameters

The mesh used to represent a portion of an 8-m-diameter main drift and backfill is illustrated in Figure 6-148. The red blocks represent the backfill material, the green blocks are the surrounding tuff, and the blue blocks represent the magma.

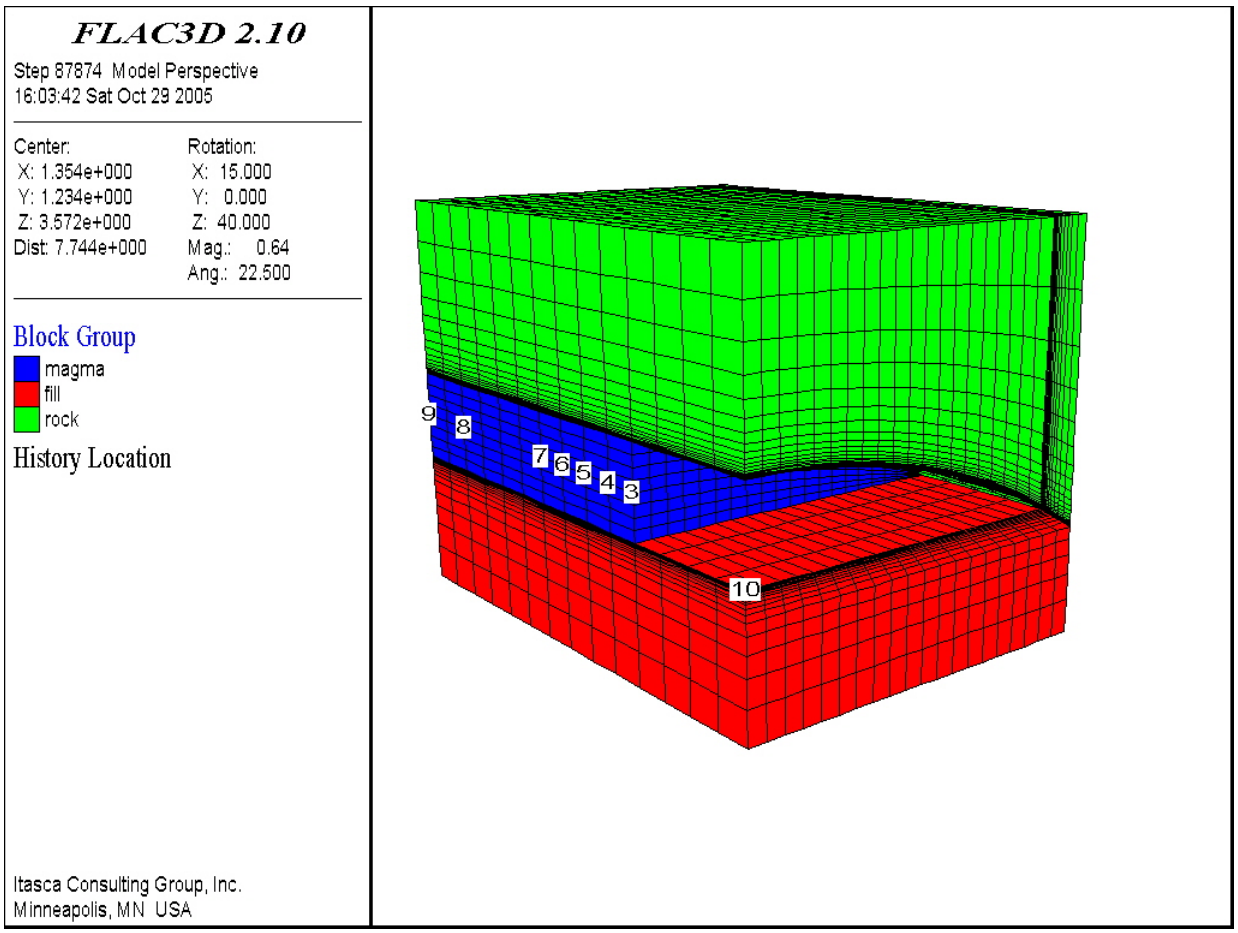

Source: Output DTN: MO0705BACKFILL.000, file \ *m0p5*\ *v0p056**fig7.jpg*.

NOTE: Graphic shows a 0.5-m gap; v = 0.056 m/s.

Figure 6-148. Grid and History Location—Three-Dimensional Simulation

The thermal properties for the analysis are listed in Table 6-28. Thermal diffusivity is defined as conductivity divided by the product of heat capacity and density. The initial temperatures for rock and magma and the magma temperature of effective solidification are listed in Table 6-29.

Two different magma velocities were considered for each gap size. The velocities were calculated by applying the formula for viscous flow in a pipe (Equation 6-95) using the hydraulic radius of the crescent-shaped opening at the top of the backfill in place of the pipe radius. The hydraulic radius is the area of the flow divided by its perimeter. The areas and perimeters are 1.308 m^2 and 7.916 m for a 0.5-m gap and 0.613 m^2 and 6.158 m for a 0.3-m gap. Two cases are considered, with viscosities of 40 Pa·s and 10 Pa·s covering the range of viscosities from *Characterize Eruptive Processes at Yucca Mountain, Nevada* (SNL 2007 [DIRS 174260]), Table 7-1). A pressure gradient of 1 MPa across 100 m was assumed. The resulting velocities are listed in Table 6-30.

Table 6-28. Thermal Properties for Rock, Fill, and Magma

Property	Value	Source
Rock		
Conductivity (W/mK)	1.18	Used value for Tptpul strata (lowest among four RHH units) DTN: SN0404T0503102.011 [DIRS 169129], Table 7-10
Heat capacity (J/kg K)	985	DTN: SN0402T0503102.010 [DIRS 170993]
Density (kg/m^3)	2,043	DTN: SN0404T0503102.011 [DIRS 169129], Table 7-10, average density for four RHH units.
Diffusivity (m^2/s)	5.86×10^{-7}	(see note)
Fill		
Conductivity (W/mK)	0.16	DTN: SN0206F3504502.012 [DIRS 159145], Table S02138_001 DTN: SN0208F3504502.019 [DIRS 161883], Table S02221_001 DTN: SN0206F3504502.013 [DIRS 159146], Table S02139_001
Heat capacity (J/kg K)	760	DTN: GS000483351030.003 [DIRS 152932], Table S01076_001
Density (kg/m^3)	1,225	DTN: GS020183351030.001 [DIRS 163107], Table S02025
Diffusivity (m^2/s)	1.72×10^{-7}	(see note)
Magma		
Conductivity (W/mK)	0.60	Detournay et al. [DIRS 169660], Table 1-2; average of upper and lower bounds
Heat capacity (J/kg K)	1,945	Assumption
Density (kg/m^3)	2,556	DTN: LA0612DK831811.001 [DIRS 179987], Table 6-5, values for water content: 2 wt %
Diffusivity (m^2/s)	1.21×10^{-7}	(see note)

NOTE: Diffusivity is calculated by dividing conductivity by heat capacity and density.

Table 6-29. Initial and Solidification Temperatures for Magma

	Value	Source
Rock and backfill initial temperature (K)	293	Assumption
Magma intrusion temperature (K)	1,379	DTN: LA0612DK831811.001 [DIRS 179987], Table 6-5, values for water content: 2 wt %
Effective solidification temperature (K)	1,174	Section 6.4.8.2.1

Table 6-30. Magma Velocity (m/s)

Gap height	0.3 m gap	0.5 m gap
Case 1	0.016	0.056
Case 2	0.063	0.22

6.4.8.4.3 Flow into Backfilled Access Main Drifts

Temperature contours around the magma front are shown in Figure 6-149 for the case of a 0.3-m-high gap. The evolution of temperature at the magma front is shown in Figure 6-150 for two cases of magma velocities: 0.063 m/s (red line) and 0.016 m/s (blue crosses). Clearly, magma front velocity has little effect on temperature evolution. The effective solidification temperature of magma is indicated by the horizontal line in Figure 6-150. It takes 34,000 s, or approximately 9.4 hours, for the magma front temperature to fall below the effective solidification temperature, halting the flow of magma. Distance from the dike intersection reached by the magma flowing inside the gap can be calculated based on magma velocities. In a favorable case, when magma velocity is relatively small (0.016 m/s), the distance reached by magma is almost 550 m (far enough to reach six emplacement drifts spaced 81 m apart). If the magma is flowing at the higher speed of 0.063 m/s, it would reach over 2 km, encountering 25 emplacement drifts.

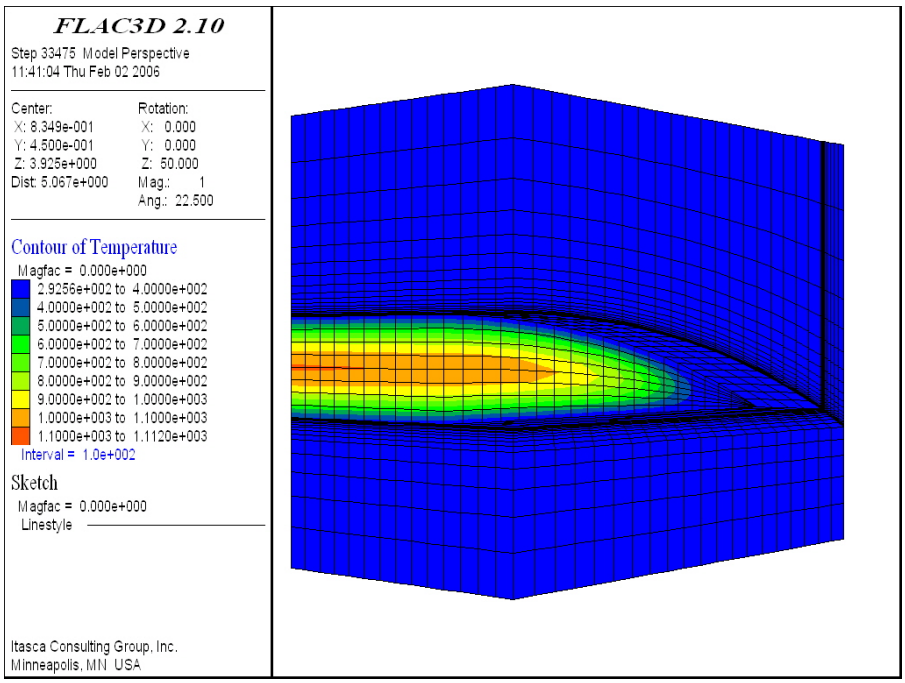

Source: Output DTN: MO0705BACKFILL.000, file *\m0p3\v0p016\m0p3.sav.*

NOTE: Graphic shows the 0.3-m gap.

Figure 6-149. Temperature Contours at the End of the Three-Dimensional Simulation

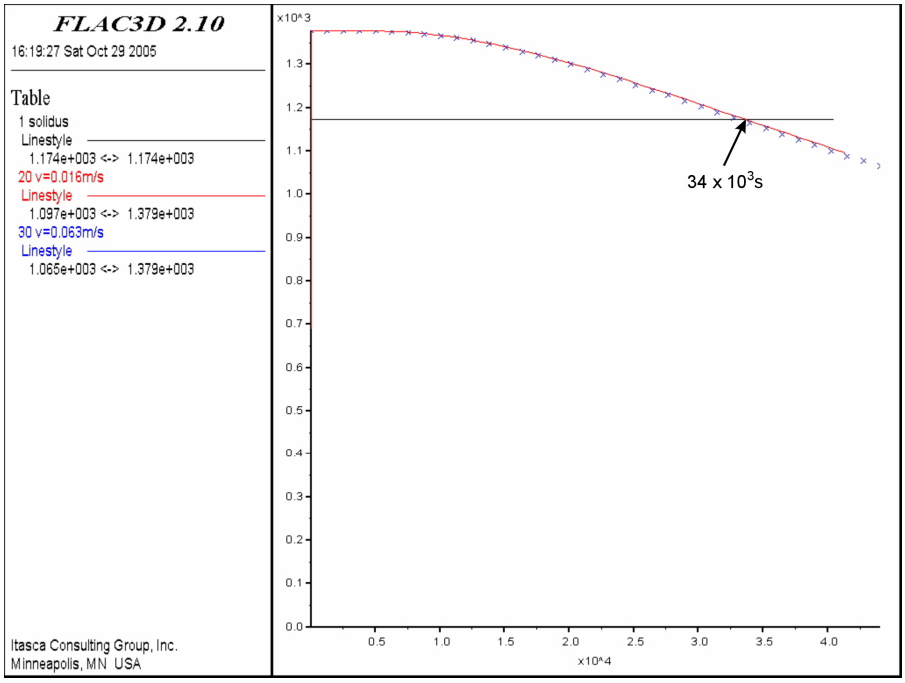

Source: Output DTN: MO0705BACKFILL.000; file: *m0p3/figm0p3/fig12.jpg*.

NOTE: Graphic shows the 0.3-m gap.

Figure 6-150. Temperature History at Mid-elevation in Magma Tip—Three-Dimensional Simulation

The gap size on top of the backfill will most likely be greater than 0.3 m. Consequently, the magma velocity will be greater, the cooling time will be longer, and the distance traveled by the magma before its front freezes will be longer. Results for magma flow in a gap of 0.5 m are given in Figure 6-151, showing temperature contours at the end of the simulation. Figure 6-152 shows the cooling history for magma velocities of 0.056 m/s (blue crosses) and 0.22 m/s (red line). As in the flow in the narrower gap, there is little difference in the time (90,000 s or just over one day) required for the magma to cool to the effective solidification temperature. With such a long cooling time, magma could flow through a length of backfilled main drifts equivalent to 5 km for the lower velocity and up to almost 20 km for the higher velocity—clearly enough time to reach all emplacement drifts in the repository.

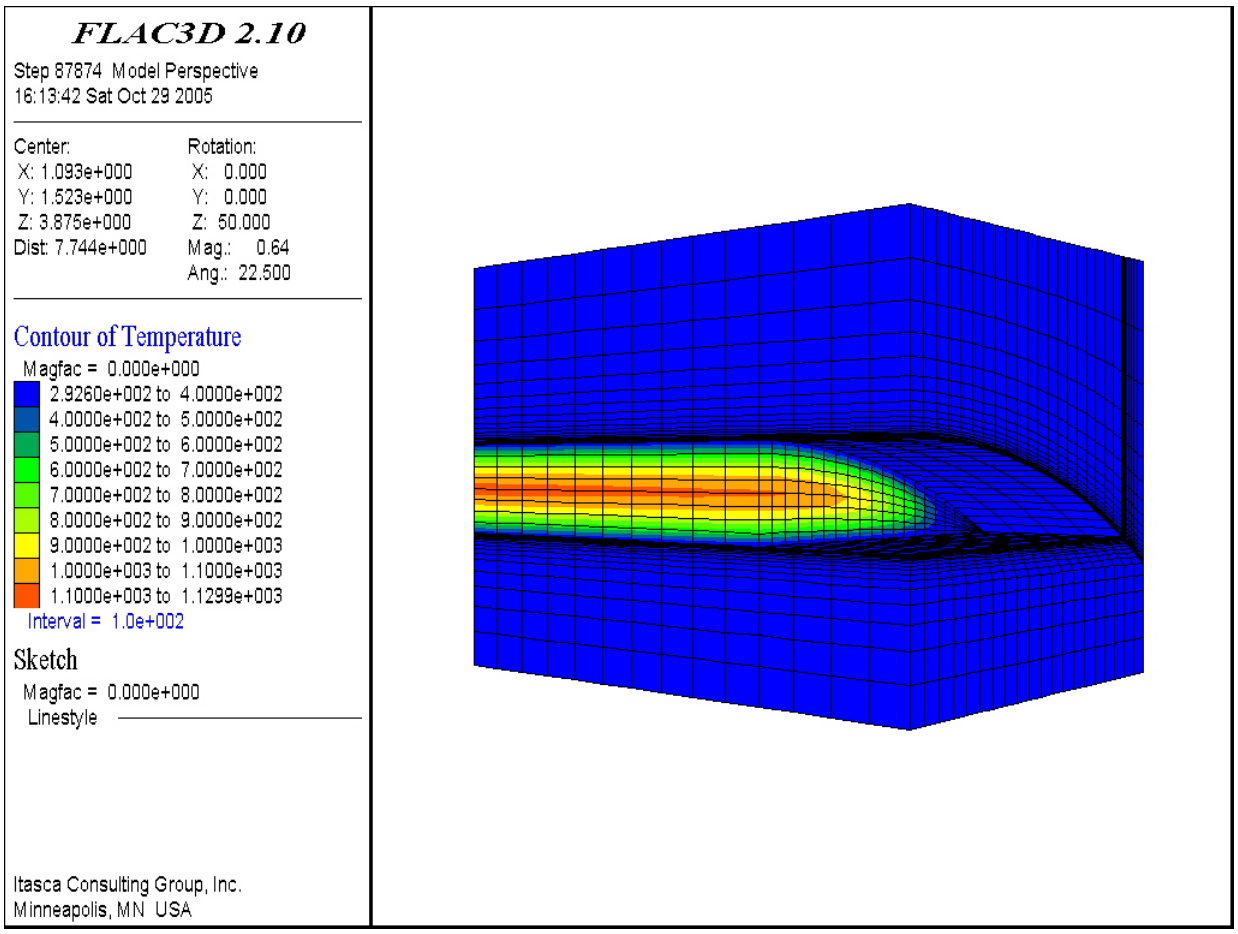

Source: Output DTN: MO0705BACKFILL.000; file: *\m0p5\v0p056\fig10.jpg*.

NOTE: Graphic shows the 0.5-m gap; v = 0.056 m/s.

Figure 6-151. Temperature Contours at the End of the Three-Dimensional Simulation

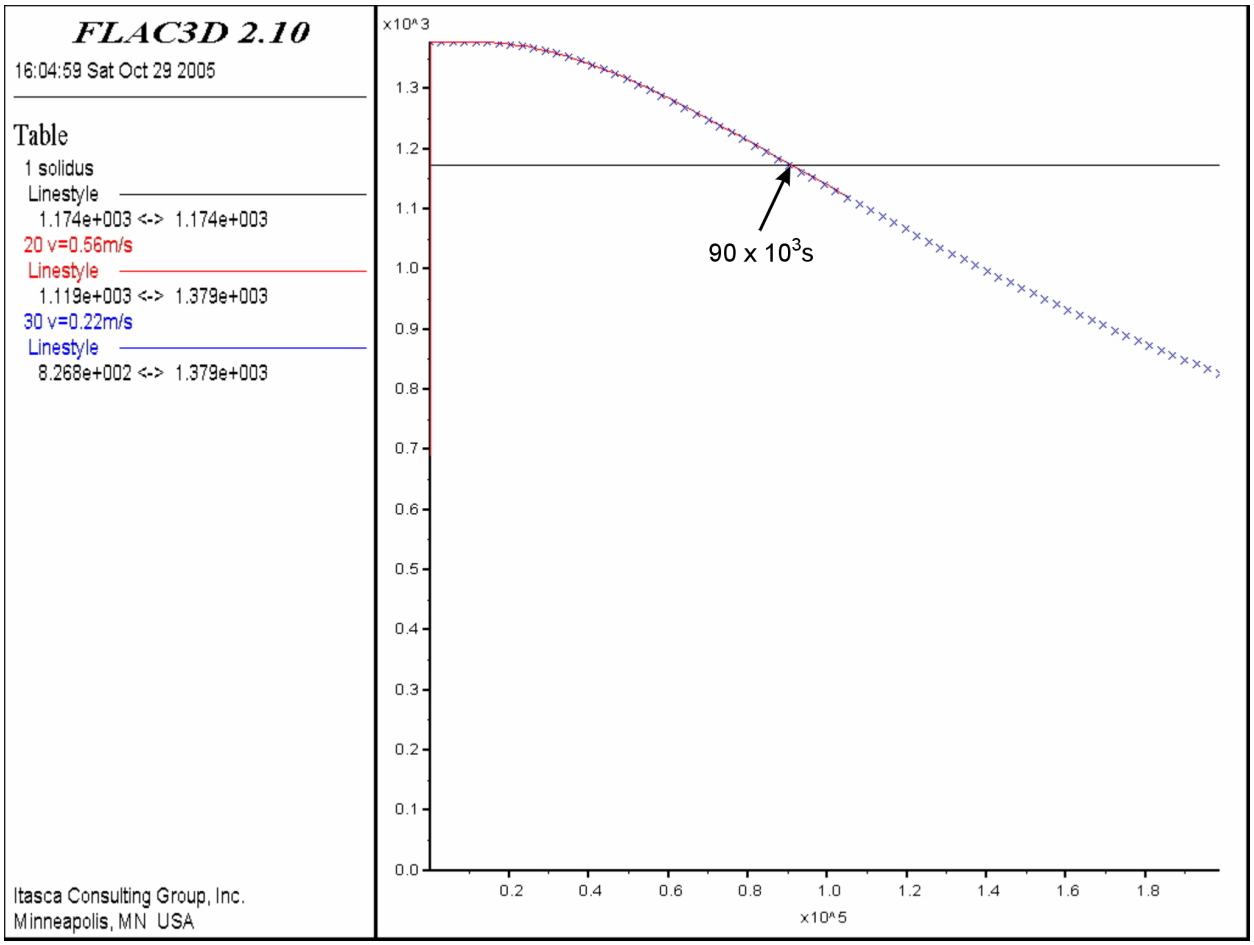

Source: Output DTN: MO0705BACKFILL.000, file *\m0p5\figm0p5\fig9.jpg.*

NOTE: Graphic is for 0.5-m gap between the backfill and the crown of the drip shield.

Figure 6-152. Temperature History at Mid-elevation of the Magma Tip—Three-Dimensional Simulation

To estimate the influence of grid size on simulation results, the calculations for a 0.3-m gap and a magma velocity of 0.016 m/s were repeated for two larger values of zone size, 10 mm and 5 mm, in the direction normal to the drift axis near the magma front. The results for temperature history at mid-elevation in the magma tip for all three zone sizes (10 mm, 5 mm, and 1 mm) are compared in Figure 6-153.

The cooling times for the three zone sizes show the influence of grid discretization on results. One important observation is that heat loss for the magma is underestimated by the use of a larger grid size, as the magma temperature is higher than the temperature of the surrounding rock or fill and the use of a larger grid size for the rock/fill in the vicinity of the magma results in a smaller thermal gradient in the first calculation step after the magma comes in the contact with cool rock/fill. Therefore, heat loss for the magma is underestimated by the use of a larger grid size. The discrepancy is not large (about 13%) for the cases investigated, and the results confirm a value that corresponds to the traveled distance of magma on the order of 500 meters for a magma velocity of 0.016 m/s and a 0.3-m gap on top of the fill.

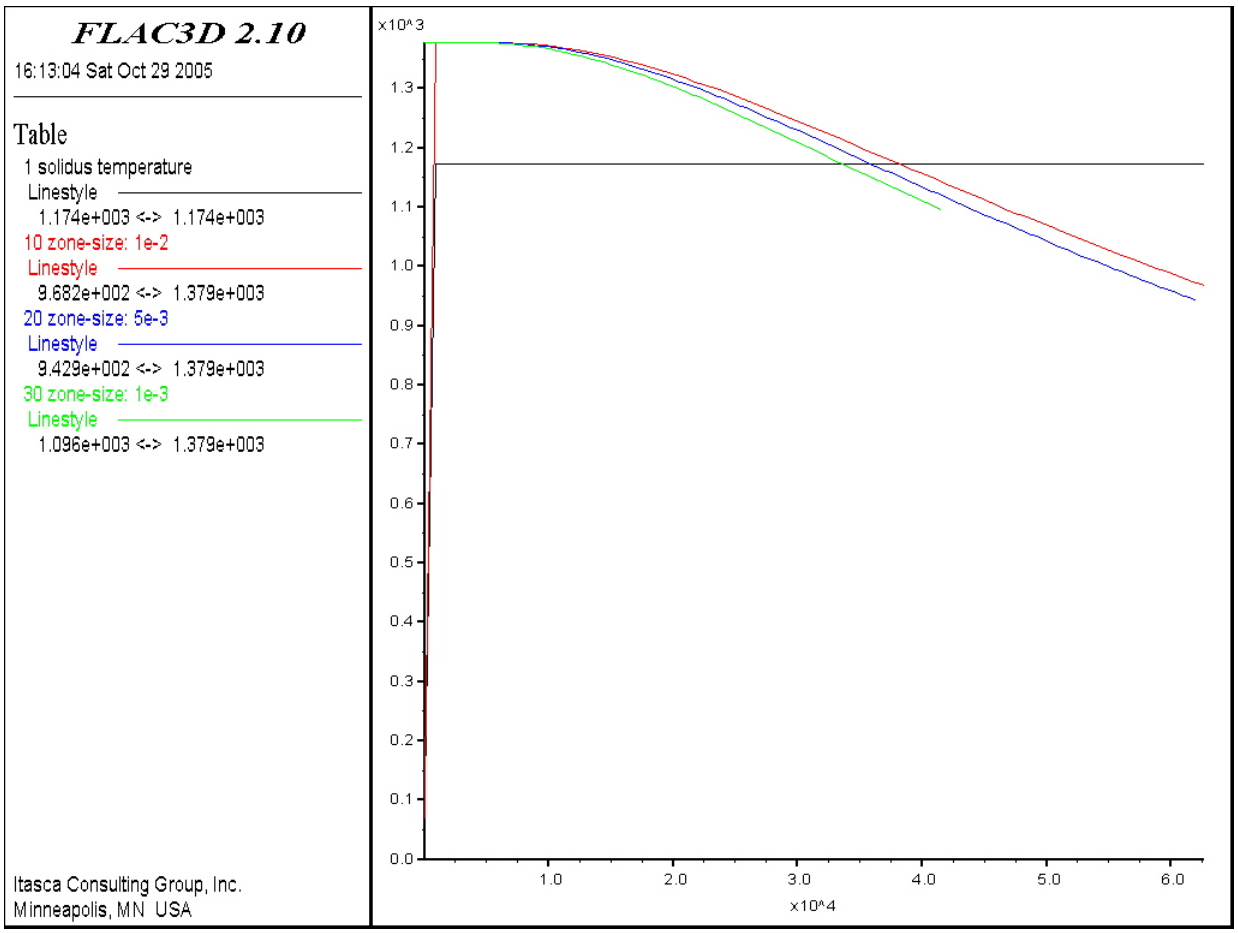

Source: Output DTN: MO0705BACKFILL.000, file *\m0p3\figm0p3\fig13.jpg*.

NOTE: Graphic shows 0.3-m gap; magma velocity is 0.016 m/s.

Figure 6-153. Temperature Histories at Mid-elevation in Magma Tip for Three Zone Sizes—Three-Dimensional Simulation

6.4.8.4.4 Conclusion

Three-dimensional analyses using a combination of fixed grid techniques and small zone sizes were conducted to simulate transfer of heat by advection and conduction for magma flowing in a gap over backfill in a drift. Increasing the gap from 0.3 m to 0.5 m results in an increase in the cooling times by a factor of 3 (and, therefore, in increase in the distance traveled before solidification). The results are linear with respect to the inverse of the magma viscosity. The results predict a maximum flow distance ranging from approximately 500 meters for a gap of 0.3 m and a magma velocity of 0.016 m/s to approximately 20 km of flow distance for a magma velocity of 0.22 m/s with a 0.5-m gap.

This analysis provides an estimate of the upper limit of the distance that magma may flow in the gap between backfill and the crown of a drift. Factors not included in the analysis that would further decrease magma flow include: increased magma viscosity as a result of cooling and partial crystallization at the edges of the flow prior to complete stoppage at the center of flow;

mixing of cold, high-silica backfill into the hot, low-silica alkali basalt magma; and radiative heat losses from the toe of the magma flow to the open gap ahead of the flow.

The analysis presented here assumes that the magma has a viscosity that is independent of temperature, which is not correct but is required by constraints of available qualified software. It was shown in Section 6.4.8.2 that the viscosity of magma increases by several orders of magnitude as the temperature drops below the liquidus. As the viscosity increases, the velocity will decrease. Thus the distances derived in this section, which are calculated by multiplying the magma speed by the time to cool to the effective solidification temperature, will be overestimates. Because of the highly nonlinear nature of the cooling flow, the extent of overestimation cannot be reliably estimated.

Calculations of drift stability for strong seismic ground shaking, discussed in *Seismic Consequence Abstraction* (SNL 2007 [DIRS 176828), show that drift crown collapse certainly occurs for a peak ground velocity (PGV) of 2.44 m/s or greater. These PGV levels correspond to a probability of annual recurrence of 10^{-6} or less. The drift crown remains stable for the majority of ground motions analyzed at the 1.05 m/s PGV level. Therefore, the annual probability that the roof will collapse and completely close the gap on top of backfill is between 10^{-6} and 10^{-5}. If seismic ground shaking and volcanic intrusion are independent processes, the probability that volcanic intrusion will take place while there is still a gap on top of backfill in the access mains is a function of time. For example, if a volcanic intrusion were to occur 10,000 years after waste emplacement, there is a 99% and 90% probability that the gap will be open if the annual probability of gap closure is 10^{-6} and 10^{-5}, respectively. Thus, if seismic ground shaking and volcanic intrusion are independent processes, the probability is high that the gap on top of the backfill will be open for a long time after backfilling of the mains.

Ascent of dikes often causes seismicity. Interaction between a rising dike and nearby (or intersected) faults can cause slip on the fault and seismic events in the vicinity of the repository that could collapse the drifts. If the access mains or the drifts are completely filled (with backfill or rubble formed by collapse of the drift crown), magma will be prevented from penetrating into unintersected emplacement drifts.

6.4.9 Summary

Section 6.4 has developed constraints on the environment in the repository that will occur in drifts following intrusion by an alkali basaltic magma.

The analysis of heat flow after an emplacement drift has been filled with magma (Section 6.4.6) found that waste packages will rise to magmatic temperatures in days to weeks, exceeding 700°C for a period of from one month to nineteen months, depending on the temperature of the magma and the radioactive heat generated by the waste. Temperatures in the invert fill supporting the pallets and waste packages will approach or exceed the glass-transition temperature of the crushed tuff for as long as three years after intrusion if the waste packages are hot at the time of intrusion; for cold waste packages and a hot, effusive intrusion, temperatures in the upper half of the invert fill may exceed that temperature for a few months.

As the magma cools, it will solidify with the progressive crystallization of mostly anhydrous minerals. Thus water is more concentrated in the residual melt. Since the edges of a drift will already be solid and there will be a plastic layer between the cooler, solid basalt and the mushy interior, the increasing water content will result in pressures in excess of 10 MPa, perhaps as high as 15 MPa, before the seal is broken. Given the expected composition of magmatic volatiles and a nominal 10 MPa pressure, it is concluded that waste packages can be subjected for several months to a highly corrosive vapor consisting of partial pressures of 7.3 MPa steam, 1.4 MPa CO_2, 945 kPa $S0_2$, 120 kPa H_2, 87 kPa HCl, 74 kPa H_2S, 57 kPa CO, 41 kPa S_2, and 17 kPa HF at temperatures of 900°C to 1,100°C.

Uncertainty exists in the magmatic effects on waste package integrity. Flow of magma into drifts is likely to result in plastic deformation of waste packages, but it is unlikely to result in movement of waste packages over large distances. Exposure of packages to the high temperatures and corrosive gases at high pressures in the magmatic environment for periods lasting from one month to tens of months is expected to enhance corrosion, with the result that waste packages may tear and magma could enter. Commercial spent nuclear fuel is expected to become comminuted due to oxidation. Other chemical effects are difficult to predict. Glassy waste forms are not expected to be significantly altered by encounters with magma. On balance, it is appropriate to adopt the conservative position that all waste packages and associated drip shields that come in contact with basalt magma will provide no protection against seepage water when seepage flow returns after an intrusive event.

An approximate analysis of heat losses during the flow of magma through a gap of 0.3 m at the top of backfill in access drifts indicates that cooling will take approximately ten hours. This is a long enough time that flow of magma with a constant viscosity would reach 500 m. However, the viscosity of the magma would increase as it cools, so the actual distance reached by magma flowing over backfill would be less.

6.5 ANALYSIS OF SECONDARY DIKE PROPAGATION

This section contains analyses intended to evaluate a portion of FEP 1.2.04.03.0A, Igneous Intrusion into Repository. Woods et al. (2002 [DIRS 163662]) described a drift filling and a secondary dike opening to the surface at some distance from the original dike, with the magma flow being diverted through the drift and carrying the entire drift contents to the surface. This is commonly called the “dog-leg” scenario. Secondary dike propagation for the case of effusive magma flow, in which the magma is similar to that considered in Section 6.3.3, is analyzed in Section 6.5.1. Analysis of secondary dike propagation driven by pyroclastic or two-phase flow is not attempted in this report. However, that scenario is considered unlikely to occur because the model in Section 6.3 demonstrates that the cross-sectional area of contact between the dike and a drift will increase gradually over a period of several seconds or even minutes, precluding development of a strong shock propagating down the drift. Section 6.5.2 summarizes the conclusions from the analyses.

6.5.1 Secondary Dike Propagation for Effusive Flow

It appears, from the analysis of dike propagation from depth, that in most cases the dike tip will have already reached the surface by the time an effusive magma arrives at the depth of the emplacement drifts and more-viscous magma would accentuate this tendency (Section 6.3.7.1). In addition, the upward progress of the magma front inside the dike may be slowed above a drift (relative to upward progress of magma in the pillars between drifts during the time that magma is flowing into the drifts; see Section 6.3.3.5.6). Both of these effects will reduce the likelihood that magma would find a path out of the repository other than along the original trajectory of the dike. However, the analysis that follows in this section addresses the unlikely potential for such a diversion.

6.5.1.1 Description of Inputs

6.5.1.1.1 Inputs for Crack-Opening Analysis

The inputs for the crack-opening analysis in Section 6.5.1.2 are in situ stress state, drift geometry (diameter of 5.5 m), elastic properties of rock mass, joint properties, and magma properties. The sources are listed in Table 4-1. Input values are listed in Tables 6-31 through 6-33.

Table 6-31. Input Parameters for Analysis of Crack-Opening Rates: Initial Stress

Overburden (m)	Ratio of Stress—Crack Perpendicular to Drift	Ratio of Stress—Crack Parallel to Drift
250, 300	0.35, 0.50	0.5

Source: BSC 2004 [DIRS 166107].

Table 6-32. Input Parameters for Analysis of Crack-Opening Rates: Rock Mass

Initial Crack Aperture (mm)[1]	Young's Modulus of Rock (GPa)[2]	Poisson's Ratio[2]	Joint Normal Stiffness (GPa/m)[3]	Joint Shear Stiffness (GPa/m)[3]
1, 3	5, 15	0.21	20	20

Sources: [1] Value postulated relative to corroborating information discussed in this section.
[2] Detournay et al. 2003 [DIRS 169660], Table 1-2.
[3] Assumed value.

NOTE: Values for Young's modulus and Poisson's ratio are representative of the Topopah Spring lower lithophysal unit.

Table 6-33. Input Parameters for Analysis of Crack-Opening Rates: Magma

	Magma Pressure in Drift (MPa)[a]	Bulk Modulus of Magma (MPa)[a]	Magma Density (kg m^3)	Magma Viscosity (Pa·s)
Value	4, 8, 10	50, 500	1,000	10, 100

[a] Specified values.

Source: Detournay et al. 2003 [DIRS 169660], except where specified.

In order to ensure internal consistency in this report, the sources of the inputs for overburden and ratios of horizontal stresses to vertical stress (referred to in Table 6-31 as coefficients along and perpendicular to the drift) are the same as the sources for the inputs discussed in Section 6.3.3.3. Also, the sources for the elastic properties of the rock mass and the magma properties are the same as the sources for the inputs discussed in Section 6.3.3.3.

Somewhat wider ranges for Young's modulus and magma viscosity were considered in the crack-opening analysis. Young's modulus of 5 GPa is representative of poor-quality rock mass at the repository level. The increased viscosity of 100 Pa·s addresses the effect of magma cooling on the viscosity.

A single value of 1,000 kg m^{-3} for the magma density was used throughout the analysis (Table 6-33). This has a negligible effect on the result because the accelerations are very low, so inertial effects are small. Furthermore, the difference resulting from using magma with a higher density is small.

Three values of magma pressure were considered. Results from Section 6.3.3.4 and Figure 6-18 indicate that the likely value of magma pressure at repository depth under in situ stress conditions is 4 MPa while drifts are filling with magma. After magma has finished filling drifts, it may continue to rise to the surface, increasing the pressure head. At the nominal repository depth of 300 m, the pressure at the base of a column of magma with the largest possible density of 2,600 kg m^3 would be 8 MPa; this exceeds the maximum pressure expected during drift filling in the first 2,000 years after closure as seen in Section 6.3.7.4 and Figure 6-87. The greatest depths of drifts are just over 400 m, at which depth the pressure head in the column of magma would be about 10 MPa.

The results of this analysis are not sensitive to the joint normal and shear stiffnesses. Those input parameters were selected to correspond to the lower bound of measured values (BSC 2004 [DIRS 166107], Table E-4). (Smaller joint stiffness results in a larger calculation time step.) The same argument was used in selection of the input for magma bulk modulus. The analysis showed that there is an insignificant effect on the results when the magma bulk modulus was increased from 50 MPa to 500 MPa. The joint openings (initial crack aperture) of 1 mm and 3 mm were used for the analysis. Measurements by Olsson and Brown (1997 [DIRS 106453]) found that initial joint openings at Yucca Mountain are less than 1 mm. A wider initial opening would be easier to enlarge and would carry more flow than a narrower one.

6.5.1.1.2 Inputs for Magma Cooling Rates Analysis

The inputs for the magma cooling-rates analysis are the thermal diffusivity and specific heat of the magma (heat capacity), the latent heat of crystallization of the magma (heat of fusion), the intrusion temperature, and the viscosity of crystal-free magma. The solution presented here makes the approximation that the thermal properties (specific heat and thermal diffusivity) of the magma and the host rock are the same. The effective solidification temperature (T_s) of the magma is also required and is derived in the analysis (Section 6.4.8.2). Table 4-1 gives input sources.

Calculations were done for the six magma compositions differing in water content and used in *Characterize Eruptive Processes at Yucca Mountain, Nevada* (SNL 2007 [DIRS 174260]).

The thermal diffusivity and specific heat of the magma, and its latent heat were selected to be consistent with the values used in *Final Report of the Igneous Consequences Peer Review Panel, with Appendices* (Detournay et al. 2003 [DIRS 169660]), which are consistent with values used by Spera (2000 [DIRS 164109]). The intrusion temperature is taken as the liquidus temperature from DTN: LA0612DK831811.001 [DIRS 179987]. The crystal-free viscosity is from the same source. The values used are presented in Table 6-34.

Table 6-34. Input Parameters for Thermal Calculations

Water (%)	Approximate Latent Heat ($J\ kg^{-1}$)[a]	Approximate Specific Heat ($J\ kg^{-1}K^{-1}$)[a]	Approximate Diffusivity (m^2s^{-1})[a]	Intrusion Temperature (°C)[b]	Crystal-free Viscosity (Pa·s)[b]	T_s (°C)[c]
0	3.50×10^5	1,100	3.00×10^{-7}	1,169	48	1,135
0.5	3.50×10^5	1,100	3.00×10^{-7}	1,153	37	1,108
1.0	3.50×10^5	1,100	3.00×10^{-7}	1,137	30	1,083
2.0	3.50×10^5	1,100	3.00×10^{-7}	1,106	19	1,034
3.0	3.50×10^5	1,100	3.00×10^{-7}	1,076	13	998
4.0	3.50×10^5	1,100	3.00×10^{-7}	1,046	9.1	964

Sources: [a] Detournay et al. 2003 [DIRS 169660].
[b] DTN: LA0612DK831811.001 [DIRS 179987].
[c] Section 6.4.8.2.

6.5.1.2 Opening of Preexisting Crack

To assess the possibility of a secondary dike propagation (i.e., magma finding a new path to the ground surface by re-opening some of the existing joints inside the drifts), the conditions of magma injection into the joints intersecting the drift were investigated. Specific evaluations were conducted to determine if the pressure in a filled drift could sustain the propagation of magma up a joint to the surface and how fast the magma would rise.

This section discusses results of simulations of magma injection into pre-existing joints inside the emplacement drifts. The simulations discussed here investigate sensitivity of the predictions to variation of the parameters, such as magma compressibility, magma viscosity, magma pressure, initial joint aperture, rock mass stiffness (Young's modulus), and initial stress state. Magma freezing inside the joints is not considered here but is analyzed in Section 6.5.1.4. This analysis does not deal with the transient magma pressures that may develop at the precise time the magma finishes filling the drift. However, because the velocity of an effusive magma in the drift is not high (not more than a few $m \cdot s^{-1}$; see Section 6.3.3.5.6), such transients will be minimal.

All analyses discussed in this section were done using one of two numerical codes: UDEC V. 3.14 or FLAC3D V. 2.14. Both codes are qualified and are used here within their range of intended use. The simulations are fully coupled hydro-mechanical computations but do not consider temperature. Starting from null initial fluid pressures everywhere, a fluid (magma)

pressure is applied inside the drift. This pressure causes the adjacent joint to open and starts the process of magma flow into the joint. Note that the pressure applied in the drift is kept constant in time.

All simulated cases of magma injection into preexisting joints inside the emplacement drifts are summarized in Table 6-35. (The order in which the cases are listed in Table 6-35 does not indicate a relation between different cases, only the sequence in which they were simulated.)

Table 6-35. Summary of Analyzed Cases of Magma Injection into Joints

Case	Crack Orientation with Respect to Drift[a]	Initial Crack Aperture (mm)	Magma Pressure in Drift (MPa)	Initial Stress			Bulk Modulus of Magma (MPa)	Young's Modulus of Rock (GPa)	Magma Viscosity (Pa·s)
				Over burden (m)	Coeff. Parallel to Drift	Coeff. Perp. to Drift			
101	Vertical Parallel	1	4	300		0.5	50	15	10
102	Vertical Parallel	1	8	300		0.5	50	15	10
103	Vertical Parallel	1	10	250		0.5	50	15	10
104	Horizontal	1	8	300		0.5	50	15	10
105	Vertical Perpendicular	1	10	300	0.35	0.5	50	15	10
106	Vertical Parallel	1	4	300		0.5	50	5	10
107	Vertical Parallel	1	4	300		0.5	500	15	10
108	Vertical Perpendicular	1	8	300	0.35	0.5	50	15	10
109	Vertical Perpendicular	1	8	300	0.5	0.35	50	15	10
110	Vertical Parallel	1	8	250		0.5	50	15	10
111	Vertical Parallel	3	8	250		0.5	50	15	10
112	Vertical Parallel	3	8	250		0.5	50	5	10
113	Vertical Parallel	3	8	250		0.5	500	5	10
114	Vertical Parallel	3	8	250		0.5	500	15	10
115	Vertical Parallel	1	8	250		0.5	50	5	10
116	Vertical Parallel	1	8	250		0.5	50	15	100
117	Vertical Parallel	1	10	250		0.5	50	15	100
118	Vertical Parallel	3	8	250		0.5	50	15	100
119	Vertical Parallel	3	8	250		0.5	50	5	100
120	Vertical Parallel	1	8	250		0.5	50	5	100

[a] Crack Orientation: Vertical Parallel = a vertical crack parallel to the drift axis; Vertical Perpendicular = a vertical crack perpendicular to the drift.

Source: For information only.

During simulations, joint apertures and magma pressures in the joint are recorded at seven different locations away from the drift. Tables 6-36 and 6-37 show the positions of these seven points relative to the drift periphery, for all cases studied.

Table 6-36. Distances from Drift Periphery to Recording Points for Cases 101 through 104, 106, 107, and 110 through 120

Point	Distance (m)
1	0.46
2	0.92
3	1.83
4	3.67
5	7.79
6	16.04
7	32.14

Source: For information only

NOTES: Distances are measured from the drift periphery to the points at which histories of aperture and pressures are recorded for the various cases.

Table 6-37. Distances from Drift Periphery to Recording Points for Cases 105, 108, and 109

Point	Distance (m)
1	0.00
2	1.40
3	3.08
4	5.08
5	10.34
6	22.71
7	43.79

Source: For information only

NOTES Distances are measured from the drift periphery to the points at which histories of aperture and pressures are recorded for the various cases.

The results for Case 101 (representative conditions) and Case 103 (extremely aggressive conditions) are shown in Figures 6-154 through 6-161. The following plots are shown for each case:

- Displacement vector field and hydraulic aperture along the joint at the end of the simulation
- Stress tensor field (colored by the magnitude of the minor principal stress) and pore pressure along the joint at the end of simulation
- Evolution of joint aperture at seven locations, as indicated in Table 6-36
- Position (distance from the drift periphery) of the magma front inside the joint as a function of time.

The results for all runs are summarized in Figures 6-162 and 6-163; plots similar to Figures 6-154 through 6-160 for each of the cases listed in Table 6-35 can be found in output DTN: MO0411EG831811.002. Appendix H provides more detail on identifying the files in the

DTN that contain these results. Figure 6-162 shows the average magma front velocity computed for each simulation. Note that such a velocity tends to decrease with time, so the velocity shown here is an overestimate of the magma velocity at later times. Figure 6-163 compares the various simulations in terms of thickness achieved by the magma intrusion at a range of 3.67 m from the wall of the drift. The figure shows, for each case studied, the time needed between the start of the injection and:

- Start of the joint opening
- 1.5-mm thickening of the joint
- 3-mm thickening of the joint opening
- 10-mm thickening of the joint
- 25-mm thickening of the joint opening.

For Case 101, the magma travels only 15 m in one hour, as shown in Figure 6-157. However, only 300 seconds after the drifts are completely filled with magma, the main dike would reach ground surface (for a magma front velocity of 1 m s^{-1}). At that time, the magma has traveled only 5 m away from the drift.

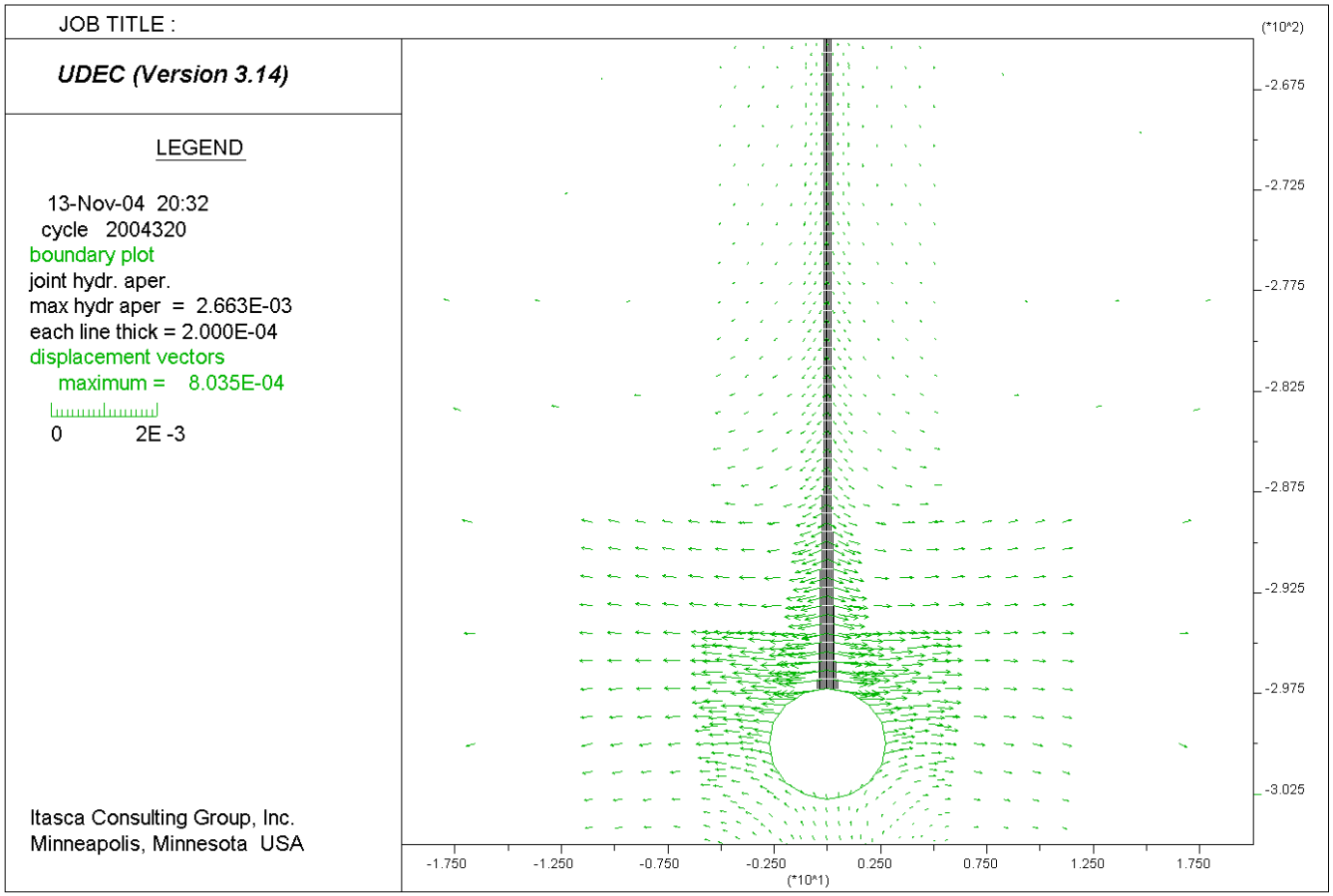

Output DTN: MO0411EG831811.002; file: *MO0411EG831811.002_Disk6\figures\fig6-53.jpg*.

Source: Output data calculation plot.

NOTE: Thickness of the black line is proportional to the hydraulic aperture of the joint. Deformation (green arrow) is due to pressure change inside the joint only. Scale in legend shows displacement vector lengths from 0 mm to 0.8 mm.

Figure 6-154. Displacement Vector Field (m) in Green and Hydraulic Aperture (m) in Black along the Vertical Fracture: Case 101

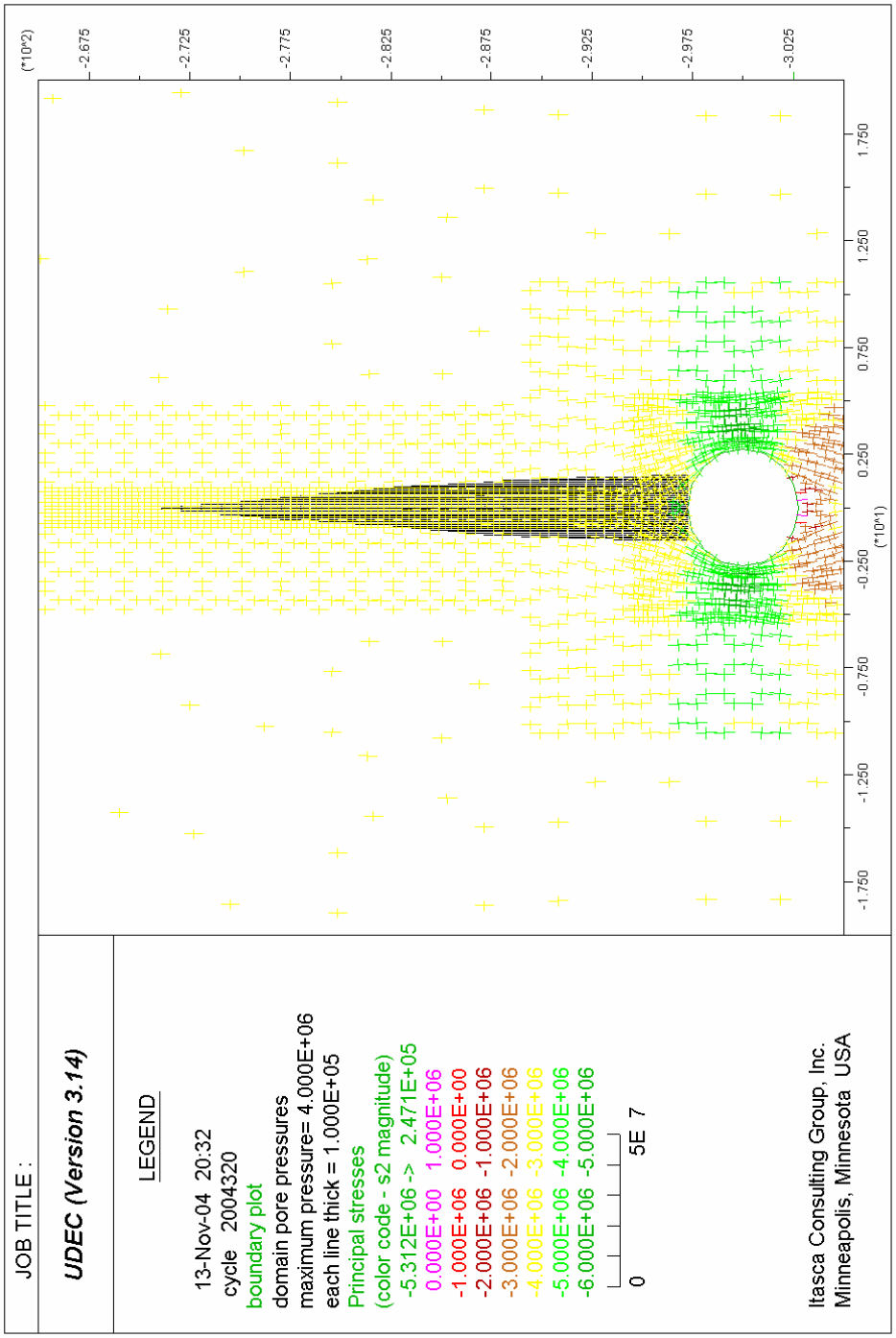

Output DTN: MO0411EG831811.002; file: *MO0411EG831811.002_Disk6\figures\fig6-54.jpg*.

Source: Output data calculation plot.

NOTE: Thickness of the black line is proportional to magma pressure in the joint; color of stress tensors indicates the magnitude of the minor principal stress.

Figure 6-155. Stress Tensor Field (Pa) (in color) and Pore Pressure (Pa) (in black) along the Joint: Case 101

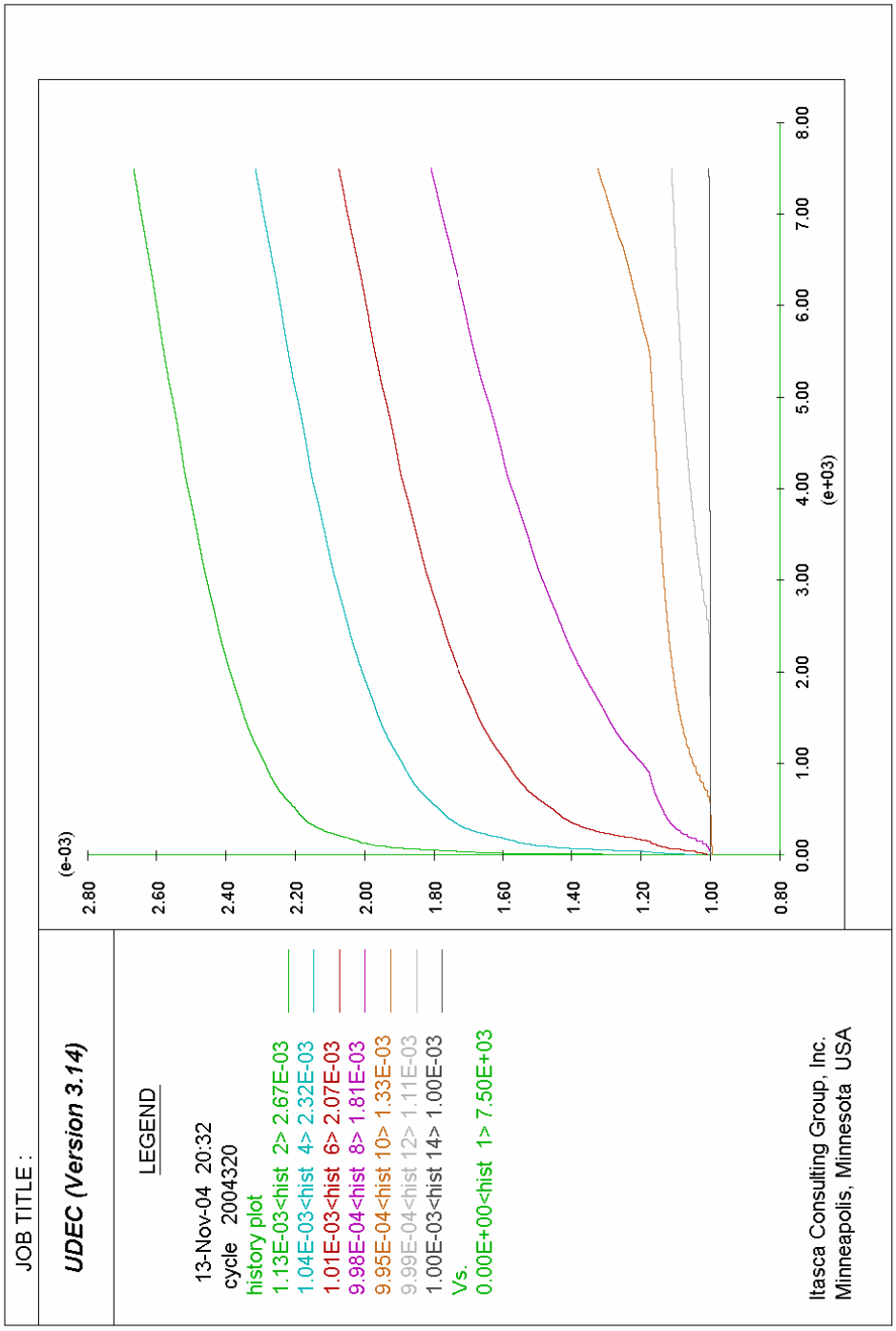

Output DTN: MO0411EG831811.002; file: *MO0411EG831811.002_Disk6\figures\fig6-55.jpg*.

Source: Output data calculation plots.

NOTE: Increasing history numbers correspond to points from Table 6-35, maintaining the same sequence. Time is in seconds.

Figure 6-156. Histories of Joint Hydraulic Aperture (m) at Seven Locations along the Joint: Case 101

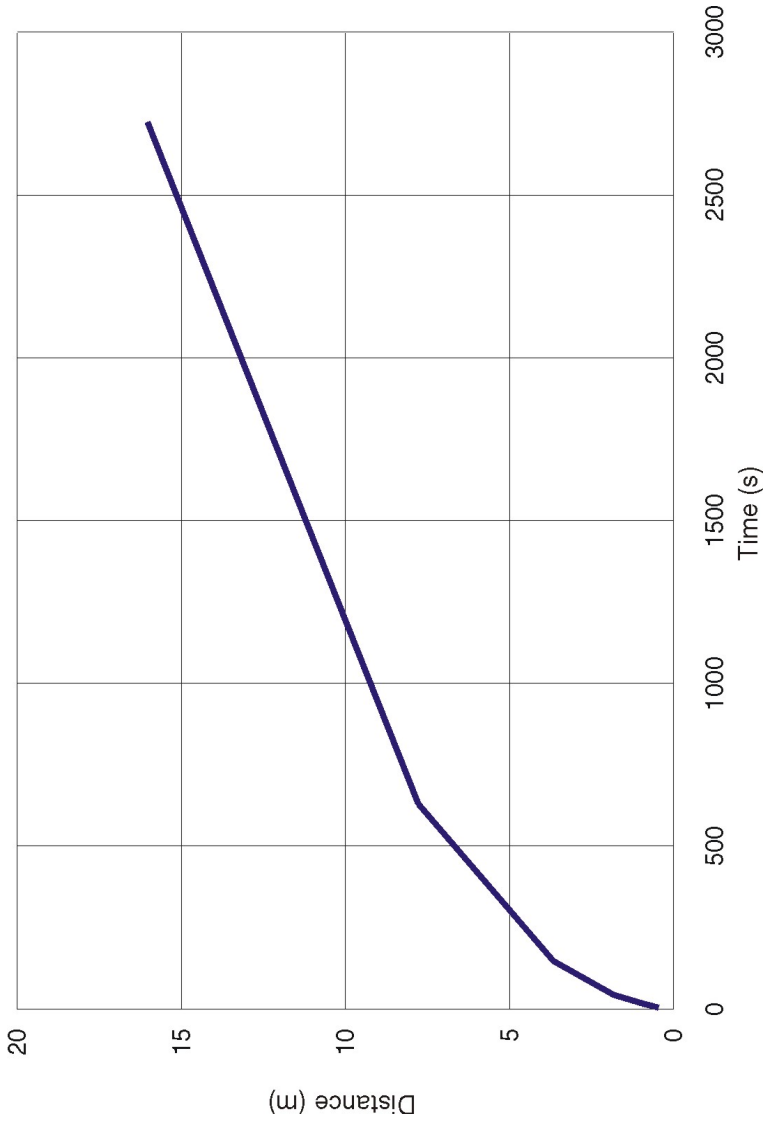

Output DTN: MO0411EG831811.002; file: *MO0411EG831811.002_Disk6\figures\fig6-56.jpg.*

Source: Output data calculation plot.

Figure 6-157. Location (Relative to the Drift Periphery) of the Magma Front inside a Joint as a Function of Time: Case 101

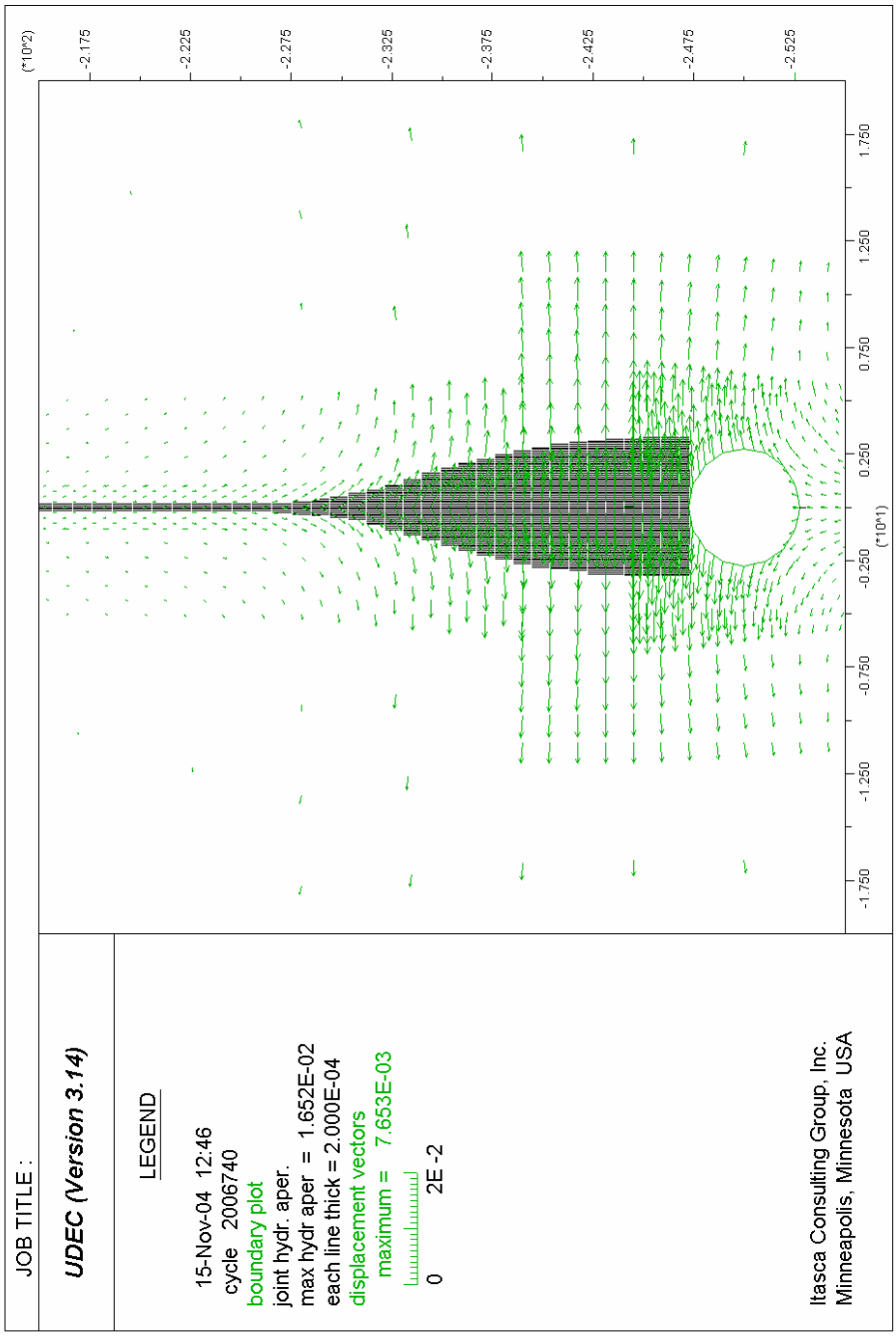

Output DTN: MO0411EG831811.002; file: *MO0411EG831811.002_Disk6\figures\fig6-57.jpg*.

Source: Output data calculation plot.

NOTE: Thickness of the black line is proportional to hydraulic aperture of the joint; deformation is due to pressure change inside the joint only.

Figure 6-158. Displacement Vector Field (m) (in green) and Hydraulic Aperture (m) (in black) along the Vertical Fracture: Case 103

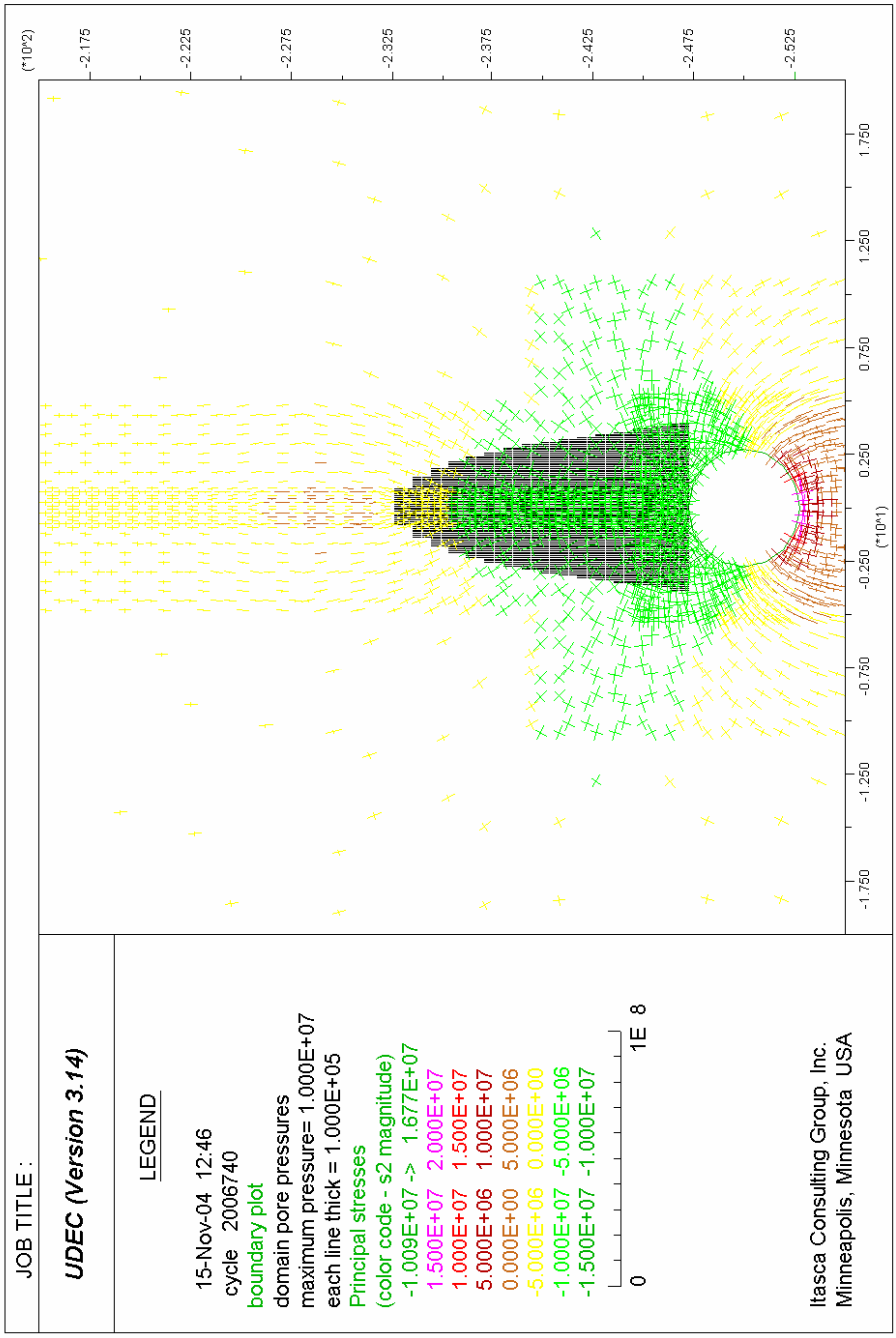

Output DTN: MO0411EG831811.002; file: *MO0411EG831811.002_Disk6\figures\fig6-58.jpg*.

Source: Output data calculation plot.

NOTE: Thickness of the black line is proportional to magma pressure in the joint; color of stress tensors indicates the magnitude of the minor principal stress.

Figure 6-159. Stress Tensor Field (Pa) (in color) and Pore Pressure (Pa) (in black) along the Joint: Case 103

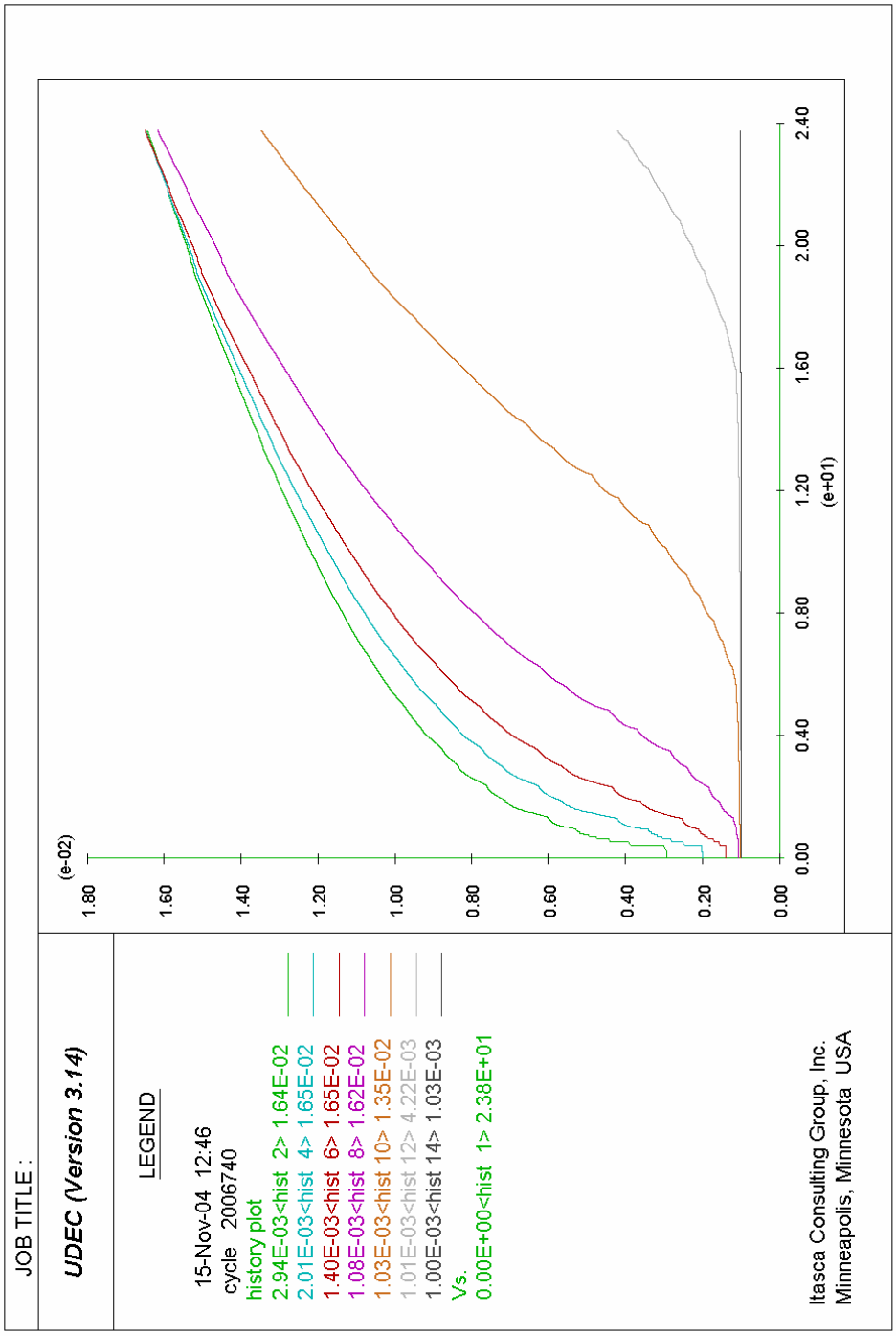

Output DTN: MO0411EG831811.002; file: *MO0411EG831811.002_Disk6\figures\fig6-59.jpg*.

Source: Output data calculation plots.

NOTE: Increasing history numbers correspond to points from Table 6-35, maintaining the same sequence. Time is in seconds.

Figure 6-160. Histories of Joint Hydraulic Aperture (m) at Seven Locations along the Joint: Case 103

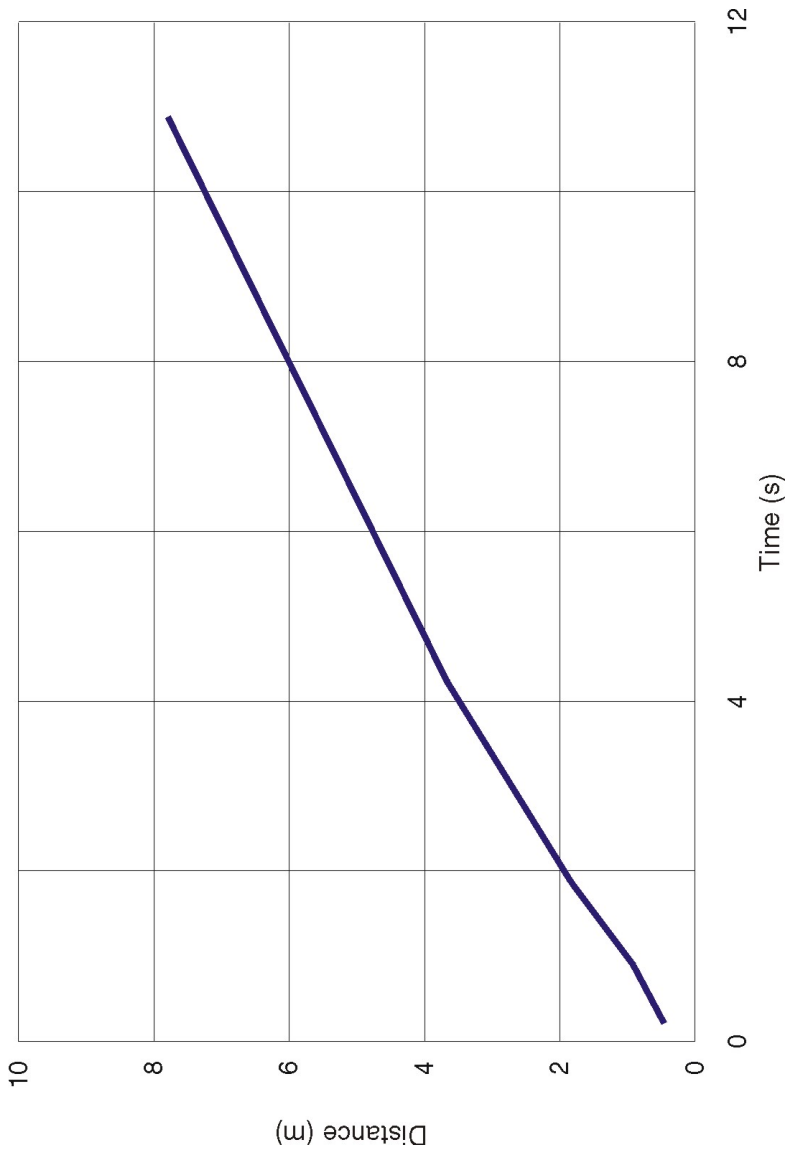

Output DTN: MO0411EG831811.002; file: *MO0411EG831811.002_Disk6\figures\fig6-60.jpg*.

Source: Output data calculation plot.

Figure 6-161. Location (relative to the drift periphery) of the Magma Front inside a Joint as a Function of Time: Case 103

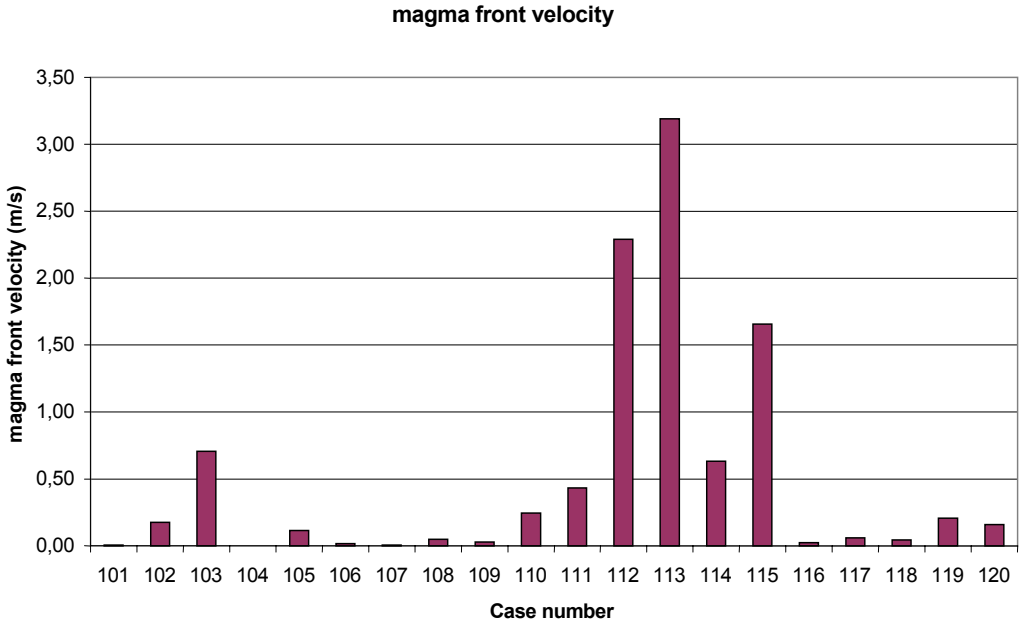

Output DTN: MO0411EG831811.002; file: *MO0411EG831811.002_Disk6\figures\fig6-61.jpg*.

Figure 6-162 Magma Front Average Velocity over the Whole Simulation, for each Case

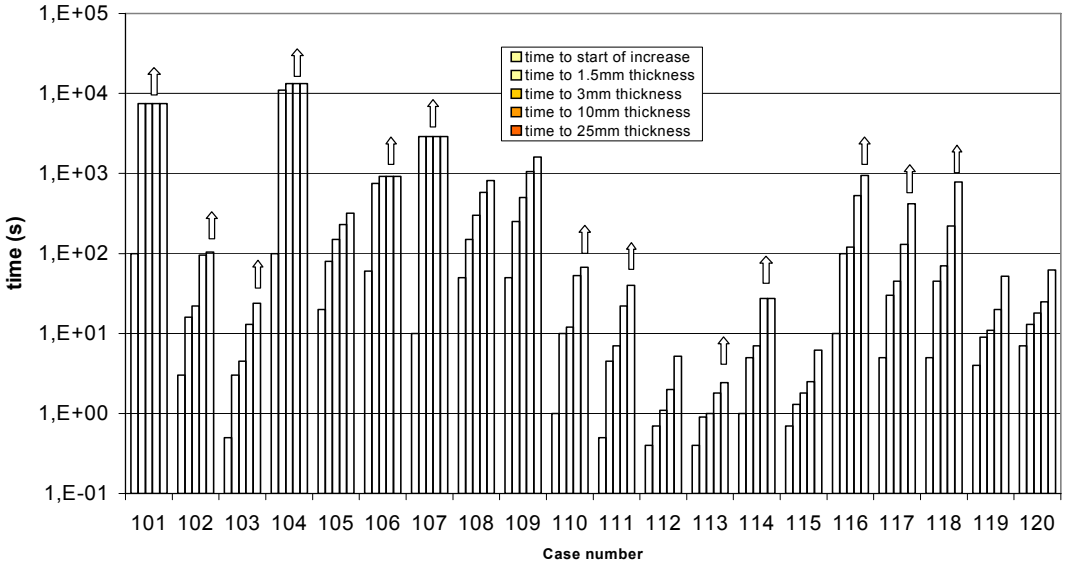

Output DTN: MO0411EG831811.002; file: *MO0411EG831811.002_Disk6\figures\fig6-62.jpg*.

NOTE: Arrows above histogram bars mean that the time given is a minimum; the simulation was stopped before the corresponding thickness increase was reached.

Figure 6-163. Time Needed for the Joint to Reach Several Thickness Increases at 3.67 m from the Drift Periphery (except for cases 105, 108, and 109, for which distance is 3.08 m)

Case 103 represents extreme conditions with a magma pressure inside the drift of 10 MPa and a shallow repository depth of only 250 m, whereas stresses in the rock mass are due to in situ far-field conditions (no thermal effects). Plugging the main dike or conduit at any elevation

above the repository level could result in an increase in magma pressure without an increase in rock-mass stresses. The analysis of magma pressures that might be generated during crystallization of magma in a drift (Figure 6-141, Section 6.4.8.1.3) indicates that pressures could exceed 10 MPa. Those pressures would be contained inside a plastically deforming seal of crystallized magma and would not have direct access to pre-existing cracks in the surrounding tuff. Hence, these high pressures could not readily escape as an effusive magma, only as a vapor-dominated hydrofracture. Even for such extreme conditions, the mean velocity of the magma front inside a joint is approximately 0.7 m s^{-1} (with a trend to decrease as the pressure gradient decreases in response to the increasing length of the magma-filled portion of the joint). This is less than the expected velocity of the magma front inside the main dike.

As shown in Figure 6-162, the remaining base cases (i.e., cases 102, 104, and 105) yielded lower magma front velocities.

The results from cases 106 through 120 investigated sensitivity of the predictions to variations of particular parameters, such as magma compressibility, magma viscosity, magma pressure, initial joint aperture, rock mass stiffness (Young's modulus), and initial stress state.

Sensitivity of case 101 to variation of Young's modulus of the rock mass was investigated in case 106. Young's modulus of the rock mass in case 106 is 5 GPa (poor quality lithophysal rock, between categories 1 and 2), which compares to 15 GPa in case 101 (good quality lithophysal rock, between Categories 4 and 5, and also representative of nonlithophysal rock mass). The results indicate that, in the case of more compliant rock mass, the increase in the joint aperture is faster (750 s needed to reach a 1.5 mm thickness increase, instead of more than 7,500 s for case 101; see Figure 6-163) but still relatively small. Even in this case, the analysis in Section 6.5.1.4 indicates that the magma would freeze due to conductive heat loss into the surrounding rock mass.

To investigate the effect of magma compressibility, case 107 was simulated using a magma bulk modulus of 500 MPa (compared to 50 MPa in case 101). The magma front velocities for cases 101 and 107 are almost identical, at 0.01 m s^{-1}. Also, in both of these cases, the joint thickness does not attain 1.5 mm during the simulation time. Magma compressibility hardly affects the results in these cases.

Cases 108 and 109 use a three-dimensional representation of a joint perpendicular to the axis of the drift for comparison with case 105. Both new cases are for 8 MPa magma pressure (case 105 is for 10 MPa). Case 109 represents the condition of a larger normal stress along the drift (perpendicular to the joint), 50% of the vertical stress compared to 35% of the vertical stress for cases 105 and 108. The simulations for all three cases indicated instability (due to the magma pressure being larger than the horizontal far-field stress perpendicular to the joint). However, Figure 6-163 shows a clear trend of reduction in the rate of joint opening from cases 105 to 108 and from case 108 to 109, as the ratio of driving pressure to confining stress decreases. The time needed for a 25-mm thickness increase varies from 320 s for case 105, to 820 s for case 108 and 1,600 s for case 109.

The maximum vertical stress at the repository level is less than 8 MPa. Under such conditions, the 10-MPa magma pressure considered in case 103 is unrealistic unless the magma is enclosed in a small (5-m- to 8-m-diameter) cylinder whose periphery is sealed. Case 110 investigates the effect of reduction in magma pressure from 10 MPa (considered in case 103) to 8 MPa with the same small overburden depth of 250 m. The rate of fracture opening declines significantly from case 103 to case 110; the time needed to reach a crack width of a 25-mm increases from 24 s (case 103) to 67 s (case 110). Also, the magma front velocity is significantly reduced from 0.71 m/s to 0.25 m/s.

All of the analyses discussed so far had the initial joint aperture set at 1 mm. This input value is reasonable considering measurements of joint apertures (Olsson and Brown 1997 [DIRS 106453]). However, to investigate the response of the initial joint aperture, six cases (cases 111 to 114, 118, and 119) were simulated using the larger value of 3 mm for the initial joint aperture. All parameters between cases 110 and 111 are the same, except that the initial joint aperture in case 110 is 1 mm and in case 111 it is 3 mm. Magma front velocity increases from 0.25 m s^{-1} to 0.43 m s^{-1}. The 25-mm thickness is reached in 40 s (case 111) instead of 67 s (case 110).

Cases 106, 112, and 115 investigate the effect of stiffness of the rock mass. Cases 106 and 101 both have 4-MPa pressure in a 1-mm-wide crack, but case 101 has a Young's modulus of 15 GPa whereas Young's modulus is only 5 GPa for case 106. Case 115, with a Young's modulus of 5 GPa, can be compared to case 110, with a Young's modulus of 5 GPa (both cases are for a 1-mm joint aperture). Similarly, case 111 is for a Young's modulus of the rock mass of 15 GPa for comparison to case 112 where Young's modulus is 5 GPa (both cases are for a 3-mm joint aperture). The effect of the stiffness of the rock mass is much more pronounced for wider joint apertures (cases 111 and 112) and for higher magma pressures (cases 110 and 115) than for narrow joints at low pressures (cases 101 and 106). It also appears that rock mass deformability has a more profound effect on the potential for the opening of a secondary dike inside the drift than the initial joint aperture.

Joints with long trace lengths exist in good quality rock (i.e., nonlithophysal rock mass and better-quality lithophysal rock mass). Such rock is characterized with a Young's modulus equal to or greater than 15 GPa. Poor-quality rock mass at the repository level in Yucca Mountain (e.g., highly fractured lower lithophysal—Tptpll) is characterized by a large number of joints that are closely spaced with short trace lengths and that are not continuous. Such poor-quality rock will not be susceptible to a mechanism of localized fracture propagation. Instead, it is more likely that magma will be injected into exposed lithophysae and into a number of noncontinuous, mutually intersecting joints. Such a process will lead to quick magma freezing due to excessive heat loss.

Cases 113 and 114 investigate the effect of an increase in magma bulk modulus from 50 MPa to 500 MPa relative to cases 112 and 111. It appears from the results that such an increase in magma bulk modulus has a minor effect on the results.

All of the results presented to this point used a magma viscosity of 10 Pa·s. As magma enters the drift and is being injected into the joints, it will cool and its viscosity will increase. Because a dimensional and scaling analysis was not carried out, simulations of cases 116 through 120 were

conducted to investigate the effect of an increase in magma viscosity from 10 Pa·s to 100 Pa·s. As expected, an increase in magma viscosity results in a proportional increase in time scale. For example, in case 103 (viscosity 10 Pa·s) it takes 13 s to reach a 10-mm thickness increase; whereas, in case 117 (viscosity 100 Pa·s) the thickness increase is reached after 130 s.

Even if the argument of partial freezing is not used, among all of the 20 analyzed cases, only in five cases, cases 103 and 112 to 115, does a magma front inside the joint move faster than 0.5 m/s. That result implies that the magma front inside the original dike (which could already be 80 m or more above the repository level) will reach the ground surface much sooner than the magma injected into joints inside the drift.

A limitation of this model of secondary dike propagation is that it considers all of the magma in the drift and in the propagating crack to be a fluid with a fixed viscosity. The effect of cooling of the magma being injected into the secondary crack is considered in Section 6.5.1.4. In Section 6.4.8.1.3.2 it was noted that the outer portions of magma in the drift would include a zone of solidified, but plastically deformable, hot basalt that would retard fracture propagation; therefore, hydrofracture at the late times needed to generate magma pressures above 10 MPa is not likely.

6.5.1.3 Potential Location of an Eventual Secondary Dike

This section presents an analysis of the altered stress field around the dike and the resultant stress concentrations to provide an assessment of where along the drift a secondary dike would be most likely to develop.

6.5.1.3.1 Stress-Related Effects

Prior to the formation of the dike, the repository is characterized by some far-field principal stresses with known orientations and values. These stresses may change with time due to heating, but calculations of those changes are available using a thermo-mechanical model of the repository. The repository is also characterized by various material properties, but only Poisson's ratio is actually required for this analysis.

Effective In Situ Stresses–The effective in situ stresses are given by:

$$\sigma_1 = S_1 - \zeta P \qquad \text{(Eq. 6-116)}$$

$$\sigma_2 = S_2 - \zeta P$$

$$\sigma_v = S_v - \zeta P$$

where

S_1, S_2, and S_v are the principal in situ stresses
P = is the pore pressure
ζ = Biot's modulus.

All subsequent equations involving the principal far-field stresses will use the effective stress form. However, because the pore pressure at the repository level is zero, the effective stresses are equal to the total stresses.

Addition of Dike-Stress Perturbation–The presence of a pressurized dike results in additional stresses that must be superposed on the in situ stresses. However, because the dike is aligned normal to the minimum principal in situ stress and the dike calculation is two-dimensional, there are perturbations to only four of the stress components. The values of these stress perturbations come from the NPHF2D code calculations and are represented by:

σ_{dv}: the stress perturbation by the dike in the vertical direction
σ_{dh}: the stress perturbation by the dike in the horizontal plane
τ_{dhv}: the shear stress perturbation by the dike in the horizontal-vertical plane
$\sigma_{dp} = v(\sigma_{dv} + \sigma_{dh})$: the stress perturbation by the dike parallel to the dike (out of plane),

where v is Poisson's ratio.

With the presence of the dike, the new stress field, $\boldsymbol{\sigma}'$, is characterized by:

$$\begin{aligned} \sigma_1' &= S_1 + v(\sigma_{dv} + \sigma_{dh}) \\ \sigma_2' &= S_2 + \sigma_{dh} \\ \sigma_v' &= S_v + \sigma_{dv} \\ \tau_{2v}' &= \tau_{dhv} \end{aligned} \qquad \text{(Eq. 6-117)}$$

Because of the existence of some shear in the minimum/vertical plane, the principal stresses would be rotated slightly by the presence of the dike.

Transformation of Principal and Dike Stresses into the Drift Plane: Due to geometric simplifications, the transformation of superposed principal and dike stresses is straightforward. The drifts are essentially horizontal so that the vertical stress is always normal to the tunnel. It is only necessary to rotate the horizontal stresses into a new plane aligned with the drift, which adds a shear stress and appropriately distributes the shear from the dike. The rotation is taken through the angle, φ, from the maximum principal horizontal in situ stress to the axis of the drift. In this rotated space, z is vertical, x is along the axis of the drift, and y is normal to the drift.

These rotations yield stresses σ_x, σ_y, and σ_z and shear stresses τ_{xy}, τ_{yz}, and τ_{xz}, given by:

$$\sigma_x = \sigma_1' \cos^2 \varphi + \sigma_2' \sin^2 \varphi$$

$$\begin{aligned}
\sigma_y &= \sigma_1' \sin^2 \varphi + \sigma_2' \cos^2 \varphi \\
\sigma_z &= \sigma_v' \\
\tau_{xy} &= \frac{1}{2}(\sigma_1' - \sigma_2') \sin(2\varphi) \\
\tau_{yz} &= \tau_{2v}' \cos(\varphi) \\
\tau_{xz} &= \tau_{2v}' \sin(\varphi)
\end{aligned} \qquad \text{(Eq. 6-118)}$$

Drift Stress Concentration: The stress concentrations around the drift in response to the far-field stresses can be calculated following "Stability of Highly Inclined Boreholes" (Aadnoy and Chenevert 1987 [DIRS 178340]). At the tunnel wall where the stress concentration is highest, the stresses are given by:

$$\begin{aligned}
\sigma_\theta &= (\sigma_x + \sigma_y) - 2(\sigma_x - \sigma_y)\cos(2\theta) - 4\tau_{xy} \sin(2\theta) \\
\sigma_{zz} &= \sigma_z - 2\nu(\sigma_x - \sigma_y)\cos(2\theta) - 4\nu\tau_{xy} \sin(2\theta) \\
\tau_{\theta z} &= 2(-\tau_{xz} \sin\theta + \tau_{yz} \cos\theta) \\
\tau_{r\theta} &= \tau_{rz} = 0
\end{aligned} \qquad \text{(Eq. 6-119)}$$

In these equations, θ is the angle around the drift as measured from the x axis towards the z axis, so σ_θ is the hoop stress. Also, σ_r (not in the equations above) is the radial stress, but it is zero at the tunnel wall until pressurized by magma, which is considered next.

Drift Pressurization: The pressurization of the drift, to a value P_w, induces additional radial and tangential components, σ_{pr} and $\sigma_{p\theta}$. These are given by:

$$\begin{aligned}
\sigma_{pr} &= P_w \\
\sigma_{p\theta} &= -P_w \\
\sigma_{pz} &= \nu(\sigma_{pr} + \sigma_{p\theta}) = 0
\end{aligned} \qquad \text{(Eq. 6-120)}$$

In this analysis, there is no leakoff of magma into the pore space to induce poroelastic stress variations. Thermoelastic stresses are not considered here, but the heating of the drift by magma would cause the drift to expand and increase the hoop stress, further reducing the potential for initiation of a fracture.

Principal Stresses–To examine if fracture initiation could occur, the principal stresses around the drift must be determined. The radial stress is always a principal stress because there are no shear components in the radial plane at the drift surface. In the z-θ plane, the principal stresses are given by:

$$\sigma_p, \sigma_q = \frac{1}{2}(\sigma_\theta + \sigma_z) \pm \frac{1}{2}\left[(\sigma_\theta - \sigma_z)^2 + 4\tau_{\theta z}^2\right]^{\frac{1}{2}}, \qquad \text{(Eq. 6-121)}$$

and the angle of failure is given by:

$$\alpha = \frac{1}{2}\tan^{-1}\left(\frac{2\tau_{xy}}{\sigma_x - \sigma_y}\right) \qquad \text{(Eq. 6-122)}$$

6.5.1.3.2 Fracture Criteria

Assessment of Fracture Re-initiation: A new fracture can initiate from the drift only if the magma pressure is sufficient to increase either the hoop stress or the axial stress to overcome the smallest compressive stress that exists on the tunnel wall. Thus, the determination of the smallest principal stress at the tunnel wall solves this aspect of the problem. This determination can be done rigorously by superposing the pressurization stresses with the stress concentration around the tunnel. However, for the particular geometry of the repository (e.g., the drifts nearly aligned with the stress field), the effects of the shear stresses are minimal, and the stress field is almost aligned with the drift. Thus, the principal stresses are essentially in the hoop, radial, and axial directions, and direct comparisons with the pressure can be made by examining the tunnel stress concentrations.

Assessment of Fracture Propagation: An assessment of fracture propagation is direct. The pressure in the drift must be greater than the minimum principal stress at that location. If it is less, the pressure cannot open the fracture and propagate.

6.5.1.3.3 Results of Stress Calculations

An evaluation of the stress field (due to the presence of the pressurized dike) around the repository drifts was performed for a number of the cases run for the dike propagation analysis (Section 6.3). This evaluation includes the stress perturbation (due to the dike) as well as the stress concentration around the drift. These calculations allow for assessment of the conditions under which a potential secondary dike could initiate from the drift and/or propagate in the far field.

Calculations using NPHF2D require some manipulation of the dimensionless parameters in order to represent the location of the repository, the distance away from the dike, the location of the dike tip and magma front, the pressure, and other parameters. An example using one of the base-case calculations is given below to demonstrate the process.

The scaled parameters derived from the input parameters described in Table 4-1 for dike propagation and developed in preceding parts of Section 6 for this case, are given by:

Length	$l^* = (\mu' E'^3 q_\infty / \delta'^4)^{1/6} = 945.01$ m
Pressure	$p^* = (\mu' E'^3 \delta'^2 q_\infty)^{1/6} = 8{,}488{,}596$ Pa
Time	$t^* = (\mu' E' / \delta'^2 q_\infty)^{1/2} = 43.309$ s

and the resultant dike far-field width and velocity are given by:

Width	$w_\infty^* = (\mu' q_\infty / \delta')^{1/3} = 0.5112$ m
Velocity	$v_\infty^* = (\delta' q_\infty^2 / \mu')^{1/3} = 19.5617$ m s^{-1}

Because the problem is formulated in terms of dimensionless parameters and only two of the dimensionless parameters are critical, a wide suite of calculations can be derived from each numerical run. In this particular case with zero cavity pressure and zero confining stress, only one dimensionless quantity needs to be considered, namely:

$$\mathcal{D} = \frac{\kappa \rho_r}{\kappa \rho_r - \rho_f} = \frac{g \kappa \rho_r}{\delta'} \qquad \text{(Eq. 6-123)}$$

Since the input conditions that will be matched are those of dike propagation rate and width at infinity (v_∞ and w_∞) and using the scaled-width equation (Equation 6-68) to substitute for δ', then the dimensionless group can be reformulated as:

$$\mathcal{D} = \frac{g \kappa \rho_r w_\infty^2}{\mu' v_\infty} \qquad \text{(Eq. 6-124)}$$

As long as this dimensionless group is kept constant, this case can be used to extract numerous other valid solutions.

To continue with this example, suppose that this is a case where:

- A lower horizontal stress is desired (e.g., as determined by the relative density difference or a lower value of κ)
- The desired infinite velocity is 1.0 m s^{-1}, as expected for locations near the repository.

The dimensionless group is kept constant if the far-field width drops from 0.5112 to 0.1634. However, making these changes alters the scaling parameters. These must be recomputed from the new values of the parameters, and it is sensible to do so using somewhat more simple relations. For this case, these are:

Length	$l_* = (E' w_\infty^3 / \mu' v_\infty)^{1/2} = 755.3$ m
Pressure	$p_* = (\mu' E' v_\infty / w_\infty)^{1/2} = 3{,}394{,}736$ Pa
Time	$t_* = (w_\infty^3 E' / \mu' v_\infty^3)^{1/2} = 755.3$ s.

The scaled length and time are the same for this case because $v_\infty = 1$ m s^{-1}.

Given this information, the output data from each calculation can be rescaled for the appropriate case. To determine the new position of the dike or the magma front or to find a new position in space (e.g., the location of the repository or the position where a stress determination is required), it is necessary to take the calculated output and rescale by:

$$\text{new length} = \text{calculated length} \times (l_*/l^*).$$

To determine the new pressure or the stress at any position, it is necessary to rescale by:

$$\text{new pressure} = \text{calculated pressure} \times (p_*/\text{p}^*).$$

To determine the new time, it is necessary to rescale by:

$$\text{new time} = \text{calculated time} \times (t_*/t^*) .$$

To determine the new opening of the dike at any depth, it is necessary to rescale by:

$$\text{new opening} = \text{calculated opening} \times (w_\infty/w_\infty^*).$$

For this same example, the repository location is nominally at a 300-m depth; however, the original location computed by the inverse of the rescaling calculation is at a depth of 375.35 m. Similarly, offset distances normal to the fracture are scaled in the same manner. For desired offset values of 10 m, 20 m, 40 m, 80 m, 160 m, 320 m, and 640 m, the original input values must be 12.51 m, 25.02 m, 50.05 m, 100.09 m, 200.19 m, 400.37 m, and 800.75 m, respectively. However, these values will not be the correct depth positions for different density or far-field velocity rescaling.

Applying this process to the case with $\mathcal{D} = 2.67$, $v_\infty = 1$ m s^{-1}, $\mu = 10$ Pa·s, and $\kappa = 0.5$ (Table 6-3), additional stress induced by the pressurized dike (at the repository level and as a function of distance from the dike) can be computed. Figures 6-164 through 6-167 show the induced horizontal, vertical, and shear stress as a function of distance at times when the dike tip is below the repository (Figure 6-164), at the repository (Figure 6-165), halfway between the repository and the surface (Figure 6-166), and as close to the surface as the calculations allow (Figure 6-167) (i.e., the time when the dike unstably propagates to the surface). Tensile stresses are negative. Since this calculation is two-dimensional, the other horizontal stress would be calculated by multiplying Poisson's ratio times the sum of the vertical and horizontal calculated stresses.

In these cases, the effect of the dike on the stress field is somewhat different from that commonly observed with hydraulic fractures occurring at depth. Of particular interest are the large size of the tensile zone and the extension of the tensile region along the dike. In most hydraulic fractures, the tensile zone is narrow and the stress becomes compressive just behind the fracture tip. In this case, however, the large size of the dike, the large cavity region, and the pressure gradient dominated by the weight of the magma, serve to generate a large amount of curvature in a sizable area around the tip resulting in a large extension of the tensile zone. For example,

Figures 6-164 and 6-165 show the horizontal stress decreasing as the dike tip approaches, but Figures 6-166 and 6-167 show that the stress around the dike remains tensile even when the fracture tip is near the surface (nearly 300 m above the repository).

Even the vertical stress becomes tensile directly over the crack tip, but it is slightly compressive at distances beyond 200 m from the dike. In addition, there is a stress reversal behind the tip that is probably due to the adjustment required to match the cavity pressure condition existing at the dike wall, or to match the magma pressure if the fluid front passed this location, as illustrated in Figure 6-167.

Finally, the stress decay length is on the order of several hundred meters. Beyond this point, the effect of the dike is minimal. Clearly, this decay length is a function of the dike tip position and other conditions.

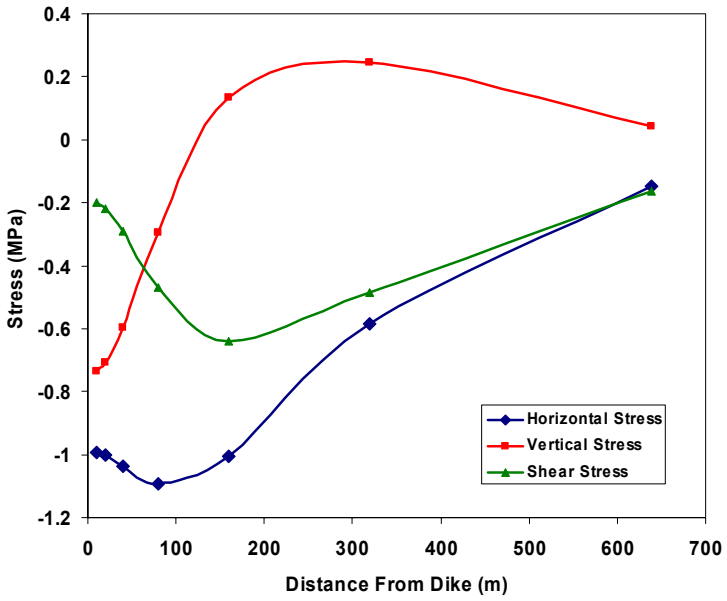

Output DTN: MO0411EG831811.002; file: *MO0411EG831811.002_Disk8\figures\Figures 6-63 & 6-64 data.xls*, tab: "Data412m."

Figure 6-164. Dike-Induced Stress Changes at a 300-m Depth as a Function of Horizontal Distance When the Tip is at a 412-m Depth

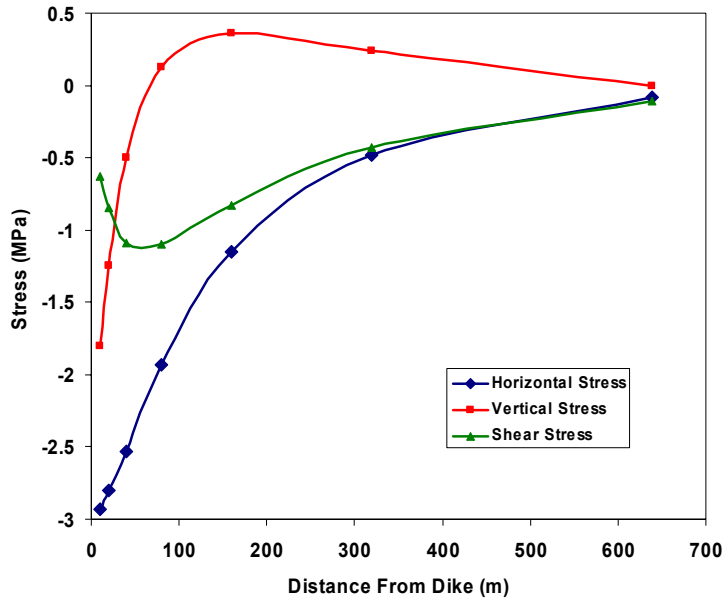

Output DTN: MO0411EG831811.002; file: *MO0411EG831811.002_Disk8\figures\Figures 6-63 & 6-64 data.xls*, tab: "Data300m."

Figure 6-165. Dike-Induced Stress Changes at a 300-m Depth as a Function of Horizontal Distance When the Tip is at a 300-m Depth

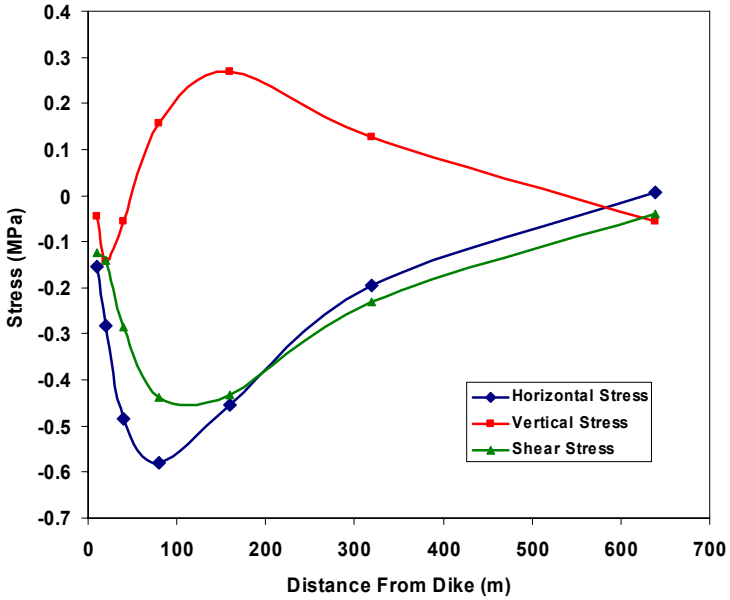

Output DTN: MO0411EG831811.002; file: *MO0411EG831811.002_Disk8\figures\Figures 6-65 to 6-74 data.xls*, tab: "Data150m."

Figure 6-166. Dike-Induced Stress Changes at a 300-m Depth as a Function of Horizontal Distance When the Tip is at a 150-m Depth

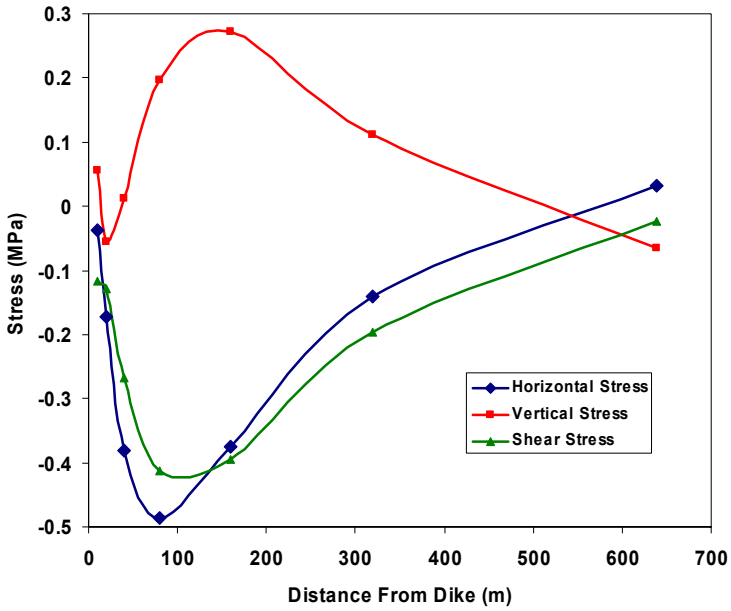

Output DTN: MO0411EG831811.002; file: *MO0411EG831811.002_Disk8\figures\Figures 6-65 to 6-74 data.xls*, tab: "Data16m."

Figure 6-167. Dike-Induced Stress Changes at a 300-m Depth as a Function of Horizontal Distance When the Tip is at a 16-m Depth

To assess the importance of these stress perturbations on the repository, it is necessary to superpose them on the existing stress field, so as to calculate the resultant effect on the stress field and the stress concentrations around the repository drifts. The boundary conditions are:

- Minimum horizontal stress of 3.6 MPa (e.g., this analysis was rescaled with κ = 0.5, which would yield a scaled stress of 3.6 MPa)
- Maximum horizontal stress somewhat greater (5.5 MPa)
- Overburden stress of 7.2 MPa
- Orientation of the maximum horizontal stress N55°E
- Drift orientation of approximately N70°E.

From these boundary conditions, the full stress field near the dike can be calculated. Figure 6-168 shows the resultant stress field acting on the repository when the dike is 412 m below the surface.

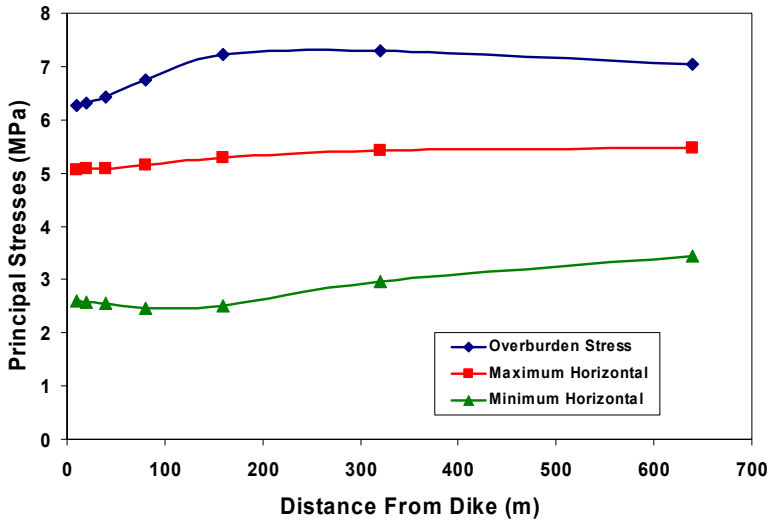

Output DTN: MO0411EG831811.002; file: *MO0411EG831811.002_Disk8\figures\Figures 6-65 to 6-74 data.xls*, tab: "Calculations-411."

Figure 6-168. Total Stresses Acting on the Repository When the Crack Tip is at a 412-m Depth

Figures 6-169 to 6-171 show the same results for dike tip positions of 300 m, 150 m, and 16 m from the surface. As expected from the previous plots, the greatest perturbation on the existing in situ stresses occurs when the dike tip is near the repository depth.

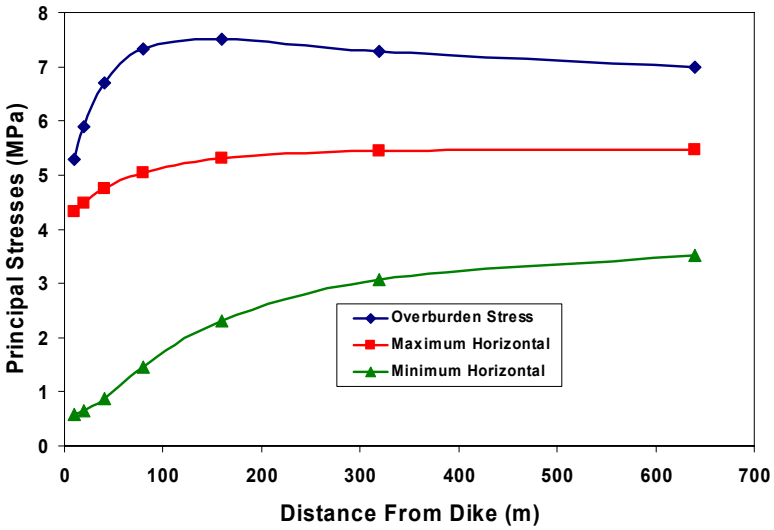

Output DTN:MO0411EG831811.002; file: *MO0411EG831811.002_Disk8\figures\Figures 6-65 to 6-74 data.xls*, tab: "Calculations-300."

Figure 6-169. Total Stresses Acting on the Repository When the Crack Tip is at a 300-m Depth

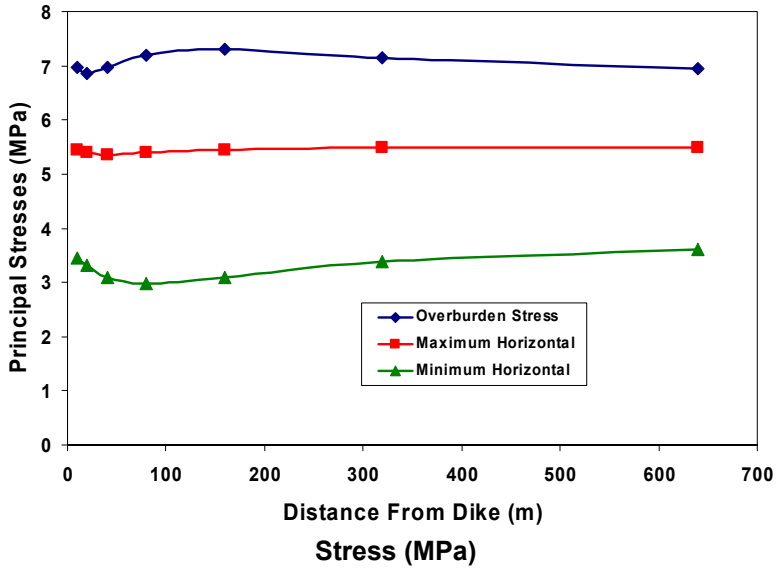

Stress (MPa)

Output DTN: MO0411EG831811.002; file: *MO0411EG831811.002_Disk8\figures\Figures 6-65 to 6-74 data.xls*, tab: "Calculations-150."

Figure 6-170. Total Stresses Acting on the Repository When the Crack Tip is at a 150-m Depth

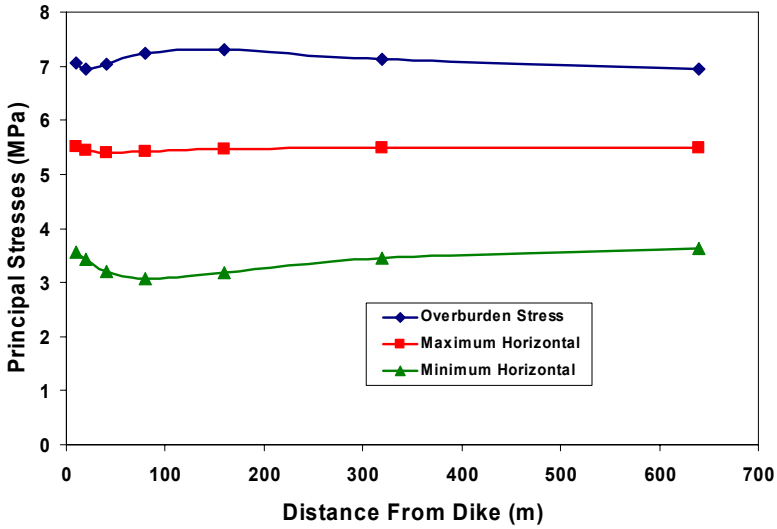

Output DTN: MO0411EG831811.002; file: *MO0411EG831811.002_Disk8\figures\Figures 6-65 to 6-74 data.xls*, tab: "Calculations-16."

Figure 6-171. Total Stresses Acting on the Repository When the Crack Tip is at a 16-m Depth

Given the principal stresses acting on the tunnel, the stress concentrations around the tunnel are calculated as a function of angular position. The principal stresses along the tunnel are also calculated for several distances from the dike. Examples are shown in Figures 6-172 through 6-174 for positions along the drift at distances of 10 m, 40 m, and 640 m from the dike, when the tip is at repository elevation, 300 m from the surface. In general, the principal stresses are not very different from hoop and axial stresses because the repository is nearly aligned with the stress field (Figure 6-174), but stress reorientation does become significant near the dike (Figures 6-172 and 6-173). The asymmetric behavior of the stress field is due to shear stresses generated by the dike and by the misalignment of the repository with the stress field. Near the dike, hoop stresses are reduced so less stress will be required to initiate the fracture than is required to propagate it far from the dike.

Taking the minimum cyclic stress values from Figures 6-172 through 6-174, along with data from other positions along the drift, the plot of Figure 6-175 can be developed. This plot shows the minimum principal stress present when the tip is at repository elevation on the drift wall at any angular position as a function of distance. This stress is the minimum pressure required to start a secondary dike at that position. In this case, the most likely place for re-initiation of a new dike is close to the original dike. Nevertheless, at this time the magma is still a long distance from reaching the repository, so the consequences are minimal. By the time the magma reaches the repository, the stress perturbation is small (e.g., Figure 6-167) and the effect on the stress concentrations around the tunnel is minimal. Of course, if the dike is to propagate any significant distance, it must also exceed the minimum stresses shown in Figures 6-168 through 6-171.

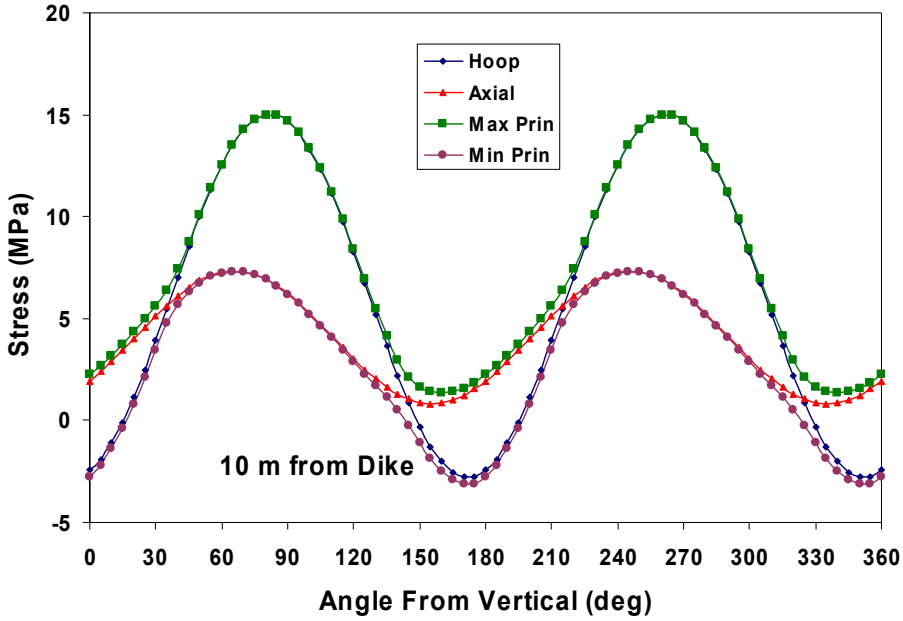

Output DTN: MO0411EG831811.002; file: *MO0411EG831811.002_Disk8\figures\Figures 6-65 to 6-74 data.xls*, tab: "Calculations-300."

Figure 6-172. Stresses around the Drift Wall at 10 m from the Dike

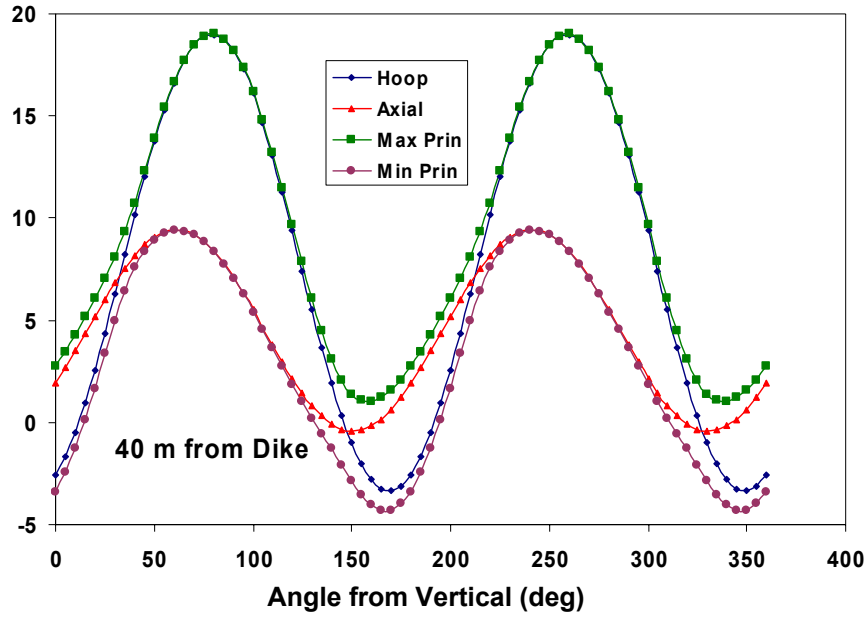

Output DTN: MO0411EG831811.002; file: *MO0411EG831811.002_Disk8\figures\Figures 6-65 to 6-74 data.xls*, tab: "Calculations-300."

Figure 6-173. Stresses around the Drift Wall at 40 m from the Dike

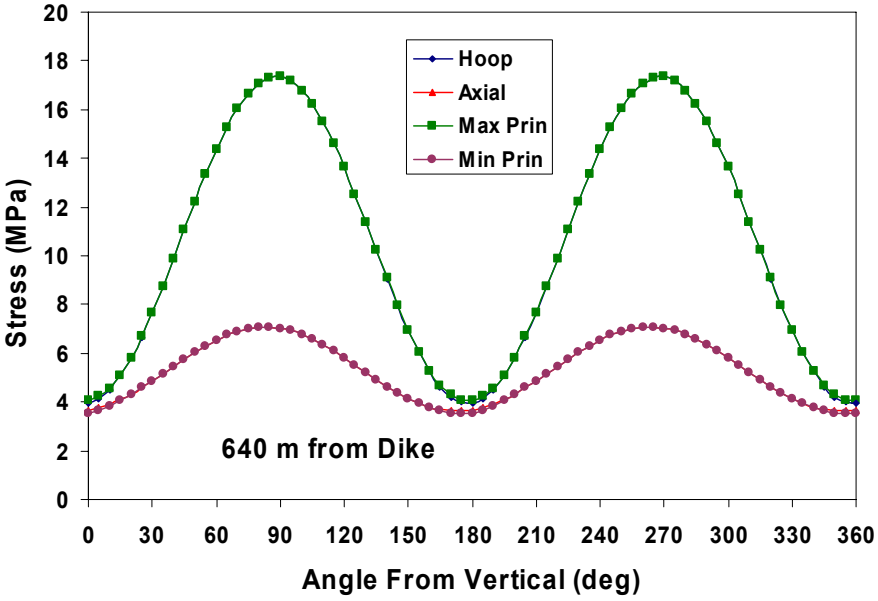

Output DTN: MO0411EG831811.002; file: *MO0411EG831811.002_Disk8\figures\Figures 6-65 to 6-74 data.xls*, tab: "Calculations-300."

Figure 6-174. Stresses around the Drift Wall at 640 m from the Dike

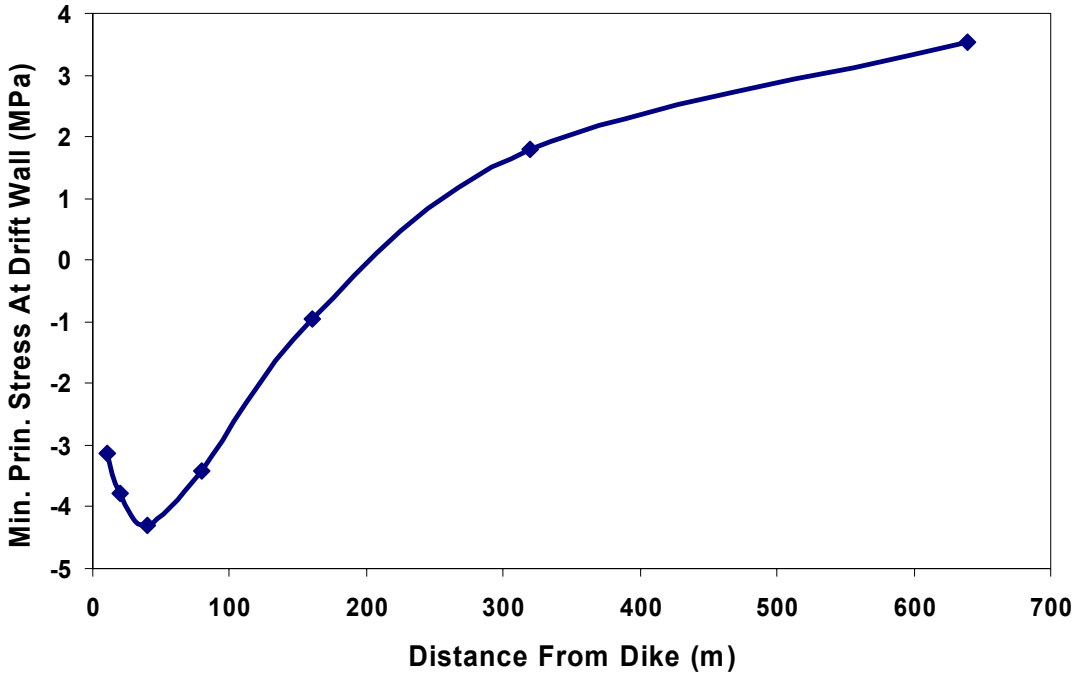

Output DTN: MO0411EG831811.002; file: *MO0411EG831811.002_Disk8\figures\Figures 6-65 to 6-74 data.xls*, tab: "Calculations-300."

Figure 6-175. Minimum Principal Stress at the Drift Wall versus Distance down a Drift away from the Dike, When the Tip is at Repository Elevation

Figures 6-168 to 6-171 indicate that stress changes at repository depth due to the dike intrusion have a strong minimum as the crack tip passes but return to less than 1 MPa by the time the magma reaches repository depth. Although the dike-induced stress change causes a minimum in the least horizontal stress at approximately 75 m to 100 m away from the dike along the drift (Figure 6-167), the magnitude of the difference (0.6 MPa) is not considered large enough to control the location of any secondary dike that may form.

6.5.1.4 Thermal Stoppage of a Secondary Dike

From the input values shown in Table 6-34, the time needed for new dikes to solidify in cold country rock can be calculated. For times larger than the calculated time, a dike of the input width will freeze before it can propagate—the "thermal death" described by Detournay et al. (2003 [DIRS 169660], Appendix 3.4, p. 53). These times vary as the square of the thickness of the dike. The results are illustrated in Figure 6-176. The points indicated in the legend with the red square labeled "new dike" are plotted in filled dark blue symbols as follows:

- For the triangles: the time for a new crack to reach the widths plotted for the most extreme case 103 of Section 6.5.1.2 when the crack has initiated parallel to the drift (the orientation of easiest crack initiation from a pressurized cylinder) and propagated 3.67 m, 7.79 m, and 16.04 m, from bottom to top, respectively, in the plot. However, by the time any new dike has reached 16 m from the drift (almost six drift radii), the local effect of pressure in the drift would be eclipsed into the regional stress field and the most

favorable direction for it to continue opening would be normal to the drift axis (similar to case 105).

- For the squares: the time for a new crack to reach the widths plotted for case 105 where the crack has initiated perpendicular to the drift axis and propagated to a range of 3.08 m, 5.08 m, and 43.8 m, from bottom to top, respectively.

- For the circle: the highly unfavorable case of sill formation where the crack has reached a distance of 3.67 m for case 104.

Clearly, such cracks will not be able to grow to any appreciable width before they are halted by solidification.

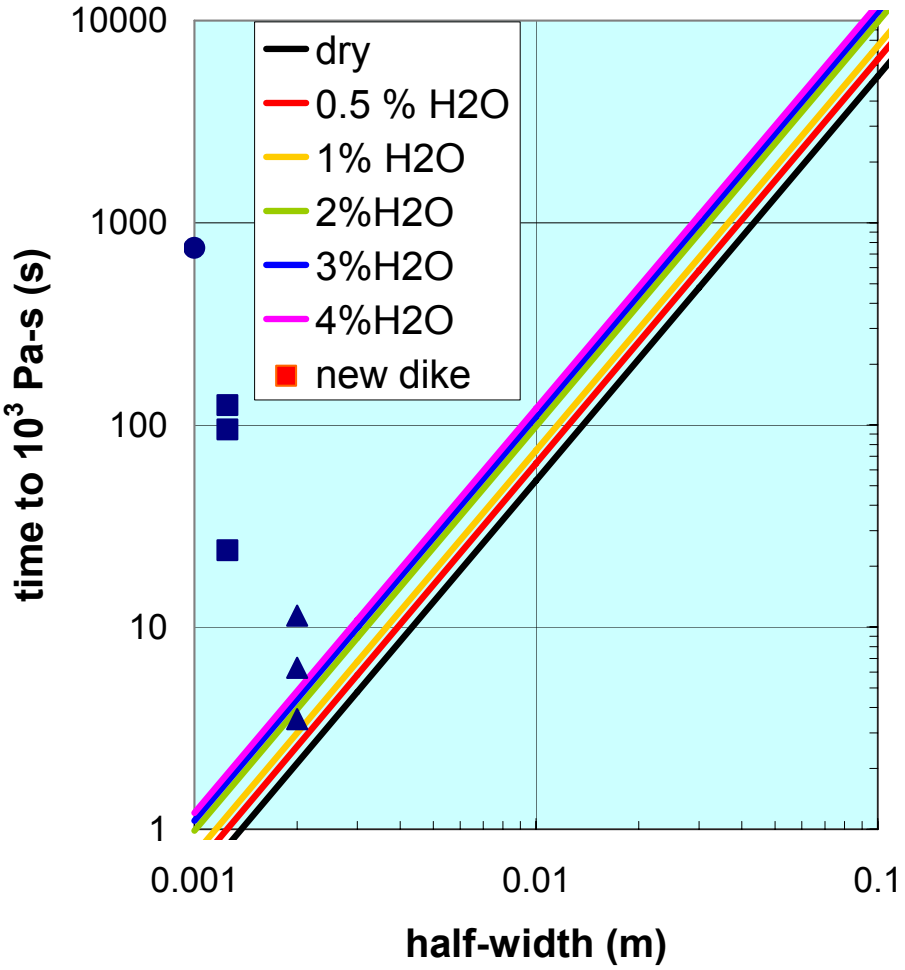

Output DTN: MO0411EG831811.002; file: *MO0411EG831811.002_Disk8.zip\Figures 6-75 & 6-76.zip\DogLeg.xls*.

NOTES: Blue triangles represent times calculated from Equation 6-108 for case 103 opening to 2-mm half-width.

Blue squares represent times for case 105 opening to 2.5 mm; blue circle represents time for case 104.

Figure 6-176. Time to Chill a Dike from Liquidus Temperature to the Temperature at Which the Apparent Viscosity is 1,000 Pa·s, the Assumed Effective "Solidus" Temperature

6.5.1.5 Synthesis: Likelihood of the Dog-Leg Scenario for Effusive Flow

Figure 6-176 shows time and width points from calculations from Section 6.5.1.2 of the growth history for a new dike under the most favorable assumptions for growth of case 103. The new dike started out at 1-mm half-width and took 13 s to grow to a width of only 11 mm at a range of 3.67 m from the edge of the drift. At greater ranges, the time to reach the same width is greater (20 s at 8 m from the drift, see Figure 6-160). Comparing this growth history for a constant viscosity magma with the results of the chill-zone growth rate, it is seen that the dike will never be able to propagate more than a few meters from the drift because the magma will chill rapidly, blocking off the flow of fluid to drive the crack growth. However, the effect of advection on the heat balance has been neglected in deriving this result.

Section 6.3.3.4.1 shows that during an encounter with a drift, for the more-realistic case of horizontal stresses equal to half the vertical stresses, the crack will intersect the drift before the magma:

- For a relatively slow magma rise velocity of 1 m s^{-1}, the crack tip will lead the magma by about 40 s if the magma viscosity is 10 Pa·s (Figures 6-13 and 6-15). Therefore, before any magma can be diverted into the drifts, the crack will already be more than 40 m above the drift. For a more-viscous magma (40 Pa·s), the tip has already broken out at the surface before the magma reaches the drift level (Figure 6-17).

- For a magma velocity of 5 m s^{-1}, the tip has already broken out at the surface before the magma reaches the drift level (Figure 6-13, for example).

Results of Section 6.3.7.3 indicate that, as magma continues up the original dike path while also being diverted into the drifts, the vertical velocity will be lower directly above a drift than at the midpoint between two drifts. This result can be seen most clearly in Figure 6-75, which is a snapshot taken shortly after magma first encounters a drift. The effect persisted at least as long as the simulation ran (Figure 6-78). It is also seen that pressures in the dike above the drift are almost an order of magnitude lower than those between drifts (Figure 6-7).

Based on the results discussed in the preceding paragraphs, it is concluded that the most likely scenario for magma to erupt to the surface after intruding the drift complex is for it to continue along the trajectory of the original dike.

6.5.2 Conclusions

Based on the discussion in this section, effusive magma will continue along the trajectory of the original dike after intruding the drift complex. In the unlikely event that an existing joint at the drift periphery is invaded by magma, the flow will be interrupted by magma freezing long before it is able to reach the surface. Therefore, it is concluded that the dog-leg scenario is not credible for effusive magma. In light of the gradual opening foreseen as the crack tip first encounters a drift, a pyroclastic dog-leg is also considered unlikely but can not be ruled out on the basis of the models in this report.

6.6 LITERATURE REVIEW OF REACTION BETWEEN WATER AND BASALT

This section describes an analysis of the chemistry of seepage water that would come into contact with basalt in emplacement drifts after an intrusion had cooled. This is in the form of a review of published reports of groundwater in analogue basalt terrains in the peer-reviewed literature. Analysis of interaction of seepage water with the intrusion before it has cooled is not necessary because the high temperatures of the cooling basalt will prevent water from entering the intrusion until its temperature has dropped below 100°C.

After postintrusive magma has cooled to ambient conditions, the seepage water is expected to flow through any contact metamorphic aureole that may form and react with the basalt in the intruded emplacement drifts, resulting in seepage water modified by chemical interaction with the basalt. The geochemical interaction of seepage water with the basalt and the resulting hydrochemistry can be estimated based on field observations at analogue sites.

6.6.1 Ground Water/Basalt Interactions

Investigation of ground waters affected by basalts was conducted by a search of peer-reviewed journal articles. Over 400 articles were reviewed for relevance, and a total of 15 sites were chosen to study basalt groundwater interactions on the basis that the papers reporting their composition had the desired data—pH and ionic strength. A total of 1,229 sample pH values were used in the statistical analyses. All 15 studies had groundwater pH values, which were summarized by mean values and standard deviation. Based on a simple chemical argument, this process was extended to lower CO_2 concentrations.

6.6.2 Assumptions and Simplifications

The use of field analogues of interaction between basalt and seepage water is based on the fact that all basalts have a roughly similar mineralogy (pyroxene + calcic plagioclase + olivine + magnetite), so reactions consuming hydrogen ions will tend to buffer pH toward a similar range of values regardless of tectonic setting.

This approach is also a simplification of reality in that no temporal variation is included in the result; there is no indication whether the earliest returning seepage waters will have the same composition as those 10,000 years after an igneous event.

6.6.3 Uncertainties and Limitations

The use of field analogues for the chemistry of seepage water interacting with basalt following an intrusion into the repository is inherently uncertain because of the natural variability of waters entering the analogue systems. Some sites will have high fluxes, others much lower fluxes. In addition the terrain from which the waters are derived will impart a specific chemical signature. This natural variability is accommodated by including a range of sites, thereby ensuring that the results will include appropriate values. Analogue values which can be identified as outliers on the basis of geologic occurrence or chemical traits are excluded from the averages.

The field analogue sites also represent a limited range of CO_2 fugacities, whereas results are desired for a range from current atmospheric (f_{CO2} = 2 [log(bar)] to only 1% of that value. Some conclusions regarding varying CO_2 fugacity can be derived from chemical arguments in Section 6.6.6.1.

6.6.4 Inputs

This section describes the fifteen sites chosen as natural field analogues for the chemistry of water in basaltic rocks. The work of Aiuppa et al. (2003, [DIRS 177256] Table 1, pp. 866 to 872) describes groundwater chemistry on and around Mount Etna, near Naples Italy. This stratovolcano is composed primarily of hawaiitic basalt composition. Angelone et al. (2005, [DIRS 177265] Table 2a, pp. 326 to 329) measured the fluid geochemistry along the Sardinian Rift-Campidano Graben that trends NW-SE through the island of Sardinia. The graben is limited by two Paleozoic granite-metamorphic horsts. The rift host rock in the southern part of the island is primarily andesites and Miocene-Pliocene sediments. The northern half of the rift is composed mostly of basalts and recent sediments derived from the Paleozoic meta-igneous basement. The 65 pH values recorded along and in the rift reacted with basaltic rock as either a major or minor component. Arnorsson and Andresdottir (1995 [DIRS 177278] Table 2, pp. 4,128 to 4,130) described boron and chlorine distributions of natural waters in Iceland and also measured pH values of groundwaters on this basaltic island.

Bath et al. (1986 [DIRS 177272] Table 1, pp. 286 to 287) sampled groundwater interaction with volcanic islands of the Vanuatu archipelago in the SW Pacific. Of particular interest to the present work is that the fact that one spring (North Spring) mimics the scenario of Yucca Mountain closely. In this case groundwater emanating from basalts passes through a zone of rhyolitic composition pumice. Cruz and Amaral (2004, [DIRS 177266] Table 1, p. 447) analyzed the groundwaters of the Azores volcanic archipelago. They list a total of 246 samples which were then reduced to statistical data for each island. Therefore the data presented below are a summary developed from the authors' median values for each island. Igneous compositions were primarily basaltic but included trachytic and up to rhyolitic compositions. Because of the nature of the geologic descriptions presented in this paper, field juxtapositions of the various igneous rock types were uncertain. Edmunds et al. (2002 [DIRS 177253] Table 1, p. 6) undertook a study of the groundwaters in the graben beneath Mexico City, Mexico. The geologic environment, from bottom to top includes Cretaceous Limestones, Tertiary volcanics (layered basalt, rhyolite, and andesites), Lower Pliocene lacustrine and pyroclastic material, Plio-Quaternary basaltic-andesites and pyroclastics, and finally, Quaternary fluvial and alluvial deposits.

Select water chemistry samples from the Rhine Graben of Germany are provided by Greisshaber et al. (1992 [DIRS 177269] Appendix I, p. 232). Six samples were selected from the Ardennes in the Rhenish Massif, where Quaternary basaltic volcanics overlie slates, quartzites, and limestones. Ingebritsen and Scholl (1993 [DIRS 177273] Tables 1 and 2, pp. 258 and 259) provided details of the hydrogeology of Kilauea volcano in Hawaii. Kebede et al. (2005 [DIRS 177267] Table 1, p. 1669) describe the groundwater geochemical evolution in the source region of the Blue Nile River, Ethiopia. The regional geology consists of Paleozoic basement (high grade gneisses and volcano-sedimentary green schists with ultramafics), Mesozoic sedimentary rocks (sandstones and minor carbonates), and widespread Cenozoic basalt

volcanics. Groundwater behavior on the island of Madiera, a basaltic volcano seamount, was investigated by Prada et al. (2005 [DIRS 177275] Table 2, p. 808). Rees et al. (1996 [DIRS 177277] Table I, p. 134) used groundwaters from the western US to perform leaching experiments from plutonium bearing radioactive waste glass.

Rose et al. (1996 [DIRS 177254] Table 1, p. 216) characterized voluminous cold springs that emanate from the Hat Creek Basin basaltic rocks in northern California. Twenty three pH analyses were performed on distinct samples from springs. Sedwick and Stuben (1996 [DIRS 177276] Table 1, p. 150) investigated the chemistry of shallow submarine warm springs near Vulcano Island in the Aeolian Archipelago, Italy. The authors have concluded that the fluids are a mixture of seawater and low-salinity groundwater that has undergone hydrothermal (>100^{o}C) alteration. Groundwaters in the State of San Paulo, Brazil have been analyzed by Szikszay et al. (1981 [DIRS 177490], Table II, p. 30). These waters were drawn from wells that collected groundwaters in basalt flows (the Serra Geral Formation). In turn, these flows are overlain by the Bauru Group, which consists of sandstone, clayey sandstone, or siltstone with or without carbonate cement. Weaver et al. (2006 [DIRS 177268] Table 1a, p. 294) determined the water chemistry of cold CO_2-bearing mineral waters emanating from fractured basalts in Daylesford, Victoria, Australia. The authors determined that the waters interacted with both the basalts and the overlying sediments.

Data for 32 waters from basalt aquifers (Hearn et al. 1985 [DIRS 166893]; White et al. 1980 [DIRS 163752]; Hem 1985 [DIRS 115670]) are used to estimate fluoride (F^-) concentrations developed from the reaction of seepage water with basalt.

6.6.5 Results

The summary pH data is compiled in Table 6-38. The average of the pH mean values is 7.31. Furthermore, high and low pH values are noted.

The mean pH value for Mount Etna, reported by Aiuppa et al. (2003 [DIRS 177256]), is 7.03 (n = 279) with a standard deviation of 0.41. The high and low pH values are 8.58 and 5.95, respectively. Both should be considered outliers, since they are more than two standard deviations from the mean. The mean pH value reported by Angelone et al. (2005, [DIRS 177265]) for the Sardinian Rift-Campidano Graben is 7.17 ± 0.07 (n = 65) with extreme high and low values of 8.58 and 5.96 respectively.

Many elevated chlorine and boron values, along with high pH levels in Iceland, are associated with mixing with either seawater or geothermal springs, according to Arnorsson and Andresdottir (1995 [DIRS 177278]. As viewed in Table 6-38, the mean pH value of 8.12 ± 1.08 (n = 398) is the highest of the values associated with large data groups. The high pH value in this study, 10.35, is most probably associated with mixing with a high pH thermal spring. This study, although situated on a basaltic composition island, indicates how relatively high pH values can occur when other mixing components are involved.

The pH range of the groundwaters from Vanuatu (Bath et al. (1986 [DIRS 177272]) are reported in Table 6-38, with a mean value of 7.13 ± 1.13 (n = 16). The highest value reported is 8.50, while the low value is 6.75. The small (n = 4) subgroup, with groundwater emanating from

basalts, passes through a zone of rhyolitic composition pumice and has a mean pH value of 7.69 ± 1.10. The pH mean value for the Azores (Cruz and Amaral (2004 [DIRS 177266]) is 7.05 ± 0.07, with a high median value of 7.45 and a low median value of 6.11. The pH values from Mexico City (Edmunds et al. (2002 [DIRS 177253]) in Table 6-38 indicate a mean value of 7.55 ± 0.30 (n = 17) with a high of 8.30 and a low of 7.00. Unfortunately, most wells are tapped slightly below the Quaternary Plio-Quaternary boundary aquatard; therefore, they sample a heterogeneous and anisotropic aquifer according to the authors. The mean pH value from the Rhine Graben of Germany (Greisshaber et al. (1992 [DIRS 177269]) is 6.95 ± 0.21, with a range from 8.3 to 5.6. Ingebritsen and Scholl (1993 [DIRS 177273]) provided a small data set of pH values from Mt. Kilauea (Hawaii) with a mean value of 7.88 ± 0.57 (n = 5) for groundwaters interacting with tholeitic basalts. The high and low pH values of 8.4 and 7.2, respectively, are close to the one standard deviation limits.

Eighty-four groundwater chemistry values from the Blue Nile River region of Ethiopia, presented by Kebede et al. (2005 [DIRS 177267]), provided the pH data summarized in Table 6-38. The mean pH value is 7.55 ± 0.56, with a high value of 9.15 and a low of 6.53. The more extreme values are beyond the 2 standard deviation limits and should not be considered representative. The mean pH value for groundwaters interacting with the basalt host rock on Madiera (Prada et al. (2005 [DIRS 177275]) is 7.37 ± 0.56 (n = 33). The high and low pH values of 8.40 and 6.13 fall reasonably well within two sigma. The mean pH value of groundwaters from the western United States (Rees et al. (1996 [DIRS 177277]), reported in Table 6-41), is 8.15 ± 0.99 (n = 4), slightly higher than most groundwaters interacting with basalts. This is most probably due to the Grande Ronde basalt value (pH = 9.3) used by those authors.

Summary results from the Hat Creek Basin (located in northeastern California; Rose et al. (1996 [DIRS 177254]) are given in Table 6-38. The mean pH value is 7.87 ± 0.49. The high pH value measured was 10.2. This value can be considered an outlier, since the rest of the twenty-two samples fall within two sigma of the mean (below pH 8.85). As can be seen in Table 6-38 for shallow submarine warm springs near Vulcano, Italy (Sedwick and Stuben 1996 [DIRS 177276]), the low mean pH value at 6.05 ± 0.63 (n = 16) reflects considerable mixing. The total range of pH values in this study is from 7.5 to 5.2. Four pH values from Sao Paulo, Brazil (Szikszay et al. 1981 [DIRS 177490]) are given in Table 6-38, with a mean value of 7.55 ± 0.86. A set of thirty-three samples from Australian basalts (Weaver et al. 2006 [DIRS 177268]) are summarized in Table 6-38, with a mean pH value of 6.3 ± 0.11. The samples ranged from a high of 6.89 to a low of 5.83. Both extreme values are beyond the two standard deviation limit.

This data set of 1,229 pH values, wherein groundwaters interact with basalts and various other rock types and sediments, provides a basis for understanding the range of pH values that could be encountered at Yucca Mountain. If one takes the average value of all the mean values presented in Table 6-38, the resulting pH is 7.31. However, the most relevant values may be taken from Bath et al. (1986 [DIRS 177272]), where one spring (North Spring) mimics the scenario of Yucca Mountain precisely. In this case groundwater emanating from basalts passes through a zone of rhyolitic composition pumice. This small subgroup (n = 4) has a mean pH value of 7.69 ± 1.10.

From the total of fifteen studies, twelve had water chemistry sufficient to calculate ionic strength. The range (by locality) of ionic strength values is tabulated in Table 6-39. A group of 111 water samples was selected to be most representative of basalt/groundwater interaction without influence from other chemical sources (i.e., seawater, limestones, shales, metamorphics). The range of ionic strength values goes from 2.9×10^{-4} to 9.59×10^{-2} moles kg^{-1}. The highest ionic strength value (9.59×10^{-2} moles kg^{-1}) measured at the island of Sardinia (sample SAR 46) was obtained from a thermal spring on the coast and is an anomalous value on all of the authors' plots (Angelone et al. [DIRS 177265]). The high sodium and chlorine values indicate a high mixing ratio with seawater. A more reasonable range for the remaining 110 samples is from 2.9×10^{-4} moles kg^{-1} to 7.2×10^{-2} moles kg^{-1}.

Of particular interest were groundwaters that interacted with both basalts and rhyolitic ignimbrites. By grouping the type of basalts that interact with groundwater, a slightly clearer picture of ionic strength values is evident. The large stratovolcanos at Mt. Etna, Italy (Aiuppa et al. 2003 [DIRS 177256]) and Mt Kilauea, Hawaii (Ingebritsen and Scholl 1993 [DIRS 177273]) have mean ionic strength values of 0.036 moles kg^{-1} and 0.039 moles kg^{-1}, respectively. Basaltic interaction with groundwaters in graben regimes have mean ionic strength values that range from 0.020 moles kg^{-1} (Sardinia, Angelone et al. 2005 [DIRS 177265]) to 0.049 moles kg^{-1} (Blue Nile, Ethiopia, Kebede et al. 2005 [DIRS 177267]). Flood-type basalts at Mexico City, Mexico (Edmunds et al. 2002 [DIRS 177253]) and Sao Paulo, Brazil (Szikszay et al. 1981 [DIRS 177490]) have mean ionic strength values that are an order of magnitude lower, 0.0053 and 0.0069 moles kg^{-1}, respectively. Those groundwaters that show the largest spread in mean ionic strength values are those associated with basalt islands that are part of archipelagos, ranging from a low of 0.0074 moles kg^{-1} at Madiera, a volcanic island in Portugal (Prada et al. 2005 [DIRS 177275]) to a high of 0.025 moles kg^{-1} on Vulcano Island, in the Aeolian Archipelago, Italy (Sedwick and Stuben 1996 [DIRS 177276]). As part of these archipelagos, the area of Vanuatu in the southwest Pacific (Bath et al. 1986 [DIRS 177272]), which contains groundwater in association with both basalts and rhyolitic pyroclastics, has mean ionic strength values of 0.0039 ± 0.001 moles kg^{-1}.

Table 6-38. Basalt/Water Interaction: Summary pH Values

Authors/Location	Number of Samples	Mean	Std. Dv.	High	Low
Aiuppa et al. 2003 [DIRS 177256], Mt. Etna	279	7.03	0.41	8.58	5.95
Angelone et al. 2005 [DIRS 177265], Sardinia	65	7.17	0.07	8.58	5.96
Arnorsson & Andresdottir 1995 [DIRS 177278], Iceland	398	8.12	1.08	10.35	5.31
Bath et al. 1986 [DIRS 177272], Vanuatu	16	7.13	1.13	8.50	6.75
Cruz and Amaral 2004 [DIRS 177266], Azores	246	7.05	0.07	7.45	6.11
Edmunds et al. 2002 [DIRS 177253], Mexico City	17	7.55	0.30	8.30	7.00
Greisshaber et al. 1992 [DIRS 177269], Rhine	6	6.95	0.21	8.3	5.6

Table 6-38. Basalt/Water Interaction: Summary pH Values (Continued)

Authors/Location	Number of Samples	Mean	Std. Dv.	High	Low
Ingebritsen and Scholl 1993 [DIRS 177273], Kilauea	5	7.88	0.57	8.4	7.2
Kebede et al. 2005 [DIRS 177267], Blue Nile	84	7.55	0.56	9.15	6.53
Prada et al. 2005 [DIRS 177275], Madiera	33	7.37	0.56	8.40	6.13
Rees et al. 1985 [DIRS 177277], Western US	3[a]	7.77	0.15	7.9[a]	7.6
Rose et al. 1996 [DIRS 177254], California	23	7.87	0.49	10.2	6.7
Sedwick and Stuben 1996 [DIRS 177276], Vulcano	16	6.05	0.63	7.5	5.2
Szikszay et al. 1981 [DIRS 177490], San Paulo, Brazil	4	7.55	0.86	8.7	6.8
Weaver et al. 2006 [DIRS 177268], Dayleford, Australia	33	6.30	0.11	6.89	5.83
	Total # of Samples	**Average of means**		**Range of means**	
	1,229	7.29		6.05 – 8.12	

[a] A single value of 9.3 has been excluded, see text for discussion.

Table 6-39. Ionic Strength Summary

Authors/Location	No. of samples	Range of Values (moles/kg)	Mean ± Std. Dv. (moles/kg)
Aiuppa et al. 2003 [DIRS 177256], Mt. Etna	23	0.029 – 0.054	0.036 ± 0.0039
Angelone et al. 2005 [DIRS 177265], Sardinia	4	0.011 – 0.100	0.020 ± 0.0128
Arnorsson and Andresdottir 1995 [DIRS 177278], Iceland	NA	–	–
Bath et al. 1986 [DIRS 177272], Vanuatu	4	0.0033 – 0.0047	0.0039 ± 0.001
Cruz and Amaral 2004 [DIRS 177266], Azores	10	0.0014 – 0.0040	0.0023 ± 0.0001
Edmunds et al. 2002 [DIRS 177253], Mexico City	17	0.0053 – 0.0193	0.0053 ± 0.0018
Greisshaber et al. 1992 [DIRS 177269], Rhine	6	0.0028 – 0.069	0.0394 ± 0.042
Ingebritsen and Scholl 1993 [DIRS 177273], Kilauea	5	0.0017 – 0.0685	0.039 ± 0.039
Kebede et al. 2005 [DIRS 177267], Blue Nile	9	0.0026 – 0.0959	0.0496 ± 0.065
Prada et al. 2005 [DIRS 177275], Madiera	5	0.0020 – 0.0099	0.0074 ± 0.0034

Table 6-39. Ionic Strength Summary (Continued)

Authors/Location	No. of samples	Range of Values (moles/kg)	Mean ± Std. Dv. (moles/kg)
Rees et al. 1985 [DIRS 177277], Western US	NA	–	–
Rose et al. 1996 [DIRS 177254], California	NA	–	–
Sedwick and Stuben 1996 [DIRS 177276], Vulcano	12	0.0237 – 0.0254	0.025 ± 8.06E-5
Szikszay et al. 1981 [DIRS 177490], Sao Paulo, Brazil	4	0.00029 – 0.0043	0.0069 ± 0.0037
Weaver et al. 2006 [DIRS 177268], Dayleford, Australia	12	0.020 – 0.059	0.0376 ± 0.0075
	Total No. of Samples	**Total Range**	**Average of Means**
	111	0.00029 – 0.0959	0.0021

NOTE: NA = not applicable.

Aiuppa et al. (2003 [DIRS 177256], Table 2) conducted a multifactor analysis to determine correlations among the several groundwater constituents that were measured. They found three factors that were important. One of these, Factor #1 of Table 2 (Aiuppa et al. 2003 [DIRS 177256]), included strong influences of both pH and pCO_2, with both having a factor of nearly 0.8 but with opposite signs. The ratio of their contributions equaled −1.03 (i.e., the two components were almost perfectly inversely correlated).

Fluoride concentrations in basalt aquifers are quite low. Data for 32 waters from basalt aquifers (Hearn et al. 1985 [DIRS 166893]; White et al. 1980 [DIRS 163752]; Hem 1985 [DIRS 115670]) have a mean F^- content of 0.8 ± 0.8 (1σ) mg/L. The median value is 0.5 mg/L, reflective of the fact that the mean is skewed on the basis of a few analyses with F^- compositions in the range of a few mg/L.

6.6.6 Discussion

The large body of data from potential analogue sites covers a very wide range of both pH and ionic strength values.

6.6.6.1 pH

Figure 6-177 shows a histogram of mean pH for the fifteen sites analyzed. Disregarding the two occurrences with pH below 6.4, the other thirteen values all lie between 6.8 and 8.2. As mentioned in Sections 6.6.1.4 and 6.6.1.5, there is a site on Vanuatu (Bath et al. 1986 [DIRS 177272] with a very similar geologic association to that which would occur at Yucca Mountain following intrusion of basalt into drifts, namely rhyolitic tuffs overlying basalt. These waters have a value of 7.69 for pH and 0.0007 moles/kg for ionic strength. The pH value is superimposed on the histogram as a white square. Similarly, mean values of 7.06 for pH and 0.0329 moles/kg for ionic strength are derived from "dry" sites with less than 400 mm mean

annual precipitation (Aiuppa et al. 2003 [DIRS 177256]; Angelone et al. 2005 [DIRS 177265]; Rees et al. 1985 [DIRS 177277]). Of the "dry" site data, the Grande Ronde basalt value (pH 9.3) was excluded based on the anomalous F value (52 mg/l), which may indicate departure from equilibrium. The mean pH of the "dry" sites is represented in Figure 6-177 as a white circle.

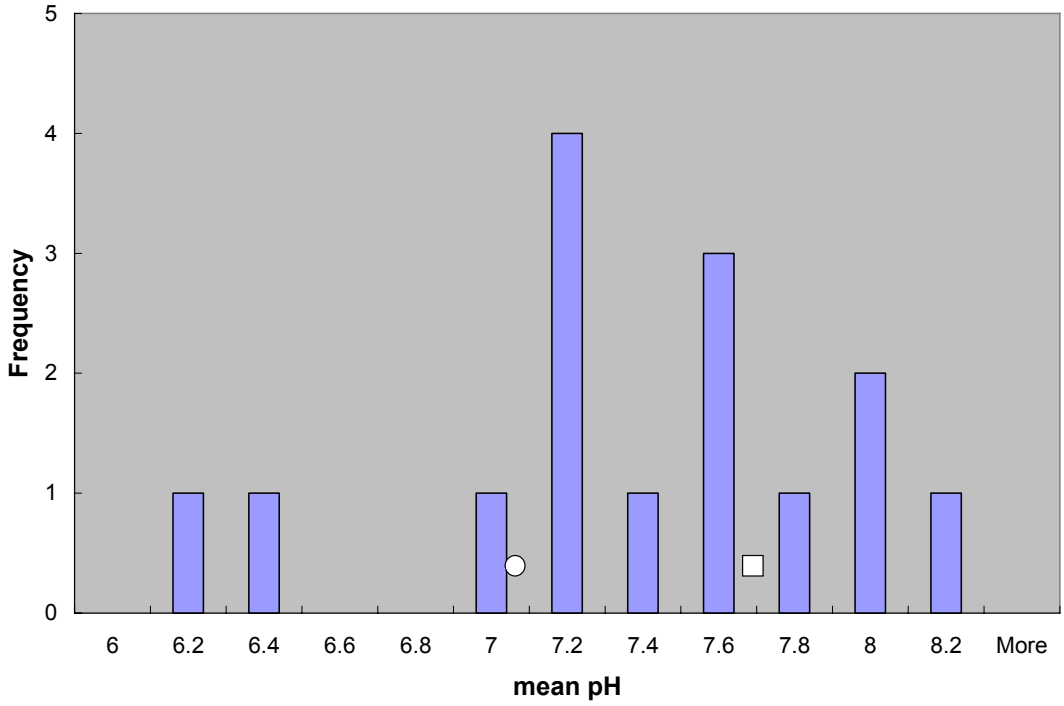

Source: For reference only.

Figure 6-177. Histogram of Mean pH from 1,229 Water Samples at Fifteen Sites

It is assumed that the mean pH values discussed above are in equilibrium with the standard atmospheric concentration of CO_2, which is $10^{-3.5}$ bars (300 Pa). The effect of pCO_2 on pH can be estimated using Equations 6-127a to 6-127c, relating pCO_2 to the activity of the bicarbonate (HCO_3) and to pH (Hem 1985 [DIRS 115670], p. 62):

$$\frac{[H_2CO_3]}{P_{CO_2}} = K_h = 10^{-1.43} \quad \text{(Eq. 6-127a)}$$

$$\frac{[HCO_3][H^+]}{[H_2CO_3]} = K_1 = 10^{-6.35} \quad \text{(Eq. 6-127b)}$$

$$\frac{[H^+][CO_3^{2-}]}{[HCO_3]} = K_2 = 10^{-10.33} \quad \text{(Eq. 6-127c)}$$

These equations indicate that, if the activity of bicarbonate is constant, pCO_2 should be proportional to the activity of the hydrogen cation.

$$P_{CO_2} = 10^{7.78}[\mathrm{HCO_3}][\mathrm{H^+}] \quad \text{(Eq. 6-128)}$$

Thus a change in log(pCO_2) by −0.5 should result in a change in pH by the same amount. This linear relation is supported by the factor analysis of Aiuppa et al. (2003 [DIRS 177256]), who found that pCO_2 and pH were almost perfectly inversely correlated. Using Equation 6-128, the modal value for pH of waters in equilibrium with pCO_2 of 1 kPa would be 1.5 higher than the mode of the analogue sites, or 6.1. The mode in equilibrium with 0.01 kPa would be 8.1.

6.6.6.2 Ionic Strength

The distribution of ionic strength in waters from "dry" sites is illustrated in Figure 6-178. There are three outliers. The 25 other values cluster between 0.01 moles/kg and 0.05 moles/kg.

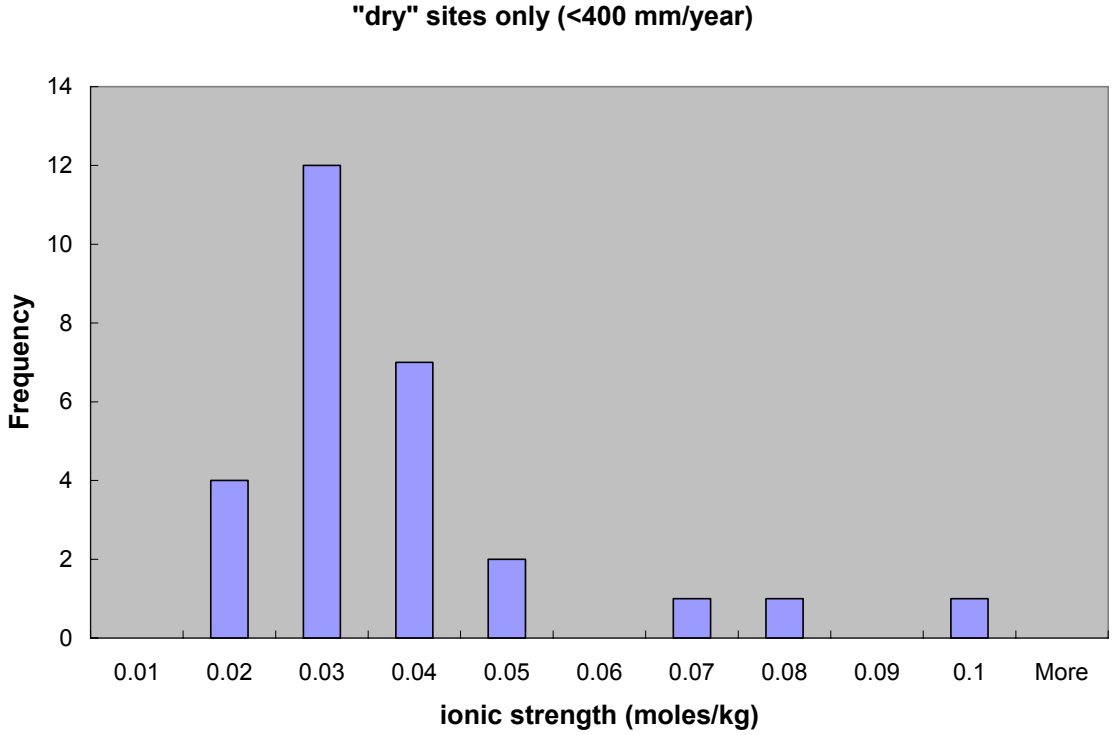

Source: For reference only.

Figure 6-178. Histogram of Ionic Strength of 28 Analogue Sites

These values are to be expected after a steady-state condition has been reached following return of seepage waters.

6.6.7 Summary

Chemical reactions between basalt intruded into a drift and water seeping through it will modify the composition of any seepage water that might encounter waste after an intrusive event. A literature review was conducted of groundwater chemistry in basaltic rocks. Over 400 articles were reviewed for relevance, and a total of fifteen sites were chosen to study basalt groundwater interactions. A total of 1,229 sample pH values were used in the statistical analyses. All fifteen

studies had groundwater pH values which were summarized by mean values and standard deviation. The mean pH of each site ranged from 6.05 to 8.12; the average of the means was 7.29. The mean ionic strengths ranged from 0.00029 moles/kg to 0.0959 moles/kg; the average of the means was 0.0021 moles/kg.

INTENTIONALLY LEFT BLANK

7. VALIDATION

Validation, or confidence building, is a way of ensuring that the processes represented and simulated by the numerical models are consistent with observed behavior to give confidence in model results. SCI-PRO-006, *Models*, requires that models supporting TSPA model components be validated to the level of confidence required by the component's relative importance to the potential performance of the repository system. SCI-PRO-002, *Planning for Science Activities*, describes two levels of model importance and corresponding validation guidelines commensurate with each level. These levels of model importance are based on the TSPA system sensitivity analyses and conclusions presented in *Risk Information to Support Prioritization of Performance Assessment Models* (BSC 2003 [DIRS 168796]). Although not all models directly support the TSPA model, some do provide input or a scientific basis for the component models that directly support the TSPA model. The dike intrusion submodel consists of one model component, the dike propagation model. It does not directly feed to the TSPA model but does address FEPS and review criteria in *Yucca Mountain Review Plan, Final Report* (NRC 2003 [DIRS 163274]). The activities necessary to build confidence and validate these models are described in the TWP (BSC 2006 [DIRS 178448]). The model component of the post-intrusion submodel, magma cooling, provides direct outputs to the model components of the TSPA model. The activities necessary to build confidence and validate these models are described in the TWP (BSC 2006 [DIRS 178448]).

7.1 IMPORTANCE LEVELS FOR MODEL VALIDATION

The TWP (BSC 2006 [DIRS 178448]) identifies the levels of importance based on the effect model uncertainty could have on repository performance. The three levels defined in the TWP (BSC 2006 [DIRS 178448]) are based on LP-2.29Q-BSC. To apply these under the current procedures, Level I and II in LP-2.29Q-BSC are both equated with Level I in SCI-PRO-002, and Level III in LP-2.29Q-BSC is equated with Level II in SCI-PRO-002. The TWP (BSC 2006 [DIRS 178448])) also identifies the validation approaches for the models presented in this model report. The levels of importance identified for this model report in terms of SCI-PRO-006 are summarized in Table 7-1. The dike propagation model provides direct input to the waste package/drip shield degradation and the number of waste packages impacted by igneous intrusion model components that support the TSPA model. The magma-cooling component of the post-intrusion submodel provides direct input to the waste package/drip shield degradation component model that supports the TSPA model.

Table 7-1. Validation Levels for Submodels of the Dike/Drift Interaction Model

Model Component	TSPA Component Models	Level of Validation
Dike Propagation from Depth	Waste Package/Drip Shield Degradation Number of Waste Packages Impacted by Igneous Intrusion	II
• Thermally Induced Stresses	Waste Package/Drip Shield Degradation Number of Waste Packages Impacted by Igneous Intrusion	II

Table 7-1. Validation Levels for Submodels of the Dike/Drift Interaction Model (Continued)

Model Component	TSPA Component Models	Level of Validation
• Topography		I
• Structural Effects		I
Basalt Cooling and Solidification	Waste Package/Drip Shield Degradation Number of Waste Packages Impacted by Igneous Intrusion	II

The approaches used for confidence building during model and postmodel development are summarized in Table 7-2. Model uncertainty, which may arise for several reasons, is addressed both during model development and after model development. Sources contributing to model uncertainty include:

- Inaccuracy of numerical solutions
- Uncertainty of input due to lack of knowledge
- Uncertainty of input due to natural, frequently stochastic, variability of properties or configurations
- Inadequate state of knowledge or understanding of phenomena or processes.

The effect of model uncertainty is discussed in Section 7.3 at the end of each postdevelopment confidence-building discussion.

Table 7-2. Confidence-Building and Postmodel Development Validation Activities

SCI-PRO-006 Validation Approaches	Location of Discussion
Confidence Building Activities Related to Model Development	
Ensure that validation of the mathematical model and its underlying conceptual model includes documentation of decisions or activities that are implemented to generate confidence in the model: Selection of input parameters and/or input data, and a discussion of how the selection process builds confidence in the model.	**Dike Intrusion Submodel:** Development is consistent with the procedures and recommendations of the ICPRP (Section 7.2). Input parameters were selected to be well within the applicability of the formulation of the model. Parameter selection is discussed for the dike propagation model in Section 7.2.1
Ensure that validation of the mathematical model and its underlying conceptual model includes documentation of decisions or activities that are implemented to generate confidence in the model: Description of calibration activities, and/or initial boundary condition runs, and/or run convergences, and a discussion of how the activity or activities build confidence in the model.	**Dike Intrusion Submodel:** Development is consistent with the findings of the ICPRP (Section 7.2.1) and includes more-complete treatment of topography and underlying geologic structure in response to requests from the IVRT and probabilistic volcanic hazard analysis panels (Section 7.3.1.2.1). Initial and boundary condition selection is addressed in Sections 6 and 7.2.

Table 7-2. Confidence-Building and Postmodel Development Validation Activities (Continued)

SCI-PRO-006 Validation Approaches	Location of Discussion
Confidence Building Activities Related to Model Development (Continued)	
Ensure that validation of the mathematical model and its underlying conceptual model includes documentation of decisions or activities that are implemented to generate confidence in the model: Discussion of the impacts of uncertainties to model results.	**Dike Intrusion-Post-Intrusion Submodels**: Parameter uncertainties are discussed in Sections 6 and 7.2.
Ensure that validation of the mathematical model and its underlying conceptual model includes documentation of decisions or activities that are implemented to generate confidence in the model: Selection of input parameters and/or input data, and a discussion of how the selection process builds confidence in the model.	**Post-Intrusion Submodel:** The magma-cooling submodel used data from qualified sources. Parameter selection is discussed in Section 7.2.2
Postdevelopment Model Validation Activities	
Dike Intrusion Submodels	
Corroboration of model results with other model results obtained from the implementation of other independent mathematical models developed for similar or comparable intended use/purpose (SCI-PRO-006, Section 6.3.2, 2nd method).	Corroboration was performed using analytical solutions for a vertical self-similar dike. The results are documented in Section 7.3.1.1.3.
Corroboration of model results with data acquired from the laboratory, field experiments, analogue studies, or other relevant observations not previously used to develop or calibrate the model (SCI-PRO-006, Section 6.3.2, 2nd method).	Calculations were performed to compare model and analysis results for a dike interacting with a free surface, to those from the Parícutin (Mexico) analogue. The results are documented in Section 7.3.1.1.1. Corroboration by comparison with independent, peer-reviewed research was conducted for the effect of topography component. The results are contained in Section 7.3.1.2.1. Corroboration with analogue studies was conducted for effect of underlying geologic structure component. The results are contained in Section 7.3.1.3.1.
Technical review through publication in a refereed professional journal or review by an external agency (SCI-PRO-006, Section 6.3.2, 8th method). (This approach must be used in combination with at least one other model validation activity from this list.)	Corroboration of aspects of the effect of topography on the dike propagation modeling approach and results was achieved by publication in peer-reviewed journals as documented in Section 7.3.1.2.2.
Conduct independent technical review, planned in the applicable TWP (SCI-PRO-006, Section 6.3.2, 5th method).	An independent technical review was performed for the dike propagation model. The results are documented in Section 7.3.1.1.2.
Post-Intrusion Submodel	
Corroboration of model results with the results of auxiliary analyses (SCI-PRO-006, Section 6.3.2, 6th method)	Corroboration was performed using an alternative analytic solution and a two-dimensional numerical solution for magma cooling. The results are documented in Section 7.3.2.1.1.
Corroboration of model results with data acquired in field experiments (SCI-PRO-006, Section 6.3.2, 7th method)	Corroboration with field data was performed for magma cooling for thermal evolution of a shallow cooling lava lake. The results are contained in Section 7.3.2.1.2.

7.2 CONFIDENCE BUILDING DURING DEVELOPMENT

All input parameters are well within the applicability of the formulation of the numerical model. Initial and boundary conditions are addressed in Section 6, as are parameter uncertainties.

7.2.1 Dike Intrusion Submodel

During development, the dike propagation model and supporting analyses related to igneous consequence were presented to the ICPRP, a group of experts chosen for their expertise in fracture mechanics, dike propagation, magma properties, flow dynamics, and igneous processes. In their evaluation, the ICPRP used similar conceptual and numerical approaches to those reported in this model report. The panel employed some of the same software that was used in this study and obtained similar results. In response to the peer-review findings, many of the models and analyses presented in this model report have been modified to be consistent with recommendations and technical information presented in the ICPRP final report (Detournay et al. 2003 [DIRS 169660]). Specific applications of the findings of the panel include:

- Many of the input parameter values used in Section 6.3 are drawn from the ICPRP report (Table 4-1)

- The ICPRP discussion of the impact of the high gas permeability of the host rock (Detournay et al. 2003 [DIRS 169660], Section 3.4.3.2, p. 50) provides support for neglecting cavity pressure in models in Section 6.3.3.4.2

- The ICPRP equations for the coupled flow from a dike into a drift (Detournay et al. 2003 [DIRS 169660], Appendix 3.5, p. 62) provides the basis for the coupled flow model in Section 6.3.3.5.6 and for the alternative analysis of effusive flow in Section 6.3.3.5.7

- The analysis in Section 6.4.8.2 of magma cooling rates is based on a similar analysis by the ICPRP (Detournay et al. 2003 [DIRS 169660], Appendix 3.4, p. 53). The extension of this analysis to include changes in magma viscosity (Section 6.4.8.2.1) and the model of magma pressurization due to partial crystallization (Section 6.4.8.1.3.1) used ICPRP values for the extent of partial crystallization as a function of temperature (Detournay et al. 2003 [DIRS 169660], Appendix 2, Table 2E).

The ICPRP found: (1) the scientific basis for the dike propagation model is adequate and reflects current scientific understanding; (2) the models and analyses are accurate for their intended use; and (3) the models and analyses incorporate appropriate data. These findings provide confidence in the analyses and models of this report.

The dike propagation model component is, in the most general case, a function of three dimensionless numbers that reflect rock and magma density, reference stress, and fracture toughness (defined in Equation 6-34). The dimensionless toughness is a small number compared to unity under very general conditions of dike propagation. This implies that fracture toughness can be neglected when considering dike propagation; thus, it is not considered in this section.

The simulations of dike ascent covered a range of relative density from 2.67 to 20.28, which is almost one order of magnitude. Such variation of the relative rock density corresponds to the variation in the difference between normal far-field stress and magma density (buoyancy) between 600 Pa/m and 9,000 Pa/m (with rock mass densities of 1,200 kg m^3 and 2,400 kg m^3). This range includes, for example, the 3,000 Pa/m assumed by Rubin (1995 [DIRS 164118] in his analysis of the propagation of magma-filled cracks. Dimensional results are generated for a number of far-field magma velocities and dike openings, which satisfy the scaling laws and are within the expected ranges for the opening, $0.1\,\text{m} \le w_\infty \le 10\,\text{m}$, and for the velocity, $0.1\,\text{m/s} \le v_\infty \le 15\,\text{m/s}$ (SNL 2007 [DIRS 174260]).

The dimensionless reference stress accounts for the effects of gas pressure inside the dike tip cavity and for changes in confining stress normal to the dike. Most of the simulations were carried out with a reference stress of zero (i.e., in situ stress conditions equal to gas pressure inside the tip cavity). The effect of the cavity gas pressure, which is unlikely to be much larger than the atmospheric pressure, is investigated by taking the cavity gas pressure to be as large as 2.1 MPa. This is very close to the pressure that would trigger dike-tip instability at the repository depth. The effect of thermal stresses in the first 2,000 years after closure on dike propagation cannot be modeled with the same approach because the effect of heating is to induce horizontal confining stresses that are not linear with depth. Thermal stresses from calculations done for *Drift Degradation Analysis* (BSC 2004 [DIRS 166107]) were used as input to a complementary implementation to estimate the effect such stress variations would have on dike intrusion during this thermal period.

The model assumes homogeneous rock mass properties. Results presented in the report were generated for a Young's modulus of 15 GPa. This value is representative of the stiffness of the rock mass at Yucca Mountain on the scale of a potential dike. However, results for any other value of Young's modulus can be obtained readily by rescaling the existing results. Section 6.3.7.1 provides an example of such rescaling.

7.2.2 Post-Intrusion Submodel

Confidence in the post-intrusion submodel was developed by the selection of input data, by calibration activities, by assessment of the impacts of uncertainties, by use of appropriate assumptions and simplifications, and by ensuring consistency with physical principles.

Input parameters for the magma cooling model were selected to be consistent with measured values for the appropriate stratigraphic units at the Yucca Mountain site as described in Section 6.4.5 and Appendix C. The sensitivity of the model to the saturation level of the host rock is discussed in Appendix C. The effect of including or excluding the latent heat of crystallization of the magma in the heat flow calculation is also assessed in Appendix C. Approximations and parameters used in development and application of the model (e.g., approximating the configuration as two-dimensional and the thermal properties of the host rock formations) are discussed in Appendix C. Assumptions regarding the thermal properties of the magma are discussed in Section 5.4.

7.3 POSTDEVELOPMENT CONFIDENCE BUILDING

7.3.1 Dike-Intrusion Submodel

This submodel consists of four model components, dike propagation for incompressible magma, the effects of topography on dike propagation, the effects of structure and stratigraphy on dike propagation, and dike propagation for compressible magma.

7.3.1.1 Dike Propagation for Incompressible Magma

Postdevelopment confidence building for the dike propagation model component was accomplished by comparing model results with a natural analogue to address accuracy (Section 7.3.1.1.1) and by independent technical review to address adequacy (Section 7.3.1.1.2). Uncertainty is addressed in Section 7.3.1.1.3.

7.3.1.1.1 Parícutin Volcano Natural Analogue

One of the best-documented historic new volcanic eruptions began near the west Mexican village of Parícutin on February 20, 1943. The eruption was preceded by earthquakes felt by the local population and the fissure (dike-tip cavity) was observed immediately by farm workers in the field as it broke through the surface. The rate of magma production is also well-documented from the very beginning of the eruption. The first lava erupted was a basaltic andesite with about 55% silica (Wilcox 1954 [DIRS 163659]). Although the propagation of the dike within the earth was not directly observed, the phenomena associated with the initial eruption of Parícutin are well-documented. Thus, the Parícutin eruption provides a good analogue for dike propagation. If the timing of events at Parícutin can be approximated using input parameters consistent with field observations and inferences by experienced geologists regarding the physical properties of the components, the model can be considered to be accurate enough to represent dike propagation at Yucca Mountain.

The first seismic activity in the Parícutin vicinity was a magnitude 4.4 event recorded on January 7, 1943, in Mexico City, 320 km to the east (Yokoyama and de la Cruz-Reyna 1990 [DIRS 108740]), with four more quakes ($3.9 < M_S < 4.2$, M_S being surface wave magnitude) over the next month. Locally-felt earthquakes began about noon on 5 February according to Luhr and Simkin (1993 [DIRS 144310]), although Yokoyama and de la Cruz-Reyna (1990 [DIRS 108740]) report an early morning event at 0455 h that day (times are reported in local time, which is GMT-0600). Thereafter, seismic events were frequent. Events of $M_S > 4.0$ are summarized in Table 7-3. The depth of the hypocenters is not well-constrained but, based on the direct-wave delays, Yokoyama and de la Cruz-Reyna (1990 [DIRS 108740]) concluded that most are probably in the range of 10 km to 15 km deep.

Table 7-3. Earthquakes (M_S > 4.0) With Epicenters in the Parícutin Area during January and February 1943

Y&D Event #	Day	Hour	Minute	M_S
1	07 Jan	17	40	4.4
4	28 Jan	19	33	4.2
6	08 Feb	04	55	4.3
13	14 Feb	03	31	4.4
14	14 Feb	03	48	4.5
16	14 Feb	13	05	4.1
19	17 Feb	17	40	4.2
20	18 Feb	18	39	4.5

Source: Yokoyama and de la Cruz-Reyna 1990 [DIRS 108740].

NOTE: Times are local time, GMT-0600.

Luhr and Simkin (1993 [DIRS 144310]) provide details from many sources on events immediately following the first surface manifestations at Parícutin. Presented here is an abbreviated outline; page references in that volume are shown as *{page#}* in the remainder of this section (Section 7.3.1.1.1).

20 Feb 1943 *{54-65}*

1600: Half-meter deep fissure noticed (approximately 5 cm wide and 30 m long).

A few minutes later, the ground swelled up to 2-2.5 m and "smoke" began rising from the fissure.

After a few more minutes, hissing sounds and "smoke" and smell of sulfur were observed.

The spring near the fissure had dried up (time not observed).

1800: A fissure approximately 1 km long appeared with activity concentrated in a central depression about 12 m wide and 20 m long; "smoke" and sulfurous vapors issued from pit; small rocks were thrown 5 m high.

~2300-0000(21Feb): Volcano began to roar, incandescent stones were hurled up with great force, column of "smoke" arose.

21 Feb 1943 *{66-68}*

8 AM: A 10-m-high hill had formed and rocks were hurled out with great violence.

By 1 PM, a 30-m high cone had been formed.

By evening, explosions and bombs had been hurled to 500 m.

22 Feb 1943

0300: Heavy seismic activity, the first lava flows, a cone about 50-60 m high were observed. *{68-69}*

That night: Ordonez reported that "lava was flowing from three vents aligned from east to west and located precisely in the center of the crater." *{65}*

25 Feb 1943 *{68-69}*

First lava flow ceases to be fed from vent.

26 Feb 1943 *{69-70}*

Volume of cone 0.0195 km^3, growing at 0.00333 km^3/day.

Volume of lava flow 0.007 km^3.

The time lag between the first opening at the surface and the arrival of substantial magma at the surface is well-constrained by these observations to be about 7 hr to 8 hr. The estimate given above of magma supply rate to Parícutin in the early days (0.0033 km^3/day or 39 m^3 s^{-1}) agrees well with the total supply rate for all of the year 1943 estimated at 0.0026 km^3/day and the later history of an exponential drop in magma flux *{314}*. The values for time-lag and magma supply rate are the best-established metrics for the Parícutin eruption.

The composition of material erupted on 22 February was reported by Wilcox (1954 [DIRS 163659]) to be a basaltic andesite with the following major oxide weight percentages: SiO_2, 55.04; Al_2O_3, 18.82; Fe_2O_3, 1.97; FeO, 5.69; CaO, 7.17; MgO, 5.68; K_2O, 0.85; Na_2O, 3.88; TiO_2, 0.94; H_2O, 0.16 *{328}*. Eggler (1972 [DIRS 163623]) estimates, on the basis of the phenocryst compositions, that the actual water content of the source lava was higher, on the order of 2.2 wt % *{362}*. Based on the compositions of glass inclusions, a "before eruption" water content of about 1.5 wt % was estimated *{351-352}*.

There were no measurements of lava temperature at this early stage. The earliest available measurements were from May 1945, when optical pyrometer measurements of lava yielded a temperature of 1,200°C to 1,250°C (1,475 K to 1,525 K) *{318}*. Wilcox (1954 [DIRS 163659]) reports compositions for material from six months earlier and six months later. Silica by that time had increased to 55.6% to 56.4% and alumina had decreased to 17.7% *{328}*. The liquidus of such a magma would be slightly lower than for the original magma, but the 1946 material had slightly fewer phenocrysts than the earliest material, so it may be assumed that the temperature of the material being erupted in February 1943 was similar. The liquidus temperature for a magma with the composition given in the previous paragraph and calculated by the method used in *Characterize Eruptive Processes at Yucca Mountain, Nevada* (SNL 2007 [DIRS 174260]) is 1,104°C (1,377 K), much lower than the measurements. Given the primitive nature of the instrumentation available at the time, the calculated temperature seems likely to be more reliable. In addition, the early Parícutin magma had about 3.3% phenocrysts *{326}*; therefore, 1,052°C (1,325 K) represents the most appropriate estimate of magma temperature. This value is slightly lower than the estimate of Eggler (1972 [DIRS 163623]), but the oldest rock he worked with was not erupted until 1947, four years after the first eruption began *{360-363}*.

The viscosity of such a magma would be higher than that expected for alkali basaltic magma at Yucca Mountain (10 Pa·s to 40 Pa·s, see Table 4-1). As calculated by the method of Shaw (SNL 2007 [DIRS 174260]), the viscosity of the Parícutin magma would range from about 60 Pa·s at 1,200°C to about 900 Pa·s at 1,000°C. This is likely to be an underestimate because the effects of phenocrysts (a few percent), xenoliths, and bubbles are not considered. Krauskopf (1948 [DIRS 163632]) calculated the viscosity of lava at Parícutin based on flow speeds, flow depths, and slope values and found viscosities of 10^4 Pa·s to 10^5 Pa·s. This is likely to be an overestimate because the surface portions of the lava were not at the same temperature as the central portions. Hence, 10^3 Pa·s to 10^4 Pa·s is considered an appropriate range of viscosities for the Parícutin magma *{320}*.

The eruption was centered in a small valley so the fracture extent of approximately 1 km should be considered a lower limit for the strike length of the feeder dike.

There is little information on the depth of the magma chamber that fed Parícutin. Eggler's experimental petrology studies (1972 [DIRS 163623]) indicated some pressure and water were needed to prevent pyroxene phenocrysts from forming, but did not establish any strong limits. His experiments that most closely replicated the real Parícutin phases were at pressures of about 550 MPa, equivalent to a depth of about 20 km. Experiments at the same water content but at 750 MPa (about 28 km) contained pyroxene, so the depth must have been less than about 25 km *{360-363}*.

Although the magma chamber feeding Parícutin may have been 20-km deep, it is unlikely that the final movement of the dike leading to the surface originated so deeply. Basaltic magma may be stored at depths in the range of 2 km to 4 km due to decreased tensile strength of near-surface rocks or neutral buoyancy (Ryan 1987 [DIRS 170320]). Physical model experiments by Mastin and Pollard (1988 [DIRS 169783)] and elastic analysis indicate that a zone of tension will exist directly above a propagating dike. This will be manifested by development of a graben where the dike will eventually emerge, but the feature will have a depth on the order of the dike width and a width on the order of the depth to the magma. No such phenomena were observed at Parícutin, although the reported ground swell may be related to sudden release of such tension.

Given that both the beginning of seismic activity related directly to dike formation and the depth of origin of the dike feeding the new Parícutin volcano are uncertain (whether from seismic data or from petrologic constraints), only a rough order of magnitude estimate of the velocity of magma moving up the dike can be developed. The range of possible values based on the seismic data and possible source depths covers 0.001 m/s to 0.1 m/s.

Based on the above discussion, Table 7-4 presents a summary of the observational constraints on the Parícutin eruptive process.

Table 7-4. Summary of Parameters for the Dike That Fed Parícutin

Feeder Dike Property	Value	Reliability
Magma flux (m^3/s)[a]	39	Well-constrained by geometric measurements
Time lag: crack to magma at surface (h)[a]	7.5	Well-constrained, ±0.5 hr
Magma viscosity (Pa·s)[a]	100 to 100,000	Estimates based on composition do not agree with values calculated from lava flow velocities
Water content (wt%)[a]	1.5 to 2.2	Well-constrained by measurement and petrology
Magma velocity in dike (m/s)	0.001 to 0.1	Little real observational constraint
Strike length (km)[a]	>~1	Approximate lower limit
Magma chamber depth (km)[a]	<25	Upper limit
Magma "holding" depth (km)[b]	2 to 4	Inferred at other sites (see text)
Origin time (days before 20Feb43)[c]	2 to 45	Little real observational constraint

Sources: [a] Luhr and Simkin 1993 [DIRS 144310].
[b] Ryan 1987 [DIRS 170320].
[c] Yokoyama and de la Cruz-Reyna 1990 [DIRS 108740].

Validation Criteria: The observed phenomena and features of the eruption at Parícutin include the times of seismicity, of first opening of the fissure at the surface, and of the beginning of magma eruption at the surface; the nature of the first emanations from the fissure and the chemical and physical properties of the magma; observations of ground displacements; and the rate of magma eruption over the first several days.

The magma volume flux rising in the dike is fixed at the observed rate of eruption, given assumptions about the length of the dike feeding Parícutin. The model output can be considered corroborated if the time between crack opening and magma arrival is within a few hours, given the observed or inferred properties of the magma and country rock. The sequence of emanations should agree with observations. The calculated magma density must be consistent with the density expected due to exsolution of volatiles at the depths of the "final" phase of intrusion (i.e., after earthquake #20 in Table 7-3) for a magma with an "original" concentration of 1.5 wt % to 2.5 wt %. Because psychological factors can affect eyewitness accounts of magnitude of ground motion, displacement amplitudes are not considered, but ground displacements from the model should be in the same direction as those observed.

Approach: The dike propagation results described in Section 6.3 were rescaled with values appropriate for Parícutin. To account for the stiffer basalts of the Trans-Mexican Volcanic Field relative to the rhyolite tuffs of Yucca Mountain, Young's modulus was taken as 30 GPa with Poisson's ratio being 0.3 as estimated by Yokoyama and de la Cruz-Reyna (1990 [DIRS 108740]). To address uncertainties in other parameters, calculations were done for three country rock densities (ρ_{rock} = 2,200 kg m^3, 2,400 kg m^3, 2,600 kg m^3), two viscosities (μ = 10 kPa, 100 kPa), and three dike strike lengths (L = 1 km, 2 km, 4 km) for each of the three values of $\mathcal{D}$ used in Section 6.3. The magma density, calculated from ρ_{rock} and $\mathcal{D}$ as $\rho_{magma} = \rho_{rock} \times (1-1/\mathcal{D})$, ranged from 1,376 km/m^3 to 2,472 kg m^3. For each combination of ρ_{rock}, μ, L and $\mathcal{D}$, the far-field width was calculated for a magma flux of 39 m^3/sec with Equations 6-52 and 6-53. The far-field magma velocity was then obtained from Equation 6-48. The scaling length and scaling time were derived from Equation 6-31. The lag time was calculated by multiplying by the scaled depth to the magma front at breakout and dividing by the dimensionless magma front velocity. For each case, three estimates of dimensionless velocity were used. Based on a plot of magma front velocity versus depth, it was seen that the magma front velocity approached v_∞, but that the value fluctuated considerably as the crack neared the surface. (Figure 7-1 shows such a plot for $\mathcal{D}$ = 6.02; plots for $\mathcal{D}$ = 2.67 and 20.3 are very similar except that scatter as the crack tip approaches the surface is lower for $\mathcal{D}$ = 20.3 and greater for $\mathcal{D}$ = 2.67). To reflect the uncertainty associated with the fluctuation, factors of 0.75 v_∞, 1.0 v_∞, and 1.25 v_∞ were used to calculate the time lag.

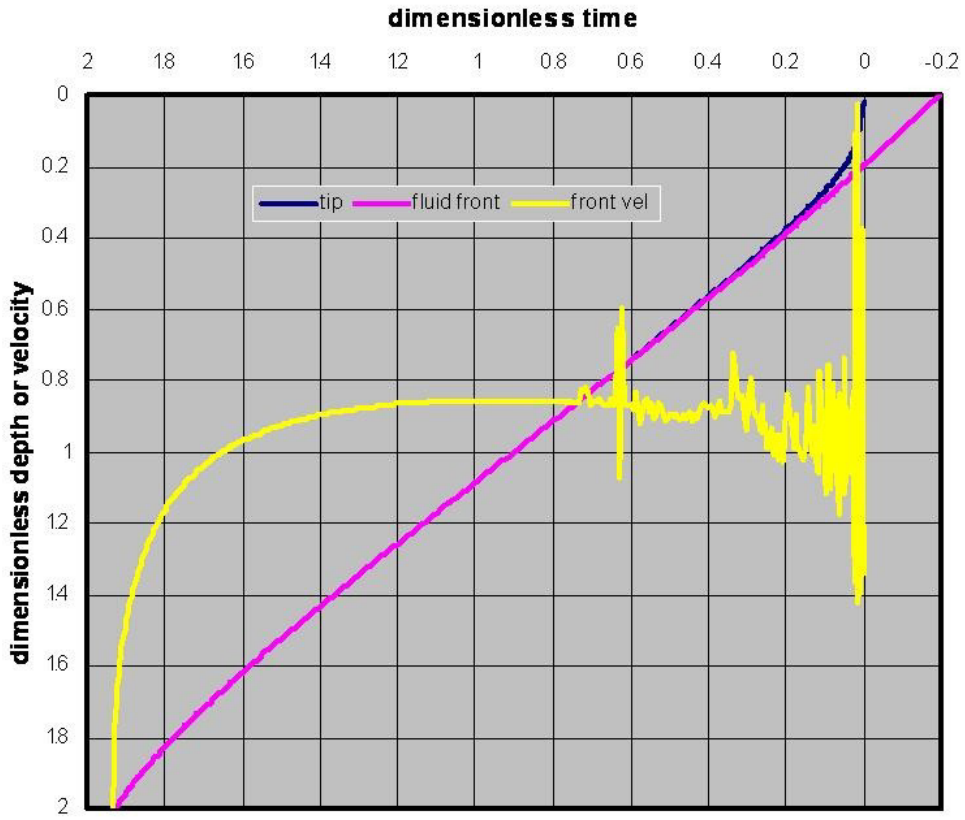

Developed Data Output DTN: MO0408EG831811.000; file *Scaling to Paricutin-27JUL04*, tab: "D=6.02."

Figure 7-1. Dimensionless Front Velocity (Yellow) for $\mathcal{D}$ = 6.02

For each rock density and viscosity combination, one set of results was selected for which the time lag fell between 5 hr and 10 hr (7.5 hr being the observed lag); if more than one set of results met that criterion, only the set nearest to 7.5 hours was carried forward.

The depth of magma at the time of the last large (M_S > 4) earthquake, which occurred on the evening of 18 February (#20 in Table 7-3), was calculated as the magma front velocity divided by the time elapsed from the earthquake to the arrival of magma at the surface. This depth was then used with Equations 6-1, 6-5a, and 6-8 of *Characterize Eruptive Processes at Yucca Mountain, Nevada* (SNL 2007 [DIRS 174260], pp. 6-22 and 6-27) to calculate the density at that depth expected for magma with a vesicle-free density of 2,600 kg m^3 and a dissolved water content of 2.5 wt %. This provided a value to compare with the magma density calculated from ρ_{rock} and $\mathcal{D}$ above.

Results: The results of these calculations are presented in Table 7-5. For the lower viscosity calculated, μ=10 kPa·s, there are cases from each value of $\mathcal{D}$ for which the time between crack opening and magma arrival is within 7.5±2.5 hours. No acceptable solutions were found with μ=100 kPa·s, providing more support for the upper limit of 10 kPa deemed appropriate above for lavas at Parícutin. For μ=10 kPa·s, there are no acceptable solutions with $\mathcal{D}$ = 20.3. Cases resulting in unacceptable solutions are indicated by dark shading in Table 7-5. The only cases for which the magma density calculated from exsolution relations is within 20% of that derived

from the scaling relations (highlighted in **boldface** and with light shading in Table 7-5) have $\mathcal{D}$ = 20.3 or 6.02; cases with unacceptable magma densities are dark-shaded in the table. One of those, with ρ_{rock} = 2,600 kg.m^3 and $\mathcal{D}$ = 20.3 (with no shading in the table), has agreement between the densities within less than 1% and is presented in ***bold italics*** in Table 7-5.

Table 7-5. Dike Intrusion/Eruption Parameters at Parícutin Scaled from Calculations Applied to Yucca Mountain

Viscosity	Strike length	$\mathcal{D}$	Magma density (scaled)	Crack-to-eruption	Far-field width	Far-field velocity	Magma front velocity	Depth to Q#20	Magma density (calc)
(kPa·s)	(km)	-	(kg m^3)	(hr)	(m)	(mm/s)	(mm/s)	(km)	(kg m^3)
ρ_{rock} = 2,200 kg m^3									
10	4.0	2.67	1,376	7.1	0.5	19	19	3.5	2,467
10	4.0	6.02	1,835	8.8	0.7	14	14	2.7	2,209
10	1.0	20.3	2,092	8.6	1.6	24	24	4.5	2,600*
ρ_{rock} = 2,400 kg m^3									
10	4.0	2.67	1,501	7.1	0.5	19	19	3.6	2,566
10	4.0	6.02	2,001	8.8	0.7	15	15	2.8	2,323
10	**2.0**	**20.3**	**2,282**	**8.2**	**1.3**	**19**	**19**	**3.7**	**2,282**
ρ_{rock} = 2,600 kg m^3									
10	4.0	2.67	1,626	6.6	0.5	16	16	3.7	2,600*
10	**4.0**	**6.02**	**2,168**	**8.1**	**0.7**	**15**	**15**	**2.8**	**2,424**
10	***2.0***	***20.3***	***2,472***	***9.5***	***1.2***	***20***	***20***	***3.0***	***2,475***

NOTE: Q#20 is seismic event number 20 from the list in Table 7-3.

* Indicates magma was below the depth for exsolution.

The sequence of emanations (several hours of gas and dust prior to actual magma) agrees with observations. The calculations indicate a length of the crack-tip cavity of about 540 m at the time of first breakout. Although not illustrated above, elastic analysis of deformation accompanying dike intrusion (Smith et al. 1996 [DIRS 101020]) indicates that the surface will be depressed in the immediate vicinity over the dike. When the dike breaks the surface, the ground would rebound upward as was observed. The observed magnitude may not agree with elastic analysis, but only the sign is included in the acceptance criteria.

Comparisons with field observations at Parícutin support the phenomenology described in the model. These results meet the acceptance criteria, and the accuracy of the model output has been corroborated by comparison with the analogue volcanic activity. Specifically, the model accurately reflects the process of dike propagation from depth and as it nears the surface. For magma viscosities and flow rates estimated from field and chemical observations, the calculated dike dimensions (aperture and strike length) and timing of the Parícutin eruption are reproduced by the model. Thus the model may be considered valid for applications that include a free surface and an appreciable lag time between the first cracking at the surface and the arrival of the magma front. The existence of a crack-tip cavity of considerable height is also corroborated.

Uncertainty–The deviations from the field observations can be attributed to:

- Uncertainties associated with lay observers and the primitiveness of the instrumentation available at the time
- Uncertainties in the material properties used in the rescaling of dimensionless results to the specific environment of the Parícutin eruption
- The fact that the model was scaled from one of the existing simulations rather than being developed specifically for the volcanic activity at Parícutin.

7.3.1.1.2 Independent Technical Review

Consistent with the requirements in SCI-PRO-006 for postdevelopment model validation of mathematical models, an independent technical review was conducted to enhance confidence that the dike propagation model presented in this model report is adequate for its intended purpose. The independent review, conducted by Dr. Allan Rubin, Professor of Structural Geology for the Department of Geosciences at Princeton University and a former member of the ICPRP, attests to the adequacy of the dike propagation model. His full report can be found in Appendix F.

Dr. Rubin was requested to consider the following five questions:

1. *Is the conceptual model reasonable and appropriate for its intended use?*

   Dr. Rubin finds the conceptual model here to be "reasonable and appropriate for its intended use." Although he mentions that some possibly rather severe simplifications (e.g., neglect of magma compressibility, magma freezing, inelastic deformation of the host rock) are made, he stresses that the goal "is not the faithful numerical reproduction of dike propagation…, but to understand in a general sense what would happen if a dike intersected the repository." He mentions the objective stated in the opening section of the report, that the "dog-leg" scenario be precluded, and asserts that this claim is not justified in the document he reviewed. The "dog-leg" scenario is in fact dealt with in an analysis, not included in the model. This analysis, which was not reviewed by Dr. Rubin, is reported in detail in Section 6.5 of the report.

2. *Are the mathematical relationships appropriate and representative of the scientific understanding of fracture/dike propagation?*

   Dr. Rubin states that he agrees in general with the main model assumptions, however, he points out that a number of them could be more accurately justified.

   Section 6.3.2, which deals with assumptions and simplifications of the dike propagation model, has been extensively revised in response to Dr. Rubin's comments. The assumption of the two-dimensional elasticity/one-dimensional flow model is now justified both for flow and geomechanical aspects of the model. The linear-elastic behavior assumption has been revised and does not state that this is always conservative. The "fracture toughness" parameter is used to investigate the effect of

any mechanism that resists fracture growth (Section 6.3.1.2). The laminar flow assumption is complemented by a qualitative discussion on the likely effect that turbulent flow would have on the solution (Section 6.3.2, Assumption 8). The assumption of a horizontal ground surface is now based only on computation results from the analysis in Section 6.2.

3. *Are the outputs of the model reasonable and representative?*

   Although he finds the outputs reasonable and representative, Dr. Rubin has concerns about the way the effect of thermal loading was represented (uniform load over the full model height). This has been changed and replaced by a computation where local thermal stresses are properly included (Section 6.3.7).

   Otherwise, Dr. Rubin questions the robustness of the statement that "the maximum magma pressure is at most 1 MPa larger than the horizontal far-field stress at the given depth." In his view, this should be changed to "a few MPa," in order to account for the range of possible dike thicknesses. In the final conclusion of the dike propagation model section of this report (Section 6.3.8), the text has been modified to coincide with Dr. Rubin's comment although such modification primarily reflects the findings of Section 6.3.7.

   He states that one of the conclusions from computations of the effect of thermal stresses is not justified by what is presented: the dike is not expected to turn and create a sill if rock mass properties are homogeneous and isotropic. The text has been revised to mention that dike deflection was not obtained for Yucca Mountain conditions (Section 6.3.7).

   Overall, Dr Rubin states that the simplifications mentioned in Question 1 above do not alter significantly the estimate of the maximum excess pressure and the pressure-versus-depth profile, although he mentions the difficulty in evaluating whether the neglected processes might introduce any qualitatively new behavior.

4. *Are limitations of the model adequately described?*

   Dr. Rubin agrees that the limitations of the model are adequately described.

5. *Are there alternative models or approaches that should be considered?*

   Dr. Rubin agrees that alternative models or approaches are adequately discussed.

Dr. Rubin's review has been addressed in the current version of this report.

7.3.1.1.3 Uncertainty

Uncertainty in the dike propagation model arises from diverse sources and has been addressed in various ways. One type of uncertainty is related to how closely the numerical solutions agree with analytical solutions when the latter are available. Results just below indicate that such uncertainty is small. Larger uncertainties arise from the natural variability of geologic

phenomena and have been addressed in application of the model and in postdevelopment model validation.

Numerical Uncertainties–The magnitude associated with numerical uncertainties can be estimated by comparing code results with analytical solutions for similar problems. The problem of propagation of a vertical dike far from any free surface is solved using NPHF2D V. 1.0. For the case in which the lag does not exist, the solution depends on dimensionless fracture toughness only. A specific subset of that case, in which the toughness is vanishingly small ($K \sim 0$), is considered here. A self-similar condition is achieved when both the dimensionless dike length and the dimensionless distance from the ground surface are larger than 2.0. Dimensionless lengths are obtained by scaling lengths to the characteristic length defined in Equation 6-31. To ensure a self-similar condition, the initial position of the fracture tip was selected to be at 4,000-m depth (a dimensionless depth of 5.208). The dike was propagated for 2,000 m (a dimensionless depth of 2.604), or halfway to the ground surface. At that point, the model results were compared with an analytic solution for a self-similar vertical dike produced by Lister (1990 [DIRS 126865]). The dimensional model parameters used in the particular simulations were:

- Young's modulus: 15 GPa
- Poisson's ratio: 0.21
- Horizontal stress gradient: 6,645 Pa/m
- Magma viscosity: 1 Pa·s
- Magma density: 400 kg m^3
- Magma injection rate: 0.2 m^2/s.

Comparisons between the numerical and analytical solutions of the dimensionless dike aperture and pressure versus scaled distance from the fracture tip are shown in Figures 7-2 and 7-3 (see Section 6.3.4 for a discussion of dimensionless, or scaled, dike properties).

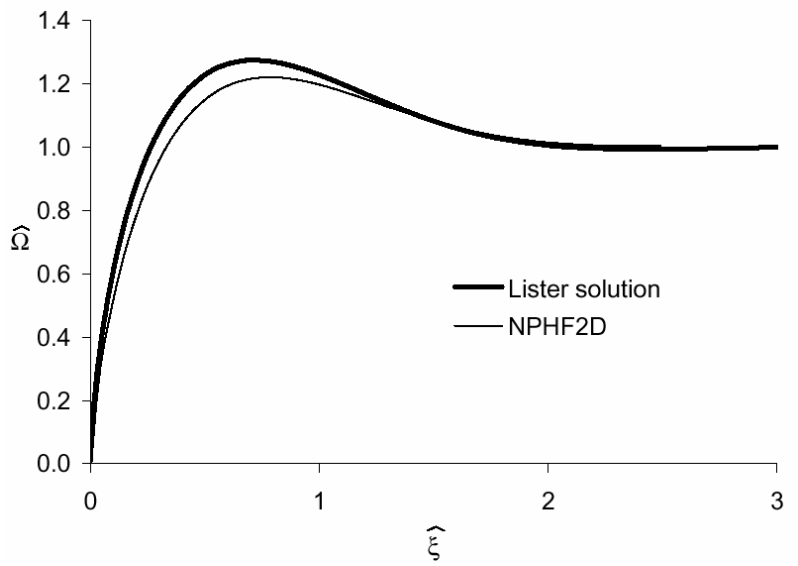

Source: Zhang et al. 2002 [DIRS 164368].

Figure 7-2. Self-Similar Dike Problem for K = 0: Dimensionless Opening (Ω) versus Dimensionless Distance from the Crack Tip (ξ)

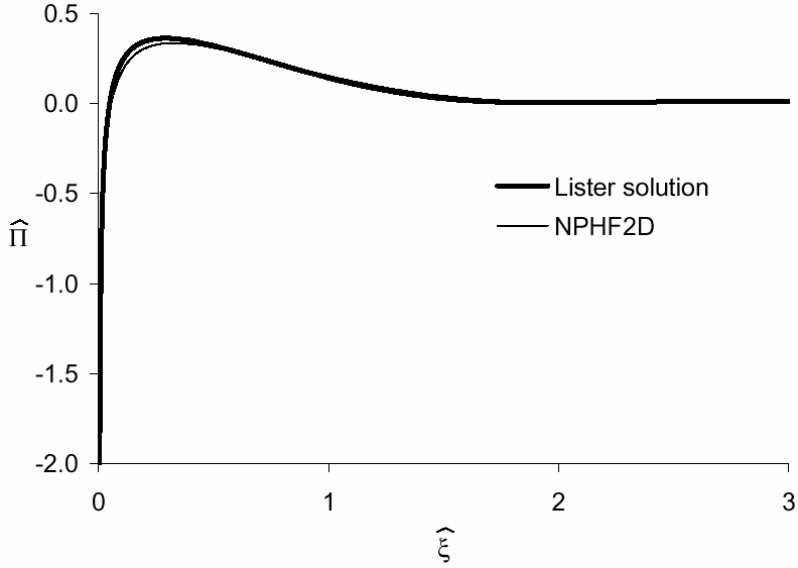

Source: Zhang et al. 2002 [DIRS 164368].

Figure 7-3. Self-Similar Dike Problem for K = 0: Dimensionless Pressure (Π) versus Dimensionless Distance from the Crack Tip (ξ)

The agreement with the analytic solution is close. The solutions far below the tip are almost coincident. The dimensionless dike opening far from the tip should be 1; the dimensionless pressure far from the tip should be 0. According to Lister's analytic solution (1990 [DIRS 126865]), the dimensionless fracture opening has a maximum of 1.274, at a dimensionless distance from the tip equal to 0.729. The NPHF2D V. 1.0 code yields a maximum opening of 1.218, which is a difference of 4.4%. The discrepancy is due to the finite fracture length and an

effect of the free surface in the model, compared to the idealized conditions of a semi-infinite fracture in an infinite elastic medium assumed in the Lister solution (1990 [DIRS 126865]).

Uncertainties associated with the fidelity of the numerical approximations used in the NPHF2D code are on the order of a few percent. Such uncertainties will not affect the applicability of the results of the dike propagation model.

Geological Uncertainties–Uncertainty is also associated with the extent to which a numerical model is a faithful representation of conditions "in the ground." The analysis provided in Section 6.3.7, addressing the effect of thermally induced stresses and the possibility of sill formation uses Voronoi polygons to represent the mechanical behavior of not only unstratified rocks but even poorly stratified rocks, which introduces its own uncertainty. In particular, the isotropic nature represented may not be as faithful as some other structure with a larger proportion of horizontal discontinuities. This may contribute to the apparent difficulty of sill formation found in the analysis.

Uncertainties of the dike propagation model associated with the variability of real geologic media can be inferred from intermediate results in the Parícutin natural analogue calculations (Section 7.3.1.1.1). For example, for dike strike lengths that differ by a factor of 2 (keeping the magma supply rate and magma density constant), variations of about 25% in dike widths and of about 60% to 65% in most other properties are found. Comparing results with different densities, it is seen that variations on the order of 50% in magma density will lead to similar variations in timing but smaller variations (10% to 15%) in dike width and magma velocity. The effect of uncertain geologic properties has also been addressed in the application of the model. For instance, the model is applied to a range of country rock densities, magma velocities, and magma viscosities; these lead to corresponding variations in calculated magma density, dike width and magma flux (Table 6-3).

Clearly, natural geological variability will be the greatest source of uncertainty in the results of the dike propagation model. Uncertainties of a factor of 2 or larger in such results as the time needed for magma to flood a drift or the depth of magma when the crack tip reaches the surface may arise from this source. This uncertainty related to dike propagation, specifically the potential for formation of a "dog-leg," has no effect on the post-intrusion model results.

7.3.1.2 Effects of Topography

Postdevelopment confidence building for the effects of topography on dike propagation was accomplished by comparing model results with the results of an independent, peer-reviewed publication (Section 7.3.1.2.1)) and by technical review through publication in a refereed professional journal or review by an external agency (Section 7.3.1.2.2). Uncertainty is addressed in Section 7.3.1.2.3.

7.3.1.2.1 Comparison with Pinel and Jaupart

Technical Work Plan for: Igneous Activity Assessment for Disruptive Events (BSC 2006 [DIRS 178448]) identifies the primary method that will be used to validate the effects-of-topography submodel as corroboration of the model with the results of an alternative model derived from different mathematical algorithms. The TWP states, "The computer code

used in the effects of topography submodel will be run with the same inputs as those used in the study of radial dike propagation from beneath a conical volcanic edifice published by Pinel and Jaupart (2004 [DIRS 176896]),” and calls for a quantitative comparison of the two models. However, due to a change in work scope, the code run with FLAC3D was not accomplished. Therefore, a qualitative comparison of the results of the two models with different geometries is provided to demonstrate the accuracy of the phenomena predicted by the model for the effects of topography on dike propagation.

Pinel and Jaupart (2004 [DIRS 176896]) found that dikes propagating radially from beneath a conical mountain would remain at depth until they reach the edge of the mountain, at which point they would begin to rise toward the surface. Since the time the TWP was written, a related publication has been identified. Dahm (2000 [DIRS 181315]) analyzed the stress field underneath a linear ridge using a two-dimensional Cartesian model. He found that the orientation of principal stresses was such that a dike originating off of the axis of the ridge but within a few half-widths of the ridge would tend to propagate toward the ridge and eventually emerge as a dike through the ridge or form a sill beneath it.

The analysis of topographic effects on dike propagation (Section 6.3.5) considers the effect of topography on the vertical propagation of a planar dike in the vicinity of a topographic ridge with a different strike than that of the dike. It was found that magma rising in a vertical dike that strikes across the trend of a topographic ridge will respond to lateral variations in confining stress and be diverted toward the surrounding lowland well before the magma reaches the surface. This effect combines with the simple geometric effect (that rising magma will first encounter a valley or lowland) to generate a preference for volcanic eruption in valleys rather than mountains.

The model results reported in Section 6.3.5.4 are similar to the findings of Pinel and Jaupart (2004), who found that magma rising under a conical edifice would frequently be diverted into radially propagating cracks and emerge some distance from the axis. They are not contradicted by the results of the analysis of dike propagation beneath linear ridges (Dahm 2000 [DIRS 181315]) because the strike of the dike considered in Section 6.3.5 is oblique to the ridge, whereas according to Dahm (2000 [DIRS 181315]), it is parallel. The radial dike considered by Pinel and Jaupart (2004 [DIRS 176896]) is more closely analogous to that of a dike striking perpendicular to the ridge. In view of the facts that the analysis yields a similar result to Pinel and Jaupart (2004 [DIRS 176896]) but with subdued effect and is not contradicted by the finding of Dahm (2000 [DIRS 181315]), the analysis of the effects of topography on dike propagation in Section 6.3.5 can be considered accurate.

7.3.1.2.2 Publication in Refereed Professional Journal

The model of the effect of topography on dike propagation in Section 6.3.5 has undergone technical review through publication in a refereed professional journal (Gaffney and Damjanac 2006 [DIRS 178144]). This demonstrates that the model is an adequate description of the effects of topography on dike propagation.

7.3.1.2.3 Uncertainty

Uncertainty associated with the analysis of the effects of topography on dike propagations from depth is related to the relative orientation of the strike of the dike and the elongation of the ridge. In the case modeled in Section 6.3.5, the angle between the two directions was 30 degrees, which is between the angles addressed by Pinel and Jaupart (2004 [DIRS 176896]) and by Dahm (2000 [DIRS 181315]). Other uncertainties associated with the natural variability of geologic media are common to all geologic engineering problems.

7.3.1.3 Effects of Structure

Postdevelopment confidence building for the effects of underlying geologic structure on dike propagation was accomplished by comparing model results with the field analogue sites reported in an independent, peer-reviewed publication (Section 7.3.1.3.1). Uncertainty is addressed in Section 7.3.1.3.2.

7.3.1.3.1 Natural Analogue

Technical Work Plan for: Igneous Activity Assessment for Disruptive Events (BSC 2006 [DIRS 178448]) identifies the primary method that will be used to validate the effects of underlying geologic structure on dike propagation as the corroboration of model results with data acquired from analogue studies. The structural submodel will be considered accurate in its description of the diversion of a dike into a fault if field observations indicate that dikes intrude into high angle faults but not into low-angle faults. Further corroboration will be achieved if the structural model adequately indicates sills may form at locations similar to where they are found in the field analogue sites.

Field studies reported by Valentine and Krogh (2006 [DIRS 177282]) have documented the intrusion of dikes along faults and sills into the hanging wall of faults in the vicinity of Paiute Ridge, Nevada. Valentine and Krogh (2006 [DIRS 177282]) mapped the geology of partially exhumed Tertiary volcanics in which basaltic dikes and sills intruded a previously faulted sequence of rhyolitic tuffs. The exposures represent a paleodepth of approximately 150 m to 300 m. They found that dikes frequently followed pre-existing faults, but only if the dip of the faults was steeper than 60 degrees. Faults with shallower dips were not intruded. They also observed several sills that developed from these faults. The sills were restricted to the hanging walls of the faults and were often also close to the depth of the much stiffer Paleozoic that underlies the tuffs.

Comparison of the structural submodel results in Section 6.3.4.5.2 is appropriate because the host and intruding rocks at Paiute Ridge are almost identical to those in the model of Section 6.3.4.5 and the depth of the rocks at the time of intrusion is well-constrained. The analogue data serve as evidence that fault structures have provided a preferred pathway for an intruding magma body only for fault dips steeper than about 60 degrees. For a fracture toughness of 0.1 MPa to 1.0 MPa $m^{1/2}$, which Table 6-10 indicates is appropriate for tuff, the largest fractures in the hanging wall would have to be larger than 0.1 m to 1 m long to permit penetration of the hanging wall of a 60-degree fault. This is in agreement with Figure 6-59.

Thus, the accuracy of the model of Section 6.3.4.5 is corroborated by the results of Valentine and Krogh (2006 [DIRS 177282]).

The intrusion of sills into the hanging wall provides further corroboration that the stress fields in the structural submodel are correctly reproduced. Such behavior is indicated in Figures 6-56 and 6-57. Although the calculation did not proceed long enough for magma to reach the level of the open stratigraphic horizons at a depth of a few hundred meters, it is clear that it would penetrate the open joints when it reached that level. Thus, the accuracy of the model discussed in Section 6.3.4.5 in describing phenomena associated with interaction between a dike and a pre-existing fault is corroborated by the results of Valentine and Krogh (2006 [DIRS 177282]).

7.3.1.3.2 Uncertainty

The largest uncertainty associated with the application of the analysis of the effect of underlying structure and stratigraphy on dike propagation is the depth at which the dikes intersected the fault that captured them. All that is known is that it is deeper than the deepest exposed paleodepth, which is a few hundred meters.

7.3.2 Post-Intrusion Submodel

Postdevelopment validations of the components of the post-intrusion submodel were conducted. The magma cooling and solidification model component is described in Section 7.3.2.1.

7.3.2.1 Magma Cooling and Solidification Model Component

The magma cooling and solidification model component is corroborated by comparison with alternative analytical solutions (Section 7.3.2.1.1) and with field observations and an associated numerical analysis (Section 7.3.2.1.2). Uncertainty is addressed in Section 7.3.2.1.3.

7.3.2.1.1 Comparison with Alternative Mathematical Models

The model results for magma cooling and solidification described in Section 6.4.6 are compared in this section with the results of two alternative models. Section 7.3.2.1.1.1 compares the model results with alternative analytic solutions. A comparison with alternative numerical models is presented in Section 7.3.2.1.1.2. Both of these sets of comparisons address the accuracy of the model results. The adequacy of the model is discussed at the end of Section 7.3.2.1.1.2.

7.3.2.1.1.1 Comparison with Alternative Analytic Solutions

The approach outlined in Sections 6.4.1 through 6.4.6 involved a finite difference methodology as summarized in Appendix C. The alternative approach, for which summary results are presented here, uses analytical solutions to the same equations, as does the model solution, but uses a very different treatment of latent heat effects. A complete discussion of the method and results is presented in Appendix D.

Acceptance Criteria: Results of both calculations at selected times and places within the repository system following an intrusive event should differ by no more than 25%.

Results–Figures 7-4 and 7-5 are included below to facilitate comparisons between base case and validation thermal models. Figure 7-4 shows the thermal evolution of a magma-filled drift using the thermal conductivity of dry tuff with latent heat not included, as discussed in Section 6.7.1.1.1. Figure 7-5 shows the estimated effects of latent heat, as determined by an alternate approach documented fully in Appendix D.

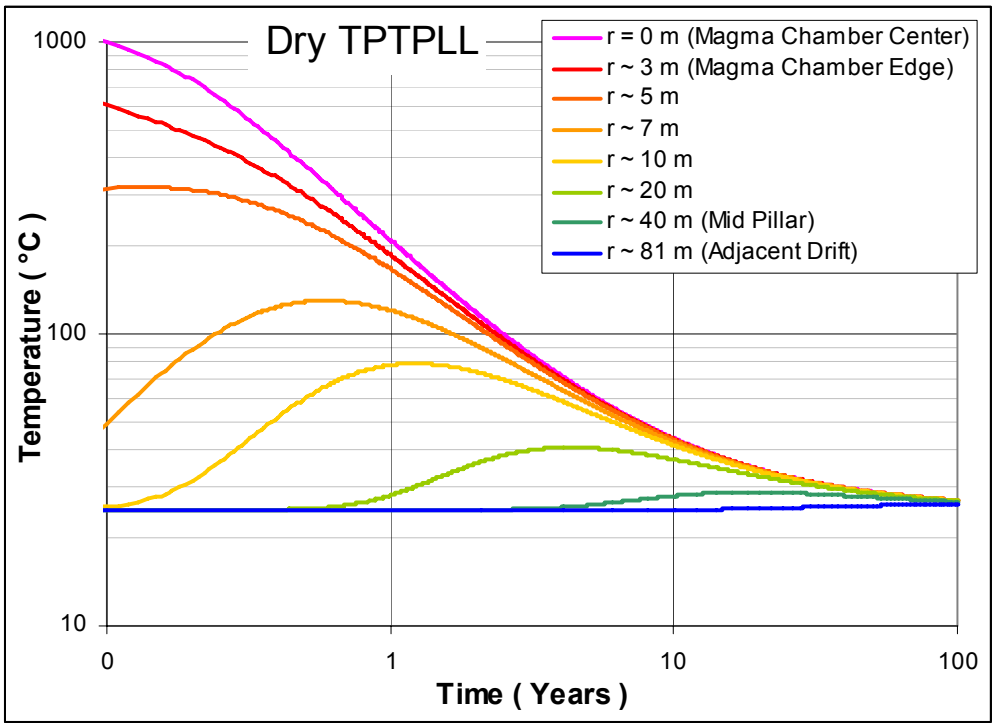

Output DTN: MO0408EG831811.008; file *MO0408EG831811.008.zip\Heat Conduction - Dry TPTPLL.xls*.

Figure 7-4. Heat Conduction from Magma Flow for Dry Tptpll

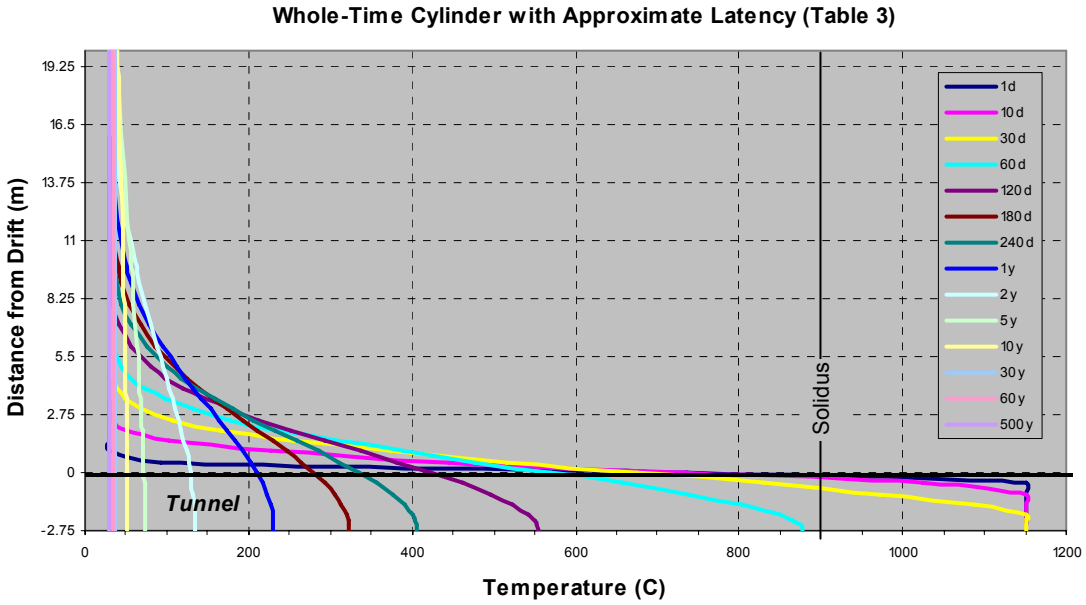

Output DTN: LA0307EG831811.001; file: *Heat_Flow_Calculations\Heat_Flow2\Analytical Solutions of Heat Flow.xls,* tab: "Chart3."

Figure 7-5. Plot of Calculated Whole-Time Temperature Profiles for Various Cooling Times Assuming a Cylindrical Drift Geometry and Showing the Approximate Effect of Latent Heat

Values listed below in Table 7-6 agree to within 20% or better relative to the models presented in Section 6.7. Note that, for short periods, finite difference models slightly under predict temperatures, whereas they over-predict thermal effects for long times. Thus, models presented in Section 6.7 above are conservative for long times. The agreement between the models is considered to be excellent given the wide range of natural variation in input parameters, as well as the simplifications of natural processes that have been made.

Table 7-6. Comparison of Cooling Model Results from Section 6.7 [Model 1] and from Alternate Model [Model 2]

Location	Model 1[a] (T°C)	Model 2[b] (T°C)
After one year:		
• drift center	~200	~215
• drift wall	~190	~205
• 20 m from drift center	~37	~40
After 10 years:		
• drift center	~55	~50
• drift wall	~55	~50
• 20 m from drift center	~48	~40

[a] Base case model: finite difference, Tptpll, no latent heat, dry pore volume. See Figure 7-4.
[b] Validation model: analytical solution, approximate latent heat effects considered. See Figure 7-5 and Figure D-2, Appendix D.

7.3.2.1.1.2 Comparison with Alternative Numerical Models

Numerical simulations were reported in Section 6.4.7.2.5 for analyses with and without a thermal source in the repository. The hot waste package (HWP) and cold waste package (CWP) scenarios study the evolution of temperature in the waste package, invert, and surrounding rock mass after magma intrusion into an emplacement drift. In the HWP scenario, magma intrusion occurs at the time the peak temperature is reached in the waste package according to results presented in *Repository Twelve Waste Package Segment Thermal Calculation* (BSC 2003 [DIRS 164726]). In the CWP scenario, the intrusion takes place after temperatures in the waste package and the rock mass have returned to ambient. The analyses are two-dimensional and are based on heat transfer by conduction after the magma fills the drift. The specific heat of magma used in the hot and cool calculations is increased to account for the latent heat of solidification. When magma temperature drops below the solidification temperature (estimated at 1,229 K), the specific heat is reduced to its original (unmodified) value of 1,100 J kg^{-1} K^{-1}. Simulations are performed for a period of 100 years after intrusion for initial temperatures of the magma, corresponding to effusive magma flow.

The results of the simulations for the HWP scenario show that, 100 years after intrusion, the temperature in the waste package (monitoring point 1) is about 555 K; the temperature in the magma (point 11) is 488 K.

The simulations for the CWP scenario show that at least 90% of the temperature drop at the monitoring points occurs during the first five years after intrusion, by which time all the temperatures are below the boiling point of water. The maximum recorded waste-package temperature (monitoring point 2) is about 1,280 K. Also, 100 years after intrusion, the temperatures at monitoring points in the waste package (point 1), magma (point 11), and invert (point 21) have equilibrated down to a value of about 295 K.

Comparison of the results of this section with the TSPA parameters identified in Appendix C, Table C-4, demonstrates the differences between the TSPA parameter values and the temperature values obtained by including the effects of latent heat, waste package radiogenic heat, and other factors described in this section. Table 7-7 presents both sets of results for the TSPA parameters with an initial temperature of 200°C (columns 2 through 4), the HWP scenario of Section 6.4.7.2.5.2 (columns 5 through 7), and the differences (columns 8 through 10). Note that the values of TSPA parameters labeled "WP" are the R = 0 m values in Table 6-13, while the R = 3 m values are listed twice and labeled "Crown" and "Invert." The second row of numbers (labeled "Max") for the results of this section provides the maximum temperature reached, which is before 0.1 year but, except for the crown temperature, not at the instant of intrusion; hence the second row of differences does not represent differences at a single time. Table 7-8 provides a similar comparison for the T_0 = 25°C TSPA parameters and the CWP scenario of Section 6.4.7.2.5.1. Note that the actual numbers listed for the "Two-dimensional Model" in Tables 7-7 and 7-8 are not reproduced in the cited sections but can be found in output DTN: MO0705FREEZING.000.

For the HWP scenario results in Table 7-7, the differences in temperature are due to latent heat, radiogenic heat from the waste package, and decrease in the "ambient" temperature due to decrease in the wattage generated by the waste packages over the 100 years represented by the

calculation. The large negative differences for all the locations between 0.5 years and 40 years are due to the radiogenic heat, which was not considered in generation of the TSPA parameters. In the waste package itself, the effects of the radiogenic heat continue to the end of the calculation; the same is true to a lesser extent in the invert. Latent heat, which is produced while the magma is crystallizing in the first half-year, is only a factor for the first year or two. Finally, the crown temperatures in the TSPA parameters after 50 years are too low because the decrease in temperature of the rock outside of the region affected by igneous heat was not considered.

For the CWP scenario results in Table 7-8, the differences are due only to latent heat and the small difference in initial temperature. The effect of latent heat is restricted to the first two years and is largest from 0.2 years to 0.6 years. The difference at late times is due to a starting temperature of 25°C for the TSPA parameters and one of 20°C for the results of this section. For applications in which the rock surrounding the repository is warmer than 20°C, a good estimate of the temperature in the waste package, the crown, or the invert can be obtained by adding to the values in Table 7-8 an amount equal to the difference between the warmer temperature and 20°C.

Although the results of the alternative model of Section 6.4.7.2 will overestimate peak temperatures (Assumption 5.4, Section 5), they are still considered to be more representative of rock mass temperatures after an igneous intrusion than the TSPA parameter values because of the more-accurate treatment of latent heat, because of the inclusion of decay in radiogenic heating, and because of the two-dimensional nature of the alternative model. The neglect of decay of the ambient temperature surrounding a hot waste packages may result in discrepancies for the TSPA igneous temperature parameters, especially for high initial temperatures, but these will not impact the TSPA adversely because temperatures will be high enough to compromise the mechanical integrity of waste packages for either result in Section 6.4.8.3 and because higher temperatures will only delay the return of seepage water. Therefore, these differences have no impact on TSPA, and the model is found to be accurate for its use in TSPA.

Table 7-7. Rock Mass Temperature for Selected Monitoring Points: HWP Scenario

Time (yr)	TSPA Parameters (Appendix C, Table C-4)			Two-dimensional Model, Section 6.4.7.2			Difference (TSPA—Two-dimensional Model)		
	WP (°C)	Crown (°C)	Invert (°C)	WP (°C)	Crown (°C)	Invert (°C)	WP (°C)	Crown (°C)	Invert (°C)
0.0	1,150	1,150	1,150	593.0	1,031.2	480.9	557.0	118.8	669.1
Max	1,150	1,150	1,150	1,157.5	1,031.2	657.5	−7.5	118.8	492.5
0.1	1,026	692	692	1,154.3	603.3	628.8	−128.3	88.8	63.2
0.2	804	583	583	1,135.5	549.0	657.5	−331.5	34.0	−74.5
0.3	655	516	516	1,057.8	498.8	643.2	−402.8	17.2	−127.2
0.4	560	468	468	977.0	465.7	618.2	−417.0	2.3	−150.2
0.5	497	431	431	904.5	437.0	588.4	−407.5	−5.9	−157.4
0.6	452	403	403	851.6	412.6	562.7	−399.6	−9.6	−159.7
0.7	418	381	381	802.9	387.8	537.2	−384.9	−6.8	−156.2
0.8	392	363	363	773.5	371.6	520.9	−381.5	−8.6	−157.9
0.9	372	349	349	750.2	358.1	507.4	−378.2	−9.1	−158.4

Table 7-7. Rock Mass Temperature for Selected Monitoring Points: HWP Scenario (Continued)

Time (yr)	TSPA Parameters (Appendix C, Table C-4)			Two-dimensional Model, Section 6.4.7.2			Difference (TSPA—Two-dimensional Model)		
	WP (°C)	Crown (°C)	Invert (°C)	WP (°C)	Crown (°C)	Invert (°C)	WP (°C)	Crown (°C)	Invert (°C)
1.0	356	336	336	731.3	346.6	496.2	−375.3	−10.6	−160.2
2.0	279	274	274	645.8	288.0	441.0	−366.8	−14.0	−167.0
3.0	253	251	251	621.2	270.6	423.9	−368.2	−19.6	−172.9
4.0	240	238	238	609.1	263.5	415.9	−369.1	−25.5	−177.9
5.0	232	231	231	600.6	259.8	410.8	−368.6	−28.8	−179.8
6.0	227	226	226	593.9	257.6	406.9	−366.9	−31.6	−180.9
7.0	223	222	222	587.6	256.0	403.5	−364.6	−34.0	−181.5
8.0	220	220	220	581.8	254.8	400.3	−361.8	−34.8	−180.3
9.0	218	217	217	576.0	253.6	397.2	−358.0	−36.6	−180.2
10.	216	216	216	570.2	252.5	394.1	−354.2	−36.5	−178.1
20.	208	208	208	510.0	239.0	360.0	−302.0	−31.0	−152.0
30.	205	205	205	461.4	224.5	330.3	−256.4	−19.5	−125.3
40.	204	204	204	421.1	211.1	304.9	−217.1	−7.1	−100.9
50.	203	203	203	386.5	198.9	282.8	−183.5	4.1	−79.8
60.	203	203	203	357.7	188.0	263.9	−154.7	15.0	−60.9
70.	202	202	202	334.0	178.6	248.0	−132.0	23.4	−46.0
80.	202	202	202	313.9	170.4	234.5	−111.9	31.6	−32.5
90.	202	202	202	297.1	163.3	223.1	−95.1	38.8	−21.1
100.	202	202	202	282.0	156.8	212.8	−80.0	45.2	−10.8

NOTE: TSPA = total system performance assessment; WP = waste package.

Table 7-8. Rock Mass Temperature for Selected Monitoring Points: Cool Scenario

Time (yr)	TSPA Parameters (Table C-4)			Two-dimensional Model, Section 6.4.7.2			Difference (TSPA—Two-dimensional Model)		
	WP (°C)	Crown (°C)	Invert (°C)	WP (°C)	Crown (°C)	Invert (°C)	WP (°C)	Crown (°C)	Invert (°C)
0.0	1150	1150	1150	402.5	959.9	302.4	747.5	190.1	847.6
Max	1150	1150	1150	973.7	959.9	490.4	176.3	190.1	659.6
0.1	1003	608	608	964.2	518.4	484.5	38.8	89.6	123.5
0.2	740	479	479	857.2	462.1	477.6	−117.2	16.9	1.4
0.3	564	399	399	675.3	402.1	420.9	−111.3	−3.1	−21.9
0.4	452	342	342	556.5	356.9	369.3	−104.5	−14.9	−27.3
0.5	377	299	299	467.3	318.6	325.2	−90.3	−19.6	−26.2
0.6	323	266	266	399.6	286.6	289.0	−76.6	−20.6	−23.0
0.7	283	240	240	335.9	253.8	252.7	−52.9	−13.8	−12.7
0.8	253	218	218	296.9	232.1	229.4	−43.9	−14.1	−11.4

Table 7-8. Rock Mass Temperature for Selected Monitoring Points: Cool Scenario (Continued)

Time (yr)	TSPA Parameters (Table C-4)			Two-dimensional Model, Section 6.4.7.2			Difference (TSPA—Two-dimensional Model)		
	WP (°C)	Crown (°C)	Invert (°C)	WP (°C)	Crown (°C)	Invert (°C)	WP (°C)	Crown (°C)	Invert (°C)
0.9	229	201	201	265.5	213.6	209.9	−36.5	−12.6	−8.9
1.0	209	186	186	239.9	197.7	193.4	−30.9	−11.7	−7.4
2.0	119	112	112	119.0	110.5	107.5	0.0	1.5	4.5
3.0	87.7	84.9	84.9	82.7	79.4	77.9	5.0	5.5	7.0
4.0	72.1	70.5	70.5	66.0	64.3	63.4	6.1	6.2	7.1
5.0	62.7	61.7	61.7	56.1	55.1	54.5	6.6	6.6	7.2
6.0	56.4	55.7	55.7	49.9	49.1	48.7	6.5	6.6	7.0
7.0	51.9	51.4	51.4	45.3	44.8	44.5	6.6	6.6	6.9
8.0	48.6	48.2	48.2	42.1	41.7	41.4	6.5	6.5	6.8
9.0	45.9	45.6	45.6	39.5	39.2	39.0	6.4	6.4	6.6
10.	43.9	43.6	43.6	37.4	37.2	37.0	6.5	6.4	6.6
20.	34.4	34.4	34.4	28.5	28.4	28.4	5.9	6.0	6.0
30.	31.3	31.3	31.3	25.6	25.5	25.5	5.7	5.8	5.8
40.	29.7	29.7	29.7	24.1	24.1	24.1	5.6	5.6	5.6
50.	28.8	28.8	28.8	23.3	23.3	23.2	5.5	5.5	5.6
60.	28.1	28.1	28.1	22.7	22.7	22.7	5.4	5.4	5.4
70.	27.7	27.7	27.7	22.3	22.3	22.3	5.4	5.4	5.4
80.	27.4	27.4	27.4	22.0	22.0	22.0	5.4	5.4	5.4
90.	27.1	27.1	27.1	21.7	21.7	21.7	5.4	5.4	5.4
100.	26.9	26.9	26.9	21.6	21.6	21.6	5.3	5.3	5.3

NOTE: TSPA = total system performance assessment; WP = waste package.

7.3.2.1.2 Comparison with Field Observations and Associated Mathematical Model

Shaw et al. (1977 [DIRS 170321]) and Peck et al. (1977 [DIRS 170318]) monitored and modeled the thermal evolution of a shallow (approximately 15-m-deep) cooling lava lake (Alae Lava Lake, formed in August 1963 during an eruptive phase of the Kilauea volcano, Hawaii) and successfully modeled and measured its cooling over the period of several years. This work illustrates that models of conductive cooling can adequately reproduce the thermal behavior of volcanic systems.

Acceptance Criteria: The acceptability of this analogue is established by a close correspondence between predicted and observed temperature profiles in which the simplifying assumptions of a constant thermal conductivity for the magma/host rock system are similar to cooling calculations in Section 6.7.

Results: Shaw et al. (1977 [DIRS 170321]) and Peck et al. (1977 [DIRS 170318]) describe the evolution of a lava lake, initially extruded at 1,160°C, as it cooled over a four-year period to less than 100°C. The modeling was more complex than that presented in this report because it had to account for the dissipation of energy through the heating and vaporization of rainwater. Nonetheless, conductive cooling models were successful in closely reproducing the temporal

thermal evolution of the lava lake. For example, the average deviation between observed and modeled profiles was 21°C. This is a remarkable correspondence given the additional complexity of the irregular shape of the bottom of the lava lake, the vaporization of rainwater, and the formation of cooling joints that accommodated the advective loss of hot gas from the cooling and solidifying magma body. This correspondence builds confidence in the adequacy of constant conductivity cooling models of magma-filled drifts, which are conceptually much simpler than a cooling lava lake, to provide estimates of the thermal history of a drift filled with magma.

7.3.2.1.3 Uncertainty

Uncertainty in the magma-cooling component of the post-intrusion model was explicitly evaluated in Section 7.3.2.1.1. The results, particularly the explicit comparison made in Table 7-8, demonstrate that the model is fairly insensitive to natural parameter variations. The comparisons in Table 7-8 were made at critical locations such as the drift center and drift wall, as well as the pillar interior. Differences after 10 years would have no significant effect on repository function. Conservatism was added to the model by using an initial magma intrusive temperature of 1,150°C which is near the maximum temperature of 1,169°C presented in *Characterize Eruptive Processes at Yucca Mountain, Nevada* (SNL 2007 [DIRS 174260]). Additionally, the drift was considered to be entirely filled with magma, effectually causing slower cool-down than would occur in a partially filled emplacement drift.

INTENTIONALLY LEFT BLANK

8. CONCLUSIONS

8.1 SUMMARY OF MODELING ACTIVITIES

Information concerning dike propagation, the fluid dynamics and thermal evolution of magma, and potential processes associated with the interaction between magma, waste package materials, and waste forms was assembled. This was done to develop a dike/drift interaction model that represents the interactions of a rising basaltic dike with a repository drift mined in silicic tuff, intrusion into that drift, and the postemplacement effects. This model is summarized in Sections 8.1.1 through 8.1.4. A series of validation activities was completed to build confidence in the model. Limitations on the use of this model are discussed in Section 1.3. *Yucca Mountain Review Plan, Final Report* (NRC 2003 [DIRS 163274]) acceptance criteria have been addressed, as described in Section 4.2 and Appendix A of this report. Results of this model are provided as outputs in Section 8.2, the associated uncertainties are discussed in Section 8.3, and restrictions are described in Section 8.4.

8.1.1 Dike Propagation

The following conclusions are drawn from modeling results presented in this report:

- The in situ state of stress at Yucca Mountain (before heating) is such that the vertical stress is the maximum principal compressive stress, whereas two other principal stresses of smaller magnitude are in the horizontal plane. Based on current understanding of the state of stress, the topography of Yucca Mountain would not cause deflection of the dike (Section 6.2.2).

- Stress changes caused by drift excavation will be of limited spatial extent and would have an insignificant effect on dike propagation (Section 6.2.3).

- A dike propagating upward from depth would consist of a vapor-filled crack tip moving ahead of the magma. Properties of the propagating dike, including the length of the crack-tip cavity, the velocity of the magma, and the width of magma in the dike, would depend on the density and viscosity of the magma and on the stiffness of the rock and the confining stresses normal to the dike plane. For an incompressible magma, properties of the magma and the environment can be reduced to two dimensionless parameters, one ($\mathcal{D}$) related to the density of the host rock and of the magma, and the other ($\mathcal{S}$) to the stress, the stiffness, and the viscosity. Large values of $\mathcal{D}$ are associated with denser magmas, and negative values of $\mathcal{S}$ are associated with excess gas pressure in the tip cavity (Section 6.3.3.1.3).

- As the dike with incompressible magma propagates upward, the length of the crack tip would increase due to the decrease in the confining stresses from the overburden. As the tip of the crack approaches the surface, it would accelerate even more. For lateral confinement typical of Yucca Mountain (κ = 0.5), appropriate later than about 2,000 years postclosure, magma with nominal (10 Pa·s) viscosity and a density of 750 kg m^3 rising at 1 m/s would arrive at drift level less than 60 s before the crack tip breached the surface 300 m above. Denser magmas would arrive at drift level even closer to the time of breaching the surface. Magmas with a density of 1,140 kg m^3 would stall just

below repository depth as the crack races to the surface. This would occur because the crack widens rapidly enough to accommodate all of the new magma arriving from depth. After the crack opened to its full extent, magma would resume its upward motion. Faster rising magma would open the crack faster, so that such magmas would not reach repository level before the crack tip breached the surface. Larger lateral stresses (up to 12 MPa during the first 2,000 years postclosure) would retard crack-tip acceleration so that magmas rising as fast as 5 m/s would reach the repository level before the crack tip breached the surface (Figures 6-10 through 6-15).

- More-viscous magma would result in wider dikes and longer tip-cavity lengths (Figures 6-16 and 6-17).

- Fluid pressure in the cavity ahead of the magma would be near atmospheric due to the high gas permeability of the host tuff. The model predicts that pressures in excess of atmospheric would increase the length of the tip cavity (Figure 6-22 vs. Figure 6-9), thereby increasing the likelihood that the crack tip will reach the surface before magma reaches the drift.

- The maximum magma pressure as the dike passes repository depth would be about 4.5 MPa under in situ stress conditions (Section 6.3.3.4.1). This would increase to 6 MPa in the case of thermally induced horizontal stresses up to 13 MPa in the first 1,500 years after closure of the repository (Section 6.3.7).

- Analysis of the effects of geologic structure and stratigraphy on dike propagation shows that intersection of a dike with a fault at depth would not be expected to divert the dike from its original upward path in the plane normal to the least compressive stress except at shallow depth and into steeply dipping faults. As a result, if such diversion were to occur, it would have a negligible effect on whether the repository would be intruded; that is, the path of the dike would not be moved more than tens of meters to either side of its original trajectory (Section 6.3.4.5). If magma were diverted into a high-angle fault, the effective stress-resisting fault slip would decrease, and slip could occur if the orientation of the fault relative to the regional stresses were favorable. Such slip could facilitate the intrusion of sills into the hanging wall if weak sub-horizontal planes occur at depths of less than approximately 500 meters (Section 6.3.4.5.2).

- A more-detailed analysis of the effects of topography on magma flow in dikes under ridges indicates that there is a tendency for magma to erupt onto lowlands adjacent to ridges rather than out from the ridge itself. This is due both to the simple geometric effect and to the increased confining stresses beneath the higher topography. Once an eruption began in the lowland, the upward progress of the dike under the ridge would stall (Section 6.3.5.4).

- Propagation of a dike driven by a compressible (expanding) magma has not been modeled directly in this report. However, a combined analysis of magma of several different densities indicates that one effect of expanding magma would be to increase the acceleration of the crack tip as it nears the surface. In addition, dimensional analysis indicates that the dike aperture when the first low-density fraction of magma in the dike reaches the repository will be considerably narrower than the aperture for a denser magma (Section 6.3.6).

- The model indicates that thermally induced stresses 1,000 years after closure would significantly affect dike propagation. As the dike approaches the region of increased horizontal stresses approximately 200 m below the repository, the ascending dike tip and magma front would slow. The dike opening would increase significantly, while the crack tip would nearly stall; the magma front would slow to approximately 0.1 m/s. A dike at the center of the repository would be more strongly affected than one near the edge because the temperature (and, hence, the thermally induced horizontal stresses) will be greatest in the middle of the repository and will decrease toward its margins. Once the dike passed through the region of increased horizontal stresses, the tip and magma front would be free to accelerate under the very large vertical stress gradient (Figure 6-79) above the repository. Below the thermal stress region, the gap between the dike tip and the magma front would be between 50 m and 100 m. The gap would almost completely disappear as the dike penetrated the repository (shown in Figure 6-82). Despite these modifications to the dike propagation, the predicted thermal stress magnitudes are not expected to be great enough to deflect the dike either toward or away from the repository or to result in sill formation beneath the repository (Section 6.3.7.4).

8.1.2 Environment in Repository after Intrusion

- The maximum temperature to which contents of waste packages would rise following intrusion of emplacement drifts depends on the temperature of the magma and on the thermal condition of the waste packages. The model calculates that the temperature in waste packages would reach the magma temperature (nominally 1,150°C; Appendices C and D), but more complete analyses that include the heat required to raise the temperature of a cold waste package indicate that peak temperatures would be approximately 150°C lower and would peak during the first 0.1 year after intrusion (Section 6.4.7.2). Temperatures would remain above 350°C for about eight months (Section 6.4.7.2). Because of inaccuracies associated with input data assumptions (Section 5.4), the peak values would likely be somewhat lower (Table H-1). If an intrusion occurred in the first 1,000 years after closure, the radiogenic heat from the waste form would combine with the magmatic heat, resulting in peak temperatures that were slightly higher than magmatic temperatures and could remain above 350°C for as long as sixty years (Section 6.4.7.2).

- Pressures within a magma-filled drift would rise after intrusion as the anhydrous minerals crystallize. The volatile species would be concentrated in the remaining liquid and would be sealed in by the hot solidified outer portions of the drift, which would act as a membrane. By the time the magma is half-crystallized, a matter of one to two months (Section 6.4.7.1), pressures would approach 10 MPa, and they could go as high as 15 MPa before the pressure can be vented through fractures (Section 6.4.8.1.3). This would result in partial pressures of

corrosive gases (at 10 MPa total pressure) on the order of 7 MPa steam, 1 MPa CO_2, 945 kPa $S0_2$, 100 kPa H_2, 100 kPa HCl, 100 kPa H_2S, 50 kPa CO, 50 kPa S_2, and 20 kPa HF (Section 6.4.8.3.1). The upper end of this range of pressures may be outside the range of conditions associated with basaltic volcanism of the type found in the Yucca Mountain region; however, they are included in this analysis for completeness.

- It is difficult to predict with certainty the effects of basaltic magma interacting with waste package materials. However, a survey of known effects suggests that they are all deleterious to waste package integrity, and often seriously so. Thus, this report is supportive of the position that all waste packages, cladding, and drip shields would be immediately and completely compromised with regard to seepage water if they come in contact with magma (Section 6.4.8.3.1).

- An analysis of elastoplastic deformation of waste packages subjected to high temperatures and pressures indicate that deformations would exceed the maximum strain limits of waste package materials by an amount large enough that the ends would fail and allow magma to flow into the interior of the waste packages (Section 6.4.8.3.1 and Appendix E). Due to the large pressures (10 MPa or more; Section 6.4.8.3.1), magma could fill the waste package. Because reverse pressure gradients are not likely to become large after magma has intruded a waste package, magma would be expected to remain in a waste package that had been filled (Section 6.4.8.3.1).

- Magmatic effects on waste forms are even more difficult to predict but are expected to include oxidation and comminuting of oxide fuel by transgranular cracks and volatilization of some fission daughter products. Because of the high temperatures at which basalt magma and waste forms would interact, oxide and silicate phases would form, and these phases would serve as the most likely hosts for radionuclides. The solubility of such phases has not been assessed. Chemical reactions between magmatic volatiles and waste forms are also possible but have not been evaluated. Glass waste forms are not expected to be devitrified. However, these conclusions should be considered in light of the large uncertainty that exists (Section 6.4.8.3.3).

8.1.3 Secondary Dike Propagation

- The opening of pre-existing cracks due to pressure build-up in the drift was analyzed. Even under the conditions of a wide initial opening of a pre-existing crack and large driving pressures, the velocity of a magma front inside a joint is approximately 0.5 m/s, which is less than the expected velocity of the magma front inside the main dike. The re-opening cracks would only be millimeters to centimeters wide so that magma would freeze due to conductive heat loss into the surrounding rock mass. Furthermore, because the highly fractured, lithophysal rock mass at the repository level in Yucca Mountain is characterized by a large number of closely spaced joints, it is more likely that magma will be injected into exposed lithophysae and into a number of intersecting joints. Such a process leads to rapid magma freezing due to heat loss (Section 6.5.1.2).

- By the time magma reaches the repository level, the stress-induced perturbation is small (e.g., Figure 6-167), and its effect on the stress concentrations around the tunnel is minimal (Section 6.5.1.3).

- Even under the most favorable assumptions for growth, a subsidiary dike will never be able to propagate effusively more than a few meters from the drift because the magma will be halted by solidification (Section 6.5.1.4).

- The most likely scenario for magma to erupt to the surface after intruding the drift complex is for it to continue along the trajectory of the original dike (Section 6.5.1.5).

8.1.4 Basalt/Water Interaction

- Published reports of ground water in contact with basaltic rock have been reviewed. There is a wide range of pH and ionic strength in such waters. Fluoride contents are low (Section 6.6).

8.2 MODEL OUTPUT

8.2.1 Developed Output Listed by Data Tracking Number

The outputs associated with the Dike/Drift Interaction model are listed in Table 8-1 by data tracking number. In addition to the output DTNs listed in this table, the results of model validation have been submitted to the Technical Data Management System separately (DTNs: MO0408EG831811.000 and SN0705DRFTTEMP.001). In addition, DTN: MO0408EG831811.008 contains intermediate product output used to develop output in Appendix C.

Table 8-1. Outputs for the Dike/Drift Interaction Model Report

Submodel/Component: Output Description	Data Tracking Number
Dike Propagation Model: Model Results Using NPHF2D	SN0304T0504203.001
Dike Propagation Model: Abstraction of Results	MO0408EG831811.004
Dike Propagation Model: Results Using NPHF2D (Figure 6-17 only)	MO0408EG831811.003
Dike/Drift Interactions: Magma Flow in Dike with Drift	MO0411EG831811.001
Dike Propagation Model: Estimates of Magma Flow from Dike into Drifts	LA0602DA831811.001
Dike Propagation Model: Effects of Structure	MO0610SPADIKEP.000
Dike Propagation Model: Effects of Topography	MO0705TOPODIKE.000
Dike Propagation Model: Expanding Magma	MO0408EG831811.002
Dike Propagation Model: Thermal Stress Results Using UDEC	MO0411EG831811.000
Post-Intrusion Model/Magma Cooling/Solidification: Temperature of Waste Forms	LA0702PADE01EG.001
Post-Intrusion Model/Magma Cooling/Solidification: Temperature Sensitivities	MO0408EG831811.008
Post-Intrusion Model/Magma Cooling/Solidification Temperature - 1D Alternative	LA0307EG831811.001
Post-Intrusion Model/Magma Cooling/Solidification: Temperature - 2D Alternative	MO0705FREEZING.000
Post-Intrusion Model/Magma Cooling/ Solidification: Magma Pressurization	SN0705MAGPRESS.001
Post-Intrusion Model/Magma Cooling/Solidification: Magma Breakout Pressures	MO0705BREAKOUT.000

Table 8-1. Outputs for the Dike/Drift Interaction Model Report (Continued)

Submodel/Component: Output Description	Data Tracking Number
Post-Intrusion Model/Magma Cooling/Solidification: Solidification Temperatures	MO0411EG831811.002
Post-Intrusion Model/Magma Cooling/Solidification: Waste Package in Magma	MO0705WPNMAGMA.000
Post-Intrusion Model/Magma Cooling/Solidification: EBS Failure Fractions	LA0702PADE01EG.002
Post-Intrusion Model/Magma Cooling/Solidification: Magma Cooling with Backfill	MO0705BACKFILL.000
Secondary Dike Propagation: Results	MO0411EG831811.002
Analysis of Natural and Induced Stresses at the Repository	SN0707ISITUTIS.001

NOTE: 1D = one-dimensional; 2D = two-dimensional; EBS = Engineered Barrier System.

8.2.2 Thermal Effects

Values of the igneous temperature parameters developed in Section 6.4.6 are listed in Table 8-2. The values were calculated using Excel in several spreadsheets listed in Appendix G. The results are contained in output DTN: LA0702PADE01EG.001. These parameters are justified by having been generated from the qualified inputs listed in Tables 4-1 under Yucca Mountain Project quality assurance standards.

Table 8-2. Lookup Tables for Temperature (°C) of Intruded Drifts

Time after Intrusion	Pre-intrusion Temperature									
	25°C		50°C		100°C		150°C		200°C	
Years	$T_{r=0m}$	$T_{r=3m}$	$T_{r=0m}$	$T_{r=3m}$	$T_{r=0m}$	$T_{r=3m}$	$T_{r=0m}$	$T_{r=3m}$	$T_{r=0m}$	$T_{r=3m}$
0	1,150	1,150	1,150	1,150	1,150	1,150	1,150	1,150	1,150	1,150
0.1	1,003	608	1006	620	1,012	644	1,019	668	1,026	692
0.2	740	479	749	494	768	524	786	553	804	583
0.3	564	399	577	416	603	449	629	483	655	516
0.4	452	342	467	360	498	396	529	432	560	468
0.5	377	299	394	318	428	356	462	394	497	431
0.6	323	266	341	286	378	325	415	364	452	403
0.7	283	240	303	260	341	300	380	341	418	381
0.8	253	218	273	239	313	281	353	322	392	363
0.9	229	201	249	222	290	264	331	306	372	349
1	209	186	230	208	272	251	314	293	356	336
2	119	112	142	136	187	182	233	228	279	274
3	87.7	84.9	111	109	158	156	206	203	253	251
4	72.1	70.5	96.0	94.5	144	142	192	190	240	238
5	62.7	61.7	86.8	85.8	135	134	183	183	232	231
6	56.4	55.7	80.7	80.0	129	129	178	177	227	226
7	51.9	51.4	76.3	75.8	125	125	174	173	223	222
8	48.6	48.2	73.0	72.6	122	122	171	171	220	220
9	45.9	45.6	70.5	70.2	120	119	169	168	218	217
10	43.9	43.6	68.4	68.2	118	117	167	167	216	216
20	34.4	34.4	59.2	59.2	109	109	158	158	208	208
30	31.3	31.3	56.1	56.1	106	106	156	156	205	205

Table 8-2. Lookup Tables for Temperature (°C) of Intruded Drifts (Continued)

Time after Intrusion	Pre-intrusion Temperature									
	25°C		50°C		100°C		150°C		200°C	
Years	$T_{r=0m}$	$T_{r=3m}$	$T_{r=0m}$	$T_{r=3m}$	$T_{r=0m}$	$T_{r=3m}$	$T_{r=0m}$	$T_{r=3m}$	$T_{r=0m}$	$T_{r=3m}$
40	29.7	29.7	54.6	54.6	104	104	154	154	204	204
50	28.8	28.8	53.7	53.7	104	104	153	153	203	203
60	28.1	28.1	53.1	53.1	103	103	153	153	203	203
70	27.7	27.7	52.6	52.6	103	103	152	152	202	202
80	27.4	27.4	52.3	52.3	102	102	152	152	202	202
90	27.1	27.1	52.0	52.0	102	102	152	152	202	202
100	26.9	26.9	51.8	51.8	102	102	152	152	202	202
Source file name	*Heat Conduction - Dry TPTPLL*		*Heat Conduction - Dry TPTPLL 50C*		*Heat Conduction - Dry TPTPLL 100C*		*Heat Conduction - Dry TPTPLL 150C*		*Heat Conduction - Dry TPTPLL 200C*	

Source: Located in tab: "Lookup Tables" in named spreadsheets in Appendix G.

Output DTN: LA0702PADE01EG.001.

NOTE: $T_{r=0}$ is the centerline temperature and $T_{r=3}$ is the temperature at the edge of the drift.

8.2.3 Igneous EBS Failure Fractions

The outputs from this section are found in output DTN: LA0702PADE01EG.002, EBS Failure Fractions. They include three parameters used in the TSPA GoldSim model. Fraction_DS_Failed_Ign_Input represents total damage of the drip shield and has a value of 1. Fraction_WP_Failed_Ign_Input represents total damage of the waste package and has a value of 1. Clad_Failure_Frac_Ign_Input represents total failure of the commercial spent nuclear fuel cladding and has a value of 1.

The TSPA parameter Fraction_DS_Failed_Ign_Input is assumed to have a value of 1 because the drip shields are considerably less robust structures than the waste packages under intrusive igneous conditions and the waste packages are expected to fail (see next paragraph).

The TSPA parameter Fraction_WP_Failed_Ign_Input has been assigned a value of 1 based on the thermal, mechanical, and chemical environment to which it would be exposed, as described in Section 6.4.8.3.1 and in Appendices C and E. The mechanical failure is corroborated by the numerical analysis in Appendix E. This analysis demonstrates that pressures experienced by a waste package surrounded by cooling magma in a drift would be sufficient to open gaps large enough that magma can be expected to fill the waste package. Chemical failure is a result of loss of integrity of cladding and of oxidative disaggregation of uranium oxide fuel.

The TSPA parameter Clad_Failure_Fract_Ign_Input has been assigned a value of 1 based on the thermal and chemical environment to which it would be exposed, as described in Section 6.4.8.3.3. Mechanical failure is a result of loss of integrity of cladding, and chemical failure is a result of oxidative disintegration of uranium oxide fuel.

The full details of the effects of magma intrusion on waste packages and cladding are not known. Nevertheless, several conclusions can be drawn. The waste packages and other drift materials would be enclosed by the magma. At the time of intrusion, temperatures inside waste packages

will rise to nearly magmatic temperatures and will remain high enough for long enough in most instances that Zircalloy cladding will be compromised by any of several mechanisms (Section 6.4.8.3.3). Upon cooling, the pressure of magmatic gases will rise, likely reaching values of 10 MPa or higher before venting into the host rock (Section 6.4.8.1.4). Pressures of this magnitude are sufficient to crush the waste packages and cause tears that will expose the contents to volcanic gases (Section 6.4.8.3.1). These high magmatic pressures will also result in partial pressures of steam on the order of 7 MPa, with values for other more corrosive gases being correspondingly high. Such gases will lead to excessive corrosion of waste package materials and to reaction with waste forms that become exposed to them (Section 6.4.8.3.3). In summary, the most likely result of an igneous intrusion is that no credit can be taken for any residual containment by remaining waste package or cladding material.

The simulation modeling of heat conduction away from the intruded drifts demonstrates that the initial 1,150°C temperature reduces to about 30°C at the center of the drift in about 30 years, and the maximum temperature rise expected in adjacent emplacement drifts is less than 1°C (Section 6.4.6). The drift-rock provides an effective thermal insulation barrier to the impacts of high temperature of the intruded magma, and there would not be any impact of igneous heat on the waste packages in adjacent emplacement drifts.

8.3 OUTPUT UNCERTAINTY

8.3.1 Heat Flow Calculation

Uncertainties from various sources have been addressed in this model report (Section 7.3.2.2.1.2 and Appendices C and D). These include thermal conductivity, grain density, specific heat capacity, matrix porosity, saturation, lithophysal porosity, and initial temperature. Of these, it was shown that only the initial temperature had any appreciable effect on the outcome of the TSPA. The uncertainty in the temperature is reflected in the comparison between the model output (Table 8-2) and the results of the two-dimensional alternative model, which is considered to be a more accurate description of the temperatures that would be expected in an actual intrusion; that comparison is in Tables 7-9 and 7-10.

8.3.2 Igneous Engineered Barrier System Failure Fractions

The range of possible interactions with waste packages, cladding, and drip shields encompasses an unusually broad range of uncertainty. As a result, it is not possible at this time to predict the precise behavior of these elements in the event of an igneous intrusion. However, the temperatures, pressures, corrosive vapors and durations of exposure associated with an igneous intrusion into emplacement drifts support the position that waste canister/assembly, cladding, and drip shields contacted by magma will provide no added protection to waste forms and that magma may flow into, but not back out of, waste packages.

8.4 RESTRICTIONS

The igneous temperature parameters found in output DTN: LA0702PADE01EG.001 are intended for use in the TSPA model only. Other applications for temperatures in drifts or surrounding rocks after intrusion should use the results of Section 6.4.7.2; however, attention is called to the potential effects of data assumptions (Table H-1 and Section 5.4).

Similarly, the igneous Engineered Barrier System failure fractions parameters found in output DTN: LA0702PADE01EG.002 are intended for use in the TSPA model only. Other applications related to the response of waste packages or waste forms after intrusion should consider the discussion of Section 6.4.8.3.

There are no other restrictions on the use of outputs from this report. For all applications, attention is directed to the limitations described in Section 1.4 of this report.

INTENTIONALLY LEFT BLANK

9. INPUTS AND REFERENCES

9.1 DOCUMENTS CITED

178340 Aadnoy, B.S. and Chenevert, M.E. 1987. "Stability of Highly Inclined Boreholes." *SPE Drilling Engineering, [2],* Pages 364-374. Richardson, Texas: Society of Petroleum Engineers. TIC: 259470.

156927 Abramowitz, M. and Stegun, I.A., eds. 1972. *Handbook of Mathematical Functions with Formulas, Graphs, and Mathematical Tables.* New York, New York: Dover Publications. TIC: 240610.

177256 Aiuppa, A.; Bellomo, S.; Brusca, L.; D'Alessandro, W.; and Federico, C. 2003. "Natural and Anthropogenic Factors Affecting Groundwater Quality of an Active Volcano (Mt. Etna, Italy)." *Applied Geochemistry, 18,* 863-882. New York, New York: Pergamon. TIC: 258387.

151409 Allegheny Ludlum. 1999. "Technical Data Blue Sheet, Stainless Steels, Chromium-Nickel-Molybdenum, Types 316 (S31600), 316L (S31603), 317 (S31700), 317L (S31703)." Pittsburgh, Pennsylvania: Allegheny Ludlum Corporation. Accessed July 31, 2000. TIC: 248631. URL: http://www.alleghenytechnologies.com/ludlum/ pages/products/t316_317.pdf.

182250 Allegheny Ludlum. 2006. *Technical Data Blue Sheet: Stainless Steels, Chromium-Nickel-Molybdenum Types 316 (S31600), 316L (S31603), 317 (S31700), 317L (S31703).* Brackenridge, PA: Allegheny Ludlum Corporation (div. Allegheny Technologies, Inc. (ATI)). TIC: 259471.

103597 Altman, W.D.; Donnelly, J.P.; and Kennedy, J.E. 1988. *Peer Review for High-Level Nuclear Waste Repositories: Generic Technical Position.* NUREG-1297. Washington, D.C.: U.S. Nuclear Regulatory Commission. TIC: 200651.

103750 Altman, W.D.; Donnelly, J.P.; and Kennedy, J.E. 1988. *Qualification of Existing Data for High-Level Nuclear Waste Repositories: Generic Technical Position.* NUREG-1298. Washington, D.C.: U.S. Nuclear Regulatory Commission. TIC: 200652.

177265 Angelone, M.; Gasparini, C.; Guerra, M.; Lombardi, S.; Pizzino, L.; Quattrocchi, F.; Sacchi, E.; and Zuppi, G.M. 2005. "Fluid Geochemistry of the Sardinian Rift-Campidano Graben (Sardinia, Italy): Fault Segmentation, Seismic Quiescence of Geochemically 'Active' Faults, and New Constraints for Selection of CO_2 Storage Sites." *Applied Geochemistry, 20,* 317-340. New York, New York: Elsevier. TIC: 258388.

177278 Arnórsson, S. and Andrésdóttir, A. 1995. "Processes Controlling the Distribution of Boron and Chlorine in Natural Waters in Iceland." *Geochimica et Cosmochimica Acta, 59,* (20), 4125-4146. New York, New York: Pergamon. TIC: 258399.

182314 Balme, M.R.; Rocchi, V.; Jones, C.; Sammonds, P.R.; Meredith, P.G.; and Boon, S. 2004. "Fracture Toughness Measurements on Igneous Rocks Using a High-Pressure, High-Temperature Rock Fracture Mechanics Cell." *Journal of Volcanology and Geothermal Research, 132,* 159-172. New York, New York: Elsevier. TIC: 257314.

178341 Bardintzeff, J-M. and Bonin, B. 1987. "The Amphibole Effect: A Possible Mechanism for Triggering Explosive Eruptions." *Journal of Volcanology and Geothermal Research, 33,* 255-262. Amsterdam, The Netherlands: Elsevier. TIC: 236165.

178342 Barsom, J.M. and Rolfe, S.T. 1987. *Fracture and Fatigue Control in Structures, Application of Fracture Mechanics.* 2nd Edition. Englewood Cliffs, New Jersey: Prentice-Hall. TIC: 259460.

182275 Basham, K.D.; Chong, K.P.; and Boresi, A.P. 1993. "A New Method to Compute Size Independent Fracture Toughness Values for Brittle Materials." *Engineering Fracture Mechanics, 46,* 357-363. New York, New York: Pergamon. TIC: 259635.

103289 Batchelor, G.K. 1967. *An Introduction to Fluid Dynamics.* Page 594. New York, New York: Cambridge University Press. TIC: 241827.

177272 Bath, A.H.; Burgess, W.G.; and Carney, J.N. 1986. "The Chemistry and Hydrology of Thermal Springs on Efate, Vanuatu, SW Pacific." *Geothermics, 15,* (3), 277-294. New York, New York: Pergamon. TIC: 258394.

181323 Bhatti, T.M.; Vuorinen, A.; Lehtinen, M.; and Tuovinen, O.H. 1998. "Dissolution of Uraninite in Acid Solutions." *Journal of Chemical Technology and Biotechnology, 73,* 259-263. New York, New York: John Wiley & Sons. TIC: 259397.

103524 Bird, R.B.; Stewart, W.E.; and Lightfoot, E.N. 1960. *Transport Phenomena.* New York, New York: John Wiley & Sons. TIC: 208957.

178343 Boorman, S.L.; McGuire, J.B.; Boudreau, A.E.; and Kruger, F.J. 2003. "Fluid Overpressure in Layered Intrusions: Formation of a Breccia Pipe in the Eastern Bushveld Complex, Republic of South Africa." *Mineralium Deposita, 38,* 356-369. New York, New York: Springer-Verlag. TIC: 259184.

178344 Boudreau, A.E. 1999. "PELE−A Version of the MELTS Software Program for the PC Platform." *Computers & Geosciences, 25,* 201-203. New York, New York: Pergamon. TIC: 259174.

163439 BSC (Bechtel SAIC Company) 2003. *Input Parameters for Ground Support Design.* 800-K0C-TEG0-00500-000-00A. Las Vegas, Nevada: Bechtel SAIC Company. ACC: ENG.20030515.0002; ENG.20050816.0016.

164726 BSC 2003. *Repository Twelve Waste Package Segment Thermal Calculation.* 800-00C-WIS0-00100-000-00A. Las Vegas, Nevada: Bechtel SAIC Company. ACC: ENG.20030915.0003; ENG.20050829.0002; ENG.20051021.0001; ENG.20050914.0017.

168796 BSC 2003. *Risk Information to Support Prioritization of Performance Assessment Models.* TDR-WIS-PA-000009 REV 01 ICN 01 [Errata 001]. Las Vegas, Nevada: Bechtel SAIC Company. ACC: MOL.20021017.0045; DOC.20031014.0003.

170835 BSC 2004. *21-PWR Waste Package Configuration [Sheet 1 of 3].* 000-MW0-DSU0-00401-000-00D. Las Vegas, Nevada: Bechtel SAIC Company. ACC: ENG.20040708.0004.

169987 BSC 2004. *CSNF Waste Form Degradation: Summary Abstraction.* ANL-EBS-MD-000015 REV 02. Las Vegas, Nevada: Bechtel SAIC Company. ACC: DOC.20040908.0001; DOC.20050620.0004.

166107 BSC 2004. *Drift Degradation Analysis.* ANL-EBS-MD-000027 REV 03. Las Vegas, Nevada: Bechtel SAIC Company. ACC: DOC.20040915.0010; DOC.20050419.0001; DOC.20051130.0002; DOC.20060731.0005.

170029 BSC 2004. *Geologic Framework Model (GFM2000).* MDL-NBS-GS-000002 REV 02. Las Vegas, Nevada: Bechtel SAIC Company. ACC: DOC.20040827.0008.

168960 BSC 2004. *Igneous Intrusion Impacts on Waste Packages and Waste Forms.* MDL-EBS-GS-000002 REV 01. Las Vegas, Nevada: Bechtel SAIC Company. ACC: DOC.20040421.0002.

169854 BSC 2004. *Thermal Conductivity of the Potential Repository Horizon.* MDL-NBS-GS-000005 REV 01. Las Vegas, Nevada: Bechtel SAIC Company. ACC: DOC.20040928.0006.

169862 BSC 2004. *Ventilation Model and Analysis Report.* ANL-EBS-MD-000030 REV 04. Las Vegas, Nevada: Bechtel SAIC Company. ACC: DOC.20041025.0002.

169734 BSC 2004. *Yucca Mountain Site Description.* TDR-CRW-GS-000001 REV 02 ICN 01. Two volumes. Las Vegas, Nevada: Bechtel SAIC Company. ACC: DOC.20040504.0008.

173981 BSC 2005. *Features, Events, and Processes: Disruptive Events.* ANL-WIS-MD-000005 REV 03. Las Vegas, Nevada: Bechtel SAIC Company. ACC: DOC.20050830.0008.

174070 BSC 2005. *Magma Dynamics at Yucca Mountain, Nevada.* ANL-MGR-GS-000005 REV 00. Las Vegas, Nevada: Bechtel SAIC Company. ACC: DOC.20050829.0006.

173447 BSC 2005. *Normal Load Bearing by Site Specific Canister.* 000-00C-HAC0-00100-000-00A. Las Vegas, Nevada: Bechtel SAIC Company. ACC: ENG.20050324.0005.

173492 BSC 2005. *Waste Package Behavior in Magma.* 000-00C-SSE0-00600-000-00A. Las Vegas, Nevada: Bechtel SAIC Company. ACC: ENG.20050502.0005; ENG.20050817.0027.

173802 BSC 2005. *Waste Package Damage Due to Interaction with Magma.* CAL-WIS-MD-000013 REV 00A. Las Vegas, Nevada: Bechtel SAIC Company. ACC: DOC.20050706.0006.

178838 BSC 2006. *Naval Long Waste Package for License Application [Sheet 1 of 4].* 000-MWK-DNF0-00101-000-00A. Las Vegas, Nevada: Bechtel SAIC Company. ACC: ENG.20060227.0002.

176681 BSC 2006. *Naval Long Waste Package for License Application [Sheet 2].* 000-MWK-DNF0-00102-000-00A. Las Vegas, Nevada: Bechtel SAIC Company. ACC: ENG.20060227.0003.

178839 BSC 2006. *Naval Long Waste Package for License Application [Sheet 3].* 000-MWK-DNF0-00103-000-00A. Las Vegas, Nevada: Bechtel SAIC Company. ACC: ENG.20060227.0004.

178448 BSC 2006. *Technical Work Plan for: Igneous Activity Assessment for Disruptive Events.* TWP-WIS-MD-000007 REV 09 ICN 01. Las Vegas, Nevada: Bechtel SAIC Company. ACC: DOC.20060814.0018.

178693 BSC (Bechtel SAIC Company) 2007. *Subsurface Geotechnical Parameters Report.* ANL-SSD-GE-000001 REV 00. Las Vegas, Nevada: Bechtel SAIC Company. ACC: ENG.20070115.0006.

163096 Carnahan, B.; Luther, H.A.; and Wilkes, J.O. 1990. *Applied Numerical Methods.* Malabar, Florida: Krieger Publishing. TIC: 224042.

100968 Carslaw, H.S. and Jaeger, J.C. 1959. *Conduction of Heat in Solids.* 2nd Edition. Oxford, Great Britain: Oxford University Press. TIC: 206085.

160928 Carter Krogh, K.E. and Valentine, G.A. 1996. *Structural Control on Basaltic Dike and Sill Emplacement, Paiute Ridge Mafic Intrusion Complex, Southern Nevada.* LA-13157-MS. Los Alamos, New Mexico: Los Alamos National Laboratories. ACC: MOL.20030828.0138.

152938 Chapman, A.J. 1974. *Heat Transfer.* 3rd Edition. New York, New York: Macmillan Publishing. TIC: 245061.

178345 Chouet, B.; Dawson, P.; Ohminato, T.; Martini, M.; Saccorotti, G.; Giudicepietro, F.; De Luca, G.; Milana, G.; and Scarpa, R. 2003. "Source Mechanisms of Explosions at Stromboli Volcano, Italy, Determined from Moment-Tensor Inversions of Very-Long-Period Data." *Journal of Geophysical Research, 108,* (B1), ESE 7-1 - ESE 7-25. Washington, D.C.: American Geophysical Union. TIC: 259172.

149935 Connor, C.B.; Stamatakos, J.A.; Ferrill, D.A.; Hill, B.E.; Ofoegbu, G.I.; Conway, F.M.; Sagar, B.; and Trapp, J. 2000. "Geologic Factors Controlling Patterns of Small-Volume Basaltic Volcanism: Application to a Volcanic Hazards Assessment at Yucca Mountain, Nevada." *Journal of Geophysical Research, 105,* (B1), 417-432. Washington, D.C.: American Geophysical Union. TIC: 247906.

139600 Crouch, S.L. and Starfield, A.M. 1983. *Boundary Element Methods in Solid Mechanics, with Applications in Rock Mechanics and Geological Engineering.* Boston, Massachusetts: Allen & Unwin. TIC: 4370.

177266 Cruz, J.V. and Amaral, C.S. 2004. "Major Ion Chemistry of Groundwater from Perched-Water Bodies of the Azores (Portugal) Volcanic Archipelago." *Applied Geochemistry, 19,* 445-459. New York, New York: Elsevier. TIC: 258389.

151552 CRWMS M&O. 2000. *Dike Propagation Near Drifts.* ANL-WIS-MD-000015 REV 00 ICN 1. Las Vegas, Nevada: CRWMS M&O. ACC: MOL.20001213.0061.

181315 Dahm, T. 2000. "Numerical Simulations of the Propagation Path and the Arrest of Fluid-Filled Fractures in the Earth." *Geophysical Journal International, 141,* 623-638. Oxford, England: Blackwell Scientific Publications. TIC: 259396.

100027 Day, W.C.; Dickerson, R.P.; Potter, C.J.; Sweetkind, D.S.; San Juan, C.A.; Drake, R.M., II; and Fridrich, C.J. 1998. *Bedrock Geologic Map of the Yucca Mountain Area, Nye County, Nevada.* Geologic Investigations Series I-2627. Denver, Colorado: U.S. Geological Survey. ACC: MOL.19981014.0301.

102776 Delaney, P.T. 1987. "Heat Transfer During Emplacement and Cooling of Mafic Dykes." *Mafic Dyke Swarms, A Collection of Papers Based on the Proceedings of an International Conference held at Erindale College, University of Toronto, Ontario, Canada, June 4 to 7, 1985.* Halls, H.C. and Fahrig, W.F., eds. Special Paper 34. Pages 31-46. St. John's, Newfoundland, Canada: Geological Association of Canada. TIC: 225006.

169660 Detournay, E.; Mastin, L.G.; Pearson, J.R.A.; Rubin, A.M.; and Spera, F.J. 2003. *Final Report of the Igneous Consequences Peer Review Panel, with Appendices.* Las Vegas, Nevada: Bechtel SAIC Company. ACC: MOL.20031014.0097; MOL.20030730.0163.

118647 Dieter, G.E. 1976. *Mechanical Metallurgy.* 2nd Edition. Materials Science and Engineering Series. New York, New York: McGraw-Hill Book Company. TIC: 247879.

182051 DOE (U.S. Department of Energy) 2007. *Quality Assurance Requirements and Description.* DOE/RW-0333P, Rev. 19. Washington, D. C.: U.S. Department of Energy, Office of Civilian Radioactive Waste Management. ACC: DOC.20070717.0006.

182316 Donovan, J.G. and Karfakis, M.G. 2004. "Adaptation of a Simple Wedge Test for the Rapid Determination of Mode I Fracture Toughness and the Assessment of Relative Fracture Resistance." *International Journal of Rock Mechanics and Mining Science & Geomechanics Abstracts, 41,* 695-701. New York, New York: Pergamon. TIC: 259636.

166999 Douglass, D.L. 1983. "The Corrosion of Ferritic Stainless Steels and High-Purity Fe–Cr Alloys in Basaltic Lava and Simulated Magmatic Gas." *Oxidation of Metals, 20,* (3/4), 161-183. New York, New York: Plenum Press. TIC: 238278.

161776 Duncan, J.M.; Byrne, P.; Wong, K.S.; and Mabry, P. 1980. *Strength, Stress-Strain and Bulk Modulus Parameters for Finite Element Analyses of Stresses and Movements in Soil Masses.* UCB/GT/80-01. Berkeley, California: University of California, College of Engineering, Office of Research Services. TIC: 253873.

177253 Edmunds, W.M.; Carrillo-Rivera, J.J.; and Cardona, A. 2002. "Geochemical Evolution of Groundwater Beneath Mexico City." *Journal of Hydrology, 258,* 1-24. New York, New York: Elsevier. TIC: 258385.

163623 Eggler, D.H. 1972. "Water-Saturated and Undersaturated Melting Relations in a Parícutin Andesite and an Estimate of Water Content in the Natural Magma." *Contributions to Mineralogy and Petrology, 34,* 261–271. Berlin, Germany: Springer-Verlag. TIC: 254481.

101097 Ehrlich, S.A. and Douglass, D.L. 1982. *The Effect of Molybdenum Plus Chromium on the Corrosion of Iron-, Nickel-, and Cobalt-Base Alloys in Basaltic Lava and Simulated Magmatic Gas at 1,150°C.* SAND82-7055. Albuquerque, New Mexico: Sandia National Laboratories. ACC: MOL.19981028.0003.

178346 Einarsson, P. and Brandsdottir, B. 1980. "Seismological Evidence for Lateral Magma Intrusion during the July 1978 Deflation of the Krafla Volcano in NE Iceland." *Journal of Geophysics, 47,* 160-165. New York, New York: Springer-Verlag.

126446 Einziger, R.E.; Marschman, S.C.; and Buchanan, H.C. 1991. "Spent-Fuel Dry-Bath Oxidation Testing." *Nuclear Technology, 94,* 383-393. Hinsdale, Illinois: American Nuclear Society. TIC: 246459.

171915 EPRI (Electric Power Research Institute) 2004. *Potential Igneous Processes Relevant to the Yucca Mountain Repository: Extrusive-Release Scenario.* EPRI TR-1008169. Palo Alto, California: Electric Power Research Institute. TIC: 256654.

178347 Fagents, S.A. and Wilson, L. 1993. "Explosive Volcanic-Eruptions--VII. The Ranges of Pyroclasts Ejected in Transient Volcanic Explosions." *Geophysics Journal International, 113,* 359-370. Oxford, United Kingdom: Blackwell Scientific. TIC: 259468.

178348 Funatsu, T.; Seto, M.; Shimada, H.; Matsui, K.; and Kuruppu, M. 2004. "Combined Effects of Increasing Temperature and Confining Pressure on the Fracture Toughness of Clay Bearing Rocks." *International Journal of Rock Mechanics & Mining Sciences, 41,* 927-938. New York, New York: Elsevier. TIC: 259408.

163631 Gaffney, E.S. 2003. Magma and Gas Flow Analysis. Scientific Notebook SN-LANL-SCI-279-V1. ACC: MOL.20031009.0141.

178144 Gaffney, E.S. and Damjanac, B. 2006. "Localization of Volcanic Activity: Topographic Effects on Dike Propagation, Eruption and Conduit Formation." *Geophysical Research Letters, 33,* 1-4. Washington, D.C.: American Geophysical Union. TIC: 258505.

163624 Geertsma, J. and de Klerk, F. 1969. "A Rapid Method of Predicting Width and Extent of Hydraulically Induced Fractures." *Journal of Petroleum Technology, [21],* ([12]), 1571–1581. Dallas, Texas: American Institute of Mining and Metallurgical Engineers. TIC: 254512.

178349 Ghiorso, M.S. and Sack, R.O. 1995. "Chemical Mass Transfer in Magmatic Processes IV. A Revised and Internally Consistent Thermodynamic Model for the Interpolation and Extrapolation of Liquid-Solid Equilibria in Magmatic Systems at Elevated Temperatures and Pressures." *Contributions to Mineralogy and Petrology, 119,* (2/3), 197-212. Heidelburg, Germany: Springer-Verlag. TIC: 238316.

178350 Giordano, D.; Nichols, A.R.L.; and Dingwell, D.B. 2005. "Glass Transition Temperatures of Natural Hydrous Melts: A Relationship with Shear Viscosity and Implications for the Welding Process." *Journal of Volcanology and Geothermal Research, 142,* 105-118. New York, New York: Elsevier. TIC: 259407.

101966 Goodman, R.E. 1980. *Introduction to Rock Mechanics.* New York, New York: John Wiley & Sons. TIC: 218828.

163357 Gordon, B.M. 2003. *Literature Review of Waste Package and Drip Shield Materials' Corrosion Performance in Magmatic-Type Environments.* SIR-02-168, Rev. 0. San Jose, California: Structural Integrity Associates. ACC: MOL.20030414.0260.

177269 Griesshaber, E.; O'Nions, R.K.; and Oxburgh, E.R. 1992. "Helium and Carbon Isotope Systematics in Crustal Fluids from the Eifel, the Rhine Graben and Black Forest, F.R.G." *Chemical Geology, 99,* 213-235. Amsterdam, The Netherlands: Elsevier. TIC: 258392.

163625 Griffiths, R.W. 2000. "The Dynamics of Lava Flows." *Annual Review of Fluid Mechanics, 32,* 477–518. Palo Alto, California: Annual Reviews. TIC: 254466.

178351 Grunder, A.L.; Laporte, D.; and Druitt, T.H. 2005. "Experimental and Textural Investigation of Welding: Effects of Compaction, Sintering, and Vapor-Phase Crystallization in the Rhyolitic Rattlesnake Tuff." *Journal of Volcanology and Geothermal Research, 142,* 89-104. New York, New York: Elsevier. TIC: 259406.

181324 Gudmundsson, A. and Philipp, S.L. 2006. "How Local Stress Fields Prevent Volcanic Eruptions." *Journal of Volcanology and Geothermal Research, 158,* 257-268. New York, New York: Elsevier. TIC: 259492.

174063 Gupta, A.S. and Rao, K.S. 2000. "Weathering Effects on the Strength and Deformational Behaviour of Crystalline Rocks under Uniaxial Compression State." *Engineering Geology, 56,* 257-274. New York, New York: Elsevier. TIC: 257315.

178352 Hagerty, M.T.; Schwartz, S.Y.; Garcés, M.A.; and Protti, M. 2000. "Analysis of Seismic and Acoustic Observations at Arenal Volcano, Costa Rica, 1995-1997." *Journal of Volcanology and Geothermal Research, 101,* 27-65. New York, New York: Elsevier. TIC: 259183.

146529 Hahn, G.J. and Shapiro, S.S. 1967. *Statistical Models in Engineering.* New York, New York: John Wiley & Sons. TIC: 247729.

171570 Haskin, F.E.; Camp, A.L.; Hodge, S.A.; and Powers, D.A. 2002. *Perspectives on Reactor Safety.* NUREG/CR-6042, Rev. 2. Washington, D.C.: U.S. Nuclear Regulatory Commission. ACC: MOL.20040910.0330.

100896 Haynes International 1997. Hastelloy C-22 Alloy. Kokomo, Indiana: Haynes International. TIC: 238121.

166893 Hearn, P.P.; Steinkampf, W.C.; Bortleson, G.C.; and Drost, B.W. 1985. *Geochemical Controls on Dissolved Sodium in Basalt Aquifers of the Columbia Plateau, Washington.* Water-Resources Investigations Report 84-4304. Tacoma, Washington: U.S. Geological Survey. TIC: 230835.

115670 Hem, J.D. 1985. *Study and Interpretation of the Chemical Characteristics of Natural Water.* 3rd Edition. Geological Survey Water-Supply Paper 2254. Washington, D.C.: U.S. Government Printing Office. ACC: NNA.19940427.0181.

164124 Henderson, F.M. 1966. *Open Channel Flow.* Upper Saddle River, New Jersey: Prentice Hall. TIC: 254509.

100455 Hillner, E.; Franklin, D.G.; and Smee, J.D. 1998. *The Corrosion of Zircaloy-Clad Fuel Assemblies in a Geologic Repository Environment.* WAPD-T-3173. West Mifflin, Pennsylvania: Bettis Atomic Power Laboratory. TIC: 237127.

163626 Hills, D.A.; Kelly, P.A.; Dai, D.N.; and Korsunsky, A.M. 1996. *Solution of Crack Problems, The Distributed Dislocation Technique.* Solid Mechanics and its Applications, Volume 44. Boston, Massachusetts: Kluwer Academic. TIC: 254533.

170501 Hoek, E. and Brown, E.T. 1997. "Practical Estimates of Rock Mass Strength." *International Journal of Rock Mechanics and Mining Science & Geomechanics Abstracts, 34,* (8), 1165-1186. Oxford, England: Pergamon. TIC: 256245.

164038 Hofmann, P. and Kerwin-Peck, D. 1984. "UO_2/Zircaloy-4 Chemical Interactions from 1,000 to 1,700°C Under Isothermal and Transient Temperature Conditions." *Journal of Nuclear Materials, 124,* 80-105. New York, New York: North-Holland. TIC: 253983.

163628 Howard, G.C. and Fast, C.R. 1958. "Optimum Fluid Characteristics for Fracture Extension." *Drilling and Production Practice.* Pages 261-270. Washington, D.C.: American Petroleum Institute. TIC: 254514.

163337 Incropera, F.P. and DeWitt, D.P. 2002. *Fundamentals of Heat and Mass Transfer.* 5th Edition. New York, New York: John Wiley & Sons. TIC: 254280.

177273 Ingebritsen, S.E. and Scholl, M.A. 1993. "The Hydrogeology of Kilauea Volcano." *Geothermics, 22,* (4), 255-270. New York, New York: Pergamon. TIC: 258395.

160331 Itasca Consulting Group 2002. *Itasca Software–Cutting Edge Tools for Computational Mechanics.* Minneapolis, Minnesota: Itasca Consulting Group. TIC: 252592.

163630 Jaeger, J.C. 1968. "Cooling and Solidification of Igneous Rocks." *Basalts, The Poldervaart Treatise on Rocks of Basaltic Composition.* Volume 2. Hess, H.H. and Poldervaart, A., eds. Pages 503–536. New York, New York: Interscience Publishers. TIC: 254505.

106219 Jaeger, J.C. and Cook, N.G.W. 1979. *Fundamentals of Rock Mechanics.* 3rd Edition. New York, New York: Chapman and Hall. TIC: 218325.

177267 Kebede, S.; Travi, Y.; Alemayehu, T.; and Ayenew, T. 2005. "Groundwater Recharge, Circulation and Geochemical Evolution in the Source Region of the Blue Nile River, Ethiopia." *Applied Geochemistry, 20,* 1658-1676. New York, New York: Elsevier. TIC: 258390.

178353 Kieffer, S.W. 1982. "Fluid Dynamics of the May 18 Blast at Mount St. Helens." *The 1980 Eruptions of Mount St. Helens, Washington.* Lipman, P.W. and Mullineaux, D.R., eds. 2nd Printing 1982. Geological Survey Professional Paper 1250. Pages 379-400. Washington, D.C.: U.S. Government Printing Office. TIC: 218260.

182964 Kokajko, L.E. 2005. "Pre-Licensing Evaluation of Key Technical Issue Agreements: Igneous Activity 2.03 Additional Information Needed, 2.09 Additional Information Needed, 2.19, and 2.20." Letter from L.E. Kokajko (NRC) to J.D. Ziegler (DOE/ORD), March 31, 2005, 0404055214, with enclosure. ACC: MOL.20050506.0101.

174026 Kokajko, L.E. 2005. "Staff Review of U.S. Department of Energy Response to Igneous Activity Agreement Item IA.2.18." Letter from L.E. Kokajko (NRC) to J.D. Ziegler (DOE/ORD), January 10, 2005, 01108054475, with enclosure. ACC: MOL.20050211.0288.

100909 Kotra, J.P.; Lee, M.P.; Eisenberg, N.A.; and DeWispelare, A.R. 1996. *Branch Technical Position on the Use of Expert Elicitation in the High-Level Radioactive Waste Program.* NUREG-1563. Washington, D.C.: U.S. Nuclear Regulatory Commission. TIC: 226832.

163632 Krauskopf, K.B. 1948. "Lava Movement at Parícutin Volcano, Mexico." *Bulletin of the Geological Society of America, 59,* (12, Part 1), 1267–1283. New York, New York: Geological Society of America. TIC: 254513.

170764 LBNL (Lawrence Berkeley National Laboratory) 2003. *Validation Test Report (VTR) for TOUGH V1.6.* Document Identifier: 10007-VTR-1.6-02. Berkeley, California: Lawrence Berkeley National Laboratory. ACC: MOL.20030312.0199.

160832 Lide, D.R., ed. 2002. *CRC Handbook of Chemistry and Physics.* 83rd Edition. Boca Raton, Florida: CRC Press. TIC: 253582.

126865 Lister, J.R. 1990. "Buoyancy-Driven Fluid Fracture: Similarity Solutions for the Horizontal and Vertical Propagation of Fluid-Filled Cracks." *Journal of Fluid Mechanics, 217,* 213-239. Cambridge, United Kingdom: Cambridge University Press. TIC: 225065.

126877 Lister, J.R. 1990. "Buoyancy-Driven Fluid Fracture: The Effects of Material Toughness and of Low-Viscosity Precursors." *Journal of Fluid Mechanics, 210,* 263-280. Cambridge, United Kingdom: Cambridge University Press. TIC: 246674.

163635 Lister, J.R. 1995. "Fluid-Mechanical Models of the Interaction Between Solidification and Flow in Dykes." *Physics and Chemistry of Dykes, Selected Papers Presented at the Third International Dyke Conference, Jerusalem, Israel, 4-8 September 1995.* Baer, G. and Heimann, A., eds. Pages 115-124. Brookfield, Vermont: A.A. Balkema. TIC: 254504.

126889 Lister, J.R. and Kerr, R.C. 1991. "Fluid-Mechanical Models of Crack Propagation and Their Application to Magma Transport in Dykes." *Journal of Geophysical Research, 96,* (B6), 10,049-10,077. Washington, D.C.: American Geophysical Union. TIC: 225066.

144310 Luhr, J.F. and Simkin, T., eds. 1993. *Paricutin, The Volcano Born in a Mexican Cornfield.* Phoenix, Arizona: Geoscience Press. TIC: 247017.

157883 Marachi, N.D.; Chan, C.K.; and Seed, H.B. 1972. "Evaluation of Properties of Rockfill Materials." *Journal of the Soil Mechanics and Foundations Division, Proceedings of the American Society of Civil Engineers, 98,* (SM1), 95-114. New York, New York: American Society of Civil Engineers. TIC: 252235.

169783 Mastin, L.G. and Pollard, D.D. 1988. "Surface Deformation and Shallow Dike Intrusion Processes at Inyo Craters, Long Valley, California." *Journal of Geophysical Research, 93,* (B11), 13,221-13,235. Washington, D.C.: American Geophysical Union. TIC: 256132.

182276 Matsuki, K.; Matsune, S.; and Takahashi, H. 1991. "Boundary Element Analysis for Standard Specimen Configurations in the ISRM Suggested Methods for Determining Fracture Toughness of Rock." *International Journal of Rock Mechanics and Mining Science & Geomechanics Abstracts, 28,* 355-363. New York, New York: Pergamon. TIC: 259634.

178354 McDuffie, S.M.; Connor, C.B.; and Mahrer, K.D. 1994. "A Simple 2-D Stress Model of Dike-Fracture Interaction." *Eos (Supplement), [75],* ([16]), 345. Washington, D.C.: American Geophysical Union. TIC: 259466.

171053 Menard, O.; Advocat, T.; Ambrosi, J.P.; and Michard, A. 1998. "Behavior of Actinides (Th, U, Np and Pu) and Rare Earths (La, Ce and Nd) During Aqueous Leaching of a Nuclear Waste Glass Under Geological Disposal Conditions." *Applied Geochemistry, 13,* 105-126. New York, New York: Pergamon. TIC: 256470.

178355 Mériaux, C.; Lister, J.R.; Lyakhovsky, V.; and Agnon, A. 1999. "Dyke Propagation with Distributed Damage of the Host Rock." *Earth and Planetary Science Letters, 165,* 177-185. New York, New York: Elsevier. TIC: 259177.

182315 Momber, A.W. 2004. "Deformation and Fracture of Rocks Loaded with Spherical Indenters." *International Journal of Fracture, 125,* (3-4), 263-279. New York, New York: Springer. TIC: 259633.

181320 Morrissey, M.M. and Chouet, B.A. 1997. "Burst Conditions of Explosive Volcanic Eruptions Recorded on Microbarographs." *Science, 275,* (5304), 1290-1293. Washington, D.C.: American Association for the Advancement of Science. TIC: 259490.

178356 Murrell, S.A.F. 1969. "Global Tectonics, Rock Mechanics, and the Mechanism of Volcanic Intrusions." Chapter 17 of *Mechanism of Igneous Intrusion.* 1st Edition. Newall, G. and Rast, N., eds. Liverpool, England: Seel House Press. TIC: 259456.

178357 Nakada, S.; Shimizu, H.; and Ohta, K. 1999. "Overview of the 1990-1995 Eruption at Unzen Volcano." *Journal of Volcanology and Geothermal Research, 89,* 1-22. New York, New York: Elsevier. TIC: 259192.

163641 Nordgren, R.P. 1972. "Propagation of a Vertical Hydraulic Fracture." *Society of Petroleum Engineers Journal, 12,* (4), 306–314. Dallas, Texas: Society of Petroleum Engineers. TIC: 254486.

163274 NRC (U.S. Nuclear Regulatory Commission) 2003. *Yucca Mountain Review Plan, Final Report.* NUREG-1804, Rev. 2. Washington, D.C.: U.S. Nuclear Regulatory Commission, Office of Nuclear Material Safety and Safeguards. TIC: 254568.

106453 Olsson, W.A. and Brown, S.R. 1997. *Mechanical Properties of Fractures from Drillholes UE25-NRG-4, USW-NRG-6, USW-NRG-7, USW-SD-9 at Yucca Mountain, Nevada.* SAND95-1736. Albuquerque, New Mexico: Sandia National Laboratories. ACC: MOL.19970224.0064.

170318 Peck, D.L.; Hamilton, M.S.; and Shaw, H.R. 1977. "Numerical Analysis of Lava Lake Cooling Models: Part II, Application to Alae Lava Lake, Hawaii." *American Journal of Science, 277,* (4), 415-437. New Haven, Connecticut: Yale University, Kline Geology Laboratory. TIC: 256756.

163644 Perkins, T.K. and Kern, L.R. 1961. "Widths of Hydraulic Fractures." *Transactions of the Society of Petroleum Engineers of the American Institute of Mining, Metallurgical, and Petroleum Engineers, Inc., 222,* 937-949. Dallas, Texas: American Institute of Mining and Metallurgical Engineers. TIC: 254487.

178358 Pinel, V. and Jaupart, C. 2004. "Likelihood of Basaltic Eruptions as a Function of Volatile Content and Volcanic Edifice Size." *Journal of Volcanology and Geothermal Research, 137,* 201-217. New York, New York: Elsevier. TIC: 259193.

176896 Pinel, V. and Jaupart, C. 2004. "Magma Storage and Horizontal Dyke Injection beneath a Volcanic Edifice." *Earth and Planetary Science Letters, 221,* (1-4), 245-262. Amsterdam, The Netherlands: Elsevier. TIC: 259726.

160060 Potter, C.J.; Dickerson, R.P.; Sweetkind, D.S.; Drake, R.M., II; Taylor, E.M.; Fridrich, C.J.; San Juan, C.A.; and Day, W.C. 2002. *Geologic Map of the Yucca Mountain Region, Nye County, Nevada.* Geologic Investigations Series I-2755. Denver, Colorado: U.S. Geological Survey. TIC: 253945.

177275 Prada, S.N.; da Silva, M.O.; and Cruz, J.V. 2005. "Groundwater Behaviour in Madeira, Volcanic Island (Portugal)." *Hydrogeology Journal, 13,* 800-812. New York, New York: Springer-Verlag. TIC: 258396.

177277 Rees, T.F.; Cleveland, J.M.; and Nash, K.L. 1985. "Leaching of Plutonium from a Radioactive Waste Glass by Eight Groundwaters from the Western United States." *Nuclear Technology, 70,* 133-140. Hinsdale, Illinois: American Nuclear Society. TIC: 258398.

164405 Rice, J.R. 1968. "Mathematical Analysis in the Mechanics of Fracture." Chapter 3 of *Fracture, An Advanced Treatise.* Volume II: Mathematical Fundamentals. Liebowitz, H., ed. New York, New York: Academic Press. TIC: 254573.

178359 Roberts, J.L. 1969. "The Intrusion of Magma into Brittle Rocks." Chapter 20 of *Mechanisms of Igneous Intrusion.* 1st Edition. Newall, G. and Rast, N., eds. Liverpool, England: Seel House Press. TIC: 259456.

178360 Rocchi, V.; Sammonds, P.R.; and Kilburn, C.R.J. 2002. "Flow and Fracture Maps for Basaltic Rock Deformation at High Temperatures." *Journal of Volcanology and Geothermal Research, 120,* 25-42. New York, New York: Elsevier. TIC: 259191.

173995 Rocchi, V.; Sammonds, P.R.; and Kilburn, C.R.J. 2004. "Fracturing of Etnean and Vesuvian Rocks at High Temperatures and Low Pressures." *Journal of Volcanology and Geothermal Research, 132,* 137-157. New York, New York: Elsevier. TIC: 257313.

177254 Rose, T.P.; Davisson, M.L.; and Criss, R.E. 1996. "Isotope Hydrology of Voluminous Cold Springs in Fractured Rock from an Active Volcanic Region, Northeastern California." *Journal of Hydrology, 179,* 207-236. New York, New York: Elsevier. TIC: 258386.

164118 Rubin, A.M. 1995. "Propagation of Magma-Filled Cracks." *Annual Review of Earth and Planetary Sciences, 23,* 287-336. Palo Alto, California: Annual Reviews. TIC: 254554.

169786 Rubin, A.M. and Gillard, D. 1998. "Dike-Induced Earthquakes: Theoretical Considerations." *Journal of Geophysical Research, 103,* (B5), 10,017-10,030. Washington, D.C.: American Geophysical Union. TIC: 256130.

169787 Rubin, A.M.; Gillard, D.; and Got, J-L. 1998. "A Reinterpretation of Seismicity Associated with the January 1983 Dike Intrusion at Kilauea Volcano, Hawaii." *Journal of Geophysical Research, 103,* (B5), 10,003-10,015. Washington, D.C.: American Geophysical Union. TIC: 256131.

178361 Rubin, A.M. and Pollard, D.D. 1987. "Origins of Blade-Like Dikes in Volcanic Rift Zones." Chapter 53 of *Volcanism in Hawaii.* Decker, R.W.; Wright, T.L.; and Stauffer, P.H., eds. U.S. Geological Survey Professional Paper 1350, Volume 2. Washington, D.C.: U.S. Government Printing Office. TIC: 250389.

176667 Russell, J.K. and Quane, S.L. 2005. "Rheology of Welding: Inversion of Field Constraints." *Journal of Volcanology and Geothermal Research, 142,* ([1-2]), 173-191. New York, New York: Elsevier. TIC: 258316.

170320 Ryan, M.P. 1987. "Neutral Buoyancy and the Mechanical Evolution of Magmatic Systems." *Magmatic Processes: Physicochemical Principles.* Mysen, B.O., ed. Special Publication No. 1. Pages 259-287. University Park, Pennsylvania: Geochemical Society, Pennsylvania State University. TIC: 256749.

177276 Sedwick, P. and Stüben, D. 1996. "Chemistry of Shallow Submarine Warm Springs in an Arc-Volcanic Setting: Vulcano Island, Aeolian Archipelago, Italy." *Marine Chemistry, 53,* 147-161. Amsterdam, The Netherlands: Elsevier. TIC: 258397.

178362 Self, S.; Wilson, L.; and Nairn, I. 1979. "Vulcanian Eruption Mechanisms." *Nature, 277,* 440-443. London, England: Macmillan Journals. TIC: 259173.

126270 Shaw, H.R. 1972. "Viscosities of Magmatic Silicate Liquids: An Empirical Method of Prediction." *American Journal of Science, 272,* 870-889. New Haven, Connecticut: Yale University, Kline Geology Laboratory. TIC: 246470.

170321 Shaw, H.R.; Hamilton, M.S.; and Peck, D.L. 1977. "Numerical Analysis of Lava Lake Cooling Models: Part I, Description of the Method." *American Journal of Science, 277,* (4), 384-414. New Haven, Connecticut: Yale University, Kline Geology Laboratory. TIC: 256755.

178363 Smart, K.J. 2004. *Examination of Effects of Geologic Features on Thermally Induced Stresses at Yucca Mountain, Nevada.* San Antonio, Texas: Center for Nuclear Waste Research and Analysis.

101020 Smith, R.P.; Jackson, S.M.; and Hackett, W.R. 1996. "Paleoseismology and Seismic Hazards Evaluations in Extensional Volcanic Terrains." *Journal of Geophysical Research, 101,* (B3), 6277-6292. Washington, D.C.: American Geophysical Union. TIC: 238265.

163648 Sneddon, I.N. 1946. "The Distribution of Stress in the Neighbourhood of a Crack in an Elastic Solid." *Proceedings of the Royal Society of London, Series A: Mathematical and Physical Sciences, 187,* 229–260. London, England: Harrison and Son. TIC: 254550.

163645 SNL (Sandia National Laboratories) 1996. *Hydraulic Fracturing Stress Measurements in Test Hole ESF-AOD-HDFR#1, Thermal Test Facility, Exploratory Studies Facility at Yucca Mountain.* WA-0065. Albuquerque, New Mexico: Sandia National Laboratories. ACC: MOL.19970717.0008.

177431 SNL 2007. *Atmospheric Dispersal and Deposition of Tephra from a Potential Volcanic Eruption at Yucca Mountain, Nevada.* MDL-MGR-GS-000002 REV 03. Las Vegas, Nevada: Sandia National Laboratories.

174260 SNL 2007. *Characterize Eruptive Processes at Yucca Mountain, Nevada.* ANL-MGR-GS-000002 REV 03. Las Vegas, Nevada: Sandia National Laboratories. ACC: DOC.20070301.0001.

180506 SNL 2007. *In-Package Chemistry Abstraction.* ANL-EBS-MD-000037 REV 04 ADD 01. Las Vegas, Nevada: Sandia National Laboratories. ACC: DOC.20051130.0007; DOC.20070816.0004.

177432 SNL 2007. *Number of Waste Packages Hit by Igneous Events.* ANL-MGR-GS-000003 REV 03. Las Vegas, Nevada: Sandia National Laboratories.

181325 SNL 2007. *Plan for the Expert Elicitation to Update the Probabilistic Volcanic Hazard Analysis (PVHA) for Yucca Mountain, Nevada.* PLN-MGR-GS-000001 REV 02. Las Vegas, Nevada: Sandia National Laboratories. ACC: DOC.20070205.0002.

176828 SNL 2007. *Seismic Consequence Abstraction.* MDL-WIS-PA-000003 REV 03. Las Vegas, Nevada: Sandia National Laboratories.

179354 SNL 2007. *Total System Performance Assessment Data Input Package for Requirements Analysis for EBS In-Drift Configuration.* TDR-TDIP-ES-000010 REV 00. Las Vegas, Nevada: Sandia National Laboratories.

179466 SNL 2007. *Total System Performance Assessment Data Input Package for Requirements Analysis for Subsurface Facilities.* TDR-TDIP-PA-000001 REV 00. Las Vegas, Nevada: Sandia National Laboratories.

179394 SNL 2007. *Total System Performance Assessment Data Input Package for Requirements Analysis for Transportation Aging and Disposal Canister and Related Waste Package Physical Attributes Basis for Performance Assessment*. TDR-TDIP-ES-000006 REV 00. Las Vegas, Nevada: Sandia National Laboratories.

127068 Spence, D.A. and Turcotte, D.L. 1985. "Magma-Driven Propagation of Cracks." *Journal of Geophysical Research, 90,* (B1), 575-580. Washington, D.C.: American Geophysical Union. TIC: 225148.

127086 Spence, D.A. and Turcotte, D.L. 1990. "Buoyancy-Driven Magma Fracture: A Mechanism for Ascent Through the Lithosphere and the Emplacement of Diamonds." *Journal of Geophysical Research, 95,* (B4), 5133-5139. Washington, D.C.: American Geophysical Union. TIC: 246860.

164109 Spera, F.J. 2000. "Physical Properties of Magma." *Encyclopedia of Volcanoes.* Sigurdsson, H., ed. Pages 171-190. San Diego, California: Academic Press. TIC: 254454.

164459 Stasiuk, M.V.; Barclay, J.; Carroll, M.R.; Jaupart, C.; Ratté, J.C.; Sparks, R.S.J.; and Tait, S.R. 1996. "Degassing During Magma Ascent in the Mule Creek Vent (USA)." *Bulletin of Volcanology, 58,* ([2-3]), 117-130. New York, New York: Springer-Verlag. TIC: 254576.

101027 Stock, J.M.; Healy, J.H.; Hickman, S.H.; and Zoback, M.D. 1985. "Hydraulic Fracturing Stress Measurements at Yucca Mountain, Nevada, and Relationship to the Regional Stress Field." *Journal of Geophysical Research, 90,* (B10), 8691-8706. Washington, D.C.: American Geophysical Union. TIC: 219009.

177490 Szikszay, M.; Teissedre, J.-M.; Barner, U.; and Matsui, E. 1981. "Geochemical and Isotopic Characteristics of Spring and Groundwater in the State of São Paulo, Brazil." *Journal of Hydrology, 54,* 23-32. Amsterdam, The Netherlands: Elsevier. TIC: 258384.

178364 Tait, S.; Jaupart, C.; and Vergniolle, S. 1989. "Pressure, Gas Content and Eruption Periodicity of a Shallow, Crystallising Magma Chamber." *Earth and Planetary Science Letters, 92,* 107-123. Amsterdam, The Netherlands: Elsevier. TIC: 259176.

181322 Tananaev, I.V.; Nikolaev, N.S.; Luk'yanychev, Yu.A.; and Opalovskii, A.A. 1961. "The Chemistry of Uranium Fluorides." *Russian Chemical Reviews, 30,* (12), 654-671. Moscow, Russian Federation: Turpion. TIC: 259398.

121096 Timoshenko, S.P. and Goodier, J.N. 1970. *Theory of Elasticity.* 3rd Edition. New York, New York: McGraw-Hill. TIC: 245469.

107735 Todreas, N.E. and Kazimi, M.S. 1990. *Nuclear Systems I, Thermal Hydraulic Fundamentals.* New York, New York: Hemisphere Publishing. TIC: 226511.

178366 Touloukian, Y.S.; Judd, W.R.; and Roy, R.F., eds. 1981. *Physical Properties of Rocks and Minerals.* McGraw-Hill/CINDAS Data Series on Material Properties II-2. New York, New York: McGraw-Hill. TIC: 209327.

139651 Turcotte, D.L. and Schubert, G. 1982. *Geodynamics, Applications of Continuum Physics to Geological Problems.* New York, New York: John Wiley & Sons. TIC: 235924.

134364 Turcotte, D.L.; Emerman, S.H.; and Spence, D.A. 1987. "Mechanics of Dyke Injection." *Mafic Dyke Swarms, A Collection of Papers Based on the Proceedings of an International Conference held at Erindale College, University of Toronto, Ontario, Canada, June 4-7, 1985.* Halls, H.C. and Fahrig, W.F., eds. Pages 25-29. St. John's, Newfoundland, Canada: Geological Association of Canada. TIC: 246897.

178367 Turcotte, D.L.; Ockendon, H.; Ockendon, J.R.; and Cowley, S.J. 1990. "A Mathematical Model of Vulcanian Eruptions." *Geophysical Journal International, 103,* 211-217. Malden, Massachusetts: Blackwell Publishing. TIC: 259457.

177282 Valentine, G.A. and Krogh, K.E.C. 2006. "Emplacement of Shallow Dikes and Sills Beneath a Small Basaltic Volcanic Center - The Role of Pre-Existing Structure (Paiute Ridge, Southern Nevada, USA)." *Earth and Planetary Science Letters, 246,* 217-230. New York, New York: Elsevier. TIC: 258400.

178371 Vergniolle, S. 1998. "Modelling Two-Phase Flow in a Volcano." *13th Australasian Fluid Mechanics Conference.* 647-650. Melbourne, Australia: Monash University.

178372 Vergniolle, S. and Caplan-Auerbach, J. 2004. "Acoustic Measurements of the 1999 Basaltic Eruption of Shishaldin Volcano, Alaska 2. Precursor to the Subplinian Phase." *Journal of Volcanology and Geothermal Research, 137,* 135-151. New York, New York: Elsevier. TIC: 259182.

115585 Vergniolle, S. and Jaupart, C. 1986. "Separated Two-Phase Flow and Basaltic Eruptions." *Journal of Geophysical Research, 91,* (B12), 12,842-12,860. Washington, D.C.: American Geophysical Union. TIC: 239308.

181321 Vergniolle, S.; Boichu, M.; and Caplan-Auerbach, J. 2004. "Acoustic Measurements of the 1999 Basaltic Eruption of Shishaldin Volcano, Alaska 1. Origin of Strombolian Activity." *Journal of Volcanology and Geothermal Research, 137,* 109-134. New York, New York: Elsevier. TIC: 259491.

163649 Warpinski, N.R.; Abou-Sayed, I.S.; Moschovidis, Z.; and Parker, C. 1993. *Hydraulic Fracture Model Comparison Study: Complete Results.* GRI-93/0109. Chicago, Illinois: Gas Research Institute. TIC: 254276.

163657 Warpinski, N.R.; Moschovidis, Z.A.; Parker, C.D.; and Abou-Sayed, I.S. 1994. "Comparison Study of Hydraulic Fracturing Models—Test Case: GRI Staged Field Experiment No. 3." *SPE Production & Facilities, 9,* (1), 7–16. Richardson, Texas: SPE Production and Facilities. TIC: 254277.

177268 Weaver, T.R.; Cartwright, I.; Tweed, S.O.; Ahearne, D.; Cooper, M.; Czapnik, K.; and Tranter, J. 2006. "Controls on Chemistry During Fracture-Hosted Flow of Cold CO_2-Bearing Mineral Waters, Daylesford, Victoria, Australia: Implications for Resource Protection." *Applied Geochemistry, 21,* ([2]), 289-304. New York, New York: Elsevier. TIC: 258391.

100492 Westrich, H.R. 1982. "The Solubility of LWR Core Debris in Sacrificial Floor Material." *Journal of Nuclear Materials, 110,* 324-332. Amsterdam, The Netherlands: North-Holland Publishing Company. TIC: 234101.

178373 Whan, G.A. and Rothfus, R.R. 1959. "Characteristics of Transition Flow Between Parallel Plates." *AIChE Journal, 5,* (2), 204-208. New York, New York: American Institute of Chemical Engineers. TIC: 259179.

163752 White, D.E.; Hem, J.D.; and Waring, G.A. 1980. "Chemical Composition of Subsurface Waters." Chapter F of *Data of Geochemistry.* 6th Edition. Geological Survey Professional Paper 440-F. Washington, D.C.: U.S. Government Printing Office. TIC: 249975.

163659 Wilcox, R.E. 1954. "Petrology of the Paricutin Volcano." *Petrology of the Parícutin Volcano Mexico, Geologic Investigations in the Parícutin Area, Mexico.* Geological Survey Bulletin 965-C. Pages 281-353. Washington, D.C: U.S. Government Printing Office. TIC: 254485.

178374 Wilson, L. 1972. "Explosive Volcanic Eruptions - II The Atmospheric Trajectories of Pyroclasts." *Geophysical Journal of the Royal Astronomical Society, 30,* 381-392. Oxford, England: Blackwell Scientific Publications. TIC: 259458.

178375 Woods, A.W. 1995. "A Model of Vulcanian Explosions." *Nuclear Engineering and Design, 155,* 345-357. New York, New York: Elsevier. TIC: 259178.

163662 Woods, A.W.; Sparks, S.; Bokhove, O.; LeJeune, A-M.; Conner, C.B.; and Hill, B.E. 2002. "Modeling Magma-Drift Interaction at the Proposed High-Level Radioactive Waste Repository at Yucca Mountain, Nevada, USA." *Geophysical Research Letters, 29,* (13), 19-1 through 19-4. Washington, D.C.: American Geophysical Union. TIC: 254467.

108740 Yokoyama, I. and de la Cruz-Reyna, S. 1990. "Precursory Earthquakes of the 1943 Eruption of Paricutin Volcano, Michoacan, Mexico." *Journal of Volcanology and Geothermal Research, 44,* 265-281. Amsterdam, The Netherlands: Elsevier. TIC: 234990.

178376 Young, S.R.; McKague, H.L.; and Terhune, R.W. 1994. *Influence of Faults on Ascent of Mafic Magma by Dike Intrusion.* CNWRA 94-025. San Antonio, Texas: Center for Nuclear Waste Regulatory Analyses. ACC: MOL.20060614.0034.

164368 Zhang, X.; Jeffrey, R.; and Detournay, E. 2002. *NPHF2D, Non-Planar Hydraulic Fracture 2D User's Manual.* Minneapolis, Minnesota: University of Minnesota, Department of Civil Engineering. TIC: 253445.

9.2 CODES, STANDARDS, REGULATIONS, AND PROCEDURES

180319 10 CFR 63. 2007. Energy: Disposal of High-Level Radioactive Wastes in a Geologic Repository at Yucca Mountain, Nevada. Internet accessible.

IM-PRO-002, *Control of the Electronic Management of Information.*

IM-PRO-003, *Software Management.*

LP-2.29Q, *Planning for Science Activities.*

SCI-PRO-001, *Qualification of Unqualified Data.*

SCI-PRO-002, *Planning for Science Activities.*

SCI-PRO-006, *Models*.

9.3 SOFTWARE

161953 FLAC V. 4.0. 2002. WINDOWS 2000/NT 4.0. STN: 10167-4.0-00.

172432 FLAC V. 4.04. 2004. WINDOWS 2000. STN: 10167-4.04-00.

161947 FLAC3D V. 2.1 Sub-Release 2.10.196. 2002. WINDOWS 2000/NT 4.0. STN: 10502-2.1-00.

172323 FLAC3D V. 2.14. 2004. WINDOWS 2000. STN: 10502-2.14-00.

163665 NPHF2D V. 1.0. 2002. WINDOWS 2000. STN: 10904-1.0-00.

161949 UDEC V. 3.1 Sub-Release 3.10.109. 2002. WINDOWS 2000/NT 4.0. STN: 10173-3.1-00.

172322 UDEC V. 3.14. 2004. WINDOWS 2000. STN: 10173-3.14-00.

9.4 SOURCE DATA, LISTED BY DATA TRACKING NUMBER

152932 GS000483351030.003. Thermal Properties Measured 12/01/99 to 12/02/99 Using the Thermolink Soil Multimeter and Thermal Properties Sensor on Selected Potential Candidate Backfill Materials Used in the Engineered Barrier System. Submittal date: 11/09/2000.

163107 GS020183351030.001. Uncompacted Bulk Density for Analyses Performed 02/02/00 to 05/23/00 on Potential Backfill Materials Used in the Engineered Barrier System. Submittal date: 01/22/2002.

179987 LA0612DK831811.001. Magma and Eruption Properties for Potential Volcano at Yucca Mountain. Submittal date: 03/23/2002.

159672 LB0207REVUZPRP.002. Matrix Properties for UZ Model Layers Developed from Field and Laboratory Data. Submittal date: 07/15/2002.

165395 MO0307MWDAC8MV.000. Analytical-LA-Coarse-800M Ventilation. Submittal date: 07/15/2003.

170679 MO0407SPAMTSHR.000. Modeled Thermal Stresses Within the Host Rock at Three Graduated Points in Time. Submittal date: 07/20/2004.

171483 MO0408MWDDDMIO.002. Drift Degradation Model Inputs and Outputs. Submittal date: 08/31/2004.

181613 MO0706SPAFEPLA.001. FY 2007 LA FEP List and Screening. Submittal date: 06/20/2007.

159145 SN0206F3504502.012. Revised Thermal Conductivity, Volumetric Heat Capacity and Thermal Diffusivity Data for ECRB Thermal K Test 1 (Two-Hole Test). Submittal date: 06/07/2002.

159146 SN0206F3504502.013. Revised Thermal Conductivity, Volumetric Heat Capacity and Thermal Diffusivity Data for ECRB Thermal K Test 3 (Three-Hole Test, with Results from 1/22/2002 through 4/9/2002). Submittal date: 06/07/2002.

161883 SN0208F3504502.019. Thermal Conductivity, Volumetric Heat Capacity and Thermal Diffusivity Data for ECRB Thermal K Test 2 (Six-Hole Test). Submittal date: 08/30/2002.

164196 SN0307T0510902.003. Updated Heat Capacity of Yucca Mountain Stratigraphic Units. Submittal date: 07/15/2003.

170993 SN0402T0503102.010. Heat Capacity Values for Lithostratigraphic Layers of Yucca Mountain. Submittal date: 02/24/2004.

169129 SN0404T0503102.011. Thermal Conductivity of the Potential Repository Horizon Rev 3. Submittal date: 04/27/2004.

131356 SNF37100195002.001. Hydraulic Fracturing Stress Measurements in Test Hole: ESF-AOD-HDFR1, Thermal Test Facility, Exploratory Studies Facility at Yucca Mountain. Submittal date: 12/18/1996.

108410 SNL02030193001.027. Summary of Bulk Property Measurements Including Saturated Bulk Density for NRG-2, NRG-2A, NRG-2B, NRG-3, NRG-4, NRG-5, NRG-6, NRG-7/7A, SD-9, and SD12. Submittal date: 08/14/1996.

9.5 OUTPUT AND DEVELOPED DATA, LISTED BY DATA TRACKING NUMBER

LA0307EG831811.001. Analytical Calculations of Heat Flow for YMP Drift Filled with Basaltic Magma. Submittal date: 07/24/2003.

LA0602DA831811.001. Estimates of Magma Flow From Dike into Drifts. Submittal date: 02/15/2006.

LA0702PADE01EG.001. Igneous Temperatures. Submittal date: 02/01/2007.

LA0702PADE01EG.002. EBS Failure Fractions. Submittal date: 02/02/2007.

MO0408EG831811.000. Dike Scaling Parameters for the 20 FEB 1943 Eruption of Paricutin. Submittal date: 09/08/2004.

MO0408EG831811.002. Expanding Magma. Submittal date: 09/07/2004.

MO0408EG831811.003. Dike Propagation Model Results Using NPHF2D. Submittal date: 09/29/2004.

MO0408EG831811.004. Dike Propagation Model Results Using NPHF2D. Submittal date: 09/13/2004.

MO0408EG831811.008. Magma Cooling and Solidification. Submittal date: 09/13/2004.

MO0411EG831811.000. Dike Propagation Model Results. Submittal date: 11/16/2004.

MO0411EG831811.001. 3D Analysis of Dike/Drift Interaction in the Vicinity of the Repository. Submittal date: 11/16/2004.

MO0411EG831811.002. Secondary Dike Propagation From a Drift. Submittal date: 11/16/2004.

MO0610SPADIKEP.000. Input and Output Data from the Analysis of Structure Effect on Dike Propagation. Submittal date: 10/11/2006.

MO0705BACKFILL.000. Magma Flow in Top of Backfill. Submittal date: 05/16/2007.

MO0705BREAKOUT.000. Magma Breakout Pressures. Submittal date: 05/16/2007.

MO0705FREEZING.000. Magma Freezing inside the Emplacement Drift. Submittal date: 05/16/2007.

MO0705TOPODIKE.000. Effect of Topography on Dike Localizations. Submittal date : 05/16/2007.

MO0705WPNMAGMA.000. Influence of Magma Pressure on Stability of Waste Package. Submittal date: 05/30/2007.

SN0304T0504203.001. Dike Propagation Model: Model Results Using NPHF2D. Submittal date: 04/02/2003.

SN0705DRFTTEMP.001. Drift Temperatures. Submittal date: 05/17/2007.

SN0705MAGPRESS.001. Magmatic Pressures. Submittal date: 05/14/2007.

SN0707ISITUTIS.001. In Situ and Thermally Induced Stresses. Submittal date: 07/10/2007

APPENDIX A
NUREG-1804 ACCEPTANCE CRITERIA ASSOCIATED WITH IGNEOUS ACTIVITY

APPENDIX A
NUREG-1804 ACCEPTANCE CRITERIA ASSOCIATED WITH IGNEOUS ACTIVITY

The discussion in this attachment identifies information in the dike/drift interactions model report that addresses *Yucca Mountain Review Plan, Final Report* acceptance criteria (NRC 2003 [DIRS 163274]) associated with the following integrated subissues:

- Mechanical disruption of engineered barriers (Section 2.2.1.3.2.3)
- Volcanic disruption of waste packages (Section 2.2.1.3.10.3)
- Airborne transport of radionuclides (Section 2.2.1.3.11.3).

This information is required by 10 CFR 63.114 (a) to (c) and (e) to (g) [DIRS 180319].

The following discussion identifies the relevant acceptance criteria associated with each of the integrated subissues and briefly summarizes the information in this report that addresses the acceptance criteria.

A1. INTEGRATED SUBISSUES MECHANICAL DISRUPTION OF ENGINEERED BARRIERS

A1.1 ACCEPTANCE CRITERION 1: SYSTEM DESCRIPTION AND MODEL INTEGRATION ARE ADEQUATE

The objective for modeling dike/drift interactions is described in Section 6 of the model report and includes describing the mechanical, thermal, and chemical environment that would be applied to waste packages should a future volcanic event disrupt the proposed repository.

1. *Total System Performance Assessment (TSPA) adequately incorporates important design features, physical phenomena, and couplings, and uses consistent and appropriate assumptions throughout the mechanical disruption of engineered barrier abstraction process.*

   Two models and supporting analyses describe the processes that could occur if an igneous intrusion were to intersect the repository. The first model describes dike propagation from depth (Section 6.3.1), and Section 6.3.3.1 provides the mathematical description of the model. Assumptions related to the model are described in Section 6.3.2, and uncertainties associated with the model are described in Section 6.3.3.2. Alternative models of dike propagation are described in Section 6.3.3.5. Results from exercise of the base-case model are described in Section 6.3.3.4, and the inputs for the analysis of magma flow into drifts are provided in Section 6.3.3.5.6.

   The second model describes heating of neighboring drifts from cooling of the emplaced magma (Section 6.4.1). The conceptual model for magma cooling and solidification is described in Section 6.4.1, and the results are described in Section 6.4.6. Sensitivity to saturation is described in Appendix C, and sensitivity to latent heat effects is described in Appendix D.

The analyses documented in this report are natural and thermal stresses (Section 6.2) and magma flow into drifts at dike/drift intersections (Section 6.3.3.5.6). Alternative models for dike propagation are described in Section 6.3.3.5. The effects of expanding magma on dike extensions to the surface are described in Section 6.3.6. Magma flow to the surface along a secondary pathway developed at some distance from the intersection is described in Section 6.5 and are summarized in Section 8.1.3.

For dike propagation, effects of pressure inside a tip cavity are described in Section 6.3.3.4.2, and effects of thermally induced increases in horizontal stress are described in Section 6.3.7.

An analysis of fully coupled dike/drift interaction is presented in Section 6.3.3.5.6, and an analysis of magma–waste package and magma–waste form interactions in intersected drifts is presented in Section 6.4.8.3.

Section 6.3.3.4 provides the results of dike propagation modeling. Section 6.3.3.5.6 summarizes the alternative models for dike propagation, including inputs for the analysis of magma flow into drifts. Section 6.5 describes the analysis of secondary dike propagation, and Sections 6.5.2 and 8.1.3 provide conclusions about secondary dike propagation and the basis on which to discount the potential for development of the shock wave scenario proposed by Woods et al. (2002 [DIRS 163662]).

Assumptions related to in situ and thermally induced stresses are described in Section 5.1. Assumptions used to model dike propagation from depth are described in Section 5.2. Assumptions related to the magma flow model are described in Section 5.3, and implementing assumptions are described in Section 6.4.7.2.1. Assumptions related to the modeling of magma cooling and solidification are described in Section 5.4.

2. *The description of geological and engineering aspects of design features, physical phenomena, and couplings that may affect mechanical disruption of engineered barriers, is adequate. For example, the description may include materials used in the construction of engineered barrier components, environmental effects (e.g., temperature, water chemistry, humidity, radiation, etc.) on these materials, and mechanical failure processes and concomitant failure criteria used to assess the performance capabilities of these materials. Conditions and assumptions in the abstraction of mechanical disruption of engineered barriers are readily identified and consistent with the body of data presented in the description.*

   Parameters used in the modeling of dike/drift interactions are summarized in Table 4-1. Assumptions related to in situ and thermally induced stresses are described in Section 5.1. Assumptions related to modeling of dike propagation are described in Sections 5.2. Assumptions related to the analysis of magma flow are described in Section 5.3. Assumptions related to modeling of magma cooling and solidification are described in Section 5.4.

Results of the modeling of dike propagation through the repository horizon are described in Sections 6.3.3.4, 6.3.7.4, and 8.1.1. Results of analysis of magma flow, including flow in drifts and the effects of structure, topography, compressible magma, and thermally induced stress on dike propagation to the surface, are described in Sections 6.3.3.5.6, 6.3.4, 6.3.5, 6.3.6, 6.3.7, 6.5.1.1, and 8.1.2. Results for modeling of magma cooling and solidification are described in Sections 6.4.9 and 8.2.2. The modeling of post-intrusion effects is summarized in Section 8.1.2.

3. *The abstraction of mechanical disruption of engineered barriers uses assumptions, technical bases, data, and models that are appropriate and consistent with other related U.S. Department of Energy abstractions. For example, assumptions used for mechanical disruption of engineered barriers are consistent with the abstraction of degradation of engineered barriers (Section 2.2.1.3.1 of the Yucca Mountain Review Plan). The descriptions and technical bases provide transparent and traceable support for the abstraction of mechanical disruption of engineered barriers.*

   Parameters used in the analysis of dike/drift interactions are summarized in Table 4-1. Modeling activities for dike propagation are summarized in Section 8.1.1, and modeling of post-intrusion effects is summarized in Section 8.1.2. Model outputs for thermal effects are summarized in Section 8.2.2. Uncertainties associated with the outputs of heat-flow calculations are described in Section 8.3.1. Restrictions on the use of information from the modeling and analyses described in this report are summarized in Section 8.4.

4. *Boundary and initial conditions used in the TSPA abstraction of mechanical disruption of engineered barriers are propagated throughout the abstraction approaches.*

   Boundary and initial conditions used in the modeling of dike propagation are described in Section 6.3.3.3.1. Boundary and initial conditions used in the analysis of magma flow into drifts are described in Section 6.3.3.5.6. Propagation of the boundary and initial conditions into the dike propagation model is presented in the mathematical description of the dike propagation model in Section 6.3.3.1, and the results are described in Section 6.3.3.4; a similar description for the analysis of magma flow in drifts is provided in Section 6.3.3.5.6. The problem definition for the modeling of effects of magma cooling is described in Section 6.4.3 and results are described in Sections 6.4.9 and 8.2.2.

5. *Sufficient data and technical bases to assess the degree to which features, events, and processes have been included in this abstraction are provided.*

   Features, events, and processes (FEPs) that are specifically addressed by information in this model report are identified in Section 6.1 and described in more detail in Table 6-1. The table identifies sections of the report addressing FEPs that are included in the total system performance assessment for the license application (TSPA-LA) through the use of the results of the calculations described in this document. Basically, the outputs of the dike/drift interactions model provide descriptions of

thermal conditions (Section 8.2.2), and the igneous Engineered Barrier System (EBS) failure fractions (Section 8.2.3), and the uncertainties associated with those outputs (Section 8.3) for application in the TSPA-LA in-drift submodels.

6. *The conclusion, with respect to the impact of transient criticality on the integrity of the engineered barriers, is defensible.*

   This model report does not address the impact of transient criticality on the integrity of the engineered barriers.

7. *Guidance in NUREG-1297 (Altman et al. 1988 [DIRS 103597]) and NUREG-1298 (Altman et al. 1988 [DIRS 103750]) or other acceptable approaches, is followed.*

   NUREG-1297 describes the generic technical position with respect to the use of peer reviews on high-level waste repository programs. The use of information from *Final Report of the Igneous Consequences Peer Review Panel* (Detournay et al. 2003 [DIRS 169660]) is summarized in Section 7.1. NUREG-1298 describes the generic technical position with respect to qualification of existing data. External sources have provided unqualified data that have been used as direct input to this document. The inputs from these sources are qualified for intended use within the document using the methods and attributes required for qualification of data per SCI-PRO-001, *Qualification of Unqualified Data.* These methods and attributes are based on those that are presented in NUREG-1298, which are meant to provide "the level of confidence in the data … commensurate with their intended use."

A1.2 ACCEPTANCE CRITERION 2: DATA ARE SUFFICIENT FOR MODEL JUSTIFICATION

1. *Geological and engineering values used in the license application to evaluate mechanical disruption of engineered barriers, are adequately justified. Adequate descriptions of how the data were used, and appropriately synthesized into the parameters, are provided.*

   Inputs for the modeling of dike propagation are described in Section 6.3.3.3, and the use of the information is described in Section 6.3.3.1. Model results are described in Section 6.3.3.4. Inputs for the analysis of effusive flow of magma into drifts are described in Section 6.3.3.5.6; the use of the information is described in Section 6.3.3.5.6, and results are provided in Section 6.3.3.5.6. Magma–waste package interactions are described in Section 6.4.8.3. Inputs for the analysis of secondary dike propagation are described in Section 6.5.1.1. The analysis examines the potential for development of secondary dikes under effusive flow conditions (Section 6.5.1). A synthesis describing the likelihood of the dog-leg scenario for effusive flow is presented in Section 6.5.1.5. Results are presented in Sections 6.5.1.5, 6.5.2, and 8.1.3. Inputs and the use of the information for the analysis of the effects of magma cooling and solidification on neighboring drift are described in Section 6.4.5, and results of the analysis are provided in Sections 6.4.9 and 8.2.2.

The outputs of the dike/drift interaction model provide descriptions of thermal conditions, the igneous EBS failure fractions (Section 8.2), and the uncertainties associated with those outputs (Section 8.3) for application in the TSPA in-drift submodels.

2. *Sufficient data have been collected on the geology of the natural system, engineering materials, and initial manufacturing defects, to establish initial and boundary conditions for the TSPA abstraction of mechanical disruption of engineered barriers.*

   This report describes the models and analysis that support the modeling of dike/drift interactions. The response to the previous criterion identifies the locations in this report where the inputs for the various models and analyses are described. The response also identifies where model results and analysis results are described. Evaluation of the descriptions of formulations of the analyses and models provides the basis to determine the sufficiency of data used as input or to establish boundary and initial conditions.

   The outputs of the dike/drift interaction model provide descriptions of thermal conditions, the igneous EBS failure fractions (Section 8.2), and the uncertainties associated with those outputs (Section 8.3) for application in the TSPA in-drift submodels.

3. *Data on geology of the natural system, engineering materials, and initial manufacturing defects used in the TSPA abstraction, are based on appropriate techniques. These techniques may include laboratory experiments, site-specific field measurements, natural analogue research, and process-level modeling studies. As appropriate, sensitivity or uncertainty analyses used to support the U.S. Department of Energy TSPA abstraction are adequate to determine the possible need for additional data.*

   The models and analyses that support the model of dike/drift interactions use input information about the geology of the natural system and engineering materials, but the analyses and models do not consider initial manufacturing defects. Parameters used in the analysis of dike/drift interactions are summarized in Table 4-1. The suitability of methods used to develop the information is established in the model reports and analysis reports that provide the information (e.g., SNL 2007 [DIRS 174260]). Natural analogue research unique to this report is described in Section 7.3.1.1.1. Comparisons with field observations and associated mathematical models used to increase postdevelopment confidence in the dike intrusion submodel are described in Section 7.3.1.

   Inputs for the modeling of dike propagation are described in Section 6.3.3.3, and the use of the information is described in Section 6.3.3.1. Model results are described in Section 6.3.3.4. Inputs for the analysis of effusive flow of magma into drifts are described in Section 6.3.3.5.6; the use of the information is described in Section 6.3.3.5.6, and results are provided in Section 6.3.3.5.6. Magma–waste package interactions are described in Section 6.4.8.3. Inputs for the analysis of

secondary dike propagation are described in Section 6.5.1.1. The analysis examines the potential for development of secondary dikes under effusive flow conditions (Section 6.5.1), and conclusions are presented in Section 6.5.2. A synthesis describing the likelihood of the dog-leg scenario for effusive flow is presented in Sections 6.5.1.5 and 8.1.3. The postintrusive magmatic thermal and chemical environment is summarized in Sections 6.4.9 and 8.2.2.

Effects of pressure inside the tip cavity and thermally induced increased horizontal stress on dike propagation are described in Sections 6.3.3.4.2 and 6.3.7. The effect of expanding magma on dike extension to the surface is described in Section 6.3.6. Sensitivity of the effects of magma cooling to saturation and latent heat effects are described in Appendices C and D.

The outputs of the dike/drift interaction model provide descriptions of thermal effects, the igneous EBS failure fractions (Section 8.2), and the uncertainties associated with those outputs (Section 8.3) for application in the TSPA in-drift submodels.

4. *Engineered barrier mechanical failure models for disruption events are adequate. For example, these models may consider effects of prolonged exposure to the expected emplacement drift environment, material test results not specifically designed or performed for the Yucca Mountain site, and engineered barrier component fabrication flaws.*

   The model of dike propagation from depth provides the inputs needed for the analysis of magma flow into drifts (Section 6.3.3.5.6). Magma–waste package interactions under effusive flow conditions are described in Section 6.4.8.3.3. Magma-cooling rates and their effects on secondary dike propagation, including the potential for stoppage of a new dike because of cooling-induced viscosity changes, are described in Section 6.4.8.2.

A1.3 ACCEPTANCE CRITERION 3: DATA UNCERTAINTY IS CHARACTERIZED AND PROPAGATED THROUGH THE MODEL ABSTRACTION

1. *Models use parameter values, assumed ranges, probability distributions, and bounding assumptions that are technically defensible, reasonably account for uncertainties, and variabilities, and do not result in an under-representation of risk.*

   Parameters used in the analysis of dike/drift interactions are summarized in Table 4-1. Inputs for the modeling of dike propagation are described in Section 6.3.3.3, and the use of the information is described in Section 6.3.3.1. Model results are described in Section 6.3.7.4. Inputs for the analysis of effusive flow of magma into drifts are described in Section 6.3.3.5.6, as are the use of the information and the results. Magma–waste package interactions are described in Section 6.4.8.3. Inputs for the analysis of secondary dike propagation are described in Section 6.5.1.1. The analysis examines the potential for development of secondary dikes under effusive flow conditions (Section 6.5.1). A synthesis describing the likelihood of the dog-leg

scenario for effusive flow is presented in Section 6.5.1.5. Conclusions are presented in Sections 6.5.2 and 8.1.3.

Boundary and initial conditions used in the modeling of dike propagation are described in Section 6.3.3.3.1. Boundary and initial conditions used in the analysis of magma flow are described in Section 6.3.3.5.6. Propagation of the boundary and initial conditions into the dike propagation model is presented in the mathematical description of the dike propagation model in Section 6.3.3.1.

Effects of pressure inside the tip cavity and thermally induced increased horizontal stress on dike propagation are described in Sections 6.3.3.4.2 and 6.3.7. The effect of expanding magma on dike extension to the surface is described in Section 6.3.6. Sensitivity of the effects of magma cooling to saturation and latent heat effects are described in Appendix C and Appendix D.

The outputs of the dike/drift interaction model provide descriptions of thermal effects (Section 8.2) and the uncertainties associated with those outputs (Section 8.3) for application in the TSPA in-drift submodels.

The representation of risk is a TSPA responsibility. This report describes no results that could be used to evaluate the representation of risk from magma–drift and magma–waste package interactions, but the review of magma–waste package interactions and recommendations for TSPA are summarized in Section 6.4.8.3.5. It is important to note that no parameters are passed from these models directly to the TSPA. Rather, parameter time histories developed in this report could be used by the waste form and waste package groups to determine possible damage states, which then would be passed to TSPA.

2. *Process-level models used to represent mechanically disruptive events, within the emplacement drifts at the proposed Yucca Mountain repository, are adequate. Parameter values are adequately constrained by Yucca Mountain site data, such that the estimates of mechanically disruptive events on engineered barrier integrity are not underestimated. Parameters within conceptual models for mechanically disruptive events are consistent with the range of characteristics observed at Yucca Mountain.*

   Two models and supporting analyses describe the processes that could occur if an igneous intrusion were to intersect the repository. The first model describes dike propagation from depth (Section 6.3.3); the mathematical description of the model is found in Section 6.3.3.1. Assumptions related to the model are described in Section 6.3.3.1, and uncertainties associated with the model are described in Section 6.3.3.2. Alternative models of dike propagation are described in Section 6.3.3.5. Results from exercise of the model are described in Section 6.3.3.4, and the inputs for the analysis of magma flow into drifts are provided in Section 6.3.3.5.6.

The second model describes heating of neighboring drifts from cooling of the emplaced magma (Section 6.4 and Appendix C). The mathematical model is described in Section 6.4.3, and the results are described in Section 6.4.9. Sensitivity to saturation is described in Appendix C, and sensitivity to latent heat effects is described in Appendix D.

The analyses documented in this report are natural and thermal stresses (Section 6.2) and magma flow into drifts at dike/drift intersections (Section 6.3.3.5.6). Alternative models for dike propagation are described in Section 6.3.3.5. The effects of expanding magma on dike extension to the surface are described in Section 6.3.6. Magma flow to the surface along a secondary pathway developed at some distance from the intersection is described in Section 6.5. Magma–waste package interactions are described in Section 6.4.8.3. Results support the TSPA assumption that waste packages in intersected drifts provide no protection for the waste. For waste packages in nonintersected drifts, results described in Sections 6.4.8.3.5 indicate that exposure to magmatic products would produce only limited damage because the repository host rock is expected to limit heat conduction to nonintersected drifts. Magma–waste form interactions are expected to form silicate and oxide minerals.

Parameters used in the analysis of dike/drift interactions are summarized in Table 4-1. Constraints on parameters and consistency of parameter values with the range of characteristics observed at Yucca Mountain is established in the model reports and analysis reports that provide the information (e.g., SNL 2007 [DIRS 174260]). Comparisons with field observations and associated mathematical models used to increase postdevelopment confidence in the dike intrusion submodel are described in Section 7.3.2.2.2. Model uncertainties associated with the dike propagation model are described in Section 6.3.3.2, and alternative models are described in Section 6.3.3.5. Output uncertainties associated with the heat-flow calculation are described in Section 8.3.2.

3. *Uncertainty is adequately represented in parameter development for conceptual models, process-level models, and alternative conceptual models considered in developing the TSPA abstraction of mechanical disruption of engineered barriers. This may be done through either sensitivity analyses or use of conservative limits.*

   Parameters used in the analysis of dike/drift interactions are summarized in Table 4-1. Uncertainties associated with the dike propagation model are described in Section 6.3.3.2, and alternative models are described in Section 6.3.3.5. Alternatives for the analysis of magma flow in drifts are described in Sections 6.3.3.5.7. Uncertainties associated with the analysis of effects on neighboring drifts of magma cooling and solidification are described in Appendix C. Boundary and initial conditions for the dike propagation model are described in Section 6.3.3.3.1. Boundary and initial conditions for the magma flow analysis are described in Section 6.3.3.5.6. Sensitivity of the modeling for effects of magma cooling and solidification on neighboring drifts to saturation is described in Appendix C, and sensitivity to latent heat effects is described in Appendix D. Model outputs and uncertainties associated with the heat flow calculation are described in Sections 8.3.1.

4. *Where sufficient data do not exist, the definitions of parameter values and conceptual models are based on appropriate use of expert elicitation, conducted in accordance with NUREG-1563 (Kotra et al. 1996 [DIRS 100909]). If other approaches are used, the U.S. Department of Energy adequately justifies their use.*

   Expert elicitation was not used in the development of the models of dike propagation, magma flow, gas flow between drifts, or magma cooling and solidification. However, results of the *Final Report of the Igneous Consequences Peer Review Panel* (Detournay et al. 2003 [DIRS 169660]) were used in the development of the dike propagation and magma flow models. Use of the peer review results is described in Section 7.3.1.1.2.

A1.4 ACCEPTANCE CRITERION 4: MODEL UNCERTAINTY IS CHARACTERIZED AND PROPAGATED THROUGH THE MODEL ABSTRACTION

1. *Alternative modeling approaches of features, events, and processes are considered and are consistent with available data and current scientific understanding, and the results and limitations are appropriately considered in the abstraction.*

   Alternative conceptual models that were considered in the development of the model of dike propagation are discussed in Section 6.3.3.5. Alternatives for the analysis of magma flow into drifts are described in Section 6.3.3.5.7. FEPs that were considered in developing these models were identified in Section 6.1 and described in Table 6-1.

   Confidence building conducted during model development is described for the dike intrusion model in Section 7.2.1 and for the post-intrusion submodel in Section 7.2.2. Postdevelopment confidence-building activities for the dike propagation model are described in Section 7.3.1. Confidence building for the model for magma cooling and solidification is summarized in Section 7.3.2.2. Uncertainties associated with the outputs from these models are described in Section 8.3.

   Limitations associated with the analysis of natural and thermal stresses are described in Section 1.4.1. Limitations associated with the dike propagation model are described in Section 1.4.2. Limitations associated with the analysis of magma flow in drifts are described in Section 1.4.3. Limitations associated with the analysis of the development of secondary dikes (dog-leg scenario) are described in Section 1.4.4. Limitations associated with the modeling of basalt cooling and solidification are described in Section 1.4.5.

2. *Consideration of conceptual model uncertainty is consistent with available site characterization data, laboratory experiments, field measurements, natural analog information and process-level modeling studies; and the treatment of conceptual model uncertainty does not result in an under-representation of the risk estimate.*

Model uncertainties associated with the dike propagation model are described in Section 6.3.3.2. Sensitivity of the modeling of effects of magma cooling and solidification on neighboring drifts to saturation is described in Section Appendix C and to latent heat effects in Section Appendix D.

Uncertainties associated with the heat flow calculation output are described in Section 8.3.1.

The representation of risk is a TSPA responsibility, but the review of magma-waste package interactions and recommendations for TSPA are summarized in Section 8.2. This report describes no results that could be used to evaluate the representation of risk from magma-drift and magma-waste package interactions.

3. *Appropriate alternative modeling approaches are investigated that are consistent with available data and current scientific knowledge and that appropriately consider their results and limitations using tests and analyses that are sensitive to the processes modeled.*

   Alternative conceptual models that were considered in the development of the model of dike propagation are discussed in Section 6.3.3.5. Alternatives for the analysis of magma flow into drifts are described in Section 6.3.3.5.7. Features, events and processes that were considered in developing these models were identified in Section 6.1 and described in Table 6-1.

   Confidence building conducted during model development is described for the dike intrusion model in Section 7.2.1 and for the post intrusion submodel in Section 7.2.2. Post-development confidence building activities for the dike propagation model are described in Section 7.3.1. Confidence building for the model for magma cooling and solidification is summarized in Section 7.3.2.2.

   Effects on dike propagation of pressure inside the tip cavity are described in Section 6.3.3.4.2, and effects of thermally induced increased horizontal stress are described in Section 6.3.7. Effects of expanding magma on dike extension to the surface are described in Section 6.3.6. Sensitivity of the modeling of effects of magma cooling and solidification on neighboring drifts to saturation is described in Section Appendix C and sensitivity to latent heat effects in Section Appendix D.

   Limitations associated with the analysis of natural and thermal stresses are described in Section 1.4.1. Limitations associated with the dike propagation model are described in Section 1.4.2. Limitations associated with the analysis of magma flow in drifts are described in Section 1.4.3. Limitations associated with the analysis of the development of secondary dikes (dog-leg scenario) are described in Section 1.4.4. Limitations associated with the modeling of basalt cooling and solidification are described in Section 1.4.5.

A1.5 ACCEPTANCE CRITERION 5: MODEL ABSTRACTION OUTPUT IS SUPPORTED BY OBJECTIVE COMPARISONS

1. *Models implemented in this TSPA abstraction provide results consistent with output from detailed process-level models and/or empirical observations (laboratory and field testings and/or natural analogues).*

   Model outputs for thermal effects are described in Section 8.2.3. Uncertainties associated with the heat-flow calculation are described in Section 8.3.1.

   Magma–waste package interactions are described in Section 6.4.8.3. Results support the TSPA assumption that waste packages in intersected drifts provide no protection for the waste. Radionuclide mobility associated with magma–waste form interactions is described in Section 6.4.8.3.3. Magma–waste form interactions are expected to form silicate and oxide minerals, although halides and sulfates can not be ruled out.

2. *Outputs of mechanical disruption of engineered barrier abstractions reasonably produce or bound the results of corresponding process-level models, empirical observations, or both.*

   Model outputs for thermal effects are described in Section 8.2.2. Uncertainties associated with the heat-flow calculation are described in Section 8.3.1, and uncertainties associated with the Igneous EBS Failure Fractions are described in Section 8.3.2. Confidence building conducted during model development is described for the dike intrusion submodel in Section 7.2.1 and for the post-intrusion submodel in Section 7.2.2. Postdevelopment confidence-building activities for the dike propagation model are described in Section 7.3.1. Postdevelopment confidence-building for the model for magma cooling and solidification is summarized in Section 7.3.2.1.

3. *Well-documented procedures that have been accepted by the scientific community to construct and test the mathematical and numerical models, are used to simulate mechanical disruption of engineered barriers.*

   The computer codes used in the modeling activities documented in this report are described in Table 3-1. Confidence building conducted during model development is described for the dike intrusion submodel in Section 7.2.1 and for the post-intrusion submodel in Section 7.2.2. Postdevelopment confidence-building activities for the dike propagation model are described in Section 7.3.1. Confidence building for the model for magma cooling and solidification is summarized in Section 7.3.2.1.

4. *Sensitivity analyses or bounding analyses are provided to support the TSPA abstraction of mechanical disruption of engineered barriers that cover ranges consistent with site data, field or laboratory experiments and tests, and natural analogue research.*

   Model outputs for thermal effects are described in Section 8.2.2. Uncertainties associated with the heat-flow calculation are described in Section 8.3.1.

Effects of pressure inside the tip cavity and thermally induced increased horizontal stress on dike propagation are described in Sections 6.3.3.4.2 and 6.3.7. The effect of expanding magma on dike extension to the surface is described in Section 6.3.6. Sensitivity of magma cooling to latent heat effects and saturation effects are described in Appendices D and C. Boundary and initial conditions for the dike propagation model are described in Section 6.3.3.3.1. Boundary and initial conditions for the magma flow analysis are described in Section 6.3.3.5.6.

A2. VOLCANIC DISRUPTION OF WASTE PACKAGES

A2.1 ACCEPTANCE CRITERION 1: SYSTEM DESCRIPTION AND MODEL INTEGRATION ARE ADEQUATE

1. *TSPA adequately incorporates important design features, physical phenomena, and couplings, and uses consistent and appropriate assumptions throughout the volcanic disruption of the waste package abstraction process.*

   Dike/Drift Interactions addresses propagation of a magma-filled fracture (dike) and the characteristics of magma for the intrusive case and not for the eruptive case. The number of waste packages contacted by magma in the igneous intrusion-groundwater transport modeling case is considered in *Number of Waste Packages Hit by Igneous Events* (SNL 2007 ([DIRS 177432]).

2. *Models used to assess volcanic disruption of waste packages are consistent with physical processes generally interpreted from igneous features in the Yucca Mountain region and/or observed at active igneous systems.*

   This report discusses models that provide some of the initial conditions needed to evaluate volcanic disruption of waste packages. The first model describes dike propagation from depth (Section 6.3.3) and the mathematical description of the model (Section 6.3.3.1). Assumptions related to the model are described in Section 6.3.2, and uncertainties associated with the model are described in Section 6.3.3.2. Alternative models of dike propagation are described in Section 6.3.5. Results from exercise of the model are described in Section 6.3.3.4, and the inputs for the analysis of magma flow into drifts are provided in Section 6.3.3.5.6.

   The second model describes heating of neighboring drifts from cooling of the emplaced magma (Section 6.4). The conceptual model is described in Section 6.4.1 and Appendix C, and the results are described in Section 6.4.6 and Appendix C. Sensitivity to latent heat effects is described in Appendix D, and sensitivity to saturation is described in Appendix C.

3. *Models account for changes in igneous processes that may occur from interactions with engineered repository systems.*

   Effects of stresses from excavation of the repository are described in Section 6.5.1.3, and thermal stresses are described in Section 6.3.7.4; effects of gas seepage on fracture and dike propagation are not explicitly discussed, but the model described in

Section 6.3.3.4.1 assumes that the pressure in the tip cavity is very small. The effects of loss of hydrofracture-driving fluid due to flow of magma into drifts are described in Section 6.3.3.5.6. Effects of vesiculation and fragmentation of a magma in a drift are also generally not included, but the restrictions on the development of the dog-leg scenario are described in Section 6.5.1.5. The mechanical effects of magmatic pressures external to waste packages have been analyzed in Section 6.4.8.3.1. A summary of the effects of drifts on dike propagation is presented in Section 8.1.1. A summary of magma-induced environments in drifts is presented in Section 8.1.2, and dike propagation to the surface is summarized in Section 8.1.1 and 8.1.3.

4. *Guidance in NUREG-1297 (Altman et al. 1988 [DIRS 103597]) and NUREG-1298 (Altman et al. 1988 [DIRS 103750], or other acceptable approaches is followed.*

NUREG-1297 describes the generic technical position with respect to the use of peer reviews on high-level waste repository programs. The use of information from the *Final Report of the Igneous Consequences Peer Review Panel* (Detournay et al. 2003 [DIRS 169660]) is summarized in Section 7.2.1. The *Final Report of the Igneous Consequences Peer Review Panel* (Detournay et al. 2003 [DIRS 169660], pp. 44 and 45) addressed the limitations of modeling dike propagation, when assuming that the magma is an incompressible fluid (whereas real magma would be compressible). Use of peer review in the development of the model is described in *Atmospheric Dispersal and Deposition of Tephra from a Potential Volcanic Eruption at Yucca Mountain, Nevada* (SNL 2007 [DIRS 177431], Section 7.4).

NUREG-1298 describes the generic technical position with respect to qualification of existing data. External sources have provided unqualified data that have been used as direct input to this document. The inputs from these sources are qualified for intended use within the document using the criteria found in SCI-PRO-006, *Models*. These criteria represent a subset of the methods and attributes required for qualification of data per SCI-PRO-001, *Qualification of Unqualified Data.* These methods and attributes are based on those that are presented in NUREG-1298, which are meant to provide "the level of confidence in the data … commensurate with their intended use."

The remaining acceptance criteria associated with the integrated subissue of volcanic disruption of waste packages in *Yucca Mountain Review Plan, Final Report* (NRC 2003 [DIRS 163274], Section 2.2.1.3.10.3) are associated with the volcanic eruption modeling case and are addressed in either *Number of Waste Packages Hit by Igneous Events* (SNL 2007 [DIRS 177432]) or *Atmospheric Dispersal and Deposition of Tephra from a Potential Volcanic Eruption at Yucca Mountain, Nevada* (SNL 2007 [DIRS 177431]) but are not addressed in this report, which focuses on conditions associated with the igneous intrusion modeling case.

A3. AIRBORNE TRANSPORT OF RADIONUCLIDES

The models of dike propagation near drifts, magma and gas flow in drifts, and drift-scale gas flow constrain the conceptual models that support generation of the source term for the analysis of airborne transport of radionuclides. The outputs from this report provide no direct parameter inputs to the analysis and modeling of airborne transport of radionuclides. The description of the modeling of airborne transport of radionuclides is provided in *Atmospheric Dispersal and Deposition of Tephra from a Potential Volcanic Eruption at Yucca Mountain, Nevada* (SNL 2007 [DIRS 177431]).

APPENDIX B
QUALIFICATION OF EXTERNAL SOURCES

APPENDIX B
QUALIFICATION OF EXTERNAL SOURCES

External sources have provided unqualified data that have been used as direct input to this document. The inputs from these sources are qualified for intended use within the document using the process found in SCI-PRO-006, *Models*, and the methods and attributes required for qualification of data per SCI-PRO-001, *Qualification of Unqualified Data.*

Data for Qualification

The following external sources of data used as direct input to this report are qualified in this appendix:

1. Parameter values for mechanical properties of scoria are provided by Duncan et al. (1980 [DIRS 161776]), and are presented in Table 6-26, Section 6.4.8.1.3.3 of this report.

2. Parameter values for material properties of solidified basalt are provided by Gupta and Rao (2000 [DIRS 174063]), and also are discussed in Table 6-26, Section 6.4.8.1.3.3 of this report.

3. Parameter values for mechanical properties of basalt are taken from Hoek and Brown (1997 [DIRS 170501]), as discussed in Table 6-26, Section 6.4.8.1.3.3 of this report.

METHOD OF QUALIFICATION SELECTED

The method for qualification of these three external sources of data is the technical assessment method. Other qualification methods described in SCI-PRO-001, Attachment 3, are not considered because they require information not available through the original source (i.e., scientific journal or publication). Qualification process attributes used in the technical assessment of each external source are selected from the list provided in Attachment 4 of SCI-PRO-001. Attributes used specifically as data qualification attributes in this report are:

1. (Criterion 1) Qualifications of personnel or organizations generating the data (such qualifications should be comparable to qualification requirements of personnel generating similar data under an approved program that supports the Yucca Mountain Project license application process or postclosure science)

2. (Criterion 3) The extent to which the data demonstrate the properties of interest (e.g., physical, chemical, geologic, mechanical)

3. (Criterion 8) Prior peer or other professional reviews of the data and their results

4. (Criterion 10) Extent and quality of corroborating data or confirmatory testing results.

Sources meeting three or more of these criteria will be deemed qualified for use in this report.

B1. DUNCAN ET AL. 1980

Reference—Duncan, J.M.; Byrne, P.; Wong, K.S.; and Mabry, P. 1980. *Strength, Stress-Strain and Bulk Modulus Parameters for Finite Element Analyses of Stresses and Movements in Soil Masses.* UCB/GT/80-01. Berkeley, California: University of California, College of Engineering, Office of Research Services. TIC: 253873. [DIRS 161776]

Description of Use–Parameter values for mechanical properties of scoria (bulk modulus, shear modulus, cohesion, friction angle, and tensile strength) from Duncan et al. (1980 [DIRS 161776]) are used in Table 6-26, Section 6.4.8.1.3.3, to analyze the failure of a scoria cone when magma flow is blocked by slumping of scoria inward, covering the vent.

Qualifications of Personnel or Organizations Generating the Data—The report was released by University of California, Berkeley, which is one of the world's leading institutions in research on constitutive behavior and numerical analysis of soils. Two of the co-authors, professors J.M. Duncan and P. Byrne, have published a large number of articles on constitutive behavior of soils.

Extent to which the Data Demonstrate the Properties of Interest—No data have been found in the literature for the deformational properties of basaltic scoria, either undisturbed or loose. The properties listed are estimated based on tabulated properties for generic gravel (Duncan et al. 1980 [DIRS 161776], Table 5 and Equation 3). The analysis presented in Section 6.5.2.1 of this document uses these values to limit the pressurization of the magma in a conduit feeding the cone if the conduit is blocked by slumping.

Prior peer or other professional reviews—There is no evidence of prior peer review of this source.

Corroborative Data—The values published in the report are in agreement with the observations of Marachi et al. (1972 [DIRS 157883]).

Qualification Decision—The data are found to be qualified, having met three of the four criteria.

B2. GUPTA AND RAO 2000

Reference—Gupta, A. S., and Rao, K. S, 2000. "Weathering Effects on the Strength and Deformational Behaviour of Crystalline Rocks under Uniaxial Compression State." *Engineering Geology, 56,* 257-274. New York, New York: Elsevier. TIC: 257315. [DIRS 174063]

Description of Use–Gupta and Rao (2000 [DIRS 174063], Tables 2 and 3) are the source of values for parameter values of material properties (density, bulk modulus, shear modulus, cohesion and tensile strength) of solidified basalt as discussed in Section 6.4.8.1.3.3, Table 6-26. This information is then employed in the analysis of the failure of basalt bodies (solidified magma or lava) to limit the pressures that may be developed in a conduit or dike blocked by either slumping scoria or cooling lava.

Extent to which the Data Demonstrate the Properties of Interest—The properties for basalt are based on measurements on small (centimeter-sized) samples (Gupta and Rao 2000 [DIRS 174063], Tables 2 and 3) and, as discussed in Section 6.4.8.1.3.3, may overestimate the strength of a larger rock mass, which is useful for this particular application.

Qualifications of Personnel or Organizations Generating the Data—A. S. Gupta is a common Indian name. It is possible to find four publications published during the period from 1997 to 2000 with both A. S. Gupta and K. S. Rao as authors that are clearly associated with this A. S. Gupta because they all deal with the subject of the strength of weathered or jointed rock. No earlier or later publications by A. S. Gupta can be unequivocally associated with this author. Therefore, qualification of this source will rely upon the qualifications of K. S. Rao, who was probably in charge of the research of his student Gupta. Dr. K. S. Rao is a professor at the Indian Institute of Technology, Delhi. He earned a Ph.D. degree from the same institution. His research specialties include rock mechanics, rock engineering, geotechnical engineering, engineering geology, and seismic microzonation. Prof. Rao is the author of over 15 papers on rock or soil mechanics since 1988. His 2005 paper "Empirical methods to estimate the strength of jointed rock masses" was among the top 25 most requested articles in *Engineering Geology* in 2004-2005.

Prior peer or other professional reviews—The reference in question (Gupta and Rao 2000 [DIRS 174063]) was published in *Engineering Geology,* a peer-reviewed journal. This paper has survived rigorous peer review and may be accepted as an authoritative description of the properties of unconsolidated granular material.

Corroborative Data—The tensile strength value from this source is considerably higher than from other reports, such as *Fracturing of Etnean and Vesuvian Rocks at High Temperatures and Low Pressures* (Rocchi et al. 2004 [DIRS 173995], Table 3, p. 146); the higher value allows the calculation to reach higher pressures so that a larger region of failure parameter space can be investigated.

Qualification Decision—The data are found to be qualified by having met all four criteria.

B3. HOEK AND BROWN 1997

Reference— Hoek, E. and Brown, E.T. 1997. "Practical Estimates of Rock Mass Strength." *International Journal of Rock Mechanics and Mining Science & Geomechanics Abstracts, 34,* (8), 1165-1186. Oxford, England: Pergamon. TIC: 256245. [DIRS 170501]

Description of Use– The method of Hoek and Brown 1997, Fig. 8, is used in Section 6.4.8.1.3.3, Table 6-26, to estimate the friction angle of basalt. This is then employed in the analysis of the failure of basalt bodies (solidified magma or lava) to limit the pressures that may be developed in a conduit or dike blocked by either slumping scoria or cooling lava.

Extent to which the Data Demonstrate the Properties of Interest— The Hoek-Brown criterion is used to generate a series of values relating uniaxial strength to confining pressure (or shear strength to normal stress) and these are treated as the results of a hypothetical large-scale in situ triaxial or shear test. A linear regression method is used to find the average slope and intercept, and these are then transformed into a cohesive strength c and a friction angle f.

Qualifications of Personnel or Organizations Generating the Data— Professors E. Hoek and E.T. Brown are leading rock-mechanic experts and researchers. Both have held distinguished positions at Imperial College, London, which is one of the leading universities in rock mechanics. Both also have considerable industry experience through Golder Associates a leading rock mechanics consulting firm.

Prior peer or other professional reviews— The article, *Practical Estimates of Rock Mass Strength* (1997 [DIRS 170501]), was published in the International Journal of Rock Mechanics and Mining Sciences, which is a peer-reviewed journal. This paper has survived rigorous peer review and may be accepted as an authoritative description of the properties of unconsolidated granular material.

The Hoek-Brown failure criterion is a basis of standard engineering practice, considered to be the most realistic failure criterion for in situ rock masses. It can be found in almost every rock mechanics text book published within the last 20 years.

Corroborative Data— The original failure criterion was developed in the early 1980s. The criterion was required in order provide input information for the design of underground excavations. Since no suitable methods for estimating rock mass strength appeared to be available at that time, the efforts were focused on developing a dimensionless equation that could be scaled in relation to geological information. The original Hoek-Brown equation was neither new nor unique—an identical equation had been used for describing the failure of concrete as early as 1936. The significant contribution that Hoek and Brown made was to link the equation to geological observations in the form of Rock Mass Rating and later to the Geological Strength Index.

One of the issues that had been problematic throughout the development of the criterion was the relationship between the Hoek-Brown criterion, with the non-linear parameters *m* and *s*, and the Mohr-Coulomb criterion, with the parameters *c* and f. Practically all software for soil and rock mechanics is written in terms of the Mohr-Coulomb criterion and it was necessary to define the relationship between *m* and *s* and *c* and f to allow the criterion to be used to provide input for this software. Addition of this modification of the Hoek-Brown equation in 1983 completed the development of the model.

This paper incorporated numerous refinements to the original 1980 criterion. In addition, a method for estimating the equivalent Mohr-Coulomb cohesion and friction angle was introduced. In this method, the Hoek-Brown criterion is used to generate a series of values relating uniaxial strength to confining pressure (or shear strength to normal stress) and these are treated as the results of a hypothetical large-scale in situ triaxial or shear test. A linear regression method is used to find the average slope and intercept, and these are then transformed into a cohesive strength *c* and a friction angle *f*. The most important aspect of this curve fitting process is to decide upon the stress range over which the hypothetical in situ 'tests' should be carried out. This was determined experimentally by carrying out a large number of comparative theoretical studies in which the results of both surface and underground excavation stability analyses, using both the Hoek-Brown and Mohr-Coulomb parameters, were compared.

Qualification Decision—The data are found to be qualified by having met all four criteria.

APPENDIX C
MAGMA COOLING AND SOLIDIFICATION

C1. HEAT-FLOW MODEL

A one-dimensional second-order partial differential equation (Chapman 1974 [DIRS 152938], p. 137), subject to initial temperature (due to the constant heat content) and a far-field temperature-boundary condition applies to the problem of magma intrusion:

$$k\left[\frac{1}{r}\cdot\frac{\partial T}{\partial r}+\frac{\partial^2 T}{\partial r^2}\right]=\rho\cdot C_p\cdot\frac{\partial T}{\partial t} \qquad \text{(Eq. C-1)}$$

The magma is considered to be at an initial intrusive temperature of 1,150°C (DTN: LA0612DK831811.001 [DIRS 179987]). The magma fills the drift entirely and instantaneously, and then the temperature spatially and temporally evolves. The temperature of the drift wall and the far field is considered to be 25°C, and up to 200°C, at the time of the intrusion. The heat-transfer thermal properties of the magma are considered to be the same as those for the densely welded tuff for a first-order analysis.

Carnahan et al. (1990 [DIRS 163096], p. 462) provide finite difference expression approximations to first and second order derivatives for the radial-heat conduction problem. The governing equation may be expressed as:

$$\frac{1}{r_i}\cdot\left(\frac{T'_{i+1}-T'_{i-1}}{2\cdot\Delta r}\right)+\frac{1}{\Delta r^2}\cdot\left[T'_{i+1}+T'_{i-1}-2\cdot T'_i\right]=\frac{1}{\alpha}\cdot\frac{T_i-T'_i}{\Delta t} \qquad \text{(Eq. C-2)}$$

Using the following definition of thermal diffusivity (Incropera and DeWitt 2002 [DIRS 163337], p. 59):

$$\alpha=\frac{k}{\rho C_p} \qquad \text{(Eq. C-3)}$$

where

Δt = change in time (time-step) [yr]

r_i = total distance to the center of the cylinder [m]

Δr = change in distance from the center of the cylinder in one time-step [m]

T_i = temperature at distance r_i from the center of the cylinder [°C]

T'_i = temperature from the previous time-step at a distance of r_i from the center of the cylinder [°C]

T'_{i+1} = temperature from the previous time-step at a distance of r_{i+1} from the center of the cylinder [°C]

T'_{i-1} = temperature from the previous time-step at a distance of r_{i-1} from the center of the cylinder [°C]

α = thermal diffusivity of the rock mass and the magma [$m^2\ yr^{-1}$]

k = thermal conductivity of the rock mass and the magma [$W\ m^{-1}\ K^{-1}$]

ρ = density [$kg\ m^{-3}$]

C_p = specific heat [$J\ kg^{-1}\ K^{-1}$]

Factoring the expression to give T_i in terms of $T`_i$, $T`_{i-1}$, and $T`_{i+1}$ in an explicit finite-difference calculation results in Equation C-4:

$$T_i = \alpha \cdot \Delta t \cdot \left[\frac{1}{r_i \cdot 2 \cdot \Delta r} + \frac{1}{\Delta r^2} \right] \cdot T'_{i+1} + \alpha \cdot \Delta t \cdot \left[\frac{-1}{r_i \cdot 2 \cdot \Delta r} + \frac{1}{\Delta r^2} \right] \cdot T'_{i-1} - \frac{2\alpha \cdot \Delta t \cdot T'_i}{\Delta r^2} + T'_i \qquad \text{(Eq. C-4)}$$

C1.1 RADIAL EQUATION ($r_i > 0$)

A simple explicit finite-difference calculation was set up in Microsoft Excel based upon the second-order finite-difference expression for radial flow. The stability of the calculation was confirmed by using an energy balance check within the spreadsheet. The explicit finite-difference calculation can be simplified by defining the coefficients for T'_{i+1}, T'_{i-1}, and T'_i as α', β', and γ', respectively:

$$\alpha' = \left[\frac{1}{r_i \cdot 2 \cdot \Delta r} + \frac{1}{\Delta r^2} \right] \qquad \text{(Eq. C-4a)}$$

$$\beta' = \left[\frac{-1}{r_i \cdot 2 \cdot \Delta r} + \frac{1}{\Delta r^2} \right] \qquad \text{(Eq. C-4b)}$$

$$\gamma' = \left(-\frac{2}{\Delta r^2} \right) \qquad \text{(Eq. C-4c)}$$

The explicit finite difference expression (Equation C-4) then becomes:

$$T_i = \alpha \cdot \Delta t \cdot \left[\alpha' \cdot T'_{i+1} + \beta' \cdot T'_{i-1} + \gamma' \cdot T'_i \right] + T'_i \qquad \text{(Eq. C-5)}$$

The far-field temperature boundary condition at a distance of 150 m (approximately 10 m less than twice the drift spacing) is set to a constant ambient temperature of 25°C. Additional calculations look at ambient temperatures up to 200°C.

C1.2 ON-AXIS EQUATION ($r_i = 0$)

To obtain an equation for the temperature on the r = 0 axis, a finite difference expression at the center of the model sets the insulated-temperature boundary condition equal to the temperature at r = 0 ($T`_{i-1} = T`_{i+1}$), resulting in Equation C-6:

$$T_i = \alpha \cdot \Delta t \cdot \left[\frac{1}{r_i \cdot 2 \cdot \Delta r} + \frac{1}{\Delta r^2} \right] \cdot T'_{i+1} + \alpha \cdot \Delta t \cdot \left[\frac{-1}{r_i \cdot 2 \cdot \Delta r} + \frac{1}{\Delta r^2} \right] \cdot T'_{i+1} - \frac{2\alpha \cdot \Delta t \cdot T'_i}{\Delta r^2} + T'_i \qquad \text{(Eq. C-6)}$$

Simplifying this equation gives Equation C-7:

$$T_i = \left[\frac{2\alpha \cdot \Delta t}{\Delta r^2} \right] \cdot [T'_{i+1} - T'_i] + T'_i \qquad \text{(Eq. C-7)}$$

The model was implemented by entering Equations C-4 and C-7 into Microsoft Excel spreadsheets (Output DTN: MO0408EG831811.008). The required thermal diffusivity (α) was calculated using the method discussed below.

C1.3 THERMAL DIFFUSIVITY

Assessment of temperature changes due to magma in a drift requires the rock-mass thermal diffusivity, which in turn requires an estimate of the rock-mass volumetric-heat capacity and thermal conductivity of the welded tuff at the repository horizon.

The volumetric heat capacity was calculated using an equation derived in *Ventilation Model and Analysis Report* (BSC 2004 [DIRS 169862], Equation II-15).

$$C_{rock} = \frac{S \cdot \frac{\phi_m}{1-\phi_m} C_{vw} + \rho_g \cdot C_p}{\left(1 + \frac{\phi_m}{1-\phi_m} + \frac{\phi_l}{1-\phi_l} \cdot \left(1 + \frac{\phi_m}{1-\phi_m} \right) \right)} \qquad \text{(Eq. C-8)}$$

Simplifying this equation gives Equation C-9:

$$C_{rock} = \frac{S \cdot \frac{\phi_m}{1-\phi_m} C_{vw} + \rho_g \cdot C_p}{\left(1 + \frac{\phi_l}{1-\phi_l} \right) \cdot \left(1 + \frac{\phi_m}{1-\phi_m} \right)} \qquad \text{(Eq. C-9)}$$

where

C_{rock} = volumetric heat capacity of the rock mass [J m^{-3} K^{-1}]
S = saturation (S = 0 meaning dry; S = 1 meaning wet)
φ_m = matrix porosity
φ_l = lithophysal porosity
C_{vw} = volumetric heat capacity of water [J m^{-3} K^{-1}]
ρ_g = grain density of solids [kg m^{-3}]
C_p = specific heat capacity of solids [J kg^{-1} K^{-1}].

The saturation in this heat-flow calculation is either completely dry (no water; S = 0), or completely wet (matrix is completely filled with water; S = 1). Real conditions of saturation are not so absolute; unsaturated conditions really lie between 10% and 20% saturation (DTN: LB0207REVUZPRP.002 [DIRS 159672]), and fully saturated conditions do not consider the lithophysae to be filled with water.

The simulations consider the four types of lithophysal and nonlithophysal units that comprise the repository horizon of the Topopah Spring Tuff, as summarized in Table C-1.

Table C-1. Summary of Lithostratigraphic Units of the Repository Horizon Considered in Thermal Calculation

Formation Symbol	Phenocryst Content Symbol	Lithophysal Content Symbol	Total Lithostratigraphic Symbol
Tpt= Topopah Spring Tuff	p = crystal poor	ul = upper lithophysal	Tptpul
		mn = middle nonlithophysal	Tptpmn
		ll = lower lithophysal	Tptpll
		ln = lower nonlithophysal	Tptpln

The Yucca Mountain Project assessed the thermal conductivity of the potential repository horizon for spatial variability and uncertainty of thermal conductivity in the host horizon (BSC 2004 [DIRS 169854]). Table C-2 presents the properties taken from that report for the rock units near the repository horizon. Note that the values used for specific heat of solids actually used as input (Table C-2, last column) differ from those listed in the source by +1 J kg^{-1} K^{-1}. The result of this difference is approximately 0.1% of the value of the specific heat of the bulk rock when the rock is dry, and less than that when the rock is wet (Equation C-8). Such a difference is smaller than the stochastic variability of the data and is, therefore, insignificant.

Table C-2. Summary of Primary Thermal Conductivity Statistics

Stratigraphic Unit	Bulk Dry Rock Mass Thermal Conductivity (W m^{-1} K^{-1})	Bulk Wet Rock Mass Thermal Conductivity (W m^{-1} K^{-1})	Matrix Porosity	Lithophysal Porosity	Dry Bulk Density (kg m^3)	Specific Heat Capacity of Solids (J kg^{-1} K^{-1})
	k_{rm} [a]	k_{rm} [a]	φ_m [a]	φ_l [a]	ρ_{bd} [a]	C_p [b]
Tptpul	1.18	1.77	0.17	0.12	1,830	934
Tptpmn	1.42	2.07	0.13	0.03	2,150	932
Tptpll	1.28	1.89	0.15	0.09	1,980	933
Tptpln	1.49	2.13	0.11	0.03	2,210	933

Sources: [a] DTN: SN0404T0503102.011 [DIRS 169129], file *ReadMe_Summery.doc*, Table 7-10.
[b] DTN: SN0307T0510902.003 [DIRS 164196], file *rock_grain_heat_capacity (edited).xls*, tab: "Cp grain 25-325," cells X8:X11.

NOTE: Porosity is the ratio of void volume to total rock volume and has units of m^3 void/m^3 rock.

The volumetric heat capacity of water (C_{vw}) is calculated (Incropera and DeWitt 2002 [DIRS 163337], pp. 58 and 59) for saturated water at 62°C by multiplying the density of water by the specific heat of water, giving Equation C-10:

$$C_{vw} = C_P \cdot \rho \qquad \text{(Eq. C-10)}$$

where

ρ = density of water ($1/v_f$) 982.3 [kg m^{-3}]

C_p = specific heat 4,186 [J kg^{-1} K^{-1}]

The grain density of solids can be calculated from the dry bulk density (ρ_{bd}) and the porosities of the matrix and lithophysae using the following equation from *Thermal Conductivity of the Potential Repository Horizon Model Report* (BSC 2004 [DIRS 169854], p. 41, Equation 6-4):

$$\rho_{bd} = (1-\phi_l)(1-\phi_m)\rho_g \qquad \text{(Eq. C-11)}$$

Solving for the grain density of solids:

$$\rho_g = \frac{\rho_{bd}}{(1-\phi_l)(1-\phi_m)} \qquad \text{(Eq. C-12)}$$

After plugging in the required values into Equation C-9 and solving for C_{rock}, the thermal diffusivity can be calculated by combining Equation C-3 with Equation C-10:

$$\alpha = \frac{k}{C_{rock}} \qquad \text{(Eq. C-13)}$$

NOTE: The units of watts are converted to joules per second (W = J s^{-1}), and then seconds are converted to years, since Δt is in terms of years.

Table C-3 contains all of the values calculated, using the values presented in Table C-2 and Equation C-10 through Equation C-13, which were then used in the heat-transfer explicit finite-difference calculation.

Table C-3. Summary of Volumetric Heat Capacity and Thermal Diffusivity Calculations

Stratigraphic Unit	Grain Density of Solids (kg m^{-3})	Dry Volumetric Heat Capacity (J m^{-3} K^{-1})	Wet Volumetric Heat Capacity (J m^{-3} K^{-1})	Dry Thermal Diffusivity (m^2 yr^{-1})	Wet Thermal Diffusivity (m^2 yr^{-1})
	ρ_g	C_{rock}	C_{rock}	α	α
Tptpul	2,504	1,709,220.0	2,335,595.2	21.84	24.13
Tptpmn	2,532	2,003,800.0	2,528,980.0	22.35	25.88
Tptpll	2,551	1,847,340.0	2,414,589.0	21.84	24.69
Tptpln	2,548	2,061,930.0	2,491,536.0	22.80	26.98

Calculated in Output DTN: MO0408EG831811.008, spreadsheet *Heat Conduction – Dry TPTPLL*: tab, "Properties" (Appendix G).

To cover a broad range of potential conditions, the analysis assumes two different alternative thermal states for the tuff matrix where (a) the matrix is saturated with water, and (b) the matrix is dry. Of course, these conditions are idealized, although they encompass the full range of possible states with respect to matrix water content.

C2. RESULTS OF MODEL SIMULATIONS

The results of the model are summarized in Table C-4.

Table C-4. Lookup Tables for Temperature (°C) of Intruded Drifts

Time after Intrusion	For an Intrusion into a Repository at 25°C		For an Intrusion into a Repository at 50°C		For an Intrusion into a Repository at 100°C		For an Intrusion into a Repository at 150°C		For an Intrusion into a Repository at 200°C	
Years	$T_{r=0m}$	$T_{r=3m}$	$T_{r=0m}$	$T_{r=3m}$	$T_{r=0m}$	$T_{r=3m}$	$T_{r=0m}$	$T_{r=3m}$	$T_{r=0m}$	$T_{r=3m}$
0	1,150	1,150	1,150	1,150	1,150	1,150	1,150	1,150	1,150	1,150
0.1	1003	608	1006	620	1012	644	1,019	668	1,026	692
0.2	740	479	749	494	768	524	786	553	804	583
0.3	564	399	577	416	603	449	629	483	655	516
0.4	452	342	467	360	498	396	529	432	560	468
0.5	377	299	394	318	428	356	462	394	497	431
0.6	323	266	341	286	378	325	415	364	452	403
0.7	283	240	303	260	341	300	380	341	418	381
0.8	253	218	273	239	313	281	353	322	392	363
0.9	229	201	249	222	290	264	331	306	372	349
1	209	186	230	208	272	251	314	293	356	336
2	119	112	142	136	187	182	233	228	279	274
3	87.7	84.9	111	109	158	156	206	203	253	251
4	72.1	70.5	96.0	94.5	144	142	192	190	240	238
5	62.7	61.7	86.8	85.8	135	134	183	183	232	231
6	56.4	55.7	80.7	80.0	129	129	178	177	227	226

Table C-4. Lookup Tables for Temperature (°C) of Intruded Drifts (Continued)

Time after Intrusion	For an Intrusion into a Repository at 25°C		For an Intrusion into a Repository at 50°C		For an Intrusion into a Repository at 100°C		For an Intrusion into a Repository at 150°C		For an Intrusion into a Repository at 200°C	
Years	$T_{r=0m}$	$T_{r=3m}$	$T_{r=0m}$	$T_{r=3m}$	$T_{r=0m}$	$T_{r=3m}$	$T_{r=0m}$	$T_{r=3m}$	$T_{r=0m}$	$T_{r=3m}$
7	51.9	51.4	76.3	75.8	125	125	174	173	223	222
8	48.6	48.2	73.0	72.6	122	122	171	171	220	220
9	45.9	45.6	70.5	70.2	120	119	169	168	218	217
10	43.9	43.6	68.4	68.2	118	117	167	167	216	216
20	34.4	34.4	59.2	59.2	109	109	158	158	208	208
30	31.3	31.3	56.1	56.1	106	106	156	156	205	205
40	29.7	29.7	54.6	54.6	104	104	154	154	204	204
50	28.8	28.8	53.7	53.7	104	104	153	153	203	203
60	28.1	28.1	53.1	53.1	103	103	153	153	203	203
70	27.7	27.7	52.6	52.6	103	103	152	152	202	202
80	27.4	27.4	52.3	52.3	102	102	152	152	202	202
90	27.1	27.1	52.0	52.0	102	102	152	152	202	202
100	26.9	26.9	51.8	51.8	102	102	152	152	202	202
Source file	*Heat Conduction - Dry TPTPLL*		*Heat Conduction - Dry TPTPLL 50C*		*Heat Conduction - Dry TPTPLL 100C*		*Heat Conduction - Dry TPTPLL 150C*		*Heat Conduction - Dry TPTPLL 200C*	

Source: Located in tab:"Lookup Tables" in named spreadsheets in output DTN: MO0408EG831811.008.

Output DTN: LA0702PADE01EG.001.

NOTE: $T_{r=0m}$ is the centerline temperature and $T_{r=3m}$ is the temperature at the edge of the drift.

The results of the analysis for different repository horizon rock units for a period of 100 years are presented in Figures C-1 and C-2 for wet and dry states of Tptpll. The results for the three other lithostratigraphic horizons are so similar to the Tptpll results that the differences cannot be distinguished graphically. Only the results for Tptpll are shown.

The calculations show that initial temperatures near the drift are high and attenuate rapidly into the surrounding tuff. Outside the drift, peak temperatures are always less than magmatic temperatures and are not reached until sufficient time has passed to accommodate conductive heating of the wall rock. For example, the peak temperature at a 10-m radius is less than boiling, and is attained only after one year for both conditions of saturation. Under end member saturations, the temperature reaches near ambient conditions of approximately 30°C at drift center in approximately 30 yr (Figures C-1 and C-2). The analysis also shows that the maximum temperature rise in an adjacent, unaffected drift is small (less than 10°C), and the rock provides an effective thermal barrier to the impacts of heat transfer from magmatic intrusion.

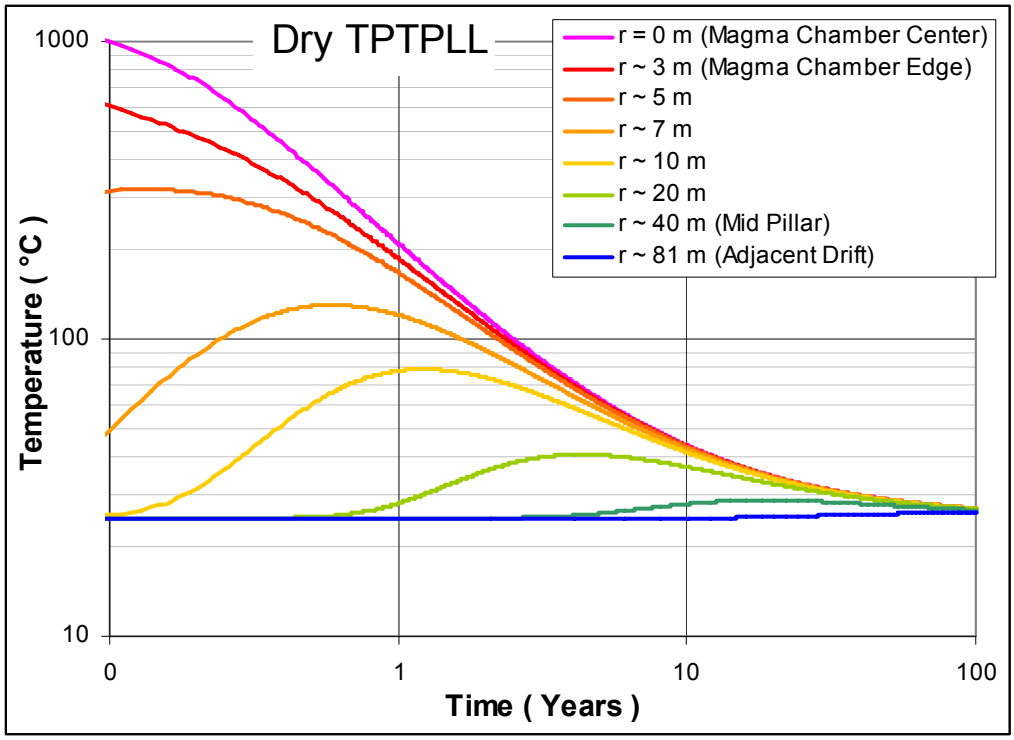

Output DTN: MO0408EG831811.008; file *MO0408EG831811.008.zip\Heat Conduction - Dry TPTPLL.xls*.

Figure C-1. Heat Conduction from Magma Flow for Dry Tptpll

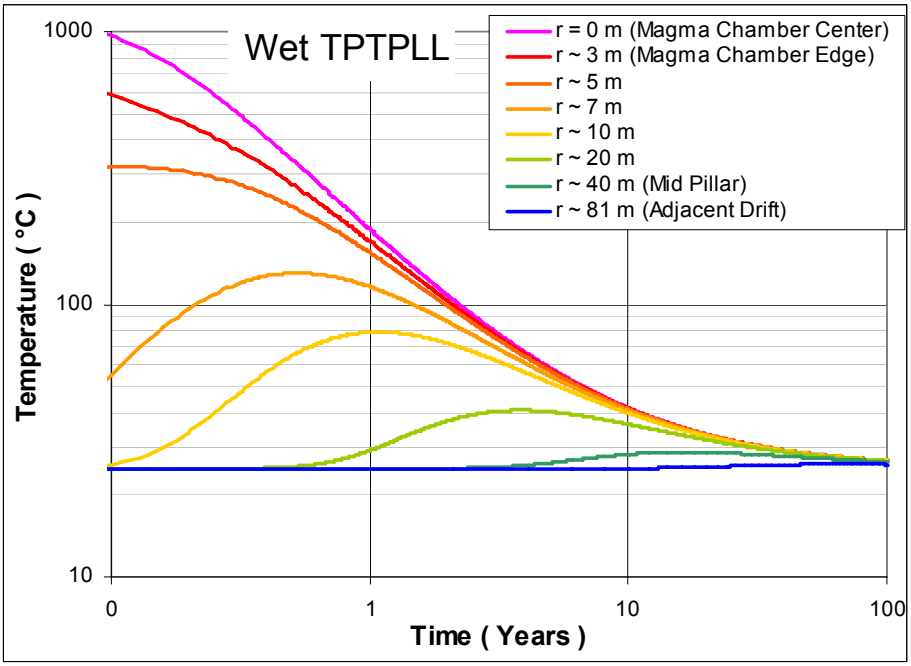

Output DTN: MO0408EG831811.008; file *MO0408EG831811.008.zip\Heat Conduction - Wet TPTPLL.xls*.

Figure C-2. Heat Conduction from Magma Flow for Wet Tptpll

This conclusion of minimal thermal impact on unintruded drifts is based on a conceptualization of the filling of a single drift with magma, when, in fact, a dike may intersect multiple drifts, raising the potential for the development of overlapping thermal aureoles. However, it can be easily shown that, for a multiple-drift-intersection scenario, the volume of intersected drifts is less than 6% of the smallest rectangular volume that can contain those drifts. For example, 10 drifts contain the following volume:

$$V = \pi r^2 L$$
$$V = \pi \cdot 2.75^2 \cdot L \qquad \text{(Eq. C-14)}$$

V = volume of a single drift [m^3] = 23.76 L m^3
R = drift radius [m] = 2.75 m (SNL 2007 [DIRS 179466])
L = drift length [m]

Thus, the volume of n drifts is 23.76 n L m^3.

The rectangular volume containing these drifts is:

$$V_1 = 81nL(2R) \qquad \text{(Eq. C-15)}$$

V_n = rectangular volume containing n drifts [m^3]
81 = drift spacing [m] (SNL 2007 [DIRS 179466])
n = number of drifts.

Thus: $\frac{V}{V_1} \cong 5.3\%$.

The additive thermal impact of multiple drift intersections is therefore necessarily small, because the surrounding rock mass presents an enormous volumetric heat sink. Therefore, the spatial and temporal heat-conduction simulations and analyses suggest that the waste packages in unintruded emplacement drifts would not be affected by the heat conduction from magma intruded into adjacent emplacement drifts.

C3. SENSITIVITY

Sensitivity to Latent Heat Effects

The latent heat generated by crystallization of cooling magma can be significant, lengthening the time required to cool a drift/rockwall system back to ambient conditions. Latent heat is liberated during crystallization of the magma; thus, its effects are most pronounced at early times while the magma is still above its solidus.

A simple way to simulate latent heat is by increasing the initial temperature of the magma. In this section, cooling calculations are repeated by raising the initial magmatic temperature by 100°C to 1,250°C to roughly account for the latent heat. The results are compared with the base case and presented in Figures C-3 and C-4. The figures show little change in the results. At the center of the drift, the temperature falls below 100°C at 2.5 yr, or at 2.7 yr if the effects of latent

heat are included. At the drift wall, the temperature falls below 100°C at 2.5 yr, or at 2.6 yr if the effects of latent heat are approximated. As shown in Section 6.4.7.2, a more conservative conceptualization of latent heat effects (i.e., higher latent heat content) shows that cooling to 100°C is accomplished within 2 yr to 5 yr. Considering the geologic timeframes of interest and the inherent uncertainty in these calculations, these differences are negligible.

Sensitivity to Saturation

Ventilation Model and Analysis Report (BSC 2004 ([DIRS 169862], Section 8) shows that the change in temperature based on the saturation of the matrix is less than 5%; therefore, the effects of enhanced vapor diffusion will be minimal. Convection in a saturated matrix is also a consideration but is expected to be minimal based on the low porosity of the rock, the rapid attenuation of temperatures over time, and the sustainability of high temperatures only over short distances.

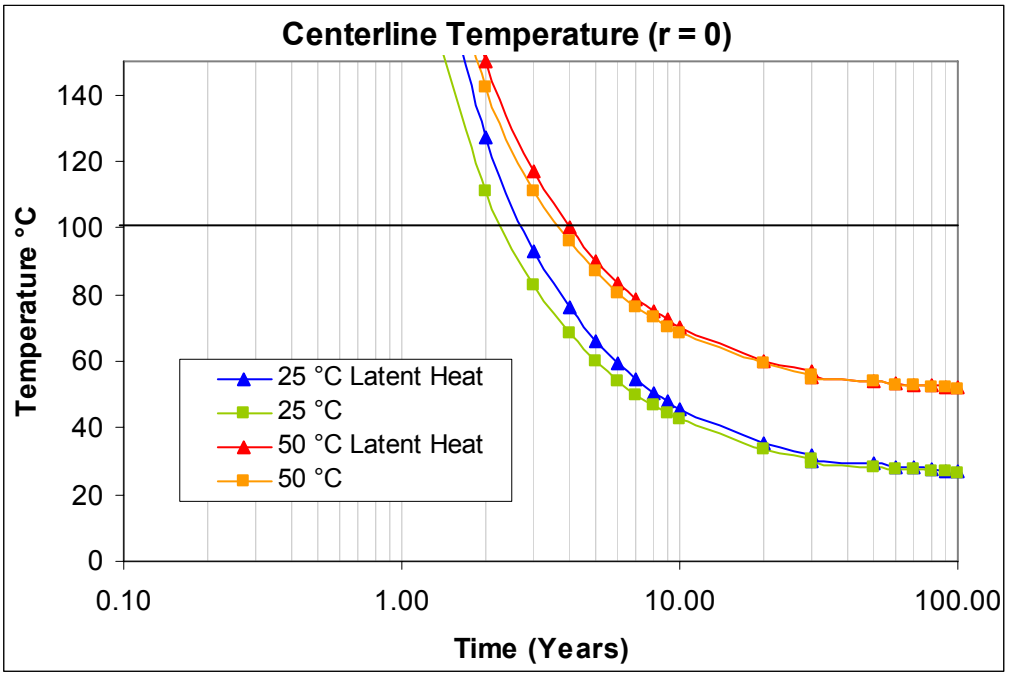

Output DTN: MO0408EG831811.008; file *MO0408EG831811.008.zip\1200 Heat Conduction - Dry TPTPLL.xls*.

Figure C-3. Latent Heat Effect at Drift Centerline

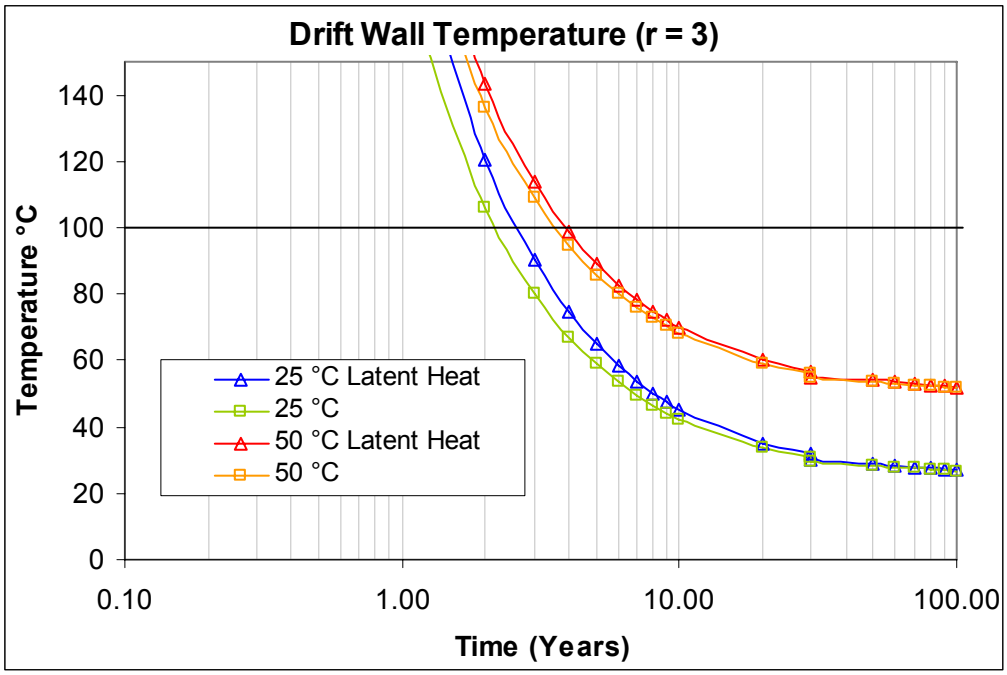

Output DTN: MO0408EG831811.008; file *MO0408EG831811.008.zip\1200 Heat Conduction - Dry TPTPLL.xls*.

Figure C-4. Latent Heat Effect at Drift Wall

C4 UNCERTAINTY ANALYSIS OF PEAK TEMPERATURE IN THE ROCK MASS AT A DISTANCE OF 10 M

The generation of system moments allows a determination of the relative importance of each component variable by examining the magnitude of its partial derivative. Hahn and Shapiro (1967 [DIRS 146529], p. 229) provide an expression for the mean system performance (for example, the maximum temperature at a radius of 10 m from the drift with magma) through the expression under the assumption that the parameters are independent for the composite model:

$$E(z) = h((E(x_1), E(x_2), ...E(x_n)) + \frac{1}{2} \cdot \sum_{i=1}^{n} \frac{\partial^2 h}{\partial x_i^2} \cdot Var(x_i) \qquad \text{(Eq. C-16)}$$

where

$E(z)$ = expectation for the system performance

$E(x_i)$ = expectation of the component variables

$x_i ... x_n$ = component variables

$h()$ = functional relationship between the component variables and the system performance

Hahn and Shapiro (1967 [DIRS 146529], p. 231) present the following relationship for the variance in which the higher order moments are not used:

$$Var(z) = \sum_{i=1}^{n} \left(\frac{\partial h}{\partial x_i} \right)^2 \cdot Var(x_i) \qquad \text{(Eq. C-17)}$$

This relation is frequently a satisfactory approximation to calculating the variance for independent parameters.

The peak temperature at a radius of 10 m for the constant heat-content process depends on the rock-mass thermal conductivity and thermal diffusivity; these, in turn, depend on the solids thermal conductivity; the solids specific-heat capacity; the solids grain density; the matrix porosity; the matrix saturation; and the lithophysal porosity. This set of parameters is taken as the independent set of parameters.

Table C-5 presents the evaluation of the system variance. The values for mean and standard deviation were obtained from *Ventilation Model and Analysis Report* (BSC 2004 [DIRS 169862], Section 6.11).

Table C-5. Sensitivity of Uncertainty in Input Parameters (with Standard Deviation for Use in Delta Method)

Input/Design Parameter	Mean Value	Standard Deviation	Rock Mass Thermal Conductivity[a]		Rock Mass Thermal Diffusivity[a]		Peak Temperature[a]			Percent Contribution[a]
			Plus	Minus	Plus	Minus	Plus	Minus	Variance	
Solids Thermal Conductivity (W/(m·K))	2.603	0.3413	2.02	1.62	26.68	21.48	78.17	78.12	5.55×10^{-04}	0%
Solids Grain Density (kg m^3)	2,593	138	1.82	1.82	23.14	25.16	78.13	78.15	8.54×10^{-05}	0%
Solids Specific Heat Capacity (J/(kg·K))	930	170	1.82	1.82	21.09	28.15	78.11	78.16	4.50×10^{-04}	0%
Matrix Porosity	14.86%	3.40%	1.74	1.91	22.59	25.79	78.13	78.16	2.08×10^{-04}	0%
Matrix Saturation	90.50%	10%	1.89	1.76	24.39	23.82	78.14	78.14	5.91×10^{-06}	0%
Lithophysal Porosity	8.83%	5.40%	1.72	1.93	24.13	24.09	78.14	78.14	1.92×10^{-08}	0%
Initial Temperature (°C)*	1,150	35.51	1.82	1.82	24.11	24.11	73.23	79.04	2.81	100%
								Sum	2.81	100%
								Standard Deviation	1.68	

[a] Calculated in *Heat Conduction – Uncertainty Analysis.xls* in output DTN: MO0408EG831811.008.

The method of moments provides information as to the source of uncertainty from the individual variables. In Equation C-16, the variance of each individual variable, x_i, is multiplied by the square of the derivative of the system function for that parameter. The square of the derivative represents the sensitivity of the system variance to the individual parameter. If the sensitivity, and the variance to an individual parameter are large, then the system variance is dominated by

this contribution. Conversely, if the sensitivity and the variance to an individual parameter are small, then the system variance is not influenced by this individual contribution.

Table C-5 represents the results of the analysis using the method of generating system moments. The analysis is performed by calculating the first-order partial derivatives of temperature to the solids thermal conductivity (k_s); the solids specific heat capacity (C_p); the solids grain density (ρ_g); matrix porosity (ϕ_m); the matrix saturation (S_m); and the lithophysal porosity (ϕ_l). Each component is perturbed from its mean value by plus or minus one standard deviation while the other components are evaluated at their mean value. The rock mass thermal conductivity and the thermal diffusivity are then calculated based upon the relations for thermal conductivity and thermal diffusivity presented previously. The finite-difference calculations are then performed, and the peak temperature at a radius of 10 m is evaluated for the parameters. The first-order partial derivatives are approximated for the mean values plus or minus one standard deviation for each component and then substituted into Equation C-17.

Figure C-5 shows that variations in key inputs other than initial temperature result in a shift in the time when the peak temperature occurs, but the actual peak temperature remains the same.

The contributions to variance are then calculated for each component as the product of the sensitivity and the variance. The contributions are then summed. The analysis provides information on the percent contributions to system variance from each of the component variables. The analysis suggests that the principal source of uncertainty is the initial temperature (100% of the uncertainty). The variance caused by the uncertainty of the initial temperature should be used as the uncertainty of the output temperatures, which is ±3°C.

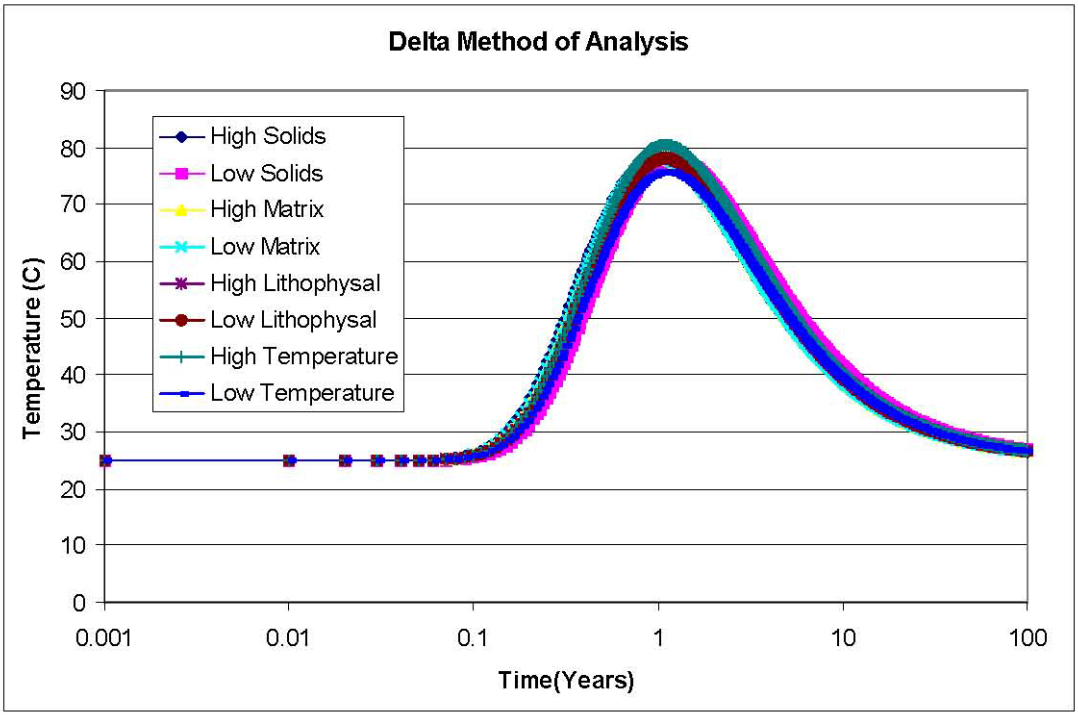

Output DTN: MO0408EG831811.008; file *MO0408EG831811.008.zip\Heat Conduction - Uncertainty Analysis.xls*.

Figure C-5. Peak Temperatures for Variations in Key Inputs

APPENDIX D
ALTERNATIVE ANALYTICAL SOLUTION TO HEAT FLOW

APPENDIX D
ALTERNATIVE ANALYTICAL SOLUTION TO HEAT FLOW

D1. DEFINITION OF THE PROBLEM

Consider a drift 5.5 m in diameter and 637-m long created in tuff at a depth of 300 m below the surface and where the ambient tuff temperature is 30°C. If that drift were to be instantaneously filled with basaltic magma at a temperature of 1150°C, the tuff surrounding the drift would begin to heat up as the magma cooled. The temperature profile through the drift and surrounding rock evolves with time.

Analysis of energy conservation can only provide exact solutions for thermal evolution when simplifying assumptions are made about the effects of dimensionality, latent heat, and contrasting thermal properties. These simplifying assumptions are necessary to make analytical solutions bear any resemblance to the problem, but the results must be regarded as approximate.

The analytical theory described below derives a solution first in Cartesian coordinates, treating the drift as a slab, and then in cylindrical coordinates, treating the drift as an infinitely long cylinder. Because solutions for the effects of latent heat are only valid for cooling times up to the point of complete solidification of the magma, late-time solutions must employ an approximate solution mated to the early time solution. To these results are added the effects of contrasting thermal properties between the magma and tuff.

Calculations based on these solutions were performed in the Microsoft Excel™ 2000 (SP 3) spreadsheet file: *Analytical Solutions of Heat Flow.xls*, which is documented in Scientific Notebook SN-LANL-SCI-279-V1 (Gaffney 2003 [DIRS 163631], pp. 17-30) and in output DTN: LA0307EG831811.001.[1] These results are shown for radial distances from the drift to 40.5 m (half of the nominal spacing between parallel drifts) and are discussed and shown in Figure D-1 through Figure D-6.

[1] IRAN #4837-A was generated to downgrade the status of output DTN: LA0307EG831811.001 to "unqualified" because of the unqualified TIC sources. Although not required, because this appendix is for corroboration only, the sources of the equations cited in this appendix are validated as follows: Jaeger (1958 [DIRS 163630]) is established fact on the basis that Prof. Jaeger's paper was the first to develop an approximate solution for heat flow within a crystallizing dike to include the approximate effects of latent heat on the crystallization; Delaney (1987 [DIRS 102776]) is a widely cited work on heat loss from dikes and sills and is particularly useful for its development of a solution with material properties contrasts, in addition his approximation for latent heat is the same as that used in the base model of Appendix A; *Geodynamics, Applications of Continuum Physics to Geological Problems* (Turcotte and Schubert 1982 [DIRS 139651]) is the standard textbook in the application of continuum physics to geological problems.

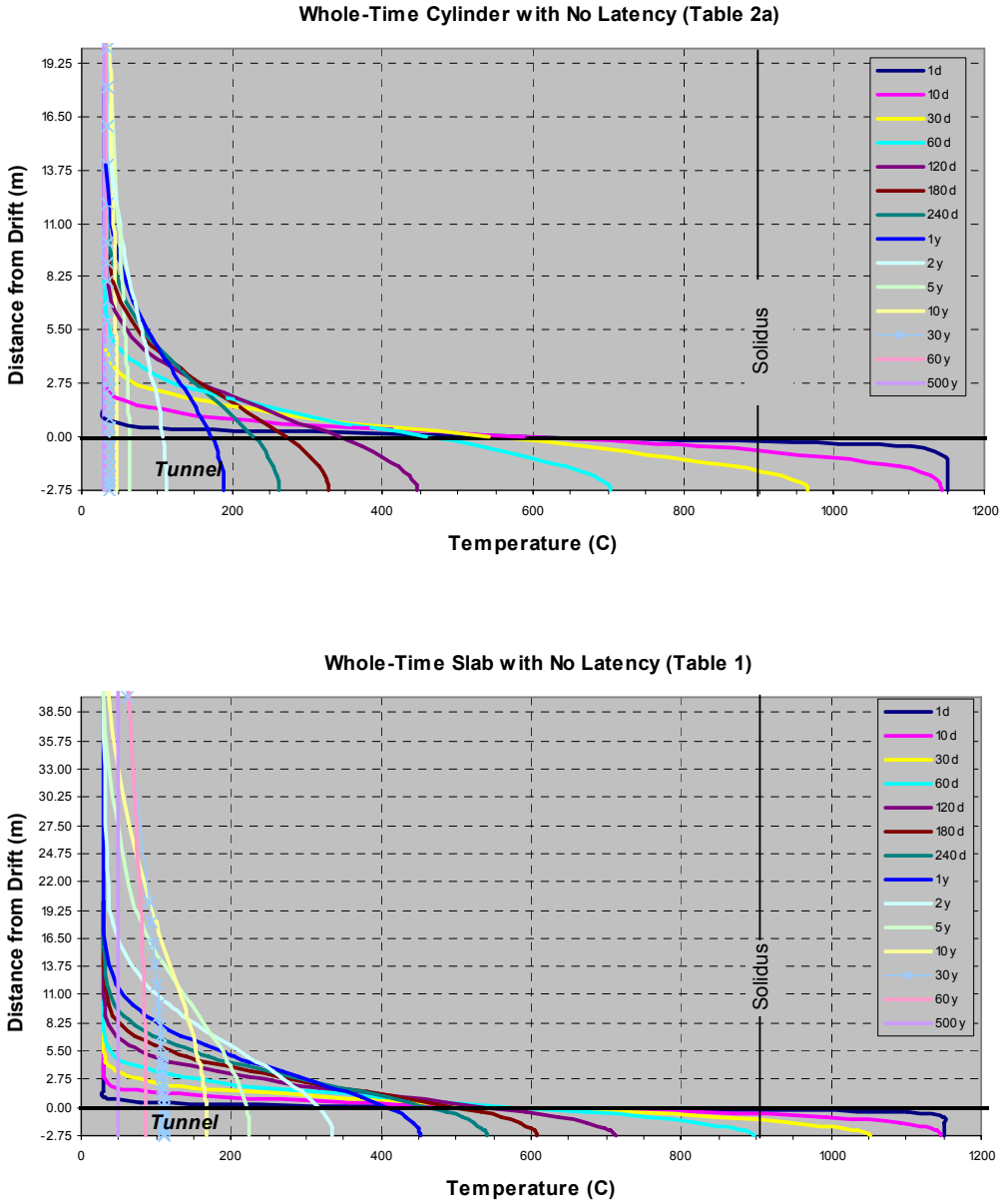

Output DTN: LA0307EG831811.001; *file Heat_Flow_Calculations\Heat_Flow2\Analytical Solutions of Heat Flow.xls,* tabs: "Chart1" & "Chart2."

NOTES: Calculations are for a drift in tuff at an initial temperature of 30°C and filled with basaltic magma at an initial temperature of 1,150°C. This whole-time solution does not account for thermal property contrasts and the effects of latent heat.

Figure D-1. Plot of Calculated Temperature Profiles for Various Cooling Times Comparing Results for a One-dimensional Slab-Like Geometry (upper plot) With Results for a Two-dimensional Cylindrical Drift Geometry (lower plot)

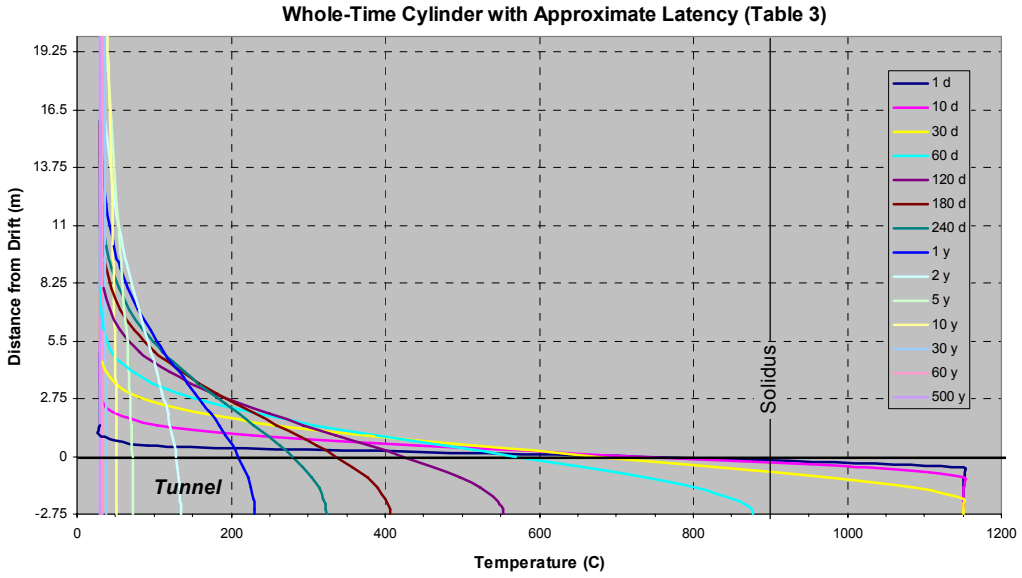

Output DTN: LA0307EG831811.001; file *Heat_Flow_Calculations\Heat_Flow2\Analytical Solutions of Heat Flow.xls,* tab: "Chart3."

Figure D-2. Plot of Calculated Whole-Time Temperature Profiles for Various Cooling Times Assuming a Cylindrical Drift Geometry and Showing the Approximate Effect of Latent Heat

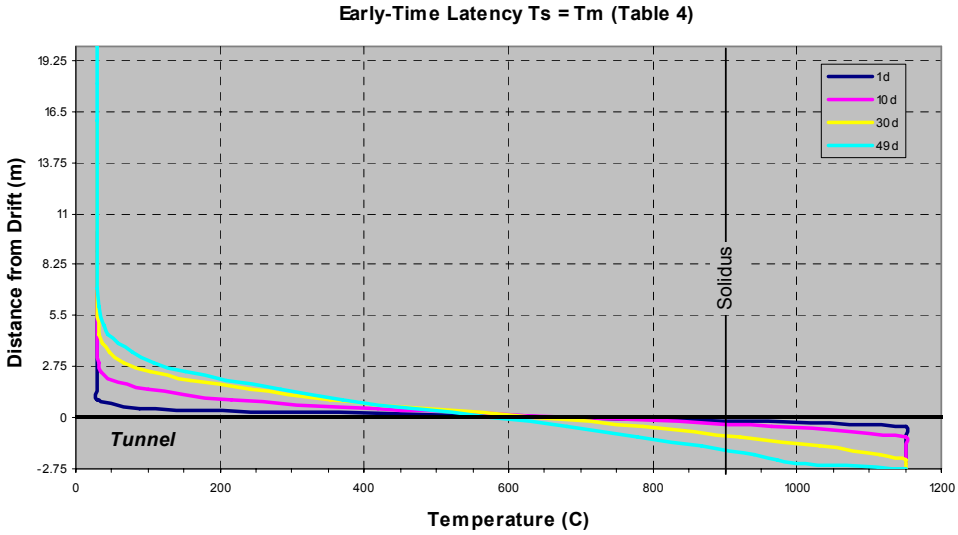

Output DTN: LA0307EG831811.001; file *Heat_Flow_Calculations\Heat_Flow2\Analytical Solutions of Heat Flow.xls*, tab: "Chart4."

NOTES: These calculations are valid only for early times when the temperature of the magma at the drift center is above the assumed solidus at 900°C.

Figure D-3. Plot of Calculated Temperature Profiles for Various Cooling Times with Latency Modeled as Occurring at a Specific Temperature (Ts = Tm)

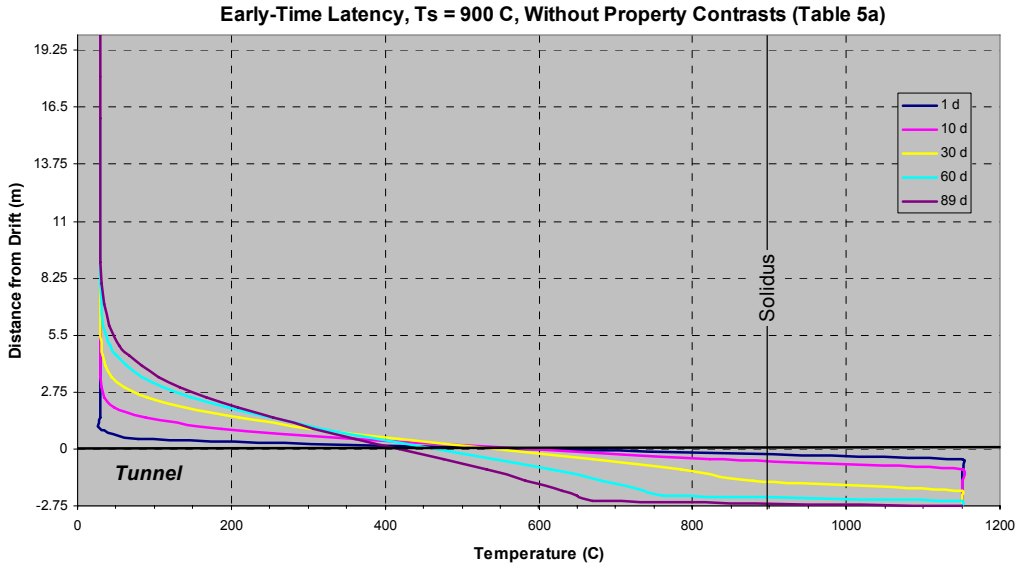

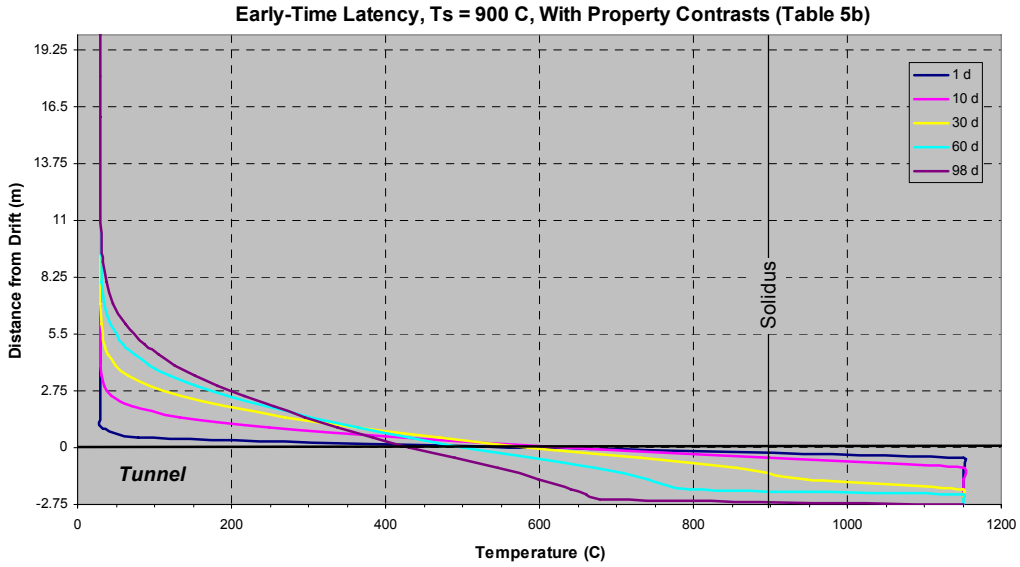

Output DTN: LA0307EG831811.001; file *Heat_Flow_Calculations\Heat_Flow2\Analytical Solutions of Heat Flow.xls*, tabs: “Chart5” & “Chart6.”

NOTES: These calculations are valid only for early times when the temperature of the magma at the drift center is above the assumed solidus at 900°C.

Figure D-4. Plot of Calculated Temperature Profiles for Various Cooling Times with Latent Heat, Calculated for T_s = 900°C and for the Cases With (lower panel) and Without (upper panel) Property Contrasts Between Magma and Tuff

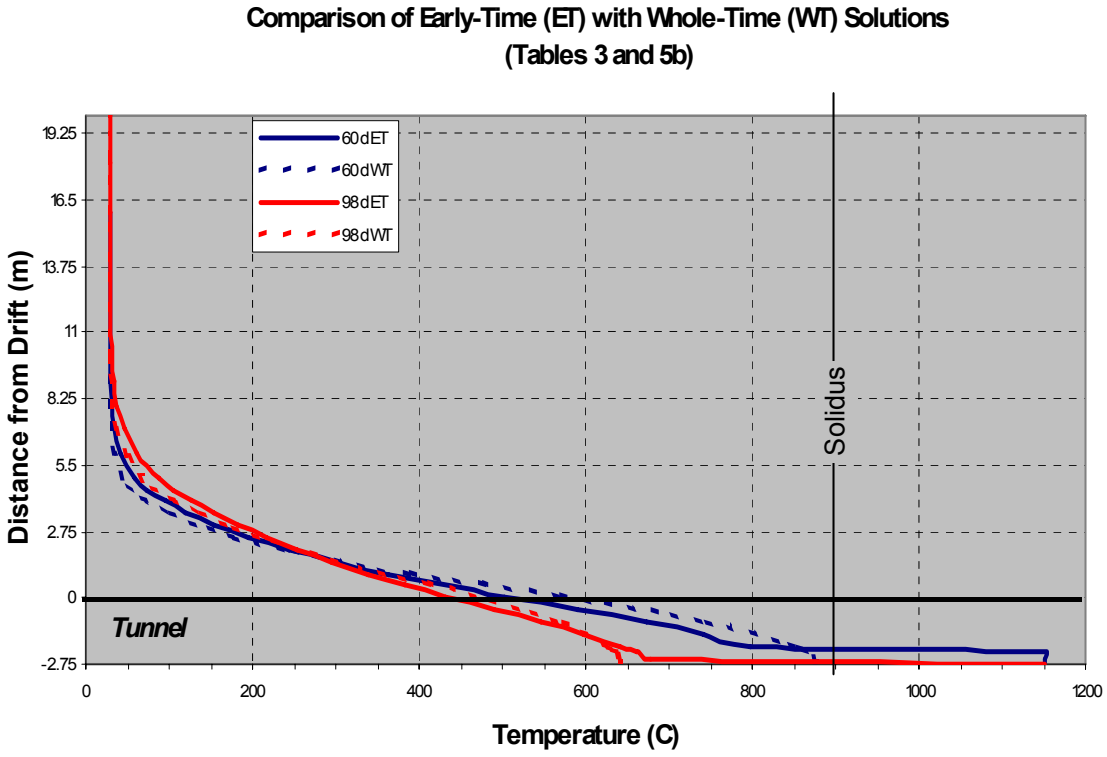

Output DTN: LA0307EG831811.001; file Heat_Flow_Calculations\Heat_Flow2*Analytical Solutions of Heat Flow.xls*, tab: "Chart7."

NOTE: Dashed curves are the whole-time solutions from Figure D-2; solid curves are early-time solutions from Figure D-4.

Figure D-5. Plot of Calculated Temperature Profiles at 60 and 98 Days Comparing the Whole-Time Solutions with Early-Time Solutions

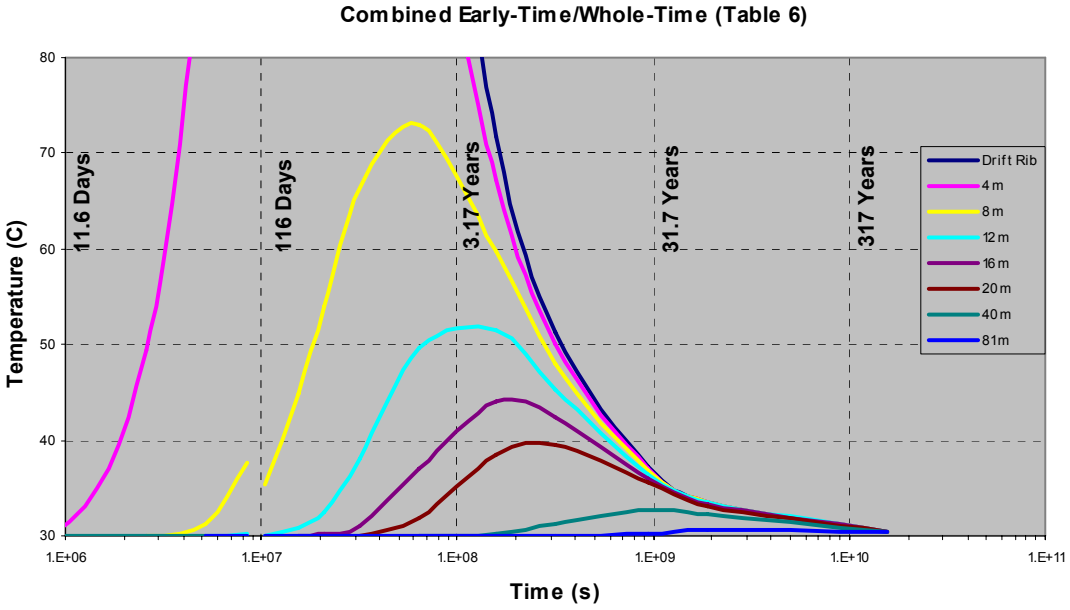

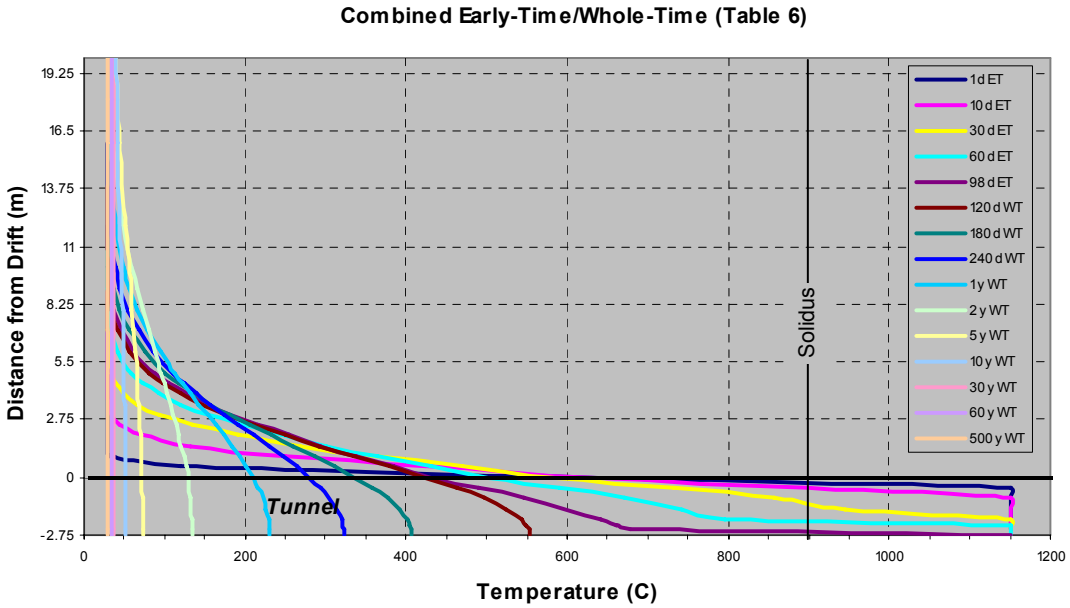

Source: Turcotte and Schubert 1982 [DIRS 139651], pp. 168 to 170, early-time latency; Delany (1987 [DIRS 102776]), late-time results using modified method.

Output DTN: LA0307EG831811.001; file Heat_Flow_Calculations\Heat_Flow2*Analytical Solutions of Heat Flow.xls*, tab: "Chart8."

Figure D-6. Whole-Time Solution Combining the Results for Early-Time Latency With Those Late-Time Results

D2. MATERIAL PROPERTY INPUTS

For the Yucca Mountain Project problem, the thermal properties shown in Table D-1 are applied, and an initial tuff temperature of 30°C without any thermal gradient is assumed. Although values are given for density (ρ), specific heat (c), and thermal conductivity (k), those properties always appear in the solutions in combination in the form of the thermal diffusivity ($\kappa = k/\rho c$). Further, for the simplest solutions presented, it is assumed that the diffusivities of the magma and the host rock are equal with a value of the mean diffusivity of the two rocks used by the Igneous Consequences Peer Review Panel in their final report (Detournay et al. 2003 [DIRS 169660]). The Panel's sources for these numbers are given in Table 4-1. For more detailed solutions presented, thermal property contrasts between the magma and the tuff are included, and these set the diffusivities of the magma and tuff to 0.3×10^{-6} m^2 s^{-1} and 0.7×10^{-6} m^2 s^{-1}, respectively.

The other property inputs affecting the results of this section are the temperatures of the magma and the host rock and the latent heat of solidification of the magma. The magma temperature used is a round number that is about 0.3% above the value listed for a magma with 0.5% water in *Characterize Eruptive Processes at Yucca Mountain, Nevada* (SNL 2007 [DIRS 174260], Table 6-5]. The host rock temperature is a round number close to room temperature. The effect of these two round-number approximations will be less than 2% difference at early times, and the percentage error will decrease with time. The latent heat of solidification is the value used by the Igneous Consequences Peer Review Panel (Detournay et al. 2003 [DIRS 169660]).

Table D-1. Thermal Properties of Magma and Tuff

Property	Value
Magma	
Temperature, T_m	1,150°C
Latent heat, Λ	350 kJ/kg
Tuff	
Temperature, T	30°C
Average	
Thermal diffusivity, κ	0.5×10^{-6} m^2 s^{-1}

Source: Detournay et al. 2003 [DIRS 169660], Table 1-2 (latent heat and thermal diffusivity).

The solutions given below are sensitive to magma temperature; an approximately 10% variation in T_m produces a 10% variation in T near the magma-tuff contact for cooling times up to 1 year but falling to approximately 3% after 30 years. The solutions are less sensitive to diffusivity, with a 10% variation in κ producing only approximately 1% to approximately 6% change in T near the magma-tuff contact during the first year or so of cooling.

D3. DERIVATION OF EQUATIONS

One-Dimensional Cartesian Equations–Assuming that the magma is emplaced in the drift instantaneously and that it experiences no further movement nor loss or gain of mass, the cooling and heat transfer is governed by the conservation of energy:

$$\frac{\partial T}{\partial t} = \nabla \cdot (\kappa \nabla T) - \mathbf{u} \cdot \nabla T + q \qquad \text{(Eq. D-1)}$$

where:

T = temperature
t = time
κ = thermal diffusivity
u = the magma convective velocity vector
q = represents heat sources and sinks.

This equation describes the change of temperature with time (left-hand side), with the right-hand side summing the effects of thermal conductivity (first term) and thermal convection (second term) with heat sources and sinks (third term). Given the height of the drift as 5.5 m, one may show by consideration of the magnitude of the thermal Rayleigh number that magma convection will not occur within the drift. No heat sinks or sources other than the latent heat of magma crystallization are considered.

To start the analysis, any latent heat released during magma crystallization is ignored and there are no thermal property contrasts between the magma and tuff. First, consider the case for one-dimensional Cartesian coordinates, such that the drift is represented by a slab of a finite thickness but of infinite length and width. These simplifications allow a one-dimensional expression of Equation D-1 as:

$$\frac{\partial T}{\partial t} = \kappa \frac{\partial^2 T}{\partial x^2} \qquad \text{(Eq. D-2)}$$

for which x represents distance measured perpendicular to the surface of the slab. An analytical solution of Equation D-2 for geological systems has most commonly been achieved by using self-similarity solutions (Carslaw and Jaeger 1959 [DIRS 100968]) in which temperature is expressed non-dimensionally as θ:

$$\theta = \frac{T - T_0}{T_m - T_0} \qquad \text{(Eq. D-3)}$$

for which subscripts m and 0 refer to the initial temperature of the magma and tuff, respectively. A single similarity variable, η, that combines both temporal and spatial effects can be defined as the ratio of distance to twice the characteristic thermal diffusion distance:

$$\eta = \frac{x}{2\sqrt{\kappa t}} \qquad \text{(Eq. D-4)}$$

Rewriting Equation D-2 using non-dimensional temperature, θ, and the similarity variable, η, requires the derivation of θ with respect to t and x in terms of η and reduces Equation D-2 from a partial differential equation to an ordinary differential equation:

$$-\eta\left[\frac{d\theta}{d\eta}\right]=\frac{1}{2}\frac{d^2\theta}{d\eta^2} \quad \text{(Eq. D-5)}$$

To solve Equation D-5, the variable, φ, may be defined as $d\theta/d\eta$ so that the equation becomes:

$$-\eta d\eta=\frac{1}{2}\frac{d\varphi}{\varphi} \quad \text{(Eq. D-6)}$$

With integration and exponentiation of Equation D-6, Equation D-7 shows:

$$\frac{d\theta}{d\eta}=ce^{-\eta^2} \quad \text{(Eq. D-7)}$$

in which c is a constant of integration. Considering the boundary between a magma and rock where $\eta = 0$ and $\theta(0) \equiv 1/2$, integration of Equation D-7 yields:

$$\theta=c\int_0^{\eta}e^{-n^2}dn+1/2 \quad \text{and} \quad \theta=c\int_{-\eta}^{0}e^{-n^2}dn-1/2, \quad \text{(Eq. D-8)}$$

for which n is an arbitrary integration variable. For the boundary condition $\theta(\infty) = 0$:

$$0=c\int_0^{\infty}e^{-n^2}dn+1/2 \quad \text{(Eq. D-9a)}$$

and for $\theta(-\infty) = 0$:

$$0=c\int_{-\infty}^{0}e^{-n^2}dn-1/2\,. \quad \text{(Eq. D-9b)}$$

For $n \geq 0$, the definite integral in Equation D-9a is equal to $\pi^{1/2}/2$, and the constant $c = -(2/\pi^{1/2})/2$, so that:

$$\theta=1/2-\left(\frac{1}{2}\right)\frac{2}{\sqrt{\pi}}\int_0^{\eta}e^{-z^2}dz=1/2-\left(\frac{1}{2}\right)\mathrm{erf}(\eta)=\left(\frac{1}{2}\right)\left[1-\mathrm{erf}\left(\frac{x}{2\sqrt{\kappa t}}\right)\right] \quad \text{(Eq. D-10a)}$$

For $n \leq 0$, $c = (2/\pi^{1/2})/2$ and recalling that $\mathrm{erf}(-\eta) = -\mathrm{erf}(\eta)$, the solution is:

$$\theta=-1/2+\left(\frac{1}{2}\right)\frac{2}{\sqrt{\pi}}\int_{-\eta}^{0}e^{-n^2}dz=-1/2-\left(\frac{1}{2}\right)\mathrm{erf}(-\eta)=\left(\frac{1}{2}\right)\left[\mathrm{erf}\left(\frac{x}{2\sqrt{\kappa t}}\right)-1\right] \quad \text{(Eq. D-10b)}$$

Jaeger (1968 [DIRS 163630], p. 54) defines a problem for cooling of a sheet-like magma body of thickness 2*a*, intruded beneath deep cover, for which the *x*-axis origin is defined at the center of the sheet. For this problem, θ must be evaluated away from both surfaces of the sheet (*x*-*a* and *x*+*a*), and because the solution of Equations D-10a and D-10b are linear, they can be summed:

$$\theta = \frac{1}{2}\left[1-\operatorname{erf}\left(\frac{x-a}{2\sqrt{\kappa t}}\right)\right]+\frac{1}{2}\left[\operatorname{erf}\left(\frac{x+a}{2\sqrt{\kappa t}}\right)-1\right]=\frac{1}{2}\left[\operatorname{erf}\left(\frac{x+a}{2\sqrt{\kappa t}}\right)-\operatorname{erf}\left(\frac{x-a}{2\sqrt{\kappa t}}\right)\right] \quad \text{(Eq. D-11)}$$

The above equations are valid only in a one-dimensional Cartesian system, which will provide a good temperature solution for the case of a sill but which is not adequate for the roughly cylindrical geometry of a magma-filled drift.

One-Dimensional Cylindrical Equations--This section derives the analysis for a drift of circular cross-section and finite length. Consider the 3-D form of Equation D-2, expressed in Cartesian coordinates:

$$\frac{\partial T}{\partial t} = \kappa\left(\frac{\partial^2 T}{\partial x^2}+\frac{\partial^2 T}{\partial y^2}+\frac{\partial^2 T}{\partial z^2}\right). \quad \text{(Eq. D-12)}$$

Carslaw and Jaeger (1959 [DIRS 100968], p. 56, Section 2.2(10)) show that the solution to Equation D-12 is similar to Equation D-11 but with added terms for the extra dimensions:

$$\theta = \left[\frac{1}{2}\left(\operatorname{erf}\frac{x+a}{2\sqrt{\kappa t}}-\operatorname{erf}\frac{x-a}{2\sqrt{\kappa t}}\right)\right]\left[\frac{1}{2}\left(\operatorname{erf}\frac{y+b}{2\sqrt{\kappa t}}-\operatorname{erf}\frac{y-b}{2\sqrt{\kappa t}}\right)\right]\left[\frac{1}{2}\left(\operatorname{erf}\frac{z+c}{2\sqrt{\kappa t}}-\operatorname{erf}\frac{z-c}{2\sqrt{\kappa t}}\right)\right] \quad \text{(Eq. D-13)}$$

for which

a = the half-height
b = the half-width
c = the half-length of the drift.

The drift cross section is best represented as a circle. Because in three dimensions the drift is a cylinder, Equation D-12 can be simplified by using cylindrical coordinates with radial distance, *r*, azimuth ϕ, and length, *z*:

$$\frac{\partial T}{\partial t} = \kappa\left(\frac{\partial^2 T}{\partial r^2}+\frac{1}{r}\frac{\partial T}{\partial r}+\frac{1}{r^2}\frac{\partial^2 T}{\partial \phi^2}+\frac{\partial^2 T}{\partial z^2}\right) \quad \text{(Eq. D-14)}$$

Assuming that magma temperature within the drift is homogeneous with azimuth then $\partial^2 T/\partial\phi^2 = 0$. Because the drift half-length *c* is more than 100 times greater than its radius *a*, $\partial^2 T/\partial z^2$ vanishes for radial solutions midway through the drift, where *z* = 0 at all times earlier than the *z*-coordinate diffusive time. This time can be easily determined for the value of the last term of Equation D-13, which is within 0.001% of unity for erf(*n*), where $n \geq \pi$. Letting $n \geq c/(2(\kappa t)^{1/2}) \geq \pi$, then $t \leq c^2/4\pi^2\kappa$ or ~200 years for *c* = 318.5 m and κ = 0.0000004 m^2/s. In

fact, even after 500 years of cooling, the *z*-component accounts for less than a half of a percent. With this consideration, Equation D-14 is suitably expressed as:

$$\frac{\partial T}{\partial t} = \kappa\left(\frac{\partial^2 T}{\partial r^2} + \frac{\partial T}{r\partial r}\right). \qquad \text{(Eq. D-15)}$$

From Carslaw and Jaeger (1959 [DIRS 100968], Section 2.2(9)), the solution of Equation D-15 is that of an infinite cylinder where ω = the cylinder radius and Carslaw and Jaeger's *x*-coordinate is replaced by *r* and their *y*-coordinate is set to zero ($z = 0$):

$$\theta = \frac{1}{2}\left(\operatorname{erf}\frac{r+\omega}{2\sqrt{\kappa t}} - \operatorname{erf}\frac{r-\omega}{2\sqrt{\kappa t}}\right)\left(\operatorname{erf}\frac{\omega}{2\sqrt{\kappa t}}\right) \qquad \text{(Eq. D-16)}$$

The above solutions assume that no latent heat is released during magma cooling and that the magma and tuff do not display thermal property contrasts (i.e., $\kappa_m/\kappa_r = k_m/k_r = 1$), where *k* is thermal conductivity ($k = \rho c \kappa$), ρ is density, *c* is heat capacity, and subscript *m* and *r* refer to magma and tuff, respectively.

The average diffusivity, κ, is applied to the following calculations based on Equations D-11 and D-16. Results using values from Tables 1 and 2a of the spreadsheet *Analytical Solutions of Heat Flow.xls*, output DTN: LA0307EG831811.001, are shown in plots of *T* versus *x* at various times (Figure D-1) for both slab-like and cylindrical geometries. The former is appropriate for dike or sill geometries; the latter is appropriate for application to drift geometry.

D4. THERMAL PROPERTY CONTRASTS AND LATENT HEAT

Addressing the issue of contrasting thermal properties between the magma and host rock, Delaney (1987 [DIRS 102776]) shows the initial contact temperature θ_{ci} as:

$$\theta_{ci} = \frac{k_m / k_t}{k_m / k_t + \sqrt{\kappa_m / \kappa_t}} \qquad \text{(Eq. D-17)}$$

where the subscripts *m* and *t* refer to the magma and tuff, respectively. Using the values listed under the heading "Assumed Thermal Properties" in Gaffney's scientific notebook (2003 [DIRS 163631], p. 17) and in output DTN: LA0307EG831811.001, then $\theta_{ci} \approx 0.54$ and the initial contact temperature is approximately 630°C, which is approximately 10°C (about 7%) higher than that predicted by no thermal-property contrasts. It must be recognized that conductivities generally rise with falling temperature; for example, at 30°C, k_m may reach 2 W m^{-1} K^{-1} or more. However, Delaney (1987 [DIRS 102776]) finds that, although thermal-property contrasts affect the maximum temperature achieved in the host rock (tuff in this case), they do not have a large influence over solutions at late times. In fact, Delaney (1987 [DIRS 102776]) points out that most workers do not consider thermal-property contrasts.

The effect of latent heat (Λ) production is not negligible, but, as Delaney (1987 [DIRS 102776]) points out, there is no analytically exact method to include its effects. Assuming Λ = 350 kJ/kg, a first approximation of its effect is to find an effective initial magma temperature T^*_m by adding to the temperature of the magma the amount Λ/c_m (Λ/c_m = 350 kJ K−1/1.2 kJ kg^{-1} K^{-1} = 292°C). Delaney (1987 [DIRS 102776]) finds that setting $T^*_m = T_m + \Lambda/c_m$ provides for adequate solutions for temperatures in host rocks at a distance of more than a quarter of a dike thickness away from the contact. Results for this consideration, documented in output DTN: LA0307EG831811.001, Table 3, are shown in Figure D-2, for which T_c is 736°C.

In Figure D-6, the upper plot shows temperatures at specific times as a function of distance from the drift, whereas the lower plot shows temperatures at specific locations as a function of time. The discontinuity at approximately 120 days in the curve at 8 m from the drift (yellow) is a result of combining calculation methods.

The main problem with this approximate approach for including the effect of latent heat is that temperature profiles within and near the magma-filled drift are not realistic and are too high. A more physically accurate method to account for latent heat is discussed by Turcotte and Schubert (1982 [DIRS 139651], pp. 168 to 170]). They follow the classical Stefan problem in which the cooling of a body of magma has a definite solidification temperature $T_s = T_m$. Considering a one-dimensional case (slab-like geometry) with magma intruded at $x < 0$, the solidification surface occurs at X_s:

$$X_s = -2\lambda\sqrt{\kappa t} \qquad \text{(Eq. D-18)}$$

for which λ is a constant to be determined. With this approach, one needs a solution that fits the conditions that $\theta = 1$ ($T = T_m = T_s$), where $x = X_s$. The solution implies that the temperature at any point, defined by η (from Equation D-12), is proportional to the position of the solidification surface defined by λ:

$$\theta = \frac{\operatorname{erfc}(\eta)}{\operatorname{erfc}(-\lambda)} \qquad \text{(Eq. D-19)}$$

For $x \le X_s$, $T = T_m$, and for $X_s < x < 0$, $T_m > T > T_t$. This solution is valid only for times at which latent heat is being released in the magma (i.e., the temperature at the hottest part of the magma, the center of the drift, is above the magma's solidus temperature).

Because $T_s = T_m$, solidification occurs immediately during cooling from T_m, releasing latent heat at a rate $\rho\Lambda(dx_m/dt)\delta_t$. Equating this rate with the rate of heat conduction by Fourier's law gives:

$$\rho\Lambda\left(\frac{dX_s}{dt}\right) = k\left(\frac{\partial T}{\partial x}\right)_{X=X_s} \qquad \text{(Eq. D-20)}$$

The derivative on the left-hand side of Equation D-20 can be found by differentiating Equation D-18:

$$\frac{dX_s}{dt} = \frac{-\lambda\sqrt{\kappa}}{\sqrt{t}}. \qquad \text{(Eq. D-21)}$$

The derivative on the right-hand side of Equation D-20 can be found by differentiating Equation D-18:

$$\left(\frac{\partial T}{\partial x}\right)_{x=X_s} = \left(\frac{d\theta}{d\eta}\right)_{\eta=-\lambda}\left(\frac{\partial \eta}{\partial x}\right)(T_m - T_0) = \frac{-(T_m - T_0)}{2\sqrt{\kappa t}}\frac{2}{\sqrt{\pi}}\frac{e^{-\lambda^2}}{[1+erf(\lambda)]} \qquad \text{(Eq. D-22)}$$

A transcendental equation of λ is derived by substituting Equations D-21 and D-22 into Equation D-20 and recalling that $k = \rho c \kappa$:

$$\frac{\Lambda\sqrt{\pi}}{c(T_m - T_0)} = \frac{e^{-\lambda^2}}{\lambda[1+erf(\lambda)]} \qquad \text{(Eq. D-23)}$$

With Equations D-19 and D-23, temperatures in time and space can be calculated for one-dimensional problems that involve release of latent heat. Furthermore, Equation D-18 can be used to calculate the time for all the magma to solidify (i.e., when the solidification surface reaches the center of the slab and $X_s^2 = a^2$, where a is the slab half-thickness). The solidification time is a function of one-quarter of the area a^2:

$$t_s = \frac{a^2}{4\kappa\lambda^2} \qquad \text{(Eq. D-24)}$$

Considering cylindrical geometry, the area expressed by the term a^2 in Equation D-24 becomes $\pi a^2/4$. Replacing the Cartesian position of the solidification surface by its cylindrical equivalent, R_s, Equation D-18 becomes:

$$R_s = -4\lambda\sqrt{\kappa t/\pi} \qquad \text{(Eq. D-25)}$$

and the transcendental equation for λ is:

$$\frac{2\Lambda}{c(T_m - T_0)} = \frac{e^{-\lambda^2}}{\lambda[1+erf(\lambda)]} \qquad \text{(Eq. D-26)}$$

For given values of Λ, c, T_m, and T_0, λ can be found by iteratively calculating the right-hand side of Equation D-26 until it equals the left-hand side. For a system for which r is 0 at the contact between magma and host rock and increases towards the center of the magma body, the following solutions depend upon the value of R_s, which is a function of λ:

$$T = T_m \quad (r \geq R_s) \qquad \text{(Eq. D-27)}$$

$$T = T_c\left(1 + erf\,\frac{r}{2\sqrt{\kappa t}}\right)\left(erf\,\frac{\omega}{2\sqrt{\kappa t}}\right) \quad (R_s > r) \qquad \text{(Eq. D-28)}$$

where:

$$T_c = T_0 + \frac{(T_s - T_0)}{1 + erf\,(\lambda)} \qquad \text{(Eq. D-29)}$$

As Carslaw and Jaeger (1959 [DIRS 100968]) point out, there is no exact solution for a cylinder beyond its radius. Equation D-28 takes into account the cylindrical geometry in the same fashion as Equation D-16. As such, this solution is approximate, but comparisons of its calculated results shown in Figure D-3 (output DTN: LA0307EG831811.001) with those shown in Figure D-2, show remarkable similarity, as will be shown later. The solutions are valid for early times when liquid magma (above its solidus) exists: T_c = 664°C and λ = 0.84. The full solidification time occurs when the solidification surface, R_s, reaches the center of the drift ($R_s(\lambda, \kappa, t)$ = 2.75 m, t_s = 49 days). This time is shorter than the approximately 81 days that would be predicted for a one-dimensional slab, using Equation D-28, which is not unexpected because of the smaller cooling surface involved with cylindrical geometry. It is interesting that calculated drift-center magma temperatures at this point in time are at 900°C, which is the assumed solidus temperature to be considered in the following discussions.

Because magma solidifies over a range of temperatures ($T_s < T_m$) and displays a small but finite contrast in thermal properties with tuff, one can follow the more complicated analysis of Carslaw and Jaeger (1959 [DIRS 100968]). For conditions for which the conductivity of liquid and solid magma are equal ($k_m = k_s$), the transcendental equation in λ from Carslaw and Jaeger (1959 [DIRS 100968]) can be modified for cylindrical geometry and property contrasts (Carslaw and Jaeger 1959 [DIRS 100968], Section 2.16 and Section 11.2[42]):

$$p\frac{\sqrt{\pi}(T_m - T_s)}{4T_s} = \frac{[1 - erf\,(p\lambda)]\exp[(p^2 - 1)\lambda^2]}{\zeta + erf\,(\lambda)} \qquad \text{(Eq. D-30)}$$

Equation D-30 accounts for the effects of latent heat by the variable p, which is the square-root of the ratio of diffusivities (κ) of the solid (subscript s) and liquid (subscript m). The magma diffusivity reflects the effect of a higher effective heat capacity from the addition of latent heat:

$$p = \left[\frac{\kappa_s}{k_m / \rho_m[c_m + \Lambda/(T_m - T_s)]}\right]^{1/2} \qquad \text{(Eq. D-31)}$$

The effect of property contrasts between the magma and tuff in Equation D-30 are accounted for by the variable ζ,

$$\zeta = \frac{k_m\sqrt{\kappa_r}}{k_r\sqrt{\kappa_m}} \qquad \text{(Eq. D-32)}$$

The solution temperatures are like those in Equations D-27 to D-29 and depend upon the temporal radial position of the cooling surface R_s.

$$T_c = T_0 + \frac{\zeta (T_s - T_0)}{[\zeta + erf\,(\lambda)]} \quad \text{(Eq. D-33)}$$

$$T = T_m \quad (r \geq R_s) \quad \text{(Eq. D-34)}$$

$$T = T_c \left(1 + \frac{1}{\zeta} erf\left(\frac{r}{2\sqrt{\kappa_m t}}\right)\right) \bullet \left(erf\left(\frac{\omega}{2\sqrt{\kappa t}}\right)\right) \quad (0 < r < R_s) \quad \text{(Eq. D-35)}$$

$$T = T_c \left(1 + erf\left(\frac{r}{2\sqrt{\kappa_t t}}\right)\right) \bullet \left(erf\left(\frac{\omega}{2\sqrt{\kappa t}}\right)\right) \quad (r < 0) \quad \text{(Eq. D-36)}$$

Again, the effect of cylindrical divergence is accounted for, as in Equation D-28. Equations D-30 to D-36 take into account latent heat being released between T_m and T_s (solidus temperature) as well as property contrasts between the magma (subscript *m*) and tuff (subscript *t*).

Assuming a solidus temperature of 900°C, the effect of $T_s < T_m$ (without property contrasts) results in a lower predicted contact temperature, T_c = 563°C, as well as a lower value of λ (0.64). If the effect of property contrasts is also calculated, then T_c rises to 600°C and λ falls to a value of 0.60. In both cases, a 50°C change in solidus temperature results in an approximately 16°C change in T_c.

Compared to the calculation for latent heat in which $T_s = T_m$, the effect of $T_s < T_m$ increases the length of time for complete solidification from 49 days to 85 days (without property contrasts) to 98 days (with property contrasts). Figure D-4 shows results from output DTN: LA0307EG831811.001, Table 5, for the cases in which ζ = 1 (no property contrast) and ζ = 1.19.

D5. WHOLE-TIME SOLUTIONS

Because the analytical results for latency are only valid at early times, a plot of whole-time solutions requires a combination of results. The whole-time calculations for approximated latency (Figure D-6 and output DTN: LA0307EG831811.001, Table 3) are valid for all times, with the caveat that they are inaccurate for temperatures in or near the magma while it is still molten. On the other hand, the early-time results shown in Figure D-4 (output DTN: LA0307EG831811.001, Table 5b) are believed to be analytically more accurate. Figure D-6 shows a comparison of results for 60 and 99 days for these whole-time and early-time solutions. The comparison demonstrates that temperatures are within approximately 10°C for the two methods at the time when solidification is complete (99 days).

Accordingly, results, as documented in output DTN: LA0307EG831811.001, Table 5b, through 99 days of calculated time, are combined with those of output DTN: LA0307EG831811.001, Table 3 (120 days to 500 years) in the upper panel of Figure D-6. The lower panel of Figure D-6 shows the evolution of temperature at specific points in space as a function of time.

D6. CONCLUSIONS

Analytical solutions for heat flow within and around a drift filled with magma and that use cylindrical symmetry, the effects of latent heat, and property contrasts can only be approximate and, thus, must be viewed as analysis results only (Figure D-6).

Several variations of analytical solutions show slight variations in predicted thermal profiles at different cooling times for a drift filled with magma. The approximate effects of thermal property contrasts between the magma and tuff host rock are shown to be small. In contrast, latent heat of crystallization, which cannot be exactly accounted for by analytical means, does have an effect. Latent heat prolongs the cooling times within the magma, increasing by one-third the time required for temperatures on the axis to drop below 325°C, and causes early-time temperatures within the magma and tuff near the contact to be approximately 100°C hotter.

The values for the thermal properties of the magma and tuff may vary from those of newer measurements, which might differ by up to 10%. Calculations based on varying these properties by 10% (with the exception of the initial magma temperature) shows that each property varied accounts for only approximately 3% of the change in calculated temperatures.

With respect to the thermal effects on neighbor drifts (approximately 81 m distant), a slight thermal pulse (approximately 1°C) might be felt after 60 years of cooling. After 500 years of cooling, the magma-filled drift and surrounding tuff has cooled to within 0.5°C of the initial temperature (30°C).

APPENDIX E
INFLUENCE OF MAGMA PRESSURE ON STABILITY OF WASTE PACKAGE

APPENDIX E
INFLUENCE OF MAGMA PRESSURE ON STABILITY OF WASTE PACKAGE

E1. INTRODUCTION

This appendix presents results of a static analysis of the waste package under high pressures and temperatures caused by magma intrusion into the emplacement drifts. The problem was analyzed for three levels of magma-induced external pressure. Internal pressure in the waste package and material properties varied as a function of pre-set temperature. Two levels of temperature were considered. Thermal calculations were not performed; instead, it was assumed that all components of the waste package are at the same temperature as the surrounding magma.

E2. MODELING

The waste package was analyzed using the finite difference code FLAC, Version 4.0 (STN: 10167-4.0-00 [DIRS 161953]), which is qualified for the calculations described in this appendix. For analytical purposes, the waste package is assumed to be axisymmetric and to have symmetry with respect to the plane perpendicular to the axis of axisymmetry at the mid-height of the container, as shown in Figure E-1a. Results are presented for the "bottom end" geometry only, which has thinner components and, consequently, would fail at lower pressures.

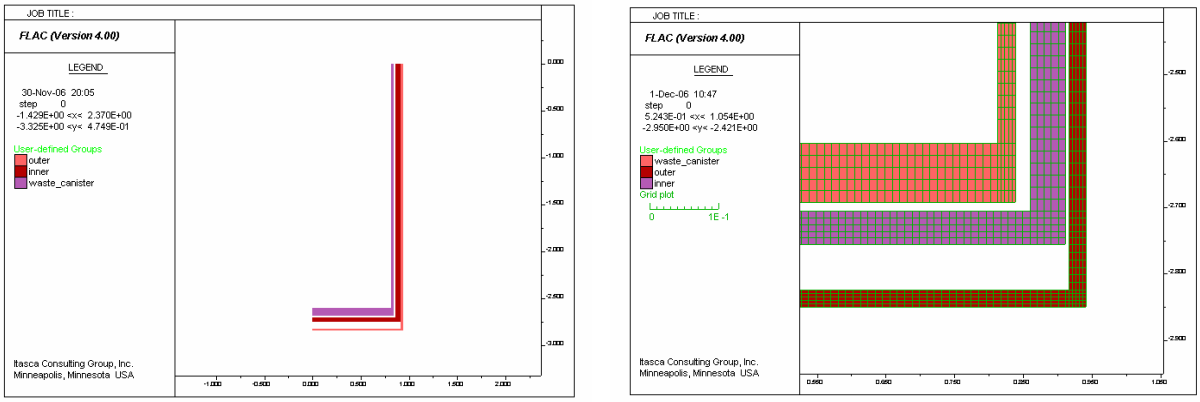

(a) ***(b)***

Source: For illustration purposes only.

Figure E-1. Model Geometry

The analyzed geometry includes the site-specific canister (SSC) located inside the Naval Long waste package. The outer corrosion barrier (OCB) of the Naval Long waste package is made of Alloy 22. The information for the Naval Long waste package was taken from sheets 1 through 3 of *Naval Long Waste Package for License Application* (BSC 2006 [DIRS 178838], [DIRS 176681], [DIRS 178839]). The information about SSC is taken from *Normal Load Bearing by Site Specific Canister* (BSC 2005 [DIRS 173447]). The inner vessel and the shell of SSC are of Stainless Steel Type 316. The mechanical properties (stiffness and strength) of the waste package components were calculated for two temperature levels corresponding to temperatures of surrounding magma (Table E-1). The mechanical properties were calculated

based on testing at elevated temperatures, and a linear extrapolation between the maximum testing temperature and the melting temperature (1,357°C for Alloy 22 (Haynes International, Inc. [DIRS 100896], sheet "data," p. 15) and 1,375°C for Stainless Steel Type 316 (Allegheny Ludlum 1999 [DIRS 151409]). Both the stiffness and strength of Alloy 22 and Stainless Steel Type 316 were assumed to be zero at melting temperature.

No limit was set in the calculation on deformation or stress of the materials that would represent its rupture. Instead, potential rupture was assessed at the end of calculation based on calculated maximum stresses and rupture strengths at elevated temperatures as provided in Table E-1 in *Waste Package Behavior in Magma* (BSC 2005 [DIRS 173492]), and Figure 2 *Waste Package Damage Due to Interaction with Magma* in (BSC 2005 [DIRS 173802]). The columns for rupture strength after 100 and 1,000 hours of creep deformation in Table E-1 are engineering stress values. The "Ultimate Strength" and "Plastic Strain" columns in Table E-1 list true stress and true strain values calculated from maximum engineering stresses and strains (e_{max} = 0.57, s_{max} = 524 MPa at 760°C for Alloy 22 (Haynes International 1997 [DIRS 100896], sheet: "data." p. 15) and e_{max} = 0.42, s_{max} = 124 MPa at 871°C for Stainless Steel Type 316 (Allegheny Ludlum 1999 [DIRS 151409]), using $\sigma=s(1+e)$ for true stress, σ, and $\varepsilon=\ln(1+e)$ for true strain, ε, where the engineering stress is s and the engineering strain is e (Dieter 1976 [DIRS 118647]). Using engineering stress to assess the potential of rupture after 100 and 1,000 hours of creep does not have significant effect because stresses in the waste package components well exceed the strengths.

Table E-1. Material Properties

T Temperature [C]	E Young's Modulus [GPa]	σ_y Yield Strength [MPa]	σ_u Ultimate Strength [MPa]	σ_u 100 hour [MPa]	σ_u 1000 hour [MPa]	ε_p Plastic Strain	K Bulk Modulus [GPa]	G Shear Modulus [GPa]
Alloy 22								
900	152[a]	184[c]	629[e]	50[f]	33[f]	0.45[c]	114[g]	59[£]
1100	99[a]	104[c]	353[e]	8[f]	3[f]	0.45[c]	75[g]	39[£]
Stainless Steel-316								
900	123[b]	102[d]	166[d]	30[f]	15[f]	0.352[d]	102[g]	47[£]
1100	106[b]	59[d]	96[d]	5.5[f]	2[f]	0.352[d]	88[g]	41[£]

Sources:
[a] BSC 2005 [DIRS 173802]: Table 4 and Figure II-4.
[b] BSC 2005 [DIRS 173802]: Table 3 and Figure II-3.
[c] Calculated based on engineering stress, s, and engineering strain, e, given in Hastelloy C-22 Alloy, (Haynes International 1997 [DIRS 100896]), using the relations $\sigma = s(1+e)$ and $\varepsilon = \ln(1+e)$.
[d] From "Technical Data Blue Sheet, Stainless Steels, Chromium-Nickel-Molybdenum Types 316 (S31600), 316L (S31603), 317 (S31700), 317L (S31703)" (Allegheny Ludlum 1999 [DIRS 151409]). Ultimate strength and plastic strain are calculated based on engineering stress, s, and engineering strain, e, given in the reference, using the relations $\sigma = s(1+e)$ and $\varepsilon = \ln(1+e)$.
[e] Calculated based on engineering stress, s, and engineering strain, e, given in *Waste Package Behavior in Magma* (BSC 2005 [DIRS 173492]), using the relation $\sigma = s(1+e)$.
[f] BSC 2005 [DIRS 173802], Figure 2.
[g] Calculated from the values for Young's modulus, E, and Poisson's ratio, ν, taken from BSC 2005 [DIRS 173802], Table 5: $K = \frac{E}{3(1-2\nu)}$ and $G = \frac{E}{2(1+\nu)}$.

The thickness of the OCB wall and lid is 25.4 mm. The inner vessel has a uniform wall thickness of 50.8 mm throughout. The SSC has a wall thickness of 25.4 mm, with an 88.9-mm-thick bottom lid. The inner vessel rests on a 68.3-mm-high support element, which is not modeled; instead, there is a gap between the bottom lids of the OCB and the inner vessel, as shown in Figure E-1b. In the radial direction, there is a 5-mm gap between the walls of the OCB and the inner vessel, and a 15.24-mm gap between the SSC and the inner vessel. The inner radius of the inner vessel is 859.8 mm (diameter = 1,719.6 mm).

Gravity loading is neglected. External magma pressure is applied to the outer boundary of the model. Analyses are repeated for three levels of external pressure: 12 MPa, generated by 60% crystallization (Section 6.4.8.1.3.1), 8 MPa (approximately equal to the pressure head of a 300-m column of magma of density 2600 kg m^{-3}), and 4 MPa (slightly less than the maximum magma pressure for an effusive dike as it passes the repository (Section 6.3.3.4.1)). Pressure inside the waste container is set to 1.75 MPa for a temperature of 900°C and to 2.04 MPa for a temperature of 1,100°C (BSC 2005 [DIRS 173492], page 10). Pressure between the vessels is neglected. Stresses in the model are due to applied mechanical loading only. A Tresca material model with bi-linear strain-hardening was used for all materials with properties as listed in Table E-1; calculations were performed in large-strain mode.

E3. RESULTS

The results of the simulation for a temperature of 900°C and a pressure of 12 MPa are shown in Figure E-2. The apparent gap between the vessels in Figure E-2 occurs because the contours do not extend to the outer surface of the bodies, only to the center of the last row of elements. The stresses are calculated for the center of the element, and the contouring algorithm does not attempt any extrapolation. Negative stresses are compressive. The maximum tensile stress of 233 MPa occurs in the lid of the OCB, on the inner surface at the axis of axisymmetry (where maximum displacement is measured) and close to the corner at which the plate is attached to the cylinder wall, as shown in Figure E-2d. The maximum stress levels in the stainless steel components are as follows: 113 MPa in the inner vessel, and 123 MPa in the SSC shell.

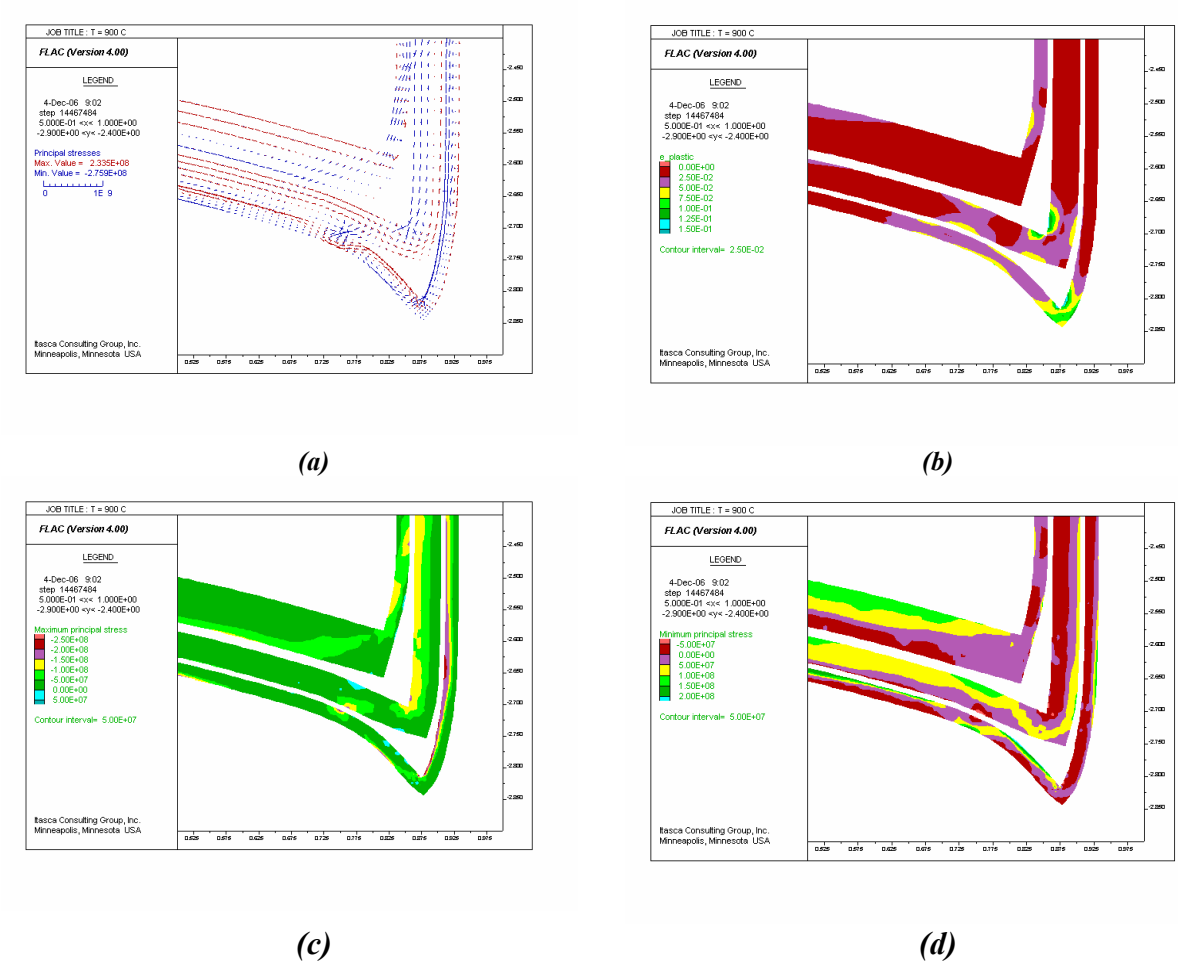

Output DTN: MO0705WPNMAGMA.000, folder 900_12MPa.

Figure E-2. (a) Principal Stress Tensor, [Pa]; (b) Plastic Strain; (c) Maximum Stress, [Pa]; (d) Minimum Stress, [Pa]—All for a Temperature of 900°C

Stress levels in both the Alloy 22 and Stainless Steel Type 316 containers are above the yield limits but below the instantaneous ultimate tensile-strength limits listed in Table E-1. The ultimate tensile strength of Stainless Steel Type 316 of 166 MPa is not exceeded, but the ultimate tensile strength of Stainless Steel Type 316 after 100 hours of exposure to a temperature of 900°C, accounting for the creep deformation, drops to 30 MPa—and that level is exceeded. For Alloy 22 after 100 hours of exposure to a temperature of 900°C, the tensile strength drops to 50 MPa, well below computed maximum tensile stress of 233 MPa. Plastic strain levels are depicted in Figure E-2b. The maximum plastic strain in the OCB reaches the value of 0.15 at the connection between the wall and the lid; for the inner stainless steel containers, the maximum plastic strain is 0.125. Principal stress tensors are depicted in Figure E-2a.

Principal stresses, maximum and minimum stress contours, and plastic strain contours due to external loading of 12 MPa at a temperature of 1,100°C are depicted in Figure E-3. For temperatures of 1,100°C, the maximum tensile stress in the OCB, made of Alloy 22, reaches 162 MPa. The ultimate instantaneous tensile strength for Alloy 22 at 1,100°C is estimated to be 353 MPa, but for 100 hours exposure at 1,100°C, the ultimate tensile strength of Alloy 22 drops to 8 MPa, and tensile stress exceeds this level.

The maximum tensile stress in the stainless steel vessels reaches the level of 67 MPa. This stress is not greater than the estimated instantaneous ultimate tensile strength of 96 MPa, but it is much greater than the ultimate tensile limit (5.5 MPa) after 100 hours of exposure to 1,100°C. A maximum plastic strain of 0.6 is reached in the outer fiber of the SSC (Stainless Steel Type 316) lid. Plastic strain reaches a maximum value of 0.225 in the inner corner of the OCB.

Similar trends are observed in results for 4 MPa and 8 MPa levels of magma-induced pressure. For an external loading of 4 MPa and temperatures of 1,100°C and 900°C, maximum stresses of 136 MPa and 213 MPa in the Alloy 22 components, and 65 MPa and 107 MPa in the stainless steel components, respectively, are above the yield values but below the true instantaneous ultimate stress values. However, for longer exposure to pressures and temperature, the strengths levels are exceeded. For the higher magnitude of external loading of 8 MPa, the maximum stresses in the Alloy 22 components for temperatures of 1,100°C and 900°C are 138 MPa and 227 MPa, and 65 MPa and 110 MPa in the stainless steel components, respectively. Again, the levels are lower than instantaneous tensile-strength levels, but much greater than the rupture strength values for cases of longer exposure to the analyzed conditions. The calculated global maximum stress levels are summarized and compared with high-temperature strengths in Table E-2.

It is concluded that cracks would be produced that would be wide enough to permit magma to flow into the interior of the waste package. The internal gases, at pressures of 0.5 MPa to 2 MPa (BSC 2005 [173492], Section 5.3), would be replaced or absorbed by the magma outside the canister that is at higher pressure.

Table E-2. Calculated Stresses and Strengths for Waste Package Components.

Temp. (°C)	Press. (MPa)	Alloy 22					SS316				
		Stress (MPa)	Yield Stress (MPa)	Ultim. Stress (MPa)	100-hr Stress (MPa)	1,000-hr Stress (MPa)	Stress (MPa)	Yield Stress (MPa)	Ultim. Stress (MPa)	100-hr Stress (MPa)	1,000-hr Stress (MPa)
900	4	213	184	629	50	33	107	102	166	30	15
	8	227					110				
	12	233					123				
1,100	4	136	104	353	8	3	65	59	96	5.5	2
	8	138					65				
	12	162					67				

Output DTN: MO0705WPNMAGMA.000, file *stresses.xls*.

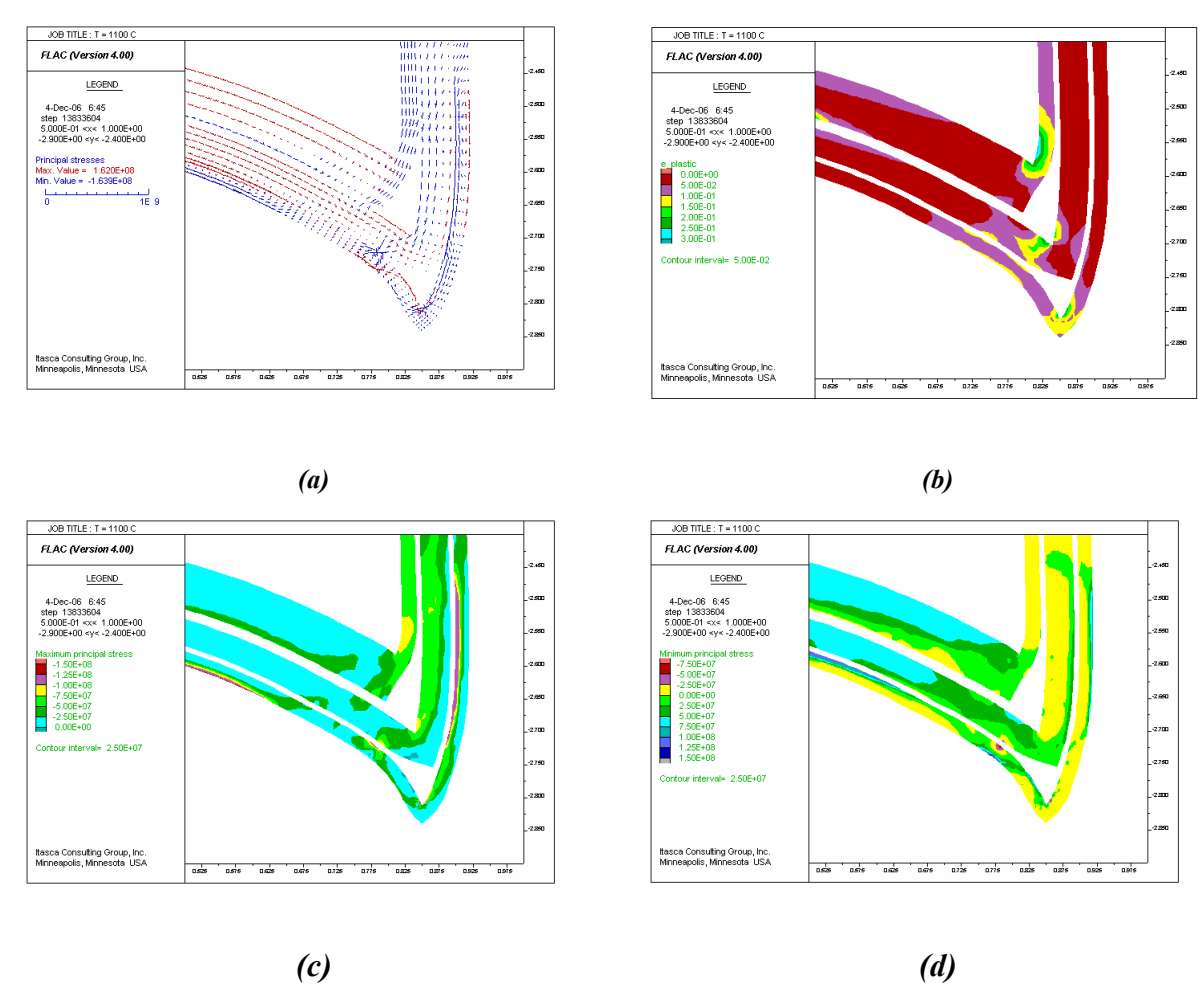

Output DTN: MO0705WPNMAGMA.000, folder 1100_12MPa.

Figure E-3. (a) Principal Stress Tensor, [Pa]; (b) Plastic Strain; (c) Maximum Stress, [Pa]; (d) Minimum Stress, [Pa]—All for a Temperature of 1,100°C

E4. CONCLUSIONS

Analyses of the waste package at 900°C and 1,100°C exposed to three different levels of external pressures and two levels of internal pressure show a barely stable instantaneous response, as tensile stresses in the stainless steel components reach values still below, but almost at, the tensile strength levels. Any prolonged exposure to pressure and temperatures of this magnitude severely reduces the strength of both materials and both fail. As a result, magma could flow into the interior voids of the waste packages.

APPENDIX F
INDEPENDENT TECHNICAL REVIEW OF DIKE PROPAGATION SUBMODEL

APPENDIX F
INDEPENDENT TECHNICAL REVIEW OF DIKE PROPAGATION SUBMODEL

This appendix includes the letter, with review criteria, requesting independent technical review of the dike propagation submodel, and the response to it by Dr. Allan Rubin. The attached letter contains an error in the designation of the version of the document that Dr. Rubin reviewed. The correct version was REV 00 ICN 01 Draft B.

BECHTEL SAIC COMPANY, LLC

JUL 02 2004

QA:N/A

RECEIVED BY BSC CCU
DATE: 07/02/2004

Allen Rubin, Professor
Department of Geosciences
Princeton University
Princeton, NJ 08544

RE: Independent Review for Model Validation of the Dike Propagation Model

Dear Dr. Rubin:

You are requested to perform a technical review of the dike propagation model as a part of the validation process to enhance confidence in the model. Model validation, as stated in the model validation procedure (AP-SIII.10Q), is the process used to establish confidence that the mathematical model (if applicable) and its technical bases adequately represent the conceptual model, system processes, and/or the phenomenon being investigated.

The models developed to represent the various aspects of repository performance or consequences of potential disruptive events are required as part of the OCRWM Quality Assurance program to have post model development validation to ensure they are applicable for their intended use. In general these models will be an integral part of demonstrating system performance and compliance with the regulatory requirements set forth by the Nuclear Regulatory Commission for licensing a repository at Yucca Mountain. Model validation can be done in a number of ways. The Administrative Procedure on models (AP-SIII.10Q) identifies a number of methods for validating models that range from simple documentation to peer review. For the dike propagation model, the *Technical Work Plan -- Igneous Activity Analysis for Disruptive Events* (TWP-WIS-MD-0000071), Rev 05 (draft) identifies the post development method to achieve the desired level of model validation (Level II):

1. "Technical review, planned in the applicable TWP, by reviewers independent of the development, checking, and interdisciplinary review of the model documentation (the Originator, Responsible Manager/Lead, Checker, QER, and interdisciplinary reviewers assigned to the model document/activity may not serve as an independent post-development model validation technical reviewer) (Section 5.4.1(c)(5))."

The TWP states that the conceptual model, developed specifically for the Yucca Mountain Project, will be validated under SIII.10Q to develop confidence in its intended use. The draft model report (*Dike Drift Interactions*, Rev 02) describes the conceptual and mathematical model for dike propagation. You are requested to perform an independent review on the application of this model to modeling the dike propagation processes for the Yucca Mountain Project. The intended use of the model is to describe the propagation of a dike through rhyolitic tuff in the vicinity of Yucca Mountain assuming an igneous event occurs.

Bechtel SAIC Company, LLC • 1180 Town Center Drive • Las Vegas, Nevada 89144

JUL 02 2004

Log# 0701042226
Page 2

The criteria for your independent review are as follows:

1. Is the conceptual model reasonable and appropriate for its intended use
2. Are the mathematical relationships appropriate and representative of the scientific understanding of fracture/dike propagation
3. Are the outputs of the model reasonable and representative
4. Are limitations of the model adequately described
5. Are there other alternative models or approaches that should be considered.

Your response (memo or letter report) should explicitly address these criteria.

The relevant parts of the *Dike Drift Interactions* Rev. 02 model report will be sent to you separately. Please initiate your review upon receipt of that material. Your response is expected to be available no later than July 8, 2004, so that we may incorporate your comments and the originator's response into the model report prior to its scheduled Project review.

Your independent technical review is an important component to the validation process for developing confidence in the use of the ash redistribution conceptual model. Your Comments (letter reports or memos) from this review will become a part of the validation process consistent with SIII.10Q.

Should you have any questions, please direct your comments me (mike_cline@ymp.gov or 702 295-4899) or Ed Gaffney (edgaffney@earthlink.net, or 712 527-4527).

Your support is greatly appreciated

Sincerely,

K. Michael Cline, Team Lead
Igneous Regulatory Integration Team

July 2, 2004
Date Signed

MC:glm - 0701042226

cc. Edward Gaffney, Las Vegas
William Hackett, Las Vegas

Bechtel SAIC Company, LLC • 1180 Town Center Drive • Las Vegas, Nevada 89144

Technical Review of "Dike/Drift Interactions", MDL-MGR-GS-000005 REV 00B ICN 01

Allan Rubin

July 9, 2004

Some general comments:

The draft was well-written and easy to read. Thank you.

I found the boundaries between some of the five "criteria for independent review" to be somewhat subjective. I have chosen a particular breakdown in this review, but mostly I aimed for completeness without worrying too much about which comments fell under which category.

1. *Is the conceptual model reasonable and appropriate for its intended use?* Section 6.1 states: "The development of a comprehensive list of features, events, and processes, potentially relevant to postclosure performance of the potential Yucca Mountain repository is an ongoing, iterative process based on site-specific information, design, and regulations". To "site-specific information, design, and regulations" I would add something to the effect of "the collective imagination of the people thinking about such processes". At least for Igneous Events, for example, it is not feasible to generate an all-encompassing model based on first principles that would produce all classes of possible outcomes if it were run with a wide enough range of initial conditions. Therefore the mode of operation is to imagine the event first and only then then to design software, with suitable approximations, to investigate it. Because the approximations are usually very specific to the event under consideration, it is unlikely that a new "potential event" will first attract attention as a result of model calculations. They must be imagined first. This means that a conceptual model that appears to be "comprehensive" must be understood as "comprehensive" in the limited sense of pertaining to all those processes that have been imagined thus far.

With the above caveat, I find the conceptual model here to be reasonable and appropriate for its intended use. By "conceptual model" I mean the combination of the particular model of dike propagation discussed at length in this document, and the idea that dike/drift interaction can be understood by first modeling dike propagation in the absence of a repository and then using the output of those models as input into a first generation of dike/drift

interacton models. One other caveat: By necessity many simplifications are made in the specific dike propagation calculation, some of them possibly rather severe (neglect of magma compressibility, magma freezing, inelastic deformation of the host rock, etc.). This is required to make the models tractable numerically and because our understanding of some of these processes is quite limited. Nonetheless, enough approximations are made that I think one could legitimately ask what the point of the calculations is. The proper response, I think, is that the goal is not the faithful numerical reproduction of dike propagation in the pre-repository environment, but to understand in a general sense what would happen if a dike intersected the repository. But the dike/drift interaction models that will be used to develop this understanding were not discussed in this document. So I find myself reviewing a model of dike propagation whose main purpose is to be used as input into a model that I cannot evaluate. In a strict sense that makes it difficult to evaluate the assumptions made in the dike propagation model. I have to imagine how the output will be used.

Details:

TSPA-LA FEP 1.2.04.03 in Table 6-1 would be more complete if it included the possibility of intrusion along a bedding plane that cuts the drifts. From analog examples this strikes me as more likely than a horizontal sill in the plane of the drifts.

In describing the dike propagation model it is stated (Table 6-1): "The output of this model provides the support for a conceptual dike propagation model that precludes development of a conduit extending from the original point of intersection to encompass the entire length of the drift (forming a "dog-leg"),...". I did not see this claim ("dog-leg is precluded") justified anywhere in the document.

2. *Are the mathematical relationships appropriate and representative of the scientific understanding of fracture/dike propagation?* I have chosen to put my evaluation of the main model assumptions here. In general I would answer "yes" to this question. Many of the comments below provide an alternate or in my view more accurate justification for the adopted assumptions, without calling into question the suitableness of that assumption. One exception might be the neglect of inelastic deformation as it pertains to the dike tip reaching the surface before the magma reaches the repository (again, whether this is important depends upon the dike/drift interaction model, which I have not seen).

The numbers below correspond to those used in: 6.3.2 Assumptions and Simplifications.

1) It is true that from the standpoint of the fluid flow the 2-D elasticity/1-D flow model becomes more appropriate as the along-strike length of the dike decreases. But from the standpoint of elasticity this model becomes *less* appropriate as the strike length decreases, because the plane of the model cross-section is vertical. From the standpoint of elasticity the 2-D elasticity/1-D flow model should be appropriate provided the along-strike length is greater than the length scale l^* defined in this document. This is discussed briefly in Appendix 4.1 of the Final Report of the Igneous Consequences Peer Review Panel (ICPRPFR).

Also, I know of no field observations supporting the claim that the limited lateral extent of dikes in this environment is "probably due to cumulative inelastic effects as the dike intersects more joints, faults, and other discontinuities and inhomogeneities" (see also the last paragraph of section 6.3). If the magma is everywhere "effectively" buoyant ($\rho_m g < dS_h/dz$), the lateral extent can be much less than the vertical extent because the pressure gradient for vertical flow exceeds that for lateral flow (provided the lateral extent is at least as large as l^*). But this explanation is not feasible if you think the least horizontal stress S_h is controlled by the frictional strength of normal faults down to depths of 10 or more kilometers, where volatile exsolution is unlikely to reduce the magma density significantly.

2) Adding magma compressibility would change the pressure profiles in the dikes noticeably, but if the ultimate goal is a qualitative statement along the lines of "the maximum magma pressure is at most 1 MPa larger [I might say 'a few MPa larger'] than the horizontal far-field stress at the given depth" (Section 6-3, p. 30), then neglecting compressibility is probably justifiable. Compressibility might be most important in how it contributes to the statement that the pressure in the tip cavity is near atmospheric (Section 60-3, p. 33), a claim that is repeated here from the ICPRPFR.

3) (see also Section 6 p. 2 PP 2, and 5.1 p. 5-10. Assumption 3): "Linear-elastic behavior would be a conservative assumption because anelastic behavior would serve to increase dike widths and reduce pressures at the repository". I think this statement is untrue, or at least an oversimplification. The actual outcome very likely depends upon the assumed boundary conditions, but take the case of a constant flux from a deep source and accept the notion that anelasticity at the repository level acts to increase the dike thickness locally. If the dike source is deep enough, the excess pressure is tied to the local confining pressure over most of the dike height and changes in thickness at shallow depth don't affect the flux significantly. Under these conditions, widening at shallow depth leads to lower flow velocities and smaller pressure drops. Because the magma pressure is tied to the host rock stress at greater depth, a smaller viscous pressure drop leads to larger pressures at the repository. Of course, I base this scenario only on my intuition, and the story is more complicated because of the coupling between elasticity and fluid flow (l^* would likely decrease somewhat, for example). But I'm guessing that the net effect would still be a pressure increase.

If it were deemed important, this question could be explored numerically (in an approximate way) by adding some arbitrary inelastic thickness to the computed elastic dike thickness over some depth interval. This approach (or a reduced confining pressure over some interval) might also be used to mimic the expected increase in host rock elastic modulus with depth. In the end this may not be an important enough question to warrant the effort. I understand the motivation for making the claim quoted above – Given that so many simplifications are required to make the problem tractable, it is nice to be able to label some of them as "conservative" and move on. But I don't think it has been established that neglecting anelasticity is conservative, and for this reason it is probably safest to just say that the pressure differences it would induce are likely to be small compared to the expected uncertainty in dike parameters. I put it in the same category as neglect of magma compressibility, turbulent flow, or magma freezing – Until you build models that

include these parameters it is difficult to quantify their effects, but perhaps we have gained enough intuition using the simpler model to state with some confidence that their effects would be small compared to natural variability from dike to dike. Therefore a better justification might be that for assumption 5 ("this is the only possible assumption for analyzing the behavior of a deep-source dike.")

(Even the statement "anelastic behavior would serve to increase dike widths ... at the repository" is questionable. The most likely form of large-scale inelastic deformation in this environment, at least more than 200 m below the repository or in the post-thermal period, is induced normal faulting because the existing normal faults are near a state of failure. If a normal fault cut by the dike had more slip on the updip than downdip extension of the fault, which seems reasonable, this would widen the dike below the intersection but narrow the dike above.)

There is one aspect of this model where neglecting inelastic deformation may be both significant and not conservative. It is stated in Section 6, p, 6-1 that "If the dike does reach the surface prior to the drifts being filled the probability of a dog-leg through the repository will be greatly reduced". Figure 3-2 of the ICPRPFR, with no free surface, shows that when the dike tip is just about to run to the surface the cavity is a very small fraction of the dike thickness (much less than 10%). A zero-pressure crack centimeters or less in thickness and hundreds of meters high would seem to be very susceptible to closure by normal faulting along in the Basin and Range environment. Normal faults intersecting the dike cavity can sometimes be seen to prevent eruption where dikes cut cinder cones. Thus, inelastic deformation makes it more difficult for the dike tip to breach the surface (deformation is diffuse, rather than being concentrated along a single plane), which in turn decreases the chance that the dike would breach the surface before the drifts fill with magma.

4) See the above comment concerning the "conservative" nature of neglecting inelastic deformation. If you really want to make this claim, support it with a few model calculations where (as an approximation) the dike thickness is artificially altered. Otherwise just state that it is neglected to make the problem tractable.

6) "The dike is a single fracture." Combine this with the statement in 6.2.3, p 6-9: "Stress changes from the drift excavation are of limited spatial extent and decay quickly as a function of distance from the drift wall... They will have insignificant effect on dike propagation." Perhaps this is true on a large scale, but on a small scale the stresses could deflect the dike near a dike-drift intersection, and cause an otherwise planar dike to intersect a drift as two en-echelon segments separated by perhaps a drift diameter (or more?), depending upon the drift orientation relative to the principal stresses. Probably this would reduce the magma flux into the drift, as the flux is so sensitive to thickness and the thickness of each overlapping tip should be less than that of the unaffected dike, so ignoring it is likely conservative. On the other hand, this might increase mechanical erosion near the dike/drift intersection and increase the likelihood that a conduit to the surface ultimately forms from that point, as opposed to elsewhere along the dike (in a 1981 USGS Professional Paper [1202] Delaney and Pollard suggested that conduits sometimes localize where dike segments

overlap). Without a dike/drift interaction model it is hard to comment on the significance of these scenarios.

8) I am not much bothered by the neglect of turbulence, but I would feel more comfortable if there were a (justifiable) qualitative description of how it would affect the solution. If this were a constant-thickness slot with a pressurized source at depth, turbulence would just uniformly slow the flow for the available pressure gradient. But the dike narrows toward the tip, and in the steady solution the average cross-sectional flow velocity is everywhere the same, so the Reynolds number decreases linearly with decreasing thickness near the tip. Probably flow would be laminar to thicknesses of several tens of centimeters, even if it were turbulent (smaller velocity for the available pressure gradient) at greater depth. How the resulting solution would compare qualitatively to the purely laminar case I don't know. Any guesses?

11) "This approach is a conservative assumption because the additional load of the mountain could serve to deflect any dike away from the mountain. However, analysis of in situ stresses in Section 6.2.2 demonstrates that topography has negligible effect on the dike path". I find the second statement here, in conjunction with figure 6-22, quite convincing. But I would throw out the first. Muller, Ito and Martel (JGR, June 2001) showed that linear loads on the surface of a half-space act to *attract* dikes by adding a quasi-radial greatest compressive stress to the existing stress distribution. Unless you have information from your simulations that contradicts this, I would throw out the conservative assumption claim.

Other:

Section 6-3, p. 2: I find it odd to justify the neglect of leak-off into the surrounding medium but never mention the neglect of magma freezing, which could have a greater influence on propagation than many of the items listed in 6.3.2. I would put it in the same category as the laminar flow or homogeneous linear elasticity assumptions. Some references to dike models that include freezing can be found on p. 46 of the ICPRPFR.

6-3, p. 4: I get ascent velocities of about 10^{-3} m/s for 1-mm bubbles (for a viscosity of 10 Pa s), which (unless I've made an error) seems small enough compared to the 1-10 m/s flow velocity that I'm surprised by the statement that they effectively separate.

Section 6.3.7.3 Effect of Thermally Induced Increased Horizontal Stress. There are several aspects of this model that I think I do not understand. The main goal seems to be the computation of the dike path and ascent velocity in the face of an increased horizontal stress, using a model that allows for non-planar propagation on a pre-defined, somewhat random network of existing cracks. I presume the fluid flow equations are being solved rigorously, as in the planar dike model described earlier. Is the discretization for those equations just more coarse (that is, on the scale of the distinct elements)? Why do the dike thickness and pressure profiles appear to be asymmetric in Figures 8 and 9? Is this just an artifact of the plotting? And what is meant by "saturation of the dike" on p. 6-14?

I guess my biggest question has to do with the ability of the code to accurately predict propagation paths in the face of variable principal stress orientations. On p. 6-21 it is stated "because of the change in stress due to the presence of the dike itself, the tip will not necessarily deviate even if the in-situ principal stresses rotate. The deviation will depend on the strength of the stress difference." But in a homogeneous elastic body the tip *will* rotate even in the face of arbitrarily small changes in the ambient principal stress orientations. I interpret the quoted statement as really meaning that, given the limited range of pre-defined orientations available to the dike tip, for small enough variability in stress the dike might propagate more-or-less straight ahead. It is true that in a homogeneous continuum the path of a propagating crack can develop a large radius of curvature if the magnitude of the resolved shear stress on the crack is small. So if it would take the dike more than 200 m to rotate I suppose it is reasonable to state that it propagates mostly straight ahead. But how has the distinct element model with a limited network of existing cracks been validated as a means of predicting crack propagation paths? The fourth conclusion on p. 6-25, that the dike "is not expected to turn and create a sill if rock mass properties are homogeneous and isotropic", strikes me as difficult to justify on the basis of what has been presented (is "homogeneous and isotropic" here intended to imply a 'random" grid of the form of Figure 3, or a continuum?). I think a useful calculation would be to put in a representation of the *expected* anisotropy, for example the existing subhorizontal bedding and any known joint set orientations. Then, if a sill does not form along the existing bedding in the presence of large thermal stresses, perhaps a meaningful conclusion can be drawn.

The conclusion that a near-vertical dike with an increased confining pressure of 13 MPa has a maximum excess pressure at the repository depth of only 6 MPa (that is, well below the confining pressure; p. 6-26) is significant. This means that the dike walls are held open at this depth by the excess pressure at greater depth or shallower depth. It would be nice to reproduce this result with the numerical planar dike code described previously, just to make sure that it is not an artifact of the limited vertical extent of the model. It also reinforces the point made in the paragraph below that the uniformly increased load may not be the most instructive case to consider.

Section 6.3.9.4 Effect of Expanding magma on Dike Extension to the Surface. I think I understand what is going on here, although more from the figure caption than the text. Of course, the more relevant point is not how much sooner the tip breaches the surface in the low-density case, but where the magma front is when the tip breaches the surface, and I'm not sure what generalizations can be made concerning this from Figure 6.3.9.4-1. The philosophy underlying this approximate approach to compressibility is hard for me to evaluate. It is clear that the pressure-time history at the repository depth would be identical to a particular case of an incompressible magma, because that is how it is computed. It is just that given some range of likely source parameters (density and flux at depth), matching the fluxes when the density goes down will shift the region of parameter space thought of as "likely". If this shift is small compared to the size of the likely parameter space, it is not terribly significant. If it is large, then the limitations of the approximation need to be considered, and this is difficult to evaluate. For example, q^{∞} is proportional to $w^{\infty}\delta'^{1/3}$, while l^{*} is proportional to $(w^{\infty}/\delta')^{1/2}$. This means that maintaining a constant flux in the manner

adopted here implies a "hidden" change in l^*, which is not accounted for when jumping from one solution to the next.

3. *Are the outputs of the model reasonable and representative?* Yes, with a few qualifications given below. I think it may be a useful result (for the dike/drift interaction model) that the pressure-time history at the repository depth can be well-approximated by "convecting" a single prior snapshot of the time-dependent calculation past the repository depth (section 6.3.7.1, p. 30). It is useful to investigate different tip cavity pressures (6.3.7.2). It is also useful to investigate the effect of an increased horizontal stress (6.3.7.3), designed to address intersection during a time of high thermal loading. But why is this load applied uniformly over the full model height? This is not necessarily a "bounding" case, as is claimed. For a uniform pressure increase, the only effect is to produce in a shorter cavity at a given depth (the source pressure just goes up in lock-step with the remote load, as does the magma pressure everywhere "far" from the cavity). But for a locally increased confining pressure, the thickness is reduced locally while the source flux remains largely unaffected (see the earlier discussion regarding the effect of inelastic deformation or elastic modulus variation). I can see that it might be more difficult to handle the localized stress increase numerically, but this is the numerical experiment that is relevant. If it can't be done for numerical reasons then this should be stated.

If I take the broadest view, the statement "the maximum magma pressure is at most 1 MPa larger than the horizontal far-field stress at the given depth" (Section 6-3, p. 30), seems to be the sort of "bottom-line" result that that one would hope to get out of simulations like this (or that statement plus a qualitative description of the variation of pressure as a function of depth below the dike tip, that might be translated into an approximate pressure-vs-time history at the repository depth). How representative is this result? The dimensional estimate of the maximum excess pressure is $\delta' \equiv (\kappa\rho_r - \rho_f)g$ times the length scale $l^* \equiv (w_* E'/\delta')^{1/2}$, or $(w_* E'\delta')^{1/2}$. For $w_* = 1$ m, $E' = 15$ GPa, and $\delta' = 10^3$ Pa/m, this yields an estimated maximum excess pressure of ~ 3 MPa. My recollection is that this dimensional estimate overestimates the actual excess pressure in a "base case" calculation by a factor of ~ 3 (ICPRPFR, Fig. 3-5). So a refined estimate is very close to the number of 1 MPa cited in this document as a maximum. On the other hand, in Figure 6M-11 a pressure of 1 MPa is reached for a dike thickness of 0.16 m. If a thick dike was assumed, say 4 m (as I believe is representative of some of the thicker dikes in the region), this would increase the maximum excess pressure by a factor of 5 (that is, $(4/0.16)^{1/2}$). This is what prompted my earlier comment that "a few MPa" may be a more robust maximum value than "1 MPa". On the other hand, an excess pressure this large will give rise to a much taller tip cavity at the same depth of the magma front.

In a practical sense, the question of the validity of the neglect of magma freezing, turbulence, inelastic deformation, etc, can be reduced to the two questions of (1) Do these additional processes introduce any qualitatively new behavior?, and (2) Do they alter the estimate of the maximum excess pressure from $\sim 0.3(w_* E'\delta')^{1/2}$ by an amount that begins to approach the variation expected from natural variations in w_*, E', and δ'? To this second question might be added a question (2a), Do these processes significantly change the

pressure-vs-depth profile (press-vs-time at the repository)? I am mostly comfortable with the neglect of these additional processes because I think the answer to questions (2) and (2a) is "no". To the extent that I have remaining doubts it is because of the difficulty in answering question (1) with certainty (e.g., does inelastic deformation greatly reduce the tip cavity length; might freezing cause the magma front to halt a short distance above the repository, etc.).

A detail:

Fig 6M-16, p 34: I am surprised that the dike tip does not appear to have gone unstable (no equilibrium position) before reaching the surface for (for example) V=1m/s. Numerical simulations and an analytic solution in Appendix 3.2 of the ICPRPFR suggest that it would do so. Admittedly this is for no free surface, which might change things. But with a constant cavity pressure, I find it hard to believe that the free surface could stabilize the tip when the cavity pressure exceeds the confining pressure, which it does in this case at 40 m depth. The analytic (no free surface) approximate solution would have it going unstable at closer to 120 m depth, for a magma front at 200 m depth as in Fig. 6M-16.

6.4.8 Summary (Should this be 6.3.8?): If 1 m/s is the "expected" velocity, perhaps this should be achieved with a larger viscosity, because 0.12-0.25 m sounds small for eroded dikes in this region. On the other hand, I am not sure of the basis upon which this is "expected". 1 m/s is a good upper-bound velocity for dikes in Iceland and Hawaii, but the viscosities there are probably 100 Pa s or somewhat larger, and if 10 Pa s is a good number, then perhaps 10 m/s should be the "expectation".

Less of a detail, perhaps, but not necessarily important:

On p. 19 of Section 6.3, it appears that a κ of 0.5, which may be appropriate throughout the brittle crust, requires very low magma densities of 751 kg/m^3. This in turn requires unreasonably large bubble fractions at depths below a few km. I bring this up because it is related to the problem of the limited lateral extent of these dikes mentioned in assumption (1) of 6.3.2. If the magma is to be locally buoyant and if the magma density is constrained by reasonable bubble fractions, κ can be significantly less than 1 only in the upper few kilometers of the crust. I am not concerned here with the possibility that a depth-variable κ is being modeled as constant; I am pointing out that there is a significant gap in our understanding of how these dikes make it up through most of the upper crust (until gas exsolution makes the magma buoyant even for a low κ). If they do it by being bounded laterally by faults, as was suggested in this document, then δ' must change sign over most of the upper crust. The flux from below can continue to drive the dike tip upward in this case, but the elastic stresses should be far different from that computed in these models, even perhaps at the depth of the repository (the dike thickness in the middle crust might be ten times that computed here). On the other hand, if κ is increased to near 1 over most of the upper crust by earlier dikes that froze, then seeing one cone at the surface implies many more non-eruptive dikes at depth, with perhaps significant implications for the probability of a future igneous event.

Model validation, Section 7.3:

I think the comparison to Lister's more analytic solution demonstrates that the code NPHF2D is perfectly adequate for its advertised task. The deviation from the Lister solution probably has more to do with the presence of the free surface than any numerical approximations made (although one should check the depth of the tip against l^* to bolster this claim). The comparison with Paricutin is an important qualitative test, although admittedly the quantitative constraints are few. Perhaps most important is just the validation of the concept that a "tip cavity" can breach the surface long before magma gets there. One question related to my earlier comment on the possibility that inelastic deformation could "short-circuit" this cavity: What is known of the stress state near Paricutin? Are there active normal faults, as at Yucca Mountain, that would allow one to infer that the least horizontal stress is quite low? Or might the least horizontal stress be much closer to the vertical stress? (As a possible erratum, I have no doubt that the numerical model can adequately reproduce the stress intensity factor and thickness for a uniformly pressurized crack, as it has passed more stringent tests. But Section 7.3.1.1.2 doesn't say this, and it looks like the wrong paragraph might have been inserted here.)

4. *Are limitations of the model adequately described?* Yes. Any concerns I might have about this have already been stated in response to question (2).

5. *Are there alternative models or approaches that should be considered?* Not really, except insofar as the more analytic ones provide some "reasonableness" checks on the calculations presented here. This is adequately discussed in the document. Some of the published dike propagation models that include freezing might be looked at, just to develop an intuition for how they might change the flow. And, as I stated earlier, it might be instructive to run some additional models where the dike thickness or confining pressure is varied only over a limited depth interval.

Errata:

5.3 Assumption 21: 88 MPa should be 8 MPa?

Section 6.2.2, p. 6-6: Figure 10, 11 should be 6-21, 6-22?

Section 6-3, p. 23, check the end of the first sentence, 2nd paragraph.

Section 6-3, p. 30, line 4: "remains invariant" should be changed to "is approximated as remaining invariant", I think.

Section 6-3, p. 30: $D = 20.28$ (Figure 6M-11) should be (Figure 6M-13).

APPENDIX G
HEAT TRANSFER CALCULATION FILE LISTING

APPENDIX G
HEAT TRANSFER CALCULATION FILE LISTING

References to this appendix (Appendix G) in the body of the report are in regard to spreadsheets in support of this model report and associated output DTN.

The following files were used in calculating the heat flow model of Appendix C. They are provided by output DTN: MO0408EG831811.008.

```
Directory of D:\heat.zip
04/07/2004  10:58a      <DIR>          Heat
               0 File(s)              0 bytes


Directory of D:\heat.zip\Heat

04/07/2004  01:45p          43,247,104 1200 Heat Conduction - Dry TPTPUL.xls
04/07/2004  01:24p          43,214,848 50 at 1200 Heat Conduction - Dry
TPTPUL.xls
12/15/2003  03:18p          38,245,376 Heat Conduction - Dry TPTPLL.xls
12/15/2003  03:21p          38,246,400 Heat Conduction - Dry TPTPLN.xls


12/15/2003  03:29p          38,246,400 Heat Conduction - Dry TPTPMN.xls
04/04/2004  02:03p          38,246,400 Heat Conduction - Dry TPTPUL.xls
12/15/2003  03:20p          38,245,888 Heat Conduction - Dry TPTPLL  300C.xls
12/15/2003  03:20p          38,245,888 Heat Conduction - Dry TPTPLL  50C.xls
12/15/2003  03:30p          38,246,400 Heat Conduction - Wet TPTPLN.xls
12/15/2003  03:30p          38,245,376 Heat Conduction - Wet TPTPLL.xls
12/15/2003  03:31p          38,246,400 Heat Conduction - Wet TPTPUL.xls
12/15/2003  03:30p          38,246,400 Heat Conduction - Wet TPTPMN.xls
03/29/2004  02:00p          43,208,192 Heat Conduction - Uncertainty
Analysis.xls
12/15/2003  03:19p          38,245,888 Heat Conduction - Dry TPTPLL  100C.xls
12/15/2003  03:19p          38,245,888 Heat Conduction - Dry TPTPLL  150C.xls
12/15/2003  03:20p          38,245,888 Heat Conduction - Dry TPTPLL  200C.xls
              16 File(s)    626,868,736 bytes
```

INTENTIONALLY LEFT BLANK

APPENDIX H
RESULTS FOR EFFUSIVE FLOW IN SECONDARY DIKES

APPENDIX H
RESULTS FOR EFFUSIVE FLOW IN SECONDARY DIKES

This appendix describes the locations of results of all of the simulations of magma injection into preexisting joints inside the emplacement drifts as described in Section 6.5.1.2 of this report.

All simulated cases of magma injection into preexisting joints inside the emplacement drifts are summarized in Table H-1. The case numbers in Table 6-35 have had 100 added to them relative to the case numbers in the output DTN: MO0411EG831811.002; the case numbers from the DTN are listed in Table H-1. The order in which the cases are listed in Table H-1 does not indicate a relation between different cases, only the sequence in which they were simulated.

Table H-1. Summary of Analyzed Cases of Magma Injection Into Joints Using Case Numbers from DTN: MO0411EG831811.002

Case	Crack Orientation with Respect to Drift*	Initial Crack Aperture (mm)	Magma Pressure in Drift (MPa)	Initial Stress			Bulk Modulus of Magma (MPa)	Young's Modulus of Rock (GPa)	Magma Viscosity (Pa-s)
				Over-burden (m)	Coeff. Along Drift	Coeff. Perp. to Drift			
1	vertical along	1	4	300		0.5	50	15	10
2	vertical along	1	8	300		0.5	50	15	10
3	vertical along	1	10	250		0.5	50	15	10
4	horizontal	1	8	300		0.5	50	15	10
5	vertical perp.	1	10	300	0.35	0.5	50	15	10
6	vertical along	1	4	300		0.5	50	5	10
7	vertical along	1	4	300		0.5	500	15	10
8	vertical perp.	1	8	300	0.35	0.5	50	15	10
9	vertical perp.	1	8	300	0.5	0.35	50	15	10
10	vertical along	1	8	250		0.5	50	15	10
11	vertical along	3	8	250		0.5	50	15	10
12	vertical along	3	8	250		0.5	50	5	10
13	vertical along	3	8	250		0.5	500	5	10
14	vertical along	3	8	250		0.5	500	15	10
15	vertical along	1	8	250		0.5	50	5	10
16	vertical along	1	8	250		0.5	50	15	100
17	vertical along	1	10	250		0.5	50	15	100
18	vertical along	3	8	250		0.5	50	15	100
19	vertical along	3	8	250		0.5	50	5	100
20	vertical along	1	8	250		0.5	50	5	100

Output DTN: MO0411EG831811.002.

NOTES: * Crack Orientation: vertical along = a vertical crack along the drift; vertical perp. = a vertical crack perpendicular to the drift.

Results for Cases 8 and 9 are in zipped folder MO0411EG831811.002_Disk7; the other cases are in zipped folder MO0411EG831811.002_Disk6. Within the "...Disk*m*" folder (where *m* is either "6" or "7" each case *n* listed in Table H-1 is contained in a zipped folder "Case *n*." File *case1aper.pcx* is the equivalent of Figure 6-154, showing the displacement vector field and hydraulic aperture along the vertical fracture (for cases listed in column 2 of Table H-1 as "vertical along") or along the horizontal fracture (for case 4). File *case1pp.pcx* is the equivalent of Figure 6-155, showing the stress tensor field around and the pore pressure along the joint for cases listed as "vertical along" or "horizontal" in Table H-1. File *case1hisaper.pcx* is the equivalent of Figure 6-156, showing histories of joint hydraulic aperture at seven locations along the joint for all cases listed in Table H-1. File *case1hispp.pcx* shows histories of joint pore pressure at seven locations along the joint, a plot not presented in Section 6, for all cases listed in Table H-1.

APPENDIX I
JUSTIFICATION OF ASSUMED THERMOMECHANICAL ROCK PROPERTIES AND PRELIMINARY DESIGN VALUES FOR EBS COMPONENTS

APPENDIX I
JUSTIFICATION OF ASSUMED THERMOMECHANICAL ROCK PROPERTIES AND PRELIMINARY DESIGN VALUES FOR EBS COMPONENTS

As described in Section 5 (see Assumption 5.1, Section 5, In Situ and Thermally Induced Stresses), the in situ stress model of Section 6.2.2 and the thermal stress model of Section 6.2.4 were developed before the completion of *Drift Degradation Analysis* (BSC 2004 [DIRS 166107]). These models used assumed values based on preliminary data available in *Drift Degradation Analysis* BSC (2004 [DIRS 166107], Appendix C) that were modified and qualified in DTN: MO0408MWDDDMIO.002 ([DIRS 171483]). As shown in Table I-1, the assumed values used for input to the models are compared with the qualified values (column "Design Value") and the impacts of the differences are assessed (column "Impact Assessment"). Table I-1 also shows the sections where the assumed values were used.

The development of the numerical representation for the alternative thermal model in Section 6.4.7.2 was completed based on preliminary design concepts for the EBS components (see Assumption 5.4, Section 5). These values are compared to the design values in Table I-1. Impact assessments are also provided in Table I-2.

Table I-1. Parameter Values Used in Numerical Simulations Compared With Design Values

Input Parameter Design	Used in Section	Assumed Value Used	Design Value	Impact Assessment
Young's Modulus of TCw-PTn Unit in Regional Thermo-mechanical Analysis (GPa)	6.2.2, 6.2.4	2.54	2.2	15% high, within geologic variability
Poisson's Ratio of TCw-PTn Unit in Regional Thermo-mechanical Analysis	6.2.2, 6.2.4	0.2	0.23	13% low, within geologic variability
Density of TCw-PTn Unit in regional Thermo-mechanical Analysis (kg m^{-3})	6.2.2, 6.2.4	1,613	1,460	10% high, within geologic variability
Thermal Conductivity of TCw-PTn Unit in Regional Thermo-mechanical Analysis (W m^{-1} K^{-1})	6.2.2, 6.2.4	T <100°C, 1.015 $T \geq$ 100°C, 0.525	1.06 0.49	4% low, within geologic variability 7% high, within geologic variability
Specific Heat of TCw-PTn Unit in Regional Thermo-mechanical Analysis (J kg^{-1} K^{-1})	6.2.2, 6.2.4	T <95°C, 1,158 95°C $\leq T <$ 114°C, 11,135 T <114°C, 1,010	1,300 9,000 1,000	11% low, within geologic variability 24% high, see Section 6.2.1 for impact 1% high, within geologic variability
Young's Modulus of TSw1 Unit in Regional Thermo-mechanical Analysis (GPa)	6.2.2, 6.2.4	15.21	17.3	12% low, within geologic variability
Poisson's Ratio of TSw1 Unit in Regional Thermo-mechanical Analysis	6.2.2, 6.2.4	0.2	0.25	20% low, within geologic variability

Table I-1. Parameter Values Used in Numerical Simulations Compared With Design Values (Continued)

Input Parameter Design	Used in Section	Assumed Value Used	Design Value	Impact Assessment
Density of TSw1 Unit in Regional Thermo-mechanical Analysis (kg m^{-3})	6.2.2, 6.2.4	1,983	1,974	0.5% high, within geologic variability
Specific Heat of TSw1 Unit in Regional Thermo-mechanical Analysis (J kg^{-1} K^{-1})	6.2.2, 6.2.4	T <95°C, 939 95°C ≤ T < 114°C 5,791 T ≥114°C, 991	920 3,200 990	3% high, within geologic variability 81% high, see Section 6.2.1 for impact within geologic variability
Density of TSw2-TSw3 Unit in Regional Thermo-mechanical Analysis (kg m^{-3})	6.2.2, 6.2.4	2,086	2,095	0.5% low, within geologic variability
Thermal Conductivity of TSw2-TSw3 Unit in Regional Thermo-mechanical Analysis (W m^{-1} K^{-1})	6.2.2, 6.2.4	T <100°C, 1.925 T ≥100°C, 1.328	1.92 1.33	0.3% high, within geologic variability within rounding error, qualified
Specific Heat of TSw2-TSw3 Unit in Regional Thermo-mechanical Analysis (J kg^{-1} K^{-1})	6.2.2, 6.2.4	T <95°C, 937 95°C ≤ T < 114°C, 5,714	910 3,000	3% high, within geologic variability 90% high, see Section 6.2.1 for impact
Young's Modulus of Units Underlying TSw3 Unit in Regional Thermo-mechanical Analysis (GPa)	6.2.2, 6.2.4	15.54	–	No design value available. Assume value to be same as Unit TSw2-TSw3 which is qualified.
Poisson's Ratio of Units Underlying TSw3 Unit in Regional Thermo-mechanical Analysis	6.2.2, 6.2.4	0.2	–	No design value available. Assume value to be same as Unit TSw2-TSw3 which is qualified.
Density of Units Underlying TSw3 Unit in Regional Thermo-mechanical Analysis (kg m^{-3})	6.2.2, 6.2.4	1,545	1,614	4% low, within geologic variability
Thermal Conductivity of Units Underlying TSw3 Unit in Regional Thermo-mechanical Analysis (W m^{-1} K^{-1})	6.2.2, 6.2.4	T <100°C, 1.201 T ≥100°C, 0.581	1.21 0.57	1% low, within geologic variability 2% high, within geologic variability
Specific Heat of Units Underlying TSw3 Unit in Regional Thermo-mechanical Analysis (J kg^{-1} K^{-1})	6.2.2, 6.2.4	T <95°C, 1,304 95°C ≤ T < 114°C, 15,775 T ≥114°C, 1,016	1,300 8,400 1,100	within rounding error, qualified value 87% high, see Section 6.2.1 for impact 8% low, within geologic variability
Coefficient of Thermal Expansion of Units Underlying TSw3 Unit in Regional Thermo-mechanical Analysis (K^{-1})	6.2.2, 6.2.4	T <50°C, 7.14×10^{-6} 50°C ≤ T < 75°C, 7.47×10^{-6} 75°C ≤ T < 100°C, 7.46×10^{-6} T ≥100°C, 9.07×10^{-6}	–	No design values available. Assume values to be same as Unit TSw2-TSw3 which is qualified.

Table I-1. Parameter Values Used in Numerical Simulations Compared With Design Values (Continued)

Input Parameter Design	Used in Section	Assumed Value Used	Design Value	Impact Assessment
Mass of Loaded TAD-Canister-Bearing Waste Package (kg)	6.4.7.2	73,573, from SNL 2007 [DIRS 179394] Table 4-1, Parameter 03-01	–	Not used as direct input
TAD WP Skirt-to-Skirt Length (m)	6.4.7.2	5.818, from SNL 2007 [DIRS 179394] Table 4-1, Parameter 03-01	–	Not used as direct input
TAD OCB Diameter (m)	6.4.7.2	1.882, from SNL 2007 [DIRS 179394] Table 4-1, Parameter 03-01	–	Not used as direct input
Homogenized Density of Loaded Waste Package (kg m^{-3})	6.4.7.2	3,470	4,546	Value used is 76% of design value. This will result in lower maximum temperature than calculated, but longer cooling times.
Waste Package Diameter (m)	6.4.7.2.1	1.72	Various	Slight variations in peak temperatures
Ventilation Efficiency	6.2.2, 6.2.4	0.9	0.86, 0.88	Slight variations in temperatures
Poisson's Ratio of TCw Unit	6.4.8.1.3.3	0.21	0.22	Value used is 5% below design value, which is within geologic variability
Young's Modulus of TCw Unit (GPa)	6.4.8.1.3.3	29.36	27.8	Value used 6% above design value, which is within geologic variability
Density of TCw Unit (Kg m^3)	6.4.8.1.3.3	2,310	2,310	Not impacted
Cohesion of TCw Unit (MPa)	6.4.8.1.3.3	3.9	2.22 to 19.81	Within geologic variability
Friction Angle of TCw Unit (degrees)	6.4.8.1.3.3	57	24 to 45	See Section 6.4.8.1.3.3 for impact
Tensile Strength of TCw Unit (MPa)	6.4.8.1.3.3	2.35	0.11 to 2.95	Within geologic variability
Waste Package Heat Capacity (J kg^{-1} K^{-1})	6.4.7.2	432	378	Slight variations in temperature

In support of the position that 10% to 20% variability in rock properties is to be expected in geologic analyses of the type presented in Sections 6.2.2 and 6.2.4, the variability of the source data from which the properties in MO0408MWDDDMIO.002 ([DIRS 171483]) are derived is reviewed. Values in BSC (2004 [DIRS 166107], Table E-1) for the density of individual stratigraphic units grouped as TSw1 and TSw2/TSw3 vary by ±12% and ±8%, respectively. Young's modulus and Poisson's ratio are even more variable. BSC (2004 [DIRS 166107], Table E-6) shows that at a single location (Busted Butte) standard deviations of measurements of these properties can range from 10% of the mean to as much as 33% of the mean. Furthermore, the means of two different groups of measurements of the same unit can differ by as much as 30%. Measurements of thermal conductivity summarized in BSC (2004 [DIRS 166107], Table E-18) for individual stratigraphic units grouped as TSw1 and TSw2/TSw3 have standard deviations of 32% and 36%, respectively, below 100°C and of 26% and 30%, respectively, above. Specific heats from BSC (2004 [DIRS 166107], Table E-19) for individual stratigraphic

units grouped as TSw1 and TSw2/TSw3 vary over a range of as much a 6% of mean values. Thermal expansivity for unit TSw1 from BSC (2004 [DIRS 166107], Table B-3) have standard deviations that are between 8% and 23% of their mean values for temperature ranges below 100°C and up to 47% above 100°C. In summary, geologic properties are highly variable, and the values given in Table I-1 are qualified for the thermo-mechanical calculations in Sections 6.2.2 and 6.2.4.

The sources of qualified design data in Table I-1 are detailed in Table I-2.

Table I-2. File Locations for Thermomechanical Data

Property	Source
Young's Modulus of TCw-PTn Unit in Regional Thermo-mechanical Analysis	DTN: MO0408MWDDDMIO.002 [DIRS 171483], file Calculation Files\Material property*rock mass strength v2.xls*, worksheet 'Summary Data'
Poisson's Ratio of TCw-PTn Unit in Regional Thermo-mechanical Analysis	DTN: MO0408MWDDDMIO.002 [DIRS 171483], file Calculation Files\Material property*rock mass strength v2.xls*, worksheet 'Intact Strength'
Density of TCw-PTn Unit in regional Thermo-mechanical Analysis	DTN: MO0408MWDDDMIO.002 [DIRS 171483], file Calculation Files\Material property*thermal properties TM units v2.xls*, worksheet 'Conductivity and Density'
Thermal Conductivity of TCw-PTn Unit in Regional Thermo-mechanical Analysis	DTN: MO0408MWDDDMIO.002 [DIRS 171483], file Calculation Files\Material property*thermal properties TM units v2.xls*, worksheet 'Conductivity and Density'
Specific Heat of TCw-PTn Unit in Regional Thermo-mechanical Analysis	DTN: MO0408MWDDDMIO.002 [DIRS 171483], file Calculation Files\Material property*thermal properties TM units v2.xls*, worksheet 'Specific Heat'
Young's Modulus of TSw1 Unit in Regional Thermo-mechanical Analysis	DTN: MO0408MWDDDMIO.002 [DIRS 171483], file Calculation Files\Material property*rock mass strength v2.xls*, worksheet 'Summary Data'
Poisson's Ratio of TSw1 Unit in Regional Thermo-mechanical Analysis	DTN: MO0408MWDDDMIO.002 [DIRS 171483], file Calculation Files\Material property*rock mass strength v2.xls*, worksheet 'Intact Strength'
Density of TSw1 Unit in Regional Thermo-mechanical Analysis	DTN: MO0408MWDDDMIO.002 [DIRS 171483], file Calculation Files\Material property*thermal properties TM units v2.xls*, worksheet 'Conductivity and Density'
Specific Heat of TSw1 Unit in Regional Thermo-mechanical Analysis	DTN: MO0408MWDDDMIO.002 [DIRS 171483], file Calculation Files\Material property*thermal properties TM units v2.xls*, worksheet 'Specific Heat'
Density of TSw2-TSw3 Unit in Regional Thermo-mechanical Analysis	DTN: MO0408MWDDDMIO.002 [DIRS 171483], file Calculation Files\Material property*thermal properties TM units v2.xls*, worksheet 'Conductivity and Density'
Thermal Conductivity of TSw2-TSw3 Unit in Regional Thermo-mechanical Analysis	DTN: MO0408MWDDDMIO.002 [DIRS 171483], file Calculation Files\Material property*thermal properties TM units v2.xls*, worksheet 'Conductivity and Density'
Specific Heat of TSw2-TSw3 Unit in Regional Thermo-mechanical Analysis	DTN: MO0408MWDDDMIO.002 [DIRS 171483], file Calculation Files\Material property*thermal properties TM units v2.xls*, worksheet 'Specific Heat'

Table I-2. File Locations for Thermomechanical Data (Continued)

Property	Source
Density of Units Underlying TSw3 Unit in Regional Thermo-mechanical Analysis	DTN: MO0408MWDDDMIO.002 [DIRS 171483], file Calculation Files\Material property*thermal properties TM units v2.xls*, worksheet 'Conductivity and Density'
Thermal Conductivity of Units Underlying TSw3 Unit in Regional Thermo-mechanical Analysis	DTN: MO0408MWDDDMIO.002 [DIRS 171483], file Calculation Files\Material property*thermal properties TM units v2.xls*, worksheet 'Conductivity and Density'
Specific Heat of Units Underlying TSw3 Unit in Regional Thermo-mechanical Analysis	DTN: MO0408MWDDDMIO.002 [DIRS 171483], file Calculation Files\Material property*thermal properties TM units v2.xls*, worksheet 'Specific Heat'
Homogenized Density of Loaded Waste Package	SNL 2007 [DIRS 179394], Table 4-1, Parameter 03-01
Waste Package Diameter	SNL 2007 [DIRS 179394], Table 4-1, Parameter 03-01
Preclosure Ventilation Efficiency	DTN: MO0307MWDAC8MV.000 [DIRS 165395], file *Analytical-LA-Coarse-800m.xls*, worksheet 'Ventilation Efficiency'
Young's Modulus of TCw Unit	DTN: MO0408MWDDDMIO.002 [DIRS 171483], file Calculation Files\Material property*rock mass strength v2.xls*, worksheet 'Summary Data'
Poisson's Ratio of TCw Unit	DTN: MO0408MWDDDMIO.002 [DIRS 171483], file Calculation Files\Material property*rock mass strength v2.xls*, worksheet 'Intact Strength'
Density, Cohesion, Friction Angle, and Tensile Strength of TCw Unit	BSC 2007 [DIRS 178693], Table 6-76
Waste Package Heat Capacity (also referred to as "Waste Package Specific Heat")	SNL 2007 [DIRS 179354], Table 4-4, Parameter 05-03

INTENTIONALLY LEFT BLANK